Journal of Sensors

Remote Sensing Technology, Regional Development, and Climate Change

Lead Guest Editor: Wei Zhang
Guest Editors: Ke-Li Xu and Xiaodong Zhang

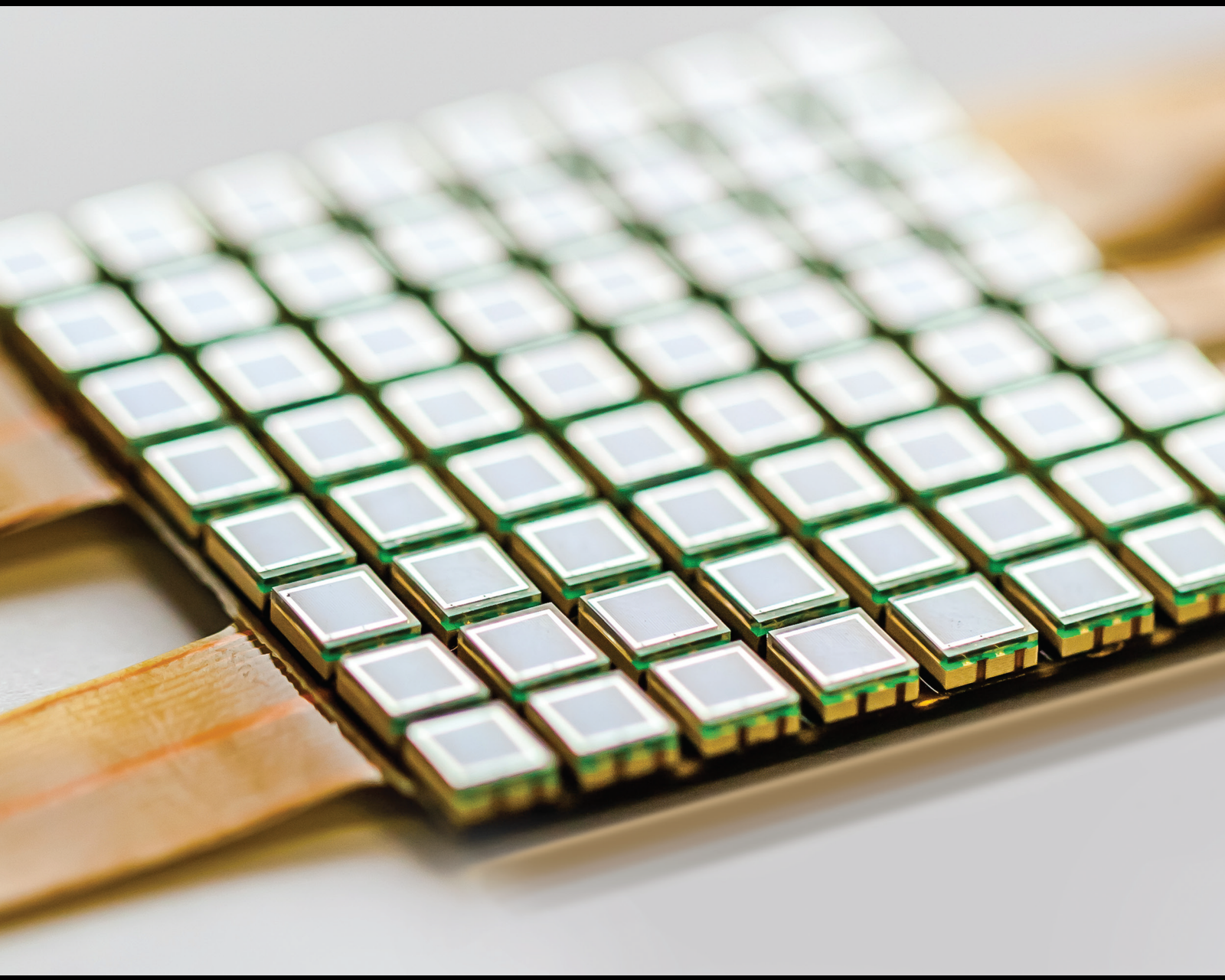

Remote Sensing Technology, Regional Development, and Climate Change

Journal of Sensors

Remote Sensing Technology, Regional Development, and Climate Change

Lead Guest Editor: Wei Zhang
Guest Editors: Ke-Li Xu and Xiaodong Zhang

Contents

Retracted: Application of Multiobjective Particle Swarm Optimization in Rural Credit System
Journal of Sensors
Retraction (1 page), Article ID 9765036, Volume 2023 (2023)

Retracted: Study on Environmental Art Design Based on Ecology Concept
Journal of Sensors
Retraction (1 page), Article ID 9804212, Volume 2023 (2023)

Retracted: Research on Intelligent Bodybuilding System Based on Machine Learning
Journal of Sensors
Retraction (1 page), Article ID 9878123, Volume 2023 (2023)

Retracted: Research on Urban Fringe Rural Design Based on Correlation Analysis of Human-Land Relationship: Taking Xiananshan Village as an Example
Journal of Sensors
Retraction (1 page), Article ID 9858401, Volume 2023 (2023)

Retracted: Mining and Evaluation of Teaching Civics Courses Based on Apriori-TIDS Algorithm
Journal of Sensors
Retraction (1 page), Article ID 9820609, Volume 2023 (2023)

[Retracted] Efficient Stochastic Galerkin Spectral Methods for Optimal Control Problems Constrained by Fractional PDEs with Uncertain Inputs
Shengzhu Shi, Dazhi Zhang, and Jiamin Li
Research Article (16 pages), Article ID 6369492, Volume 2022 (2022)

[Retracted] Research on Intelligent Bodybuilding System Based on Machine Learning
Chen Chen
Research Article (8 pages), Article ID 6293856, Volume 2022 (2022)

[Retracted] Research on Urban Fringe Rural Design Based on Correlation Analysis of Human-Land Relationship: Taking Xiananshan Village as an Example
Donghong Zhou
Research Article (11 pages), Article ID 4938311, Volume 2022 (2022)

Complex Traffic Network Analysis Method Based on a Multiscale Aggregation Model
Yingying Pei, Xia Zhu, Guohong Li, Yongtao Jin, Yuyan Liu, Yuanping Liu, Gang Liu, and Jiangxia Fan
Research Article (15 pages), Article ID 7311117, Volume 2022 (2022)

[Retracted] English-Chinese Machine Translation Model Based on Bidirectional Neural Network with Attention Mechanism
Li Yonglan and He Wenjia
Research Article (11 pages), Article ID 5199248, Volume 2022 (2022)

Contents

Hindawi
Journal of Sensors
Volume 2024, Article ID 9798467, 1 page
https://doi.org/10.1155/2024/9798467

Retraction

Retracted: Efficient Stochastic Galerkin Spectral Methods for Optimal Control Problems Constrained by Fractional PDEs with Uncertain Inputs

Journal of Sensors

Received 30 January 2024; Accepted 30 January 2024; Published 31 January 2024

This article has been retracted by Hindawi following an investigation undertaken by the publisher [1]. This investigation has uncovered evidence of one or more of the following indicators of systematic manipulation of the publication process:

(1) Discrepancies in scope
(2) Discrepancies in the description of the research reported
(3) Discrepancies between the availability of data and the research described
(4) Inappropriate citations
(5) Incoherent, meaningless and/or irrelevant content included in the article
(6) Manipulated or compromised peer review

The presence of these indicators undermines our confidence in the integrity of the article's content and we cannot, therefore, vouch for its reliability. Please note that this notice is intended solely to alert readers that the content of this article is unreliable. We have not investigated whether authors were aware of or involved in the systematic manipulation of the publication process.

Wiley and Hindawi regrets that the usual quality checks did not identify these issues before publication and have since put additional measures in place to safeguard research integrity.

We wish to credit our own Research Integrity and Research Publishing teams and anonymous and named external researchers and research integrity experts for contributing to this investigation.

The corresponding author, as the representative of all authors, has been given the opportunity to register their agreement or disagreement to this retraction. We have kept a record of any response received.

References

[1] S. Shi, D. Zhang, and J. Li, "Efficient Stochastic Galerkin Spectral Methods for Optimal Control Problems Constrained by Fractional PDEs with Uncertain Inputs," *Journal of Sensors*, vol. 2022, Article ID 6369492, 16 pages, 2022.

Hindawi
Journal of Sensors
Volume 2024, Article ID 9873845, 1 page
https://doi.org/10.1155/2024/9873845

Retraction

Retracted: English-Chinese Machine Translation Model Based on Bidirectional Neural Network with Attention Mechanism

Journal of Sensors

Received 23 January 2024; Accepted 23 January 2024; Published 24 January 2024

This article has been retracted by Hindawi following an investigation undertaken by the publisher [1]. This investigation has uncovered evidence of one or more of the following indicators of systematic manipulation of the publication process:

(1) Discrepancies in scope
(2) Discrepancies in the description of the research reported
(3) Discrepancies between the availability of data and the research described
(4) Inappropriate citations
(5) Incoherent, meaningless and/or irrelevant content included in the article
(6) Manipulated or compromised peer review

The presence of these indicators undermines our confidence in the integrity of the article's content and we cannot, therefore, vouch for its reliability. Please note that this notice is intended solely to alert readers that the content of this article is unreliable. We have not investigated whether authors were aware of or involved in the systematic manipulation of the publication process.

Wiley and Hindawi regrets that the usual quality checks did not identify these issues before publication and have since put additional measures in place to safeguard research integrity.

We wish to credit our own Research Integrity and Research Publishing teams and anonymous and named external researchers and research integrity experts for contributing to this investigation.

The corresponding author, as the representative of all authors, has been given the opportunity to register their agreement or disagreement to this retraction. We have kept a record of any response received.

References

[1] L. Yonglan and H. Wenjia, "English-Chinese Machine Translation Model Based on Bidirectional Neural Network with Attention Mechanism," *Journal of Sensors*, vol. 2022, Article ID 5199248, 11 pages, 2022.

Hindawi
Journal of Sensors
Volume 2023, Article ID 9895286, 1 page
https://doi.org/10.1155/2023/9895286

Retraction

Retracted: An Advertising Recommendation Algorithm Based on Deep Learning Fusion Model

Journal of Sensors

Received 19 December 2023; Accepted 19 December 2023; Published 20 December 2023

This article has been retracted by Hindawi following an investigation undertaken by the publisher [1]. This investigation has uncovered evidence of one or more of the following indicators of systematic manipulation of the publication process:

(1) Discrepancies in scope
(2) Discrepancies in the description of the research reported
(3) Discrepancies between the availability of data and the research described
(4) Inappropriate citations
(5) Incoherent, meaningless and/or irrelevant content included in the article
(6) Manipulated or compromised peer review

The presence of these indicators undermines our confidence in the integrity of the article's content and we cannot, therefore, vouch for its reliability. Please note that this notice is intended solely to alert readers that the content of this article is unreliable. We have not investigated whether authors were aware of or involved in the systematic manipulation of the publication process.

Wiley and Hindawi regrets that the usual quality checks did not identify these issues before publication and have since put additional measures in place to safeguard research integrity.

We wish to credit our own Research Integrity and Research Publishing teams and anonymous and named external researchers and research integrity experts for contributing to this investigation.

The corresponding author, as the representative of all authors, has been given the opportunity to register their agreement or disagreement to this retraction. We have kept a record of any response received.

References

[1] C. Li, "An Advertising Recommendation Algorithm Based on Deep Learning Fusion Model," *Journal of Sensors*, vol. 2022, Article ID 1632735, 9 pages, 2022.

Hindawi
Journal of Sensors
Volume 2023, Article ID 9836872, 1 page
https://doi.org/10.1155/2023/9836872

Retraction

Retracted: Comprehensive Decision Analysis of Industry 4.0 Virtual Enterprises considering the Personalized Customization Model of Product Life Cycle

Journal of Sensors

Received 19 December 2023; Accepted 19 December 2023; Published 20 December 2023

This article has been retracted by Hindawi following an investigation undertaken by the publisher [1]. This investigation has uncovered evidence of one or more of the following indicators of systematic manipulation of the publication process:

(1) Discrepancies in scope
(2) Discrepancies in the description of the research reported
(3) Discrepancies between the availability of data and the research described
(4) Inappropriate citations
(5) Incoherent, meaningless and/or irrelevant content included in the article
(6) Manipulated or compromised peer review

The presence of these indicators undermines our confidence in the integrity of the article's content and we cannot, therefore, vouch for its reliability. Please note that this notice is intended solely to alert readers that the content of this article is unreliable. We have not investigated whether authors were aware of or involved in the systematic manipulation of the publication process.

Wiley and Hindawi regrets that the usual quality checks did not identify these issues before publication and have since put additional measures in place to safeguard research integrity.

We wish to credit our own Research Integrity and Research Publishing teams and anonymous and named external researchers and research integrity experts for contributing to this investigation.

The corresponding author, as the representative of all authors, has been given the opportunity to register their agreement or disagreement to this retraction. We have kept a record of any response received.

References

[1] D. Ma, "Comprehensive Decision Analysis of Industry 4.0 Virtual Enterprises considering the Personalized Customization Model of Product Life Cycle," *Journal of Sensors*, vol. 2022, Article ID 1175565, 11 pages, 2022.

Hindawi
Journal of Sensors
Volume 2023, Article ID 9813624, 1 page
https://doi.org/10.1155/2023/9813624

Retraction

Retracted: English Education Translation System Based on 5G Network Virtualization

Journal of Sensors

Received 19 December 2023; Accepted 19 December 2023; Published 20 December 2023

This article has been retracted by Hindawi following an investigation undertaken by the publisher [1]. This investigation has uncovered evidence of one or more of the following indicators of systematic manipulation of the publication process:

(1) Discrepancies in scope
(2) Discrepancies in the description of the research reported
(3) Discrepancies between the availability of data and the research described
(4) Inappropriate citations
(5) Incoherent, meaningless and/or irrelevant content included in the article
(6) Manipulated or compromised peer review

The presence of these indicators undermines our confidence in the integrity of the article's content and we cannot, therefore, vouch for its reliability. Please note that this notice is intended solely to alert readers that the content of this article is unreliable. We have not investigated whether authors were aware of or involved in the systematic manipulation of the publication process.

Wiley and Hindawi regrets that the usual quality checks did not identify these issues before publication and have since put additional measures in place to safeguard research integrity.

We wish to credit our own Research Integrity and Research Publishing teams and anonymous and named external researchers and research integrity experts for contributing to this investigation.

The corresponding author, as the representative of all authors, has been given the opportunity to register their agreement or disagreement to this retraction. We have kept a record of any response received.

References

[1] M. Hou, "English Education Translation System Based on 5G Network Virtualization," *Journal of Sensors*, vol. 2022, Article ID 8763849, 12 pages, 2022.

Hindawi
Journal of Sensors
Volume 2023, Article ID 9812126, 1 page
https://doi.org/10.1155/2023/9812126

Retraction

Retracted: A Systematic Pipelaying Control Method Based on the Sliding Matrix for Dynamically Positioned Surface Vessels

Journal of Sensors

Received 19 December 2023; Accepted 19 December 2023; Published 20 December 2023

This article has been retracted by Hindawi following an investigation undertaken by the publisher [1]. This investigation has uncovered evidence of one or more of the following indicators of systematic manipulation of the publication process:

(1) Discrepancies in scope
(2) Discrepancies in the description of the research reported
(3) Discrepancies between the availability of data and the research described
(4) Inappropriate citations
(5) Incoherent, meaningless and/or irrelevant content included in the article
(6) Manipulated or compromised peer review

The presence of these indicators undermines our confidence in the integrity of the article's content and we cannot, therefore, vouch for its reliability. Please note that this notice is intended solely to alert readers that the content of this article is unreliable. We have not investigated whether authors were aware of or involved in the systematic manipulation of the publication process.

Wiley and Hindawi regrets that the usual quality checks did not identify these issues before publication and have since put additional measures in place to safeguard research integrity.

We wish to credit our own Research Integrity and Research Publishing teams and anonymous and named external researchers and research integrity experts for contributing to this investigation.

The corresponding author, as the representative of all authors, has been given the opportunity to register their agreement or disagreement to this retraction. We have kept a record of any response received.

References

[1] X. Li, Z. Jin, and L. Wang, "A Systematic Pipelaying Control Method Based on the Sliding Matrix for Dynamically Positioned Surface Vessels," *Journal of Sensors*, vol. 2022, Article ID 9702532, 16 pages, 2022.

Hindawi
Journal of Sensors
Volume 2023, Article ID 9810962, 1 page
https://doi.org/10.1155/2023/9810962

Retraction

Retracted: Research on the Architecture of Digital Song and Dance Costume Design System Based on Intelligent Deep Learning Algorithm

Journal of Sensors

Received 19 December 2023; Accepted 19 December 2023; Published 20 December 2023

This article has been retracted by Hindawi following an investigation undertaken by the publisher [1]. This investigation has uncovered evidence of one or more of the following indicators of systematic manipulation of the publication process:

(1) Discrepancies in scope
(2) Discrepancies in the description of the research reported
(3) Discrepancies between the availability of data and the research described
(4) Inappropriate citations
(5) Incoherent, meaningless and/or irrelevant content included in the article
(6) Manipulated or compromised peer review

The presence of these indicators undermines our confidence in the integrity of the article's content and we cannot, therefore, vouch for its reliability. Please note that this notice is intended solely to alert readers that the content of this article is unreliable. We have not investigated whether authors were aware of or involved in the systematic manipulation of the publication process.

Wiley and Hindawi regrets that the usual quality checks did not identify these issues before publication and have since put additional measures in place to safeguard research integrity.

We wish to credit our own Research Integrity and Research Publishing teams and anonymous and named external researchers and research integrity experts for contributing to this investigation.

The corresponding author, as the representative of all authors, has been given the opportunity to register their agreement or disagreement to this retraction. We have kept a record of any response received.

References

[1] W. Wang, "Research on the Architecture of Digital Song and Dance Costume Design System Based on Intelligent Deep Learning Algorithm," *Journal of Sensors*, vol. 2022, Article ID 1545334, 10 pages, 2022.

Hindawi
Journal of Sensors
Volume 2023, Article ID 9806065, 1 page
https://doi.org/10.1155/2023/9806065

Retraction

Retracted: Research on the Immersive Classroom Teaching Mode of Colleges and Universities Based on Virtual Reality

Journal of Sensors

Received 19 December 2023; Accepted 19 December 2023; Published 20 December 2023

This article has been retracted by Hindawi following an investigation undertaken by the publisher [1]. This investigation has uncovered evidence of one or more of the following indicators of systematic manipulation of the publication process:

(1) Discrepancies in scope
(2) Discrepancies in the description of the research reported
(3) Discrepancies between the availability of data and the research described
(4) Inappropriate citations
(5) Incoherent, meaningless and/or irrelevant content included in the article
(6) Manipulated or compromised peer review

The presence of these indicators undermines our confidence in the integrity of the article's content and we cannot, therefore, vouch for its reliability. Please note that this notice is intended solely to alert readers that the content of this article is unreliable. We have not investigated whether authors were aware of or involved in the systematic manipulation of the publication process.

Wiley and Hindawi regrets that the usual quality checks did not identify these issues before publication and have since put additional measures in place to safeguard research integrity.

We wish to credit our own Research Integrity and Research Publishing teams and anonymous and named external researchers and research integrity experts for contributing to this investigation.

The corresponding author, as the representative of all authors, has been given the opportunity to register their agreement or disagreement to this retraction. We have kept a record of any response received.

References

[1] C. Hu and J. Li, "Research on the Immersive Classroom Teaching Mode of Colleges and Universities Based on Virtual Reality," *Journal of Sensors*, vol. 2022, Article ID 3585149, 10 pages, 2022.

Hindawi
Journal of Sensors
Volume 2023, Article ID 9804026, 1 page
https://doi.org/10.1155/2023/9804026

Retraction

Retracted: Optimization of Agricultural Machinery Task Scheduling Algorithm Based on Multiobjective Optimization

Journal of Sensors

Received 19 December 2023; Accepted 19 December 2023; Published 20 December 2023

This article has been retracted by Hindawi following an investigation undertaken by the publisher [1]. This investigation has uncovered evidence of one or more of the following indicators of systematic manipulation of the publication process:

(1) Discrepancies in scope
(2) Discrepancies in the description of the research reported
(3) Discrepancies between the availability of data and the research described
(4) Inappropriate citations
(5) Incoherent, meaningless and/or irrelevant content included in the article
(6) Manipulated or compromised peer review

The presence of these indicators undermines our confidence in the integrity of the article's content and we cannot, therefore, vouch for its reliability. Please note that this notice is intended solely to alert readers that the content of this article is unreliable. We have not investigated whether authors were aware of or involved in the systematic manipulation of the publication process.

Wiley and Hindawi regrets that the usual quality checks did not identify these issues before publication and have since put additional measures in place to safeguard research integrity.

We wish to credit our own Research Integrity and Research Publishing teams and anonymous and named external researchers and research integrity experts for contributing to this investigation.

The corresponding author, as the representative of all authors, has been given the opportunity to register their agreement or disagreement to this retraction. We have kept a record of any response received.

References

[1] L. Zheng, "Optimization of Agricultural Machinery Task Scheduling Algorithm Based on Multiobjective Optimization," *Journal of Sensors*, vol. 2022, Article ID 5800332, 12 pages, 2022.

Hindawi
Journal of Sensors
Volume 2023, Article ID 9798106, 1 page
https://doi.org/10.1155/2023/9798106

Retraction

Retracted: The Construction of a Smart Education System in Colleges and Universities Based on Cloud-Side Collaborative Computing Task Scheduling Algorithm

Journal of Sensors

Received 19 December 2023; Accepted 19 December 2023; Published 20 December 2023

This article has been retracted by Hindawi following an investigation undertaken by the publisher [1]. This investigation has uncovered evidence of one or more of the following indicators of systematic manipulation of the publication process:

(1) Discrepancies in scope
(2) Discrepancies in the description of the research reported
(3) Discrepancies between the availability of data and the research described
(4) Inappropriate citations
(5) Incoherent, meaningless and/or irrelevant content included in the article
(6) Manipulated or compromised peer review

The presence of these indicators undermines our confidence in the integrity of the article's content and we cannot, therefore, vouch for its reliability. Please note that this notice is intended solely to alert readers that the content of this article is unreliable. We have not investigated whether authors were aware of or involved in the systematic manipulation of the publication process.

Wiley and Hindawi regrets that the usual quality checks did not identify these issues before publication and have since put additional measures in place to safeguard research integrity.

We wish to credit our own Research Integrity and Research Publishing teams and anonymous and named external researchers and research integrity experts for contributing to this investigation.

The corresponding author, as the representative of all authors, has been given the opportunity to register their agreement or disagreement to this retraction. We have kept a record of any response received.

References

[1] L. Yu, "The Construction of a Smart Education System in Colleges and Universities Based on Cloud-Side Collaborative Computing Task Scheduling Algorithm," *Journal of Sensors*, vol. 2022, Article ID 8949974, 12 pages, 2022.

Hindawi
Journal of Sensors
Volume 2023, Article ID 9765036, 1 page
https://doi.org/10.1155/2023/9765036

Retraction

Retracted: Application of Multiobjective Particle Swarm Optimization in Rural Credit System

Journal of Sensors

Received 19 December 2023; Accepted 19 December 2023; Published 20 December 2023

This article has been retracted by Hindawi following an investigation undertaken by the publisher [1]. This investigation has uncovered evidence of one or more of the following indicators of systematic manipulation of the publication process:

(1) Discrepancies in scope
(2) Discrepancies in the description of the research reported
(3) Discrepancies between the availability of data and the research described
(4) Inappropriate citations
(5) Incoherent, meaningless and/or irrelevant content included in the article
(6) Manipulated or compromised peer review

The presence of these indicators undermines our confidence in the integrity of the article's content and we cannot, therefore, vouch for its reliability. Please note that this notice is intended solely to alert readers that the content of this article is unreliable. We have not investigated whether authors were aware of or involved in the systematic manipulation of the publication process.

Wiley and Hindawi regrets that the usual quality checks did not identify these issues before publication and have since put additional measures in place to safeguard research integrity.

We wish to credit our own Research Integrity and Research Publishing teams and anonymous and named external researchers and research integrity experts for contributing to this investigation.

The corresponding author, as the representative of all authors, has been given the opportunity to register their agreement or disagreement to this retraction. We have kept a record of any response received.

References

[1] W. Xue, "Application of Multiobjective Particle Swarm Optimization in Rural Credit System," *Journal of Sensors*, vol. 2021, Article ID 3468479, 9 pages, 2021.

Hindawi
Journal of Sensors
Volume 2023, Article ID 9804212, 1 page
https://doi.org/10.1155/2023/9804212

Retraction

Retracted: Study on Environmental Art Design Based on Ecology Concept

Journal of Sensors

Received 17 October 2023; Accepted 17 October 2023; Published 18 October 2023

This article has been retracted by Hindawi following an investigation undertaken by the publisher [1]. This investigation has uncovered evidence of one or more of the following indicators of systematic manipulation of the publication process:

(1) Discrepancies in scope
(2) Discrepancies in the description of the research reported
(3) Discrepancies between the availability of data and the research described
(4) Inappropriate citations
(5) Incoherent, meaningless and/or irrelevant content included in the article
(6) Peer-review manipulation

The presence of these indicators undermines our confidence in the integrity of the article's content and we cannot, therefore, vouch for its reliability. Please note that this notice is intended solely to alert readers that the content of this article is unreliable. We have not investigated whether authors were aware of or involved in the systematic manipulation of the publication process.

Wiley and Hindawi regrets that the usual quality checks did not identify these issues before publication and have since put additional measures in place to safeguard research integrity.

We wish to credit our own Research Integrity and Research Publishing teams and anonymous and named external researchers and research integrity experts for contributing to this investigation.

The corresponding author, as the representative of all authors, has been given the opportunity to register their agreement or disagreement to this retraction. We have kept a record of any response received.

References

[1] Z. Jiang and F. Wang, "Study on Environmental Art Design Based on Ecology Concept," *Journal of Sensors*, vol. 2022, Article ID 8034930, 8 pages, 2022.

Hindawi
Journal of Sensors
Volume 2023, Article ID 9878123, 1 page
https://doi.org/10.1155/2023/9878123

Retraction

Retracted: Research on Intelligent Bodybuilding System Based on Machine Learning

Journal of Sensors

Received 19 September 2023; Accepted 19 September 2023; Published 20 September 2023

This article has been retracted by Hindawi following an investigation undertaken by the publisher [1]. This investigation has uncovered evidence of one or more of the following indicators of systematic manipulation of the publication process:

(1) Discrepancies in scope
(2) Discrepancies in the description of the research reported
(3) Discrepancies between the availability of data and the research described
(4) Inappropriate citations
(5) Incoherent, meaningless and/or irrelevant content included in the article
(6) Peer-review manipulation

The presence of these indicators undermines our confidence in the integrity of the article's content and we cannot, therefore, vouch for its reliability. Please note that this notice is intended solely to alert readers that the content of this article is unreliable. We have not investigated whether authors were aware of or involved in the systematic manipulation of the publication process.

Wiley and Hindawi regrets that the usual quality checks did not identify these issues before publication and have since put additional measures in place to safeguard research integrity.

We wish to credit our own Research Integrity and Research Publishing teams and anonymous and named external researchers and research integrity experts for contributing to this investigation.

The corresponding author, as the representative of all authors, has been given the opportunity to register their agreement or disagreement to this retraction. We have kept a record of any response received.

References

[1] C. Chen, "Research on Intelligent Bodybuilding System Based on Machine Learning," *Journal of Sensors*, vol. 2022, Article ID 6293856, 8 pages, 2022.

Hindawi
Journal of Sensors
Volume 2023, Article ID 9858401, 1 page
https://doi.org/10.1155/2023/9858401

Retraction

Retracted: Research on Urban Fringe Rural Design Based on Correlation Analysis of Human-Land Relationship: Taking Xiananshan Village as an Example

Journal of Sensors

Received 19 September 2023; Accepted 19 September 2023; Published 20 September 2023

This article has been retracted by Hindawi following an investigation undertaken by the publisher [1]. This investigation has uncovered evidence of one or more of the following indicators of systematic manipulation of the publication process:

(1) Discrepancies in scope
(2) Discrepancies in the description of the research reported
(3) Discrepancies between the availability of data and the research described
(4) Inappropriate citations
(5) Incoherent, meaningless and/or irrelevant content included in the article
(6) Peer-review manipulation

The presence of these indicators undermines our confidence in the integrity of the article's content and we cannot, therefore, vouch for its reliability. Please note that this notice is intended solely to alert readers that the content of this article is unreliable. We have not investigated whether authors were aware of or involved in the systematic manipulation of the publication process.

Wiley and Hindawi regrets that the usual quality checks did not identify these issues before publication and have since put additional measures in place to safeguard research integrity.

We wish to credit our own Research Integrity and Research Publishing teams and anonymous and named external researchers and research integrity experts for contributing to this investigation.

The corresponding author, as the representative of all authors, has been given the opportunity to register their agreement or disagreement to this retraction. We have kept a record of any response received.

References

[1] D. Zhou, "Research on Urban Fringe Rural Design Based on Correlation Analysis of Human-Land Relationship: Taking Xiananshan Village as an Example," *Journal of Sensors*, vol. 2022, Article ID 4938311, 11 pages, 2022.

Hindawi
Journal of Sensors
Volume 2023, Article ID 9820609, 1 page
https://doi.org/10.1155/2023/9820609

Retraction

Retracted: Mining and Evaluation of Teaching Civics Courses Based on Apriori-TIDS Algorithm

Journal of Sensors

Received 19 September 2023; Accepted 19 September 2023; Published 20 September 2023

This article has been retracted by Hindawi following an investigation undertaken by the publisher [1]. This investigation has uncovered evidence of one or more of the following indicators of systematic manipulation of the publication process:

(1) Discrepancies in scope
(2) Discrepancies in the description of the research reported
(3) Discrepancies between the availability of data and the research described
(4) Inappropriate citations
(5) Incoherent, meaningless and/or irrelevant content included in the article
(6) Peer-review manipulation

The presence of these indicators undermines our confidence in the integrity of the article's content and we cannot, therefore, vouch for its reliability. Please note that this notice is intended solely to alert readers that the content of this article is unreliable. We have not investigated whether authors were aware of or involved in the systematic manipulation of the publication process.

Wiley and Hindawi regrets that the usual quality checks did not identify these issues before publication and have since put additional measures in place to safeguard research integrity.

We wish to credit our own Research Integrity and Research Publishing teams and anonymous and named external researchers and research integrity experts for contributing to this investigation.

The corresponding author, as the representative of all authors, has been given the opportunity to register their agreement or disagreement to this retraction. We have kept a record of any response received.

References

[1] H. Yang, "Mining and Evaluation of Teaching Civics Courses Based on Apriori-TIDS Algorithm," *Journal of Sensors*, vol. 2021, Article ID 5956429, 10 pages, 2021.

Hindawi
Journal of Sensors
Volume 2024, Article ID 9798467, 1 page
https://doi.org/10.1155/2024/9798467

Retraction

Retracted: Efficient Stochastic Galerkin Spectral Methods for Optimal Control Problems Constrained by Fractional PDEs with Uncertain Inputs

Journal of Sensors

Received 30 January 2024; Accepted 30 January 2024; Published 31 January 2024

This article has been retracted by Hindawi following an investigation undertaken by the publisher [1]. This investigation has uncovered evidence of one or more of the following indicators of systematic manipulation of the publication process:

(1) Discrepancies in scope
(2) Discrepancies in the description of the research reported
(3) Discrepancies between the availability of data and the research described
(4) Inappropriate citations
(5) Incoherent, meaningless and/or irrelevant content included in the article
(6) Manipulated or compromised peer review

The presence of these indicators undermines our confidence in the integrity of the article's content and we cannot, therefore, vouch for its reliability. Please note that this notice is intended solely to alert readers that the content of this article is unreliable. We have not investigated whether authors were aware of or involved in the systematic manipulation of the publication process.

Wiley and Hindawi regrets that the usual quality checks did not identify these issues before publication and have since put additional measures in place to safeguard research integrity.

We wish to credit our own Research Integrity and Research Publishing teams and anonymous and named external researchers and research integrity experts for contributing to this investigation.

The corresponding author, as the representative of all authors, has been given the opportunity to register their agreement or disagreement to this retraction. We have kept a record of any response received.

References

[1] S. Shi, D. Zhang, and J. Li, "Efficient Stochastic Galerkin Spectral Methods for Optimal Control Problems Constrained by Fractional PDEs with Uncertain Inputs," *Journal of Sensors*, vol. 2022, Article ID 6369492, 16 pages, 2022.

Hindawi
Journal of Sensors
Volume 2022, Article ID 6369492, 16 pages
https://doi.org/10.1155/2022/6369492

Research Article

Efficient Stochastic Galerkin Spectral Methods for Optimal Control Problems Constrained by Fractional PDEs with Uncertain Inputs

Shengzhu Shi,[1] **Dazhi Zhang**,[1] **and Jiamin Li**[2]

[1]*School of Mathematics, Harbin Institute of Technology, Harbin, 150001 Heilongjiang, China*
[2]*School of Mathematics, Jilin University, Changchun, 130012 Jilin, China*

Correspondence should be addressed to Shengzhu Shi; 15b912007@hit.edu.cn

Received 27 November 2021; Accepted 16 May 2022; Published 22 July 2022

Academic Editor: Wei Zhang

This paper is devoted to designing fast solvers and efficient preconditioners for the optimal control problems (OCPs) constrained by stochastic fractional elliptic equations. We first prove the existence and uniqueness of the stochastic optimal control solution and then derive the stochastic optimality system. For the numerical approximation, we use the stochastic Galerkin spectral methods, which apply the stochastic Galerkin method for the discretization of random variables and employ the spectral-Galerkin approach for the approximation of spatial variables. To solve the large coupled saddle-point system resulted from discretization, we adopt the most commonly used MINRES method and a more effective PPCG method in low-rank matrix iteration format. Specially, we develop the efficient preconditioners based on the matrix decomposition method and the virtual variable method. We also study the eigenvalue distribution of the corresponding preconditioned matrix. Besides, for the approximation of the discretized state equation, we use the mean-based approximation and the Ullmann approximation to handle different values of the variance of the random inputs. Finally, we present numerical experiments to demonstrate the effectiveness of our solvers and preconditioners.

1. Introduction

Optimal control theory is an important field of applied mathematics. It is usually of interest on how to determine forces or boundary conditions such that the result of engineering or physical PDE systems arrives at some desired state. Recently, investigations have demonstrated that the PDEs involving fractional order tend to provide a better description for modeling complex process in various fields, e.g., in mechanics [1], biology [2], finance [3], and image processing [4]. Because of their high accuracy and wild applications, the fractional PDEs have been a new and active research area in scientific study. We also see a growing interest on their related optimal control problems (OCPs) [5–9]. Furthermore, the considered control systems are modeled with measurement data [10, 11] or random variable inputs (see, for instance, groundwater flows simulation [12]). These factors may cause uncertainties in coefficients, boundary conditions, forcing terms, and the geometry of the domain [13]. Therefore, the deterministic modeling sometimes cannot satisfy the real industrial demand. The study on uncertainty quantification (UQ) has attracted more and more attention nowadays [13–16].

In this paper, we shall focus on the fast solvers and the efficient preconditioners for the optimal control problems constrained by the fractional model investigated in [17]. To provide more reliable predictions, we take into account the uncertainties in coefficients. Usually, these uncertainties are described as random processes. We make use of the finite-dimensional noise assumption [18] and approximate the uncertainties by a finite number of random variables. Then, the stochastic OCPs are transferred to parametric OCPs. The existence and uniqueness are consequently derived by Lion's argument [19] and the well-posedness of the solution of the fractional PDEs [17]. The stochastic optimality system is obtained via a variational inequality

method. Especially, we employ the formal Lagrangian method to provide a more intuitive way to construct the adjoint system [20]. The uncertain inputs and nonlocal property of the fractional operator bring the challenges in the design of the efficient numerical algorithms and the corresponding fast solvers.

To address the uncertain inputs, we mention some works in UQ study. With the introduction of the generalized polynomial chaos [14], there are mainly two approaches for the discretization of the stochastic part: the stochastic collocation method (SCM) [16] and the stochastic Galerkin method (SGM) [15]. The SCM is more popular since it leads to a set of uncoupled deterministic systems and enjoys the advantage to use the existing spatial algorithms. SCM and its related research have received fruitful results on stochastic OCPs [10, 11, 21]. However, as mentioned in [22], when considering the stochastic OCPs, both spatial and stochastic dimensions are involved in the formulation of the cost functionals. Hence, the cost functional may also include the standard derivation of the state function, which is of our concern. The SCM and its related methods lose their advantage in this case since they no longer lead to uncoupled deterministic systems because of the standard derivation term. The SGM appears to be more competitive for this case; however, the finite-dimensional noise assumption usually leads to a moderate or high dimension in stochastic space and hence brings huge computational cost when solving the discretized optimality system. The fast solvers and preconditioning technique play the key role of the SGM implementation.

In addition, due to the nonlocal property of the fractional operator, we employ the efficient spectral approach for the discretization of the spatial part [17]. Although Mao and Shen [17] have developed efficient numerical algorithms for the fractional PDEs, how to establish the fast solvers for the discretized optimality system, which is a saddle-point system of large scale, remains to be studied.

Since the preconditioning technique plays a crucial rule in accelerating the convergence of the iterative algorithms, we pay our attention to the construction of the efficient preconditioners. To handle the discretization of the spatial part, we apply the matrix decomposition method [17, 23] and propose a new virtual variable method, which is suited for the discretized optimality system. For the stochastic part, we consider the mean-based preconditioner (MBP) and the Ullmann preconditioner (UP). We develop the preconditioners for the most commonly used MINRES iteration method and a more efficient PPCG iteration method [24]. The fast solvers for the preconditioners and the eigenvalue distribution of the preconditioned matrix are studied. In addition, to reduce the computational cost, the iterative methods are presented in the low-rank matrix format [25–27] when the variance of the uncertainty inputs are small.

The rest of the paper is organized as follows. Section 2 is devoted to the study of the stochastic OCPs and the stochastic optimality system. We present the numerical algorithm in Section 3. We introduce the MINRES and PPCG methods in the low-rank matrix format and propose the corresponding efficient preconditioners in Sections 4 and 5, respectively. In Section 6, we present some numerical experiments to demonstrate the effectiveness of our solvers. Finally, in Section 7, we draw some conclusions.

2. The Stochastic Optimal Control Problems and the Optimality Systems

In this section, we shall consider the fractional OCPs with uncertain inputs. We first demonstrate the well-posedness of the stochastic fractional elliptic PDEs. Then, we prove the existence and uniqueness of the corresponding OCPs. Besides these, we derive the optimality systems which will be used in the numerical approximation later.

2.1. The Stochastic Fractional Elliptic PDEs. Let $(\Omega, \mathcal{F}, P)$ denote a complete probability space, where Ω is a sample space, $\mathcal{F} \subset 2^{\Omega}$ is a σ-algebra of events, and $P : \mathcal{F} \longrightarrow [0, 1]$, $P(\Omega) = 1$ is an appropriate probability measure. Let $I = (-1, 1)$ and $D = I \times I$. Let $a : D \times \Omega \longrightarrow \mathbb{R}$ represent a random field, which means that $a(\mathbf{x}, \cdot)$ is a real-valued random variable defined on $(\Omega, \mathcal{F}, P)$ for each $\mathbf{x} \in D$.

Let ${}_{-1}\partial_x^s$ and ${}_x\partial_1^s$ be the left-sided and right-sided Riemann-Liouville fractional derivatives of order s, respectively [28]. Consider the following fractional elliptic PDEs with fractional derivatives from both sides [17]:

$$\begin{cases} L^{s,\gamma} u(\mathbf{x}, \omega) = g(\mathbf{x}, \omega), & (\mathbf{x}, \omega) \in D \times \Omega, \\ u(\mathbf{x}, \omega) = 0, & (\mathbf{x}, \omega) \in \partial D \times \Omega, \end{cases} \tag{1}$$

where $1 < s, \gamma < 2$, $\mathbf{x} = (x, y) \in D$, $g \in L^2(D) \otimes L^2(\Omega)$ is a random field representing the distributed control, and $L^{s,\gamma}$ is a fractional elliptic operator with uncertain inputs given by

$$\begin{aligned} L^{s,\gamma} u(\mathbf{x}, \omega) = {}_x\partial_1^{s/2} \left[d^+(\mathbf{x}, \omega) {}_{-1}\partial_x^{s/2} u \right] + {}_{-1}\partial_x^{s/2} \left[d^-(\mathbf{x}, \omega) {}_x\partial_1^{s/2} u \right] \\ + {}_y\partial_1^{\gamma/2} \left[e^+(\mathbf{x}, \omega) {}_{-1}\partial_y^{\gamma/2} u \right] + {}_{-1}\partial_y^{\gamma/2} \left[e^-(\mathbf{x}, \omega) {}_y\partial_1^{\gamma/2} u \right]. \end{aligned} \tag{2}$$

To ensure the well-posedness of the solution for (1), we suppose that the random diffusion coefficients d^+, d^-, e^+, and e^- are bounded and uniformly coercive; i.e., there exist constants $0 < \underline{d} < \bar{d} < \infty$ and $0 < \underline{e} < \bar{e} < \infty$ such that

$$\begin{cases} \underline{d} \le d^+(\mathbf{x}, \omega), d^-(\mathbf{x}, \omega) \le \bar{d}, \\ \underline{e} \le e^+(\mathbf{x}, \omega), e^-(\mathbf{x}, \omega) \le \bar{e}, \end{cases} \text{a.e.} (\mathbf{x}, \omega) \in D \times \Omega. \tag{3}$$

In this paper, we assume that the coefficients adopt the finite-dimensional noise assumption. That is, they can be represented by a finite number of prescribed centered, normalized, and mutually uncorrelated random variables $\xi = \{\xi_m\}_{m=1}^M$, where $M \in \mathbb{N}$ and $\xi_m = \xi_m(\omega) : \Omega \longrightarrow \Gamma_m \subset \mathbb{R}$. The preceding assumptions enable the transformation from the stochastic system with random event ω to the deterministic parametric system with variable ξ. Thus, for any random field $v(\mathbf{x}, \omega)$ in this paper, we assume that

$$v(\mathbf{x},\omega)=v(\mathbf{x},\xi(\omega))=v_0(\mathbf{x})+\sum_{m=1}^{M}v_m(\mathbf{x})\xi_m(\omega) \coloneqq \sum_{m=0}^{M}v_m(\mathbf{x})\xi_m,\ \xi_0=1. \tag{4}$$

We also suppose that the random variables $\{\xi_m\}_{m=1}^{M}$ are independent and ξ_m is characterized by a probability density function $\rho_m:\Gamma_m\longrightarrow[0,1]$. Let $\rho(\xi)=\prod_{m=1}^{M}\rho_m(\xi_m)$ be the joint probability density of ξ and $\Gamma=\prod_{m=1}^{M}\Gamma_m\subset\mathbb{R}^M$ be the support of such probability density. Then, given the joint probability density of $\rho(\xi)$ and a deterministic Banach space $B(D)$, we define the associated stochastic space $\mathscr{B}_\rho(D)=B(D)\otimes L^2_\rho(\Gamma)$ equipped with the norm $\|v\|_{\mathscr{B}_\rho(D)}\coloneqq\left(\int_\Gamma\|v(\cdot,\xi)\|^2_{B(D)}\rho(\xi)d\xi\right)^{1/2}<\infty$. And, for any $u,v\in\mathscr{L}^2_\rho(D)=L^2(D)\otimes L^2_\rho(\Gamma)$, the inner product is given by $(u,v)_{D,\rho}=\int_\Gamma\int_D u(\mathbf{x},\xi)v(\mathbf{x},\xi)\rho(\xi)d\mathbf{x}d\xi$.

In addition, let $s>0$ and denote by $H^s(I)$ the usual Sobolev space equipped with the norm $\|\cdot\|_{H^s(I)}$. For $s,\gamma>0$, define the Hilbert space

$$H^{s,\gamma}(D)\coloneqq\left\{v\in L^2(D):\ \|v(\cdot,y)\|_{H^s(I)}\in L^2(I)\text{ and }\|v(x,\cdot)\|_{H^\gamma(I)}\in L^2(I)\right\}, \tag{5}$$

endowed with the norm:

$$\|v\|_{H^{s,\gamma}(D)}\coloneqq\left(\left\|\|v(\cdot,y)\|_{H^s(I)}\right\|^2_{L^2(I)}+\left\|\|v(x,\cdot)\|_{H^\gamma(I)}\right\|^2_{L^2(I)}\right)^{1/2}. \tag{6}$$

In addition, for $s,\gamma>1/2$, zero trace spaces $H^{s,\gamma}_0(D)$ can be defined as the closure of $C^\infty_0(D)$ with respect to the $H^{s,\gamma}(D)$ norm.

Notice that

$$\langle{}_{-1}\partial^s_x u,v\rangle_I=\left({}_{-1}\partial^{s/2}_x u,{}_x\partial^{s/2}_1 v\right)_I,\forall u,v\in H^{s/2}_0(I), \tag{7}$$

and

$$\langle{}_x\partial^s_1 u,v\rangle_I=\left({}_x\partial^{s/2}_1 u,{}_{-1}\partial^{s/2}_x v\right)_I,\forall u,v\in H^{s/2}_0(I), \tag{8}$$

hold for $1<s<2$, where $\langle\cdot,\cdot\rangle_I$ is the duality between $H^{s/2}_0(I)$ and its dual space $H^{s/2}_0(I)'$ [17]. Define the weak deterministic formulation of the stochastic equation (1) as follows: for a given $g\in(\mathscr{H}^{s/2,\gamma/2}_0)'_\rho(D)$, find $u\in(\mathscr{H}^{s/2,\gamma/2}_0)_\rho(D)$, such that

$$\mathscr{A}(u,v)=\mathscr{G}(v),\forall v\in\left(\mathscr{H}^{s/2,\gamma/2}_0\right)_\rho(D), \tag{9}$$

where $\mathscr{A}(u,v):(\mathscr{H}^{s/2,\gamma/2}_0)_\rho(D)\times(\mathscr{H}^{s/2,\gamma/2}_0)_\rho(D)\longrightarrow\mathbb{R}$ is the bilinear form defined as

$$\begin{aligned}\mathscr{A}(u,v)\coloneqq&\left(d^+(\mathbf{x},\xi)_{-1}\partial^{s/2}_x u,{}_{-1}\partial^{s/2}_x v\right)_{D,\rho}\\&+\left(d^-(\mathbf{x},\xi)_x\partial^{s/2}_1 u,{}_x\partial^{s/2}_1 v\right)_{D,\rho}\\&+\left(e^+(\mathbf{x},\xi)_{-1}\partial^{\gamma/2}_y u,{}_{-1}\partial^{\gamma/2}_y v\right)_{D,\rho}\\&+\left(e^-(\mathbf{x},\xi)_y\partial^{\gamma/2}_1 u,{}_y\partial^{\gamma/2}_1 v\right)_{D,\rho},\end{aligned} \tag{10}$$

and $\mathscr{G}(v):(\mathscr{H}^{s/2,\gamma/2}_0)'_\rho(D)\longrightarrow\mathbb{R}$ is the functional defined as $\mathscr{G}(v)=(g,v)_{D,\rho}$.

We obtain the following theorem.

Theorem 1. *For $1<s,\gamma<2$ and $g\in(\mathscr{H}^{s/2,\gamma/2}_0)'_\rho(D)$, problem (9) admits a unique solution satisfying*

$$\|u\|_{\left(\mathscr{H}^{s/2,\gamma/2}_0\right)_\rho(D)}\le C\|g\|_{\left(\mathscr{H}^{s/2,\gamma/2}_0\right)'_\rho(D)}. \tag{11}$$

Proof. By the assumption (3) and Lemma 3 in [17], one can prove that $\mathscr{A}(\cdot,\cdot)$ is continuous and coercive in $(\mathscr{H}^{s/2,\gamma/2}_0)_\rho(D)\times(\mathscr{H}^{s/2,\gamma/2}_0)_\rho(D)$, which implies this theorem in view of the well-known Lax-Milgram lemma (for more information, we refer to [17], which consider the case of the deterministic fractional equation). □

2.2. The Stochastic Optimal Control Problems. The goal of the stochastic OCPs is to find the appropriate distributed control function g such that the associated state function u of the fractional system (1) is the best attainable approximation to the prescribed target function u_d by some measure.

In this paper, we consider the case where the cost functional not only involves the expectation of the distance between the state function and the target function but also the standard deviation of the state function. We model this in the following way: for any given $u_d\in\mathscr{L}^2_\rho(D)$, find $(u,g)\in\mathscr{U}=(\mathscr{H}^{s/2,\gamma/2}_0)_\rho(D)\otimes\mathscr{L}^2_\rho(D)$ such that

$$\min_{(u,g)\in\mathscr{U}}\mathscr{J}(u,g)=\frac{\alpha}{2}\|u-u_d\|^2_{\mathscr{L}^2_\rho(D)}+\frac{\beta}{2}\|\mathrm{std}(u)\|^2_{L^2(D)}+\frac{\lambda}{2}\|g\|^2_{\mathscr{L}^2_\rho(D)}, \tag{12}$$

subject to the state equation (1).

The first term in the cost functional (12) measures the expectation of the distance between the state function u and the target function u_d. The second term penalizes the standard deviation $\mathrm{std}(u)$ which is given by $\mathrm{std}(u(\mathbf{x},\cdot))=\left(\mathbb{E}[(u(\mathbf{x},\cdot)-\mathbb{E}[u(\mathbf{x},\cdot)])^2]\right)^{1/2}$. The positive constants α and β can be adjusted to measure the importance of the first two terms. The last term, called the Tikhonov regularization term, is added to avoid the ill-posedness. Usually, the Tikhonov parameter λ is a value around $\lambda=10^{-2}$, but it can be showed later that our algorithms also work for smaller λ.

Theorem 2. *There exists a unique optimal solution $(\widehat{u}, \widehat{g}) \in \mathcal{U}$ to problems (12) and (1).*

Proof. Define the fractional control-to-state operator $S : \mathscr{L}^2_\rho(D) \longrightarrow \mathscr{L}^2_\rho(D)$, $g \longrightarrow u$, where u is the associated weak solution of system (1) with the given distributed control function g. Then, the cost functional (12) reduces to the following quadratic optimization problem:

$$\min_{g \in U_{ad} = \mathscr{L}^2_\rho(D)} \mathscr{J}(g) = \frac{\alpha}{2} \|Sg - u_d\|^2_{\mathscr{L}^2_\rho(D)} + \frac{\beta}{2} \|\mathrm{std}(Sg)\|^2_{L^2(D)} + \frac{\lambda}{2} \|g\|^2_{\mathscr{L}^2_\rho(D)}. \tag{13}$$

By virtual of Theorem 1, $(\mathscr{H}_0^{s/2,\gamma/2})_\rho(D) \hookrightarrow \mathscr{L}^2_\rho(D)$ and S is a linear and continuous mapping from $\mathscr{L}^2_\rho(D)$ into $\mathscr{L}^2_\rho(D)$, $\mathscr{J}$ is continuous and strictly convex. Therefore, $\mathscr{J}$ is weakly lower semicontinuous. Furthermore, since $\lambda > 0$, one can restrict the control problem on a closed, convex, and bounded subset of $\mathscr{L}^2_\rho(D)$ (see [20], Theorem 2.16). Finally, with the above conditions, we derive the existence and uniqueness of the optimal solution $(\widehat{u}, \widehat{g})$ with the minimizing sequence argument (see [20], Theorem 2.14). □

2.3. The Stochastic Optimality Systems. We devote this subsection to deriving the optimality systems of our model problems. The optimality systems, which are also called the first-order necessary optimality conditions, are essential since they provide a better description for the solution of the OCPs and pave a way for the construction of the numerical algorithms. According to the Lagrange method, we derive the following theorem demonstrating the stochastic optimality systems.

Theorem 3. *The control g, together with the optimal state u and the adjoint state p, is optimal for problems (12) and (1) if and only if the triple (g, u, p) satisfies the optimality system*

$$\begin{aligned} &\mathscr{A}(u, v) = (g, v)_{D,\rho}, \forall v \in \left(\mathscr{H}_0^{s/2,\gamma/2}\right)_\rho(D), \\ &\mathscr{A}(p, q) = (\alpha u_d - (\alpha + \beta)u + \beta \mathbb{E}[u], q)_{D,\rho}, \forall q \in \left(\mathscr{H}_0^{s/2,\gamma/2}\right)_\rho(D), \\ &(\lambda g - p, h)_{D,\rho} = 0, \forall h \in \mathscr{L}^2_\rho(D). \end{aligned} \tag{14}$$

Proof. Let us start with recalling the condition that the optimal solution has to satisfy. If $\widehat{g}$ is a solution of problems (12) and (1), then it solves the variational inequality

$$\mathscr{J}'(\widehat{g})(g - \widehat{g}) \geq 0, \quad \forall g \in U_{ad} = \mathscr{L}^2_\rho(D), \tag{15}$$

where $\mathscr{J}'(\widehat{g})$ is the Gâteaux derivative of the reduced cost functional (13) with respect to g at $\widehat{g}$. Then, with some calculations [20, 22], it appears that

$$\begin{aligned} \mathscr{J}'(\widehat{g})(g - \widehat{g}) &= (\alpha(S\widehat{g} - u_d) + \beta(S\widehat{g} - \mathbb{E}[S\widehat{g}]), S^*(g - \widehat{g}))_{D,\rho} \\ &\quad + (\lambda \widehat{g}, g - \widehat{g})_{D,\rho} = (-S^*(\alpha u_d - (\alpha + \beta)S\widehat{g} + \beta \mathbb{E}[S\widehat{g}]) + \lambda \widehat{g}, g - \widehat{g})_{D,\rho}, \end{aligned} \tag{16}$$

where S^* is the adjoint operator of the fractional control-to-state operator S satisfying

$$(Su, v)_{D,\rho} = (u, S^* v)_{D,\rho}, \forall u, v \in \mathscr{L}^2_\rho(D). \tag{17}$$

In the sequel, let us determine the adjoint operator S^*. Recalling (9) and observing that

$$(L^{s,\gamma} u, v)_{D,\rho} = \mathscr{A}(u, v) = (u, L^{s,\gamma} v)_{D,\rho}, \forall u, v \in \left(\mathscr{H}_0^{s/2,\gamma/2}\right)_\rho(D), \tag{18}$$

we define the following adjoint equation:

$$\begin{cases} L^{s,\gamma} p(\mathbf{x}, \omega) = v(\mathbf{x}, \omega), & (\mathbf{x}, \omega) \in D \times \Omega, \\ p(\mathbf{x}, \omega) = 0, & (\mathbf{x}, \omega) \in \partial D \times \Omega. \end{cases} \tag{19}$$

Since $u = Sg$ is the weak solution of system (1) with the distributed control g, one obtains that

$$(Sg, v)_{D,\rho} = (Sg, L^{s,\gamma} p)_{D,\rho} = (u, L^{s,\gamma} p)_{D,\rho} = \mathscr{A}(u, p) = (g, p)_{D,\rho}, \tag{20}$$

holds for all $g, v \in \mathscr{L}^2_\rho(D)$. Thus, from (17) and (20), one derives the adjoint operator $S^* : \mathscr{L}^2_\rho(D) \longrightarrow \mathscr{L}^2_\rho(D)$ and $S^* v = p$, where $p \in (\mathscr{H}_0^{s/2,\gamma/2})_\rho(D)$ is the associate weak solution of the adjoint system (19) with right-hand side input v. In addition, in view of $U_{ad} = \mathscr{L}^2_\rho(D)$, one can rewrite the variational inequality (15) as

$$(-p + \lambda \widehat{g}, h)_{D,\rho} = 0, \forall h \in \mathscr{L}^2_\rho(D), \tag{21}$$

where p is the associate weak solution of the adjoint system (19) with right-hand side input $v = (\alpha u_d - (\alpha + \beta)S\widehat{g} + \beta \mathbb{E}[S\widehat{g}])$. The identity (21) is also referred as the gradient equation. On the other hand, it can be verified that the above conditions are also sufficient due to the convexity of the reduced cost functional (13).

In conclusion, the above method for deriving the optimality systems starts with the variational inequality, invoking the first-order derivative of the cost functional and the concept of the adjoint operator. It remains for us on how to construct the adjoint operator S^* in a more intuitive way. For this purpose, we refer to the formal Lagrange method. Let p be the Lagrange multiplier. Define a Lagrangian function associated with the cost functional (12) and the weak formulation of the state equation (9) as

$$\mathscr{J}_L(u, g; p) = \mathscr{J}(u, g) + \mathscr{A}(u, p) - \mathscr{G}(p). \tag{22}$$

By setting the Gâteaux derivative of the Lagrangian

function (22) with respect to the control variable u equal to zero, one gets the adjoint equation (19) with $v = (\alpha u_d - (\alpha + \beta)u + \beta\mathbb{E}[u])$. Notice that the procedure above is similar to the computing part of the exact Lagrange method. However, the theory analysis of the latter one is more difficult and complicated. We refer to [20] and the references therein for more detail descriptions about the formal Lagrange method and the exact Lagrange method. □

3. Numerical Approximation

By virtue of Theorem 3, one can derive the optimal solution (g, u, p) by solving the stochastic optimality system (14). In this section, we consider the numerical approximation to (14) which involves both deterministic part in the physical domain D and stochastic part in the probability domain Γ.

3.1. Spatial Discretization and the Jacobi Polynomials. For the spatial part, due to the nonlocal property of the fractional derivatives, the main challenge in developing numerical scheme is how to form and compute mass matrix and stiffness matrix efficiently. To this end, we adopt the spectral approach and take the advantage of the properties of the Jacobi polynomials. Let $\mathscr{P}_N$ be the space of polynomials of degree less than or equal to N and denote $X_N = \{v \in \mathscr{P}_N : v(\pm 1) = 0\}$. For two-dimensional spatial case, take the same number of modes in each direction and define $\mathbf{X}_N = X_N \times X_N$. It can be verified that [23, 29]

$$\mathbf{X}_N = \operatorname{span}\left\{\phi_{kj}(\mathbf{x}) = \phi_k(x)\phi_j(y):\ k, j = 0, 1, \cdots, N-2\right\}, \quad (23)$$

where $\phi_k(\cdot) = L_k(\cdot) - L_{k+2}(\cdot)$ and $L_k(\cdot)$ is the Legendre polynomial of degree k.

Then, the spatial mass matrix can be written as $M_{\mathbf{x}} = M_y \otimes M_x$, where

$$(M_x)_{lk} = \int_I \phi_{k-1}(x)\phi_{l-1}(x)dx, M_y = M_x, \quad k, l = 1, \cdots, N-1. \quad (24)$$

It can be shown that, with the given basis ϕ_k, M_x and M_y are symmetric penta-diagonal and can be solved easily [23].

In what follows, we shall exploit the structure of the stiffness matrix $S_{\mathbf{x}}$.

Let ${}^{t,L}S_a$, ${}^{t,R}S_a$, and M_a be the matrixes with respect to the coefficient function a and the fractional order t, which elements are defined as

$$\begin{aligned}
\left({}^{t,L}S_a\right)_{lk} &= \int_I a(z)\left({}_{-1}\partial_z^{t/2}\phi_{k-1}(z)\right)\left({}_{-1}\partial_z^{t/2}\phi_{l-1}(z)\right)dz,\\
\left({}^{t,R}S_a\right)_{lk} &= \int_I a(z)\left({}_{z}\partial_1^{t/2}\phi_{k-1}(z)\right)\left({}_{z}\partial_1^{t/2}\phi_{l-1}(z)\right)dz,\\
(M_a)_{lk} &= \int_I a(z)\phi_{k-1}(z)\phi_{l-1}(z)dz,
\end{aligned} \quad (25)$$

where $k, l = 1, \cdots, N-1$, $z = x$, or $z = y$.

Then, if the coefficients adopt the one-dimensional finite chaos assumption

$$\begin{aligned}
d^{\pm}(x, y, \xi) = d^{\pm}(x, \xi) &= \sum_{m=0}^{M} d_m^{\pm}(x)\xi_m \coloneqq \sum_{m=0}^{M} d_{m,x}^{\pm}\xi_m,\\
e^{\pm}(x, y, \xi) = e^{\pm}(y, \xi) &= \sum_{m=0}^{M} e_m^{\pm}(y)\xi_m \coloneqq \sum_{m=0}^{M} e_{m,y}^{\pm}\xi_m,
\end{aligned} \quad (26)$$

we obtain the m_{th} spatial stiffness matrix

$$S_{\mathbf{x}}^m = M_y \otimes \left({}^{s,L}S_{d_{m,x}^+} + {}^{s,R}S_{d_{m,x}^-}\right) + \left({}^{\gamma,L}S_{e_{m,y}^+} + {}^{\gamma,R}S_{e_{m,y}^-}\right) \otimes M_x. \quad (27)$$

More generally, if the coefficients adopt the two-dimensional finite chaos assumption, we assume that the covariance kernel is separable. According to [30], the two-dimensional eigen-problem of the separable covariance kernel can be expressed as the products of two corresponding one-dimensional eigen-problem. Thus, we assume that

$$\begin{aligned}
d^{\pm}(x, y, \xi) &= \sum_{m=0}^{M} d_m^{\pm}(x)\tilde{d}_m^{\pm}(y)\xi_m \coloneqq \sum_{m=0}^{M} d_{m,x}^{\pm}d_{m,y}^{\pm}\xi_m,\\
e^{\pm}(x, y, \xi) &= \sum_{m=0}^{M} e_m^{\pm}(x)\tilde{e}_m^{\pm}(y)\xi_m \coloneqq \sum_{m=0}^{M} e_{m,x}^{\pm}e_{m,y}^{\pm}\xi_m.
\end{aligned} \quad (28)$$

And consequently, we obtain the m_{th} spatial stiffness matrix

$$S_{\mathbf{x}}^m = M_{d_{m,y}^+} \otimes {}^{s,L}S_{d_{m,x}^+} + M_{d_{m,y}^-} \otimes {}^{s,R}S_{d_{m,x}^-} + {}^{\gamma,L}S_{e_{m,y}^+} \otimes M_{e_{m,x}^+} + {}^{\gamma,R}S_{e_{m,y}^-} \otimes M_{e_{m,x}^-}. \quad (29)$$

Next, we recall how to form (25) efficiently. Let $J_n^{s,\gamma}(z)$ $(s, \gamma > -1)$ be the n_{th} Jacobi polynomial with respect to the weight function $\omega^{s,\gamma}(z) \coloneqq (1-z)^s(1+z)^\gamma$ [29]. Then, by virtue of Lemma 4 in [17], one can rewrite $\left({}^{t,L}S_a\right)_{lk}$ and $\left({}^{t,R}S_a\right)_{lk}$ as

$$\begin{aligned}
\left({}^{t,L}S_a\right)_{lk} &= \int_I (1+z)^{2-t}a(z)\widehat{\phi}_{k-1}(z)\widehat{\phi}_{l-1}(z)dz,\\
\left({}^{t,R}S_a\right)_{lk} &= \int_I (1-z)^{2-t}a(z)\widetilde{\phi}_{k-1}(z)\widetilde{\phi}_{l-1}(z)dz,
\end{aligned} \quad (30)$$

where

$$\begin{aligned}
\widehat{\phi}_k(z) &= \frac{\Gamma(k+2)}{\Gamma(k-(t/2)+2)}J_k^{t/2,1-(t/2)}(z) - \frac{\Gamma(k+3)}{\Gamma(k-(t/2)+3)}J_{k+1}^{t/2,1-(t/2)}(z),\\
\widetilde{\phi}_k(z) &= \frac{\Gamma(k+2)}{\Gamma(k-(t/2)+2)}J_k^{1-(t/2),t/2}(z) + \frac{\Gamma(k+3)}{\Gamma(k-(t/2)+3)}J_{k+1}^{1-(t/2),t/2}(z).
\end{aligned} \quad (31)$$

It can be shown that (30) and the rest part of (25) can be efficiently formed by Jacobi-Gauss quadrature formula [29].

3.2. Stochastic Discretization and the Generalized Polynomial Chaos Expansion. For the approximation in stochastic space, we use the stochastic Galerkin method. Let us recall the definition of generalized polynomial chaos [14]. Let $\psi_q(\xi) : \Gamma \longrightarrow \mathbb{R}$ be the multivariate polynomials represented by the products of orthonormal univariate polynomials

$$\psi_q(\xi) \coloneqq \prod_{m=1}^{M} \varphi_{q_m}(\xi_m), q = (q_1, \cdots, q_M), \tag{32}$$

where φ_{q_m} is the orthogonal polynomial which is determined by the distribution of the given data. Define the total degree (TD) set by

$$\mathscr{M}_p = \left\{ q \in \mathbb{N}^M : |q| = \sum_{m=1}^{M} q_m \le p \right\}. \tag{33}$$

Then, we have the stochastic approximation space

$$\mathbf{Y}_{M,p} = \left\{ \psi_q(\xi) \colon q \in \mathscr{M}_p \right\} \in L^2_\rho(\Gamma), \tag{34}$$

which is referred as the set of basis functions for the generalized polynomial chaos expansion (generalized PCE). The number of the generalized PCE basis functions is $P = \dim(\mathbf{Y}_{M,p}) = \dim(\mathscr{M}_p) = (M+p)!/M!p!$, where p is the highest degree of the orthogonal polynomial $\{\varphi_{q_m}\}$. Then, one can use generalized PCE to approximate the stochastic part of the random field.

3.3. Stochastic Galerkin Spectral Methods (SGSMs). In a nutshell, SGSMs employ the spectral approach for spatial approximation and the generalized PCE for stochastic approximation. The SGSMs for (14) read: find $u_N^P, p_N^P, g_N^P \in \mathbf{X}_N \otimes \mathbf{Y}_{M,p}$ such that

$$\begin{aligned} \mathscr{A}(u_N^P, v_{np}) &= (g_N^P, v_{np})_{D,\rho}, \forall v_{np} \in \mathbf{X}_N \otimes \mathbf{Y}_{M,p}, \\ \mathscr{A}\left(p_N^P, q_{np}\right) &= \left(\alpha \mathbb{I}_N u_d - (\alpha+\beta) u_N^P + \beta \mathbb{E}\left[u_N^P\right], q_{np}\right)_{D,\rho}, \forall q_{np} \in \mathbf{X}_N \otimes \mathbf{Y}_{M,p}, \\ \left(\lambda g_N^P - p_N^P, h_{np}\right)_{D,\rho} &= 0, \forall h_{np} \in \mathbf{X}_N \otimes \mathbf{Y}_{M,p}, \end{aligned} \tag{35}$$

where $\mathbb{I}_N$ is the interpolation operator associated with tensor product of Legendre-Gauss-Lobatto points in spatial part. Since $\mathbf{X}_N \otimes \mathbf{Y}_{M,p} \in (\mathscr{H}_0^{s/2,\gamma/2})_\rho(D)$, the existence and uniqueness of the discretized optimality system (35) can be established as in Theorems 2 and 3. Then, with the above spaces $\mathbf{X}_N$ and $\mathbf{Y}_{M,p}$, we expand the numerical solution u_N^P, p_N^P, g_N^P as

$$u_N^P = \sum_{n,p} u_{np} \phi_n \psi_p, p_N^P = \sum_{n,p} p_{np} \phi_n \psi_p, g_N^P = \sum_{n,p} g_{np} \phi_n \psi_p, \tag{36}$$

where $\phi_n = \phi_{kj}(\mathbf{x})$ with $n = (N-1) * (j-1) + k$, $1 \le k, j \le N-1$ and $\psi_p = \psi_p(\xi)$. Let U, P, and G be the matrix of size $J \times P$ with elements u_{np}, p_{np}, and g_{np}, respectively.

Set $\mathbf{u} = \mathrm{vec}(U)$, $\mathbf{p} = \mathrm{vec}(P)$, and $\mathbf{g} = \mathrm{vec}(G)$. Here, by $x = \mathrm{vec}(X)$, we denote the column vector of size $m \cdot n$ obtained by stacking $X \in \mathbb{R}^{m \times n}$ atop one another from left to right, and we define the operator $\mathrm{mat}(\cdot)$ such that $X = \mathrm{mat}(\mathbf{x})$. In addition, we denote the right-hand side as

$$(U_d)_{li} = \alpha(\mathbb{I}_N u_d, \phi_l \psi_i)_{D,\rho}, \mathbf{u}_d = \mathrm{vec}(U_d). \tag{37}$$

Then, subsisting (36) into (35) and taking $v_{np} = q_{np} = h_{np} = \phi_n(\mathbf{x})\psi_p(\xi)$, we present (35) in tensor product notation

$$\begin{bmatrix} \lambda M & 0 & -M \\ 0 & M^{\alpha,\beta} & S \\ -M & S & 0 \end{bmatrix} \begin{bmatrix} \mathbf{g} \\ \mathbf{u} \\ \mathbf{p} \end{bmatrix} = \begin{bmatrix} \mathbf{0} \\ \mathbf{u}_d \\ \mathbf{0} \end{bmatrix}, \tag{38}$$

where $M = M_\xi \otimes M_{\mathbf{x}}$, $M^{\alpha,\beta} = M_\xi^{\alpha,\beta} \otimes M_{\mathbf{x}}$, and $S = \sum_{m=0}^{M} M_\xi^m \otimes S_{\mathbf{x}}^m$. Here, $\otimes$ is the Kronecker product, $S_{\mathbf{x}}^m$ is the m^{th} spatial stiffness matrix, and $M_{\mathbf{x}}$ is the spatial mass matrix which are given in Section 3.1. M_ξ, M_ξ^m, and $M_\xi^{\alpha,\beta}$ are referred to the stochastic matrixes defined via

$$\begin{aligned} \left(M_\xi^m\right)_{ij} &= \int_\Gamma \xi_m \psi_i(\xi) \psi_j(\xi) \rho(\xi) d\xi, 0 \le m \le M, \quad M_\xi = M_\xi^0, \\ M_\xi^{\alpha,\beta} &= (\alpha+\beta) M_\xi - \beta \bar{M}_\xi, \quad \bar{M}_\xi = \mathrm{diag}\left(\int_\Gamma \psi_0^2(\xi) \rho(\xi) d\xi, 0, \cdots, 0 \right). \end{aligned} \tag{39}$$

By virtue of the orthogonality and the three term formulation, the matrix M_ξ and $M_\xi^{\alpha,\beta}$ are diagonal and M_ξ^m are symmetric and sparse.

4. The Preconditioned MINRES Method in Low-Rank Matrix Format

Noticing that the coefficient matrix of (38) is of a saddle-point form [24], we denote it by $\mathscr{A}$ and rewrite it in saddle-point structure

$$\mathscr{A} = \begin{bmatrix} A & B^T \\ B & 0 \end{bmatrix}, \tag{40}$$

where $A = [\lambda M, 0; 0, M^{\alpha,\beta}]$ is a symmetric and positive definite matrix and $B = [-M, S]$ is a full row rank matrix. The matrix (40) is generally symmetric but indefinite. Therefore, the preconditioned MINRES method arises naturally to solve the system (38) with the preconditioner of the following form

$$\mathscr{P}_M = \begin{bmatrix} A & 0 \\ 0 & BA^{-1}B^T \end{bmatrix}. \tag{41}$$

The detailed algorithm of MINRES can be found in [31]. Next, we introduce the MINRES method in low-rank matrix format and then consider the preconditioning technique when using the stochastic Galerkin method.

4.1. The Low-Rank Representations. The stochastic Galerkin approximation always results in solving large coupled system. Therefore, we proceed the above iterative methods in matrix format, and we do not form the matrixes and the preconditioners explicitly. When the variance of the input is small compared with their mean, we employ the low-rank (LR) technique in the iterative method [25]. The LR technique is an effective and popular technique to reduce the storage and computational cost when solving the stochastic problems with the stochastic Galerkin method [26, 27, 32, 33].

With right-hand side of (38) in the low-rank matrix format, all operations of the algorithm can be implemented efficiently in low-rank format (see, for instance, [25] and the references therein). More precisely, the matrix-vector products $M \cdot x$, $M^{\alpha,\beta} \cdot x$, and $S \cdot x$ are performed in matrix-function format. For $X = \mathrm{mat}(x) = X_L X_R$ with $X_L \in \mathbb{R}^{J\times r}$ and $X_R \in \mathbb{R}^{r\times P}$ $(r \ll J, P)$ of low-rank format, one has

$$\begin{aligned}
\mathscr{M}(X) &= M_{\mathbf{x}} X M_\xi \coloneqq \mathscr{M}_{\mathbf{x}}(X_L)\left(X_R M_\xi\right),\\
\mathscr{M}^{\alpha,\beta}(X) &= M_{\mathbf{x}} X M_\xi^{\alpha,\beta} \coloneqq \mathscr{M}_{\mathbf{x}}(X_L)\left(X_R M_\xi^{\alpha,\beta}\right),\\
\mathscr{S}(X) &= \sum_{m=0}^{M} S_{\mathbf{x}}^m X M_\xi^m \coloneqq \sum_{m=0}^{M} \mathscr{S}_{\mathbf{x}}^m(X_L)\left(X_R M_\xi^m\right).
\end{aligned} \tag{42}$$

Therefore, define

$$\begin{aligned}
[Y_L, Y_R] &= \mathscr{M}(X_L, X_R):\ Y_L = \mathscr{M}_{\mathbf{x}}(X_L),\ Y_R = X_R M_\xi,\\
[Y_L, Y_R] &= \mathscr{M}^{\alpha,\beta}(X_L, X_R):\ Y_L = \mathscr{M}_{\mathbf{x}}(X_L),\ Y_R = X_R M_\xi^{\alpha,\beta},\\
Y &= \mathscr{S}(X_L, X_R):\ Y = \sum_{m=0}^{M} \mathscr{S}_{\mathbf{x}}^m(X_L)\left(X_R M_\xi^m\right),
\end{aligned} \tag{43}$$

where $\mathscr{M}_{\mathbf{x}}$ is the spatial mass matrix operators and $\mathscr{S}_{\mathbf{x}}^m$ are the spatial stiffness matrix operators.

As mentioned above, to reduce the computational and storage cost, neither $M_{\mathbf{x}}$ nor $S_{\mathbf{x}}^m$ are formed explicitly. Let x_L^p be the p_{th} column of X_L, $X_L^p = \mathrm{mat}(x_L^p)$. We set the spatial mass matrix operator as

$$\mathscr{M}_{\mathbf{x}}(X_L) = \left\{\mathrm{vec}\left(M_x X_L^p M_y\right)\right\}_{p=1}^{r} \in \mathbb{R}^{J\times r}. \tag{44}$$

We denote the m_{th} spatial stiffness matrix operator as

$$\begin{aligned}
\mathscr{S}_{\mathbf{x}}^m(X_L) = \Big\{\mathrm{vec}\Big(&{}^{s,L}S_{d_{m,x}^+}\left(X_L^p\right)M_{d_{m,y}^+} + {}^{s,R}S_{d_{m,x}^-}\left(X_L^p\right)M_{d_{m,y}^-}\\
&+ M_{e_{m,x}^+}\left(X_L^p\right)^{\gamma,L}S_{e_{m,y}^+} + M_{e_{m,x}^-}\left(X_L^p\right)^{\gamma,R}S_{e_{m,y}^-}\Big)\Big\}_{p=1}^{r} \in \mathbb{R}^{J\times r}.
\end{aligned} \tag{45}$$

As for the truncation operator $\mathscr{T}$, we adopt the most standard QR and SVD (singular value decomposition) truncation method [25]. The other truncation operator options can be found in [33, 34]. Furthermore, for low-rank matrix $X = X_L X_R$, $Y = Y_L Y_R \in \mathbb{R}^{J\times P}$ where $X_L \in \mathbb{R}^{J\times r_X}$, $X_R \in \mathbb{R}^{r_X\times P}$, $Y_L \in \mathbb{R}^{J\times r_Y}$, and $Y_R \in \mathbb{R}^{r_Y\times P}$, we compute the low-rank matrix inner product $\langle X, Y\rangle_{LR}$ as [25]

$$\begin{aligned}
\langle X, Y\rangle_{LR} &= \mathrm{vec}(X)^T\mathrm{vec}(Y) = \mathrm{trace}\left(X^T Y\right) = \mathrm{trace}\left(X_R^T X_L^T Y_L Y_R\right)\\
&= \mathrm{trace}\left(Y_R X_R^T X_L^T Y_L\right) = \mathrm{vec}\left(X_R Y_R^T\right)^T\mathrm{vec}\left(X_L^T Y_L\right).
\end{aligned} \tag{46}$$

With the above low-rank representations and by virtue of [34], we obtain the LR-MINRES matrix iterative method.

4.2. Preconditioning for the MINRES Method. Now, we consider the preconditioning for the MINRES method. Rewrite (41) as

$$\mathscr{P}_M = \begin{bmatrix} \lambda M & 0 & 0\\ 0 & M^{\alpha,\beta} & 0\\ 0 & 0 & E \end{bmatrix}, \tag{47}$$

where $E = (1/\lambda)M + S\left(M^{\alpha,\beta}\right)^{-1}S$.

The spectrum analysis shows that the MINRES method will terminate in at most three iterations with preconditioner $\mathscr{P}_M$. However, it is expansive to solve the above preconditioners in real practical implement. One needs to find suitable approximations which not only lead to less iteration count but also can be solved cheaply. Notice that the matrixes M and $M^{\alpha,\beta}$ can be solved cheaply. Hence, the difficulty arises from how to approximate the (3,3) block E in (47).

Moreover, different from the deterministic OCPs, one challenge in constructing the preconditioner for the system derived from the stochastic Galerkin method is how to approximate the stiffness matrix $S = \sum_{m=0}^{M} M_\xi^m \otimes S_{\mathbf{x}}^m$ effectively.

Let $\widehat{S}$ represent some approximation for S. Enlightened by the deterministic problem [24, 35], one can construct approximations

$$\mathscr{P}_{E1} = \widehat{S}\left(M^{\alpha,\beta}\right)^{-1}\widehat{S} \tag{48}$$

or

$$\mathscr{P}_{E2} = \frac{1}{\alpha+\beta}\left(\widehat{S} + \sqrt{\frac{\alpha+\beta}{\lambda}}M\right)M^{-1}\left(\widehat{S} + \sqrt{\frac{\alpha+\beta}{\lambda}}M\right) \tag{49}$$

for E. The above approximations can be easily solved once the fast solver for $\widehat{S}$ or $\widehat{S} + \sqrt{((\alpha+\beta)/\lambda)}M$ is developed.

We note here that $\mathscr{P}_{E1}$ is the most commonly used approximation and achieves good behavior when λ is not too small. However, the spectrum analysis in [24] shows that the eigenvalues of $\mathscr{P}_{E1}$ depend to a large extent on the

Tikhonov parameter λ; thus, the iteration count grows quickly as λ decreases. To solve this, [35] proposed a more robust approach $\mathscr{P}_{E2}$ which can effectively reduce the affection of the Tikhonov parameter λ and was adopted widely in solving stochastic OCPs [27].

In view of the spectral approach in spatial space and the matrix decomposition method [17, 23], we construct a new, more accurate, and efficient approximation

$$\mathscr{P}_{E3} = \frac{1}{\alpha+\beta}\widehat{S}M^{-1}\widehat{S} + \frac{1}{\lambda}M, \tag{50}$$

with respect for the most commonly used mean-based preconditioner (MBP) and Ullmann preconditioner (UP) for $\widehat{S}$. We will develop the detailed fast solver algorithms for (50) with respect to MBP and UP in Subsections 4.3 and 4.4, respectively.

Here, we present the spectral bounds of the preconditioned system coupled with $\mathscr{P}_M$, where $E = \mathscr{P}_{E3}$.

Theorem 4. *Let $\mathscr{A}$ be preconditioned by $\mathscr{P}_M$ defined by (47) with $E = \mathscr{P}_{E3}$ defined by (50). Let μ be an eigenvalue of $\mathscr{P}_M^{-1}\mathscr{A}$. If $\widehat{S}$ satisfies $\|\widehat{S}^{-1}S - I\| \le \eta < 1$, then μ satisfies one of the following:*

$$\begin{aligned} &\mu = 1, -\sqrt{c_M\frac{\alpha+\beta}{\alpha}}(1+\eta) \le \mu \le \frac{1}{2}\left(1 - \sqrt{1 + \frac{4}{c_M}(1-\eta)^2}\right), \\ &\text{or } \frac{1}{2} + \frac{1}{\sqrt{c_M}}(1-\eta) \le \mu \le 1 + \sqrt{c_M\frac{\alpha+\beta}{\alpha}}(1+\eta), \end{aligned} \tag{51}$$

where $c_M = \lambda_{\max}(M)/\lambda_{\min}(M)$ is the condition number of M.

Proof. Let $\mathscr{A} = \begin{bmatrix} A & B^T \\ B & 0 \end{bmatrix}$ be preconditioned by $\mathscr{P} = \begin{bmatrix} A & 0 \\ 0 & E \end{bmatrix}$. Similar to the process of Proposition 3.2 in [24], the eigenvalues of $\mathscr{P}^{-1}\mathscr{A}$ are either

$$1, \frac{1}{2}\left(1 - \sqrt{1+4t}\right) \text{ or } \frac{1}{2}\left(1 + \sqrt{1+4t}\right), \tag{52}$$

where t is the eigenvalue of $E^{-1}(BA^{-1}B^T)$.

To obtain the bounds of the eigenvalues of $E^{-1}(BA^{-1}B^T)$ where $E = \mathscr{P}_{E3}$, we consider the Raleigh quotient

$$R(x) = \frac{x^T\left(S\left(M^{\alpha,\beta}\right)^{-1}S + (1/\lambda)M\right)x}{x^T\left((1/(\alpha+\beta))\widehat{S}M^{-1}\widehat{S} + (1/\lambda)M\right)x}, \tag{53}$$

for nonzero vector x of suitable size. Since $\|\widehat{S}^{-1}S - I\| \le \eta < 1$ implies $(1-\eta)^2 \le ((x^TS^2x)/(x^T\widehat{S}^2x)) \le (1+\eta)^2$, it can be proved that

$$\begin{aligned} R(x) &\le \max\left\{\frac{\alpha+\beta}{\alpha}\frac{x^TSM^{-1}Sx}{x^T\widehat{S}M^{-1}\widehat{S}x}, 1\right\} \\ &\le \max\left\{\frac{\alpha+\beta}{\alpha}\frac{\lambda_{\max}\left(M^{-1}\right)x^TS^2x}{\lambda_{\min}\left(M^{-1}\right)x^T\widehat{S}^2x}, 1\right\} \\ &\le c_M\frac{\alpha+\beta}{\alpha}(1+\eta)^2, \\ R(x) &\ge \min\left\{\frac{x^TSM^{-1}Sx}{x^T\widehat{S}M^{-1}\widehat{S}x}, 1\right\} \ge \frac{1}{c_M}(1-\eta)^2, \end{aligned} \tag{54}$$

where $c_M = \lambda_{\max}(M)/\lambda_{\min}(M)$.

Finally, using (52) and the above estimates yields the spectral bounds (51). □

4.3. Fast Solver for $\mathscr{P}_{E3}$ Coupled with Mean-Based Preconditioner. Consider the mean-based preconditioner (MBP) which is given by

$$\widehat{S} := S_M = M_\xi \otimes S_{\mathbf{x}}^0. \tag{55}$$

Then, with the MBP and the low-rank input $F = F_LF_R$ with $F_L \in \mathbb{R}^{J\times r}$, $F_R \in \mathbb{R}^{r\times P}$, we rewrite $X = (\mathscr{P}_{E3})^{-1}(F)$ as

$$\left(\frac{1}{\alpha+\beta}S_{\boldsymbol{x}}^0M_{\boldsymbol{x}}^{-1}S_{\boldsymbol{x}}^0 + \frac{1}{\lambda}M_{\boldsymbol{x}}\right)X_L\left(X_RM_\xi\right) = F_LF_R, \tag{56}$$

or equivalently

$$\begin{cases} \left(\dfrac{1}{\alpha+\beta}S_{\mathbf{x}}^0M_{\mathbf{x}}^{-1}S_{\mathbf{x}}^0 + \dfrac{1}{\lambda}M_{\mathbf{x}}\right)x_L^p = f_L^p, \quad p = 1, \cdots, r, \\ X_R = F_RM_\xi^{-1} \in \mathbb{R}^{r\times P}, \end{cases} \tag{57}$$

where x_L^p represents the p_{th} column of matrix $X_L \in \mathbb{R}^{J\times r}$. Since M_ξ is diagonal, one can easily decompose the large $(J\times P)\times(J\times P)$ coupled system into P (r with low-rank notation) uncoupled small $J\times J$ spatial systems.

Recall (30) and notice that the spatial stiffness matrices S_x^0 and S_y^0 are full even when the coefficients are constants; therefore, it is expensive to solve the first r equations of (57) in a direct version. [17, 29] provide an efficient separation of variables method—matrix decomposition method to solve $M_{\mathbf{x}}$ and $S_{\mathbf{x}}^0$ efficiently. The total cost of this method is only $O(N^3)$.

To this end, we introduce the variable $y_L^p = M_{\mathbf{x}}^{-1}S_{\mathbf{x}}^0x_L^p$ and rewrite the equality w.r.t. x_L^p of (57) as the following system in a matrix format

$$\begin{cases} \dfrac{1}{\alpha+\beta}\left(S_x^0Y_L^pM_y + M_xY_L^pS_y^0\right) + \dfrac{1}{\lambda}M_xX_L^pM_y = F_L^p, \\ \qquad\qquad\qquad\qquad\qquad\qquad\qquad\qquad p = 1, \cdots, r, \\ M_xY_L^pM_y - \left(S_x^0X_L^pM_y + M_xX_L^pS_y^0\right) = 0, \end{cases} \tag{58}$$

where $X_L^p = \mathrm{mat}(x_L^p)$, $Y_L^p = \mathrm{mat}(y_L^p)$, and $F_L^p = \mathrm{mat}(f_L^p)$. Next, following the process of full matrix decomposition method, we consider the generalized eigenvalue problem of M_x and S_x^0 (resp. M_y and S_y^0) and denote

$$M_x E_x = S_x^0 E_x \Lambda_x, M_y E_y = S_y^0 E_y \Lambda_y, \tag{59}$$

where $\Lambda_x (\mathrm{resp.}\Lambda_y)$ is the diagonal matrix with diagonal entries $\{\lambda_i^x\}_{i=1}^{N-1}$ (resp. $\{\lambda_j^y\}_{j=1}^{N-1}$) and the columns of E_x (resp. E_y) are the corresponding eigenvectors. Set $X_L^p = E_x \tilde{X}_L^p E_y^T$ and $Y_L^p = E_x \tilde{Y}_L^p E_y^T$. Multiplying the left of system (58) by $(S_x^0 E_x)^{-1}$, right by $(S_y^0 E_y)^{-T}$ and by virtue of (59), we arrive at

$$\begin{cases} \dfrac{1}{\alpha+\beta}\left(\tilde{Y}_L^p \Lambda_y + \Lambda_x \tilde{Y}_L^p\right) + \dfrac{1}{\lambda}\Lambda_x \tilde{X}_L^p \Lambda_y = \tilde{F}_L^p, \\ \Lambda_x \tilde{Y}_L^p \Lambda_y - \left(\tilde{X}_L^p \Lambda_y + \Lambda_x \tilde{X}_L^p\right) = 0, \end{cases} \quad p = 1, \cdots, r, \tag{60}$$

where $\tilde{F}_L^p = (S_x^0 E_x)^{-1} F_L^p (S_y^0 E_y)^{-T}$. Then, it follows from (60) that

$$\left(\tilde{X}_L^p\right)_{ij} = \frac{\lambda(\alpha+\beta)\left(\lambda_i^x \lambda_j^y\right)\left(\tilde{F}_L^p\right)_{ij}}{\lambda\left(\lambda_i^x + \lambda_j^y\right)^2 + (\alpha+\beta)\left(\lambda_i^x \lambda_j^y\right)^2}, \quad \begin{matrix} p = 1, \cdots, r, \\ i, j = 1, \cdots, N-1. \end{matrix} \tag{61}$$

Finally, we have $X_L^p = E_x \tilde{X}_L^p E_y^T$ and $x_L^p = \mathrm{vec}(X_L^p)$. We note here that, though we denote the new variable y_L^p, it does not need to be computed and do not add any computational cost. We define this strategy as virtual variable method, which is very useful in solving the preconditioner of such structure. This technique will be repeatedly used in the remainder of this section.

In summary, the full matrix decomposition and virtual variable method for solving

$$\left(\frac{1}{\alpha+\beta} S_M M^{-1} S_M + \frac{1}{\lambda} M\right) x = f \tag{62}$$

with MBP ($S_M = M_\xi \otimes S_{\mathbf{x}}^0$) in low-rank format consists of the following steps:

(1) Let $F = \mathrm{mat}(f)$ and decompose it into low-rank format $F = F_L F_R$

(2) Compute $X_R = F_R M_\xi^{-1}$

(3) Let x_L^p be the p_{th} column of $X_L \in \mathbb{R}^{J \times r}$. For $p = 1, \cdots, r$, compute x_L^p by the following steps:

(i) Compute the eigenvalues and eigenvectors of the generalized eigenvalue problems (59)

(ii) Compute $\tilde{F}_L^p = (S_x^0 E_x)^{-1} F_L^p (S_y^0 E_y)^{-T}$

(iii) Obtain $\tilde{X}_L^p$ from (61)

(iv) Set $X_L^p = E_x \tilde{X}_L^p E_y^T$ and $x_L^p = \mathrm{vec}(X_L^p)$

(4) Set $X = X_L X_R$ and $x = \mathrm{vec}(X)$

4.4. Fast Solver for $\mathscr{P}_{E3}$ Coupled with Ullmann Preconditioner. MBP is best suited for most uncertain problems; however, its performance deteriorates as the variance of the random inputs increases. This is mainly because the off-diagonal blocks of S become more significant. To this end, [36] developed the Ullmann preconditioner (UP) which is constructed by all components of S.

$$\widehat{S} \coloneqq S_U = \sum_{m=0}^{M} \frac{\mathrm{trace}\left(\left(S_{\mathbf{x}}^m\right)^T S_{\mathbf{x}}^0\right)}{\mathrm{trace}\left(\left(S_{\mathbf{x}}^0\right)^T S_{\mathbf{x}}^0\right)} M_\xi^m \otimes S_{\mathbf{x}}^0 \coloneqq M_\xi^U \otimes S_x^0. \tag{63}$$

It has been proved that S_U is sparse, symmetric, positive definite and M_ξ^U minimizes $\|S - \widehat{M}_\xi \otimes S_{\mathbf{x}}^0\|_F$ for all $\widehat{M}_\xi \in \mathbb{R}^{P \times P}$ [26].

Notice that a traditional method to compute $t_m = \mathrm{trace}((S_{\mathbf{x}}^m)^T S_{\mathbf{x}}^0)$ is

$$t_m = \mathrm{trace}\left(\left(S_{\mathbf{x}}^m\right)^T S_{\mathbf{x}}^0\right) = \mathrm{vec}\left(S_{\mathbf{x}}^m\right)^T \cdot \mathrm{vec}\left(S_{\mathbf{x}}^0\right). \tag{64}$$

However, when solving the problem involving the fractional order, to achieve the desired result, the discretization parameter J is usually very large. Therefore, the computational cost of forming S_U by the traditional method might be very expensive.

To solve this, recall the structure of the spatial stiffness matrix $S_{\mathbf{x}}^m$ given in (27) for one-dimensional case and (29) for two-dimensional case and the fact that

$$\mathrm{trace}(A \otimes B) = \mathrm{trace}(A) \otimes \mathrm{trace}(B). \tag{65}$$

For one-dimensional case (27), setting $S_x^m = ({}^{s,L}S_{d_{m,x}^+} + {}^{s,R}S_{d_{m,x}^-})$ and $S_y^m = ({}^{\gamma,L}S_{e_{m,y}^+} + {}^{\gamma,R}S_{e_{m,y}^-})$, we have

$$\begin{aligned} t_m &= \mathrm{trace}\left(\left(S_{\mathbf{x}}^m\right)^T S_{\mathbf{x}}^0\right) = \mathrm{trace}\left(M_y^T M_y\right)\mathrm{trace}\left(\left(S_x^m\right)^T S_x^0\right) \\ &\quad + \mathrm{trace}\left(M_y^T S_y^0\right)\mathrm{trace}\left(\left(S_x^m\right)^T M_x\right) \\ &\quad + \mathrm{trace}\left(\left(S_y^m\right)^T M_y\right)\mathrm{trace}\left(M_x^T S_x^0\right) \\ &\quad + \mathrm{trace}\left(\left(S_y^m\right)^T S_y^0\right)\mathrm{trace}\left(M_x^T M_x\right) \\ &= \left(m^T m\right)\left(a_m^T a_0 + b_m^T b_0\right) + \left(m^T b_0\right)\left(a_m^T m\right) + \left(b_m^T m\right)\left(m^T a_0\right), \end{aligned} \tag{66}$$

where $m = \mathrm{vec}(M_x) = \mathrm{vec}(M_y)$, $a_m = \mathrm{vec}(S_x^m)$, and $b_m = \mathrm{vec}(S_y^m)$. For two-dimensional case, one can compute t_m in a similar way, which we omit the detailed computation

here. In this way, we can obtain S_U with much less computational cost compared with the traditional method (64).

Next, we give the fast solver for $\mathscr{P}_{E3}$ coupled with the approximation S_U. Letting $x = \mathrm{vec}(X)$, $y = M^{-1}S_U x$, and $Y = \mathrm{mat}(y)$, we rewrite $X = (\mathscr{P}_{E3})^{-1}(F)$ as the following system in matrix format

$$\begin{cases} \dfrac{1}{\alpha+\beta} S_{\mathbf{x}}^0 Y M_\xi^U + \dfrac{1}{\lambda} M_{\mathbf{x}} X M_\xi = F, \\ M_{\mathbf{x}} Y M_\xi - S_{\mathbf{x}}^0 X M_\xi^U = 0. \end{cases} \tag{67}$$

Different from the MBP case, we cannot decompose the large coupled system (67) into P uncoupled spatial systems directly. To solve this, we recall the partial matrix decomposition method [29]. Consider the generalized eigenvalue problem of M_ξ^U and M_ξ and denote

$$M_\xi^U E_U = M_\xi E_U \Lambda_U. \tag{68}$$

Let $X = \tilde{X}E_U^T$ and $Y = \tilde{Y}E_U^T$ and multiply the right of (67) by $(M_\xi E_U)^{-T}$. It can be verified that (67) is equivalent to

$$\begin{cases} \dfrac{1}{\alpha+\beta} S_{\mathbf{x}}^0 \tilde{Y} \Lambda_U + \dfrac{1}{\lambda} M_{\mathbf{x}} \tilde{X} = \tilde{F}, \\ M_{\mathbf{x}} \tilde{Y} - S_{\mathbf{x}}^0 \tilde{X} \Lambda_U = 0, \end{cases} \tag{69}$$

where $\tilde{F} = F(M_\xi E_U)^{-T}$. More precisely, letting $\tilde{x}_p$ (resp. $\tilde{f}_p$) be the p_{th} column of $\tilde{X}$ (resp. $\tilde{F}$) and λ_U^p be the p_{th} diagonal entry of the diagonal matrix Λ_U, we rewrite (69) as

$$(\lambda_U^p)^2 \frac{1}{\alpha+\beta} (S_{\mathbf{x}}^0 M_{\mathbf{x}}^{-1} S_{\mathbf{x}}^0) \tilde{x}_p + \frac{1}{\lambda} M_{\mathbf{x}} \tilde{x}_p = \tilde{f}_p, p = 1, \cdots, P. \tag{70}$$

It is observed that the structure of (70) is similar to that of the first r equations in (57). Then, letting $\tilde{X}_p = \mathrm{mat}(\tilde{x}_p)$ and following the process of the full matrix decomposition method introduced above, we deduce that

$$\left(\widetilde{\tilde{X}}_p\right)_{ij} = \frac{\lambda(\alpha+\beta)\left(\lambda_i^x \lambda_j^y\right)\left(\widetilde{\tilde{F}}_p\right)_{ij}}{(\lambda_U^p)^2 \lambda\left(\lambda_i^x + \lambda_j^y\right)^2 + (\alpha+\beta)\left(\lambda_i^x \lambda_j^y\right)^2}, \quad \begin{matrix} p = 1, \cdots, P, \\ i, j = 1, \cdots, N-1, \end{matrix} \tag{71}$$

where $\widetilde{\tilde{F}}_p = (S_x^0 E_x)^{-1} \tilde{F}_p (S_y^0 E_y)^{-T}$ and the parameters λ_i^x, λ_j^y, E_x, E_y are given in (59). Finally, we obtain $\tilde{X}_p = E_x \widetilde{\tilde{X}}_p E_y^T$ and $X = \tilde{X}E_U^T$.

In general, the UP can reduce the iteration counts and thus does a better job than MBP when handling the system with large variance inputs.

In summary, the full matrix decomposition and virtual variable method for solving

$$\left(\frac{1}{\alpha+\beta} S_U M^{-1} S_U + \frac{1}{\lambda} M\right) x = f, \tag{72}$$

with UP ($S_U = M_\xi^U \otimes S_{\mathbf{x}}^0$) consists of the following steps:

(1) Compute the eigenvalues and eigenvectors of the generalized eigenvalue problems (68)

(2) Let $F = \mathrm{mat}(f)$ and compute $\tilde{F} = F(M_\xi E_U)^{-T}$

(3) Let $\tilde{x}_p$ be the p_{th} column of $\tilde{X} \in \mathbb{R}^{J \times P}$. For $p = 1, \cdots, P$, compute $\tilde{x}_p$ by the following steps:

(i) Compute the eigenvalues and eigenvectors of the generalized eigenvalue problems (59)

(ii) Let $\tilde{f}_p$ be the p_{th} column of $\tilde{F}$, $\tilde{F}_p = \mathrm{mat}(\tilde{f}_p)$ and compute $\widetilde{\tilde{F}}_p = (S_x^0 E_x)^{-1} \tilde{F}_p (S_y^0 E_y)^{-T}$

(iii) Obtain $\widetilde{\tilde{X}}_p$ from (71)

(iv) Set $\tilde{X}_p = E_x \widetilde{\tilde{X}}_p E_y^T$ and $\tilde{x}_p = \mathrm{vec}(\tilde{X}_p)$

(4) Set $X = \tilde{X}E_U^T$ and $x = \mathrm{vec}(X)$

5. The PPCG Method in Low-Rank Matrix Format

Enlightened by [24, 37], we find another more efficient symmetric Krylov subspace iterative method—the preconditioned projected conjugate gradient (PPCG) method whose preconditioner takes the form

$$\mathscr{P}_P = \begin{bmatrix} 0 & 0 & -M \\ 0 & F & S \\ -M & S & 0 \end{bmatrix}, \tag{73}$$

where $F = \lambda S M^{-1} S + M^{\alpha,\beta}$.

In this section, we first introduce the PPCG method in low-rank matrix format and then consider the preconditioning technique.

5.1. The Algorithm of PPCG Method in Low-Rank Matrix Format. We present the PPCG method in the low-rank matrix format in Algorithm 1.

In Algorithm 1, the matrix functions $\mathscr{M}$, $\mathscr{M}^{\alpha,\beta}$, and $\mathscr{S}$ and the low-rank matrix inner-product $\langle X, Y \rangle_{LR}$ are defined the same as in Subsection 4.1. $\mathscr{P}_F$ is the approximation for the (2,2) block of (73), which will be discussed in the next subsection.

5.2. Preconditioning for the PPCG Method. Notice that the PPCG method will terminate in only one iteration with preconditioner $\mathscr{P}_P$ defined by (73). However, similar to the case of the

Intput: Matrix functions $\mathscr{M}$, $\mathscr{M}^{\alpha,\beta}$, $\mathscr{S}$ and $\mathscr{P}^{-1}$. Right-hand side U_d in low-rank format. Truncation operator $\mathscr{T}$ w.r.t. relative accuracy ε_{rel}.
Output: Matrixes G, U.
$R_2^+ = -U_d$
$[G_L^+, G_R^+, U_L^+, U_R^+, R_2, R_{2,L}, R_{2,R}] = \mathscr{P}^{-1}(\mathbf{0}, \mathbf{0}, R_2^+)$
$Q_{1,L} = -G_L^+,\ Q_{1,R} = G_R^+$
$Q_{2,L} = -U_L^+,\ Q_{2,R} = U_R^+$
$\gamma_0 = \langle R_2, U^+ \rangle_{LR}$
$\alpha_0 = \gamma_0 / (\lambda \langle Q_1, \mathscr{M}(Q_1) \rangle_{LR} + \langle Q_2, \mathscr{M}^{\alpha,\beta}(Q_2) \rangle_{LR})$
$G_L = \alpha_0 Q_{1,L},\ G_R = Q_{1,R}$
$U_L = \alpha_0 Q_{2,L},\ U_R = Q_{2,R}$
$r = \|\mathscr{M}^{\alpha,\beta}(U_L, U_R) + \lambda \mathscr{S}(G_L, G_R) - U_d\|_F / \|U_d\|_F$
$k = 0$
while $r >$ tol **do**
  $[R_{1,L}^+, R_{1,R}^+] = \alpha_k \lambda \mathscr{M}((Q_{1,L}, Q_{1,R})$
  $R_2^+ = R_2 + \alpha_k \mathscr{M}^{\alpha,\beta}(Q_{2,L}, Q_{2,R})$
  $[G_L^+, G_R^+, U_L^+, U_R^+, R_2, R_{2,L}, R_{2,R}] = \mathscr{P}^{-1}(R_{1,L}^+, R_{1,R}^+, R_2^+)$
  $\delta = (\langle R_1^+, G^+ \rangle_{LR} + \langle R_2^+, U^+ \rangle) / \gamma_k$
  $Q_1 = -G_L^+ G_R^+ + \delta Q_1,\ [Q_{1,L}, Q_{1,R}] = \mathscr{T}(Q_1)$
  $Q_2 = -U_L^+ U_R^+ + \delta Q_2,\ [Q_{2,L}, Q_{2,R}] = \mathscr{T}(Q_2)$
  $\gamma_{k+1} = \langle R_2, U^+ \rangle_{LR}$
  $\alpha_{k+1} = \gamma_{k+1} / (\lambda \langle Q_1, \mathscr{M}(Q_1) \rangle_{LR} + \langle Q_2, \mathscr{M}^{\alpha,\beta}(Q_2) \rangle_{LR})$
  $G = G + \alpha_{k+1} Q_1,\ [G_L, G_R] = \mathscr{T}(G)$
  $U = U + \alpha_{k+1} Q_2,\ [U_L, U_R] = \mathscr{T}(U)$
  $r = \|\mathscr{M}^{\alpha,\beta}(U_L, U_R) + \lambda \mathscr{S}(G_L, G_R) - U_d\|_F / \|U_d\|_F$
  $k = k + 1$
end while

Algorithm 1: LR-PPCG matrix iterative method.

Intput: Matrix functions $\mathscr{M}$, $\mathscr{M}^{-1}$, $\mathscr{S}$ and $\mathscr{P}_F^{-1}$. Input variables $R_{1,L}^+ \in \mathbb{R}^{J \times r}$, $R_{1,R}^+ \in \mathbb{R}^{r \times P}$ and $R_2^+ \in \mathbb{R}^{J \times R}$.
Output: Matrixes G_L^+, G_R^+, U_L^+, U_R^+, R_2, $R_{2,L}$ and $R_{2,R}$.
$[V_L, V_R] = \mathscr{M}^{-1}(-R_{1,L}^+, R_{2,L}^+)$
$H = \mathscr{S}(V_L, V_R)$
$R_2 = R_2^+ - H,\ [R_{2,L}, R_{2,R}] = \mathscr{T}(R_2)$
$[U_L^+, U_R^+] = \mathscr{P}_F^{-1}(R_{2,L}, R_{2,R})$
$W = \mathscr{S}(U_L^+, U_R^+),\ [W_L, W_R] = \mathscr{T}(W)$
$[G_L^+, G_R^+] = \mathscr{M}^{-1}(W_L, W_R)$

Algorithm 2: Algorithm for $[G_L^+, G_R^+, U_L^+, U_R^+, R_2, R_{2,L}, R_{2,R}] = \mathscr{P}^{-1}(R_{1,L}^+, R_{1,R}^+, R_2^+)$ in Algorithm 1.

MINRES iteration, it is not cheap to solve the (2,2) block F of (73) directly. Usually, the following two approximations

$$\mathscr{P}_{F1} = \lambda \widehat{S} M^{-1} \widehat{S},$$
$$\mathscr{P}_{F2} = \lambda \left(\widehat{S} + \sqrt{\frac{(\alpha+\beta)}{\lambda}} M \right) M^{-1} \left(\widehat{S} + \sqrt{\frac{(\alpha+\beta)}{\lambda}} M \right), \tag{74}$$

are used for approximating F. Again, by virtue of the matrix decomposition method, we propose a new approximation for F as

$$\mathscr{P}_{F3} = \lambda \widehat{S} M^{-1} \widehat{S} + (\alpha+\beta) M, \tag{75}$$

where $\widehat{S}$ is the mean-based preconditioner or Ullmann preconditioner for the global stiffness matrix S.

Next, we give the spectral bounds of the preconditioned system coupled with $\mathscr{P}_P$, where $F = \mathscr{P}_{F3}$.

Theorem 5. *Let $\mathscr{A}$ be preconditioned by $\mathscr{P}_P$ defined by (73) with $F = \mathscr{P}_{F3}$ defined by (75). Let μ be an eigenvalue of $\mathscr{P}_P^{-1}\mathscr{A}$. If $\widehat{S}$ satisfies $\|\widehat{S}^{-1}S - I\| \le \eta < 1$, then μ satisfies*

$$\min\left\{ \frac{\alpha}{\alpha+\beta}, \frac{1}{c_M}(1-\eta)^2 \right\} \le \mu \le c_M (1+\eta)^2 \tag{76}$$

where $c_M = \lambda_{\max}(M)/\lambda_{\min}(M)$.

Table 1: Comparison of iterations and CPU times (in seconds) to solve system (38) with given random inputs using MINRES/PPCG method with $\mathscr{P}_{E1}$, $\mathscr{P}_{E2}$, $\mathscr{P}_{E3}/\mathscr{P}_{F1}$, $\mathscr{P}_{F2}$, $\mathscr{P}_{F3}$, and S_M for $J = 16384$, $l_2 = 2$, $M = 13$, $P = 560$, $\sigma = 0.01$, and $\lambda \in \{10^{-2}, 10^{-3}, 10^{-4}, 10^{-5}\}$.

Standard format		MINRES + S_M			PPCG + S_M		
		$\mathscr{P}_{E1}$	$\mathscr{P}_{E2}$	$\mathscr{P}_{E3}$	$\mathscr{P}_{F1}$	$\mathscr{P}_{F2}$	$\mathscr{P}_{F3}$
$\lambda = 10^{-2}$	# iter	21	29	15	7	8	3
	CPU time	305.40	426.96	216.56	81.73	92.98	40.42
$\lambda = 10^{-3}$	# iter	39	31	17	14	8	4
	CPU time	565.98	455.33	244.29	154.23	92.50	50.44
$\lambda = 10^{-4}$	# iter	91	29	19	25	8	5
	CPU time	1318.06	425.05	272.84	266.75	92.26	60.06
$\lambda = 10^{-5}$	# iter	227	29	19	62	7	5
	CPU time	3290.50	425.95	273.38	645.23	82.55	60.31

Table 2: Comparison of iterations and CPU times (in seconds) to solve system (38) with given random inputs using MINRES/PPCG method in low-rank format with $\mathscr{P}_{E1}$, $\mathscr{P}_{E2}$, $\mathscr{P}_{E3}/\mathscr{P}_{F1}$, $\mathscr{P}_{F2}$, $\mathscr{P}_{F3}$, and S_M for $J = 16384$, $l_2 = 2$, $M = 13$, $P = 560$, $\sigma = 0.01$, and $\lambda \in \{10^{-2}, 1$ $0^{-3}, 10^{-4}, 10^{-5}\}$.

Low-rank format		MINRES + S_M			PPCG + S_M		
		$\mathscr{P}_{E1}$	$\mathscr{P}_{E2}$	$\mathscr{P}_{E3}$	$\mathscr{P}_{F1}$	$\mathscr{P}_{F2}$	$\mathscr{P}_{F3}$
$\lambda = 10^{-2}$	# iter	21	29	15	7	8	3
	CPU time	224.93	339.58	152.72	52.02	66.31	20.80
$\lambda = 10^{-3}$	# iter	39	31	17	14	8	4
	CPU time	424.36	360.87	171.61	104.40	66.12	28.49
$\lambda = 10^{-4}$	# iter	93	29	19	26	8	5
	CPU time	1021.96	332.70	194.26	186.70	66.23	35.30
$\lambda = 10^{-5}$	# iter	233	29	19	63	7	5
	CPU time	2490.11	325.26	178.45	446.27	52.82	34.81

Table 3: The number of the stochastic discretization parameter P and the parameter $(\sum_{m=1}^{M}\lambda_m)/|D|$ with variant tuples (l_2, M).

(l_2, M)	(1,15)	(2,13)	(2,12)	(3,9)	(4,6)
P	816	560	455	220	84
$\sum_{m=1}^{M}\lambda_m/\lvert D\rvert$	0.8124	0.9034	0.8975	0.9205	0.9203

Proof. By virtue of Theorem 4.2 in [24], the eigenvalue of $\mathscr{P}_P^{-1}\mathscr{A}$ with $F = \mathscr{P}_{F3}$ satisfies either

$$\mu = 1 \text{ or } \left(\lambda SM^{-1}S + M^{\alpha,\beta}\right)x = \mu\left(\lambda\widehat{S}M^{-1}\widehat{S} + (\alpha+\beta)M\right)x. \tag{77}$$

To obtain the bounds of μ, we consider the Raleigh quotient

$$R(x) = \frac{x^T\left(\lambda SM^{-1}S + M^{\alpha+\beta}\right)x}{x^T\left(\lambda\widehat{S}M^{-1}\widehat{S} + (\alpha+\beta)M\right)x}. \tag{78}$$

Similar to the proof of Theorem 4, we get the desired result (76).

The detailed fast solver algorithms for (75) with respect to MBP and UP can be obtained similar to that of Subsections 4.3 and 4.4, respectively. We omit the detailed process here. □

6. Numerical Results

In this section, we present some numerical experiments to show the computational efficiency of our algorithms. Without loss of generality, we assume that $e^{\pm} = 1$ and $d^{+} = d^{-}$. We assume that the random inputs $d^{+} = d^{-}$ is represented by the truncated KL expansion characterized by the covariance function

$$C_2(\mathbf{x}_1, \mathbf{x}_2) = \sigma^2 \exp\left(-\frac{|x_1 - x_2|}{l_2} - \frac{|y_1 - y_2|}{l_2}\right), \forall \mathbf{x}_i = (x_i, y_i) \in D, i = 1, 2, \tag{79}$$

respectively, where σ is the standard deviations. According to [30], the eigenpairs $\{\lambda_i, \psi_i(\mathbf{x})\}_{k=1}^{\infty}$ of (79) can be expressed as $\lambda_i = \sigma\lambda_k^1\lambda_j^2$ and $\psi_i(\mathbf{x}) = \psi_k^1(x)\psi_j^2(y)$ where $\{\lambda_k^1, \psi_k^1(x)\}_{k=1}^{\infty}$ and $\{\lambda_j^2, \psi_j^2(y)\}_{j=1}^{\infty}$ are eigenpairs of

$$C_1(x_1, x_2) = \exp\left(-\frac{|x_1 - x_2|}{l}\right), \forall x_1, x_2 \in I, \tag{80}$$

with $l_2 = l$. The analytical expressions for the eigenpairs $\{\lambda_k, \psi_k(x)\}_{k=1}^{\infty}$ of (80) are given explicitly in [18]. More

Table 4: Comparison of iterations and CPU times (in seconds) to solve system (38) with given random inputs and the ranks of truncated solutions (g_N^P/u_N^P) using MINRES method in standard format and low-rank format with $\mathscr{P}_{E3}$ and S_M for $J = 16384$, $\sigma \in \{0.01,0.04,0.09,0.16\}$, and variant tuples (l_2, M, P).

(l_2, M, P)		MINRES + $\mathscr{P}_{E3}$ + S_M (standard/low-rank)			
		(1,15, 816)	(2,12,455)	(3,9,220)	(4,6,84)
$\sigma = 0.01$	# iter	15/15	15/15	15/15	15/15
	CPU time	387.12/268.39	159.15/115.65	57.91/45.01	15.53/13.07
	Rank(g/u)	85/99	59/68	45/48	24/29
$\sigma = 0.04$	# iter	21/21	21/21	21/19	19/19
	CPU time	535.80/433.87	223.14/186.27	81.09/64.21	19.70/18.84
	Rank(g/u)	157/173	109/121	81/90	47/51
$\sigma = 0.09$	# iter	27/27	27/27	27/27	25/25
	CPU time	687.16/612.64	287.02/261.78	104.28/100.06	25.84/26.69
	Rank(g/u)	211/232	145/159	107/115	58/59
$\sigma = 0.16$	# iter	35/35	35/35	35/35	35/35
	CPU time	887.52/867.63	372.22/365.40	135.07/137.40	36.17/38.82
	Rank(g/u)	275/362	180/217	126/136	65/66

Table 5: Comparison of iterations and CPU times (in seconds) to solve system (38) with given random inputs and the ranks of truncated solutions (g_N^P/u_N^P) using PPCG method in standard format and low-rank format with $\mathscr{P}_{F3}$ and S_M for $J = 16384$, $\sigma \in \{0.01,0.04,0.09,0.16\}$, and variant tuples (l_2, M, P).

(l_2, M, P)		PPCG + $\mathscr{P}_{F3}$ + S_M (standard/low-rank)			
		(1,15, 816)	(2,12,455)	(3,9,220)	(4,6,84)
$\sigma = 0.01$	# iter	3/3	3/3	3/3	3/3
	CPU time	71.96/35.39	29.82/16.01	10.50/6.62	2.77/1.95
	Rank(g/u)	115/104	79/71	58/52	32/32
$\sigma = 0.04$	# iter	6/6	6/6	5/5	5/5
	CPU time	127.06/98.87	52.06/41.90	15.70/13.22	4.12/3.71
	Rank(g/u)	168/156	117/110	92/84	51/48
$\sigma = 0.09$	# iter	8/8	8/8	8/8	8/8
	CPU time	162.43/147.41	66.63/62.04	23.52/23.73	6.19/6.32
	Rank(g/u)	229/204	161/141	116/108	60/55
$\sigma = 0.16$	# iter	12/12	12/12	12/12	11/11
	CPU time	234.40/244.09	96.63/101.52	33.92/37.37	8.28/9.00
	Rank(g/u)	286/255	191/171	135/122	67/64

precisely, the independent random variables $\{\xi_m\}_{m=1}^M$ considered here are uniformly distributed over $[-\sqrt{3}, \sqrt{3}]$.

We assume that the desired state $u_d = \sin(\pi x)\sin(\pi y)$. Unless otherwise stated, we always set the parameters $\alpha = \beta = 1$, the fractional orders $s = \gamma = 1.8$, the mean of the random input $\mathbb{E}_{d^+} = \mathbb{E}_{d^-} = 1$, the order of the TD space $p = 3$, and discretization parameter $J = (N-1)^2 = 16384$. All matrix iterations herein are terminated when the relative residual error, measured in the Frobenius norm, is reduced to $tol = 10^{-6}$. We note here that the truncation tolerance *tr unctol* should be smaller enough to guarantee the convergence of the iterative method. However, the smaller the *tru nctol* is, the more CPU time will cost. Therefore, the parameter *trunctol* should be chosen carefully when implementing the iterative method in low-rank format. In our experiments, we set $trunctol = 10^{-8}$.

We first investigate the efficiency of the MINRES preconditioner coupled with $\mathscr{P}_{E3}$ and the PPCG preconditioner coupled with $\mathscr{P}_{F3}$ compared with the traditional approaches $\mathscr{P}_{E1}$, $\mathscr{P}_{E2}$, $\mathscr{P}_{F1}$, and $\mathscr{P}_{F2}$ with different values of the Tikhonov parameter λ. More precisely, we consider the system (38) with two-dimensional (2D) random inputs characterized by (79), and we assume that $\sigma = 0.01$ and $l_2 = 2$. Noticing that the behavior of the above preconditioners does not affect by the choice of $\widehat{S}$, we employ the simplest MBP $\widehat{S} = S_M$.

Tables 1 and 2 report the total iteration counts, the total CPU times of the simulations in standard format and low-rank format, respectively. We observe that in both formats, all preconditioners behave well when $\lambda = 10^{-2}$. However, the iteration count increases significantly as λ decreases when using the preconditioner $\mathscr{P}_{E1}$ and $\mathscr{P}_{F1}$. The rest preconditioners behave robust. They maintain a relatively equal iteration count with the different value of λ. Moreover, the preconditioners $\mathscr{P}_{E3}$ and $\mathscr{P}_{F3}$ we construct tend to cost less iteration count and perform better than the traditional options. This is because the effectiveness of the iterative solver depends largely on how well the approximation can be. We also did further experiments with different values

Table 6: Comparison of iterations and CPU times (in seconds) to solve system (38) with given random inputs using standard MINRES method with $\mathscr{P}_{E3}$ and PPCG method with $\mathscr{P}_{F3}$ and S_M, S_U for $J = 16384$, $\sigma \in \{0.1,0.2,0.3,0.4\}$, and $l \in \{1, 2, 3, 4\}$.

			MINRES + $\mathscr{P}_{E3}$		PPCG + $\mathscr{P}_{F3}$	
			S_M	S_U	S_M	S_U
$\sigma = 0.1$	$l = 1, M = 15$	# iter	27	27	8	8
		CPU time	682.38	702.92	162.88	164.70
	$l = 2, M = 12$	# iter	27	25	8	7
		CPU time	287.43	270.79	66.59	59.95
	$l = 3, M = 9$	# iter	27	23	8	7
		CPU time	104.69	90.23	23.50	21.33
	$l = 4, M = 6$	# iter	27	23	8	7
		CPU time	28.24	24.32	6.22	5.63
$\sigma = 0.2$	$l = 1, M = 15$	# iter	41	37	15	13
		CPU time	1032.48	961.34	288.44	256.28
	$l = 2, M = 12$	# iter	41	37	15	13
		CPU time	436.18	400.24	118.54	105.33
	$l = 3, M = 9$	# iter	41	35	15	12
		CPU time	158.60	137.36	41.71	34.39
	$l = 4, M = 6$	# iter	39	31	14	11
		CPU time	40.76	32.82	10.35	8.42
$\sigma = 0.3$	$l = 1, M = 15$	# iter	67	59	26	23
		CPU time	1687.23	1534.70	486.24	439.89
	$l = 2, M = 12$	# iter	69	57	27	21
		CPU time	734.39	616.97	209.03	164.89
	$l = 3, M = 9$	# iter	67	53	25	19
		CPU time	258.98	208.15	67.72	52.99
	$l = 4, M = 6$	# iter	63	47	24	17
		CPU time	65.79	49.69	17.29	12.59
$\sigma = 0.4$	$l = 1, M = 15$	# iter	135	115	54	45
		CPU time	3400.25	2990.26	995.13	840.50
	$l = 2, M = 12$	# iter	141	109	55	43
		CPU time	1500.56	1178.25	414.50	329.64
	$l = 3, M = 9$	# iter	127	93	51	36
		CPU time	491.62	364.82	135.53	98.02
	$l = 4, M = 6$	# iter	111	77	44	29
		CPU time	115.56	81.40	31.11	21.11

of J, M, and p, and we obtain similar observations. Specially, the results show that the iteration count keeps the same for different parameters J, M, and p with preconditioners $\mathscr{P}_{E3}$ and $\mathscr{P}_{F3}$, which coincides with the spectrum analysis Theorems 4 and 5.

Next, we demonstrate how the standard derivation σ and the number of the truncated term M influence the behavior of the solvers. Notice that the truncated term M is usually based on the speed of decay of the eigenvalues since $\sum_{m=1}^{\infty}\lambda_m = |D|$. We consider the covariance function $C_2(\mathbf{x}_1, \mathbf{x}_2)$ with different length l_2. We report the number of the stochastic discretization parameter P and the parameter $(\sum_{m=1}^{M}\lambda_m)/|D|$ in Table 3 with different variant tuples (l_2, M). We use the MINRES preconditioner $\mathscr{P}_{E3}$ and the PPCG preconditioner $\mathscr{P}_{F3}$ coupled with the approximation S_M.

It is first indeed evident from Tables 4 and 5 that the low-rank approach is more efficient for large-scale simulations and small variance problems. This can be explained by the fact that the efficiency of the low-rank format method mainly depends on the ranks of the numerical solutions. The smaller the rank (compared with P) is, the better the performance is. The ranks of G and U are reported in the tables denoted by rank(g/u). It is second observed from Tables 4 and 5 that the iteration count also increases as the increase of σ. This is caused by that the MBP S_M cannot approximate S well when σ is large, which means the off-diagonal blocks of S become more significant.

Finally, we study the behavior of the preconditioners S_M and S_U. Notice that the mean we considered here is the constant 1. Table 6 reports the total iteration counts and the total CPU times of solving the system (38) with given random inputs with different σ and different correlation length l_2. We can see that S_U can reduce the iteration count compared with S_M, especially for large variance problems.

7. Conclusions

In this paper, we derived the theory analysis and efficient numerical algorithms for the stochastic optimal control problems constrained by fractional elliptic equations. We presented the proof of the uniqueness and existence of the optimal control problems, and we deduced the stochastic optimality system. We applied the stochastic Galerkin spectral methods (SGSMs) to the numerical approximation.

To solve the large coupled system resulted from the SGSMs, we adopt the MINRES and PPCG methods in both standard and low-rank format. Specially, to handle the system with different value of the variance, we consider the mean-based preconditioner (MBP) and Ullmann preconditioner (UP) to approximate the stiffness matrix S. We can see that the MBP achieves a better behavior when the standard derivation σ is small and UP can reduce the iteration count when the standard derivation σ is large.

More importantly, with spectral approach in spatial space, we developed more accurate and efficient preconditioners $\mathscr{P}_{E3}$ and $\mathscr{P}_{F3}$ with respect to the above two approximations (MBP and UP) by the matrix decomposition method and the virtual variable method for both MINRES method and PPCG method. These preconditioners are proved to achieve better performance than the traditional approach.

Finally, let us mention that the MINRES method can be applied to the more general case only if the derived system is symmetric, and it is the most commonly used method when handling the large saddle-point system. However, we can see that the PPCG method is more suitable for our problems. The PPCG method can reduce the iteration count and CPU time effectively compared with the MINRES method.

Data Availability

No data were used to support this study.

Conflicts of Interest

The authors declare that they have no conflicts of interest.

Acknowledgments

This paper is supported by the Guangdong Basic and Applied Basic Research Foundation (No. 2020B1515310006).

References

[1] T. M. Atanackovic, S. Pilipovic, B. Stankovic, and D. Zorica, *Fractional Calculus with Applications in Mechanics: Wave Propagation, Impact and Variational Principles*, John Wiley & Sons, 2014.

[2] S. B. Yuste and K. Lindenberg, "Subdiffusion-limited reactions," *Chemical Physics*, vol. 284, no. 1-2, pp. 169–180, 2002.

[3] E. Scalas, R. Goreno, and F. Mainardi, "Fractional calculus and continuous-time finance," *Physica A: Statistical Mechanics and its Applications*, vol. 284, no. 1-4, pp. 376–384, 2000.

[4] P. Gatto and J. S. Hesthaven, "Numerical approximation of the fractional laplacian via hp-finite elements, with an application to image denoising," *Journal of Scientific Computing*, vol. 65, no. 1, pp. 249–270, 2015.

[5] O. P. Agrawal, "A general formulation and solution scheme for fractional optimal control problems," *Nonlinear Dynamics*, vol. 38, no. 1-4, pp. 323–337, 2004.

[6] H. Antil and E. Otarola, "A fem for an optimal control problem of fractional powers of elliptic operators," *SIAM Journal on Control and Optimization*, vol. 53, no. 6, pp. 3432–3456, 2015.

[7] H. Antil, E. Otarola, and A. J. Salgado, "A space-time fractional optimal control problem: analysis and discretization," *SIAM Journal on Control and Optimization*, vol. 54, no. 3, pp. 1295–1328, 2016.

[8] S. Dolgov, J. W. Pearson, D. V. Savostyanov, and M. Stoll, "Fast tensor product solvers for optimization problems with fractional differential equations as constraints," *Applied Mathematics and Computation*, vol. 273, pp. 604–623, 2016.

[9] N. Du, H. Wang, and W. Liu, "A fast gradient projection method for a constrained fractional optimal control," *Computing*, vol. 68, no. 1, pp. 1–20, 2016.

[10] H. Tiesler, R. M. Kirby, D. Xiu, and T. Preusser, "Stochastic collocation for optimal control problems with stochastic PDE constraints," *SIAM Journal on Control and Optimization*, vol. 50, no. 5, pp. 2659–2682, 2012.

[11] P. Chen and A. Quarteroni, "Weighted reduced basis method for stochastic optimal control problems with elliptic pde constraint," *SIAM/ASA Journal on Uncertainty Quantication*, vol. 2, no. 1, pp. 364–396, 2014.

[12] K. A. Cliffe, M. B. Giles, R. Scheichl, and A. L. Teckentrup, "Multilevel monte carlo methods and applications to elliptic pdes with random coefficients," *Computing and Visualization in Science*, vol. 14, no. 1, pp. 3–15, 2011.

[13] D. Xiu and J. Shen, "An efficient spectral method for acoustic scattering from rough surfaces," *Communications in Computational Physics*, vol. 2, no. 1, pp. 54–72, 2007.

[14] D. Xiu and G. Karniadakis, "The Wiener–Askey polynomial chaos for stochastic differential equations," *Computing*, vol. 24, no. 2, pp. 619–644, 2002.

[15] I. Babuska, R. Tempone, and G. E. Zouraris, "Galerkin finite element approximations of stochastic elliptic partial differential equations," *SIAM Journal on Numerical Analysis*, vol. 42, no. 2, pp. 800–825, 2004.

[16] I. Babuška, F. Nobile, and R. Tempone, "A stochastic collocation method for elliptic partial differential equations with random input data," *SIAM Journal on Numerical Analysis*, vol. 45, no. 3, pp. 1005–1034, 2007.

[17] Z. Mao and J. Shen, "Efficient spectral-Galerkin methods for fractional partial differential equations with variable coefficients," *Journal of Computational Physics*, vol. 307, pp. 243–261, 2016.

[18] R. G. Ghanem and P. D. Spanos, *Stochastic finite elements: a spectral approach*, Springer- Verlag, New York, 2003.

[19] J. L. Lions, *Optimal Control of Systems Governed by Partial Differential Equations*, Springer, Berlin, 1971.

[20] F. Tröltzsch and J. Sprekels, "Optimal control of partial differential equations: theory, methods, and applications," *Graduate studies in mathematics*, vol. 112, 2010.

[21] P. Chen, A. Quarteroni, and G. Rozza, "Multilevel and weighted reduced basis method for stochastic optimal control

Hindawi
Journal of Sensors
Volume 2023, Article ID 9878123, 1 page
https://doi.org/10.1155/2023/9878123

Retraction

Retracted: Research on Intelligent Bodybuilding System Based on Machine Learning

Journal of Sensors

Received 19 September 2023; Accepted 19 September 2023; Published 20 September 2023

This article has been retracted by Hindawi following an investigation undertaken by the publisher [1]. This investigation has uncovered evidence of one or more of the following indicators of systematic manipulation of the publication process:

(1) Discrepancies in scope
(2) Discrepancies in the description of the research reported
(3) Discrepancies between the availability of data and the research described
(4) Inappropriate citations
(5) Incoherent, meaningless and/or irrelevant content included in the article
(6) Peer-review manipulation

The presence of these indicators undermines our confidence in the integrity of the article's content and we cannot, therefore, vouch for its reliability. Please note that this notice is intended solely to alert readers that the content of this article is unreliable. We have not investigated whether authors were aware of or involved in the systematic manipulation of the publication process.

Wiley and Hindawi regrets that the usual quality checks did not identify these issues before publication and have since put additional measures in place to safeguard research integrity.

We wish to credit our own Research Integrity and Research Publishing teams and anonymous and named external researchers and research integrity experts for contributing to this investigation.

The corresponding author, as the representative of all authors, has been given the opportunity to register their agreement or disagreement to this retraction. We have kept a record of any response received.

References

[1] C. Chen, "Research on Intelligent Bodybuilding System Based on Machine Learning," *Journal of Sensors*, vol. 2022, Article ID 6293856, 8 pages, 2022.

Hindawi
Journal of Sensors
Volume 2022, Article ID 6293856, 8 pages
https://doi.org/10.1155/2022/6293856

Research Article

Research on Intelligent Bodybuilding System Based on Machine Learning

Chen Chen

Sports and Military Training Department, Zhejiang A&F University, Hangzhou, 311300 Zhejiang, China

Correspondence should be addressed to Chen Chen; 20060008@zafu.edu.cn

Received 25 November 2021; Accepted 29 March 2022; Published 5 May 2022

Academic Editor: Abdellah Touhafi

In recent years, people's health is facing many challenges as their workload is increasing and their lives are becoming more and more stressful. In this context, healthy living has become a topic of concern and more and more people are choosing to promote their bodies through fitness. To address these existing problems in action recognition research, this paper designs and implements a machine learning-based intelligent fitness system to monitor three important parameters in physical activity: the type of action, the number of actions, and the period of action. Through the action recognition algorithm and the period calculation method, the three important parameters of action type, number of actions, and action period are calculated to generate a more comprehensive description of the limb actions. Experiments are conducted to show that the proposed deep neural network learns well on small datasets, achieving 97.61% action recognition accuracy and SVM achieving over 96% recognition accuracy.

1. Introduction

Targeted physical activity is an important and effective improvement and treatment for these conditions [1–4]. For athletes, injuries occur during sport, and timely and appropriate rehabilitation is an important part of ensuring that athletes recover and return to play. Physical rehabilitation is also an important part of treatment for patients whose physical activity is affected by illnesses such as strokes [5]. In addition, with the increase in work intensity and the explosion of information, people are often working long hours and at high intensity, which has led to a decline in physical function and an increase in obesity, directly affecting physical health, and this highlights the importance of timely fitness and exercise [6].

However, effective fitness and exercise need to follow a certain scientific approach; otherwise, not only will it fail to achieve the purpose of strengthening the body and treating diseases, but it may even backfire and cause secondary damage to the body. For example, many athletes train with repetitive loads for long periods of time in order to improve their performance, and in a study by Hussain et al. [7], they found that repetitive activities and unreasonable technical movements for long periods of time are likely to cause sports injuries. In addition, some athletes who undergo firmness band reconstruction perform low-intensity recovery procedures during postoperative rehabilitation, but studies have shown that performing high-intensity recovery procedures is more beneficial for later functional performance. In a survey of sports injuries among university students, Moreno-Guerrero et al. [8] found that over 40% of students suffered injuries due to incorrect technical movements or lack of knowledge about them.

A wireless body area network consisting of multiple sensors can assist doctors in the initial remote consultation of patients [9]. And artificial intelligence technologies such as machine learning and deep learning have not only given smarter performance to the network's edge devices but have also made progress in aiding the diagnosis of difficult diseases. In areas such as personal fitness and healthcare, there is also a growing use of microelectromechanical system-based posture modules (containing accelerometers, gyroscopes, magnetometers, etc.) to recognise and monitor the body's movements and to share them in social networks or

sports sharing with others in social networks or sports communities [10].

It is thus clear that technological advances have made it possible to assist sports and exercise with electronic technology, and it is therefore necessary to propose a multiuser-oriented exercise monitoring system [11]. It refers to the ease with which instructors can monitor the physical movements of exercise participants, thus improving to a certain extent the difficulty of accessing professional guidance in the physical ridge exercise scenario. Such a system can be deployed in places such as gyms or body curfew classes, where the instructor can easily understand each participant's exercise, including whether the movement categories are correct and whether the number and period of movements are appropriate [12].

Consider a rehabilitation centre scenario: two athletes who have undergone surgery for an Achilles tendon rupture are now recovering. Postsurgical weight-bearing training is crucial for the recovery of the Achilles tendon, so they are rehabilitating with centrifugal contractions of the Achilles tendon [13]. At the same time, several other elderly people with mild strokes are undergoing periodic gait training of the lower limbs [14]. In addition, there were people using dumbbells for upper limb strength training in the same building. As the limbs are equipped with wearable devices, each of their limb movements is recorded and uploaded to the data centre via a wireless LAN. The medical staff can clearly see on the screen what type of exercise each person is performing and whether they are moving too fast or too many times. The medical staff will give timely guidance on inappropriate movements, thus ensuring their safety and improving the effectiveness of their workouts [15]. As can be seen, the existence of such a system makes it possible to monitor exercise for multiple users, making it easier for people to access professional exercise guidance when participating in physical exercise, thus improving the professionalism of sports and exercise participants, effectively avoiding sports injuries, and improving the effectiveness of physical exercise.

In view of this, it is of practical importance and scientific and theoretical value to propose and develop a multiuser motion monitoring system with the abovementioned features.

2. Related Work

Human motion recognition is an important application of modern computer technology. The aim of motion recognition is to enable computers to perceive and understand the type of human activity, leading to related applications such as gesture control in human-computer interaction, fitness data tracking in wearable devices, and physical games in entertainment.

Research on human movement recognition can be further subdivided into two categories, namely, human activity recognition and body movement recognition [16]. Human activity recognition is a macrolevel study of how to distinguish between the daily activity statuses of humans, such as walking, sitting, running, lying down, cycling, and walking up and down the stairs. On the other hand, by combining it with the IoT and multimodal sensing technologies (inferring the user's type of activity from a combination of sound, movement, and expression), human activity recognition can be used for intelligent healthcare, such as automatically locating and sending distress messages to healthcare professionals when an elderly person is recognised to have fallen [17]. The user can perform specific actions to interact with the computer system and trigger corresponding events, e.g., Wang [18] used recognition algorithms based on symbolic sequences and template matching to recognise seven gestures, including up, down, left, right, drawing a circle, etc. In addition, the recognition of specific body movements can be applied to the field of sport to record and analyse sport data and improve movement postures or as signal input in entertainment and gaming-related scenarios. For example, Cao et al. [19] used a 3-axis accelerometer built into a mobile phone to recognise three types of strokes in tennis and applied it to a tennis video game.

In terms of recognition algorithms, classical machine learning models are currently the most commonly used. For example, Wang et al. [20] used SVM and artificial neural nets as classifiers to achieve the recognition of six upper limb movements by fusing several MEMS posture modules. Martin and Gavey [21] used SVM and BP neural network to achieve the recognition of horizontal, vertical, diagonal, and closed lines drawn on the human arm. Slavityak [22] used a similarity matching model based on least squares to achieve the classification of six dumbbell movements.

However, there are few applications of deep learning techniques in the field of MEMS-based emotion recognition. Compared with classical machine learning algorithms, deep learning algorithms can better understand inter-interval sequence data and do not require tedious feature extraction and feature selection, but they require a high amount of training data. Convolutional neural network (CNN) and long short-term memory (LSTM) are two typical deep learning models. Convolutional neural networks were first proposed by [12, 15, 23] and used for image recognition, and later, 1D CNNs were also used for natural language processing (NLP). LSTM is a variant of recurrent neural networks, which are suitable for processing time series signals and have been widely used in speech recognition, stock prediction, etc. However, deep learning algorithms have not yet been applied to MEMS-based body movement recognition and have only been used in the field of HAR.

2.1. Machine Learning-Based Action Recognition. This section begins with an introduction to action recognition, where the data from the pose sensor are analysed using a classification model to identify the patterns embedded in the data and lose the classification of the actions. For the implementation of action recognition, two models are used, namely, SVM and deep neural networks [24]. For scenarios where the computing power is weak and the requirement for real-time performance is high, a simple and low computational model such as SVM is used for action recognition; for scenarios where the computing power is strong or the

type of action is complex, a complex and computationally intensive deep neural network is used for action recognition.

2.2. Motion Recognition Algorithms. There are two key steps in SVM-based action recognition, namely, feature selection, feature extraction, and parameter optimisation, of which feature selection has the most significant impact on recognition results. Feature selection is a method of data dimensionality reduction [25]. For most practical applications of machine learning, the features of the original data in the original space may be redundant or noisy, and the features of the data are stacked together in a way that cannot be easily processed directly by the algorithm or affects the speed of computation, so feature extraction is required. Feature extraction is the transformation of the original data into a new space so that the patterns implied by the data can be more easily identified. Generally, the dimensionality of the extracted features is much smaller than that of the original data, so feature extraction can significantly speed up the algorithm. However, some of the original information are inevitably lost in the feature extraction process. If the information lost is not significant for the classification result, then this effect can be ignored. Otherwise, the loss of important information will significantly reduce the classification accuracy [26]. The penalty factor affects how much importance the SVM places on outliers in the data, and different penalty factors will produce different classification bounds. In the process of parameter optimisation, it is necessary to experiment with different kernel functions and penalty coefficients depending on the type of data in order to achieve the best classification results [27].

The approach to feature extraction varies from application to application. For example, physically meaningful elements of an image are often used as features in image processing, including geometric features, texture features, Gabor features, and statistical features. In NLP, the feature extraction process often ignores the order and syntax of words and treats them as a collection of words that are independent of each other. In addition, principal component analysis (PCA), linear discriminant analysis (LDA), and singular value decomposition (SVD) are all common feature extraction algorithms [28].

In this paper, four statistical features are extracted from the limb movement data, including the maximum value, minimum value, standard deviation, and mean value. The original signal generated by the posture sensor is a time series signal, for which the most common feature extraction method is to calculate the statistical values. The maximum and minimum values represent the limits of the amplitude of the action and reflect the range of the action, which can vary significantly from one action to another [29]. The mean value reflects the overall state of the movement and can also be associated with the type of movement. For example, for some movements, the limb is always moving horizontally, so the mean value of acceleration along the limb direction axis is always around zero; for other movements, the limb is always moving in the vertical plane, so the mean value of acceleration along the limb direction axis is around 1. The more vigorous the movement, the larger the standard deviation, and the smoother the movement, the smaller the standard deviation. As showed in Figure 1, by calculating these four statistics for each axis of the sensor output, a total of 36 statistical features were obtained.

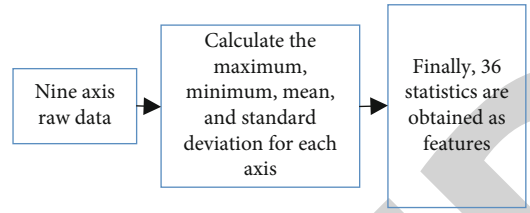

Figure 1: Feature extraction method.

2.3. Deep Learning-Based Action Recognition. The main difficulty in deep learning-based action recognition is how to train the network to converge using small datasets. For limb movement recognition, the sample size of a white-built database is much smaller than the currently popular publicly available data, and deep learning generally requires a high sample size, so it is difficult to learn enough information on a small dataset. There are two ways to solve this problem: first is the proper data preprocessing to ensure that the input requirements of the net terminal are met and no information is lost and second is the designing a suitable structure of the net terminal so that it can explore the information implied in the data while reducing the sample size requirement.

There are many different types of deep learning models, including CNN, RNN, LSTM, self-encoders (AE), restricted Boltzmann machines (RBM), and generative adversarial networks (GAN). Different network structures are suitable for different problems, e.g., CNN is mostly used for image processing, long- and short-term memory networks for time series processing, self-encoders for clustering and data compression, and generative adversarial networks for image conversion. Typically, deep learning models require large datasets to be trained. Large public datasets are usually published by research institutions, but no large-scale datasets have been published in the field of limb movement recognition, which is one of the reasons why deep learning is difficult to apply to MEMS-based limb movement recognition.

In this paper, a combined network model based on 1D CNN and LSTM is developed, which combines the features of both and can be well used to process time series signals from attitude sensors with low data volume requirements [30].

The structure of the network and the way it preprocesses data is shown in Figure 2. The network has two one-dimensional convolutional layers, a maximum pooling layer, a LSTM layer, and an output layer. Convolutional and LSTM layers each have 32 neurons, and P1-P7 represent the probability that the current input action data belongs to a certain category. The input to the network is a matrix with two dimensions, the time step and the sample wood dimension, respectively. As mentioned above, each of the sample logs connects the first and last nine axes of the original data. The time step corresponds to the value sampled by the sensor at a given moment in time. In addition, the total length of

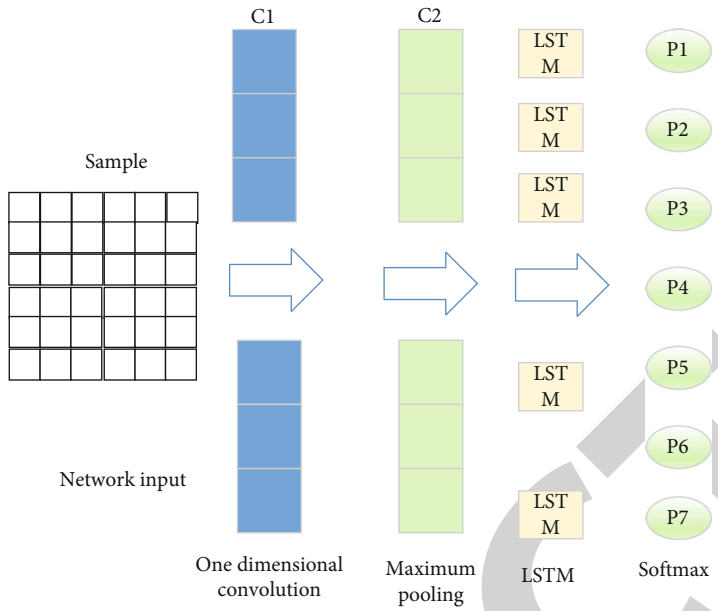

Figure 2: Structure of the network and data preprocessing process.

each data sample varies as the duration of each action recorded by the sensor varies. For programming reasons, zero values can be used in the application to fill each sample with the same length [31].

2.4. Movement Count and Cycle Calculation Method. The raw data output from the posture sensor consists of acceleration, angular velocity, and Euler angles in the X, Y, and Z axes, the sensitive axis being the one that best characterises the movement of the limb. The sensitive axis is the one that best characterises the movement state of the limb among the nine axes of data. For each movement, there is a plane of movement, with some movements mainly in the X plane and others in the Z plane.

The reason for this is twofold. Firstly, some of the nine axes often show jumps in the waveform for a raw signal. This phenomenon is concentrated in the three angular axes. For example, suppose the angle of an axis starts at 0 and as it increases to +180° and continues to increase, the angle suddenly changes to -180°. This phenomenon is caused by the attitude module's own way of calculating angles, but it can have a negative effect on the period calculation, so the three angular axes should be excluded from the selection of the sensitive axes [32]. Next, the sensitive axes are selected as follows:

$$A = [A_1, A_2, \cdots, A_6]^{\mathrm{T}},$$

$$S_i^2 = \frac{1}{m}\left[\left(A_{i1} - \bar{A}_i\right)^2 + \left(A_{22} - \bar{A}_3\right)^2 + \cdots + \left(A_{im} - \bar{A}_i\right)^2\right], \quad (1)$$

$$i' = \arg\max S_1^2,$$

where A_i is the vector representation of the i-th axis data in the original data and m is the number of data sampling points, i.e., the length of the data. The method calculates the variance of each axis, and the axis with the highest variance has the serial number $\bar{A}_i$, so that the i'rd axis is the selected sensitive axis. By performing the sensitive axis selection, the counting and periodic calculation method only needs to be performed on one axis, which not only increases the efficiency of the calculation but also allows for a higher accuracy rate. For the same type of movement, the sensitive axis is usually fixed as long as the sensor is worn in the same way. Therefore, after the initial selection of the sensitive axis, the sensitive axis can be tied to the type of action, and in subsequent actions, the sensitive axis can be determined directly from the tied relationship between the sensitive axis and the type of action, thus reducing the amount of system operations.

Suppose a signal $\psi(t) \in L^2(R)$ with a Fourier variation of $\widehat{\psi}(\omega)$. When $\widehat{\psi}(\omega)$ satisfies the condition

$$C_\psi = \int_R \frac{\left|\widehat{\psi}(\omega)\right|^2}{|\omega|} d\omega < \infty, \quad (2)$$

$\psi(t)$ is known as a wavelet basis. The wavelet basis used in this paper is a cgau wavelet, which is a Gauss wavelet in complex form. When the wavelet basis $\psi(t)$ is telescoped or translated, we can obtain a wavelet sequence, namely,

$$\psi_{(a,b)}(t) = \frac{1}{\sqrt{|a|}}\psi\left(\frac{t-b}{a}\right), \quad a, b \in R, a \neq 0, \quad (3)$$

where a is the scale factor of the wavelet transform and b is the translation factor.

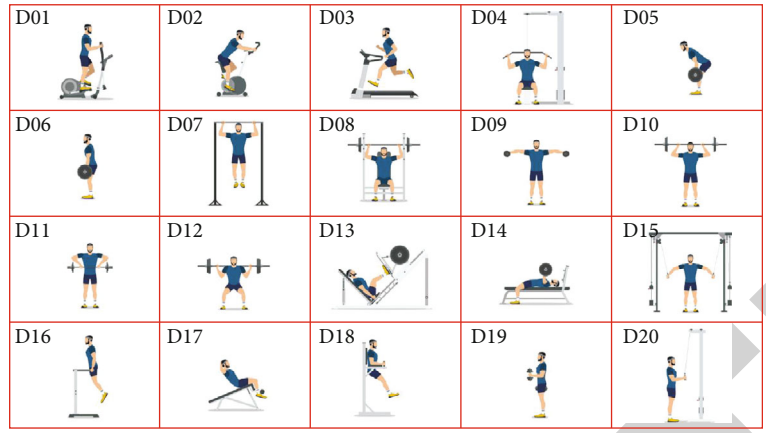

Figure 3: Diagram of the seven body movements.

For the selected key axis signal 111, the continuous wavelet transform is as follows:

$$W_f(a,b) \le f, \psi_{a,b} \ge |a|^{-1/2} \int_R f(t)\psi\left(\frac{t-b}{a}\right)dt. \quad (4)$$

Inverse conversion is calculated as follows:

$$f(t) = \frac{1}{C_\psi}\int_{-\infty}^{\infty}\int_{-\infty}^{\infty}\frac{1}{a^2}W_f(a,b)\psi\left(\frac{t-b}{a}\right)dadb. \quad (5)$$

After the wavelet transform of the key axis signal, the wavelet coefficient matrix can be obtained $A_{m\times n}$, where m denotes the number of layers of the wavelet transform and n denotes the number of sampling points, i.e., the length of the signal.

$$a_{ij} \in A_{m\times n}, 0 < i \le m, 0 < j \le n, \quad i \in N, j \in N. \quad (6)$$

The wavelet energy matrix P is as follows:

$$P = \begin{bmatrix} a_{11}^2 & a_{12}^2 & \cdots & a_{1n}^2 \\ a_{21}^2 & a_{22}^2 & \cdots & a_{2n}^2 \\ \vdots & \vdots & \ddots & \vdots \\ a_{m1}^2 & a_{m2}^2 & \cdots & a_{mn}^2 \end{bmatrix}, \quad (7)$$

where the elements in the energy matrix represent the amplitude of each harmonic component.

Next, use the following vector:

$$C = \left\{c_1, \cdots, c_m, c_l = \underset{k}{\operatorname{argmax}}(p_{lk})\right\} 1 \le l \le m, 1 \le k \le n, \quad l, k \in N. \quad (8)$$

This means that the position of the component of maximum energy in each harmonic component occurs at each moment, i.e., the position of the fundamental frequency of the sensor signal, i.e., the wavelet scale, where p_l denotes the kth row of the matrix P and p_{lk} denotes the kth element of the p_lrd row.

Table 1: Accuracy of different preprocessing methods.

Data preprocessing method of deep neural network	Motion recognition accuracy
LDA dimensionality reduction	87.79%
Data end to end	97.61%

Each wavelet scale in the wavelet transforms corresponds to a frequency vector F, which is determined by both the number of layers and the scale of the specific wavelet transform. The vector T, which reflects the period of the action at each sampling moment, can be expressed as follows:

$$T = \left[\frac{1}{F_{c_1}}, \frac{1}{F_{c_2}}, \cdots, \frac{1}{F_{c_m}}\right]. \quad (9)$$

The period of each action can be obtained by calculating the difference between adjacent elements in this list. Furthermore, another way to calculate this is to bring the list T into Equation (9), thus obtaining the vector T':

$$T' = \left[T_{L_1}, T_{L_2}, \cdots, T_{L_d}\right]. \quad (10)$$

This vector represents the period of each action, where d is the length of the list Z, i.e., the number of actions, and the element T_i in T' represents the i-th element of the vector T.

3. Experimental Procedure and Analysis of Results

In the previous presentation of this paper, the hardware and software design scheme, the data preprocessing, and identification methods as well as the counting and periodic calculation methods for the actions of multiuser action monitoring system were explained. Next, the relevant experimental procedure and the experimental results are presented [2].

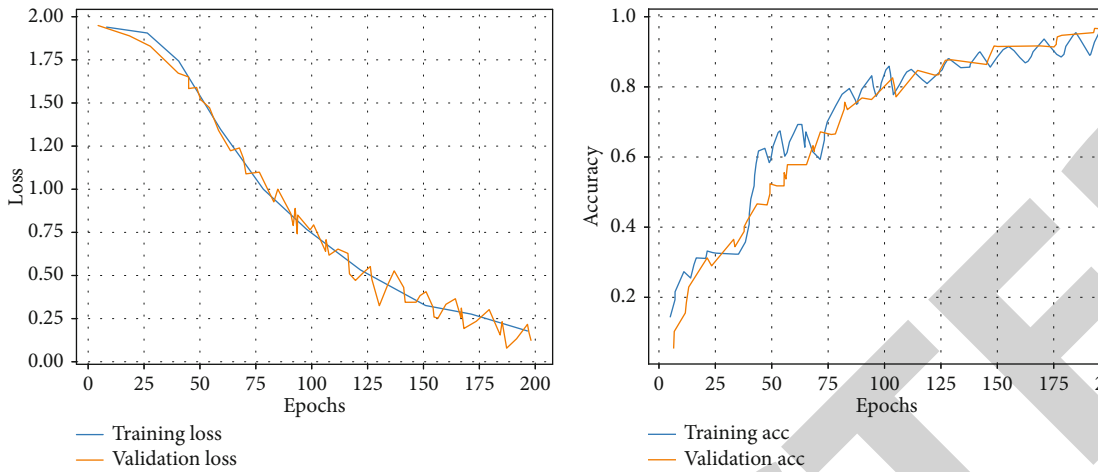

(a) Variation in training loss and validation loss

(b) Changes in training accuracy and validation accuracy

Figure 4: Loss and accuracy change curve of the network during training.

3.1. Experimental Setup. In this paper, body movements were selected for identification, as showed in Figure 3. These included four types of dumbbell movements and three types of leg exercises, namely, the dumbbell curling, side lifting, dumbbell shoulder press, dumbbell flying, sitting posture calf raising, standing posture calf raising, and heel raising. [14].

Of the data, this study used a self-constructed dataset, which consisted of a total of 420 samples. A total of six participants, three males and three females, contributed to the dataset, each providing a sample of 70 data items, with 10 items for each type of movement. Only one stance acquisition module was worn by each participant when recording the data. For the dumbbell movements, the posture acquisition module was worn at the wrist and the lower limb movements; the posture acquisition module was worn at the ankle. The weight of the dumbbell used in the dumbbell movement was 25 kg. 80% of the total samples were used as the training set and 20% as the test set. For the deep learning model, 20% of the training set was used as the validation set.

3.2. Motion Recognition Experiments. For deep neural networks, one type of preprocessing is to join the first and last nine axes, as described in Section 3 of this paper, and the other is to use linear discriminant analysis (LDA) to reduce their dimensionality.

The results of the comparison experiments between the two processing methods are shown in Table 1, which indicate that linear discriminant analysis is less accurate when used for action recognition. Figure 4 shows the trend of accuracy and loss in the training of the deep neural network. In Figure 4(a), we can see that the training and validation losses continue to decrease until the 200th round of training. Figure 4(b) represents changes in training accuracy and validation accuracy, during which the validation and training losses are basically the same.

In order to compare the effectiveness of different classification models, this paper next conducts experiments using different models. In addition to SVM and deep neural networks, a multilayer perceptron and least squares based on similarity matching model proposed by Akpan and Aldabbagh [12] was chosen as the two comparison algorithms in this paper. The final accuracy of each model was obtained through experiments on the test set. The multilayer perceptron is a representative forward neural network, and its use as a comparison algorithm can effectively set an accurate reference. As the number of layers implied by a multilayer perceptron is generally small, it is slow and ineffective on higher dimensional datasets, while the raw pose sensor data can often be thousands to tens of thousands of dimensions, so dimensionality reduction is required to feed the data into a multilayer perceptron. In this paper, the same feature extraction method as SVM is used, and the same 36 statistics are selected as features to compare the performance difference between the two on the same dataset.

Another comparison algorithm is the least squares-based similarity matching algorithm proposed by Akpan and Aldabbagh [12]. This method first performs operations such as acceleration decomposition and period normalisation on the data and then builds a feature database and judges the action category based on the similarity between the test sample and the standard action in the database during classification; the details are shown in Figure 5.

From the above experimental results, it can be seen that both the deep learning model and the SVM achieved recognition accuracies above 96%, which are higher than the comparison algorithms, while the multilayer perceptron achieved the lowest accuracy among the four models. The deep learning model achieved a recognition accuracy of 97.61%, and the confusion matrix showed that only two dumbbell shoulder presses were misconceived as dumbbell side planks in the 84 test samples, indicating that the deep learning model proposed in this paper can be used well for small datasets and action recognition. The confusion matrix of the SVM shows that the method is prone to misclassification of the two types of leg movements because the two types of movements are similar and the SVM cannot perfectly separate the two types of movements based on the features from a single sensor alone.

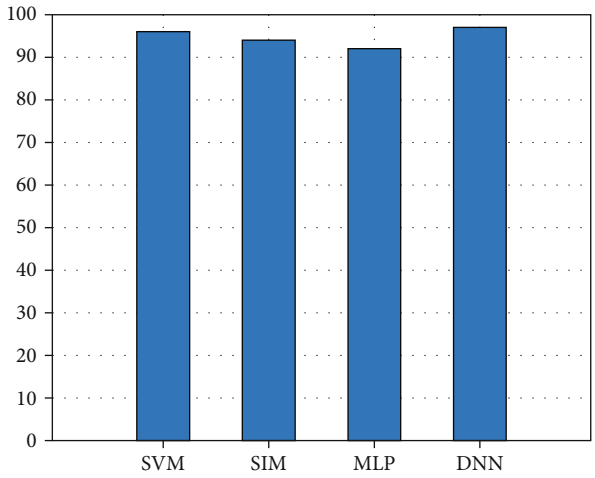

Figure 5: Action recognition accuracy of the four algorithms.

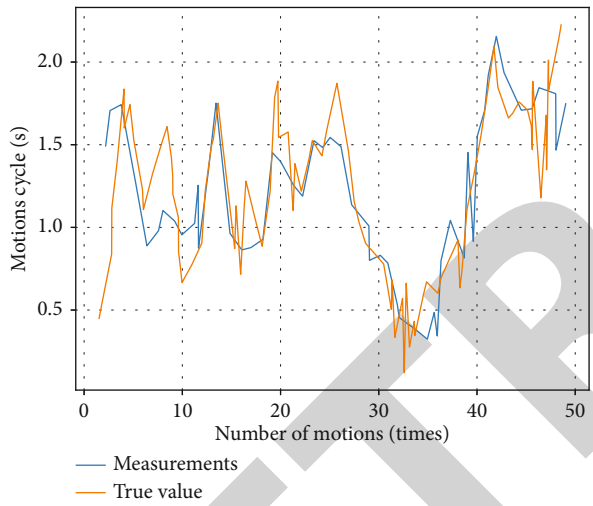

Figure 6: Action count and cycle calculation results.

3.3. Motion Counting and Cycle Calculation Experiments. The purpose of the action counting and cycle calculation experiment is to verify the accuracy of the counts and cycle calculations. For this experiment, the objectivity of the results is influenced to a large extent by the number of trials. In particular, the action counts and the validity of the analysis method can only be demonstrated by ensuring that the results are accurate for a sufficient number of trials. In this experiment, 50 repetitions were performed, a value which is much higher than the number of time required for a single exercise and which verifies the accuracy of the algorithm. In addition to recording the movements using the sensors, a stopwatch was used to time the cycles of each movement as a practical standard. The exact cycle counted and actual values for the 50 movements in this experiment are shown in Figure 6.

Firstly, as can be seen from the length of the two curves in the graph, the algorithm's action counts are very accurate, with the count statistics of 50 times agreeing exactly with the actual values. Secondly, the overall fit of the two curves in the graph is good, with an average error of only 0.08 s and an average error rate of 4.03%. The maximum error in the calculation is 0.25 s, with a maximum error rate of 13.5%, occurring only at the end points of the curves. Therefore, this experiment proves that the overall effect of the over-zero detection and wavelet analysis method is good, and that the action counting and cycle calculation can be achieved more accurately even with a high number of actions.

4. Conclusions

This paper presents two types of algorithms for motion monitoring, namely, motion recognition algorithms and cycle computation algorithms. Firstly, two types of active recognition models are introduced, namely, SVM and deep neural networks. For SVM, the feature range is first introduced, then the county body method for feature extraction and feature recognition is introduced, and finally, the classification principle and the selection of key parameters for SVM are introduced. For deep neural networks, the purpose of data preprocessing and the specific ways are introduced first, then the common types of deep networks and their uses are introduced, then the characteristics of 1D CNN and LSTM are analysed and why these two types of networks are chosen to build the classification model are introduced, and the accuracy of action recognition reaches 97.61%, and the accuracy of support vector machine recognition reaches more than 96%.

Data Availability

The raw data supporting the conclusions of this article will be made available by the author, without undue reservation.

Conflicts of Interest

The author declared that there are no conflicts of interest regarding this work.

References

[1] B. Yong, Z. Xu, X. Wang et al., "IoT-based intelligent fitness system," *Journal of Parallel and Distributed Computing*, vol. 118, pp. 14–21, 2018.

[2] I. García-Magariño, R. Muttukrishnan, and J. Lloret, "Human-centric AI for trustworthy IoT systems with explainable multilayer perceptrons," *IEEE Access*, vol. 7, pp. 125562–125574, 2019.

[3] W. G. de Oliveira Junior, J. M. de Oliveira, R. Munoz, and V. H. C. de Albuquerque, "A proposal for Internet of Smart Home Things based on BCI system to aid patients with amyotrophic lateral sclerosis," *Neural Computing and Applications*, vol. 32, no. 15, pp. 11007–11017, 2020.

[4] J. A. Kim and J. Jeong, "Smart warehouse management system utilizing IoT-based autonomous mobile robot for SME manufacturing factory," *The Journal of the Institute of Internet, Broadcasting and Communication*, vol. 18, no. 5, pp. 237–244, 2018.

[5] L. Wang, C. Zhang, Q. Chen et al., "A communication strategy of proactive nodes based on loop theorem in wireless sensor

Hindawi
Journal of Sensors
Volume 2023, Article ID 9858401, 1 page
https://doi.org/10.1155/2023/9858401

Retraction

Retracted: Research on Urban Fringe Rural Design Based on Correlation Analysis of Human-Land Relationship: Taking Xiananshan Village as an Example

Journal of Sensors

Received 19 September 2023; Accepted 19 September 2023; Published 20 September 2023

This article has been retracted by Hindawi following an investigation undertaken by the publisher [1]. This investigation has uncovered evidence of one or more of the following indicators of systematic manipulation of the publication process:

(1) Discrepancies in scope
(2) Discrepancies in the description of the research reported
(3) Discrepancies between the availability of data and the research described
(4) Inappropriate citations
(5) Incoherent, meaningless and/or irrelevant content included in the article
(6) Peer-review manipulation

The presence of these indicators undermines our confidence in the integrity of the article's content and we cannot, therefore, vouch for its reliability. Please note that this notice is intended solely to alert readers that the content of this article is unreliable. We have not investigated whether authors were aware of or involved in the systematic manipulation of the publication process.

Wiley and Hindawi regrets that the usual quality checks did not identify these issues before publication and have since put additional measures in place to safeguard research integrity.

We wish to credit our own Research Integrity and Research Publishing teams and anonymous and named external researchers and research integrity experts for contributing to this investigation.

The corresponding author, as the representative of all authors, has been given the opportunity to register their agreement or disagreement to this retraction. We have kept a record of any response received.

References

[1] D. Zhou, "Research on Urban Fringe Rural Design Based on Correlation Analysis of Human-Land Relationship: Taking Xiananshan Village as an Example," *Journal of Sensors*, vol. 2022, Article ID 4938311, 11 pages, 2022.

Hindawi
Journal of Sensors
Volume 2022, Article ID 4938311, 11 pages
https://doi.org/10.1155/2022/4938311

Research Article

Research on Urban Fringe Rural Design Based on Correlation Analysis of Human-Land Relationship: Taking Xiananshan Village as an Example

Donghong Zhou

School of Design and Art, China Academy of Art, Hangzhou 310000 Zhejiang, China

Correspondence should be addressed to Donghong Zhou; 0106018@caa.edu.cn

Received 22 November 2021; Accepted 8 March 2022; Published 25 March 2022

Academic Editor: Wei Zhang

Based on system theory and human-land relationship theory, the evolution characteristics of the habitat environment of scenic fringe rural tourism sites are summarized in three aspects, including self-organisation, periodicity, and volatility. Taking the tourism circle of Xiananshan Village in Liandu District in Lishui as an example, the spatial and temporal changes in the flow of tourism factors are taken as the main driving factors, and a dynamic model of the evolution of the habitat environment of scenic fringe rural tourism sites is constructed. The regulation process is to clarify the inner connection between the spatial and temporal patterns of rural habitat environment and the tourism development process and to seek the habitat environment of rural tourism sites on the edge of scenic areas.

1. Introduction

Scenic-edge rural tourism sites are rural tourism destinations developed on the edge of famous scenic areas and with scenic areas as their core, relying on rural-specific tourism resources and stable sources of tourists from scenic areas [1, 2]. This special type of tourism place has both the general characteristics of rural tourism places and its own uniqueness, often combining many features such as geographical spatial dependence, complementary tourism resources, shared source markets, and relatively lagging regional economy and complexity of interest subjects, becoming a key support area for coordinating integrated regional development and an important geographical support for tourism transformation and expansion of quality in core scenic areas. It is also one of the important areas of concern for human geography and tourism geography in China. With the transformation of the tourism life cycle in core scenic areas, rural tourism sites on the periphery of scenic areas have gained rapid development opportunities, but they have also triggered a series of human-land relationship crises, prompting widespread concern for the habitat of this type of area [3]. Therefore, how to deal with the potential threat of tourism development to the habitat of scenic rural tourism areas, explore the spatial and temporal characteristics and mechanisms of the evolution of the habitat of scenic rural tourism areas, and seek appropriate models for the construction of the habitat of scenic rural tourism areas has become one of the important issues facing various disciplines, including tourism science [4].

Since 2006, the comprehensive development of China's new rural construction and the upgrading and adjustment of the rural industrial structure have provided good conditions for carrying out rural habitat construction and research, and the research horizon has shifted from the evaluation and improvement of rural habitat at different spatial scales [5, 6] to the integration of multidisciplinary research, in which the planning and design [7], evolutionary laws [8], construction methods of rural habitat [9], and other issues have attracted the continuous attention of scholars. Overseas rural habitats have mainly focused on the theoretical system of rural settlements [10], the evolution and mechanism of rural habitats [10, 11], and the sustainable development of rural habitats [12]. However, there is still room for further research on the habitat environment of this unique geographical unit, which is the edge of the scenic

area. The spatial and temporal evolution characteristics and mechanisms of the habitat environment of this type of area are obviously unique, involving many disciplines such as tourism geography, ecology, economics, and sociology, and need to be explored and expanded innovatively under a new research idea and theoretical framework [13].

It is noteworthy that some Chinese tourism scholars have become aware of the interaction between tourism and habitat and have conducted exploratory studies. Some scholars have analysed the intrinsic relationship between tourism development and the quality of urban habitat [14] and through quantitative analysis have found a significant positive correlation between the level of habitat development and the attractiveness of urban tourism [15]. Some scholars have also studied that rural habitat from the perspective of urban-rural integration has attracted the attention of scholars [16]. Although Chinese tourism scholars have begun to engage in research on the habitat environment, the research results are still rather scattered and thin, and the habitat environment of rural tourism sites on the edge of scenic areas has not received sufficient attention, and the relevant basic theoretical research is particularly insufficient. Related to this is the multiperspective study of rural tourism sites; for example, in the social and cultural aspects of rural tourism sites, the residents' perceptions [17], dynamics, processes, types, and inheritance patterns of cultural changes in rural tourism sites have been analysed [18–20]. In terms of the spatial structure of rural tourism sites, the spatial structure characteristics, evolutionary patterns, and optimization paths of rural tourism sites around cities are analysed from different spatial scales [21–23]. All these show that rural tourism land as an independent geographical unit has greater research value and application space and also provide a good academic reference for the design of this paper.

2. Related Work

2.1. Current Status of Research in the Urban Fringe. In 1936, the German geographer Herbert Louis first proposed the urban fringe zone when he studied the geographic structure of Berlin from an urban morphological perspective [24], and in the 1960s, the British MRG Conzen, who focused on the urban landscape, proposed the urban fringe zone not only as a way of explaining changes in the urban landscape [25] but also as a means of ordering the complex process of urban development. He argues that the urban fringe is the frontier of urban territorial diffusion but that this expansion is not a steady progression but rather a cyclical change in three states, acceleration, stasis, and deceleration, and graphically compares this cyclical structure of urban development to the annual rings of trees. In his study of the structure of the edge zone of the town of Alnwick in Northumberland, he identified three components: the inner edge zone, the middle edge zone, and the outer edge zone. In China, the study of the urban fringe began in the 1980s and developed rapidly in the 1990s, when the theoretical framework for the study of the urban fringe in China took shape [26]. Many scholars have discussed and researched the concept, geographical definition, and characteristics of urban fringe areas. In addition, [27] planning and land use methods of urban fringe areas have been studied in some detail. In recent years, the emergence of urban villages has become a new direction of research related to urban fringe areas. [3] analyses the formation mechanism of urban villages from the perspective of land use, argues that the prerequisite for urban village transformation is land conversion, and proposes a specific policy framework for land and housing conversion in urban villages, putting forward the idea of "bottom-up" village-oriented urban village transformation.

2.2. The Current State of Research in Rural Settlement Landscapes. In China, ecological research on rural landscapes has mainly focused on the construction of "equivalence." The rising movement of "ecovillages" has positive theoretical and practical implications for the ecological construction of rural landscapes in China, and the construction model of "ecovillages" provides new ideas for the design of rural landscapes [12].

The Danish scholar Giman was the first to propose the concept of "equivalence," which is defined as "a human-scaled settlement." Within the settlement, human activities do not damage and be integrated into the natural environment, support healthy human development, and are sustainable into an unknown future. In Japan, [13] has designed three models of ecovillages, depending on the urban influence on rural areas: (1) the ecovillage model for large urban fringe areas; (2) the ecovillage model for typical agricultural areas; and (3) the ecovillage model for remote mountainous areas.

The pattern of landscape evolution is different for villages near large cities, urbanised villages, and remote isolated villages. [14] also found that the trend towards industrial agriculture led to a concentration of population and the expansion of new villages, but at the same time, thousands of small villages were abandoned and gradually disappeared, resulting in a fundamental change in the structure of rural settlements. [15] systematically explores the evolution of rural settlements from prehistory to the present, selects three types of villages, agricultural, mining, and pastoral, and illustrates their evolution in terms of different time periods, natural environments, village sizes, cultural contexts, and differences in people's perceptions of the landscape.

In Europe, [16] suggests that the sustainable development of the countryside and healthy village life requires the revitalisation of the entire rural area in terms of its nature, human, and built environment, with a focus on the preservation of rural settlements. The cultural landscape of rural settlements is actually a socioecological adaptation of people to the natural ecological environment of the countryside, and each landscape is an active adaptation to the natural geographical environment [28]. The study finds that the cultural landscape of rural settlements in China is a kind of kinship culture, with specific cultural forms and forms, forming a pluralistic regional culture, which works together with other human cultures. [29] introduces the rural settlement landscape as a dynamic interweaving of natural and human landscapes, reflecting the common values of the group formed by nature, social, humanistic, technological,

historical, mythological, and psychological consciousness in the region.

3. Definition of Urban Fringe Areas

Over the years, scholars in China and abroad have held different views on the definition of urban fringe, and the use of the concept is rather confusing. Similar to the term "urban fringe," there are other terms such as city country fringe, urban fringe, area of urban sprawl, and urban shadow area.

One of the first people to address the concept of a transition zone between urban and rural areas was the German geographer Herbert Louis. In his year in Berlin, he identified certain areas that were formerly part of the city boundaries but were later encroached upon by the built-up area and became part of the urban area, which he called the urban fringe, and pointed out that this zone had many significant differences from the built-up area, with its unique spatial structure, housing types, services, and so on. This concept was subsequently deepened and refined by many planners, architects, geographers, and other scholars from all walks of life. A more precise definition of the urban fringe was provided by [10], who described it as "a zone of change in land-use, social and demographic characteristics, located in a land use transition zone between a contiguous built-up area and a suburban area, and a purely agricultural hinterland with an almost complete absence of non-agricultural housing, non-agricultural land-use and non-agricultural land-use." At present, most Chinese scholars consider the urban fringe as a kind of discontinuous territorial entity formed at a specific stage of urban development, close to urban areas, and a zone continent in which the social and economic elements between urban and rural areas are intensely transformed. This paper argues that the urban fringe is a transitional zone where the urban and rural hinterlands meet and is a product of the combination of urban and rural areas, with obvious mixed urban-rural characteristics, and its landscape features also combine the landscape characteristics of urban and rural areas.

The urban and rural areas are two very different heterogeneous bodies, and the urban fringe is the part where these two heterogeneous bodies are combined. However, where this combined part starts and how to define the scope of the urban fringe has been the focus of academic discussion.

According to Friedman's qualitative approach, which is based directly on the daily commuting range of people's experience, the area around the city is classified as the urban fringe, where the inner fringe is about 10-15 km and the outer fringe extends up to 2550 km [11]. Some Chinese scholars have used the length of people's commuting time to measure the urban fringe from a psychological perspective. They argue from the actual situation in China that urban transport in China is still dominated by public transport, and therefore, the extent of the urban fringe in China should take into account the spatial and temporal distance of a one-hour commute by public transport (including buses as well as BRT and rail transport) [14].

3.1. The Human-Place Relationship in Tourism. Based on the theories related to human-territory relations proposed by [15] and the characteristics of tourism geography, the theoretical content of tourism human-territory relations can be summarized from a philosophical perspective as shown in Figure 1.

This system is engaged in tourism activities of human and geographic environment elements in a certain territorial space range, in accordance with certain laws intertwined, constituting a certain structure and function of the complex open system [21], with distinctive tourism, regional, open, dynamic, and comprehensive characteristics. The "people" are in the active position in the tourism-human-land relationship and can passively recognize, use, change, and protect the geographical environment; the study of "people" is about improving tourism satisfaction. "Geographical environment" refers to the geographical environment related to tourism activities, including the natural environment, human environment, and its composite environment of tourism places; geographical environment is the material basis and spatial place of human tourism activities, geographical environment affects the geographical characteristics of human tourism activities and restricts the depth, breadth, and speed of tourism activities; in research, the "land" is the effective protection and sustainable use of tourism resources and environment. Tourism "human-territory relationship" refers to the formation of a specific tourism region in the relevant constraints and interdependence of objective relations, including human tourism activities on the geographical environment of the relationship of dependence, the geographical environment on human tourism activities constraints, and the geographical environment of the interaction of cause-and-effect relationships, and human tourism activities affect the geographical environment.

Although most scholars believe that the tourism experience is the essence of tourism [28], there is no consensus on the nature of tourism geography phenomenon and the nature and research core of tourism geography. Based on the theoretical perception of tourism human-terrestrial relations, tourism geography is a science that object is the "tourism territorial system." The theory of human-territory relations is an important basis for the construction of the theoretical framework of tourism geography. The human-territorial relationship in tourism is not static; the material cycle and energy transformation between the two subsystems of human tourism activities and the geographical environment lead to dynamic changes and developmental evolution of the human-territorial system of tourism [22].

Scientific methodology is an important tool for exploring scientific issues in tourism geography. Empiricist, positivist, humanistic, and structuralist methodologies are undoubtedly common and effective research methods in tourism geography. The analysis of the territorial system of human-territory relations in tourism is not enough to rely on qualitative research alone but needs to be combined with quantitative analysis [21]. The two major methodologies are derived from the characteristics of the discipline of geography, namely, the comprehensive and systematic analysis method and the regional and area analysis method [24].

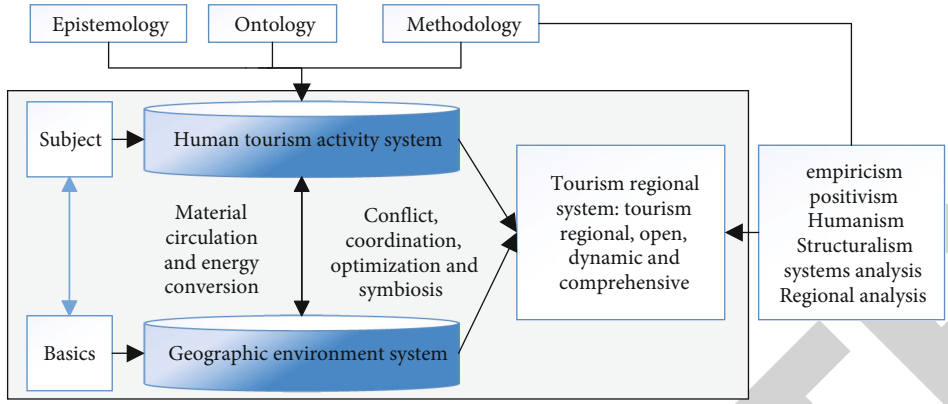

Figure 1: Theoretical framework of tourism-man-land relationship.

3.2. The Basic Framework of Tourism Geography Theory. Based on the theoretical perspective of the relationship between people and place, the theoretical framework of tourism geography is constructed based on the tourism activity system and the geographical environment system, with the theory of the relationship between people and place as the core and the theories of related disciplines integrated, in accordance with the development requirements of the systematization and scientificization of tourism geography theory, taking into full consideration the disciplinary attributes of tourism, regional, comprehensive, and application of tourism geography. The theory of tourism geography includes both the theory of tourism geography science from the perspective of "people" and the theory of tourism geography science from the perspective of "place," while the theory of tourism human-territory relationship from the perspective of "people-territory synthesis" is always the most important one. Through interdisciplinary exchanges and theoretical borrowing and integration, the theoretical essence of tourism geography from related disciplines (such as tourism, geography, philosophy, history, sociology, economics, ecology, environment, management, and ethics) can be absorbed to enrich the theoretical content of tourism geography and build a complete theoretical system of tourism geography as shown in Figure 2.

"People" are the dominant factor in the interaction between tourism and human-territory relations. All people involved in tourism activities are the object of studying in tourism geography. Theories related to the study of "people," such as tourism demand theory, tourism psychology, tourism anthropology theory, tourism marketing theory, stakeholder theory, experience tourism theory, tourism sociology theory, and tourism aesthetics theory, can be used as the theoretical basis of tourism geography.

"Land" is the special place where human beings carry out tourism activities and the basic factor of tourism human-land relationship. Any geographical environment related to tourism activities, including the natural environment, human environment, social environment, and even artificial environment, can become the object of tourism geography research. Theories related to the study of "place," such as theories of physical geography, human geography, landscape ecology, and environmental science, can also be used as the theoretical basis of tourism geography.

The theory of tourism geography is from the perspective of "human-land integration." Tourism geographic phenomena and patterns are the product of the interaction between the natural environmental complex and the tourism activity complex. Between human tourism activities and the geographical environment, there are complex relationships of human visitation behaviour, tourism development and utilization, industry operation and economy, community participation, government policy regulation and control, and tourism spatial organisation. Theories related to the study of these relationships, such as regional economic theory, urban planning and tourism planning theory, tourism industry geography theory, tourism transportation geography theory, tourism community participation theory, and tourism enterprise management theory, can also be used as the theoretical basis of tourism geography.

4. Case Area Overview

Located in the town of Bihu, Liandu District, Lishui City, Zhejiang Province, the village of Xiananshan is a Lishui Municipal Cultural Heritage Protection Unit, with more than 40 old houses with rammed earth facades in existence, the oldest of which is more than 400 years old and was built during the Wanli period of the Ming Dynasty, making it a veritable ancient village [27]. In recent years, as the standard of living has improved, villagers have moved to live outside, and the village once became a hollow village. In order to protect the ancient village, the government has carried out two maintenance repairs on Ha Nan Shan, but it remained uninhabited and the village gradually went into decline.

Nowadays, every courtyard in Ha Nan Shan is a landscape and every dwelling is a story, truly achieving "five hundred years outside, five stars inside." The village of Xiananshan, like a pearl swaying in the town of Bihu in Lishui's Liandu District, attracts visitors from all over the world, both vibrant and inheriting the original village culture, with its landscape layout as showed in Figure 3.

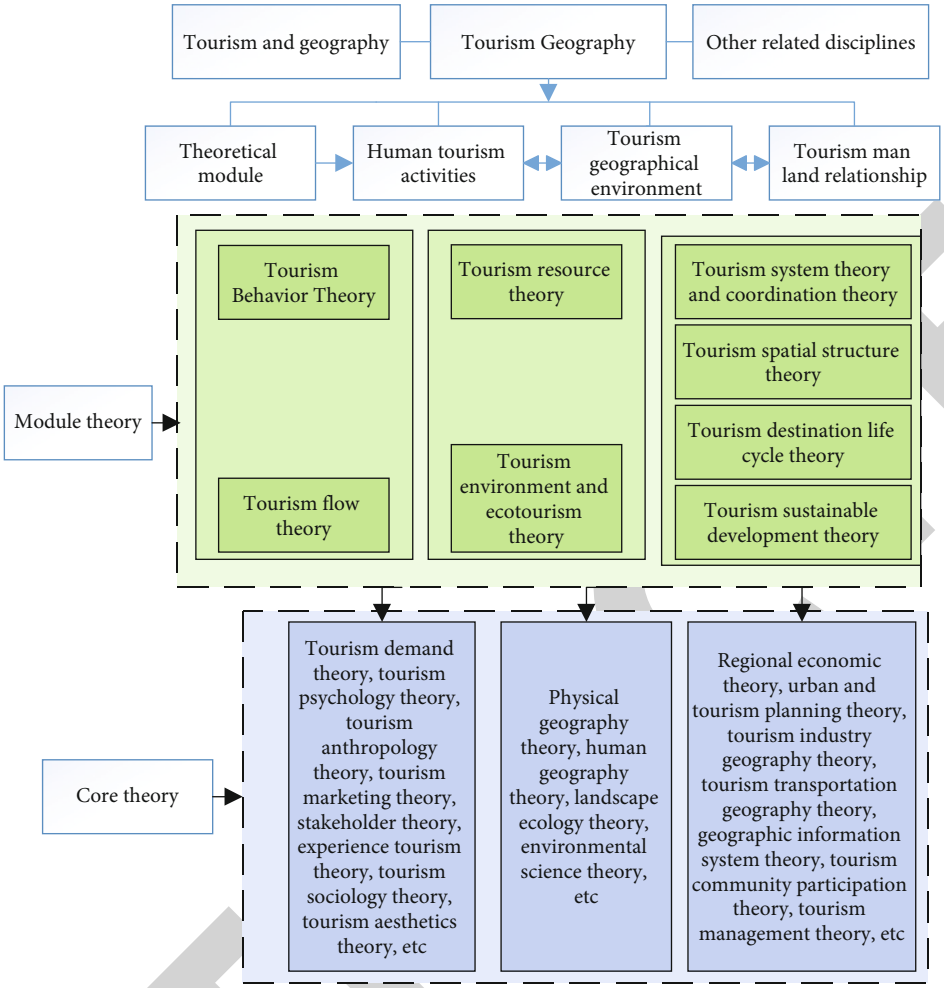

Figure 2: Theoretical framework system of tourism geography.

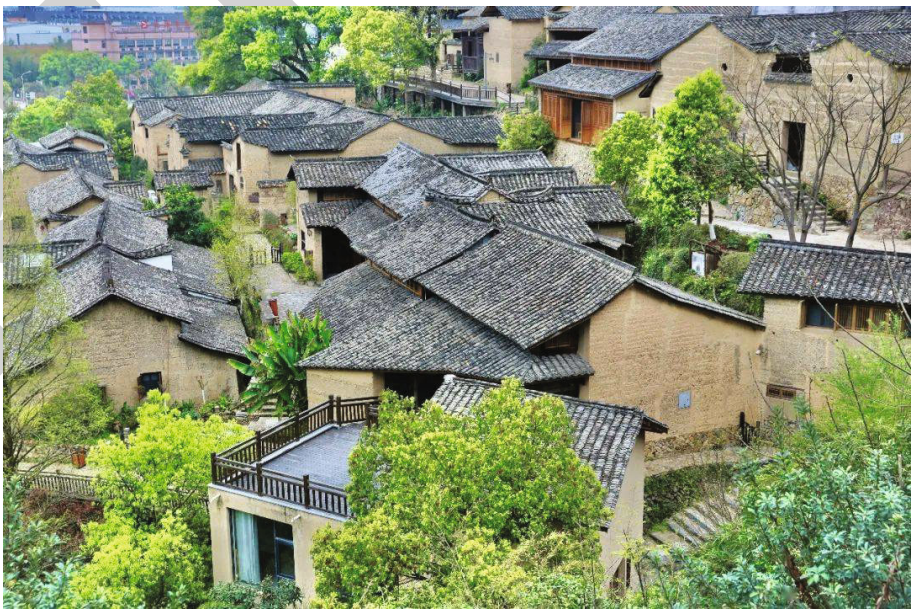

Figure 3: View of Ha Nam San village.

4.1. The Self-Organising Nature of System Evolution. The growth and evolution of the system mainly relies on the exchange of material and energy between the system and the outside world and is subject to the interaction of various internal and external dynamics, which is the result of the interaction between the system's self-organisation and other organisations. The evolution of the state of the habitat system of the rural tourism edge of the landscape has a temporal procedure, with its own movement process of creation, development, and extinction, through the nonlinear action of various elements under the rise and fall movement, to promote the generation of a new orderly structure within the system. However, not all ups and downs will cause sudden changes in the system, small ups and downs have no direct impact on the generation of new orderly structure of the system, and it only allows the system state to deviate temporarily, as long as the system does not exceed the critical point of sudden changes, eventually will return to the original stable state. If the system continues to exchange material, energy, and information with the outside world, quantitative changes may lead to qualitative changes, and a small random disturbance may be amplified by nonlinear effects near the critical point, crossing a certain threshold, which may cause structural instability in time, space, and function of the habitat system, and the habitat system enters a new evolutionary stage (Figure 4).

This dynamic movement process shows a strong correlation with the development process of the core landscape. In the primary stage of the development of the core scenic area, the core scenic area has absolute advantages and is extremely attractive to the development of the surrounding rural tourism areas, and the flow of tourism factors is concentrated in the core area, and the corresponding rural tourism area habitat system is in a slow and spontaneous evolutionary stage. With the development of social and economic development, the core scenic area development tends to saturate, and the corresponding flow of tourism factors began at the core scenic area around the rural area diffusion, and the continuous input of external energy and the original system gradually disintegrated and jumped to a new, stable, and orderly structure state.

4.2. The Cyclical Nature of System Evolution. From the perspective of the self-organised evolutionary path of the habitat system and the "core-edge" territorial structure, the evolution of the habitat system in rural tourism areas shows a strong cyclical nature. With the transformation of the tourism life cycle of the core scenic area, there is a complex energy output-input relationship between the surrounding rural tourism site habitat system and the core scenic area, and its system stability is poor:

$$\frac{dC}{dt} = rC\left(\frac{K-C}{K}\right), \tag{1}$$

where dC/dt represents the instantaneous increment of the habitat capacity of a rural tourism site, r is the growth rate of the habitat capacity of a rural tourism site, C is the existing rural habitat capacity, and K represents the saturation of the rural habitat system under a certain socioeconomic environment (the indicator varies from period to period, i.e., the threshold for the synergistic development of the system elements. In general, at $r > 0$, the steady state of the rural habitat system changes abruptly from $C = 0$ to $C = K$. At the same time, the rate of system evolution varies depending on the value of K, thus forming a different picture of system evolution (Figure 5).

When the C value is infinitely close to the K value at a certain stage, the saturation state of the period is reached, and the rural habitat system in the peripheral area is at a critical point, which is also a key stage for the government and enterprises to intervene strongly, and the threshold of the system needs to be increased K. The government can replan and develop the tourist attractions from the perspective of sustainable tourism development on a larger spatial scale and link up with the surrounding rural tourist areas for development. The government can create a second attraction in addition to the core scenic area and create a regional integrated barrier-free tourism area, while the surrounding rural tourism areas will be integrated and optimised within the system, leading to the upgrading of the structure and function of the habitat system and entering a new evolutionary cycle. Overall, the evolution of the rural habitat system shows a spiral trend. According to the system dynamics mechanism proposed by [30], it is known that the evolution of the habitat system of the rural tourist areas in the fringe area is a combination of segmented continuous logistic curves, and the combined evolution model of the system is

$$\frac{dC}{dt} = r_i\left(C - \sum_{j=1}^{i-1} K_j\right)\left(\sum_{j=1}^{i} K_j - C\right)/K_j, \quad (i = 1, 2, 3 \cdots \cdots, n\,;\, j = 1, 2, 3 \cdots \cdots, m), \tag{2}$$

where r_i is the growth rate of habitat capacity at each stage and $K_j$is the threshold value for the jth stage of habitat evolution. Based on this mathematical model of system evolution, the trajectory of the evolution of the habitat system of the scenic fringe rural tourism site can be modelled (Figure 5).

4.3. Fluctuations in the Evolution of Systems. At a macrolevel, the stages of evolution, direction of evolution, and rate of evolution of the habitat system of scenic fringe rural tourism sites are closely linked to the spatial and temporal transformation of the flow of tourism elements in the core scenic area, which means that the external driving forces of the evolution of the habitat system are relatively certain, and the coupling mode, degree of action, and development trend of the two systems can also be determined. In a sense, therefore, the cyclical nature of the evolution of habitat systems in scenic fringe rural tourism is definable and predictable. The basic factors mainly refer to the natural geographical conditions, traditional farming patterns, traditional cultural customs and traditional living habits, etc. These factors, which have been accumulated over a long period of time,

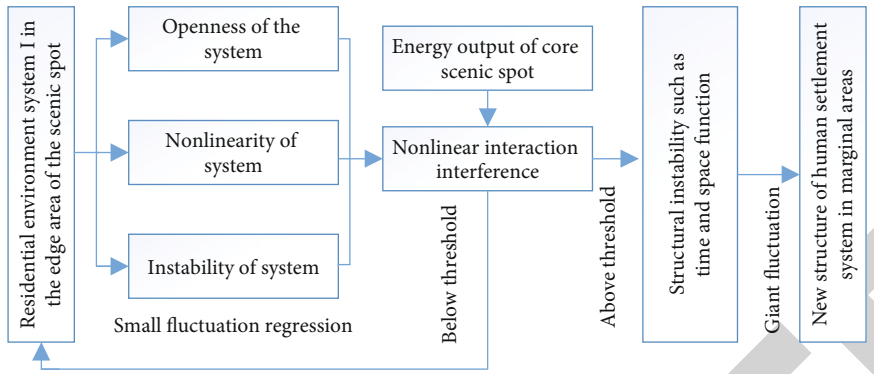

Figure 4: Self-organisation evolutionary path.

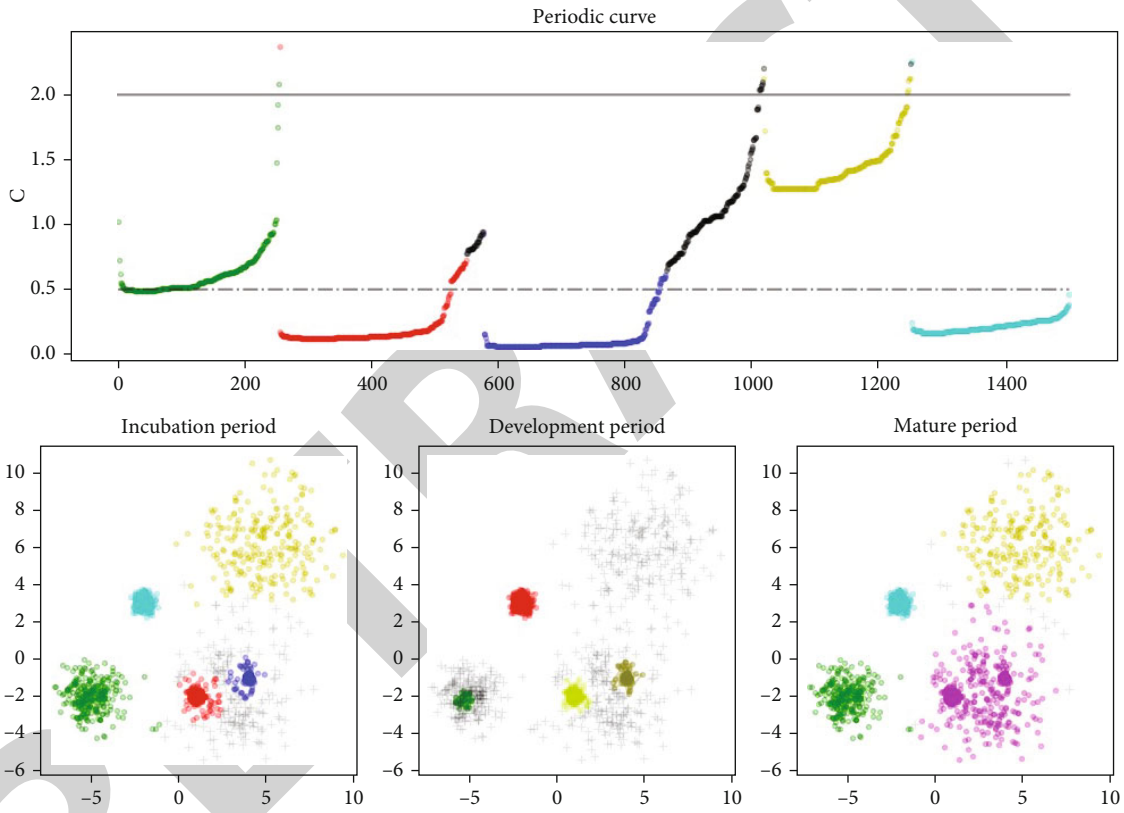

Figure 5: Rural tourism attractions of scenic spot edge type.

play a relatively stable role in the formation and development of the habitat environment in rural tourism areas, and the relationship between people and land is relatively harmonious (Figure 6(a)). The new factors include the innovation of the grassroots organisational system, the introduction of national rural tourism and rural development policies, and the change of the rural land system and household registration system. These new factors accelerate the evolution of the habitat environment in rural tourism areas, and the evolution is faster, but due to the instability, complexity, and intersectionality of these new factors themselves and the process of action, the development of the habitat environment in rural tourism areas shows a certain degree of oscillation (Figure 6(b)). Mutation factors mainly refer to events with unforeseen impacts, such as the construction of major development texts for regional tourism, major pollution events in the ecological environment or natural disasters. These sudden change factors may achieve significant changes in the habitat of rural tourism sites in a relatively short period of time (Figure 6(c)).

4.4. Influence Mechanisms on the Evolution of the Habitat of Rural Tourism Sites on the Edge of the Landscape. The habitat system of scenic fringe rural tourism sites is a dynamic and open composite ecosystem, and the ecological-geographical process of its evolution is more intense under

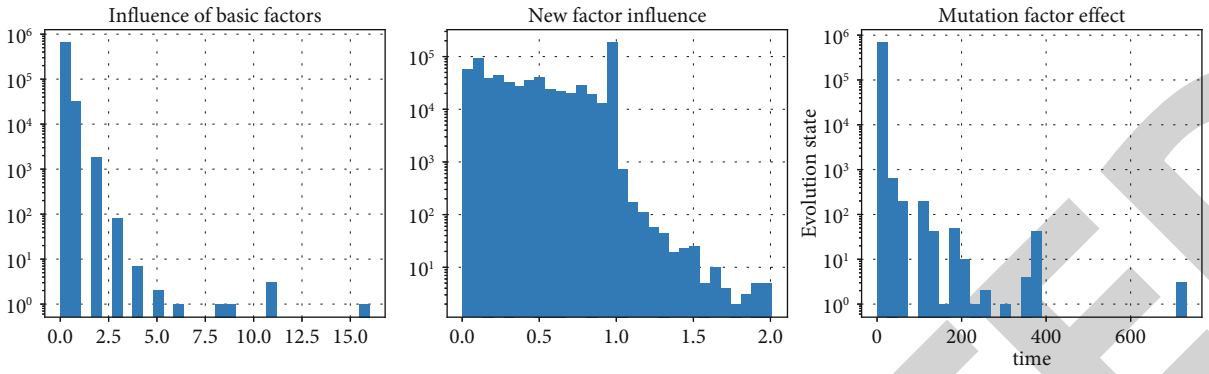

Figure 6: Evolution of rural tourism attractions human settlements.

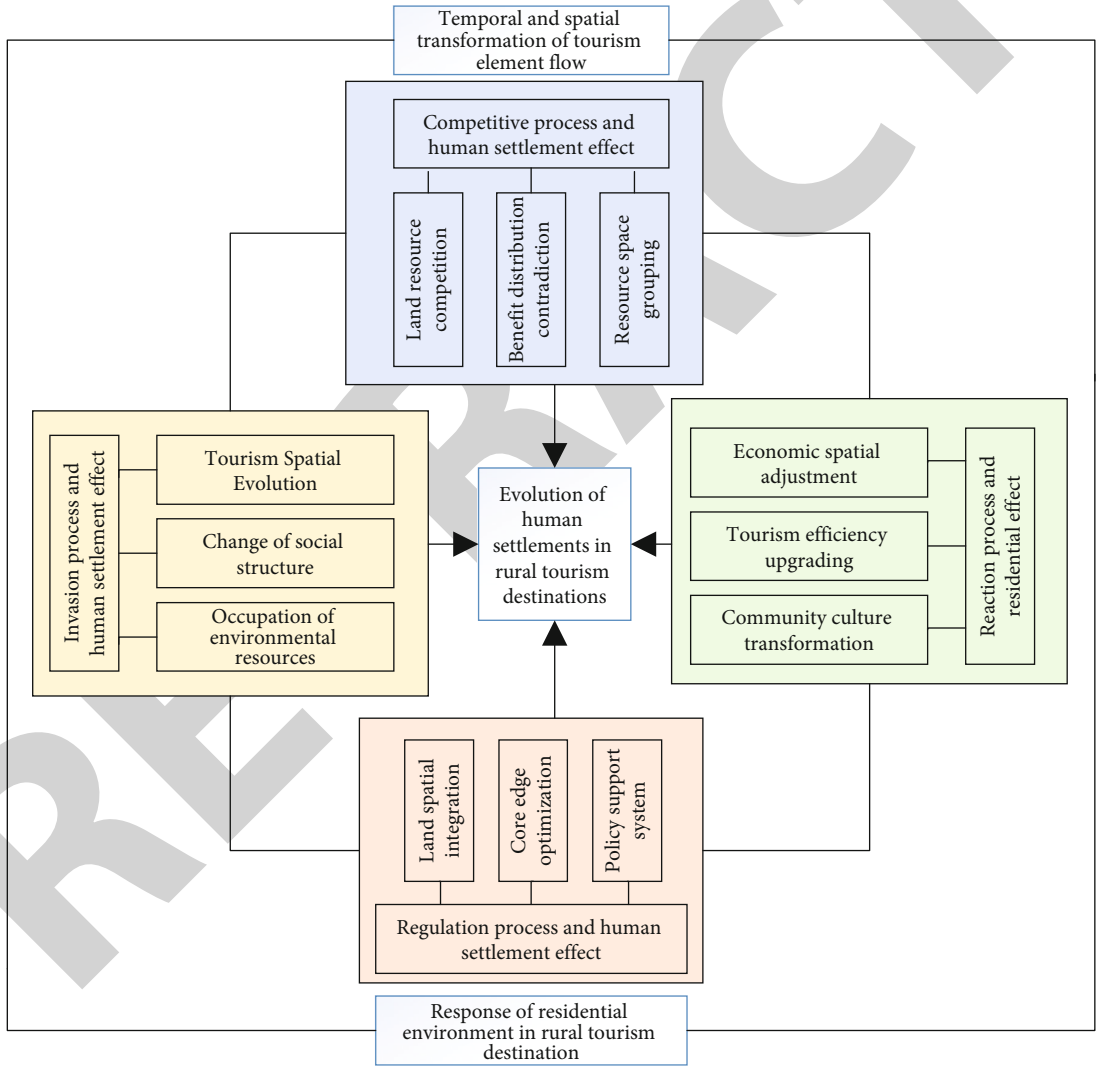

Figure 7: Influence mechanism.

the periodic stimulation of the material and energy flow of the core scenic area; therefore, it is necessary to sort out and summarize the process of the evolution of the habitat system in this typical region. The evolution of the habitat environment in rural tourism areas on the edge of the landscape follows the general rules of system evolution but at the same time has its own special requirements, which are reflected in the general trends and special dynamic mechanisms of system evolution. The structure of the habitat system is in the process of continuous evolution, and when it exceeds a certain

Figure 8: View of the courtyard.

threshold, it breaks the boundary of the original system and realises the structural upgrade and functional transformation of the system. This quantitative to qualitative spatiotemporal coupling process is driven by the spatiotemporal transformation of the flow of tourism elements, which takes the form of spatiotemporal evolution of tourism flows, capital flows, and land use patterns and the spatial structure of settlements. As the habitat environment is a composite ecosystem, its evolution process has certain similarities with the ecological community succession. Borrowing some ideas from biology, ecology, and environmental science, the spatial process of the evolution of the habitat environment in the scenic fringe-type rural tourism area is divided into four processes, namely, invasion, competition, reaction, and regulation, to build a dynamic model of the evolution of the habitat environment in the scenic fringe-type rural tourism area as shown in Figure 7.

The competition process is essentially the unification of the differentiation process and the symbiosis process of the habitat system in the core and peripheral areas. The differentiation process is the main motive force in the evolution of the habitat environment in rural tourism sites, and the symbiosis process is the key stage for the orderly development of the habitat environment in rural tourism sites. The inflow of tourism factors interferes with the self-organising function of the rural tourism habitat system, and the coupling strength of the two systems, the core scenic area and the peripheral area, hovers at the critical point of the qualitative change of the system, at which time the rural tourism habitat system is in a chaotic, disorderly, and conflicting vortex. Beyond the critical point, the various functions of the system will show the characteristics of homogeneous convergence and heterogeneous exclusion and eventually form a new state of the habitat environment in the geographical space, as showed in Figure 8.

The regulation process is to clarify the inner connection between the spatial and temporal pattern of rural habitat environment and the tourism development process and to seek the path of constructing the habitat environment of scenic fringe-type rural tourism sites. The competition process can achieve the maximization of resources and spatial value, but there are also serious divisions and social inequity. At this point, the timely intervention of other organisations can ensure the sustainable development of the habitat system in rural tourism sites, and therefore, effective regulation by the government is particularly important. Before regulation, it is necessary to summarize the process of habitat evolution and habitat effects in scenic fringe rural tourism sites, in order to provide a basis for the government's intervention and regulation content.

5. Conclusions

Based on the theory of system theory and human-land relationship, the system characteristics of the habitat environment of rural tourism sites in the edge of scenic areas are summarized in three aspects, including self-organisation, periodicity, and fluctuation of system evolution. This cyclical fluctuation is influenced by many factors and presents uncertainty and diversity in the evolutionary path and rate.

Drawing on some concepts from biology, ecology, and environmental science, the process of habitat evolution in rural tourism sites on the edge of scenic areas is divided into four processes, namely, invasion, competition, reaction, and regulation, and a dynamic model of habitat evolution in rural tourism sites on the edge of scenic areas is constructed.

Data Availability

The dataset used in this paper are available from the corresponding author upon request.

Conflicts of Interest

The author declared no conflicts of interest regarding this work.

References

[1] P. H. Gude, A. J. Hansen, R. Rasker, and B. Maxwell, "Rates and drivers of rural residential development in the Greater Yellowstone," *Landscape & Urban Planning*, vol. 77, no. 1-2, pp. 131–151, 2006.

[2] W. Sarah, E. Annette, and A. Felix, "Urban air temperature anomalies and their relation to soil moisture observed in the city of Hamburg," *Meteorologische Zeitschrift*, vol. 23, no. 2, pp. 143–157, 2014.

[3] L. Peeters, "Selective in-migration and income convergence and divergence across Belgian municipalities," *Regional Studies*, vol. 42, no. 7, pp. 905–921, 2008.

[4] B. Huang and H. Zhang, "The relationship between humans and the environment at the urban-rural interface:research progress and prospects," *Acta Ecologica Sinica*, vol. 32, no. 23, pp. 7607–7621, 2012.

[5] L. Soler, M. Escada, and P. H. Verburg, "Quantifying deforestation and secondary forest determinants for different spatial extents in an Amazonian colonization frontier (Rondonia)," *Applied Geography*, vol. 29, no. 2, pp. 182–193, 2009.

[6] Y. S. Seo, S. P. Jeong, T. M. Holsen et al., "Characteristics of total gaseous mercury (TGM) concentrations in an industrial complex in South Korea: impacts from local sources," *Atmospheric Chemistry and Physics*, vol. 16, no. 15, pp. 10215–10228, 2016.

[7] T. Song, "Technological methods of information interpretation and analysis of land use change in urban fringe area —taking Wuxi City as an example," *Progress in Geography*, vol. 23, no. 2, 2010.

[8] X. Yang, X. Li, Z. Kong, and L. Lei, "Research on residential differentiation in urban fringe areas from the perspective of spatial justice – a case study of Xi'an city," *IOP Conference Series Materials Science and Engineering*, vol. 780, no. 7, article 072043, 2020.

[9] N. Shin and C. Choi, "Research on the relationship between participation motivation, commitment, satisfaction and behavior intention of PyeongChang winter olympic volunteers," *Journal of Tourism Management Research*, vol. 23, no. 3, pp. 85–106, 2019.

[10] L. L. Zhang, X. You, J. R. Jiao, and P. Helo, "Supply chain configuration with co-ordinated product, process and logistics decisions: an approach based on Petri nets," *International Journal of Production Research*, vol. 47, no. 23, pp. 6681–6706, 2009.

[11] J. P. Wiebe and G. Zhang, "Progesterone metabolites regulate induction, growth, and suppression of estrogen- and progesterone receptor-negative human breast cell tumors," *Breast Cancer Research: BCR*, vol. 15, no. 3, p. R38, 2013.

[12] X. Zhang and C. Liu, "Image annotation based on feature fusion and semantic similarity," *Neurocomputing*, vol. 177, pp. 75–88, 2016.

[13] E. Ritter and D. Dauksta, "Human–forest relationships: ancient values in modern perspectives," *Environment Development & Sustainability*, vol. 15, no. 3, pp. 645–662, 2013.

[14] C. H. Cao, Y. N. Tang, D. Y. Huang, W. M. Gan, and C. Zhang, "IIBE: an improved identity-based encryption algorithm for WSN security," *Networks*, vol. 2021, pp. 1–8, 2021.

[15] B. Halder, J. Bandyopadhyay, and P. Banik, "Monitoring the effect of urban development on urban heat island based on remote sensing and geo-spatial approach in Kolkata and adjacent areas, India," *India. Sustainable Cities and Society*, vol. 74, article 103186, 2021.

[16] H. Hu, L. Han, L. Li, H. Wang, and T. Xu, "Soil heavy metal pollution source analysis based on the land use type in Fengdong District of Xi'an, China," *Environmental Monitoring and Assessment*, vol. 193, no. 10, pp. 1–14, 2021.

[17] H. Liu, Y. Ma, Q. Liu, and Y. Song, "Decision-making of green space utilization and protection in urban fringe based on biodiversity trade-off," *Sustainability*, vol. 12, no. 4, p. 1373, 2020.

[18] D. Wu, C. Zhang, L. Ji, R. Ran, H. Wu, and Y. Xu, "Forest fire recognition based on feature extraction from multi-view images," *Traitement du Signal*, vol. 38, no. 3, pp. 775–783, 2021.

[19] M. Dennis, D. Barlow, G. Cavan et al., "Mapping urban green infrastructure: a novel landscape-based approach to incorporating land use and land cover in the mapping of human-dominated systems," *Land*, vol. 7, no. 1, 2018.

[20] L. Hou, F. Wu, and X. Xie, "The spatial characteristics and relationships between landscape pattern and ecosystem service value along an urban-rural gradient in Xi'an city, China," *Ecological Indicators*, vol. 108, article 105720, 2020.

[21] L. Wang, C. Zhang, and Q. Chen, "A communication strategy of proactive nodes based on loop theorem in wireless sensor networks," in *2018 Ninth International Conference on Intelligent Control and Information Processing (ICICIP)*, pp. 160–167, IEEE, 2018.

[22] H. Wang and F. Qiu, "Investigation of the dynamics of agricultural land at the urban fringe: a comparison of two peri-urban areas in Canada," *The Canadian Geographer/Le Géographe canadien*, vol. 61, no. 3, pp. 457–470, 2017.

[23] D. Zhao, "Spatial allocation model of ecological land in the urban fringe of Xi'an City based on geosynclinal fold belt structure," *Arabian Journal of Geosciences*, vol. 13, no. 16, pp. 1–10, 2020.

[24] X. Chen, D. Xu, S. Fadelelseed, and L. Li, "Spatiotemporal analysis and control of landscape eco-security at the urban fringe in shrinking resource cities: a case study in Daqing, China," *International Journal of Environmental Research and Public Health*, vol. 16, no. 23, p. 4640, 2019.

[25] H. Li, D. Zeng, L. Chen, Q. Chen, M. Wang, and C. Zhang, "Immune multipath reliable transmission with fault tolerance in wireless sensor networks," in *International Conference on Bio-Inspired Computing: Theories and Applications*, pp. 513–517, Springer, Singapore, 2016.

[26] G. Erdoğan, "Identifiying urban fringe spatial character with fractal analysis: Akhan, Denizli.," *Qualitative Studies*, vol. 14, no. 2, pp. 11–17, 2019.

[27] J. Peng, Q. Liu, T. Blaschke et al., "Integrating land development size, pattern, and density to identify urban–rural fringe in a metropolitan region," *Landscape Ecology*, vol. 35, no. 9, pp. 2045–2059, 2020.

[28] Y. B. Bai, L. I. Hong-Tao, and L. U. Hao, "Analysis of spatial pattern of urban-rural construction land:with Shenyang city as an example," *Scientific and Technological Management of Land and Resources*, vol. 359, pp. 217–225, 2011.

Hindawi
Journal of Sensors
Volume 2022, Article ID 7311117, 15 pages
https://doi.org/10.1155/2022/7311117

Research Article

Complex Traffic Network Analysis Method Based on a Multiscale Aggregation Model

Yingying Pei,[1] Xia Zhu,[1,2] Guohong Li,[1,2,3] Yongtao Jin,[1,2] Yuyan Liu,[1,2] Yuanping Liu,[1,2] Gang Liu,[4] and Jiangxia Fan[1]

[1]*School of Remote Sensing and Information Engineering, North China Institute of Aerospace Engineering, Langfang 065000, China*
[2]*Hebei Aerospace Remote Sensing Information Processing and Application Collaborative Innovation Center, Langfang 065000, China*
[3]*National Local Joint Engineering Research Center for Aerospace Remote Sensing Information Application Technology, Langfang 065000, China*
[4]*School of Computing, North China Institute of Aerospace Engineering, Langfang 065000, China*

Correspondence should be addressed to Xia Zhu; zhuxia1201@126.com

Received 4 October 2021; Revised 2 February 2022; Accepted 9 March 2022; Published 25 March 2022

Academic Editor: Aijun Yin

Identifying the aggregation characteristics of the geospatial network is an important aspect of analyzing highway traffic networks. Based on the complex network theory, this paper studies the block aggregation characteristics of the highway traffic network and proposes an Improved PageRank Spectral Clustering (IPSC) Algorithm to divide the functional blocks of highway traffic networks. Firstly, the theoretical model of a highway traffic network is constructed by adding location attribute weight, geographical distance weight, road grade weight, and dynamic traffic congestion weight. Secondly, the improved PageRank algorithm is used to get the ranking of key nodes of the highway traffic network. The clustering center and the number of clusters are determined by the ranking of key nodes and the shortest path distance. Then the improved spectral clustering algorithm is used to divide the functional blocks of the highway transportation network and identify the special common blocks of the highway transportation network. Finally, the IPSC Algorithm is used to analyze the aggregation mode of complex traffic networks at city and district scales. Crossing the limit of administrative division, the division results of special common blocks of highway transportation networks are obtained. Maintaining the connectivity between blocks can improve the overall efficiency of highway transportation networks.

1. Introduction

The highway transportation network is an important infrastructure to serve the economy, society, and public. In recent years, with the continuous expansion of the urban scale, the rapid growth of the urban population has brought great pressure to urban road traffic. The optimization and intelligent management of road traffic are effective ways to alleviate traffic pressure. Therefore, it is of great significance to analyze and study the road traffic network.

With the rapid development of computers, research on complex networks at home and abroad has become a hot topic in academic circles. Highway transportation network has the characteristics of complex structure, diverse connections, and many road intersections. The mathematical model of highway traffic networks based on complex network theory can analyze the network structure as a whole. The functional block of the highway transportation network is the leading structure showing different characteristics and multiple functions of a complex highway transportation network. In recent years, Du et al. [1] pointed out that the highway transportation network is a complex network with the structural characteristics of a complex network. Qian et al. [2] built a complex road traffic network using the dual method. The time-delay and recovery characteristics of complex road traffic networks are analyzed and compared, and the cascade failure models of complex networks are simulated. Based on complex network and graph theory, Sun

et al. [3] analyzed the network structure of the urban rail transit system and deeply studied the vulnerability of stations. Zeng et al. [4] analyzed the static characteristics of Tianjin urban rail transit represented by the current network and forward network based on complex network theory. In the research, the global efficiency is selected as the evaluation index, and the evolution characteristics of the network are analyzed. Fortunato and Hric [5] proposed that network block detection is one of the most popular topics in modern network science. Yang et al. [6, 7] applied the concept of block detection to the association network of urban traffic state and proposed a new perspective to identify the spatial association mode of traffic state.

Analyzing the highway traffic network based on complex network theory, mining the functional blocks of network structure, and identifying the distribution characteristics of a network from the perspective of geospatial are important aspects of analyzing highway the traffic network. Firstly, a multiscale analysis of a complex traffic network is necessary. Yang [8] proposed that scale is the basic feature of the objective world, and multiscale research is an important means to understand the complex system of the objective world. A highway traffic network has its complexity and systematicness. In order to obtain the scientific and reasonable design strategies and principles of a highway traffic network, the road network should be analyzed from multiple levels and angles. Multiscale research undoubtedly provides a unique perspective for road network analysis. Secondly, there are deficiencies in data types in the existing research on the construction of a highway traffic network model. Tian et al. [9] proposed that urban road traffic is a typical network. Considering the functional characteristics of the urban road network, the weighted network model of the urban road traffic is redefined. However, the influence factors of dynamic weight are not considered when constructing the weighted model of the road traffic network. Zheng et al. [10] studied the dynamic flow information on a scale-free traffic network and found that congestion behavior has an impact on the traffic network. Adding weight influence factors such as dynamic traffic congestion degree to build the theoretical model of a road network can provide more comprehensive theoretical support for traffic decision-making and service personnel. In addition, an appropriate clustering algorithm needs to be selected for road traffic network block division. There are many algorithms for identifying modules in complex networks, such as vertex clustering algorithm [11], density-based algorithm [12, 13], random walk method [14, 15], circuit approximation method [16], and spectral clustering algorithm [17]. Zhu et al. [18] used the k-means clustering algorithm to analyze the highway traffic network. However, highway transportation network data is typically high-dimensional data. And the ideal cluster of road traffic network data is not necessarily spherical. Therefore, the research results obtained by using the k-means clustering algorithm to divide the functional blocks of the highway transportation network have certain limitations.

Based on the above background, this paper analyzes the complex traffic network of the multiscale aggregation model. An Improved PageRank Spectral Clustering (IPSC) Algorithm is proposed to divide the functional blocks of the highway traffic network. Firstly, the theoretical analysis model of a highway traffic network with dynamic traffic congestion degree weight influence factor is constructed. Then, an improved PageRank algorithm is used to get the ranking of key nodes in the highway traffic network and scientifically determine the clustering center and the number of clusters. Considering that the spectral clustering algorithm is suitable for processing high-dimensional data and is more adaptable to data distribution, in this paper, an improved spectral clustering algorithm is used to divide the functional blocks of the highway traffic network. The improved PageRank algorithm and the improved spectral clustering form the IPSC Algorithm. The block aggregation characteristics of a highway traffic network across administrative divisions are analyzed using the IPSC Algorithm. Thereby, it can provide decision-making references for traffic planning, design work, and maintenance work.

The rest of the organizational structure of this paper is as follows: Section 2 introduces the multiscale aggregation model. Section 3 introduces the construction of a highway traffic network theoretical model considering dynamic influence factors. Section 4 introduces the functional block division method of highway transportation network (IPSC Algorithm). Section 5 introduces an example of spatial analysis in a multiscale aggregation model. Finally, the conclusion is given in Section 6.

2. Multiscale Aggregation Model

A multiscale analysis is one of the important methods to correctly understand things and phenomena. From coarse to fine or from fine to coarse, analyzing things at different scales (resolution) is called multiscale analysis, also known as multiresolution analysis. Like the human visual mechanism, people's understanding of things, phenomena, or processes will draw different conclusions due to different scale choices. Some of these conclusions may reflect the essence of things, some may partially reflect, and some may even be wrong understanding. Obviously, only using a single scale can only make a one-sided understanding of things. Different scales are adopted. The details are seen on a small scale, and the whole is seen on a large scale. The combination of multiple scales can have a comprehensive and clear understanding of things. On the other hand, in nature and engineering practice, many phenomena or processes have multiscale characteristics or multiscale effects. At the same time, people often observe and measure phenomena or processes on different scales. Therefore, a multiscale analysis is one of the important methods to correctly understand things and phenomena.

The aggregation model refers to the movement mode formed by a group of moving objects moving together under certain time and space constraints. Aggregation pattern analysis was first proposed in the literature [19, 20]. It is defined as a trajectory model that simulates various mass events, such as celebrations, parades, protests, and traffic jams. In particular, the gathering area is also considered a long-lasting and stable high-density region. Based on the

complex network theory, this paper deeply analyzes the characteristics of network structure and finds that it is generally characterized by agglomeration in actual network structure. Accurate analysis of a road network aggregation pattern has always been the focus of researchers.

This paper analyzes the multiscale aggregation model of a highway traffic network. This refers to analyzing the special common aggregation of the network from different geospatial angles. Crossing the limits of existing administrative divisions, this paper deeply analyzes the spatial structure characteristics of a highway traffic network and the regional aggregation range produced by traffic operation. The results of block aggregation characteristics of a highway traffic network across administrative divisions at multiple levels are obtained. Then it can provide new scientific decision-making references for traffic planning, design, and maintenance. At the same time, the multiscale aggregation model analysis makes the research method popularized.

3. Construction of Theoretical Model of the Highway Traffic Network considering Dynamic Influence Factors

A complex network is the complex network topology and dynamic behavior of a complex large-scale network. It consists of a large number of nodes, which are formed by connecting edges with each other. There are two main ways to map highway transport network into a complex network. One is called the Primal Approach, which means that intersections of highway network represent nodes and connecting roads of intersections represent edges. The other is called the Dual Approach, which means that the highway represents the nodes in the transportation network, and the intersections of the highway network represent the connecting edges between the nodes, because the effect of using the original method is very clear and intuitive. And the road network constructed by the original method contains the meaning of realistic geospatial distance. It can achieve everyone's spatial cognition. Therefore, this paper uses the Primal Approach to construct the topology of highway transport network.

The next step is to consider the practical significance of the highway transportation network. In this paper, the weight factors that affect the network analysis are added to construct the theoretical analysis model of the highway traffic network. The dynamic influence factor is not considered in the theoretical analysis model of the highway transportation network. This results in a gap between the theoretical model and the actual highway transportation network. Based on this situation, this paper builds a theoretical analysis model of a highway traffic network by adding static data including properties of ground objects and facilities, topological distance, highway network grade, and dynamic traffic congestion degree weight influencing factor. This model provides a basic model for subsequent highway transportation network analysis. The theoretical analysis model of the highway transportation network is shown in Figure 1.

Specifically, the structure of the highway transportation network is defined as

$$RTN = \{\mathrm{N}, E\}. \tag{1}$$

where $N = \{n_i \mid i = 1, 2, \cdots, N\}$ represents the traffic network node set, $N = |N|$ which is the number of nodes in the traffic network, and $E = \{e_{ij} \mid i \neq j, i, j \in \{1, 2, \cdots, N\}\}$ is a collection of edges. If there is an edge between nodes i and j, then $e_{ij} = 1$; otherwise, $e_{ij} = 0$. If each edge is given a corresponding weight, this network is called a weighted network.

3.1. Location. Location attribute is an important factor to measure the importance of road segments. Location characteristics are usually related to the presence of some facilities. Referring to the POI Classification, Layering, and Attribute Structure of Geographic Information Public Service Platform published by Esri China (Beijing) Co., Ltd., the POI of catering, shopping, and other POIs are selected as location prominent attributes. The specific POI categories and codes are shown in Table 1. These POIs are used as 500-meter buffer ranges to view customized location attribute values for covered road network nodes. If the node is within the 500-meter buffer range, it will be a node weighted value of 1. Otherwise, the weighted value is 0. The location attribute weight settings are shown in Table 2.

Assume that the size of vector v is $N \times 1$, N is the number of road nodes in the road traffic network. Element $v_i = 1 (1 \leq i \leq N)$ means that node i is relatively important and has important ground feature service facilities around it. Otherwise, $v_i = 0$. The location attribute matrix is defined as

$$F = (v_1, v_2, \cdots, v_N). \tag{2}$$

3.2. Distance. In terms of geospatial correlation, highway traffic network has significant distance attenuation characteristics. The spatial correlation generally decreases with the increase of the two distances. Suppose $W = (w_{ij})_{i,j=1}^{N}$ is the distance weight matrix, where w_{ij} represents the reciprocal of the shortest path length between node i and node j.

$$w_{ij} = \begin{cases} \dfrac{1}{d_{ij}} & i \neq j \\ 0 & i = j \end{cases}, \quad 1 \leq i, j \leq N, \tag{3}$$

where d_{ij} is the shortest path length between node i and node j in the initial transportation network structure, and the unit is "km."

3.3. Road Level. Different grades of highways have different limited speeds and traffic volumes. According to China's current Technical Standard for Highway Engineering (JTG B01-2014) [21], highways are divided into five grades including expressways, first-class highways, second-class highways, third-class highways, and fourth-class highways according to their use tasks, functions, and traffic volume. According to the different speeds of highways at all levels,

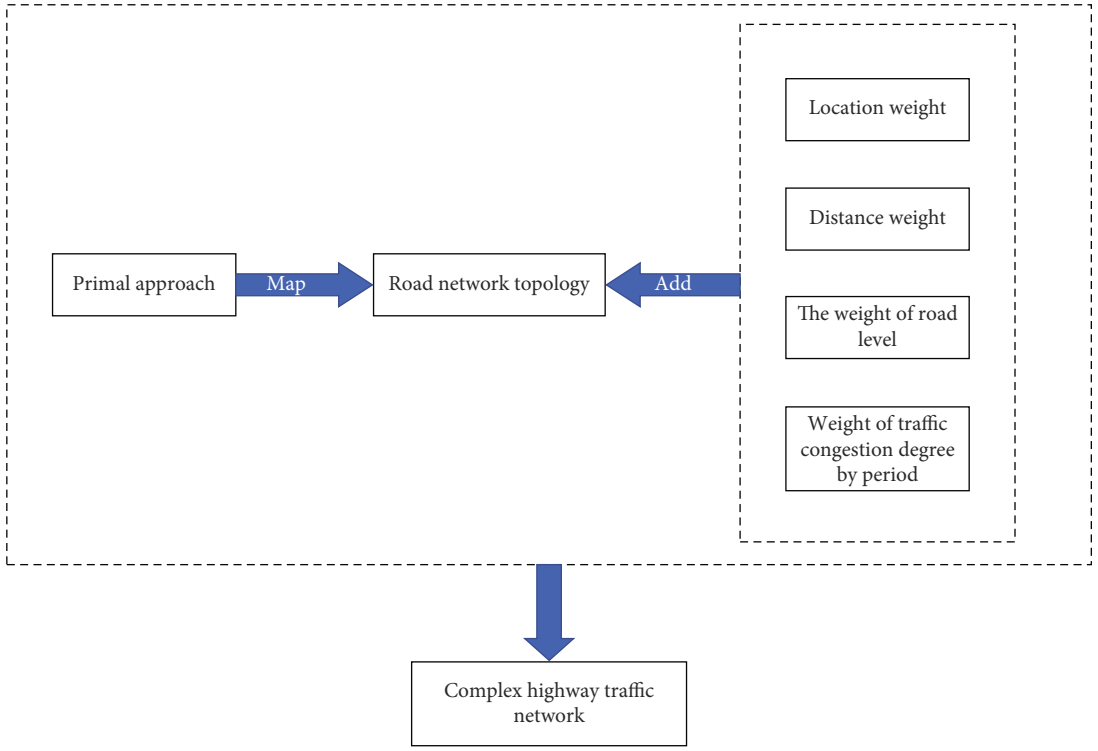

Figure 1: Theoretical analysis model of highway transport network.

Table 1: Selected POI categories.

Category name	Food	Shopping	Lodging	Journey	Sports and entertainment	Education	Medical treatment	Travel
Category code	01	02	03	04	05	09	10	12

Table 2: Weight distribution of location attributes.

Node position status	Node exists in the selected POI buffer	Node does not exist in the selected POI buffer
Weight	1	0

the weights of highways at different levels are set. The higher the speed, the greater the weight. The specific weight settings are shown in Table 3.

Suppose $L = (l_{ij})_{i,j=1}^{N}$ is a road grade matrix, and element l_{ij} refers to the weighted value of the road grade in Table 3.

3.4. The Degree of Traffic Congestion. Dynamic traffic congestion information is also one of the important factors that affect people's travel road choice. This paper uses the average travel speed of interval sections (average travel speed of interval sections = number of vehicles measured × length of interval sections/sum of all measured times of vehicles passing through the interval sections) to determine the traffic congestion level during peak travel. The degree of traffic congestion is divided into grade I (severe congestion), grade II (moderate congestion), grade III (mild congestion), and grade IV (unblocked). The lower the average travel speed, the higher the traffic congestion level and the higher the road weight during peak travel period. The weight settings for different traffic congestion levels are shown in Table 4.

Suppose $T = (t_{ij})_{i,j=1}^{N}$ is the traffic congestion level matrix, and element t_{ij} refers to the weighted value of the traffic congestion level in Table 4.

4. Highway Transportation Network Functional Block Partition Method (IPSC Algorithm)

This paper proposes the IPSC Algorithm to divide the functional blocks of a highway traffic network. The IPSC Algorithm is divided into two core parts. One is the improved PageRank algorithm part. This section is used to determine the ordering of critical nodes. The second is the improved spectral clustering algorithm part. This part is used to divide the functional blocks of the road traffic network.

Alex Rodriguez and Alessandro Laio proposed that the core idea of the clustering algorithm lies in the selection of cluster centers [22]. Therefore, the cluster center selection of the clustering algorithm has a very large impact on the clustering results. However, there is currently no standard

Table 3: Distribution of road grade weights.

Road	Expressway	First-class highway	Second-class highway	Third-class highway	Fourth-class highway
Weight	0.333	0.267	0.200	0.133	0.067

Table 4: Distribution of road traffic congestion level weight.

Traffic congestion degree grade	Pass unimpeded (IV)	Mild congestion (III)	Moderate congestion (II)	Serious congestion (I)
Weight	0.0875	0.1875	0.3125	0.4125

method for selecting cluster centers, generally selected randomly or by experience. This has obvious subjectivity, which makes it difficult to guarantee good clustering results. In this paper, the PageRank algorithm is used to determine the ranking of key nodes in the road traffic network by adding the dynamic weight factors of the road traffic network. Then the clustering center is determined by combining the key node sorting and the shortest path distance.

In addition, road traffic network data is typical high-dimensional data. And the ideal cluster of road traffic network data is not necessarily spherical. The k-means algorithm used in previous studies is not effective in identifying nonspherical clusters. Moreover, the k-means algorithm converges to the local optimal solution rather than the global optimal solution. Spectral clustering is an algorithm that evolves from graph theory and is widely used in cluster analysis. It is characterized by the use of dimension reduction techniques and is more suitable for clustering analysis of high-dimensional data such as highway transportation networks. Meanwhile, the spectral clustering algorithm is based on the spectral graph theory. Compared with traditional clustering algorithms, spectral clustering algorithms have the ability to cluster in the arbitrary shape of sample space and converge to the global optimal solution. Therefore, this paper uses a spectral clustering algorithm to partition highway transportation network functional blocks.

At the same time, considering the actual characteristics of highway transportation network itself, this paper adds weight factors such as location, distance, highway grade, and dynamic traffic congestion degree to improve the spectral clustering algorithm, using the improved spectral clustering algorithm to divide the functional blocks of the highway traffic network. This makes the clustering results more in line with the actual road network situation.

4.1. The Improved PageRank Algorithm Determines the Ranking of Key Nodes. The PageRank algorithm itself is the only standard used by the Google browser to measure the quality of a website. Google defines the level of websites as 0 to 10, of which 10 means full marks. The higher the PageRank value, the more important (very popular) the web page is. The advantage of the PageRank algorithm is that it considers the important feedback of connecting other pages. It is suitable for analyzing highway transport network.

Without considering the influence of any weight, the higher the connection degree of the road node, the more important the road node is in the highway traffic network. However, the disadvantage of the PageRank algorithm is that it does not consider the importance of the node itself. Considering the importance of road nodes, this paper adds the weight influence factors of location, road grade, distance, and dynamic traffic congestion degree in the real traffic network to improve the PageRank algorithm. The ranking of key nodes of highway transportation network obtained by using the improved PageRank algorithm is more in line with the actual situation of highway transportation network.

The flow of the improved PageRank algorithm is as follows.

(1) PageRank's Google matrix, represented by G, is defined as

$$G = \alpha A^* + \frac{(1-\alpha)}{N} I_{N\times N}, \tag{4}$$

where A^* is the transfer matrix of the adjacency matrix A obtained from the original traffic network, α is the damping factor, which is generally used $\alpha = 0.85$, N represents the number of nodes in the traffic network, and $I_{N\times N}$ is an N -order element matrix

(2) A new weighting matrix K is defined by using location attribute matrix F, distance weight matrix W, road grade matrix L, and time-division traffic congestion degree matrix T. k_j is the j-th column of matrix K:

$$K = \left(k_1, k_2, \cdots, k_j, \cdots, k_N\right) \tag{5}$$

(3) In order to make matrix K irreducible and random, it is necessary to standardize each column vector k_j of matrix K to obtain standard matrix K_N

(4) Construct a new matrix G^*. Use formula $(1-\alpha)K_N$ instead of formula $(1-\alpha)/N * I_{N\times N}$, and get

$$G^* = \alpha A^* + (1-\alpha)K_N \tag{6}$$

According to the Perron-Frobenius theorem [23], take the eigenvalue of the eigenvector $\lambda = 1$, and calculate the main eigenvector $X_1^* = \{g(1), g(2), \cdots, g(N)\}(\lambda = 1)$ of G^* to obtain the level of key nodes; $g(1), g(2), \cdots, g(N)$ represents each component of the principal eigenvector X_1^*. The size of the component value represents the importance of the node. The larger the value, the more important the node is, that is, the higher the criticality level.

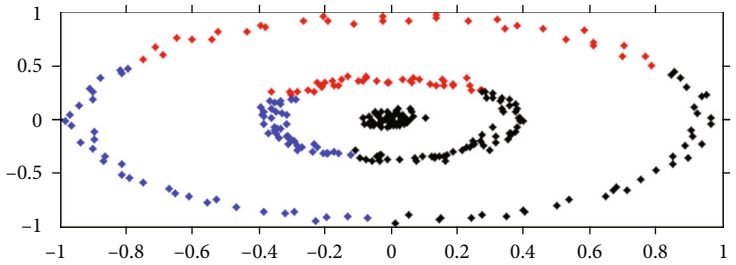

Figure 2: Partition results using the k-means clustering algorithm.

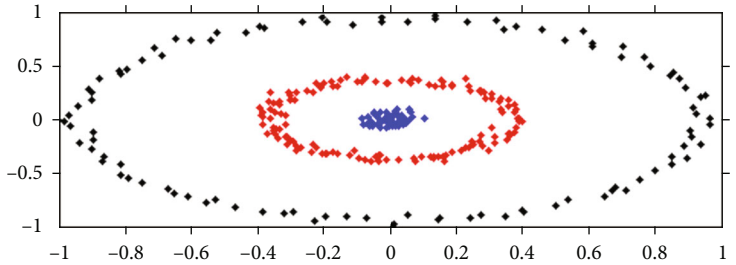

Figure 3: Partition results using the spectral clustering algorithm.

Input: n sample points $X = \{x_1, x_2, \cdots, x_n\}$ and the number of clusters m
1. Calculate the similarity matrix S of $n \times n$;
2. Based on the similarity matrix S, calculate the weighting matrix E considering the weight influence factors of location, distance, road grade, and traffic congestion degree;
3. Calculate the degree matrix D;
4. Calculate the Laplace matrix $P = D^{-1/2}PD^{-1/2} = D^{-1/2}(D - E)D^{-1/2}$;
5. Calculate the eigenvalues of Laplace matrix P and sort the eigenvalues from small to large;
6. According to the two-dimensional decision diagram in 4.2, select the central nodes and get the number of categories m;
7. Take the first m eigenvalues of Laplace matrix P and calculate the eigenvectors of the first m eigenvalues $u_1, u_2, \cdots, u_m$;
8. Form the above m column vectors into a matrix $U = \{u_1, u_2, \cdots, u_m\}$, $U \in R^{n+m}$;
9. Let $y_i \in R^m$ be the vector of line i of U, where $i = 1, 2, \cdots, n$;
10. For $i = 1, 2, \cdots, n$, $y_i \in R^m$ is sequentially united so that $|y_i| = 1$;
11. Clustering new sample point $Y = \{y_1, y_2, \cdots, y_n\}$ into cluster $C_1, C_2, \cdots, C_m$ using k-means algorithm;
12. Get the clustering result cluster $A_1, A_2, \cdots, A_m$, where $A_m = \{y_i \mid y_i \in C_m\}$, $i \in n$.
Output: clusters $A_1, A_2, \cdots, A_m$

Algorithm 1: Improved spectral clustering algorithm flow.

4.2. Determine the Cluster Center and the Number of Clusters. Alex Rodriguez and Alessandro Laio pointed out that the cluster center has the following two attributes:

(1) Cluster center is an important node surrounded by low-impact neighbors

(2) The initial cluster centers are evenly distributed in the physical network, and the "distance" between the center points is relatively larger

In this paper, the method of two-dimensional decision graph is used to select the cluster center and the number of clusters. It is easy to understand that the number of cluster centers is the number of clusters. The center point of block detection can be determined by considering ρ and δ, where ρ is the horizontal axis and δ is the vertical axis:

$$\gamma_i = \rho_i \delta_i, i \in I_S. \tag{7}$$

ρ_i, that is, the i-th component of vector X_i^*, evaluates the importance of node i and represents the shortest path distance between node i and higher critical nodes. A comprehensive value sequence $\{\gamma_i\}_{i=1}^N$ is calculated, where $\gamma_i = \rho_i \delta_i, i \in I_S$ represents the comprehensive value of node i. The larger the reference γ value, the more likely it is to be the cluster center. Therefore, it is necessary to arrange $\{\gamma_i\}_{i=1}^N$, in descending order, and then intercept several data points from front to back as the clustering center. Select m nodes distributed at the top right of the decision graph as

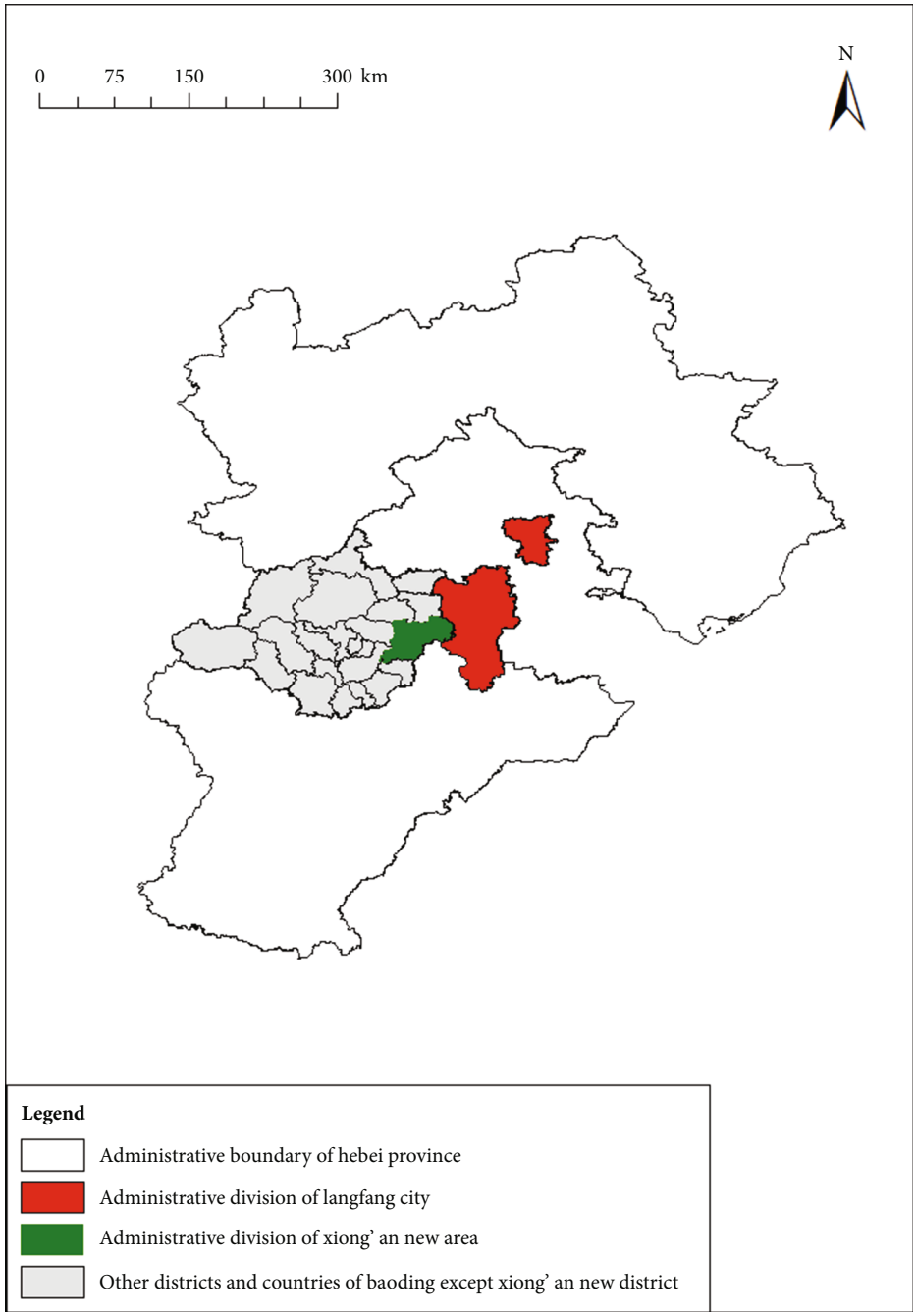

Figure 4: A display map of administrative divisions of Langfang city and Xiong'an New Area.

the clustering center, and "m" is the number of clustering clusters.

4.3. Improved Spectral Clustering Algorithm for Functional Block Division of a Highway Traffic Network. At present, the k-means clustering algorithm is mostly used in the research of functional block division of a highway traffic network. However, the k-means clustering algorithm is a prototype-based clustering. Its premise is that the cluster is spherical. Therefore, when using k-means clustering, the original clusters will be spliced to make them appear closer to spherical shape. Therefore, k-means has a better grouping effect on spherical clusters, but not on nonspherical clusters, clusters with different sizes and densities. The spectral clustering algorithm is based on the spectral graph theory. It has the characteristics of being able to cluster in any shape of the sample space and converging to the global optimal solution. It is more adaptable to data distribution. For example, when clustering clusters with three concentric circles in shape, the ideal clustering result should be that the three concentric circles form a class, respectively. The division results of k-means clustering algorithm are shown in Figure 2. Blue, black, and red represent the three categories. The k-means algorithm does not divide each concentric

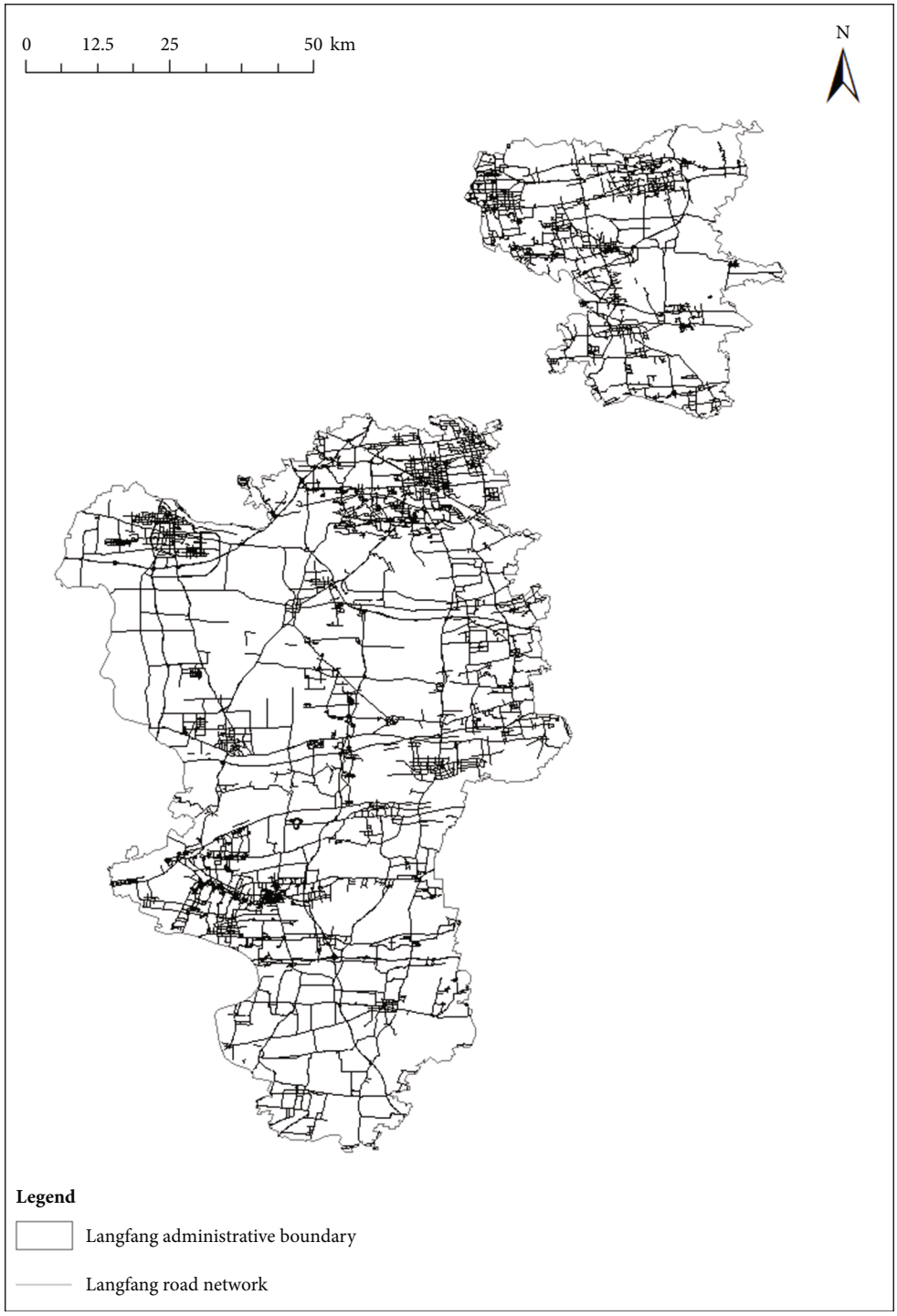

Figure 5: Road network distribution in Langfang city.

circle into one category. The division results using the spectral clustering algorithm are shown in Figure 3. The three colors of blue, black, and red represent the three categories. The spectral clustering algorithm divides each concentric circle into one category. The comparison shows that the division result of the spectral clustering algorithm is in line with the expected situation.

The spectral clustering algorithm is not only more adaptable to the data distribution but also uses the dimensionality reduction technology. It is more suitable for processing high-dimensional data such as road traffic networks. Based on the above considerations, this paper uses a spectral clustering algorithm to divide the functional blocks of a highway traffic network. The basic idea of spectral clustering is to decompose the Laplace matrix of sample data. Using the characteristics of Laplace matrix eigenvector data, cluster it based on data mining technology to form a specific clustering scheme. Considering the actual situation

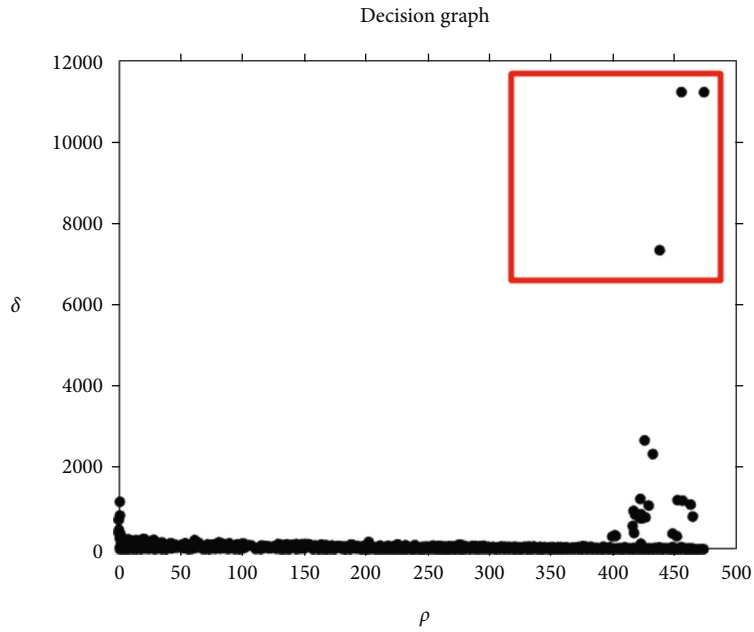

Figure 6: Selection results of cluster centers of functional blocks of Langfang highway transportation network.

of a highway traffic network, this paper improves the spectral clustering algorithm. On the basis of the similarity matrix, the weight matrix of location, distance, road grade, and traffic congestion degree is added to obtain a new weight matrix in line with the actual road network situation. Then, clustering is carried out to obtain the division results of functional blocks of a highway traffic network.

The flow of the improved spectral clustering algorithm is shown in Algorithm 1.

To sum up, the procedure for dividing the functional blocks of the highway transportation network can be described as the following steps.

Step 1: in the highway traffic network, calculate the adjacency matrix A, location attribute matrix F, distance weight matrix W, road grade matrix L, and time-division traffic congestion degree matrix T

Step 2: get the ranking of key nodes of a highway traffic network through the improved PageRank algorithm

Step 3: draw a two-dimensional decision diagram according to the ranking of key nodes and the shortest path distance, and select the cluster center. The number of cluster centers is the number of cluster clusters

Step 4: divide the road traffic network into functional blocks based on the improved spectral clustering algorithm

5. Experiment and Analysis

In this paper, a multiscale case study is carried out based on Langfang and Xiong'an New Area demonstration areas. Langfang city and Xiong'an New Area are two administrative regions with different scales. Xiong'an New Area is located in Baoding City, and both Baoding city and Langfang city are located in Hebei Province. The administrative divisions of Langfang city and Xiong'an New Area are shown in Figure 4. Using the IPSC Algorithm, the road network block division results are obtained, and the road traffic network aggregation in Langfang and Xiong'an New Area is obtained. Maintaining the connectivity of the center of each block can improve the operation efficiency of the whole transportation network, so as to provide theoretical reference for traffic management and service system personnel and provide a new model reference for the subsequent maintenance and construction of highway transport network.

5.1. City Level Case Study-Langfang Demonstration Area. Langfang is located between Beijing and Tianjin and in the hinterland of Bohai Economic Circle. It enjoys the reputation of "Pearl on Beijing-Tianjin Corridor," "Corridor connecting Beijing and Tianjin, Square around Bohai Sea," etc. It is 40 kilometers away from Tiananmen Square, 60 kilometers away from the central area of Tianjin, 70 kilometers away from the capital and Tianjin airports, and 100 kilometers away from Tianjin Xingang. There are 6 main railway lines, 8 expressways, and 25 national and provincial highways criss-crossing in the urban area. Langfang expressway runs through the south-central part of Langfang, Beijing-Shanghai high-speed railway, and Beijing New Airport, which further makes Langfang seamlessly connect with Beijing and Tianjin. By the end of 2017, there were 26 ordinary national and provincial trunk highways with a total length of 775.046 kilometers in Langfang City and 25 highways above grade II, accounting for 100% of the total mileage of maintenance and management highways.

From the perspective of the whole city, the IPSC Algorithm is used to divide the functional blocks of Langfang highway traffic network. Figure 5 shows the distribution of the highway traffic network in Langfang city. Firstly, the Primal Approach is used to construct the topology of Langfang highway traffic network. The theoretical analysis model of Langfang highway traffic network is constructed by adding

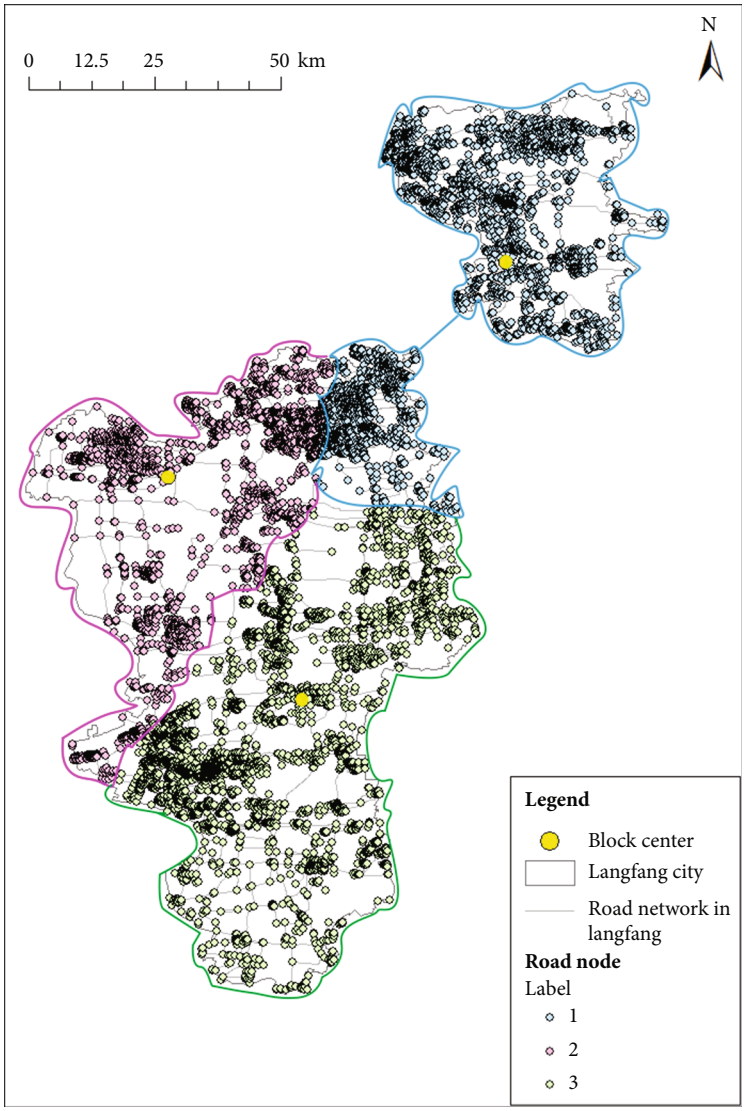

Figure 7: The block division results of Langfang highway traffic network obtained by IPSC Algorithm.

the weight influence factors including ground feature and facility attributes, topological distance, highway network grade, and dynamic traffic congestion degree. Then the improved PageRank algorithm is used to determine the ranking of key nodes. A two-dimensional decision graph is constructed by combining the ranking of key nodes and the shortest path distance. According to the two-dimensional decision graph theory in 4.2, the nodes distributed at the top right of the decision graph are selected as the clustering center of Langfang highway transportation network. The red box in Figure 6 shows the selection results of cluster centers in Langfang city obtained from the decision map. It can be seen from Figure 6 that there are three cluster centers of the road traffic network in Langfang City. The number of functional block structures of the road traffic network in Langfang City is three. Using the improved spectral clustering algorithm, the road nodes of Langfang highway traffic network are classified into the corresponding block structure to identify the block division results of the target. Figure 7 shows the final result of using the IPSC Algorithm to divide the functional blocks of the Langfang highway traffic network.

We analyze the practical significance of the experimental results in Langfang city. The blue area in Figure 7 is block 1. The purplish-red area is block 2. The green area is block 3. As the result of block division shows, the road nodes in the block are more closely connected with each other. From the figure, the center positions of the three blocks can be clearly found. From the perspective of geospatial structure, improving the connectivity and convenience of these three block structures can effectively improve the highway traffic situation in Langfang. The route at the center point in the connected graph is the key route. This provides a certain reference basis for relevant departments, showing the trend of highway transportation network connectivity. At the same time, the location of the road traffic network that is mainly maintained and improved can also be determined on the road network connected by the block structure. Improving

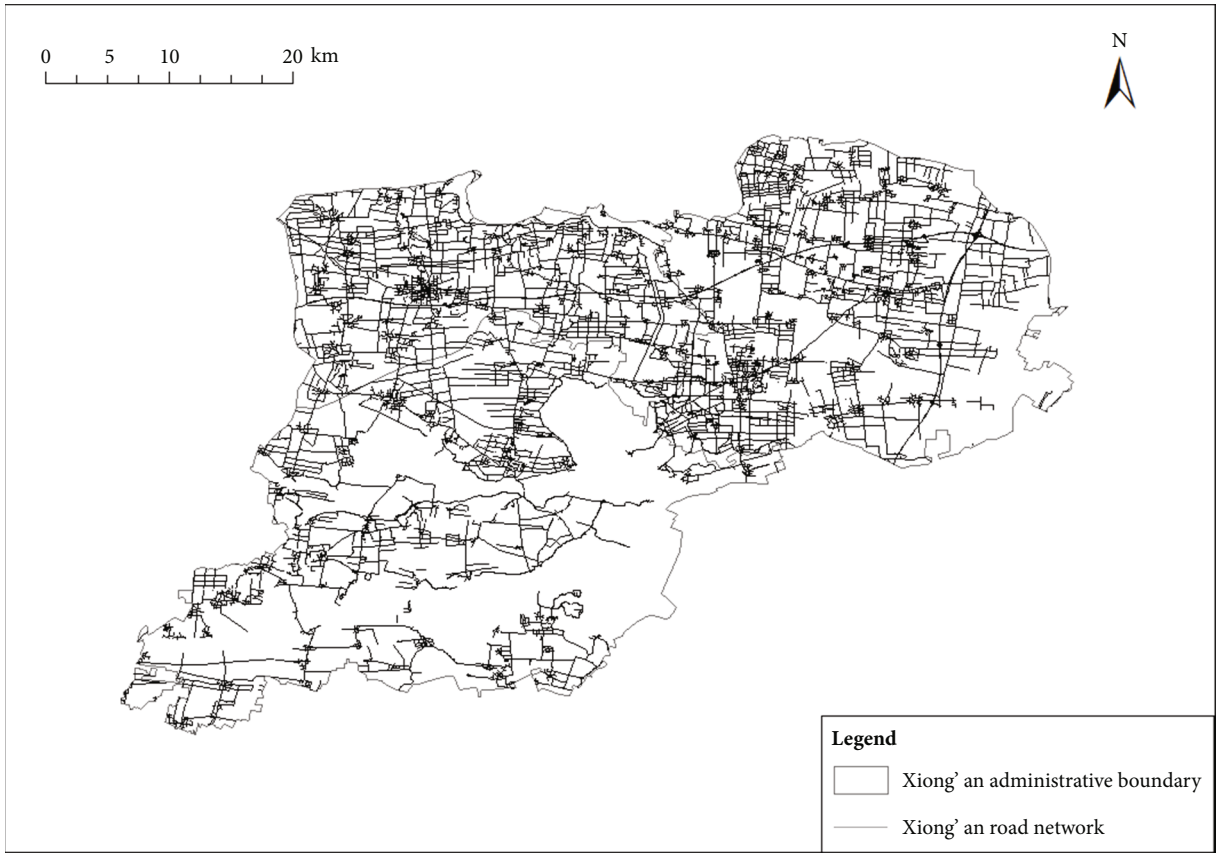

Figure 8: Road network distribution in Xiong'an New Area.

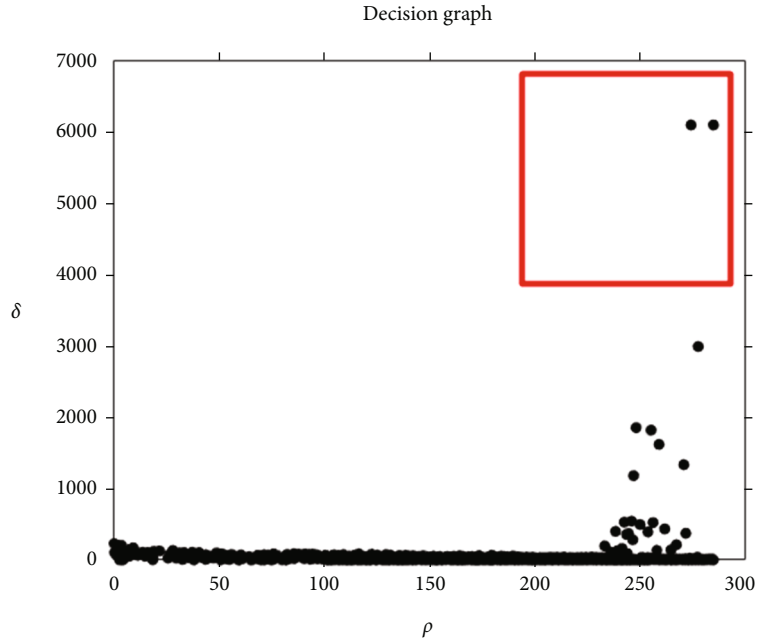

Figure 9: Selection results of cluster centers of functional blocks of Xiong'an highway transportation network.

the connectivity of central points can improve the connectivity of the whole highway transportation network in Langfang. At the same time, it also maintains the operation efficiency of highway transport network.

5.2. Case Study of District Level-Xiong'an New Area Demonstration Area. Xiong'an New Area is a state-level new area under the jurisdiction of Hebei Province, including Xiong'an County, Rongcheng County, Anxin County, and

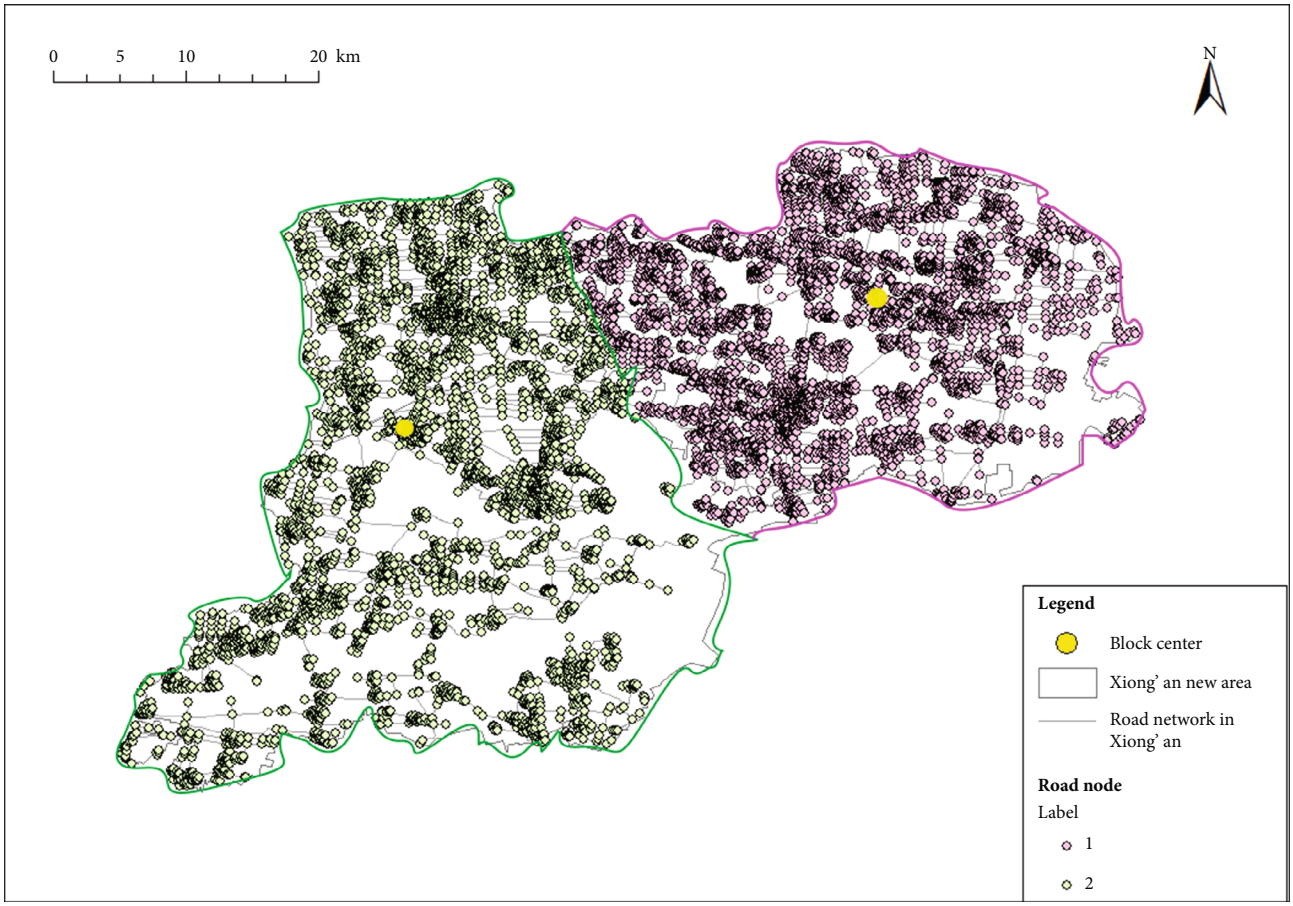

Figure 10: The block division results of Xiong'an highway traffic network obtained by the IPSC Algorithm.

some surrounding areas. On April 1, 2017, the Central Committee of the Communist Party of China and the State Council issued a notice deciding to set up a state-level new area, Xiong'an New Area, Hebei Province. There are Beijing-Xiong'an Intercity Railway, TianJin- Xiong'an Intercity Railway, Gu'an-Baoding Intercity Railway, and Beijing-Shijiazhuang Intercity Railway in Xiong'an New Area and G18 Rongcheng-Wuhai Expressway, G0211 TianJin-Shijiazhuang Expressway, G45 Daqing-Guangzhou Expressway, S7 TianJin-Baoding Expressway, and Beijing-Xiong'an Expressway that run through the whole territory. On August 30, 2019, Xiong'an New Area set up Xiong'an District of China (Hebei) Pilot Free Trade Zone. In December 2019, Xiong'an New District was selected as the first batch of pilot areas for the construction of a strong transportation country.

Based on the district perspective, the IPSC Algorithm is used to divide the functional blocks of the highway traffic network in Xiong'an New Area. Figure 8 shows the distribution of the highway traffic network in Xiong'an New Area. First, use the Primal Approach to construct the topology of the highway traffic network in Xiong'an New Area. The theoretical analysis model of the road traffic network in Xiong'an New Area is constructed by adding factors including the attributes of ground objects and facilities, topological distance, road network level, and dynamic traffic congestion degree weight. Then use the improved PageRank algorithm to determine the critical node ordering. A two-dimensional decision graph is constructed by combining key node ranking and shortest path distance. According to the two-dimensional decision graph theory in 4.2, the nodes distributed at the top right of the decision graph are selected as the clustering center of the highway traffic network in Xiong'an New Area. The red box in Figure 9 shows the selection results of cluster centers in Xiong'an New Area obtained from the decision diagram. As can be seen from Figure 9, there are two highway traffic network clustering centers in Xiong'an New Area. The number of functional block structures of the highway transportation network in Xiong'an New Area is two.

The improved spectral clustering algorithm is used to classify the road nodes of the road traffic network in Xiong'an New Area into the corresponding block structure. Thereby, the block division result of the target is identified. Figure 10 shows the results of dividing the functional blocks of the highway traffic network in Xiong'an New Area using the IPSC Algorithm.

We analyze the practical significance of the experimental results in Xiong'an New Area. The purple-red area in Figure 10 is block 1. The green area is block 2. The central points of the two blocks can be clearly seen from the figure. The center points of the two blocks can be clearly seen from the figure. From the perspective of geospatial structure, improving the connectivity and convenience of these two block structures can effectively improve the highway traffic

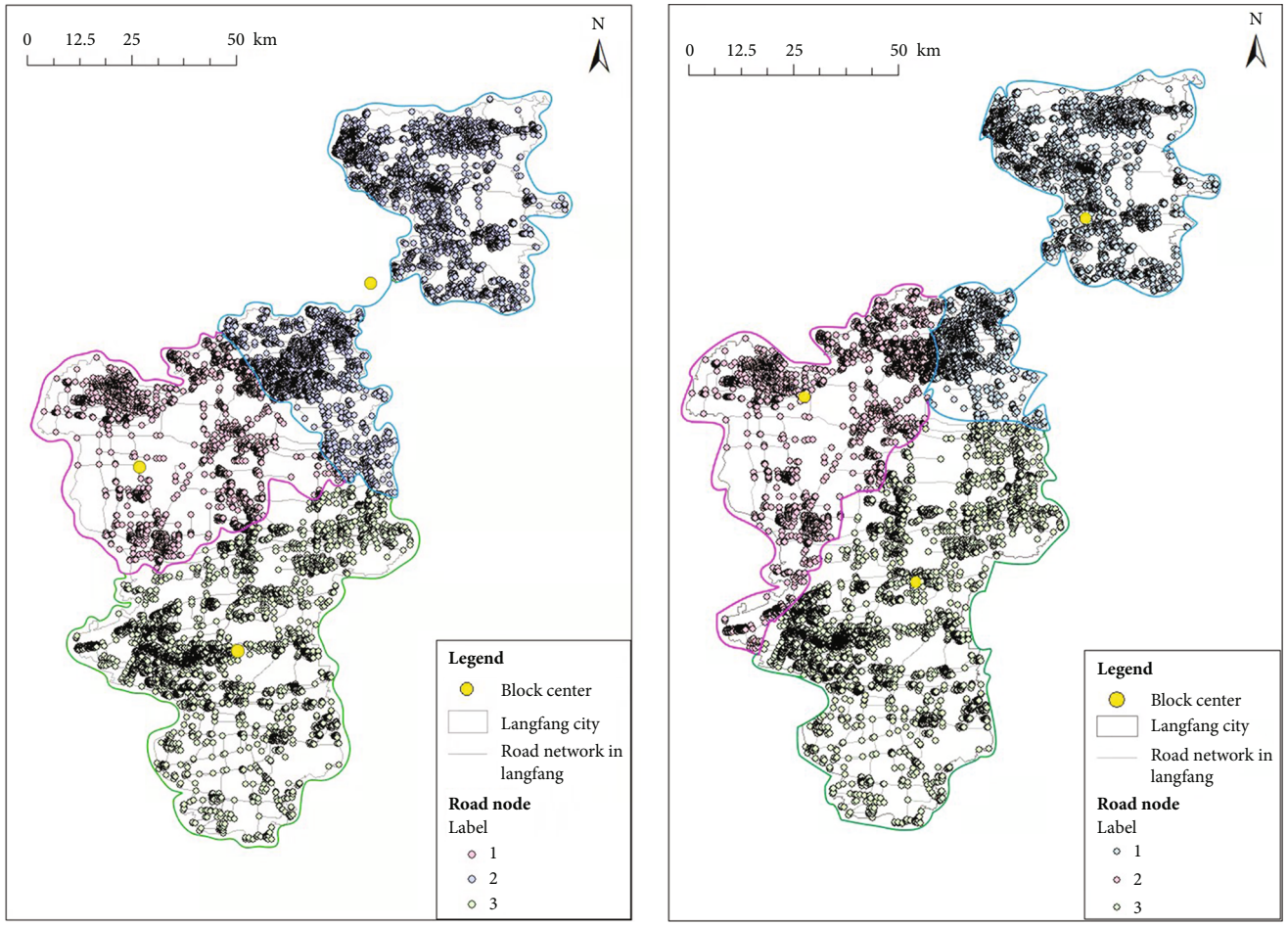

FIGURE 11: Comparison of the division results of functional blocks of the highway traffic network in Langfang City. (a) *k*-means algorithm. (b) IPSC algorithm.

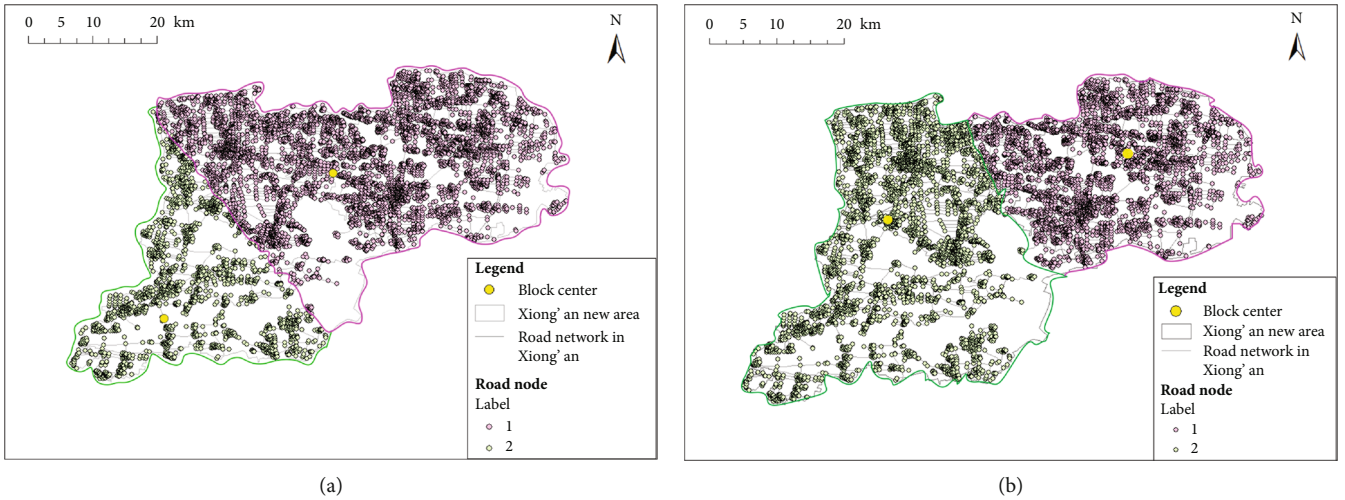

FIGURE 12: Comparison of the division results of functional blocks of the highway traffic network in Xiong'an New Area. (a) *k*-means algorithm. (b) IPSC algorithm.

situation in Xiong'an New Area. At the same time, the connecting route between the central points of the two blocks will be built and maintained, which will reduce the occurrence of dangerous accidents on this road section, ensure highway utilization efficiency, and facilitate people's living and service facilities. At present, the highway traffic network construction in Xiong'an New Area is not complete. The results of this paper can provide decision-making references for the highway construction in Xiong'an New Area.

5.3. Comparison of k-Means Clustering Algorithm and IPSC Algorithm Example Analysis Results. Figures 11(a) and 12(a) show the results of dividing the functional blocks of the highway traffic network in Langfang City and Xiong'an New Area using the *k*-means algorithm, respectively. Figures 11(b) and 12(b) show the results of road traffic network function block division in Langfang city and Xiong'an New Area, respectively, using the IPSC Algorithm.

Comparing the results obtained by the two algorithms, it can be seen that the cluster centers in the functional block division results of the highway traffic network obtained by the *k*-means algorithm are not located in the important positions that connect many roads. This is due to the random selection of clustering centers by the *k*-means algorithm. In addition, each cluster in the functional block division result of the highway transportation network obtained by using the *k*-means algorithm is close to a spherical cluster. This is due to the characteristics of the *k*-means algorithm (that is, it will splice the original clusters to make them closer to spherical shape). The IPSC Algorithm is used to divide the functional blocks of the road traffic network avoids these problems. There are three reasons for this. First, the improved PageRank algorithm in the IPSC Algorithm scientifically determines the cluster center and the number of clusters. Second, the spectral clustering algorithm in the IPSC Algorithm has the advantage of being more adaptable to the data distribution. Third, when the IPSC Algorithm divides the functional blocks of the highway traffic network, the weight factors such as the location attribute, distance, highway grade, and traffic congestion degree of the highway are added. It takes into account the actual situation of the road traffic network. Therefore, the division result of a highway traffic network functional blocks obtained by the IPSC Algorithm is more in line with the actual situation.

6. Conclusion

On the basis of predecessors, this paper analyzes the complex traffic network of the multiscale aggregation model. An Improved PageRank-Spectral Clustering (IPSC) Algorithm is proposed to divide the functional blocks of a highway traffic network. Firstly, the theoretical analysis model of a highway traffic network with dynamic weight influence factors is constructed to provide a basic model for the subsequent research on the functional block division of a highway traffic network. Then, for the problem that the cluster center is difficult to determine, the improved PageRank algorithm is used to determine the ranking of key nodes. Combined with the ranking of key nodes and the shortest path distance, the clustering center and the number of clusters are determined. Then, an improved spectral clustering algorithm is used to divide the functional blocks of a highway traffic network. Finally, combined with the two scales of Langfang city and Xiong'an New Area, the multiscale aggregation model of a complex traffic network is analyzed, and the functional block division results of the highway traffic network in Langfang city and Xiong'an New Area are obtained. It will provide decision-making references for highway construction in both areas.

Data Availability

The traffic network data of Langfang city and Xiong'an New Area used to support the results of this study have not been available because the original road network data is the traffic situation of the real county location in China. It can reflect the real data of China's geographical location. Therefore, it cannot be made public. However, the results of the later results can be referenced and applied.

Conflicts of Interest

The authors declare that there is no conflict of interest regarding the publication of this paper.

Acknowledgments

This paper is supported by the Doctoral Research Startup Fund Project (BKY-2021-30), Major Special Project-The China High-Resolution Earth Observation System (30-Y30F06-9003-20/22), Graduate Innovation Funding Project of North China Institute of Aerospace Engineering (YKY-2021-27), Langfang City Science and Technology Support Plan Project (2021011074), National Key R&D Projects (2019YFE0127300), National Defense Basic Scientific Research Project (JCKY2020908B001), and National Defense Basic Scientific Research Program (JCKY2019407D004).

References

[1] Y. Du, F. Chen, and Z. Zhang, "Analysis of urban rail transit based on complex network," *Applied Mechanics and Materials*, vol. 90-93, no. 90-93, pp. 770–773, 2011.

[2] Y. Qian, B. Wang, X. Yuan, J. Zeng, and N. Wang, "A simulation of the cascading failure of a complex network model by considering the characteristics of road traffic conditions," *Nonlinear Dynamics*, vol. 80, no. 1-2, pp. 413–420, 2015.

[3] D. Sun, Y. Zhao, and Q. C. Lu, "Vulnerability analysis of urban rail transit networks: a case study of Shanghai, China," *Sustainability*, vol. 7, no. 6, pp. 6919–6936, 2015.

[4] J. Zeng, Y. Qian, X. Liu, C. Zhang, D. Xu, and X. Wei, "Reliability analysis of Tianjin urban rail transit network based on complex network evolution characteristics," *Modern Physics Letters B*, vol. 35, no. 4, article 2150075, 2021.

[5] S. Fortunato and D. Hric, "Community detection in networks: a user guide," *Physics Reports*, vol. 659, no. none, pp. 1–44, 2016.

[6] Y. Yang, L. Jia, Y. Qin, S. Han, and H. Dong, "Understanding structure of urban traffic network based on spatial-temporal correlation analysis," *Modern Physics Letters B*, vol. 31, no. 22, p. 1750230, 2017.

[7] Y. Yang, J. Cao, Y. Qin, L. Jia, H. Dong, and A. Zhang, "Spatial correlation analysis of urban traffic state under a perspective of community detection," *International Journal of Modern Physics B*, vol. 32, no. 12, p. 1850150, 2018.

[8] P. Yang, *Multi-Scale Study of Street Furniture Color-Taking Hefei as an Example*, Hefei University of Technology, 2019.

[9] Z. Tian, L. Jia, H. Dong, F. Su, and Z. Zhang, "Analysis of urban road traffic network based on complex network," *Procedia Engineering*, vol. 137, no. none, pp. 537–546, 2016.

[10] J. F. Zheng, Z. Y. Gao, and X. Zhao, "Properties of transportation dynamics on scale-free networks," *Physica A*, vol. 373, no. none, pp. 837–844, 2007.

[11] X. Ma, L. Gao, X. Yong, and L. Fu, "Semi-supervised clustering algorithm for community structure detection in complex networks," *Physica A*, vol. 389, no. 1, pp. 187–197, 2010.

[12] H. Jin, S. Wang, and C. Li, "Community detection in complex networks by density-based clustering," *Physica A: Statistical Mechanics and its Applications*, vol. 392, no. 19, pp. 4606–4618, 2013.

[13] M. Gong, J. Liu, L. Ma, Q. Cai, and L. Jiao, "Novel heuristic density-based method for community detection in networks," *Physica A: Statistical Mechanics and its Applications*, vol. 403, pp. 71–84, 2014.

[14] D. Lai, H. Lu, and C. Nardini, "Finding communities in directed networks by PageRank random walk induced network embedding," *Physica A: Statistical Mechanics & Its Applications*, vol. 389, no. 12, pp. 2443–2454, 2010.

[15] W. Wang, D. Liu, X. Liu, and L. Pan, "Fuzzy overlapping community detection based on local random walk and multidimensional scaling," *Physica A: Statistical Mechanics and its Applications*, vol. 392, no. 24, pp. 6578–6586, 2013.

[16] F. Wu and B. A. Huberman, "Finding communities in linear time: a physics approach," *European Physical Journal B-Condensed Matter*, vol. 38, no. 2, pp. 331–338, 2004.

[17] D. Ye, *Distance Based Spectral Clustering Algorithm for Network Community Discovery*, Huazhong University of Science and Technology, 2016.

[18] X. Zhu, W. Song, and L. Gao, "Regional patch detection of road traffic network," *Journal of Sensors*, vol. 2020, Article ID 6836091, 6 pages, 2020.

[19] K. Zheng, Y. Zheng, N. J. Yuan et al., "On discovery of gathering patterns from trajectories," in *IEEE 29th Internationl Conference on Data Engineering*, pp. 242–253, Brisbane, Australia, 2013.

[20] K. Zheng, Y. Zheng, N. J. Yuan, S. Shang, and X. Zhou, "Online discovery of gathering patterns over trajectories," *IEEE Transactions on Knowledge and Data Enginering*, vol. 8, no. 26, pp. 1974–1988, 2013.

[21] JTG B01-2017, "Technical standard of highway engineering," *Beijing : China Communications Press Co.,Ltd.*, vol. 12, 2014.

[22] C. Stanfill and D. Waltz, "Toward memory-based reasoning," *Communications of the ACM*, vol. 29, no. 12, pp. 1213–1228, 1986.

[23] G. H. Golub and C. F. V. Loan, *Matrix Computation*, The Johns Hopkins University Press, Baltimore, MA, USA, 1996.

Hindawi
Journal of Sensors
Volume 2024, Article ID 9873845, 1 page
https://doi.org/10.1155/2024/9873845

Retraction

Retracted: English-Chinese Machine Translation Model Based on Bidirectional Neural Network with Attention Mechanism

Journal of Sensors

Received 23 January 2024; Accepted 23 January 2024; Published 24 January 2024

This article has been retracted by Hindawi following an investigation undertaken by the publisher [1]. This investigation has uncovered evidence of one or more of the following indicators of systematic manipulation of the publication process:

(1) Discrepancies in scope
(2) Discrepancies in the description of the research reported
(3) Discrepancies between the availability of data and the research described
(4) Inappropriate citations
(5) Incoherent, meaningless and/or irrelevant content included in the article
(6) Manipulated or compromised peer review

The presence of these indicators undermines our confidence in the integrity of the article's content and we cannot, therefore, vouch for its reliability. Please note that this notice is intended solely to alert readers that the content of this article is unreliable. We have not investigated whether authors were aware of or involved in the systematic manipulation of the publication process.

Wiley and Hindawi regrets that the usual quality checks did not identify these issues before publication and have since put additional measures in place to safeguard research integrity.

We wish to credit our own Research Integrity and Research Publishing teams and anonymous and named external researchers and research integrity experts for contributing to this investigation.

The corresponding author, as the representative of all authors, has been given the opportunity to register their agreement or disagreement to this retraction. We have kept a record of any response received.

References

[1] L. Yonglan and H. Wenjia, "English-Chinese Machine Translation Model Based on Bidirectional Neural Network with Attention Mechanism," *Journal of Sensors*, vol. 2022, Article ID 5199248, 11 pages, 2022.

Hindawi
Journal of Sensors
Volume 2022, Article ID 5199248, 11 pages
https://doi.org/10.1155/2022/5199248

Research Article

English-Chinese Machine Translation Model Based on Bidirectional Neural Network with Attention Mechanism

Li Yonglan[1] **and He Wenjia**[2]

[1]*School of Foreign Languages, Guizhou University of Finance & Economics, 550025, China*
[2]*Research Centre of Big-Data Corpus & Language Projects, School of Foreign Languages, Guizhou University of Finance & Economics, 550025, China*

Correspondence should be addressed to Li Yonglan; abbylyl@mail.gufe.edu.cn

Received 25 November 2021; Revised 20 December 2021; Accepted 1 March 2022; Published 16 March 2022

Academic Editor: Wei Zhang

In recent years, with the development of deep learning, machine translation using neural network has gradually become the mainstream method in industry and academia. The existing Chinese-English machine translation models generally adopt the deep neural network architecture based on attention mechanism. However, it is still a challenging problem to model short and long sequences simultaneously. Therefore, a bidirectional LSTM model integrating attention mechanism is proposed. Firstly, by using the word vector as the input data of the translation model, the linguistic symbols used in the translation process are mathematized. Secondly, two attention mechanisms are designed: local attention mechanism and global attention mechanism. The local attention mechanism is mainly used to learn which words or phrases in the input sequence are more important for modeling, while the global attention mechanism is used to learn which layer of expression vector in the input sequence is more critical. Bidirectional LSTM can better fuse the feature information in the input sequence, while bidirectional LSTM with attention mechanism can simultaneously model short and long sequences. The experimental results show that compared with many existing translation models, the bidirectional LSTM model with attention mechanism can effectively improve the quality of machine translation.

1. Introduction

Machine translation is an important part of natural language processing. Machine translation (MT) mainly studies the process of how to automatically translate one human language into another by computer [1–5], so as to realize the mutual conversion between different languages. With the rapid development of science and technology and social economy, the cultural exchanges at home and abroad are increasing, which leads to the increasing demand for Chinese-English translation. Google, Microsoft, Baidu, Sogou, and other companies are constantly developing and perfecting machine translation systems. Compared with human translation, machine translation, as a low-cost and efficient communication method, has become an indispensable part of the translation industry. The mainstream machine translation models mainly include statistical machine translation (SMT) [6–8] and neural machine translation (NMT) [9–11]. The traditional machine translation method is the SMT model, which counts information such as word pairs, parallel phrase pairs, and parallel syntactic structures from large-scale parallel corpus to establish a statistical model for the translation process. The research methods mainly include word-based statistical methods [12], phrase-based statistical methods [13], and syntactic structure-based statistical methods [14]. Among them, the phrase-based statistical machine translation takes phrases (that is, any consecutive words) as the basic translation unit, which can well solve the dependency relationship between the local contexts of sentences, and the translation quality has been greatly improved compared with the word-based statistical method. In recent years, with the development of deep learning, a translation model using neural network to map Chinese to English has emerged, which is called NMT

model [15, 16]. NMT model significantly improves the quality of machine translation, surpasses the performance of traditional SMT methods, and becomes the mainstream method in industry and academia at present. Different from the traditional SMT, NMT is committed to building a separate neural network to achieve the best translation performance through joint training and adjustment. The benchmark NMT system is the encoder-decoder framework [17], which uses bilingual parallel corpus to realize the end-to-end [18] training process. Coding and decoding functions are realized by recurrent neural networks (RNN) [19, 20]. These two cyclic neural networks are modeled by an attention layer connection, which detects the information related to all the words at the source when translating the target words. This process is called attention mechanism [21]. RNN is a connection model, which can capture the dynamic information of input sequence through cyclic operation in network nodes. Unlike the standard feedforward neural network, the circular neural network can maintain a state, which can represent information in any long context window. Gulcehre et al. [22] proposed the method of integrating RNN language model into NMT. Sano et al. [23] expanded the RNN structure, transferred the derivative to historical information, and improved the memory ability of translation model for long-distance information. In view of the difficulty in introducing translation rules into NMT, Wu et al. [24] coded the rules and selected the rules through attention mechanism in the process of translation, which achieved good translation results, but it also caused high time complexity. In recent years, the long short-term memory (LSTM) network has made breakthrough progress in many learning tasks in the computer field, such as adding subtitles to images, language translation, and handwriting font recognition. Ren et al. [25] extended the LSTM network structure to 16 layers, which made the single model translation result better than SMT. However, the general neural network model will not save the intermediate information and will give the same weight to the short sequence or phrase in the input sequence. Therefore, this paper proposes an attention bidirectional LSTM (A-BLSTM) model which integrates attention mechanism. Because different words and phrases in an input sequence will contain different amounts of information, the A-BLSTM model contains a local attention mechanism. Local attention mechanism is mainly used to learn which word or phrase in the input sequence contains more information. Global attention mechanism is used to learn which layer of representation vector of input sequence should be given more attention (weight). Our main contributions are as follows: Firstly, for the simultaneous modeling of short sequences and long sequences, a hierarchical structure integrating attention mechanism is proposed, which can obtain multilayer intermediate representation vectors of input sequences instead of a single fixed-length word vector. Secondly, the number of network layers in A-BLSTM model can change with the complexity of tasks. Finally, the local attention mechanism can effectively select relatively important words or phrases, and the global attention mechanism can effectively select more credible intermediate representation vectors.

2. Word Vector Generation

To transform the machine translation problem into a machine learning problem, it is first necessary to mathematize the language symbols used in the translation process. As the input data of the translation model, word vector has a great influence on the quality of the final model. As the transmission form of data in NMT, the acquisition of word vector is the basis of all research work.

2.1. Word Vector Model. Skip-gram model is used for word vector model. Skip-gram model [26], also known as skip model, takes a word as input and predicts its context around a text sequence. For example, for an example text sequence ["that", "is", "a", "question"]. Given "is", assuming that the window size is 2, what the model needs to obtain is the probability of its neighboring words "that", "a", and "question". At this time, "is" is called the head word, and other words are called background words. The basic idea of this model is to encode all words in One-Hot mode, input them into the neural network with only one hidden layer for training, and use the weight of hidden layer as the expression vector of words after training. The Skip-gram network structure is shown in Figure 1.

In this network, the dimensions of the input and output vectors of the neural network are the same, and there is no activation function in the hidden layer. In order to ensure that the output vector is a probability distribution, the output layer uses softmax. The number of neurons in the hidden layer depends on the dimension of word vector, and the number of neurons in the output layer is equal to the number of words in the corpus. Suppose the dictionary size is $|v|$. Match each word in the dictionary with integers from 0 to $|v|-1$ one by one, and establish the dictionary index set $v = \{0, 1, \cdots, |v|-1\}$. For any word in the dictionary, its corresponding integer in the dictionary is the index of the word. Assuming that a text sequence of length T is given, the word corresponding to time t is w^t, and the size of time window is m, then the Skip-gram model maximizes the probability of any central word generating background words, and the calculation method is shown in formula (1):

$$J = \prod_{t=1}^{T} \prod_{-m \le j \le m, j \ne 0} P\left(w^{t+j} \middle| w^t\right). \tag{1}$$

In order to maximize the objective function, the original maximum likelihood estimation becomes the minimization of formula (2).

$$J = -\frac{1}{T} \sum_{t=1}^{T} \sum_{-m \le j \le m, j \ne 0} \log\left\{P\left(w^{+j} \middle| w^t\right)\right\}. \tag{2}$$

v and u represent the vector of the central word and the background word, respectively. For the word with index i in the dictionary, the vector of the word as the central word and the background word is expressed as v_i and u_i, respectively. In order to embed the model parameters into the loss function, it is necessary to use the model parameters to

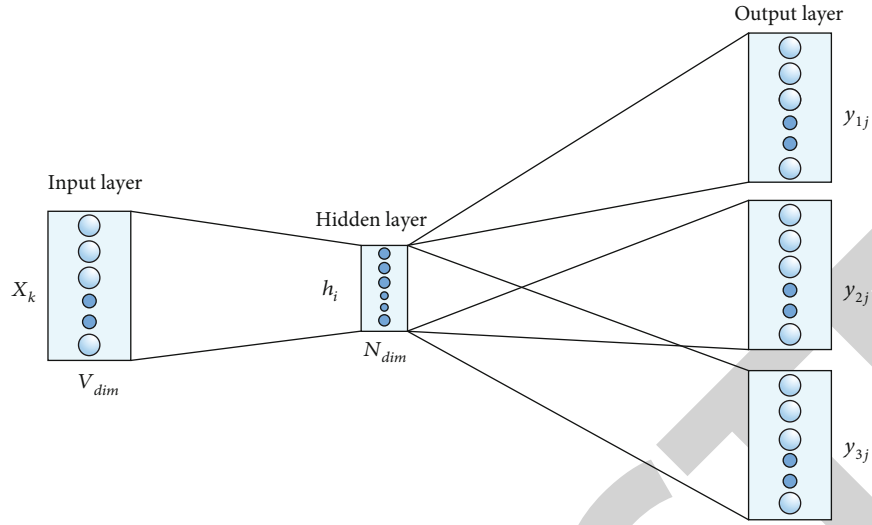

Figure 1: Structure of Skip-gram.

calculate the probability of generating background words from the center words in the loss function. Assume that the probabilities of generating background words from the central word are independent of each other. For the center word w_c and the background word w_o, the probability that the center word in the loss function generates the background word is calculated by the softmax function.

$$P(w_o|w_c) = \frac{\exp\left(u_o^T v_c\right)}{\sum_{i\in v}\exp\left(u_i^T v_c\right)}. \tag{3}$$

When the sequence length is large, a smaller subsequence is usually randomly sampled to calculate the loss function, and the random gradient descent method is used to optimize the loss function. Then, the gradient of the generation probability is as follows:

$$\frac{\partial \log P(w_o|w_c)}{\partial v_c} = u_o - \sum_{j\in v}\frac{\exp\left(u_j^T v_c\right)}{\sum_{i\in v}\exp\left(u_i^T v_c\right)}u_j. \tag{4}$$

The formula is equivalent to the following:

$$\frac{\partial \log P(w_o|w_c)}{\partial v_c} = u_o - \sum_{j\in v}P\left(w_j|w_c\right)u_j. \tag{5}$$

After the gradient is calculated by this formula, the stochastic gradient descent method is used to update the model parameter v_c iteratively. Similarly, the model parameter v_o can be obtained. After the final training, for the word with index i in the dictionary, two groups of word vectors v_i and $u_i$with this word as the central word and background word can be obtained.

2.2. Model Optimization. It can be found that the cost of gradient calculation in each step of the word vector model is related to the dictionary size $|v|$. When the dictionary is large in scale, ordinary training methods will consume a lot of space resources. Therefore, it is necessary to use approximate method to calculate the gradient, so as to reduce the calculation cost and improve the operation performance. The approximate training method adopted is sequence softmax. Sequence softmax uses a Huffman-coded binary tree to represent all words in the vocabulary. Each leaf node in the tree independently represents a word. There is a unique path from the root node to the leaf node for each leaf node. This path is used to estimate the probability of words represented by leaf nodes. Sequence softmax binary tree structure is shown in Figure 2.

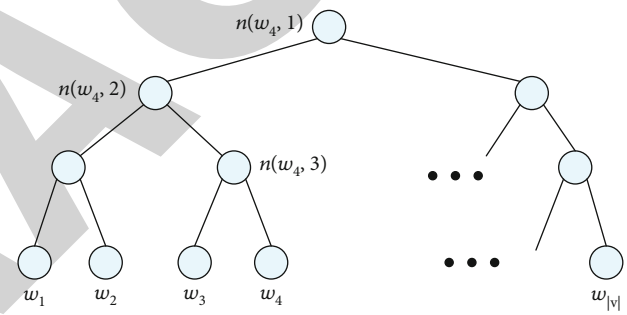

Figure 2: Binary tree structure of sequence softmax.

Suppose $L(w)$ represents the number of nodes on the path from the root node to the leaf node. Let $n(w, i)$ be the i-th node on this path, and the vector of this node is expressed as $u_{n(w,i)}$. Then, the probability of word vector model generating word w from arbitrary word w_i is as follows:

$$P(w|w_i) = \prod_{j=1}^{L(w)-1}\sigma\left(\left[n(w, j+1) = \text{leftChild}(n(w, j))\right]\right)\cdot u_{n(w,j)}^T v_i, \tag{6}$$

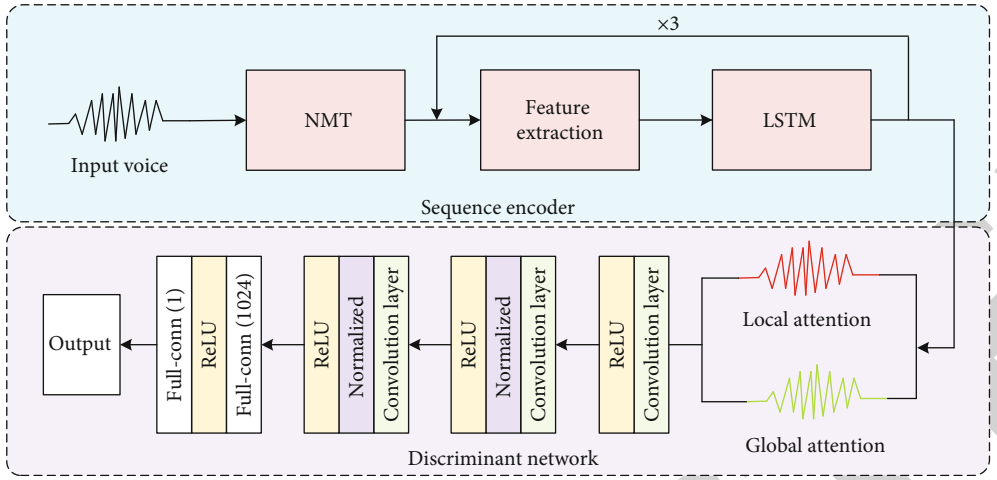

Figure 3: Overall architecture of A-BLSTM.

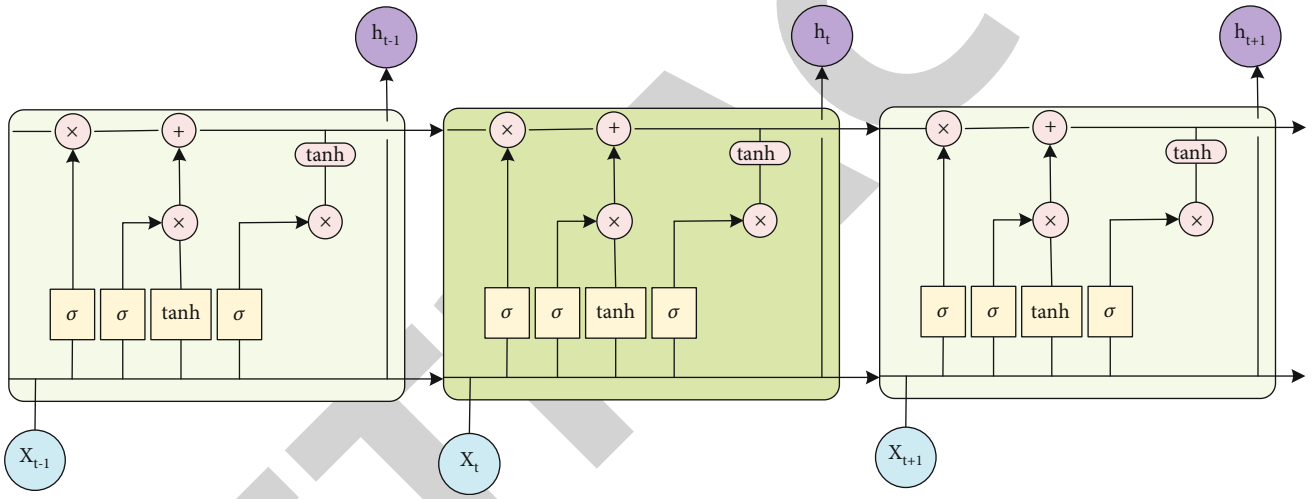

Figure 4: The architecture of LSTM.

where σ represents sigmoid function and leftChild represents the left branch.

3. Machine Translation Model Integrating Attention Mechanism

The whole structure of the proposed A-BLSTM model is shown in Figure 3. Compared with other RNN models, one advantage of this model is that the number of model layers can change with the complexity of tasks. Moreover, with the increase of network layers, the number of nodes of A-BLSTM decreases layer by layer, and the computational complexity of each layer also decreases. We will take the three-tier network structure as an example to elaborate. Specifically, A-BLSTM includes the following three parts: sequence encoder based on BLSTM, local attention mechanism structure, and global attention mechanism structure.

3.1. Sequence Encoder Based on BLSTM. In RNN, the hidden layer state h_t at time t is calculated by a function f, as shown in formula (7):

$$h_t = \begin{cases} 0, & t = 0, \\ f(h_{t-1}, X_t), & \text{others}, \end{cases} \tag{7}$$

where x_t represents the current input state and f represents a nonlinear radiation transfer function.

LSTM is an improved time recursive neural network, which can effectively deal with the problem of long-term dependence in time series, so it has strong advantages in speech recognition. LSTM can effectively solve the problem that traditional RNN cannot learn long-distance dependence in the training process. LSTM contains a single memory cell unit, which will update its stored information as needed. Figure 4 shows the structure of LSTM network, in which the repeated modules represent the hidden layer in each iteration.

The LSTM unit at time t is composed of a group of vectors, which include an input gate i_t, a forgetting gate f_t, an output gate o_t, a memory cell c_t, and a hidden state h_t. The conversion equation in LSTM network is as follows:

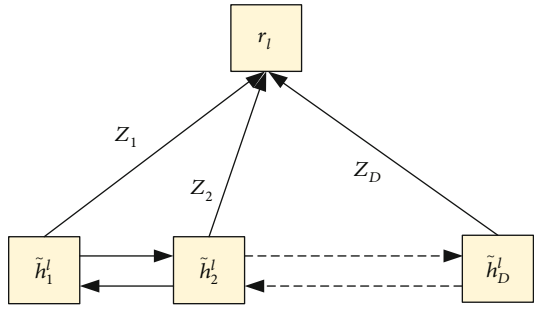

Figure 5: Local attention mechanism.

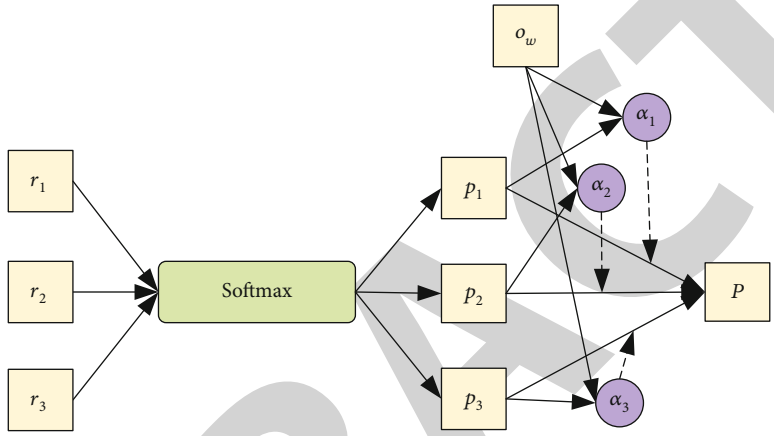

Figure 6: Global attention mechanism.

$$\begin{aligned} i_t &= \sigma(W_i X_t + U_i h_{t-1} + b_i), \\ f_t &= \sigma\left(W_f X_t + U_f h_{t-1} + b_f\right), \\ o_t &= \sigma(W_o X_t + U_o h_{t-1} + b_o), \\ z_t &= \text{thah}(W_z X_t + U_z h_{t-1} + b_z), \\ c_t &= i_t \odot z_t + f_t \odot c_{t-1}, \\ h_t &= o_t \odot \tanh(c_t), \end{aligned} \tag{8}$$

where $\odot$ represents the multiplication by element, b represents the bias vector parameter, and z_t represents an update gate.

Compared with unidirectional LSTM, bidirectional long short-term memory network (BLSTM) [27] uses extra backward information, which has the advantage of enhancing the memory ability of the network. The hidden state of each node in BLSTM can be calculated by the following formula.

$$\tilde{h}_j^l = \left[\overrightarrow{h_j^l} \oplus \overleftarrow{h_j^l}\right], \tag{9}$$

where $\oplus$ represents the connection operation, and $\sim$ represents the output of BLSTM unit.

3.2. Local Attention Mechanism and Global Attention Mechanism. Traditional LSTM modeling uses the last hidden state as the sequence vector or averages to get the final sequence vector. However, the importance of different words or phrases in sentences is different [28]. Therefore, we introduce local attention mechanism into BLSTM. The mechanism of local attention is shown in Figure 5.

For the l-th layer in the network structure, r_l represents a representation vector of the input sequence, and its calculation formula is as follows:

$$r_l = \sum_{j=1}^{D} Z_j \odot \tilde{h}_j^l, \tag{10}$$

Table 1: Parameter settings.

Parameter type	Value
Glossary size	30000
Word vector dimension	512
Number of hidden layer nodes	512
Number of neural network layer	1, 2, 3, 4, and 5
Learning rate	0.1
Dropout	0.5
Batch_size	128
Optimizer	Stochastic gradient descent

Table 2: Examples of Chinese word segmentation.

Chinese sentence	2021年初⊠因感染新冠病毒而死亡的人数达到最高值.
After word segmentation	2021 年 初⊠ 因 感染 新冠 病毒 而 死亡 的 人数 达到 最高 值.

Table 3: Examples of English symbol processing.

English sentence	At the beginning of 2021, the number of people who died from COVID-19 reached the highest value.
After symbol processing	At the beginning of 2021, the number of people who died from COVID-19 reached the highest value.

where $l \in [1, 3]$, Z_j represents the normalized coefficient vector, and D represents the length of the input sequence.

$$Z_j = \sum_{j=1}^{D} \exp \begin{bmatrix} u_1^l \\ u_2^I \\ \vdots \\ u_D^l \end{bmatrix}, \quad u_j^l = \tanh\left(W_u \tilde{h}_j^l + b_u\right), \tag{11}$$

where W_u and b_u are parameters in the network.

The higher the number of layers of the network, the less original information retained in the obtained sentence vector, and the higher the abstract level of sentence meaning. Therefore, with the different input sequences and tasks, the trust weight of each layer in the network should be different. In order to reward the layer that is more meaningful for correctly classifying labels, we introduce the global attention mechanism in the network. The global attention mechanism is shown in Figure 6.

The principle of global attention mechanism is to give a weight to the classification probability of each layer, which represents how much probability the neural network trusts the output of this layer. The formula of global attention mechanism is as follows:

$$\begin{aligned} p_l &= P\left(\bullet \middle| x_j; \theta\right) = \operatorname{softmax}\left(W_p r_l + b_p\right), \\ o_l &= \tanh\left(W_g p_l + b_g\right), \\ \alpha_l &= \frac{\exp\left(o_l^T o_g\right)}{\sum_l \exp\left(o_l^T o_g\right)}, \\ P &= \sum_l \alpha_l p_l, \end{aligned} \tag{12}$$

where W_p, W_g, b_p, b_g, and o_g are all parameters in the network. We can calculate an overall classification probability distribution P through the classification probability of each layer and the trust weight of each layer in the network structure.

3.3. A-BLSTM. The proposed A-BLSTM model is a hierarchical structure, which continuously integrates the information of each layer in a bottom-up way and finally can effectively model the combined features. The layer number of A-BLSTM is expressed by $l \in [0, 3]$. For the l layer, the input h_j^l of the j -th node is calculated as follows:

$$\begin{aligned} h_j^l &= \left[\tilde{h}_{2j}^{l-1} \oplus \tilde{h}_{2j+1}^{l-1}\right], \\ \tilde{h}_{2j}^{l-1} &= \mathrm{BLSTM}\left(h_{2j}^{l-1}\right), \\ \tilde{h}_{2j+1}^{l-1} &= \mathrm{BLSTM}\left(h_{2j+1}^{l-1}\right), \end{aligned} \tag{13}$$

where $\tilde{h}_{2j}^{l-1}$ and $\tilde{h}_{2j+1}^{l-1}$ are the outputs of BLSTM unit. A word is the input of the first layer in the network structure, and then, the output of each layer recursively becomes the input of the upper layer until the top layer of the network structure.

4. Experiment and Result Analysis

4.1. Machine Translation Evaluation Index. In order to evaluate the translation effect of the model, we use BLEU (bilingual evaluation under study) [29] proposed by IBM as the evaluation index of machine translation quality. BLEU is an internationally accepted evaluation method of machine translation. This method obtains the evaluation value by calculating the similarity between machine translation results and human translation results. The higher the similarity, the higher the score, that is, the higher the translation quality. The calculation formula of BLEU value is as follows:

$$\mathrm{BLEU} = \mathrm{BP} \cdot \exp\left(\sum_{n=1}^{N} \omega_n \log p_n\right), \tag{14}$$

where BP represents the penalty factor, N represents the total number, ω_n represents the weight, and p_n is the matching accuracy.

$$\mathrm{BP} = \begin{cases} 1, & l_c > l_s, \\ \exp\left(1 - \dfrac{l_s}{l_c}\right), & l_c \le l_s, \end{cases} \tag{15}$$

where l_c represents the length of the candidate translation and l_s represents the effective length of the reference translation.

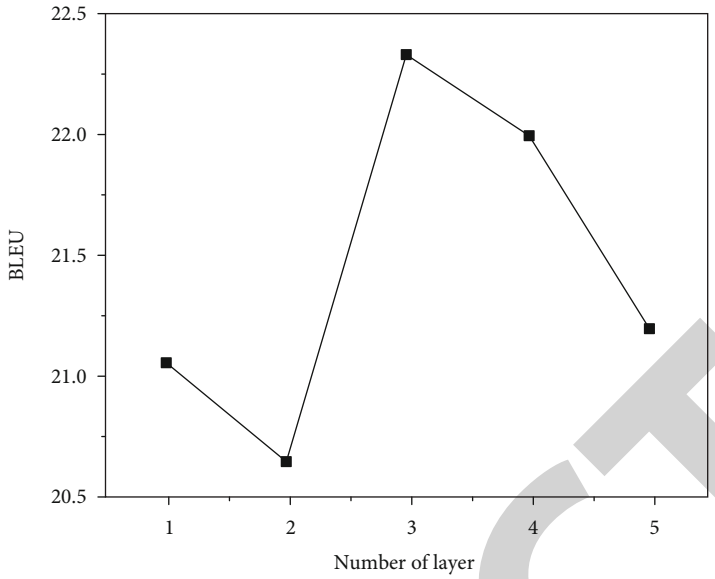

(a)

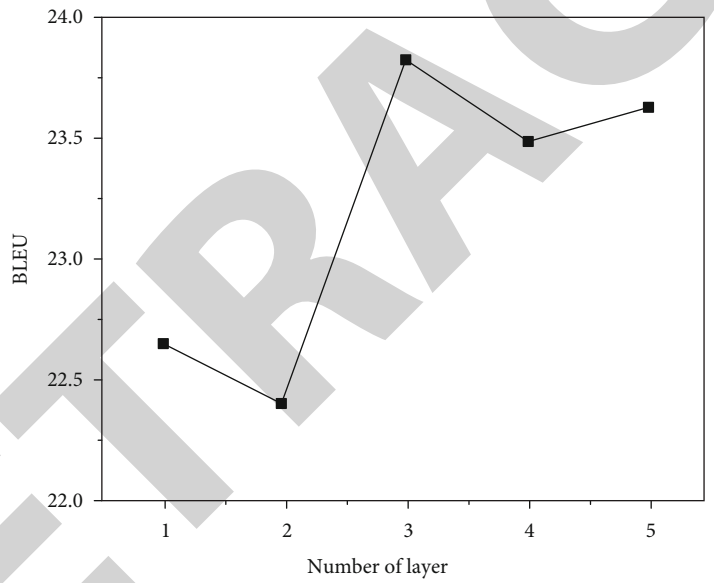

(b)

Figure 7: Continued.

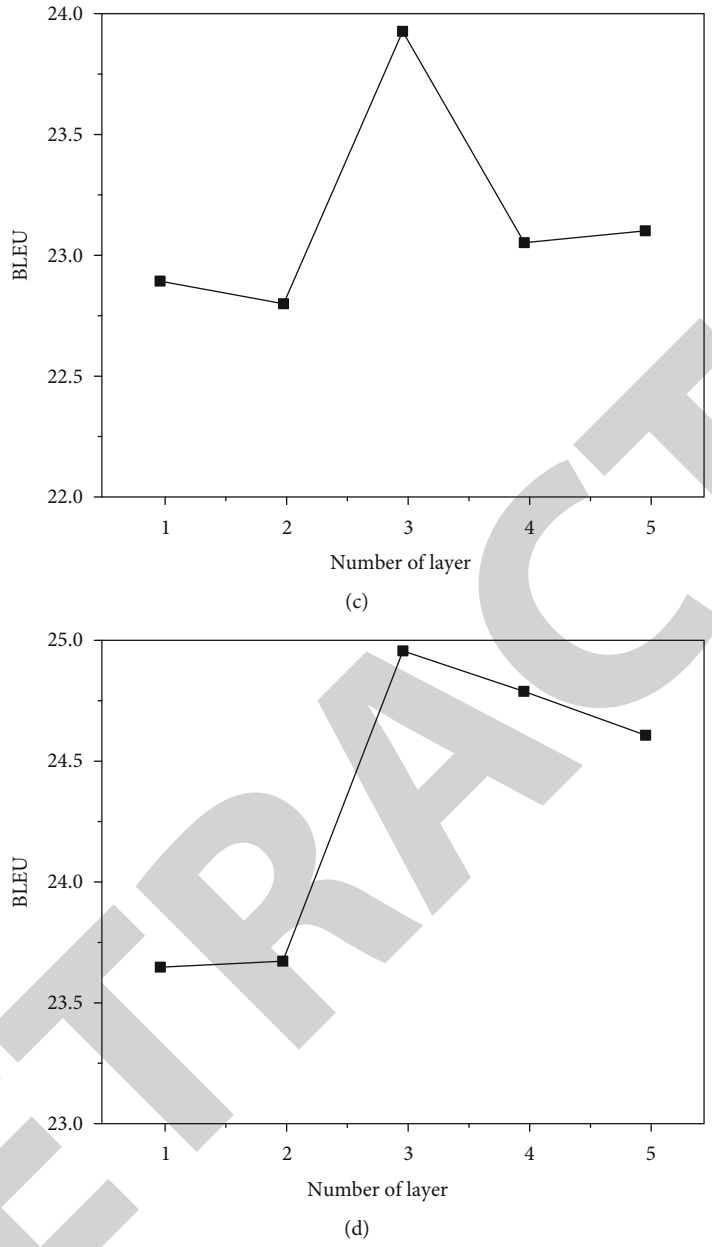

Figure 7: The BLEU change of translation model with one layer to five layers.

4.2. Experimental Data and Data Processing. The experimental data is selected from the smaller data set of International Workshop on Spoken Language Translation (IWSLT). IWSLT is the most influential oral machine translation evaluation competition in the world. IWSLT 2015 data set includes 220,000 Chinese-English parallel sentences, including one development set data dev and three test set data (test1, test2, and test3). A variety of NMT models including A-BLSTM are built on TensorFlow, a deep learning framework. Parameters related to neural network are set as shown in Table 1.

During the experiment, firstly, preprocess the corpus: (1) segment the corpus—mainly for Chinese data, use Stanford word segmentation to divide Chinese sentences into words, as shown in Table 2; (2) symbol processing of corpus—-mainly for English data, use tokenizer.per, a word segmentation script in Moses system, to insert spaces between words and punctuation marks in English data, as listed in Table 3; (3) converting uppercase into lowercase in English data; and (4) select the first 30000 high-frequency words from the processed training corpus and replace the rest words with < unk >.

4.3. Function Analysis of Network Layer Number. The influence of different layer number on the A-BLSTM model in Chinese-English machine translation tasks is shown in Figure 7.

It can be seen that compared with the deeper or shallower hierarchical structure, the three-layer A-BLSTM structure has achieved the best results in both the development

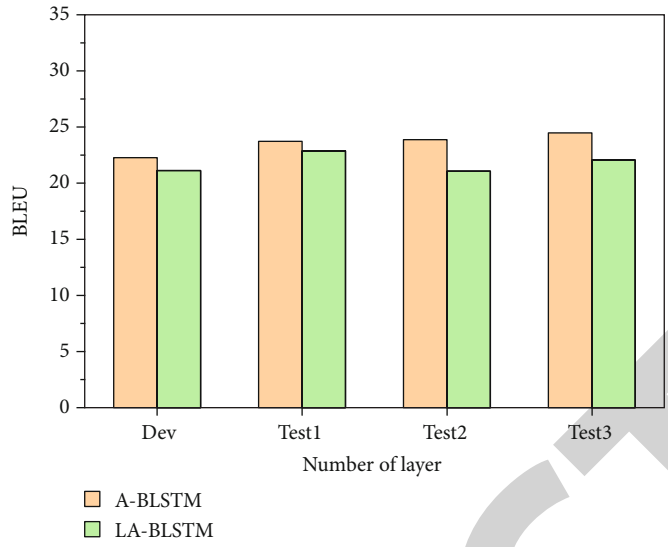

Figure 8: Comparison between LA-BLSTM and A-BLSTM.

Table 4: Comparison of translation model performance.

Translation model	Dev	Test1	Test2	Test3
RNN	10.87	11.63	11.79	12.39
LSTM	12.15	13.83	13.99	14.47
GRU	12.16	13.85	14.01	14.49
BiGRU	13.82	15.49	15.58	16.21
Attention+RNN	14.75	16.41	16.62	20.34
Attention+LSTM	20.74	22.47	22.53	23.27
Attention+GRU	20.77	22.49	22.55	23.31
Attention+BiGRU	21.86	23.37	23.41	24.28
A-BLSTM	22.27	23.73	23.87	24.48

set and the test set. The performance of the two-layer A-BLSTM structure is poor, because only one abstract level of text vector representation can be obtained, so there is no advantage brought by applying the global attention mechanism. Generally speaking, with the increase of network layers, the network can learn more abstract semantic representation information, and the translation accuracy (BLEU value) will also be continuously improved. However, when there are too many network layers in the network structure (more than three layers), the translation accuracy will begin to decline. This is because for sequence modeling, too many layers are unnecessary, and extra noise will be introduced, which will reduce the accuracy of Chinese-English machine translation. In the follow-up experiments, A-BLSTM adopts three-layer architecture.

4.4. Analysis of the Effectiveness of Attention Mechanism. To illustrate the effectiveness of global attention mechanism, we compared the local attention BLSTM (LA-BLSTM) with A-BLSTM. The result of comparison between LA-BLSTM and A-BLSTM is shown in Figure 8. Obviously, the performance of A-BLSTM model is better than that of LA-BLSTM, especially on test2 data set and test3 data set. The experimental results show that the global attention mechanism can accurately identify which layer of the network structure's representation vector is more reliable for translation.

4.5. Performance Comparison of Translation Models. Different neural networks are used for training and testing in the translation model, and the experimental results are shown in Table 4. In order to compare the translation performance of different models more intuitively, the data in Table 4 are displayed by histogram. The BLEU values of different translation models on the development set and the test set are shown in Figure 9.

From the results in Table 4 and Figure 9, we can find that the attention mechanism can improve the translation performance of NMT model and the proposed A-BLSTM model structure can effectively improve the machine translation performance by modeling both short sequences and long sequences. The main reason is that the global attention mechanism can determine which layer of representation vector in the input sequence should be given more attention (weight).

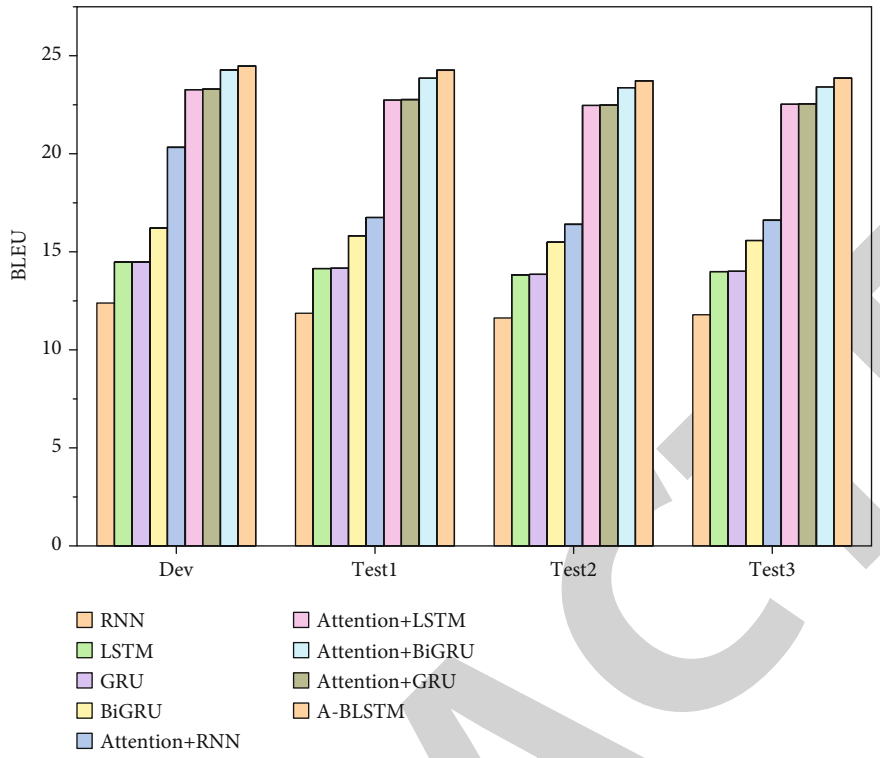

Figure 9: BLEU values of different translation models in development set and test set.

5. Conclusions

This paper proposes a neural machine translation model, A-BLSTM, which integrates attention mechanism. A hierarchical structure is adopted to represent the input sequence as a multilayer representation vector instead of a single fixed-length representation vector. The introduction of local attention mechanism can effectively select words or phrases with large amount of information in the input sequence. The introduction of global attention mechanism can effectively select a more credible intermediate representation vector. Experimental results show that the A-BLSTM model has achieved relatively high BLEU values in both Chinese and English machine translation tasks, which has surpassed other existing neural machine translation models. Subsequently, we will try to use quantum weak measurement to simulate the reader's understanding of sentences from the perspective of quantum cognition, so as to further improve the translation performance.

Data Availability

The experimental data used to support the findings of this study are available from the corresponding author upon request.

Conflicts of Interest

The authors declare that they have no conflicts of interest to report regarding the present study.

References

[1] C. Brodbeck, A. Presacco, and J. Z. Simon, "Neural source dynamics of brain responses to continuous stimuli: speech processing from acoustics to comprehension," *NeuroImage*, vol. 172, no. 11, pp. 162–174, 2018.

[2] H. Choi, K. Cho, and Y. Bengio, "Fine-grained attention mechanism for neural machine translation," *Neurocomputing*, vol. 284, no. 4, pp. 171–176, 2018.

[3] B. Erik, H. Xiang, and L. Meng, "Does machine translation affect international trade? Evidence from a large digital platform," *Social Science Electronic Publishing*, vol. 12, no. 8, pp. 29–42, 2018.

[4] M. S. Kumar, D. Dipankar, and B. Sivaji, "MTIL2017: machine translation using recurrent neural network on statistical machine translation," *Journal of Intelligent Systems*, vol. 36, no. 1, pp. 3–19, 2018.

[5] J. Su, J. Zeng, D. Xiong, Y. Liu, M. Wang, and J. Xie, "A hierarchy-to-sequence attentional neural machine translation model," *IEEE/ACM Transactions on Audio, Speech, and Language Processing*, vol. 26, no. 3, pp. 623–632, 2018.

[6] Z. Tan, J. Su, B. Wang, Y. Chen, and X. Shi, "Lattice-to-sequence attentional neural machine translation models," *Neurocomputing*, vol. 284, no. 4, pp. 138–147, 2018.

[7] J. Huang, Y. Sun, W. Zhang, H. Wang, and T. Liu, "Entity highlight generation as statistical and neural machine translation," *IEEE/ACM Transactions on Audio, Speech, and Language Processing*, vol. 26, no. 10, pp. 1860–1872, 2018.

[8] V. Mann and V. Venkatasubramanian, "Retrosynthesis prediction using grammar-based neural machine translation: an information-theoretic approach," *Computers & Chemical Engineering*, vol. 23, no. 1, pp. 23–41, 2021.

Hindawi
Journal of Sensors
Volume 2023, Article ID 9895286, 1 page
https://doi.org/10.1155/2023/9895286

Retraction

Retracted: An Advertising Recommendation Algorithm Based on Deep Learning Fusion Model

Journal of Sensors

Received 19 December 2023; Accepted 19 December 2023; Published 20 December 2023

This article has been retracted by Hindawi following an investigation undertaken by the publisher [1]. This investigation has uncovered evidence of one or more of the following indicators of systematic manipulation of the publication process:

(1) Discrepancies in scope
(2) Discrepancies in the description of the research reported
(3) Discrepancies between the availability of data and the research described
(4) Inappropriate citations
(5) Incoherent, meaningless and/or irrelevant content included in the article
(6) Manipulated or compromised peer review

The presence of these indicators undermines our confidence in the integrity of the article's content and we cannot, therefore, vouch for its reliability. Please note that this notice is intended solely to alert readers that the content of this article is unreliable. We have not investigated whether authors were aware of or involved in the systematic manipulation of the publication process.

Wiley and Hindawi regrets that the usual quality checks did not identify these issues before publication and have since put additional measures in place to safeguard research integrity.

We wish to credit our own Research Integrity and Research Publishing teams and anonymous and named external researchers and research integrity experts for contributing to this investigation.

The corresponding author, as the representative of all authors, has been given the opportunity to register their agreement or disagreement to this retraction. We have kept a record of any response received.

References

[1] C. Li, "An Advertising Recommendation Algorithm Based on Deep Learning Fusion Model," *Journal of Sensors*, vol. 2022, Article ID 1632735, 9 pages, 2022.

Hindawi
Journal of Sensors
Volume 2022, Article ID 1632735, 9 pages
https://doi.org/10.1155/2022/1632735

Research Article

An Advertising Recommendation Algorithm Based on Deep Learning Fusion Model

Chunhui Li

College of Business Administration, Guangzhou Huashang Vocational College, Guangzhou 511300, China

Correspondence should be addressed to Chunhui Li; lch33112715@163.com

Received 2 December 2021; Revised 4 January 2022; Accepted 15 January 2022; Published 1 March 2022

Academic Editor: Wei Zhang

With the rapid evolution of the Internet and smart mobile devices, personalized advertising is becoming increasingly acceptive on we-media platforms. Traditional advertising push cannot meet users' demand for personalized advertising, leading to users' resistance to advertising. Aiming to realize personalized advertising recommendation, an advertising recommendation algorithm based on deep learning fusion model is proposed. The bipartite graph model is applied to network representation learning method to decompose user and advertising content into two networks. The embedded representations of two types of nodes are obtained by training GraphSAGE model on their respective networks. The relation matrix of two kinds of nodes is obtained by using the crossproduct operation. Finally, feature information is extracted by convolutional neural network to achieve personalized advertising recommendation. Experimental results verify the effectiveness of the proposed algorithm, which also achieves good results in accuracy and convergence speed.

1. Introduction

In recent years, with the rapid development of the Internet and intelligent mobile devices, human society has entered the era of information explosion since mobile Internet advertising is booming, and higher requirements for advertising recommendation are put forward [1]. The traditional advertising recommendation method often pushes some uninteresting or even irrelevant advertising content to users, which will reduce the normal access of users, and some of which will even steal users' privacy. This kind of "carpet bombing" promotion method causes great dislike of users [2]. Therefore, how to tap the potential needs of users according to their hobbies and behaviors and personalized advertising recommendation according to their needs becomes particularly important [3]. On the other hand, the rapid development of mobile Internet has led to geometric growth of mobile Internet information and explosive growth of mobile users, resulting in an increasingly sharp contradiction between limited network resources and users' growing network needs [4]. Under the current limited resources, better algorithms to accurately capture user characteristics need exploring so as to accurately and efficiently extract user behavior characteristics, analyze their interests and needs, and carry out targeted advertising needs.

In today's era, the Internet has become the fastest and most convenient medium to transmit information in daily life, and we-media has become the main force of Internet information transmission [5]. "We-media" is short for "We-media" platform. "We-media" is a way for the general public to begin to understand how they provide and share their own facts and news after being strengthened by digital technology and connected with the global knowledge system [6]. In other words, we-media platform is a carrier for users to publish events they have seen and heard with their own eyes, such as WeChat, Douyin, Toutiao, Weibo, and BBS [7]. With the popularity of intelligent mobile terminals, we-media platforms are more interactive and lively. We-media advertising recommendation system arises at the historic moment [8], when personalized advertising recom-

mendation can provide different forms of advertising and information for different users.

In recent years, there have been many reviews about recommender systems. For example, literature [9] reviewed hybrid recommendation system. Literature [10] studied collaborative filtering technology. Literature [11] analyzed mobile news recommendation technology. Literature [12] reassessed recommendation system based on deep learning, etc. Although the above articles give a comprehensive overview of some subfields and methods and technologies of recommendation system, most of these articles are highly targeted and professional; that is, they summarize and discuss a certain field and technology [13]. Similar articles can provide reference and help for the overview of personalized advertising recommendation system, but the methods or technologies cannot completely adapt to personalized advertising recommendation system.

The problem of advertising recommendation can be generally understood as the problem of CTR (click through rate) [14]. The prediction of advertisement CTR is one of the most important contents in the advertising field. However, there are still some difficult problems, such as large amount of data, sparse data, and abnormal data [15]. In the selection of models, it is difficult to train complex models, while it is easy to produce overfitting phenomenon, and the effect of trained models is generally poor. Therefore, some relatively shallow models are generally used in industry, and two-feature engineering is an important step in solving problems [16]. Feature often determines the upper limit of the model; so, it has become one of the difficulties to solve the feature construction problem of feature engineering.

In order to realize personalized advertising recommendation, this paper proposes an advertising recommendation algorithm based on deep learning fusion model. The innovations and contributions of this paper are listed below. (1) In order to divide the user and the advertising information into two disjoint subsets, the bipartite graph model is applied to the network representation learning method to divide the user and the advertising content into two networks. (2) The embedded representations of two types of nodes are obtained by training the GraphSAGE model. The relation matrix of each dimension of two kinds of nodes is obtained by crossproduct operation. (3) The convolutional neural network is used to extract the interaction relations in the features to complete the personalized recommendation task. Experimental results demonstrate that the proposed algorithm is effective and achieves good results in accuracy and convergence speed.

The chapter structure of the paper is listed as follows. The next section mainly introduces the proposed algorithm model. The third section is experiment and analysis. The fourth section is the conclusion.

2. The Proposed Algorithm in This Paper

2.1. GraphSAGE Model. GraphSAGE [17] model was applied to complete the task of network representation learning. The GraphSAGE model is used for supervised and unsupervised learning, and you can choose whether to use node attributes for training. This method is suitable for solving the recommendation problem with various external information. When new nodes are added to the graph, the whole model does not need to be retrained, which improves the universality of the algorithm.

The GraphSAGE model is constructed for the problem of homogeneous graph, and the embedded representation of nodes is generated through node attribute information and network structure information. Embedding representation is that each node learns its own aggregation function and aggregates node's neighborhood information through this function. The forward propagation of the algorithm is divided into three steps: sampling, aggregation, and prediction [18].

In aggregation and prediction, each order of neighbor nodes aggregates neighbor node features by using different functions. After the feature representation of the target node is connected with the aggregation attribute of the neighbor node, the updated embedded representation of the target node is obtained through nonlinear transformation, and all nodes are iterated layer by layer. Mean aggregator, LSTM (long-short-term memory) aggregator, and pooling aggregator are proposed in this algorithm. The mean aggregation function averages each dimension of the feature vector of the sampled neighbor node as the feature vector of the target node. LSTM aggregator [19] has strong data expression ability and is sensitive to data order. The pooling aggregator performs nonlinear transformation on the neighbor nodes of the target node and pools them. The Pseudocode 1 of GraphSAGE forward propagation algorithm is displayed as follows.

$\{b_p^{z-1}, \forall p \in T(q)\}$ represents the neighbor node features of node q in layer $z-1$; $b_{N(p)}^{z}$ represents the feature aggregation of neighbor nodes of node z at layer q.

For the part of back propagation, unsupervised learning is adopted. Referring to SkipGram model [20], loss function based on graph is adopted to make the adjacent nodes have more similar feature expression. The loss function is shown in

$$L_A(k_p) = \& -\exp\left(\sigma\left(k_p^{\top} \mathrm{k}_q\right)\right) - V \cdot G_{q_t - U_t(q)} \exp\left(\sigma\left(-k_p^{\top} k_{q_t}\right)\right), \tag{1}$$

where k_p is the embedded representation of node p generated by GraphSAGE. Node q is the neighborhood of node p sampled in z layer, and σ is the sigmoid function. U_t is the probability distribution of negative sampling, and V is the number of negative samples.

2.2. Design and Implementation of the Proposed Algorithm

2.2.1. Overall Design of Algorithm. For the binary network of user and advertisement, the algorithm in this paper decomposes the binary graph into the homogenous network of advertisement and advertisement and the homogenous network of user and user. The GraphSAGE model was used to fuse user's network feature structure and attribute feature, and the embedded expression with the same dimension

The output: node embedding representation k_q.
(1) $b_q^0 \longleftarrow x_q, \forall q \in Q$
(2) for $\forall z \in \{1, 2, \cdots, Z\}$ do
(3) for $\forall q \in Q$ do
(4) $b_{T(q)}^z \longleftarrow \text{AGGERGATE}_q\{b_p^{z-1}, \forall p \in T(q)\}$
(5) $b_q^z \longleftarrow \sigma(G^z \bullet \text{CONCAT}(b_q^{z-1}, b_{T(q)}^z))$
(6) end for
(7) $b_q^z \longleftarrow b_q^z / \|b_q^z\|_2, \forall q \in Q$
(8) end for
(9) $k_q \longleftarrow b_q^z, \forall q \in Q$

Pseudocode 1: The input: graph $A(Q, E)$, nodal eigenvector $\{x_q, \forall q \in Q\}$, nonlinear function σ, node connection weight matrix $G^z, \forall z \in \{1, 2, \cdots, Z\}$, the aggregation depth Z, aggregation function $\text{AGGERGATE}_z, \forall z \in \{1, 2, \cdots, Z\}$, and neighbor function Z.

was obtained. The crossproduct operation of feature vectors between users and advertisements is carried out, i.e., the relationship between users and each dimension of advertising features is represented by a matrix, and then, the potential relationship between them is extracted through the convolutional neural network. The algorithm flow in this paper is shown in Figure 1.

In the scenario of user and advertisement recommendation, usually, the attribute information of advertisement and user and the interaction information of advertisement and user are known. In this context, the relationship between them is represented by the structure of the graph. Users and advertising nodes are nodes of the graph, and the interactive relationship between advertising and users is the edge of the graph. The bipartite graph model of advertisement and user is formed through mapping. In addition, it is assumed that the recommendation scenario contains m users and n ads. The user node set is represented by $= \{p_1, p_2, \cdots, p_w\}$, and the advertising node set is represented by $Q = \{q_1, q_2, \cdots, q_t\}$. For the above recommendation problem, the corresponding user-advertising bipartite graph is expressed as $A = (P, Q, G, M)$, G is the set of all edges in graph A, and g_{xy} represents the connecting edge of nodes p_x and q_y. M is the interaction weight matrix between users and advertisements in graph A, and m_{xy} is the corresponding weight of g_{xy} in graph A.

The problem of homogenous network includes user network and advertising network. Taking the advertising network as an example, different ads have similar applicable groups. For user networks, if both users are sports enthusiasts, they will have similar hobbies. Therefore, homogenous networks also have profound connections. The user-advertising bipartite graph is decomposed into two homogeneous graphs. For graph A, the first-order similarity m_{xy}^P of the user node is defined as follows:

$$m_{xy}^P = \sum_{z \epsilon Q} m_{xz} m_{yz}. \tag{2}$$

The first-order similarity m_{xy}^Q of the advertising node is defined as follows.

$$m_{xy}^Q = \sum_{z \epsilon Q} m_{zx} m_{zy}. \tag{3}$$

Get advertising similarity matrix $M^Q = [m_{xy}^Q]$ and user similarity matrix $M^P = [m_{xy}^P]$. The user homogenous graph A^Q and the advertising homogenous graph A^P are constructed based on M^P and M^Q. Before using M^Q and M^P to construct user homogeneity graph and advertisement homogeneity graph, the edges with low weight should be appropriately removed to avoid noise interference affecting subsequent calculation results according to the weight distribution of M^Q and M^P.

Attribute information types of users and advertisements should be considered to construct attribute characteristics of users and advertisements. For structured data, the nondiscrete data is discretized, and one-hot coding is performed to obtain feature coding. For unstructured data, TF-IDF [21] or LDA algorithm [22] is often used for structured processing if it is the information in this paper. In the case of audio, video, image, and other information, the corresponding deep learning method is used to transform it into structured data. User attribute characteristics are obtained by the GraphSAGE model. Matrix C^P and advertising attribute feature matrix C^Q are transformed into user feature matrix C^P and C^Q, as shown below.

$$W^P = H_{\text{GraphSAGE}}\left(A^P, C^P\right), \tag{4}$$

$$W^Q = H_{\text{GraphSAGE}}\left(A^Q, C^Q\right). \tag{5}$$

Assuming that the obtained embedding representation dimensions are n, the user feature matrix $W^P \in \mathbb{R}^{w \times n}$ and advertising feature matrix $W^Q \in \mathbb{R}^{t \times n}$ can be represented.

The crossproduct operation is used to obtain the interaction matrix between users and advertising features. For user p and advertisement x, w_p^P represents the feature vector of user P, and $W_{p,x}$ represents the feature vector of

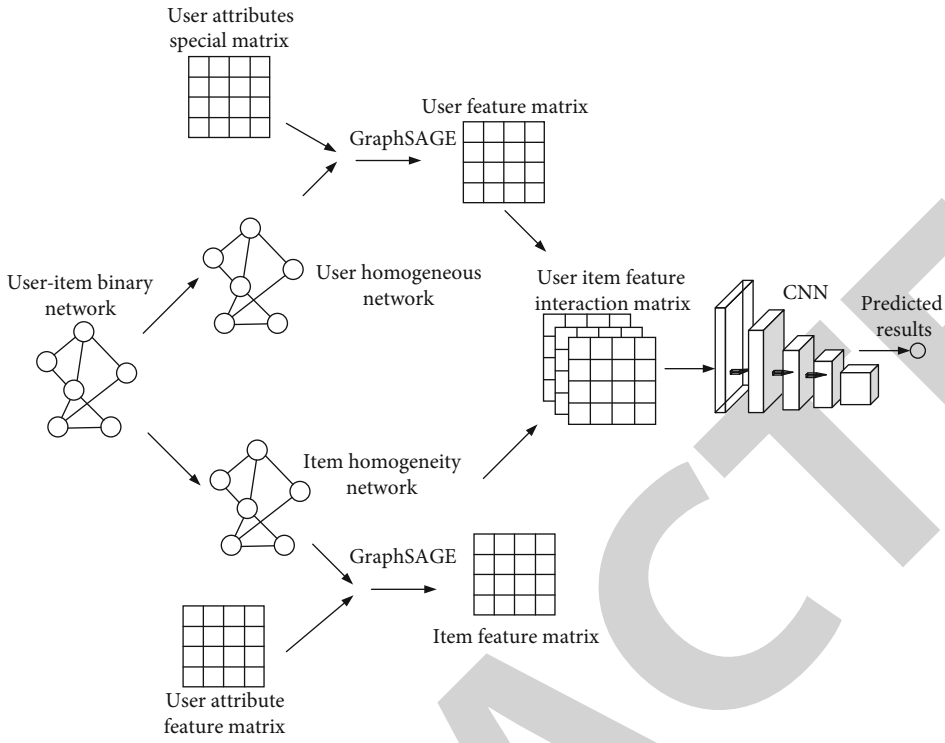

Figure 1: The flow of the proposed algorithm.

advertisement x. Then, the calculation equation of $W_{p,x}$ is as follows.

$$W_{p,x} = w_p^P \otimes w_x^Q = \begin{bmatrix} w_{p1}^P w_{x1}^Q & w_{p1}^P w_{x2}^Q & \cdots & w_{p1}^P w_{xn}^Q \\ w_{p2}^P w_{xl}^Q & w_{p2}^P w_{x2}^Q & \cdots & w_{p2}^P w_{xn}^Q \\ \vdots & \vdots & & \vdots \\ w_{pn}^P w_{xl}^Q & w_{pn}^P w_{x2}^Q & \cdots & w_{pn}^P w_{xn}^Q \end{bmatrix}. \tag{6}$$

In collaborative filtering, matrix decomposition is usually used to represent the relationship between advertising and users, the relationship between advertising and users is inner product, and only the information on the diagonal in $W_{p,x}$ is used.

The multilayer perceptron (MLP) [23] algorithm can fit any function relationship theoretically, but it needs a lot of data for training. In the user and advertisement recommendation system, the behavior information of each user is limited. Therefore, this algorithm does not adopt the scheme of learning through MLP after directly combining the features of users and advertisements. The deep network trained with limited data will degrade its performance, and it is difficult to ensure the convergence of MLP to the real model. Meanwhile, in the experimental part, users and advertising features are directly spliced without convolutional neural network training. MLP was directly used for comparison experiments, which further showed that adding convolutional neural network enhanced the effect of the algorithm.

This algorithm uses crossproduct to model the information interaction between advertisement and user and adopts convolutional neural network to train. The amount of data required for training is reduced, and the parameters required for training in the model are also cut down.

2.2.2. Structural Design of Convolutional Neural Network. In the convolutional neural network (CNN) model [24], the definition of parameters is more complex than that of traditional models, and the general rules of parameter design can be summarized as the following four aspects.

(1) The convolution layer generally uses a smaller convolution kernel. The larger the convolution kernel is, the smaller the output feature graph is, and it is difficult to extract the features of the data. And the smaller the convolution kernel, the smaller the corresponding parameter

(2) The convolution step size is generally set small to facilitate better feature extraction

(3) The pooling layer often uses a 2×2 pooling window. The function of the pooling layer is to reduce the spatial dimension of the input data. If the pooling operation is too large, data may be lost, and the network performance deteriorates

(4) The number of fully connected layers should not exceed 3. The more fully connected layers there are,

the more difficult the training is, and the more likely it is to cause overfitting and gradient dissipation

The CNN part of this model is shown in Figure 2, and the common convolutional network model is used for design. In order to avoid losing too much structural information, the convolution layer and pooling layer are not used to compress the matrix data into one dimension. The model is composed of 3 fully connected layers and 6 convolution layers. The convolution kernel size is 3×3, and the step size is 1×1. To keep the size of the input and output feature graphs constant, a padding operation is performed. After every two convolution layers, the pooling layer is added for maximum pooling. The pooling core size is 2×2, and the step size is 2×2. The feature graph was downsampled, and the number of channels was doubled in the next two convolution layers. Similarly, in the last convolution layer, flatten layer is added to flatten the data and connect the MLP network, gradually reducing the output dimension to one dimension. The total process is represented in Equation (7), where $\widehat{j}_{px}$ is the output of the final neural network.

$$\widehat{j}_{px} = \sigma\left(m_t^{\top}\left(\sigma\left(m_{t-1}^{\top}\left(\cdots\sigma\left(m_1^{\top}\mathrm{CNN}\left(W_{p,x}\right) + d_1\right)\cdots\right) + d_{t-1}\right)\right) + d_t\right), \tag{7}$$

where σ is a nonlinear function. ReLu activators are used in all convolution layers and full connection layers except sigmoid activation function at the last full connection layer. The number of modal parameters of the total body is shown in Table 1.

2.2.3. The Loss Function. The loss function is mainly a square loss function, which is defined on the premise that the observation results obey the Gaussian distribution. In practical problems, the interactive information between users and advertisements does not necessarily follow the Gaussian distribution function design. This algorithm adopts the idea of binary classification and uses "0" and "1" to represent the relationship between users and advertisements, "0" means irrelevant, and "1" means relevant. $\widehat{j}_{px}$ represents the convolutional networks. Output represents the likelihood of predicting that advertising x is related to user p. To ensure and celebrate $\widehat{j}_{px}$ probabilistic meanings, limit their values to [0, 1]. Therefore, the activation function of the last layer of the neural network is sigmoid function, and the loss function used is shown in

$$L = -\sum_{(p,x)\in J\cup J^-} j_{px}\exp\widehat{j}_{px} + \left(1 - j_{px}\right)\exp\left(1 - \widehat{j}_{px}\right), \tag{8}$$

where J is the positive sample set, J^- is the negative sample set, j_{px} represents the connection between user p and advertising x, and $\widehat{j}_{px}$ represents the final output of the convolutional network. Adam optimization algorithm [25] was adopted in the final model training. The dropout layer was added to the MLP part of the model to solve the problem of trained fitting and enhance the model generalization ability.

3. Experimental Results and Analysis

3.1. Data Collection and Preprocessing. The data set adopted in this paper comes from the real we-media advertising technology application platform WeChat public account. The whole process of personalized advertising recommendation system starts from data collection. The relevant data to be collected mainly includes user basic information, advertising data, contextual information such as time and location, interactive behavior information such as user comments, and user browsing history. The basic user information mainly comes from user registration and information improvement functions in the relevant platform system. Advertising data can be obtained from public data sets of some equation agencies or by self-scraping, but most of the datasets in the study were not exposed or used internal data. Time and position light context information is obtained by device time, GPS, etc. Interactive information can be obtained such as user comments and user browsing history from related logs such as cookies.

The data acquired in the above data acquisition stage may be accumulated in data noise, data loss, and other situations, which will affect the user preference acquisition and the effect of subsequent recommendation process. Therefore, in order to standardize the input data of personalized advertising recommendation system, it is necessary to preprocess further acquired data, such as calculation and quantification. It can be divided into shallow processing and deep processing according to the complexity of data processing and the intuitive degree of processing effect. The shallow processing mainly applied user's intuitive data, through the relatively simple standard and method, and obtains the high quantification degree result, such as a hierarchical (1-5) representation of user interest, or a self-defined project score, and the impact of missing link data. A distributed representation of user's browsing history yields a vector representation of the user. By comparing with the set threshold, the data noise can be filtered. Different quantized values are set for different time periods to distinguish, for example, assign different quantitative values to working days and rest days to distinguish. The old state of the data set is integrated into a single historical state, while the latest state of limited data is retained, etc. In addition, data classification criteria can be altered in order to have a comprehensive evaluation of research results. For example, the threshold used to filter data is modified, or the proportion of training set and test set is reformed.

The abovementioned data processing or expansion of shallow methods is of limited help to the recommendation process, and it is difficult to deal with complex scenes. Therefore, in-depth data processing should be considered. However, deep processing mainly aims at complex data of users and uses relevant mining or acquisition techniques to obtain potentially extensible data features or representations. For example, the topic acquisition or mining technology can be used to map user behaviors such as historical posting and forwarding into the potential topic space to help obtain user preferences by click, behavioral data and advertising information, parameterizing potential space, etc. Keywords are

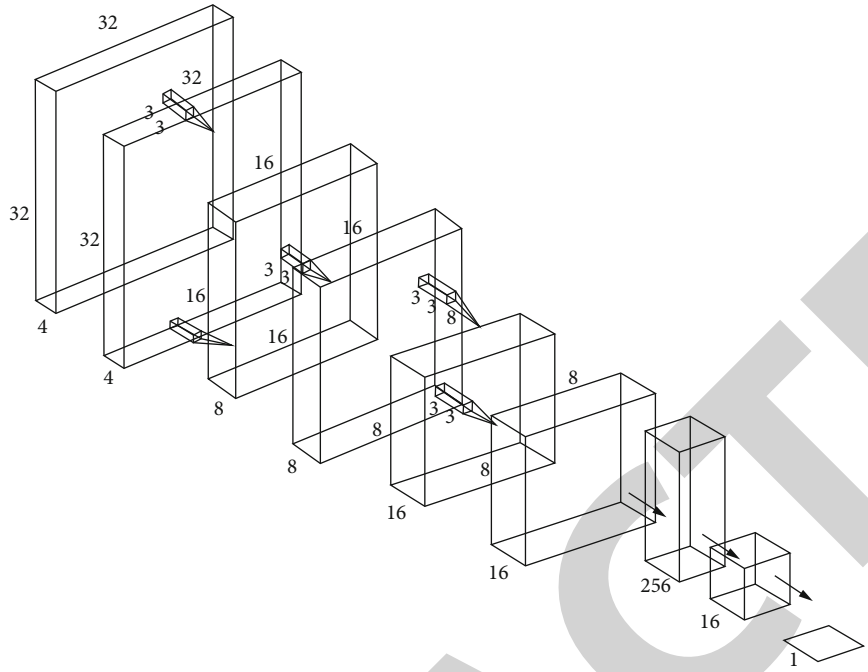

Figure 2: The structure diagram of CNN model in this paper.

Table 1: Convolutional neural network partial model parameter.

Network layer	Model parameter	Output size
Convolution layer 1	3×3 convolution kernels, step length 1, same size filling	$32 \times 32 \times 4$
Convolution layer 2	3×3 convolution kernels, step length 1, same size filling	$32 \times 32 \times 4$
Pooling layer 1	2×2 pooling kernels, step length 2, without filling	$16 \times 16 \times 4$
Convolution layer 3	3×3 convolution kernels, step length 1, same size filling	$16 \times 16 \times 8$
Convolution layer 4	3×3 convolution kernels, step length 1, same size filling	$16 \times 16 \times 8$
Pooling layer 2	2×2 pooling kernels, step length 2, without filling	$8 \times 8 \times 8$
Convolution layer 5	3×3 convolution kernels, step length 1, same size filling	$8 \times 8 \times 16$
Convolution layer 6	3×3 convolution kernels, step length 1, same size filling	$8 \times 8 \times 16$
Full connection layer 1	—	256
Full connection layer 2	—	16
Full connection layer 3	—	1

Table 2: The confusion matrix table.

Predict the actual	Predicting Positive	Positive
Positive	TP	FP
Negative	FN	TN

Table 3: Original data set results.

Model	AUC value
DCN [27]	0.728614
VSM [28]	0.737315
Proposed	0.759341

obtained through user comments and feedback on advertising, and users' attitudes toward related topics are analyzed. Additionally, users' emotional data can be acquired via processing microblog data.

3.2. Algorithm Performance Analysis. The data set adopted in this paper has about 8 million users, including 1 numerical feature and 31 categorical features (including 11 multivalued categorical feature). The data set has about 8 million users and contains 1 numerical feature and 31 categorical features (including 11 multivalued categorical feature). AUC (area under curve) scoring was adopted for model evaluation because the sample positive and negative ratio was imbalanced (the ratio of positive and negative samples was about 1 : 20) [26]. AUC is defined as the area under the ROC

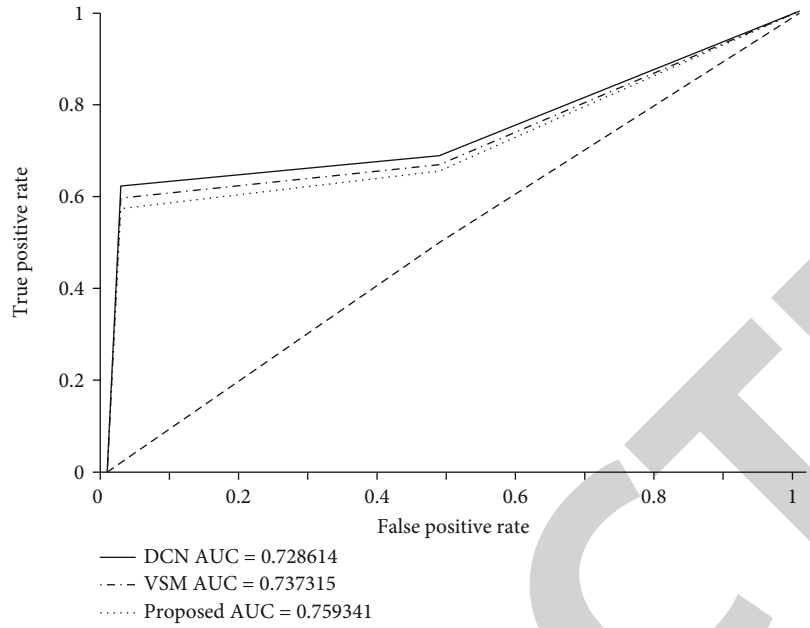

Figure 3: The ROC curve.

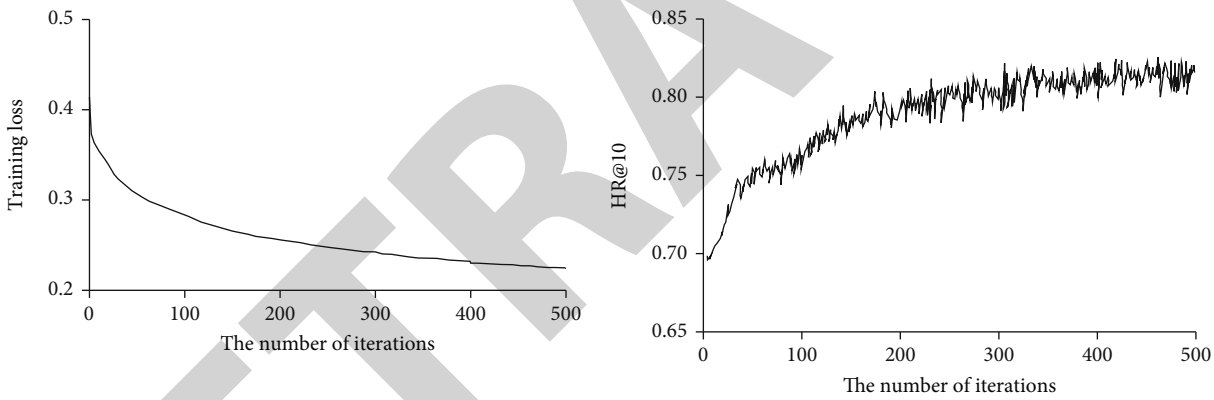

(a) The training loss

(b) The training results of HR@10

Figure 4: The training loss and training results of HR@10.

(receiver-operating characteristic curve) curve bounded by the coordinate axes. The horizontal and vertical coordinates of the ROC curve were false positive rate (FPR: FP/(TN+FP)) and true rate (TPR: TP/(TP+FN)). AUC score can be understood as the probability that positive samples rank ahead of negative samples. When the prediction result is completely correct, the AUC value is 1; so, the larger the AUC value is, the more accurate the classification result is. Table 2 is the confusion matrix table.

In this experiment, the three models were trained for several times, and the final result was the average AUC of many experiments. The experimental results are shown in Table 3 and Figure 3.

As can be indicated from the results in Table 3, the AUC value of the VSM vector space model [27] is higher than that of DCN model [28] due to its second-order combination characteristics. However, the proposed GraphSAGE model, due to the addition of deep neural network to learn high-order feature combination, has higher AUC values than LR and FM models. As can be concluded from Figure 3, the front of the ROC curve is approximately a straight line $x = 0$ due to the unbalanced proportion of positive and negative samples. The true rate of GraphSAGE behind the ROC curve is higher than that of VSM vector space model and DCN model; so, the AUC value of GraphSAGE is higher than that of VSM vector space model and DCN model. Combined with the results in Table 3 and Figure 3, it can be shown that the GraphSAGE model can effectively mine high-order combination features and has better recommendation effect than VSM vector space model and DCN model.

3.3. Comparative Analysis of Algorithm Performance. In order to verify the performance of algorithm personalized recommendation, HR@k was selected as an evaluation index

to comprehensively measure the performance of algorithm results under two indexes, namely, disorder and order. Let $R(p)$ be the recommendation list of user' p on the test set and $N(p)$ be the advertisement list of user interaction. Recall rate is defined as the proportion of ads in $R(p)$ that end up interacting with users in the test set. The calculation equation is as follows:

$$R_g = \frac{\sum_{p \in P} |R(p) \bigcap N(p)|}{\sum_{p \in P} |N(p)|}. \quad (9)$$

The larger the R_g value is, the higher the recall rate of the recommendation algorithm is. Since the value of R_g is closely related to the length of the recommended list, the conditional setting is often indicated directly with $R_g@k$, represented as HR@k.

Equation (7) is the basic model of the recommendation algorithm in this paper. Since it is a dichotomous problem, "0" and "1" can be used to indicate whether the advertisement is recommended. The sigmoid function is selected to limit the result between 0 and 1 to obtain the specific loss function. As shown in Equation (8), model parameters are trained by minimizing loss function.

The convergence of the model is verified by experiments. In the process of training and learning, early stop method is used to avoid the occurrence of overfitting phenomenon. 500 iterations were trained on the data set of WeChat public account, and the experimental results are shown in Figure 4. With the increase of training times, both of them show stable state, so the convergence performance of the algorithm is good.

4. Conclusion

With the evolution and acceptance of we-media platforms, traditional advertising recommendation algorithms can no longer meet the personalized needs. Personalized advertising recommendation is increasingly favored by "we-media" platforms and has become the main way for advertisers to identify user preferences and boost advertising revenue. In this paper, a deep learning fusion model algorithm is proposed to finalize the task of network representation learning by the GraphSAGE model. The bipartite graph model is applied to network representation learning method to decompose user and advertisement into two homogeneous networks. Each dimensional relationship matrix between user and advertising feature is obtained by crossproduct operation. Convolutional neural network is used to capture the high-order interaction relations in each dimension of the feature. Compared with other algorithms, there is no need to retrain the whole model when new nodes are added to the graph. The recall rate and discount rate of the recommendation algorithm are improved greatly and have good convergence. The GraphSAGE model can optimize advertising strategy, reduce advertising cost, and improve the conversion rate of advertising. Simultaneously, users can avoid accepting irrelevant advertising messages and better protect their privacy. The efficiency of the proposed algorithm will be analyzed in the future work.

Data Availability

The labeled dataset used to support the findings of this study are available from the corresponding author upon request.

Conflicts of Interest

The author declares no competing interests.

Acknowledgments

This work was supported in part by the Research Platform of Guangdong Provincial Department of Education 2018 Characteristic Innovation Project: "Innovation proactive behavior development and innovation performance improvement of scientific and technological personnel-a case study of high-tech enterprises in Guangdong-Hongkong-Macao Greater Bay Area (no. 2018GWTSCX051)."

References

[1] C. H. Wong, G. W. H. Tan, B. I. Tan, and K. B. Ooi, "Mobile advertising: the changing landscape of the advertising industry," *Telematics and Informatics*, vol. 32, no. 4, pp. 720–734, 2015.

[2] L. Chen and S. Tang, "Physical-layer security on mobile edge computing for emerging cyber physical systems," *Computer Communications*, vol. 99, pp. 1–12, 2022.

[3] G. Theocharous, P. S. Thomas, and M. Ghavamzadeh, "Personalized ad recommendation systems for life-time value optimization with guarantees," in *Twenty-Fourth International Joint Conference on Artificial Intelligence*, Chengdu, 2015.

[4] K. Zhao and L. Ge, "A survey on the Internet of Things security," in *2013 ninth international conference on computational intelligence and security*, pp. 663–667, Emeishan, China, 2013.

[5] Y. Wu, Y. Song, F. Wang, Y. Zhou, and M. Li, "Online public opinion guidance strategy for college students in the era of we media," *Journal of Computer and Communications*, vol. 7, no. 12, pp. 79–87, 2019.

[6] L. He and K. He, "Efficient memory-bounded optimal detection for GSM-MIMO systems," *EEE Transactions on Communications*, vol. 99, pp. 1–15, 2022.

[7] L. Ma, *An analysis of Chinese Documentary in We-Media Times*, Bangkok University, 2019.

[8] W. Jie-Feng, "Research on the innovation of ideological and political education of university students in the we-media and big data era," in *2017 9th International Conference on Measuring Technology and Mechatronics Automation (ICMTMA)*, pp. 403–407, Changsha, China, 2017.

[9] G. Manogaran, R. Varatharajan, and M. K. Priyan, "Hybrid recommendation system for heart disease diagnosis based on multiple kernel learning with adaptive neuro-fuzzy inference system," *Multimedia Tools and Applications*, vol. 77, no. 4, pp. 4379–4399, 2018.

[10] X. Lai and L. Fan, "Outdated access point selection for mobile edge computing with cochannel interference," *IEEE Transactions on Vehicular Technology*, vol. 99, pp. 1–10, 2022.

Hindawi
Journal of Sensors
Volume 2023, Article ID 9836872, 1 page
https://doi.org/10.1155/2023/9836872

Retraction

Retracted: Comprehensive Decision Analysis of Industry 4.0 Virtual Enterprises considering the Personalized Customization Model of Product Life Cycle

Journal of Sensors

Received 19 December 2023; Accepted 19 December 2023; Published 20 December 2023

This article has been retracted by Hindawi following an investigation undertaken by the publisher [1]. This investigation has uncovered evidence of one or more of the following indicators of systematic manipulation of the publication process:

(1) Discrepancies in scope
(2) Discrepancies in the description of the research reported
(3) Discrepancies between the availability of data and the research described
(4) Inappropriate citations
(5) Incoherent, meaningless and/or irrelevant content included in the article
(6) Manipulated or compromised peer review

The presence of these indicators undermines our confidence in the integrity of the article's content and we cannot, therefore, vouch for its reliability. Please note that this notice is intended solely to alert readers that the content of this article is unreliable. We have not investigated whether authors were aware of or involved in the systematic manipulation of the publication process.

Wiley and Hindawi regrets that the usual quality checks did not identify these issues before publication and have since put additional measures in place to safeguard research integrity.

We wish to credit our own Research Integrity and Research Publishing teams and anonymous and named external researchers and research integrity experts for contributing to this investigation.

The corresponding author, as the representative of all authors, has been given the opportunity to register their agreement or disagreement to this retraction. We have kept a record of any response received.

References

[1] D. Ma, "Comprehensive Decision Analysis of Industry 4.0 Virtual Enterprises considering the Personalized Customization Model of Product Life Cycle," *Journal of Sensors*, vol. 2022, Article ID 1175565, 11 pages, 2022.

Hindawi
Journal of Sensors
Volume 2022, Article ID 1175565, 11 pages
https://doi.org/10.1155/2022/1175565

Research Article

Comprehensive Decision Analysis of Industry 4.0 Virtual Enterprises considering the Personalized Customization Model of Product Life Cycle

Dongjun Ma

School of Journalism and Communication, Xinxiang University, Xinxiang 453003, China

Correspondence should be addressed to Dongjun Ma; mdj@xxu.edu.cn

Received 29 November 2021; Revised 18 January 2022; Accepted 7 February 2022; Published 25 February 2022

Academic Editor: Wei Zhang

In the era of Industry 4.0, various types of information accumulated by enterprises in the production process have become a sea of data. These manufacturing-related data originate from enterprises and are used by enterprises and include not only process data such as documents and pictures but also complex information such as video and sound. Moreover, these data are not only large in quantity and wide in variety but also have the characteristics of fast generation speed and low value density. The model constructed in this paper can be applied to the personalized customization of product life cycle and can help enterprises make comprehensive decision-making. In particular, it can perform intelligent decision analysis under the background of Industry 4.0. In addition, this article combines intelligent algorithms to build an intelligent enterprise comprehensive decision-making system. The experimental research results show that the decision-making system proposed in this paper can play an important role in the comprehensive decision-making of Industry 4.0 enterprises, and this decision-making can be spread throughout the entire life cycle of the product.

1. Introduction

With the rapid development of economy and social industry, the carrying capacity of the environment is no longer sufficient to support people's current development model with a traditional high investment, high pollution, and high energy consumption. In response to this situation, the German Federal Ministry of Education and Research and the Federal Ministry of Economics and Technology took the lead in proposing the concept of "Industry 4.0." The Chinese government also immediately proposed the Chinese version of the "Industry 4.0 Plan" or "Made in China 2025" development strategy. The basic policy pointed out that in order to promote the industrial structure to the middle and high end, we must adhere to green development, and green development is an inevitable choice for China [1].

In actual production activities, the core issue for the effective operation of the closed-loop supply chain is its actual operation and management process. The above-mentioned resource recovery and remanufacturing and the impact of remanufactured products on the production of new products have become important factors that companies need to consider in terms of production and operation. By rationally formulating production plans under the closed-loop supply chain, it is not only conducive to enterprises to make full use of production resources to meet market demand but also to minimize production costs and achieve optimal and profitable goals [2]. However, in a competitive closed-loop supply chain environment, companies tend to negatively treat the construction of closed-loop supply chains in enterprises due to the large upfront resource input and long cost recovery periods. In addition, due to the differences in quality and price of new products and remanufactured products, there is uncertainty in the demand market, which makes it difficult for companies to make production decisions. Therefore, how to make reasonable production decisions for new products or remanufactured products and make full use of recycled resources and

their own production capacity to better adapt to the ever-changing market environment will also become an inevitable choice for enterprises [3].

The innovation opportunity decision-making model is a scientific and objective expression of the process, method, and mechanism of innovation opportunity decision-making. As an important part of opportunity management, opportunity decision-making is the final foothold of opportunity identification and evaluation, so its status is beyond doubt. However, the current research on the decision-making process of innovative enterprises' continuous innovation opportunities is still in the stage of theoretical exploration, and effective decision-making models have not yet been constructed and applied to actual business operations. There are also certain controversies about opportunity decision-making itself. Some scholars believe that it is only the selection of decision-making schemes or the implementation of countermeasures and suggestions, while other scholars believe that "management is decision-making," and decision-making refers to the entire process from the beginning to the end of decision-making.

The model constructed in this article can be applied to the personalized customization of the product life cycle and can help companies make comprehensive decisions. In particular, it can perform intelligent decision-making analysis under the background of Industry 4.0.

2. Related Work

In the era of Industry 4.0, intelligent manufacturing is the leading factor, and information technology can be used to obtain the real-time status of every product, machine, and even every employee in the factory at any time [4]. It is specifically embodied in the organic combination of products, machines, resources, and people through the Cyber-Physical System (referred to as CPS), thereby promoting the manufacturing industry to intelligently transform based on big data analysis and application and realize products. Dialogue with machines, products, and people creates an intelligent manufacturing model that can independently allocate production resources and output products [5]. With the advent of the Industry 4.0 era, the smart manufacturing industry is bound to usher in a new wave. The CPS is used to coordinate and process manufacturing in real time the industrial chain to achieve high-quality and low-cost goals, while meeting the diverse and personalized needs of users, to achieve smart factory [6]. Industry 4.0 has brought amazing efficiency improvements to the manufacturing industry. The current domestic and foreign applications are mainly reflected in the high degree of automation of intelligent production equipment, making the production system not only simple and flexible but also capable of handling various events in real time during the entire production process to ensure the thorough intelligence of the production process [7]. At the same time, this intelligent production model is not only a manifestation of basic automation in a specific environment, but more importantly, it can also achieve the optimization of a world-class network formed by different factories and different production units [8]. This means that in the realization of intelligent manufacturing, the CPS system is used to effectively connect the production equipment and the control network, and the innovative technology is used to integrate the three elements of intelligent machines, efficient analysis, and staff to improve the production of the manufacturing industry, namely, efficiency, reduce cost, and time resource consumption [9].

Many scholars are more in-depth and mature in the research of information behavior from the cognitive perspective. Literature [10] believes that a variety of factors such as personal experience, organization, and education level in a specific situation will affect the cognitive structure and cognitive ability of an individual. Entrepreneur decision-making research from the perspective of ability focuses on the ability of entrepreneurs to use information to make decisions in the decision-making process. Research from this perspective is mostly based on entrepreneurial ability theory, resource management theory, and competitive advantage theory to study entrepreneurial decision-making. The connotation of ability, the influencing factors of entrepreneur's decision-making ability, the relationship between entrepreneur's decision-making ability and enterprise competition, the relationship between enterprise growth, and the improvement path of entrepreneur's decision-making ability are explored [11]. Literature [12] incorporates the entrepreneur's decision-making ability into the measurement system of entrepreneur's core competence and analyzes the relationship between entrepreneurial decision-making ability, innovation ability, communication ability, and learning ability. Entrepreneur's core competence is expanded, and the relationship between entrepreneur's strategic decision-making ability and corporate performance is explored; the literature [13] summarizes these factors into two major categories: economic structural constraints and entrepreneurial background factors after combing through relevant literature. It also conducts a more detailed analysis and discussion on two types of factors; literature [14] analyzes the performance of entrepreneurs in corporate transformation and analyzes the factors that affect entrepreneurs' decision-making capabilities in various dimensions; literature [15] focuses on entrepreneurs' decision-making capabilities to test the logical relationship between the decision-making ability and the competitive advantage of the enterprise and prove that the decision-making ability directly contributes to the competitive advantage of the enterprise and is the source of the core ability; in the research on the relationship between the decision-making ability of entrepreneurs and the growth of the enterprise, the literature [16] combines the research results of entrepreneurs' decision-making ability and influencing factors that have promoted the growth of enterprises in recent years, the mechanism of entrepreneurial decision-making ability on enterprise growth, the research results of entrepreneurial decision-making ability, and the process of enterprise growth and makes prospects for future research [17]. From the perspectives of exogenous theory and endogenous theory, it explores the relationship between the transformation of entrepreneurial decision-making ability and the growth of enterprises. Literature [18] formulated information literacy standards for corporate managers, from the perspective of information behavior, and proposed ways to improve the decision-making ability of corporate managers.

3. Enterprise Decision-Making Model Based on Virtual Machine Scheduling Model

Infrastructure layer services mainly include image management, system management, user management, system monitoring, and account billing. These services correspond to the functions provided by the virtualization integration manager and are the interfaces for users to obtain infrastructure layer resources. The schematic diagram of the infrastructure layer system structure is shown in Figure 1.

Based on the analysis of the cloud computing infrastructure layer architecture, this paper designs a virtual machine scheduling model in the cloud environment. The virtual machine scheduling model is shown in Figure 2.

In fact, the global manager can be regarded as a scheduling algorithm in essence, which realizes the replanning of the mapping relationship between virtual machines and physical hosts based on the resource monitoring data of the virtualized environment. It can be implemented using a greedy algorithm, a divide-and-conquer algorithm, or a heuristic algorithm.

The virtual machine scheduling process can be regarded as a control loop composed of three parts: data collection, data analysis and decision-making, and operation execution. Among them, the receipt collection corresponds to the detection process of the resource status and application load status of the data center node. Data analysis decision-making is to predict application load based on the collected monitoring data and determine the selection of virtual machines to be migrated and the placement of virtual machines for scheduling goals such as energy saving and load balancing. The final operation execution stage is to use virtual machine real-time migration technology to migrate virtual machines according to the virtual machine placement plan. The flowchart of the virtual machine scheduling process is shown in Figure 3.

By periodically performing the virtual machine scheduling process described in the above figure in the data center, the resource allocation of the data center can be continuously optimized, thereby improving the energy efficiency of the data center.

In order to facilitate a detailed and in-depth study of the status changes of the physical host, according to the real-time operating status and load status of the physical host in the data center, this paper divides the physical host into 4 statuses and defines them as follows:

Definition 1. Low-load status. It refers to the status when the utilization rate of various resources of the physical host is lower than the lower load threshold T_{low} preset by the system. All physical hosts in a low-load state in the data center form a low-load host set $H_{\text{low}} = \langle h_1, h_2, h_3, \cdots, h_n \rangle$. For a physical host in this state, all virtual machines running on it must be the target to be migrated.

Definition 2. High-load status. It refers to the state when the utilization rate of various resources of the physical host exceeds the upper limit threshold T_{high} of load set by the system. All physical hosts in a high-load state in the data center form a high-load host set $H_{\text{high}} = \langle h_1, h_2, h_3, \cdots, h_n \rangle$. For the physical host in this state, the migration object needs to be selected according to the virtual machine selection policy to be migrated set by the system.

Definition 3. Normal status. It refers to the state when the utilization of various resources of the physical host is between the upper limit threshold T_{high} and the lower limit threshold T_{low} set by the system. All physical hosts in a normal state in the data center form a normal load host set $H_{\text{high}} = \langle h_1, h_2, h_3, \cdots, h_n \rangle$. The physical host in this state can be used as a candidate target host for receiving the virtual machine to be migrated.

Definition 4. Idle status. It refers to the state that there is no virtual machine performing cloud tasks on the physical host. All physical hosts in an idle state in a data center form an idle host set $H_{\text{idle}} = \langle h_1, h_2, h_3, \cdots, h_n \rangle$, and they are generally shut down in a dormant state as alternate hosts in the data center [19].

The state of the physical host will change as the load on it changes and the virtual machine scheduling mechanism of the data center. The data center host state transition diagram is shown in Figure 4.

From the above figure, we can see the main reason for the host status changes when the virtual machine scheduling and load changes in the data center. The state of the physical host will change as the load on it changes and the specific virtual machine scheduling mechanism. From this perspective, the virtual machine scheduling of the data center can be seen as a process of reducing the high-load and low-load hosts in the data center by optimizing scheduling measures and maximizing the idle state hosts.

Definition 5. CPU utilization. Generally, the percentage of the total CPU time slice allocated by the running host to the total statistical time is called CPU utilization, which is recorded as U^{CPU}.

Definition 6. Memory utilization. Generally, the percentage of the memory currently used by the running node to the total memory of the node is called the memory utilization, which is recorded as U^{MEM}.

Definition 7. Bandwidth utilization. Generally, the percentage of the bandwidth currently used by the running node to the total bandwidth of the node is called the bandwidth utilization, which is recorded as u^{BW}.

Virtual machine scheduling in a data center needs to monitor the usage of various resources of the physical host and the virtual machines running on it at the same time. If we ignore the resource usage consumed by the physical host itself, this article believes that there is the following relationship between the resource utilization of a physical host and

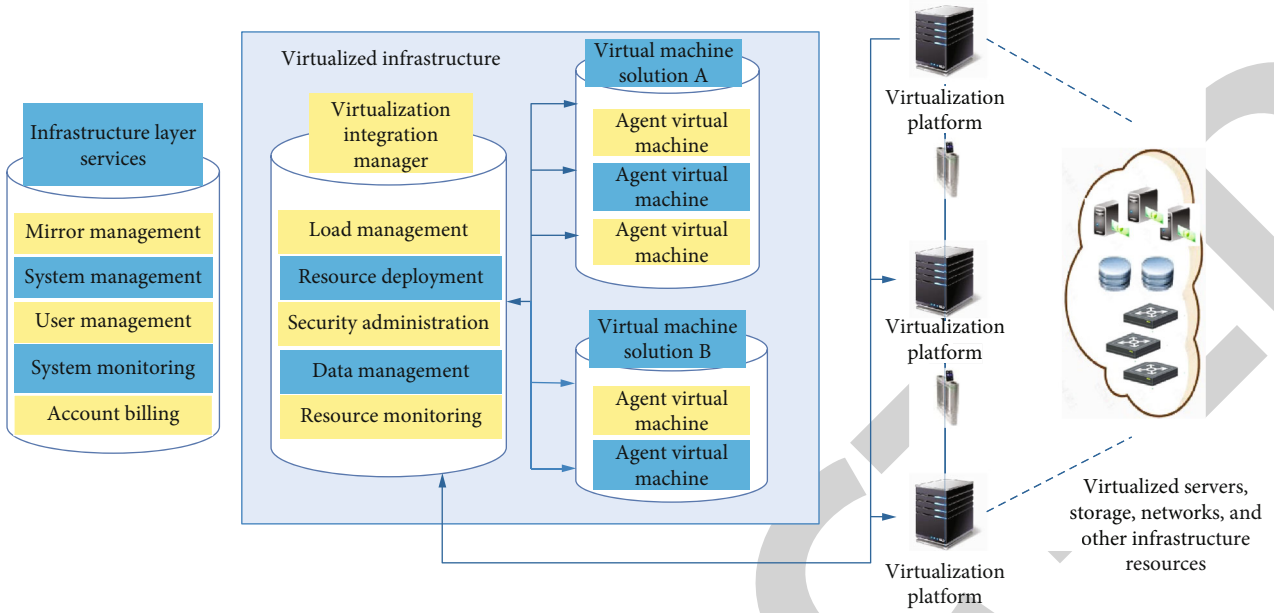

Figure 1: Schematic diagram of infrastructure layer architecture.

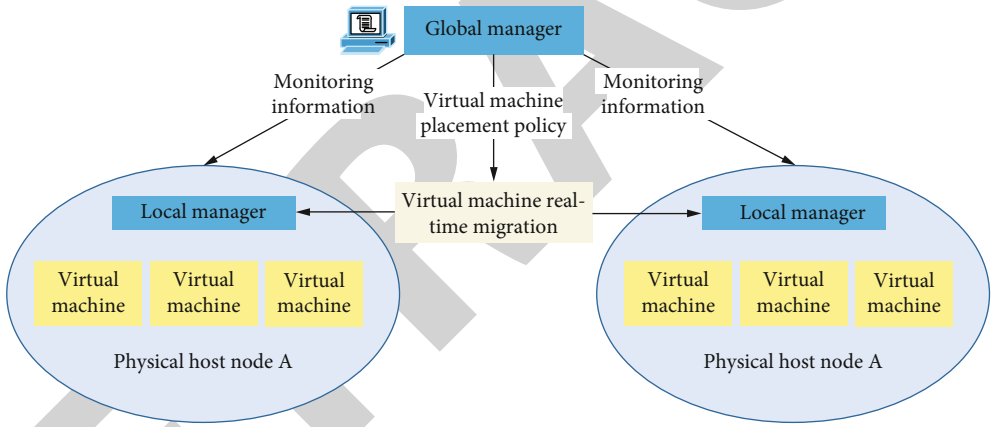

Figure 2: Virtual machine scheduling model.

the virtual machine running on it [20]:

$$U^{\mathrm{CPU}} \approx \sum_{i=1}^{n} u_i^{\mathrm{cpu}}, \tag{1}$$

$$U^{\mathrm{mem}} \approx \sum_{i=1}^{n} u_i^{\mathrm{MEM}}, \tag{2}$$

$$U^{\mathrm{BW}} \approx \sum_{i=1}^{n} u_i^{\mathrm{BW}}. \tag{3}$$

Among them, u_i^{cpu}, u_i^{MEM}, and u_i^{BW}, respectively, represent the CPU, memory, and network bandwidth utilization of the i-th virtual machine VMJ on the physical server H, and n represents the total number of virtual machines running on the host server H.

The effect of virtual machine scheduling on data centers, physical hosts, and applications is comprehensively evaluated for its effectiveness, and a comprehensive evaluation index system is established. Several main evaluation indexes are introduced below.

The energy consumption of data center servers is usually divided into two parts. Among them, part of the energy consumption comes from the overhead of the CPU. A large number of studies have shown that the power consumption of the CPU is basically linearly related to its utilization rate, so the power consumption of the CPU will increase as its utilization rate increases. The remaining part of the energy consumption comes from other components such as the motherboard, network, and memory. This part of the energy consumption is only related to the switch state of the host and is usually a fixed value. Therefore, the energy consumption model of the server can be expressed as follows:

$$P = \begin{cases} (P_{\mathrm{full}} - P_{\mathrm{idle}}) \times U^{\mathrm{CPU}} + P_{\mathrm{idle}}, & U^{\mathrm{CPU}} > 0 \\ 0, & \text{otherwise} \end{cases}. \tag{4}$$

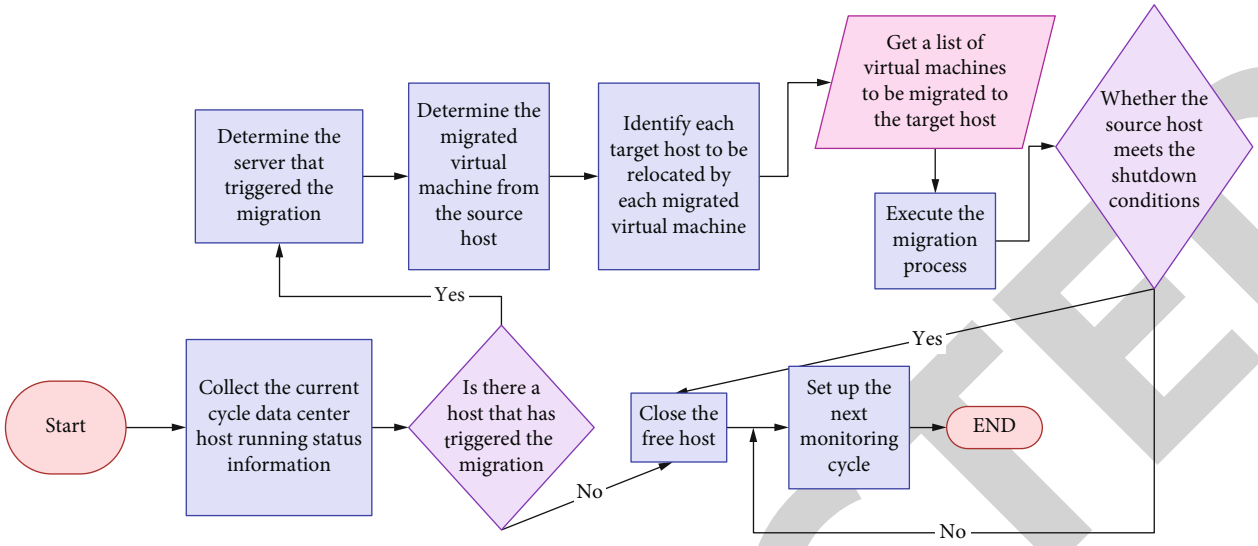

Figure 3: Flow chart of virtual machine scheduling process.

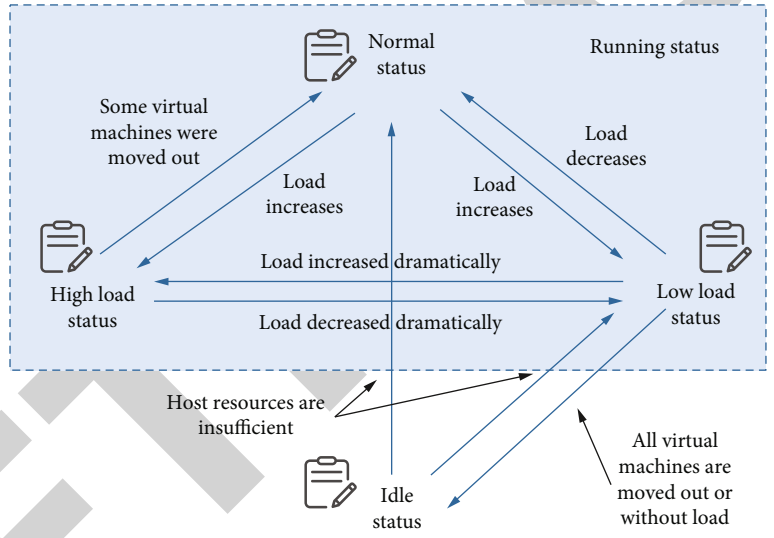

Figure 4: State transition diagram of host in data center.

Among them, P represents the total energy consumption of the physical host, P_{full} represents the maximum energy consumption of the physical host when the CPU is fully loaded (CPU utilization reaches 100%), and P_{idle} represents the energy consumption when the physical host is idle without any load.

In order to facilitate the application, the energy consumption model of the physical host can also be converted into the following form:

$$P = \begin{cases} k \times P_{\text{full}} + (1-k) \times P_{\text{full}} \times U^{\text{CPU}}, & U^{\text{CPU}} > 0 \\ 0, & \text{otherwise} \end{cases}. \quad (5)$$

Among them, k is a constant, called the energy consumption coefficient, and g represents the ratio of the energy consumption (P_{idle}) when the physical server is idle to the energy consumption (P_{full}) when the physical server is fully loaded (usually 0.7). It should be noted that for heterogeneous servers, the energy consumption coefficient k and the maximum energy consumption of the server will also be different.

This article simply uses the physical host CPU usage rate not to exceed the upper limit utilization threshold set by the system as the service level goal of the SLA. That is, when the CPU utilization is greater than the upper threshold, an SLA violation is triggered, which is recorded as SLAV. The definition of the data center SLA violation rate is as follows:

$$\text{Rate}(\text{SLAV}) = \frac{\sum_i^n T_v(vm_i)}{\sum_i^n T_r(vm_i)}. \quad (6)$$

Among them, $T_v(vm_i)$ represents the duration of the

SLA violation of the i-th virtual machine in the data center, $T_r(vm_i)$ represents the total running time of the i-th virtual machine, and n represents the total number of virtual machines in the data center. The SLA violation rate reflects the ability of the data center to provide service stability, and the lower the value, the better the service quality of the data center.

In this paper, the utilization rate of each type of resource is normalized, and the product of the utilization rate of these three resources is used to represent the load of the physical node. The load of the physical node i is defined as follows:

$$L_i = \frac{1}{1 - U_i^{\text{cpu}}} \times \frac{1}{1 - U_i^{\text{mem}}} \times \frac{1}{1 - U_i^{\text{bw}}}. \tag{7}$$

From the above definition of node load, it can be seen that the node load will change in a positive correlation with the changes of various resources. For example, no matter which resource utilization increases, the overall load of the node will increase accordingly. Using this definition is more comprehensive and accurate than considering only a single resource. By quantifying the load value of the physical host, the standard analysis of variance method can be used to represent the load balance of the data center, which is defined as follows:

$$\text{Degree} = \sqrt{\frac{1}{n}\sum_{i=0}^{n}\left(L_i - \bar{L}\right)^2}, \tag{8}$$

$$\bar{L} = \frac{1}{n}\sum_{i=0}^{n} L_i. \tag{9}$$

Different from the load balancing of a data center, the load balancing of a single physical node refers to the relative balance of the usage of various types of resources (such as CPU, memory, and network bandwidth). We assume that the CPU, memory, and network bandwidth utilization rate of physical node A is 50%, 50%, and 50%, and the corresponding resource utilization rate of physical node B is 40%, 70%, and 20%. Then, this article believes that the load balance of node A is better than that of node B. The reason is that node B is more likely to encounter a bottleneck in the use of a single type of resource and affect the performance of the node. According to the utilization rate of various types of resources, this article defines the load balance of physical nodes as follows:

$$\text{degree}_i = \sqrt{\left(U_i^{\text{cpu}} - U_i^{\text{mem}}\right)^2 + \left(U_i^{\text{cpu}} - U_i^{\text{bw}}\right)^2 + \left(U_i^{\text{mem}} - U_i^{\text{bw}}\right)^2} \tag{10}$$

Among them, degree_i represents the load balance of physical node i, that is, the balance of various resource consumption.

3.1. Number of Virtual Machine Migrations. An example diagram of virtual machine selection is shown in Figure 5.

Using the TOPSIS method, the optimal combination of virtual machines to be migrated can be selected. The specific process is as follows:

(1) The algorithm establishes the initial decision matrix X. We assume that there are m virtual machine selection schemes that can eliminate the overload of the host and form a scheme set $S_i(i = 1, 2, 3, \cdots, m)$. For each selection scheme, there are n targets to form a set $I_i(i = 1, 2, 3, \cdots, n)$. And, the goal is divided into positive attribute l^+ and negative attribute l^-, and there is $l = l^+ \cup l^-$. The constructed decision matrix is:

$$x = \begin{array}{c} \\ S_1 \\ S_2 \\ \vdots \\ S_m \end{array} \begin{array}{c} \begin{array}{cccc} l_1 & l_2 & \cdots & l_n \end{array} \\ \begin{bmatrix} x_{11} & x_{12} & \cdots & x_{1n} \\ x_{21} & x_{22} & \cdots & x_{2n} \\ \vdots & \vdots & \ddots & \vdots \\ x_{m1} & x_{m2} & \cdots & x_{mn} \end{bmatrix} \end{array}. \tag{11}$$

Because the dimensions of each evaluation index may be different, it is necessary to normalize the initial decision matrix to obtain the normalized matrix R as follows:

$$R = \begin{bmatrix} r_{11} & r_{12} & \cdots & r_{1n} \\ r_{21} & r_{22} & \cdots & r_{2n} \\ \vdots & \vdots & \ddots & \vdots \\ r_{m1} & r_{m2} & \cdots & r_{mn} \end{bmatrix}. \tag{12}$$

Among them, $r_{ij} = x_{ij} / \sqrt{\sum_{i=1}^{m} x_{ij}^2}, \quad i = 1, 2, 3, \cdots, m, \quad j = 1, 2, 3, \cdots, n$

(2) The algorithm calculates the normalized weighted decision matrix T. The algorithm assigns weights w , according to the importance of each goal, and needs to satisfy $\sum_{j=1}^{m} w_j$ at the same time. At present, the methods for determining weights include expert scoring, logarithmic least squares method, and analytic hierarchy process,. The weighting matrix is as follows:

$$W = \begin{bmatrix} w_1 & 0 & \cdots & 0 \\ 0 & w_2 & \cdots & 0 \\ \vdots & \vdots & \ddots & \vdots \\ 0 & 0 & \cdots & w_n \end{bmatrix}. \tag{13}$$

The element of the weighted decision matrix is $t_{ij} = r_{ij} * w_j$, and the weighted decision matrix can be obtained as

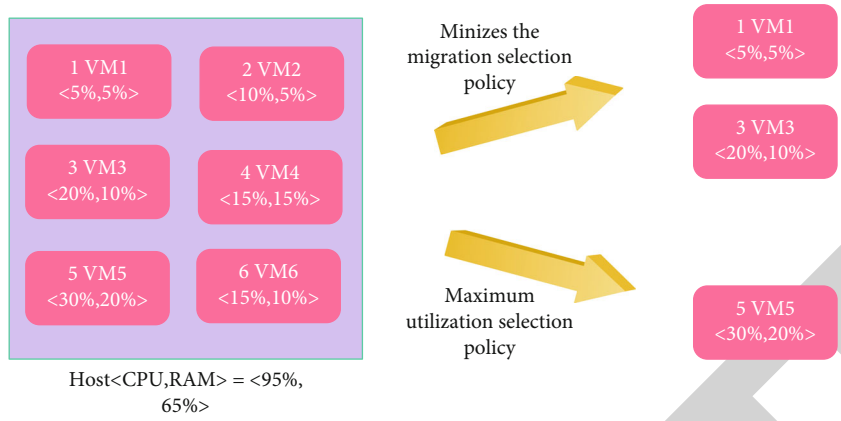

Figure 5: Sample diagram of virtual machine selection.

follows:

$$T = R \times W = \begin{bmatrix} t_{11} & t_{12} & \cdots & t_{1n} \\ t_{21} & t_{22} & \cdots & t_{2n} \\ \vdots & \vdots & \ddots & \vdots \\ t_{m1} & t_{m2} & \cdots & t_{mn} \end{bmatrix} \quad (14)$$

(3) The algorithm determines the ideal solution and the negative ideal solution. The algorithm determines the ideal solution Z∗ and the negative ideal solution Z- according to the profitability index set, the loss index set, and the weighted decision matrix, which are defined as follows:

$$Z^+ = \left\{ \left[\underset{1 \le i \le m}{\text{Max}} t_{ij} \mid I_j \in 1^+ \right], \left[\underset{1 \le i \le m}{\text{Min}} t_{ij} \mid I_j \in 1^- \right] \right\} = \{z_1^+, z_2^+, \cdots, z_n^+\}, \quad (15)$$

$$Z^- = \left\{ \left[\underset{1 \le i \le m}{\text{Min}} t_{ij} \mid I_j \in 1^+ \right], \left[\underset{1 \le i \le m}{\text{Max}} t_{ij} \mid I_j \in 1^- \right] \right\} = \{z_1^-, z_2^-, \cdots, z_n^-\}. \quad (16)$$

Among them, l+ is the profitability index set, and 1- is the loss index set. The larger the value of the profitability index, the more beneficial to the evaluation result; while for the loss index, the smaller the value is, the more beneficial the evaluation result is. On the contrary, it is unfavorable to the evaluation result

(4) The algorithm calculates the distance from each scheme to the positive and negative ideal solutions. The distance scale can be calculated with the n-dimensional Euclidean distance. The distance to the positive ideal solution Z^+ is denoted by S^+, and the distance to the negative ideal solution is denoted by S^-:

$$s_1^+ = \sqrt{\sum_{j=1}^{m} \left(t_{ij} - z_1^+\right)^2}, \quad (i = 1, 2, 3, \cdots, m), \quad (17)$$

$$s_1^- = \sqrt{\sum_{j=1}^{n} \left(t_{ij} - z_1^-\right)^2}, \quad (i = 1, 2, 3, \cdots, m) \quad (18)$$

(5) The algorithm calculates the relative closeness of each scheme to the positive ideal solution and obtains the final comprehensive evaluation result value. The calculation method is as follows:

$$C_1 = \frac{s_i^-}{s_i^- + s_i^+} (0 \le C_1 \le 1, i = 1, 2, 3, \cdots, m). \quad (19)$$

Among them, C_i represents the comprehensive evaluation value of the plan S_i. When the value of C_i is closer to 1, it means that the plan is closer to the ideal solution and the comprehensive evaluation is better. On the contrary, the comprehensive evaluation is worse

(6) The algorithm sorts based on the relative closeness c of each plan, so as to determine the priority of each plan to form the basis for decision-making. Obviously, choosing the virtual machine selection scheme with the largest c value can ensure that the optimization and trade-off of multiple objectives are met

The energy consumption of the physical host in the data center is related to the utilization rate of the CPU. This article has conducted an in-depth analysis and established an energy consumption model (formula (5)), which will continue to be used as a way to calculate the energy consumption of the physical server. Therefore, the energy consumption difference before and after the selected virtual machine is migrated from the host which can be calculated as a measure of the energy-saving benefit of a selected

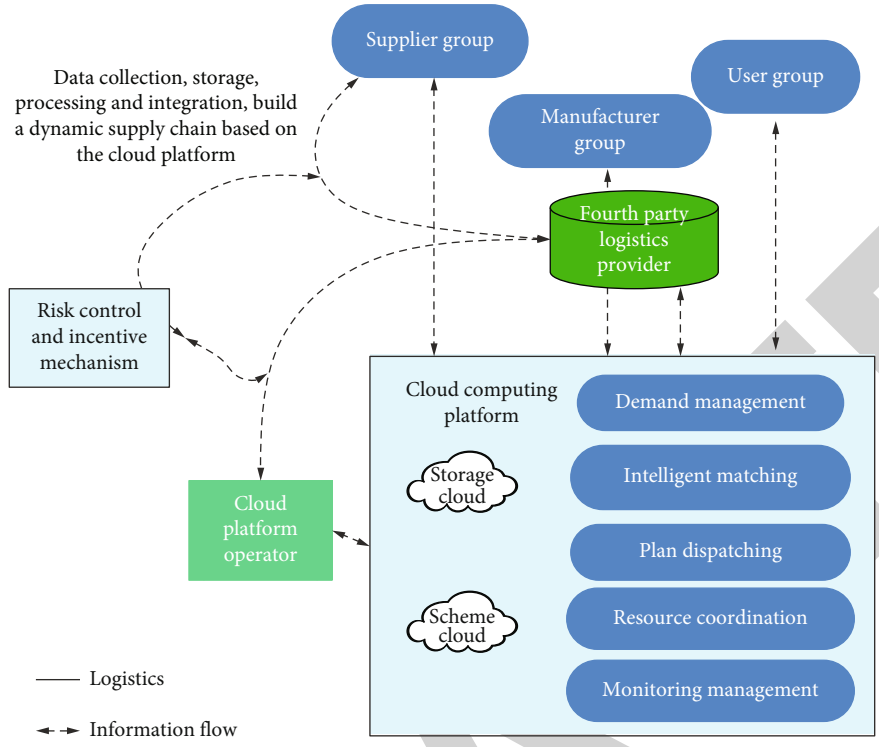

Figure 6: Model diagram of dynamic supply chain construction based on cloud platform.

scheme, which is expressed as follows:

$$\Delta P = P\left(U_{\text{after}}^{\text{cpu}}\right) - P\left(U_{\text{before}}^{\text{cpu}}\right). \tag{20}$$

Obviously, the energy consumption reduction index belongs to the profitability index. The larger the value, the more favorable the evaluation result of the scheme.

The longer the migration time of the virtual machine, the worse the quality of service for users. Therefore, in the virtual machine scheduling process, the shorter the migration time, the better the quality of service for users. From the previous discussion on the virtual machine real-time migration technology, it can be seen that the current virtual machine real-time migration technology is mainly realized by iteratively copying the virtual machine memory image. Therefore, the migration time is related to the network bandwidth of the host and the target host. However, since the target host to be migrated cannot be determined during the virtual machine selection stage, the migration time is defined as follows:

$$T_{\text{mig}} = \frac{\text{MEM}_u}{\text{BW}}. \tag{21}$$

Among them, T_{mig} represents the migration time of a single virtual machine and is the ratio of the used memory (MEM) of the virtual machine to the network bandwidth (BW). Obviously, the migration time is a loss index, and the smaller its value, the better the evaluation result. It should be noted that the virtual machine selection scheme may include one or more selected virtual machines, and the sum of their migration time needs to be calculated as the evaluation value.

If the dispersion of the evaluation value of the virtual machine selection scheme on an evaluation index is very small, it means that the evaluation index has a small impact on the evaluation result, so the index should be given a smaller weight. Therefore, this article proposes an objective weight calculation method based on standard deviation:

$$\sigma_j = \sqrt{\frac{1}{m}\sum_{i=1}^{m}\left(r_{ij} - \bar{r}_j\right)^2}, \tag{22}$$

$$w_j = \sigma_j / \sum_{j=1}^{m} \sigma_j. \tag{23}$$

Among them, σ_j represents the standard deviation of the evaluation value of the j-th index in each selection scheme after the standardization, and w_j represents the weight of the j-th index, that is, the ratio of the standard deviation of the index to the sum of the standard deviations of each index.

In the case of obtaining expert scores or empirical values, such subjective weights and calculated objective weights can usually be combined to obtain the comprehensive weights of each evaluation index, which can more comprehensively reflect the importance of each evaluation index.

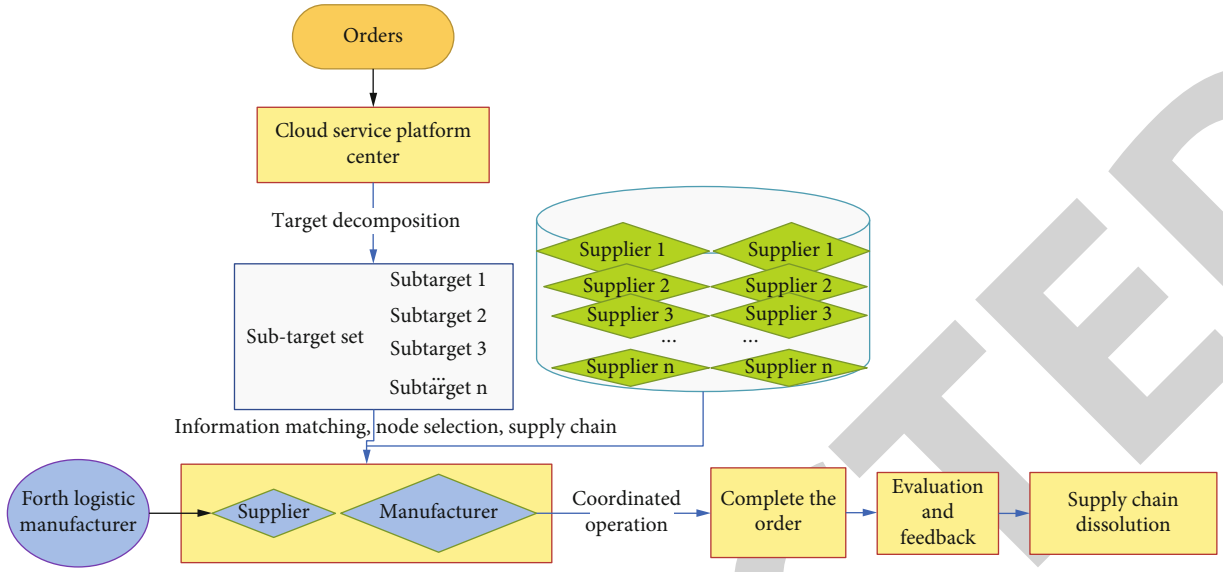

Figure 7: Schematic diagram of the operation process of a dynamic supply chain system based on a cloud platform.

4. Comprehensive Decision-Making System for Industry 4.0 Virtual Enterprises Based on the Personalized Customization Model of Product Life Cycle

The construction model of dynamic supply chain based on cloud platform proposed in this paper is driven by customer demand and characterized by customization and individualization. With the support of modern smart technology, it takes the manufacturer enterprise group and supplier enterprise group as the resource basis of the whole model and is operated by a cloud platform and a fourth-party logistics service provider to provide customers with high-quality, low-cost, and highly flexible modern products. The dynamic supply chain construction model based on the cloud platform is shown in Figure 6.

During the operation of the entire system, a stable and followable process is required to ensure the efficient operation of the system. Although fourth-party logistics providers also have the ability to select node companies to form a supply chain, the decisions made after scientific processing of relevant data through the cloud platform are more scientific and fair. Therefore, the fourth-party logistics provider in this model does not make supply chain node selection decisions. The operation process of the dynamic supply chain system based on the cloud platform is shown in Figure 7.

The model in this chapter considers the situation where the manufacturer produces new products at the same time and remanufactures products by recycling waste products/problem products. For the two products, although new products are generally slightly better than remanufactured products in terms of functions and service life, remanufactured products have certain price advantages compared to new products, so new products and remanufactured products are mutually replaceable. That is, when there is a shortage of goods in the demand market for reproducts, new products can enter the reproduct market to replace them with demand when the supply exceeds demand. Similarly, when new products are in short supply, remanufactured products can supplement the demand market for new products with sufficient inventory. Through the mutual demand substitution among products, it can meet the market demand of consumers and make up for the total profit loss of the manufacturer due to product shortage or surplus inventory. The manufacturer's production model with upward/downward substitution is shown in Figure 8.

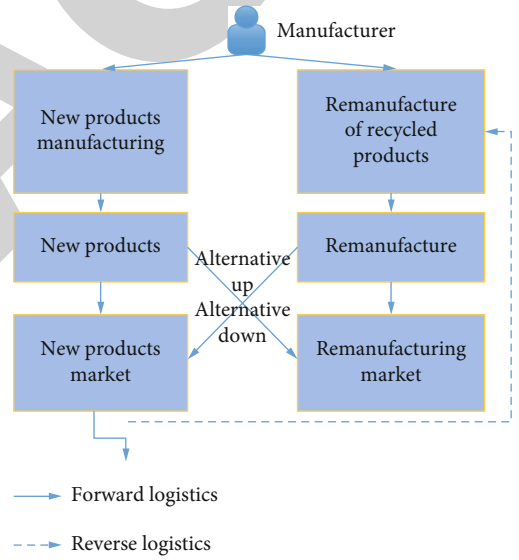

Figure 8: Manufacturer's production model with upward/downward substitution.

As a specific product of Industry 4.0, the core of smart factory lies in whether CPS technology can be deeply integrated with enterprise information system to realize the integration of workshop equipment, people, and materials and other entities with advanced information technology.

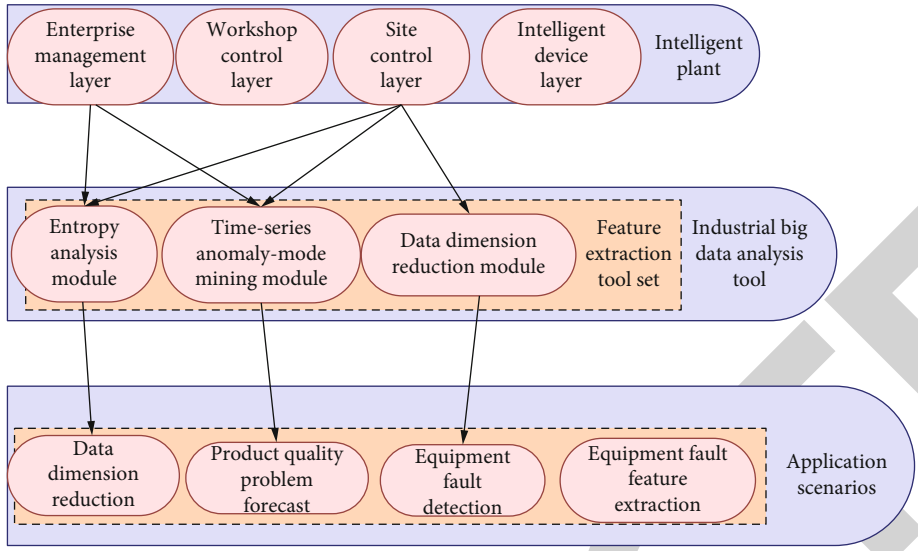

Figure 9: The overall framework of the industrial big data analysis tool set for smart factories.

Table 1: Evaluation of the comprehensive decision-making analysis effect of Industry 4.0 virtual enterprises considering the personalized customization model of product life cycle.

No.	Data processing	Decision effect	NO	Data processing	Decision effect
1	89.15	79.01	19	93.02	78.26
2	93.88	83.50	20	86.63	82.24
3	87.01	83.39	21	92.28	72.54
4	91.28	75.47	22	91.13	76.71
5	92.72	86.75	23	87.88	87.30
6	89.11	80.73	24	89.63	81.80
7	87.75	76.03	25	88.20	76.26
8	88.91	84.02	26	93.71	83.58
9	93.80	75.50	27	87.43	77.13
10	86.08	80.84	28	90.05	82.38
11	91.83	71.95	29	89.83	77.09
12	91.68	85.97	30	86.11	79.02
13	93.64	80.88	31	93.40	73.38
14	86.82	82.36	32	90.12	73.14
15	86.62	83.30	33	87.80	83.07
16	86.59	83.19	34	89.43	83.17
17	91.17	71.99	35	86.42	72.24
18	92.47	71.67	36	90.96	74.75

Moreover, it comprehensively uses big data analysis methods and means to complete the conversion of data to information to enhance the value of data and assist enterprise management and decision-making. Therefore, the construction and normal operation of smart factories must increase data utilization, use big data methods or tools to achieve value creation, and enhance corporate competitiveness. Based on this, this article preliminarily studies the feature extraction tool set in the industrial big data analysis tools for smart factories and improves the commonly used

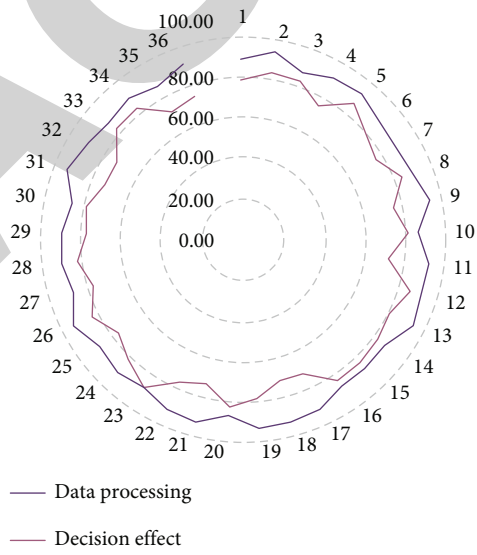

Figure 10: System performance evaluation.

mining algorithms to cope with some of the problems faced in the application of smart factories. The overall framework is shown in Figure 9:

The model constructed in this paper can be applied to the personalized customization of product life cycle and can help enterprises make comprehensive decision-making. In particular, it can perform intelligent decision-making analysis under the background of Industry 4.0. On this basis, this article evaluates the effects of this article's intelligent model from production data processing and enterprise comprehensive decision-making through experimental research and obtains the results shown in Table 1 and Figure 10.

It can be seen from the above research that the decision-making system proposed in this article can play an important role in the comprehensive decision-making of Industry 4.0 enterprises, and this decision-making can be spread throughout the entire product life cycle.

Hindawi
Journal of Sensors
Volume 2023, Article ID 9798106, 1 page
https://doi.org/10.1155/2023/9798106

Retraction

Retracted: The Construction of a Smart Education System in Colleges and Universities Based on Cloud-Side Collaborative Computing Task Scheduling Algorithm

Journal of Sensors

Received 19 December 2023; Accepted 19 December 2023; Published 20 December 2023

This article has been retracted by Hindawi following an investigation undertaken by the publisher [1]. This investigation has uncovered evidence of one or more of the following indicators of systematic manipulation of the publication process:

(1) Discrepancies in scope
(2) Discrepancies in the description of the research reported
(3) Discrepancies between the availability of data and the research described
(4) Inappropriate citations
(5) Incoherent, meaningless and/or irrelevant content included in the article
(6) Manipulated or compromised peer review

The presence of these indicators undermines our confidence in the integrity of the article's content and we cannot, therefore, vouch for its reliability. Please note that this notice is intended solely to alert readers that the content of this article is unreliable. We have not investigated whether authors were aware of or involved in the systematic manipulation of the publication process.

Wiley and Hindawi regrets that the usual quality checks did not identify these issues before publication and have since put additional measures in place to safeguard research integrity.

We wish to credit our own Research Integrity and Research Publishing teams and anonymous and named external researchers and research integrity experts for contributing to this investigation.

The corresponding author, as the representative of all authors, has been given the opportunity to register their agreement or disagreement to this retraction. We have kept a record of any response received.

References

[1] L. Yu, "The Construction of a Smart Education System in Colleges and Universities Based on Cloud-Side Collaborative Computing Task Scheduling Algorithm," *Journal of Sensors*, vol. 2022, Article ID 8949974, 12 pages, 2022.

Hindawi
Journal of Sensors
Volume 2022, Article ID 8949974, 12 pages
https://doi.org/10.1155/2022/8949974

Research Article

The Construction of a Smart Education System in Colleges and Universities Based on Cloud-Side Collaborative Computing Task Scheduling Algorithm

Lingyun Yu

Academic Affairs Office, Xiamen University of Technology, Xiamen 361024, China

Correspondence should be addressed to Lingyun Yu; yulingyun@xmut.edu.cn

Received 1 December 2021; Revised 2 January 2022; Accepted 15 January 2022; Published 10 February 2022

Academic Editor: Wei Zhang

In order to improve the resource scheduling efficiency of the smart education system in colleges and universities and improve the stability and security of educational resource processing, this paper combines cloud-side collaborative computing technology to improve the cloud computing task scheduling algorithm and uses the improved algorithm for task scheduling. Moreover, this paper combines the global optimization and local optimization processes to make the final optimal solution performance better and further reduce the task scheduling execution time in the cluster, thereby improving the computing efficiency of cloud computing. In addition, this paper combines the improved algorithm to construct the system structure framework and verifies the system performance through experiments. The experimental research results show that the smart education system in colleges and universities based on the cloud-side collaborative computing task scheduling algorithm constructed in this paper is very good in all aspects and has a greater advantage in processing educational resources.

1. Introduction

Today, when Internet information technology is becoming more and more mature, the concept of teaching interaction is becoming more and more abundant, which also makes the choice of learning methods and content more diversified. At present, it is more and more common to use portable mobile devices to realize the teaching interaction of courses. In evaluation theory and interactive teaching theory, both students and teachers are the subjects of evaluation. Moreover, students' evaluation of their own learning achievements is mainly through mutual evaluation and self-evaluation, and students can also evaluate teachers' teaching behavior [1]. Such technical means can not only help students form better learning habits and strong learning interests but also enable teachers to more intuitively understand the learning situation of each student. In particular, this method is even more important when most teachers are still subjectively evaluating the learning behavior of students, making it possible to evaluate what was previously considered impossible [2]. Cloud storage [3] is a new network storage technology extended and developed on the basis of cloud computing. Under the premise of high-speed network and Web 2.0 technology, it uses cluster technology, distributed file system technology, network technology, data compression technology, and other related technologies to connect a large number of hardware storage devices of various types, scattered in various places, and work together, and provides data storage, access, and other functions by forming an expandable storage resource pool.

This article combines the cloud-side collaborative computing task scheduling algorithm to construct a smart education system in colleges and universities, analyzes the process of smart education in colleges and universities, and further improves the effect of smart education on this basis.

2. Related Work

The rise of the concept of cloud computing drives the development of cloud storage technology. The cloud storage service models provided by cloud storage service providers are mainly divided into two types [4]: one is large-capacity file

sharing, which focuses on the storage and sharing of large files by users; the other one is cloud synchronous storage, which is the synchronous storage of files. However, due to the chaos in the cloud storage market and because there are so many cloud storage products, it is difficult to define the two storage modes [5]. Dropbox is an online file storage service developed by Dropbox. It synchronizes files through cloud computing and other advanced technologies in a network environment. Users can store and share various files and folders and support different operating systems and multiple smart clients [6]. Google Drive is an online cloud storage service launched by Google. It can not only provide free capacity space but also pay for expansion; at the same time, Google Docs is built-in, and users can collaborate with others in real time; in addition, Google will also provide third-party provider API interface, allowing people to save content from other programs to Google Drive [7]. OneDrive (formerly known as Sky Drive) is a cloud storage service launched by Microsoft, capable of file storage, file management, permission control, online office, and other services [8]. It can access the research status of informatization and intelligence in the field of education at home and abroad through multiple clients. Literature [9] mainly studies how to achieve system integration and resource sharing and improve hardware utilization, but it lacks research on massive data processing. Literature [10] proposes to solve the problem of information islands of enterprises with a hybrid architecture model of the two, but there is no introduction to resource integration and on how to improve resource utilization. Literature [11] proposed a cloud-based virtual desktop system to study the use of virtual classrooms in the education field. Literature [12] proposes to integrate knowledge organization and knowledge management and treat knowledge as a service (KAAS), demonstrating how this concept can be used in British universities. Literature [13] mainly studies the sharing and utilization of resources, but it does not solve the problem of unbalanced utilization of resources. Literature [14] proposes to model the complex causal relationship in the system by constructing a system model and verify the result-factor relationship existing in the system model through model analysis. Literature [15] proposes a new teaching system that integrates Web Services of courseware resources through the SOAP protocol. Literature [16] summarizes the transformation from traditional education informatization to education services under the cloud computing environment and the computing architecture of cloud education.

For the problems of mutual independence and closure of education systems, most of the researches are carried out on the integration of heterogeneous system resources of SOA, and the operability of interconnection between systems is also studied through a large number of aspects such as integration, redevelopment, and adaptation. Literature [17] describes the architecture and basic characteristics of modern distance education based on cloud computing, analyzes the changes that distance education cloud brings to education and teaching methods, and looks forward to its deployment. Literature [18] summarizes the fundamentals of education cloud advanced features such as efficient facility organization, educational resource sharing, reduction of R&D investment, and management and operation cost savings. Computer science disciplines are more concerned with issues such as the infrastructure and implementation technology of educational cloud services. Literature [19] proposed a cloud architecture model based on the shared content object reference model, which breaks through the solidified learning methods of traditional learning systems and realizes the unified storage and flexible distribution of educational resources such as courses and learning materials by constructing content access middleware. Literature [20] describes the transformation from traditional E-learning to cloud services and cloud service architecture and discusses the commercialization model of education cloud services and the potential risks of their promotion and operation.

3. Educational Resource Cloud Task Scheduling

The task scheduling process in the cloud computing system involves the user level, task scheduling mechanism, virtual machine level, and data center level. The user submits the task, and the service agent connecting the user and the virtual machine will assign the task to the virtual machine to execute the task according to the scheduling policy provided by the task scheduling mechanism. The process is shown in Figure 1.

Task scheduling is to map tasks submitted by users with virtual machine resources in the data center, and the mapping process is implemented through a certain algorithm. The cloud computing task scheduling process is based on the process of performing tasks on virtual machines. It can be divided into two levels of task scheduling: the first level scheduling is mainly the scheduling between the user and the virtual machine, and the second level scheduling is mainly the scheduling between the host and the virtual machine. Figure 1 shows the first-level scheduling process.

The difference between the task scheduling process in cloud computing and the task scheduling process in other systems is caused by the particularity of the cloud computing platform. First of all, the network environment in which cloud computing is located determines the diversity of resources available in the task scheduling process. Second, the distributed nature of cloud computing determines the larger scale of task scheduling. Finally, the diversity of cloud computing use groups determines the difference. The task scheduling must comply with different constraints.

In the process of task scheduling, cloud computing needs to consider various requirements put forward by users, such as how to reduce costs, improve resource utilization, and improve work efficiency. At present, the optimization goals that are more considered in the process of cloud computing task scheduling are as follows:

(1) *Time*: when taking time as the optimization goal. The time here can be considered from many aspects, such as the completion time of the task. Average completion time: both users and cloud computing service providers hope to complete their work in a relatively small amount of time or to complete more work in the same time, so time is an important optimization goal in the task scheduling process.

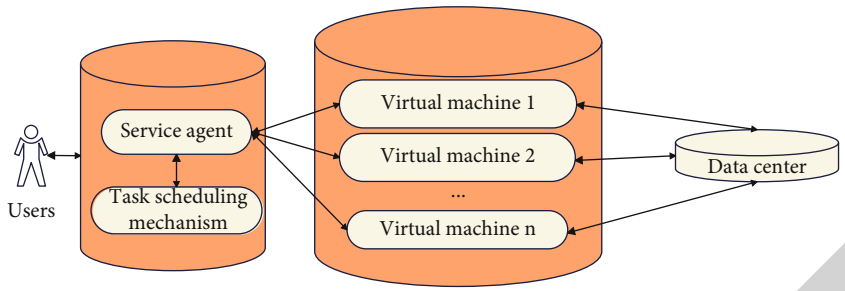

Figure 1: Flow chart of user acquisition service in cloud computing.

(2) *Resource utilization*: resource utilization refers to the rational allocation of physical resources in the process of task scheduling to maximize the use of virtual machines in the system. The improvement of resource utilization is also a way to improve work efficiency, so resource utilization is a very important optimization goal in the task scheduling process.

(3) *Cost*: cost refers to the amount of expenditure required for the user to submit the job task for processing on the virtual machine. The cost issue is the common concern of users and suppliers, so the cost issue is worth studying.

(4) *System load*: system load rationalization can ensure that the system virtual machines are allocated reasonably, that is, to ensure the task completion progress, but also to improve the work efficiency of the virtual machines, which depends on the pros and cons of the scheduling algorithm used by the system. Therefore, the system load is one of the optimization goals, and its status is self-evident.

The chaotic cat group algorithm used in the scheduling model of the chaotic cat group algorithm proposed in this paper is an improvement based on the cat group algorithm. Among them, at the beginning of the implementation of the chaotic cat group algorithm, the cat group needs to be initialized. According to the grouping rate MR (mixture ratio), the cat group is divided into the search mode and the tracking mode. The search mode can be regarded as a local optimization, and the tracking mode can be regarded as a global optimization. After two optimization processes, the optimal solution is finally obtained. Cats will have different activity states in the two modes. In the search mode, the speed and position of the cat are updated through a series of operations according to the mode state of the cat at this time. According to the fitness function developed in this paper, the fitness value of the cat at the current position is calculated, and the optimal value is retained. In the tracking mode, update the speed component and position component of the cat and check whether the value exceeds the set maximum and minimum range. For those within the range, no processing is performed, the individual values outside the range are set to the corresponding boundary values through mapping transformation, and the individual fitness value after the position change is calculated. More detailed operation steps of the two modes will be given below. The algorithm compares the cat population fitness values in the two modes and selects the largest fitness value in the population and keeps it as the optimal solution for this iteration. After that, the algorithm compares the experimental results according to the end conditions set in the algorithm in advance. If the requirements are met, the program will end, and if the requirements are not met, we continue to the next step. In the next step, the cat in the search mode and the cat in the tracking mode will exchange information, and the cat's position information will be chaotically mapped. The chaotic mapping is mainly to improve the diversity of the population and avoid the algorithm "premature." The population after chaos mapping has returned to the mode division, and the next generation of population optimization will be started from then on. The specific solution steps of the cat group algorithm are simplified to the following steps:

(1) The algorithm initializes the cat group, that is, initializes the position t and velocity component of the cat group, the population size is N, the maximum number of iterations Kmax, the grouping rate (mixture ratio MR), and so on. The range of activities of the cat group is $[a\ b]$. The size of the grouping rate MR determines the number of cats in the tracking mode. According to the actual situation, most cats are in a lazy state, most cats are in search mode, and a few are in tracking mode, so the value of MR is generally set to be small

(2) The algorithm calculates the fitness value of all cats in the population and records the maximum fitness value

(3) The algorithm randomly groups the cat group according to the MR grouping rate: it is judged whether the cat is in the tracking mode or the searching mode in the next step

(4) Tracking mode

(5) Search mode

(6) The algorithm calculates the fitness values of the individuals in the two modes and selects the individual with the largest current optimal fitness

(7) The algorithm judges whether the termination condition is met at the moment. If it is satisfied, the algorithm outputs the optimal solution and ends the procedure: otherwise, use the chaotic map to update the position of the cat and repeat the processes (3)-(6) for optimization and iterative processing. The general algorithm has two termination conditions: the number of iterations reaches the upper limit and the optimal solution meets the requirements. This article uses the maximum number of iterations to be executed

The flowchart of the chaotic cat swarm algorithm is shown in Figure 2 [21].

The cloud computing task scheduling process can be divided into two levels of task scheduling: the first level is to complete the scheduling between the user and the virtual machine and the second level is to complete the scheduling between the host and the virtual machine. In the task scheduling process of cloud computing, the task division between users and virtual machines needs to be considered, and the scheduling between hosts and virtual machines needs to consider the mapping relationship between them. The task scheduling studied in this paper belongs to the first-level scheduling. In this task scheduling process, the large task submitted by the user is divided into n smaller subtasks. Then, using task scheduling strategies and following the principles of load balancing, optimal span, QoS, etc., these subtasks are reasonably allocated to the corresponding m computing resource nodes for execution ($n > m$). The scheduling model is shown in Figure 3.

As shown in Figure 3, the task scheduling process involves users, tasks, schedulers, and virtual machines. The user submits the task, and the system divides the large-scale task into multiple subtasks and distributes the tasks to the designated virtual machines for execution according to the scheduling strategy in the scheduler. The scheduling mechanism mentioned here refers to different scheduling algorithms proposed by users according to their own needs.

3.1. Task Execution Time Function. From the task scheduling model established above, in the task scheduling process, n tasks submitted by users are allocated to m virtual machines, and the number of tasks n is much larger than the number of virtual machines m. The virtual machine list is defined as $\text{VMlist} = \{\text{VM1}, \text{vW2}, \text{VM3}, \text{V}M4, \cdots, \text{vwm}\}$, where m is the number of virtual machines. The list of all submitted task length sets is defined as $\text{TaskLengthlist} - \{\text{TaskLength1}, \text{TaskLength2}, \text{TaskLength3}, \text{TaskLength4}, \cdots \text{TaskLengthn}\}$, where TaskLength is the length corresponding to each task. The execution time of a task submitted by the user on the virtual machine is set to Exetime, and the formula is as follows:

$$\text{Exetime} = \frac{\text{TaskLength}}{\text{VMdeal}}, \tag{1}$$

Among them, VMdeal is the computing power of each virtual machine, and its calculation formula is shown in the following formula:

$$\text{dealE}_j = \text{proNum}_j * \text{MIPs}_j + \text{BW}_j. \tag{2}$$

Among them, proNum$j$ represents the number of CPUs of each virtual machine, MIPsj represents the instructions processed by the CPU per second, and BW is the virtual machine network bandwidth. In the actual task scheduling process, due to the randomness of task allocation, each task may be allocated to more than one virtual machine. Therefore, in the calculation of the virtual machine time, it is not possible to simply add up. Now, we give the total time_{ij} when all tasks are executed on the virtual machine, and the formula is shown as follows:

$$\text{Totaltime}_{ij} = \sum_{j=1}^{n} \left(\text{avg} \left(\sum_{i=1}^{m} \text{Exetime}_i \right) \right). \tag{3}$$

It means that the running time of a task on multiple virtual machines is averaged first, and then, the execution time of all tasks is summed.

3.2. Load Balancing Function. The load of a virtual machine is defined as follows: in a task allocation scheme X, the load rTime_j of a virtual machine is the task execution time allocated to all tasks on the j-th virtual machine. The formula is shown as follows:

$$\text{rTime}_j = \frac{\text{VMload}_j}{\text{deal}E_j}. \tag{4}$$

Among them, VMload is the sum of all task instruction lengths on the virtual machine, and its formula is shown as follows:

$$\text{VMload}_j = \sum_{j=1}^{n} \text{TaskLength}_j. \tag{5}$$

Therefore, the load value of all virtual machines is as follows:

$$\text{VMsload} = \sum_{j=1}^{m} \text{VMload}_j. \tag{6}$$

According to the computing power dealE_j of each virtual machine mentioned above, the maximum computing power of the system is shown as follows:

$$\text{dealE}_{\text{sum}} = \sum_{j=1}^{m} \text{dealE}_j. \tag{7}$$

The average calculation time of all virtual machines in the system is defined as $\text{rTime}_{\text{avg}}$, and its formula is shown as follows:

$$\text{rTime}_{\text{arg}} = \frac{\text{VMsload}}{\text{dealE}_{\text{sum}}}. \tag{8}$$

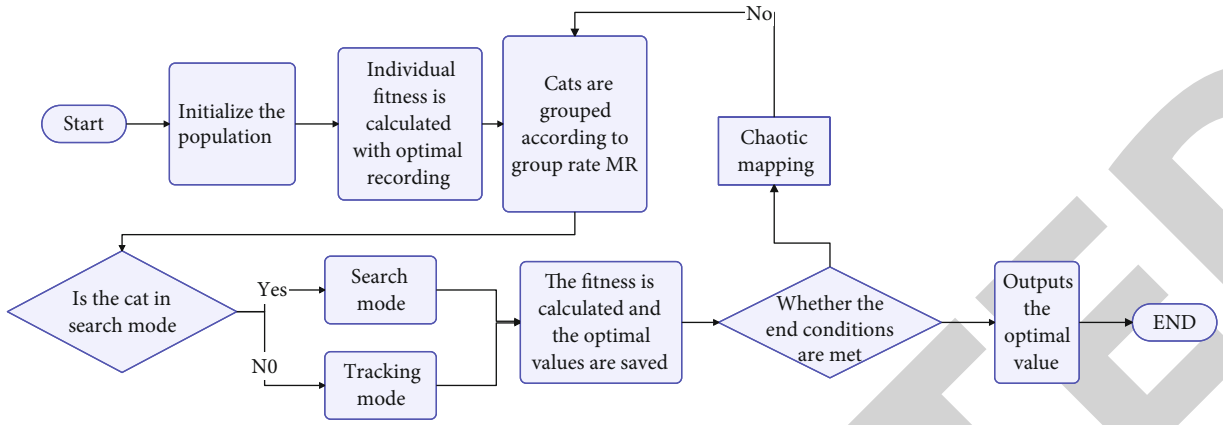

Figure 2: Algorithm flow chart.

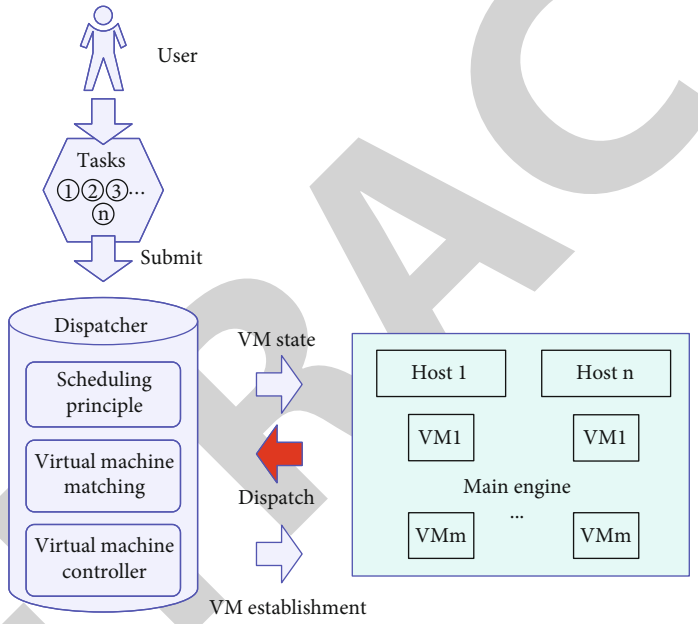

Figure 3: Scheduling model diagram.

First, the system load balance degree is given, and its function is shown as follows:

$$\text{Loadsys} = \sqrt{\frac{1}{m}\sum_{j=1}^{m}\left(\text{rTime}_j - \text{rTime}_{\text{arg}}\right)}. \quad (9)$$

Loadsys is not only the standard deviation of the system load; it also represents the load balance of the system. In order to make the system more balanced, Loadsys should be made as small as possible.

In the process of multiobjective task scheduling in this paper, two objectives are selected as the optimization objects, and the objective function is formulated according to the optimization objectives to achieve the optimization effect. The designed objective function is mainly used to calculate the size of the individual's fitness value. The size of the fitness value is also called the individual's fitness value. Generally, the fitness value is nonnegative, and the size of the fitness value reflects the individual's fitness. The greater the fitness value, the greater the individual fitness. Based on the principle of survival of the fittest in the iterative process of populations, people prefer to choose individuals with greater fitness to retain, so the final design of the fitness function also shows that the fitness value is proportional to individual superiority. However, for the design of the objective function, because the objectives to be optimized are diverse, and the degree to be achieved is also different, the positive and negative results are not required. For example, in order to obtain a smaller value, the objective function is to be smaller, and then, the fitness value of the individual will be larger.

In this paper, the chaotic cat swarm algorithm is used to optimize the multiobjective function, and the function selects execution time and load balance as the optimization objective. When the population is iteratively selected, fitness

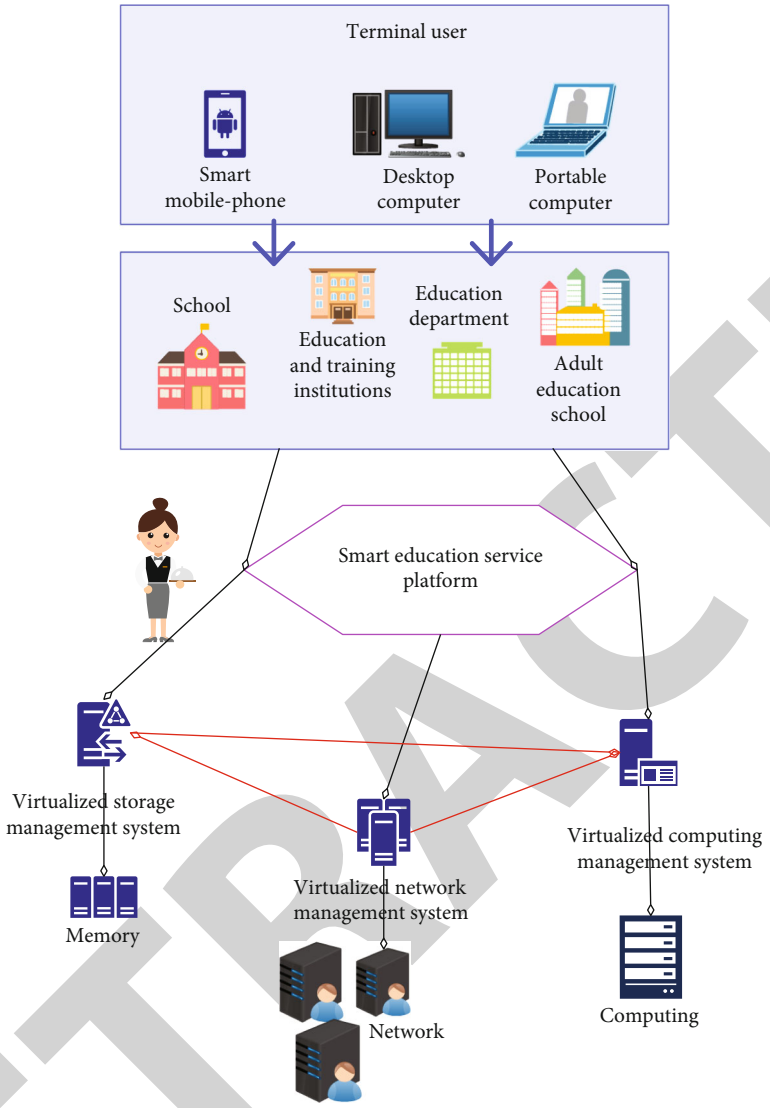

Figure 4: Smart education cloud service computing model diagram.

is used as the selection condition. Individuals with greater fitness are better, and the fitness function is set according to user needs. According to the fitness principle, it is set as the position of the i-th cat after t iterations, and then, the fitness function is designed to calculate its value. The fitness function is shown as follows:

$$F_1\left(x_1'\right) = \frac{1}{\log_2 \text{Excetime}\left(x_1'\right)}, \tag{10}$$

$$F_2\left(x_1'\right) = \frac{1}{\log_2 \text{VMload}\left(x_1'\right)}. \tag{11}$$

Among them, formula (10) is the fitness function of the execution time of the individuals in the population, and formula (11) is the fitness function of the load calculation of the individuals in the population.

In order to integrate the two functions with large differences, the value of each function takes the logarithm and then takes the reciprocal and finally adds up to obtain the objective function as shown in (12).

In the iterative process of the chaotic cat group, the cat group is divided into two working modes according to the grouping rate MR. The tracking mode is analyzed here. In the chaotic cat group tracking mode, the change of the position information of the cat group is relatively simpler than the change in the search mode, but its search range becomes larger as a result, so this mode corresponds to the global optimization process of the algorithm. Due to the large search range, when updating the cat group information, it is necessary to consider whether the updated cat group has run out of the prescribed range of activities. Once the range is exceeded, the information of the exceeding part needs to be changed, and the way to change is to map the position of the exceeding part. The specific steps of the tracking mode are as follows:

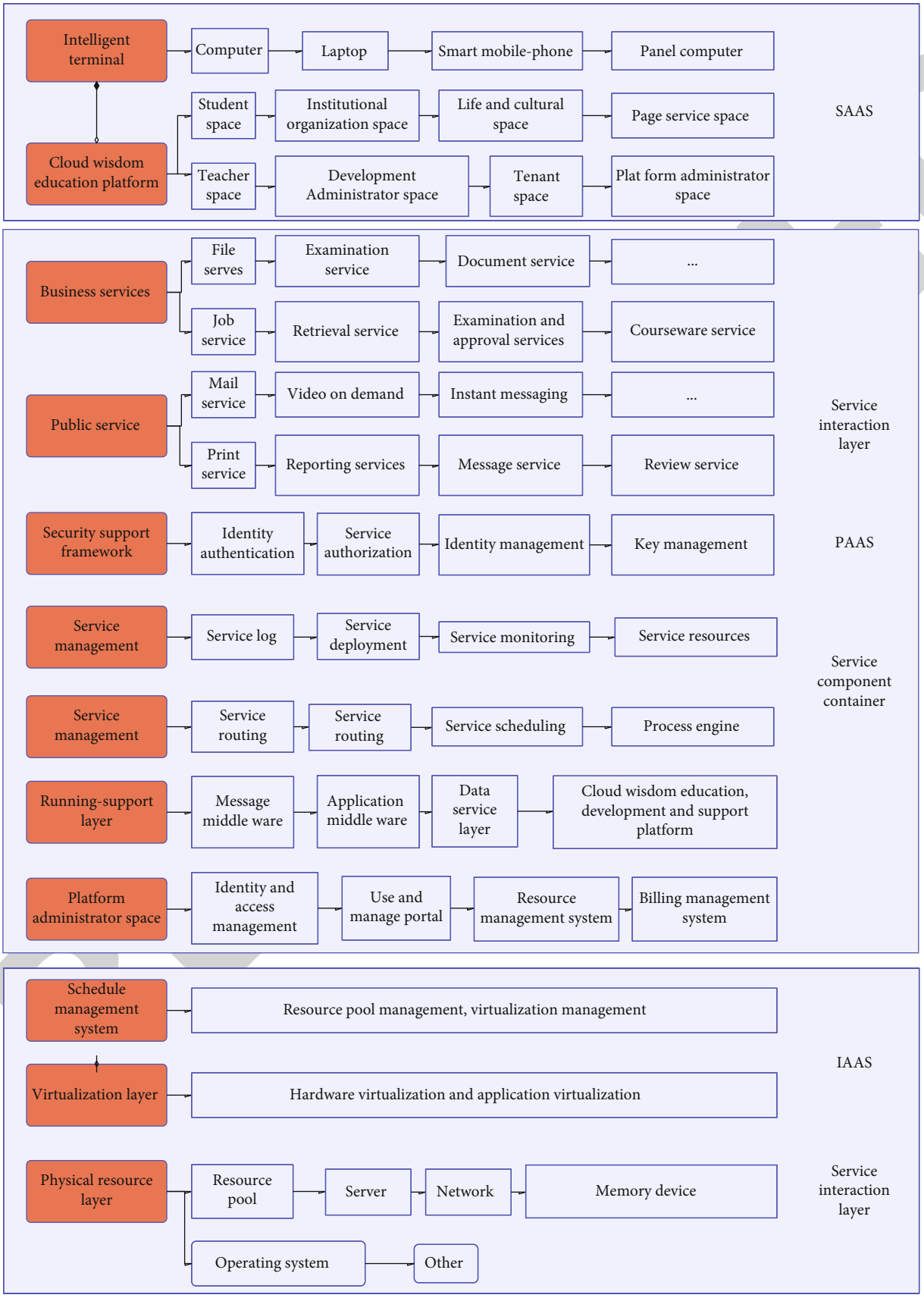

Figure 5: Smart education cloud service system structure diagram.

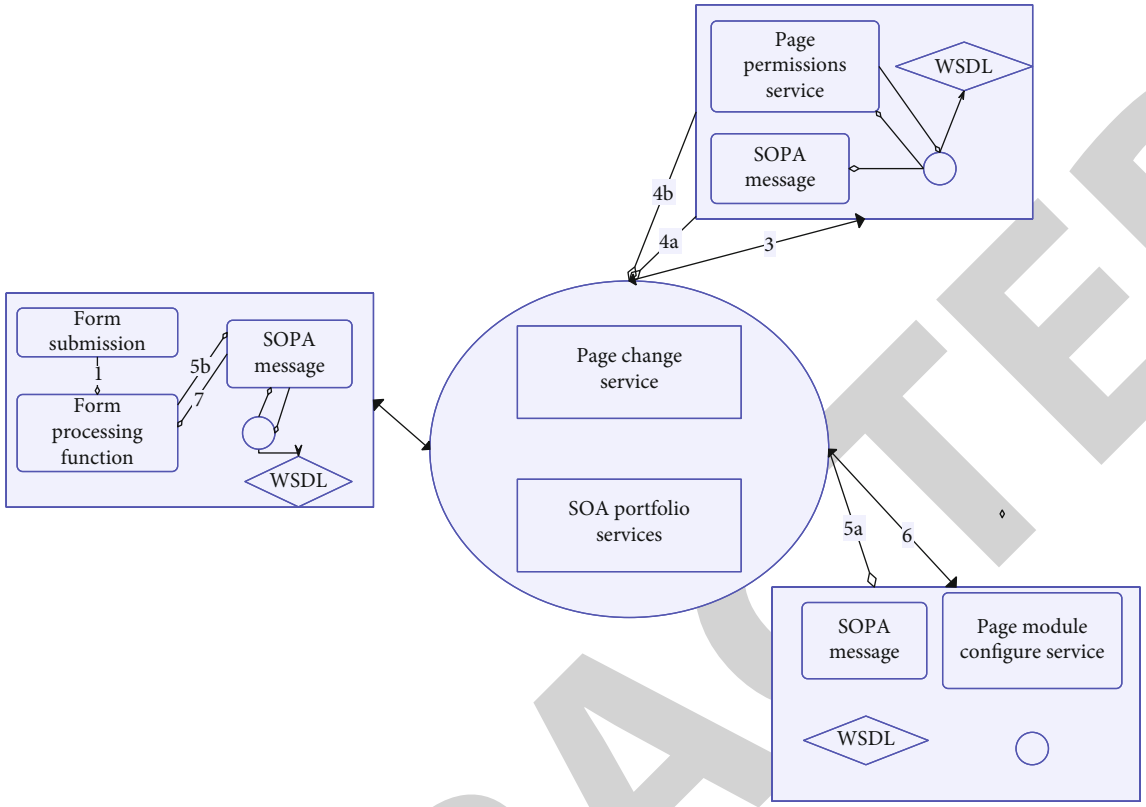

Figure 6: Work flow chart of page service.

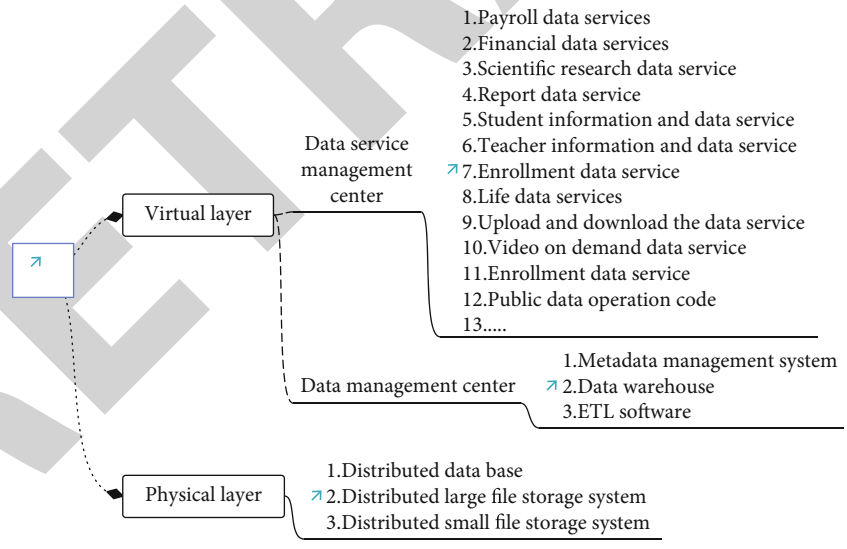

Figure 7: Data resource structure diagram.

(1) The algorithm uses formulas (12) and (13) to update the speed variable of each cat and compare it with the set speed boundary value. If it exceeds the range, it will be set to its neighboring boundary value

$$V_{k,d,t+1} = V_{k,d,t} + r1 \times c1 \times (X_{\text{best},d,t} + X_{k,d,t}), \quad d = 1, 2, \cdots, M, \quad (12)$$

$$V_{k,d,k+1} = \begin{cases} V_{\max,d,t}, V_{k,d,t} > V_{\max,d,t}, \\ V_{\min,d,t}, V_{k,d,t} > V_{\min,d,t}. \end{cases} \quad (13)$$

(2) The algorithm uses formulas (14) and (15) to update the position variable of each cat and compare it with

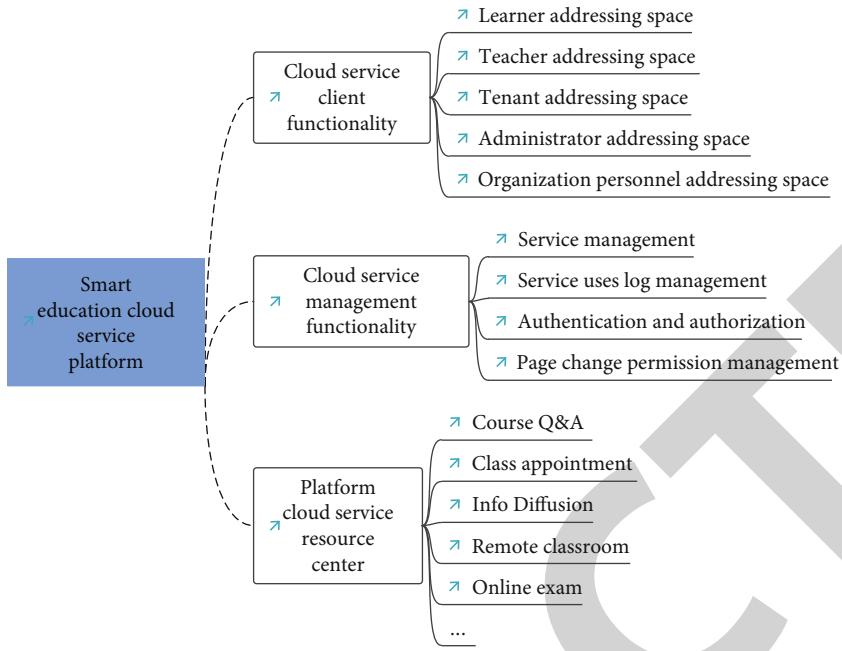

Figure 8: Data resource structure diagram.

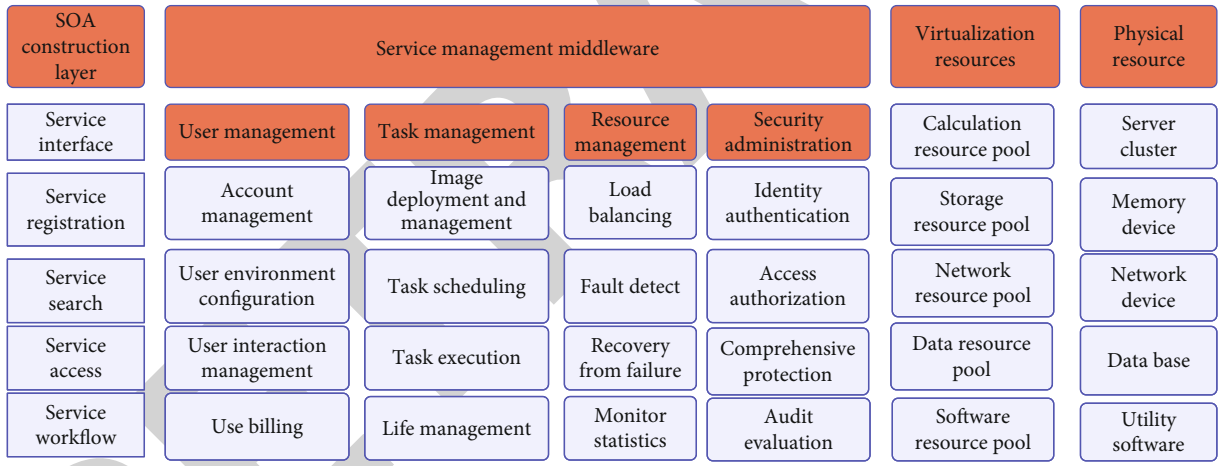

Figure 9: SOA-based cloud service architecture.

the set position boundary value. If it exceeds the range, it will be set to its neighboring boundary value

$$X_{k,d,t+1} = X_{k,d,t-1} + V_{k,d,t}, \tag{14}$$

$$X_{k,d,k+1} = \begin{cases} X_{\max,d,t}, X_{k,d,t} > X_{\max,d,t}, \\ X_{\min,d,t}, X_{k,d,t} > X_{\min,d,t}. \end{cases} \tag{15}$$

Among them, $x_{\text{best},d,i}$ is the optimal value of the fitness function of the k-th cat, $r1$ is a constant, and $c1$ is a variable, usually in the range of [0,1].

The chaos-improved cat swarm algorithm is mainly used to improve global optimization. First, we used seven different chaotic maps to improve the model steps of the algorithm. Through research and analysis, we concluded that logistic and sinograms are considered to be the best. Finally, we compare the algorithm before and after the improvement through experiments to prove the superiority of the improved algorithm. Therefore, the mapping used in this paper is a logistic chaotic mapping.

The addition of the logistic chaotic map enables the entire population to achieve a balance between global search ability and local search ability and has a good advantage in resource allocation task scheduling. The logistic chaotic map is used in the chaotic cat swarm algorithm, and its expression is shown as follows:

$$x(n+1) = u \times x(n) \times (1 - x(n)). \tag{16}$$

Among them, n is the number of iterations, u is the chaos parameter, $u \in [0, 4]$, $x \in [0, 1]$. In the classic logistic

Table 1: Evaluation of cloud task scheduling effect.

No.	Task scheduling
1	84.7
2	92.1
3	86.4
4	90.0
5	92.6
6	88.6
7	93.0
8	89.7
9	91.1
10	89.7
11	94.0
12	93.7
13	93.3
14	90.7
15	89.9
16	90.0
17	86.4
18	86.5
19	89.5
20	91.5
21	86.6
22	85.9
23	92.8
24	86.7
25	88.3
26	85.9
27	91.1
28	85.8
29	92.2
30	92.6
31	92.9
32	86.6
33	92.2
34	93.6

mapping, u is a variable. It can be seen from equation (16) that u affects the state of the logistic mapping. The value of u is also affected by xn. When u increases, the value range of xn also increases, and the distribution is more uniform. When the value of u increases to 4, the logistic mapping also tends to be surjective, and the xn sequence distribution is the most uniform at this time. This is further confirmed by calculations. After calculation, it is found that when $u = 4$, $x \in [0.1]$, and $x \notin \{0.25, 0.50, 0.75\}$, the chaotic state of the system is safe. The conventional variable is $Cx(n)$. After that, we use formulas (17) and (18) to map and transform chaotic variables. The formula is as follows:

$$x(n) = \frac{[Cx(n) - a]}{(b - a)}, \quad n = 1, 2, \cdots, N, \tag{17}$$

Table 2: Evaluation of the processing effect of cloud computing education resources.

No.	Resource handling
1	92.6
2	83.6
3	83.9
4	92.6
5	82.1
6	82.0
7	85.8
8	86.1
9	86.0
10	91.5
11	84.1
12	92.7
13	91.6
14	94.6
15	88.5
16	91.5
17	94.6
18	81.4
19	87.3
20	93.2
21	93.0
22	91.3
23	84.4
24	85.4
25	93.0
26	85.5
27	94.2
28	85.5
29	93.1
30	89.7
31	93.5
32	93.7
33	82.7
34	92.0

$$Cx(n) = a + x(n) \times (b - a), \quad n = 1, 2, \cdots, N. \tag{18}$$

Among them, a and b are the range of activity of the cat group, and $Cx(n)$ is the position of the cat group.

4. Construction of Smart Education System in Colleges and Universities Based on Cloud Computing Task Scheduling Algorithm

A low-cost, multitenant-oriented, and scalable digital education cloud service architecture needs to be established. The layers of the architecture are interrelated and independent of each other, and the upper layer has implementation dependence characteristics on the lower layer, but the result

Table 3: Evaluation of system education effect.

No.	Teaching effect
1	90.7
2	86.6
3	85.3
4	84.2
5	80.2
6	90.4
7	82.5
8	87.1
9	81.8
10	81.3
11	82.8
12	90.3
13	84.0
14	82.4
15	91.5
16	80.1
17	83.7
18	89.8
19	84.7
20	90.2
21	81.6
22	82.0
23	83.8
24	87.5
25	84.7
26	90.7
27	82.0
28	84.4
29	83.3
30	85.0
31	85.7
32	83.6
33	89.6
34	83.7

of the lower layer needs to be delivered to the user by the upper layer, as shown in Figure 4.

From the division of the cloud computing service level and scope, the architecture of the high-performance smart education cloud service platform is divided into three layers. It consists of an education cloud infrastructure layer, an education cloud service platform layer, and an education software and system application layer as shown in Figure 5.

Education cloud service users find the option to change the service in the page service. The page change service here is the change of the public service on the specific page. For example, ordinary students want to add a comment module under the remote course. The specific page service workflow is shown in Figure 6.

The data center of the smart education cloud service platform solves the problems of low utilization rate of high-quality education resources and low data processing efficiency by building data services. By building a cloud storage environment, the problem of scattered, unshared, and low storage capacity of educational resources is solved. The data center includes a physical layer and a virtual layer, and its data resource structure diagram is shown in Figure 7.

Figure 8 shows the overall service level structure of the smart education cloud service platform.

From the perspective of system layering, the SOA-based cloud service architecture can be divided into the physical resource layer, virtualized resource pool layer, service middleware layer, and SOA building layer. Its architecture model is shown in Figure 9.

This paper calculates the performance of the smart education system of colleges and universities based on the cloud-side collaborative computing task scheduling algorithm proposed in this paper and separately counts cloud task scheduling, education resource processing, and education system effect evaluation. The results are shown in Tables 1–3.

From the artistic research, we can see that the smart education system of colleges and universities based on the cloud-side collaborative computing task scheduling algorithm constructed in this paper is very good in all aspects and has a greater advantage in processing educational resources.

5. Conclusion

Using the distributed storage technology of cloud storage, educational resources are divided into multiple blocks and stored on nodes in the cloud, and cloud storage technology is used to improve backup management and capacity management, which greatly guarantees the security of educational data. Therefore, according to the many bottlenecks faced by the current education system, cloud storage technology is used to establish a smart education cloud storage system, and cloud computing technology is used to centralize and virtualize the management of various types of hardware infrastructure equipment for education. Moreover, through the efficient storage and high sharing of various educational resources and data, it breaks the isolated educational system construction model; guarantees the security, flexibility, stability, and reliability of educational data resources; and avoids multilevel repetitive construction. This paper combines the cloud-side collaborative computing task scheduling algorithm to construct a smart education system in colleges and universities, analyzes the process of smart education in colleges and universities, and further enhances the effect of smart education on this basis. The smart education system of colleges and universities based on cloud-side collaborative computing task scheduling algorithm constructed in this paper is very good in all aspects and has a greater advantage in processing educational resources.

Data Availability

The labeled dataset used to support the findings of this study are available from the corresponding author upon request.

Hindawi
Journal of Sensors
Volume 2023, Article ID 9804212, 1 page
https://doi.org/10.1155/2023/9804212

Retraction

Retracted: Study on Environmental Art Design Based on Ecology Concept

Journal of Sensors

Received 17 October 2023; Accepted 17 October 2023; Published 18 October 2023

This article has been retracted by Hindawi following an investigation undertaken by the publisher [1]. This investigation has uncovered evidence of one or more of the following indicators of systematic manipulation of the publication process:

(1) Discrepancies in scope
(2) Discrepancies in the description of the research reported
(3) Discrepancies between the availability of data and the research described
(4) Inappropriate citations
(5) Incoherent, meaningless and/or irrelevant content included in the article
(6) Peer-review manipulation

The presence of these indicators undermines our confidence in the integrity of the article's content and we cannot, therefore, vouch for its reliability. Please note that this notice is intended solely to alert readers that the content of this article is unreliable. We have not investigated whether authors were aware of or involved in the systematic manipulation of the publication process.

Wiley and Hindawi regrets that the usual quality checks did not identify these issues before publication and have since put additional measures in place to safeguard research integrity.

We wish to credit our own Research Integrity and Research Publishing teams and anonymous and named external researchers and research integrity experts for contributing to this investigation.

The corresponding author, as the representative of all authors, has been given the opportunity to register their agreement or disagreement to this retraction. We have kept a record of any response received.

References

[1] Z. Jiang and F. Wang, "Study on Environmental Art Design Based on Ecology Concept," *Journal of Sensors*, vol. 2022, Article ID 8034930, 8 pages, 2022.

Hindawi
Journal of Sensors
Volume 2022, Article ID 8034930, 8 pages
https://doi.org/10.1155/2022/8034930

Research Article

Study on Environmental Art Design Based on Ecology Concept

ZiWen Jiang and Feng Wang

School of Design, Jiangnan University, Jiangsu, Wuxi 214122, China

Correspondence should be addressed to ZiWen Jiang; 6211507005@stu.jiangnan.edu.cn

Received 29 November 2021; Revised 23 December 2021; Accepted 17 January 2022; Published 8 February 2022

Academic Editor: Wei Zhang

Ecological design concept is a design concept aimed at advocating green environmental protection and sustainable development, which is widely used in different cases of environmental design including urban and kindergarten. In our study, using literature research, case reference, and field research as research methods, through the theoretical research of domestic and foreign kindergarten environment design and interpretation of typical cases to summarize the ecological design method and design strategy, can be further applied in larger field such as urban, basin, and/or region. Then, take "Chenguang" kindergarten in Beijing as example to analyze ecological element in there. Aiming at ecological landscape, ecological humanities, and ecological experience as the goal, the kindergarten's architectural appearance and indoor and outdoor environment have been transformed and redesigned. Ecological principle and ecological strategy from our study present an important reference meaning in improving the quality of urban space environment and shaping a good city image which are of great significance.

1. Introduction

Urban environmental art design plays an important role in improving the quality of urban space environment and shaping a good city image which are of great significance. Urbanization has brought adverse effects on the urban ecological environment [1]. In recent years, urban ecological environmental problems have become increasingly severe. Under this background, the concepts of ecological design have increasingly penetrated the hearts of designers. Its application in urban environmental art design has also become a necessity, which is conducive to alleviate the problems of urban environmental pollution and excessive consumption of resources. Only a correct understanding and sufficient attention to environmental issues and a positive measure can these problems be better solved. Integrating life into urban environmental art design has been a trend of the modern times and meets the requirements of urban sustainable development. The integration of ecological concepts in the field of environmental art design is to ensure the society to optimize environmental space resource allocation and improve the efficiency of comprehensive utilization of resources under the premise of regular operation of society and daily life in an efficient and orderly manner, so as to keep the ecological balance from being broken [2].

As a discipline that integrates the knowledge of fine arts, architecture, urban planning, etc., the connotation of environmental art design is continuously extending with the development of society. From the environmental point of view, architecture should focus on the relationship between itself and nature, through the combination of artistic aesthetics and architectural functions, providing a guaranteed for completing the environmental art work. It can be seen that the framework of environmental art design is art, the embodiment is the architecture, and the two are indispensable [3]. In essence, task carried out in city for the environmental art design is the work of enhancing the environmental art of the urban landscape, which involved humanities, history, geography, and many other factors; the purpose is to compare the development prospects of the city in a more intuitive way. Researches have shown that environmental art design follows mainly the rules of nature, on basis of above, adjusts the design plan according to the urban development situation, makes it more scientific and reasonable, and highlights the "people-oriented" concepts [4].

However, we should acknowledge that current environmental art design still has following disadvantages [5]: (1) have no consideration on ecological concept. Since the reform and opening of China, the society and economy have developed rapidly. The urban environment has also undergone tremendous changes, urban construction is in full swing, and urbanization is progressing. As a part of urban construction, urban environmental art design has received more attention in modern society. More and more cities have created a beautiful space environment for the public through environmental art design [6]. Urban environmental art design is also developing in a good direction. However, in the current urban environmental art design, ecological design is lacking, some designers lack environmental awareness, and they do not fully realize the seriousness of ecological environmental problems. Although this improves and enhances the quality of urban space environment, it has an impact on urban ecology. The environment has caused a negative impact and is not conducive to the sustainable development of the city. All in all, it is under the background of continuously serious ecological environment. Designers should pay more attention to the artistic design of ecological urban environment, improve the quality of urban space environment, and promote the sustainable and good development of the city. (2) Blindly pursuing grade. In the current urban environmental art design, some designers blindly pursue "grade." Whether in the selection of materials or in the construction of gardens and green spaces, we blindly pursue luxury and style, palace gardens, and green spaces. The urban environment seems to be "high, large, and superior," but it is not related to the current development of the city. Therefore, urban environmental art design should start with the status quo of urban development and pay attention to the suitability, popularity, and timeliness of environmental art design, so as to design and create an urban space environment that can meet the diverse needs of the public territory. (3) Serious homogeneity problem. Under the background of information environment, the ways for the public to obtain information are becoming more and more diversified; in this context, the disseminating of design methods and design concepts becomes more quick and broad. In the current urban environmental art design, landscape projects with very similar design elements and design techniques are not uncommon; some designers are innovative and possess insufficient ability, who imitate, plagiarize, copy, and paste in the design and also ignore the differences in regional culture and natural environment between cities, so as to lead to the same design homogeneity [7]. Innovation is the soul of design; designers should enhance their sense of innovation and ability to combine with the city's regional culture, innovative design of the natural environment, etc., to create a unique urban environment.

Putting ecological concept into environmental art design has a very important significance, which can build green society and make environment protection and resource saving come true. What needs to do for combining ecological concept with environmental art design is that designers should possess holistic concept, improve measures of environment protection, and promote ecological service level of building [8]. Among the many characteristics of ecological design, the most representative one is naturalness, that is, ecological design can improve the quality of the living environment created by making full and reasonable use of resources. Ecological design applied to environmental art also has unique characteristics. The specific performance is as follows: (1) artistry. Designers usually take artistry as their main pursuit. Therefore, in the process of environmental art design, designers should be guided by the concept of ecological design, combining with the conditions and characteristics of the urban environment; designers should complete the design of environmental art design work; the design works not only conform to the laws of nature, but also, performance is very outstanding. (2) Naturalness. The naturalness as the basis of ecological design has very distinctive characteristics, which can be adapted to the impact of social development in a relatively short period of time. Designers who take meticulous carving as their main pursuit often have large deviations from the ecological design concept. It can be seen that environmental art emphasizes the comfortable and harmonious beauty between humans and nature [9].

In order to integrate ecological concepts into the environmental art design process, designers should organically integrate the ecological environment with the living space of human beings [10]. To achieve the integration of ecological concepts and environmental art design, principles should be followed. (1) Art design should fully integrate public aesthetics. Environmental art is a highly personalized and unique artistic style that can highlight the space environment of a building. People should integrate aesthetic thinking and design concepts in the art field in the process of environmental art design, so that while highlighting the artistic aesthetic value of the work, make the created artwork conform to the basic principles of design aesthetics. (2) Follows objective regular. Related research shows that at the end of the 20th century, many environmental art design masters used the most primitive materials and resources in the process of designing their works, fully respected objective laws, integrated natural resources well, and maintained the sound development of the ecological environment. Many famous cities at home and abroad are built in compliance with the concept of nature. (3) Improve design and eliminate noise. In the design process, the designer must follow the following requirements. Firstly, make full use of and develop the original natural landscape; secondly, in the selection of materials, use recycled materials to reduce energy consumption; thirdly, waste materials after using should be reused rationally; finally, waste materials cannot be discarded at will, and they must be recycled. (4) Show characteristics of ecological aesthetics. With the development of social productivity and the improvement of people's living standards and cultural level, contemporary environmental art design requires a return to nature. Ecological aesthetics require a high degree of integration of social civilization, human development, and ecological environment. Therefore, in the design process of environmental art, the materials that best demonstrate the characteristics of ecological aesthetics should be used first [11].

There are a large number of examples on integration ecological concepts with environment art design [12]. They applied this technology in different fields. But two common points in their all studies can be concluded: (1) prefer recyclable natural materials. The basic principles of ecological concept can provide necessary theoretical guidance for environmental art design. In order to highlight the characteristics of ecological concepts in environmental art design works, designers need to process them through some means. The use of natural materials is a good way, and it is also the key to achieving this goal. Environmental art designers should choose corresponding natural materials according to specific environmental conditions, such as decorating the wall with shells, starfish, etc., in the ocean park, which can make the environment more suitable for the target theme and make people feel like being on the scene. (2) Pursuit of sustainable development theory. Environmental art design needs to uphold the concept of sustainable development and adhere to the concept of scientific development. In recent years, under the five-in-one ecological construction goal, ensuring an ecological and environmental protection of the building space has become a long-term trend. In other words, as a fashionable sunrise industry, the creative design industry can better tap Du Fu's culture, make it more "local," and conform to the requirements of the market of the times. However, this method of making Du Fu's culture trendy does not mean blindly catering to the market. Instead, we should develop excellent culture on the basis of respect for market needs, optimize and fashion Du Fu culture with high-quality sincere market means, and realize cultural consciousness. For example, the Q version of Du Fu dolls launched by the Three Gorges Museum at the 2012 ICIF of China is the result of innovative entertainment, cartoonization, and personalization of Du Fu culture. The "Q version" trend is closely related and is a direct manifestation of culture serving the public. Among them, the designer combined the well-known image of Du Fu with modern entertainment dolls, so that poets such as Du Fu successfully transformed into modern Q version of the little people [13].

In our study, we firstly compared some examples between China and abroad on integrating ecological concepts into kindergarten environmental art design and summarized the ecological design methods and design strategies; we summarized the indoor and outdoor design elements and main spaces, including the shape, material, and color related to the renovation of the building appearance; we discussed the environmental design of the kindergarten under the ecological design concept in view of the problems in the domestic kindergarten space environment goals and design principles. And then, we take the space environment of the "Chenguang" kindergarten in Beijing city, as the research object; through field investigation, the method of combining theory with practice was adopted. Ecological design was the guiding ideology; ecological landscape, ecological humanities, and ecological experience were the goals. The exterior of the building and the indoor and outdoor environment have been redesigned to create a kindergarten environment that mainly focused on children's perspective, emphasized natural ecological experience, considered children's physical and psychological states, and promoted children's physical and mental development and communication.

Our study is organized as follows. Study methods, contents, and research ideas are discussed in Section 2; major results and discussion are presented in Section 3. Section 4 is the main conclusion of study.

2. Study Methods, Contents, and Ideas

2.1. Research Method and Contents. In our study, three methods were used to achieve our aim: (1) Literature review. Collect domestic and foreign kindergarten environmental design examples related research literature, journals, and books, understand the topic selection research and design status, provide scientific theoretical basis for thesis writing, and analyze, typical design cases to achieve theoretical and combining practical design; (2) practical investigation. Mainly investigate the representative kindergartens in Beijing, understand their architectural appearance and outdoor activity space, find out the current problems that need to be solved, take field photos and record their current situation during the field inspection, and understand specific circumstances of the kindergartens' environment; (3) comparative analysis. The successful process and experience of domestic and foreign kindergarten construction and environmental design cases were compared and used for reference with the actual situation of Chenguang kindergarten design, and the methods and models suitable for local landscape construction were extracted. In the design, refer to the same type of kindergarten design plan and learn excellent design concepts and design ideas.

This article is mainly based on the research of ecological design concept, and using this as the guiding ideology, the "Chenguang" kindergarten environment was transformed and designed, and study on how to fully reflect the ecological concept in the kindergarten environment design, achieve adaptive design, and meet the needs of children's physical and mental development. Through the research on the characteristics, design elements and main space design of the kindergarten's indoor and outdoor environment and build appearance transformation and summarize the environmental design goals and design principles of the kindergarten under the ecological design concept. Then, based on the concept of ecological design, the "Chenguang" kindergarten in Beijing city was taken as an example to design and transform to create a kindergarten area that is conducive for the physical and mental development of children.

2.2. Study Ideas. In order to effectively study the environmental renovation design of "Chenguang" kindergarten based on the ecological design concept, this topic firstly started with the core concept of the research theme, analyzed the current research status and design cases at home and abroad and the related concepts of the kindergarten space design, considered children psychological and behavioral characteristics, and analyzed the impact of kindergarten environment design on the growth of children from the aspects of cognitive learning development, social development, and character training. We summarized the indoor

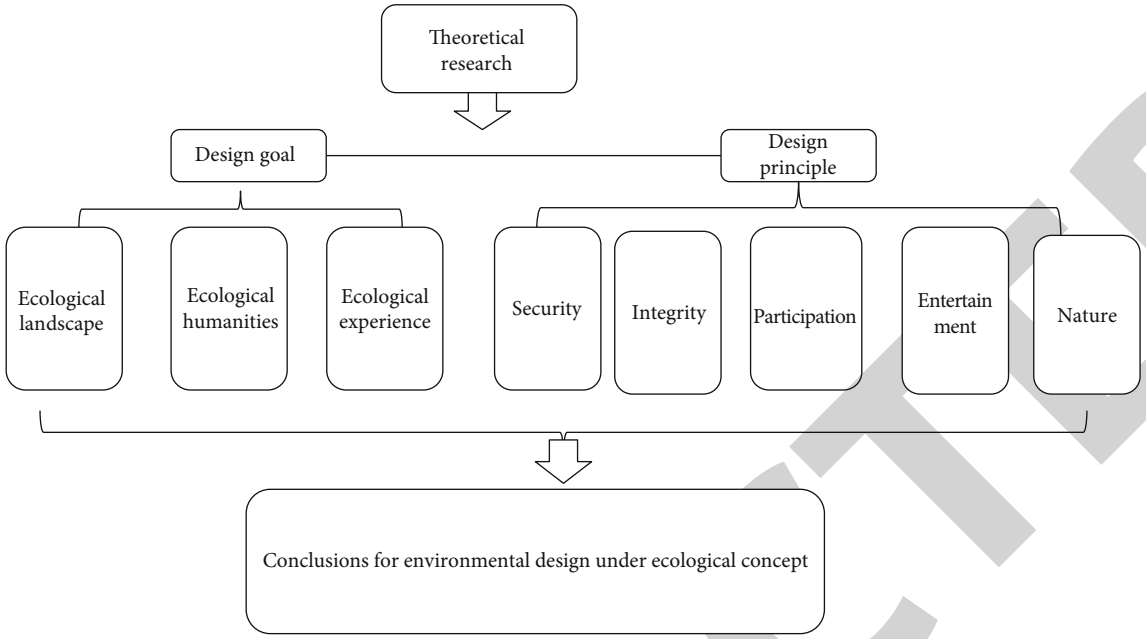

Figure 1: Workflow in our study.

and outdoor design elements of the kindergarten and the main space design functions, including the application of materials, colors, and graphics related to the renovation of the architectural appearance; then, in view of the problems in the domestic kindergarten space environment design, the kindergarten environment design goals and principle under the ecological design concept were discussed and studied on relative theory. Workflow in our study is presented in Figure 1.

3. Results and Discuss

3.1. Design Examples in China. From the perspective of design practice, there are many successful cases of domestic kindergarten environment design. For example, Beijing Siheyuan Kindergarten, Shanghai East China Normal University Bilingual Kindergarten, and the successful experience of Aibobi International Kindergarten design all reflect the importance of experience and ecology in the creation of the kindergarten environment; these successful examples provide a valuable reference for our study.

Beijing Siheyuan Kindergarten was designed by MAD Architectural Design Office led by Ma Yansong. The main body of the project is a courtyard building which was built since 1725. With the theme of "floating roof, children's world," the rational use of resources was carried out on the premise of respecting and protecting historical and cultural relics. At the same time, it is in good condition with the surrounding ecological vegetation cohesion. The overall design environment of the kindergarten expands in a horizontal posture, transforming the limited roof space into an outdoor sports and activity platform to the greatest extent. Incorporating the natural design elements of "hills" and "plains" and flowing spatial layout created a free and inclusive space atmosphere; preserve the old trees in the original site, use the microtopography design, and combine transparent floor-to-ceiling glass so that a good landscape viewing effect will be created (Figure 2).

The courtyard from Shanghai East China Normal University Bilingual Kindergarten can enhance the cohesion of the family and communicate with the world and nature in this way. The project site was located in the new community south of Anting, Shanghai, and is one of the first public buildings to be constructed. The 7,400 square meters of land needs to accommodate 15 activity classes. The designer used the three-dimensional settlement design form of stacked honeycomb classroom units to create a children's space environment with a natural urban courtyard. The design plan of the whole kindergarten complex is in the shape of "W," and the corresponding retreat space design has the largest scale of natural lighting in the three directions of east, west, and south. The honeycomb-shaped combination can better adapt to the turning of the bevel. At the same time, the corridors in the garden were arranged along the edge of the hexagon, which can effectively meet the daily traffic. Teachers and students can walk along the winding corridors, passing through the courtyard and the entrance class. The overall material is mainly wood, giving people a warm feeling. The hexagonal corridor space connects various indoor and courtyard spaces in series, so that children can get more opportunities to interact with nature through the courtyard (Figure 3).

The Aibobi International Kindergarten site is located in a residential area of Shenzhen, surrounded by a good natural environment, aiming to transform the old and outdated buildings into an ecological, environmentally friendly, comfortable, and healthy contemporary education space. The space environment design of Aibobi International Kindergarten follows the "Montessori" educational philosophy

Figure 2: Partial profile of Beijing Siheyuan Kindergarten (comes from https://www.gooood.cn).

Figure 3: Structure profile from the courtyard from Shanghai East China Normal University Bilingual Kindergarten (comes from https://www.gooood.cn).

proposed by the Italian educator Dr. Maria Montessori, which is to respect children's nature and cultivate children's conscious and active learning in the environment and the spirit of exploration. The overall design of the kindergarten used wood with clean white walls to create a harmonious and warm learning environment for children in the simplest way. The designer used concise lines as the design language to enhance children's more intuitive spatial cognition brought by the linear space. The grasp of details in the design is also particularly important. In the renovation, attention is paid to the treatment of details such as stairs, handrails, doors, windows, and safe barrier-free passages, as well as the soft rubber on the ground and the slope design. From the perspective, respect the law of children's growth and carry out adaptive design to create a teaching environment that enables children to develop in an all-round way (Figure 4).

3.2. Examples from Abroad. The education of children in foreign countries is generally based on open education, which encourages the cultivation of children's creativity and autonomy in the environment. Since the mid-20th century, modern ecological environment design concepts have gradually been applied to various spatial environments. By the end of the 20th century, people have become more aware that "the stimulation of the environment on children's sense organs is vital to children's development." Then, attention awareness of the kindergarten environment has begun to strengthen, and its typical research results include the "Model of Designing Children's Center" by Fred and the Japanese "Kindergarten Design" (Japan Co., Ltd. New Architecture, 2011), which mentioned the impact of the environment on children growth; a good kindergarten environment can make children's growth space more social; Frost's "Children's Games and Playing Environment" takes a wide range of outdoor activities for children as the research object and discusses on how to create an environment that is free, tends to nature, and is in line with children's development. It can be seen in the environmental design of foreign kindergarten areas that more emphasis is placed on nature and nature, so that children and the environment form a subtle interaction. Its environmental design and architectural design forms are also tending to diversify. Typical practical cases are Japan's Roppongatsu Kindergarten, Japan's KM Kindergarten, and Denmark's Red Kindergarten.

Roppongatsu Kindergarten is located in a residential area in Fukuoka City, Japan. It can accommodate 90 children from 0 to 6 years old. The goal is to create a kindergarten that allows children to develop freely physically and mentally. The façade of the building is arranged in a sparse and uniform combination of "color tree branches." The simple white exterior wall and large area of transparent glass make it clear and stand out in the architectural environment of the entire district. The large area of floor-to-ceiling glass gives people a comfortable sense of openness and keeps a distance from the outside world, allowing children to enjoy plenty of sunlight during classroom activities and at the same time strengthen the design of child safety protection (Figure 5).

Japan's KM Kindergarten is located in Osaka, Japan. The original building is a ruined kindergarten. The owner asked the designer to redesign and remodel to solve basic problems

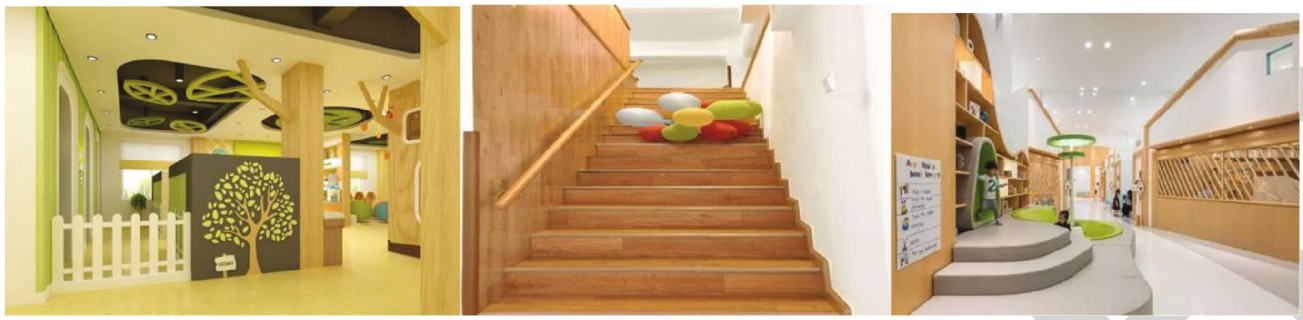

Figure 4: Structure profile from the Aibobi International Kindergarten (comes from https://www.gooood.cn).

Figure 5: Structure design for Roppongatsu Kindergarten of Japan (comes from https://www.gooood.cn).

Figure 6: Structure design outlook for Japan's KM Kindergarten (comes from https://www.gooood.cn).

such as children's daily activities. The kindergarten creates a fluid space environment that indirectly guides children to outdoor sports. Part of the building is integrated with the playground full of ecological greenery through a ramp, which satisfies the normal traffic function while allowing children to get close to nature. Many spaces in the park are also designed with humanity, such as the cafeteria can be fully opened towards the playground, to form a seamless connection between the playground and the canteen, so that the architectural space and the natural ecology are integrated (Figure 6).

Denmark's Red Kindergarten site is located in Copenhagen, Denmark. This kindergarten has a prominent curved wall and an ecological green roof garden. It used local thin brick materials to decorate the facade of the building in the form of a grille. At the same time, the color name is lined to maintain the characteristics of the kindergarten building. The designer hopes to create a world-class day care center for children through this project and create the best learning and growth environment for children. The grid form of the transparent building satisfies the natural lighting and ventilation; an open children's outdoor space is also set up in the atrium area to satisfy children's curiosity for outdoor space and provide children with a free and happy growth atmosphere and a good learning environment (Figure 7).

3.3. Renovation Based on Ecological Concepts for "Chenguang" Kindergarten. The renovation design of Chenguang Kindergarten mainly renovated the environment from the perspective of "ecological landscape, ecological humanities, and ecological experience," clarified functional divisions and improved the environment, and built a healthy and ecological park environment on the premise of satisfying its functions.

The spatial layout of the outdoor landscape is not just a simple stacking of constituent elements, but a reasonable configuration and organic unity among various elements, focusing on coordinating the harmonious factors between people and the environment and creating a good spatial effect. In the process of outdoor environment design, rational landscape design was carried out with natural ecological elements, highlighting the natural ecological attributes of the kindergarten and meeting the needs of children's own development.

Figure 7: Structure design profile of Denmark's Red Kindergarten (comes from https://www.gooood.cn).

The overall indoor space layout was divided into a first-floor space layout and a second-floor space layout, which were connected to each other to meet the needs of different functions.

At present, Chenguang Kindergarten has problems such as imperfect facilities and lack of features. The architectural image is dull and characteristic, and the outdoor environment function is not clear. The artificial lawn and large area of hard paving cannot meet the needs of the kindergarten's ecological environment design. The building appearance needs to be changed. Coordinating with the outdoor environment space, combine the theme to optimize the transformation and redesign.

In the process of designing the environment of the kindergarten area, it is necessary to fully consider the activity characteristics of children, try to ensure that there is a flat site, use steps or coexist with gentle slopes for places with height differences, and smoothly and excessively carry out barrier-free design.

Our results show that core of building ecological kindergarten is combing design elements with regional culture, for example, humanities, environment, culture, and health. These are applicable not only for our study object-kindergarten but also are a helpful reference for urban environmental design. We can conclude from our study that urban environmental art design should follow the following: (1) focus on highlighting cultural characteristics, (2) reasonable planning of land resources, (3) cultivate professional talents of modern urban environmental art design, (4) adhere to the human-oriented design concept, (5) build a multilevel urban environmental system, and (6) scientific management of urban construction and environmental art design. Only do this can we create more innovative urban outlook.

4. Conclusions

Based on the perspective of ecological concepts, this article has carried out research and practice on the kindergarten environment design. On the basis of our result, design principle and methods can be used for urban environmental art design. First, we summarized the current situation of domestic and foreign kindergarten environmental design; second, the problems and shortcomings of domestic kindergartens were presented. Finally, we combined theory with practice, taking Beijing "Chenguang" kindergarten space environment transformation as the design object; according to the status quo and problems, the kindergarten environment design goals and strategies were proposed. In the design process, with the goal of "ecological landscape, ecological humanities, and ecological experience," we strive to create learning with children an ecologically comfortable kindergarten area that is integrated with the growth environment. At the same time, through the practical application of ecological design concepts, people will be inspired to pay attention to and experience the ecology and natural environment and create a beautiful and happy life.

Data Availability

The experimental data used to support the findings of this study are available from the corresponding author upon request.

Conflicts of Interest

The authors declare that they have no conflicts of interest to report regarding the present study.

References

[1] Y. Zhibing and G. Chen, "Research project of small town environmental art design based on feature orientation," *International Core Journal of Engineering*, vol. 6, no. 12, 2020.

[2] G. M. Marchetti and F. Scapini, "Use of multiple regression models in the study of sandhopper orientation under natural conditions," *Estuarine, Coastal and Shelf Science*, vol. 58, pp. 207–215, 2003.

[3] Y. Fang, Q. Que, R. Tu, Y. Liu, and W. Gao, "How do landscape elements affect public health in subtropical high-density city: the pathway through the neighborhood physical environmental factors," *Building and Environment*, vol. 206, 2021.

[4] J. Wu, Y. Wu, W. Yu, J. Lin, and Q. He, "Residential landscapes in suburban China from the perspective of growth coalitions: evidence from Beijing," *Journal of Cleaner Production*, vol. 223, pp. 620–630, 2019.

[5] W. Zhifeng and Y. Ren, "The influence of greenspace characteristics and building configuration on depression in the elderly," *Building and Environment*, vol. 188, 2021.

[6] A. Jia and C. Xu, "Smart city image landscape design based on wireless sensors," *Microprocessors and Microsystems*, vol. 83, 2021.

Hindawi
Journal of Sensors
Volume 2023, Article ID 9806065, 1 page
https://doi.org/10.1155/2023/9806065

Retraction

Retracted: Research on the Immersive Classroom Teaching Mode of Colleges and Universities Based on Virtual Reality

Journal of Sensors

Received 19 December 2023; Accepted 19 December 2023; Published 20 December 2023

This article has been retracted by Hindawi following an investigation undertaken by the publisher [1]. This investigation has uncovered evidence of one or more of the following indicators of systematic manipulation of the publication process:

(1) Discrepancies in scope
(2) Discrepancies in the description of the research reported
(3) Discrepancies between the availability of data and the research described
(4) Inappropriate citations
(5) Incoherent, meaningless and/or irrelevant content included in the article
(6) Manipulated or compromised peer review

The presence of these indicators undermines our confidence in the integrity of the article's content and we cannot, therefore, vouch for its reliability. Please note that this notice is intended solely to alert readers that the content of this article is unreliable. We have not investigated whether authors were aware of or involved in the systematic manipulation of the publication process.

Wiley and Hindawi regrets that the usual quality checks did not identify these issues before publication and have since put additional measures in place to safeguard research integrity.

We wish to credit our own Research Integrity and Research Publishing teams and anonymous and named external researchers and research integrity experts for contributing to this investigation.

The corresponding author, as the representative of all authors, has been given the opportunity to register their agreement or disagreement to this retraction. We have kept a record of any response received.

References

[1] C. Hu and J. Li, "Research on the Immersive Classroom Teaching Mode of Colleges and Universities Based on Virtual Reality," *Journal of Sensors*, vol. 2022, Article ID 3585149, 10 pages, 2022.

Hindawi
Journal of Sensors
Volume 2022, Article ID 3585149, 10 pages
https://doi.org/10.1155/2022/3585149

Research Article

Research on the Immersive Classroom Teaching Mode of Colleges and Universities Based on Virtual Reality

Chuili Hu and Jianxin Li

School of Engineering, Guangzhou College of Technology and Business, Guangzhou 510850, China

Correspondence should be addressed to Chuili Hu; 1818200001@e.gzhu.edu.cn

Received 30 November 2021; Revised 23 December 2021; Accepted 5 January 2022; Published 7 February 2022

Academic Editor: Wei Zhang

In order to improve the teaching effect of colleges and universities and eliminate the disadvantage Figures of the traditional teaching mode, this paper applies virtual reality technology to the immersive teaching mode of colleges and universities and uses four-dimensional light field parameterization to describe the acquisition process and reproduction process of integrated imaging. Moreover, this paper studies the propagation characteristics of the light field during the reproduction of the integrated imaging system and establishes an evaluation method for the 3D scene reproduction capability of the integrated imaging system using light field parameters. In addition, this paper analyzes the problem of parameter matching between the acquisition end and the display end in the current integrated imaging system and does a detailed study on the method of light field conversion and gives the interpolation method of the light field image. Finally, this paper constructs an immersive teaching system for colleges and universities based on virtual reality and verifies the performance of the system through experimental research. From the experimental research results, it can be seen that the immersive classroom teaching model in colleges and universities based on virtual reality proposed in this paper has good teaching effects.

1. Introduction

With the continuous development of MOOCs, microclasses, and flipped classrooms, their shortcomings have also become more prominent. Although they can satisfy people's desire for knowledge, the boring video teaching also makes the learning process lack of immersion, interactivity, and interest. However, the emergence of virtual reality technology can make up for the shortcomings presented by the current MOOC, microclass, and flipped classroom. Therefore, classroom design research based on immersive virtual reality has a strong practical significance [1]. The immersive virtual reality classroom is a bold attempt to combine current information science technology with innovative teaching concepts. It inherits the short-cut, large-scale, and free and open characteristics of the existing online education, and it combines immersive virtual reality technology. Moreover, the virtual reality classroom will present a strong sense of immersion, interactivity, and conception [2]. Immersive classrooms in colleges and universities are studying how to integrate immersive virtual reality technology into modern classrooms to supplement existing teaching media and methods, which provide students with a more personalized learning space and achieve classroom optimization [3].

Virtual reality technology originated in the United States. The first country to apply virtual reality technology to teaching was the United States. At the same time, the highest level of virtual reality technology is also represented by American universities and research institutes. East Carolina University in the United States established the first virtual reality technology laboratory in 1992. In addition, the University of Houston, Harvard University, and other universities have also begun to use the virtual reality technology for teaching. In addition to the United States, virtual reality education in developed countries such as Japan and Europe is also at a leading level. Compared with the United States, China started relatively late in the VR field. However, with the expansion of China's network technology and the

improvement of the level of science and technology, VR education has attracted the interest and attention of the Chinese people.

This article combines virtual reality technology to reform the teaching mode of colleges and universities, constructs an immersive teaching classroom in colleges and universities, adopts the immersive teaching model for teaching, and improves the teaching quality of colleges and universities.

2. Related Work

The teaching process should be full of concrete experience and gradually extend to abstract experience. Learning activity theory believes that real or simulated learning environment can promote learners' cognition and internalization. The immersive virtual reality system is based on a variety of perception technologies, such as visual sensing, somatosensory and voice recognition, and tactile feedback, forming a full range of perceptual experience [4]. It can render a realistic teaching environment through audiovisual elements, such as light, pictures, sound effects, and colors, which is conducive for learners to actively construct knowledge in an intuitive learning context [5], and inspire learners to have a strong scientific research interest. The characteristic of science classroom is to construct scientific concepts and form correct scientific values through observation and experimentation. Therefore, real natural scenes are essential for the understanding and memory of knowledge [6]. In traditional classrooms, it is difficult for students to have access to real natural objects and landscapes, while virtual reality technology can use computers and other hardware devices to create highly simulated teaching situations and solve the problems of traditional classroom site factors and excessive practical expenses. [7]. At the same time, students can be completely immersed in the teaching environment closely related to the learning content, carry out repeated practice, and gain experience, thereby improving scientific literacy [8]. In a science classroom based on immersive virtual reality, learners use head-mounted high-definition displays to project themselves into a full-scene 3D environment. By operating and controlling the teaching scene, learners can naturally realize interactive learning activities. In the classroom, students use virtual reality equipment to enter the virtual environment as virtual characters of the teaching content to observe and experience scientific phenomena immersively. Science classrooms based on immersive virtual reality technology can provide students with an interactive and intuitive learning environment and stimulate students' interest in learning through strong senses, thereby enhancing students' cognition.

Virtual reality science classrooms can provide students with a variety of learning methods and practice the educational concept of "teach students in accordance with their aptitude." Virtual reality science classrooms will change the boringness of traditional classrooms and provide students with opportunities for active exploration. Students can communicate and discuss online or offline with classmates and teachers at any time and conduct interactive learning [9]. With the support of immersive virtual reality technology, teaching strategies can produce better learning effects than traditional teaching classrooms. In terms of interaction methods, immersive virtual reality technology breaks through the keyboard input and mouse operation of traditional virtual technology and adopts technologies, such as head-eye tracking, gesture recognition, and voice recognition, which are more in line with people's interaction habits [10]. Virtual reality technology provides support for various teaching strategies of learning activities and effectively improves the efficiency of learning activities. Through the creation of a highly immersive simulation environment [11], virtual reality technology can effectively stimulate the various senses of learners to observe and can internalize abstract concepts through experiential learning and actively test knowledge and skills. Learners use virtual reality equipment to observe scientific phenomena and experience scientific changes personally, learn to actively think about scientific phenomena, ask scientific questions, and achieve the effect of inferring from one another. Virtual reality technology can also promote the exploratory learning of scientific knowledge. Students can actively discover scientific problems and carry out exploratory experiences through hands-on and middle school in a virtual teaching context [12], thereby drawing conclusions. Inquiry-based teaching methods can stimulate students' research interest and learning activities, and simulation operations can also enhance students' sense of participation, improve hands-on ability and cultivate creative thinking, and enhance the effect of inquiry-based learning.

Virtual reality classrooms can improve students' learning motivation and promote the development of scientific thinking. The powerful interactive function of virtual reality technology transfers operations to the virtual teaching environment in a natural way in real time, realizing immersive learning activities [13]. Learners use input devices such as operating handles or data gloves to form a time series of learning behaviors and then use human-computer interaction interfaces to transmit data to the computer [14] to realize the analysis of students' learning behaviors and give operational results to form data feedback. Students can check for omissions based on detailed scores, thereby consolidating knowledge. Teachers can also log in to the learning management system to inquire about the learning situation of students and analyze the important and difficult points in teaching through visual data, so as to improve the teaching process and teaching methods and improve the quality of teaching [15].

3. Four-Dimensional Light Field Model of Integrated Imaging System

When all the light distribution in a three-dimensional scene is recorded and described, the optical appearance of the scene can be recorded. Correspondingly, when all the recorded light distribution is reproduced, the appearance of the three-dimensional scene is also reproduced, so that people can directly observe the three-dimensional scene.

The light distribution in the scene can be completely described by the plenoptic function, which uses seven

variables to describe the radiation of any light in the light field with a wavelength of λ at time t:

$$P = P(x, y, z, \theta, \phi, \lambda, t). \quad (1)$$

The light equation uses (x, y, and z) to describe the position of the light and (θ, ϕ) describe the direction of the light. The plenoptic function must describe all the lights in a scene. Due to the complexity of the plenoptic function, it is almost impossible to obtain the plenoptic function of a scene completely. Therefore, people use reduced-dimensional and discretized light field functions to approximate the light in the light field.

According to the principle of light color perception, the spectrum can be decomposed into three primary colors (red, green, and blue) to be perceived. Therefore, the spectral dimension in the light field can be reflected on the output of the function through color and intensity information. The time dimension can also be subtracted from the function when the optical properties of the scene are not considered to change with time. When the radiation intensity of light along a straight line is assumed to be constant, the three-dimensional space coordinates in the plenoptic function can be reduced to two-dimensional space coordinates, which together with the two-directional dimensions describe the position and direction information of the light. The light field function after the above-mentioned dimensionality reduction processing is called the four-dimensional light field function.

Two planes are used to characterize the light in the light field, as shown in Figure 1:

The four-dimensional light field function is [16]

$$L = L(u, v, s, t). \quad (2)$$

The function uses four parameters u, v, s, and t to describe the position and direction information of the light and describe the intensity and color (spectrum) information of the light through the R, G, and B values of the light L. Camahort uses points and directions on two spheres or one sphere to characterize the light in the light field, as shown in Figure 2.

Integrated imaging is to record three-dimensional scenes through planar devices. Therefore, the use of a planar four-dimensional light field can greatly simplify the process of combining the four-dimensional light field with integrated imaging. In the four-dimensional light field model given below, a reference plane is used, and the light is described by the intersection of a certain ray and the plane and the direction of light propagation, as shown in Figure 3.

The four-dimensional light field function is [17]

$$L = L(x, y, \alpha, \beta). \quad (3)$$

In the formula, x and y represent the position of the intersection of the light and the display plane on the plane, and α and β represent the angle of the light deviating from the horizontal plane and the vertical plane. For the convenience of writing, the four-dimensional light field mentioned below all adopt the four-dimensional light field model given here.

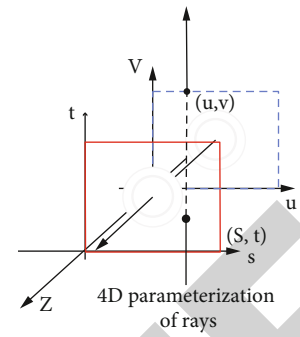

Figure 1: Points on two planes are used to describe the light in the light field.

In order to measure the imaging performance of an integrated imaging system, the performance parameters of a four-dimensional light field can be used to characterize the parameter performance of an integrated imaging system:

$$\left\{N_{pt(x,y)}, L_{(x,y)}, N_{\text{angle}(x,y)}, \Theta_{\text{angle}(x,y)}\right\}. \quad (4)$$

The sampling plane is the plane where the integrated imaging microlens array is located. On this sampling plane, N_{pl} represents the number of macro pixels, that is, the number of sampling points, which corresponds to the number of microunit lenses (pinholes) in integrated imaging. $L_{(x,y)}$ represents the sampling range, that is, the width and height of the sampling area. N_{angle} refers to the number of viewpoints in each macro pixel, that is, in the recording process, how much light from different directions can be recorded by each macro pixel, which is equivalent to the number of pixels in each micro unit image in integrated imaging. Θ_{angle} is used to represent the field of view angle of each macro pixel, L/N_{pt} represents the spatial sampling frequency, and $\Theta_{\text{angle}}/N_{\text{angle}}$ represents the angular sampling frequency.

Each parameter may have different values in the horizontal and vertical directions, so x and y are used to refer to the horizontal and vertical directions, respectively. In order to facilitate the analysis, the following article only analyzes in one direction.

In a real scene, the collection of all optical radiation constitutes a plenoptic function. However, during the acquisition process, it is impossible to record all the optical radiation in the scene. We can only discretize and record the radiation intensity of a certain wavelength or a few wavelengths within a certain spatial range and angle range in the scene for a certain period of time. Next, we analyze the capture process of traditional cameras and integrated imaging systems and quantitatively analyze and compare the two systems' ability to collect and record light field information in the scene.

The shooting process of a traditional camera can be considered as a process of recording the light passing through

(a) Select two points on the sphere to describe any light L

(b) Use the normal plane C of the in-sphere optical L and the intersection P of the intersection P of L and C to describe the L

Figure 2: A spherical surface is used to describe the light in the light field.

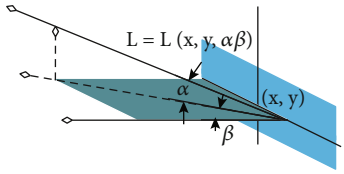

Figure 3: A point on a plane and the propagation direction angle of a ray are used to describe a ray.

the focal plane. This process integrates the light rays that can enter the camera at each point on the focus plane to obtain the pixel value of its corresponding pixel, as shown in Figure 4.

By analyzing the photographing process of a traditional camera from the perspective of the light field, we can understand as follows. The traditional photography process collects light emitted in a certain direction on a plane (focusing surface), and the number of spatial sampling points of the light field on the focus plane is the same as the number of pixels. There is only one angular sampling point, that is, only the rays that propagate from the sampling point on the focus plane to the camera lens can be sampled. Considering that most of the objects in the real scene can be approximately regarded as Lambertians, the optical observation results of the same object point from different angles are approximately unchanged. Therefore, when the focus plane is approximately coincident with the object in the scene, the integral of the light from the object to the camera lens can accurately reflect the optical appearance of the object point on the object. When the focus plane of the camera does not coincide with the object, the light propagating toward the lens through a point on the focus plane contains information about different objects. After integration, neither object A nor object B can be reflected, which becomes a blur point. At this time, objects A and B are out of the camera's depth of field.

From the above analysis, it can be seen that when in focus, the light emitted from a point on the focusing surface toward the camera is approximately the same, which can reflect the same object point information. However, when defocusing, the light emitted from the points on the focusing surface in different directions reflects the information of different object points. After the integration of the camera, blurred pixels are obtained. By reducing the clear aperture of the camera (increasing the F-number), the integration of light in different directions on the focusing surface can be reduced, thereby increasing the depth of field. In addition, through analysis, it can be considered that when the clear aperture of the camera is small enough and the objects in the scene are within the depth of field, the camera collects the light emitted in different directions through the point of the aperture on the plane where the lens is located, as shown in Figure 5.

When the clear aperture of the camera is small enough, the lens can be equivalent to a small hole, and only the light that propagates toward this small hole in the scene can be recorded. At this time, the plane where the small hole is located, that is, the plane where the camera lens is located, can be regarded as an equivalent sampling plane. On this sampling plane, the number of spatial sampling points is 1, and the number of angular sampling points is the number of pixels. The spatial sampling points in the scene are transformed into angular sampling points on the plane where the lens is located.

The acquisition results of traditional cameras are two-dimensional, which cannot reproduce the near and far position and depth information of the object. The reason can be attributed to the collected scene images only have spatial sampling and lack angle sampling. However, from the analysis of a camera with a sufficiently small lens aperture, the recording process of the camera can be equivalent to the recording process of the plane light field where the lens is located, but because there is only one spatial sampling point, only the angle information of this light field can be recorded. In other words, by increasing the number of lenses on this plane, the number of spatial sampling points for this light field can be increased. In integrated imaging, the microlens array used to collect the scene can just meet the needs of multiple lenses for collecting different sampling points of the same light field.

As mentioned earlier, only when the space of the lens can be approximated as a pinhole can there be an equivalent sampling plane of the light field. However, the use efficiency of the pinhole array for light is too low, so people generally use a microlens array as an optical element for imaging. There must be a depth of field problem when using a lens, and the depth of field can be calculated by the depth of field formula [18]:

$$\Delta L_1 = \frac{F\delta L^2}{f^2 + f\delta L},$$
$$\Delta L_2 = \frac{F\delta L^2}{f^2 - f\delta L}. \tag{5}$$

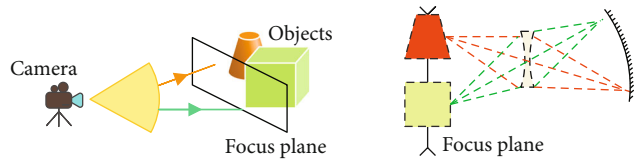

(a) The situation of defocusing

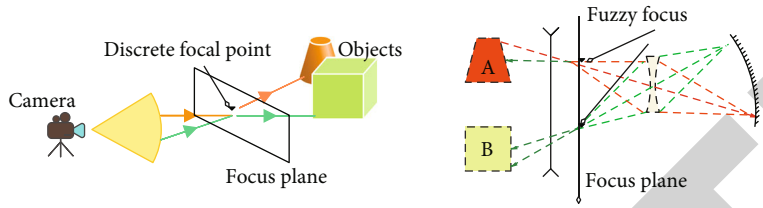

(b) The situation of defocusing

Figure 4: Acquisition mode of traditional camera.

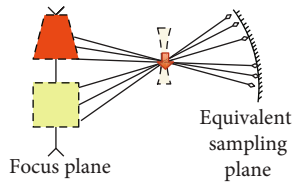

Figure 5: Focus plane and its equivalent sampling plane.

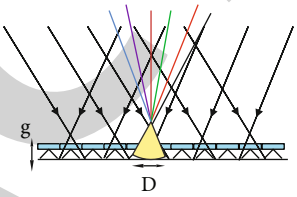

Figure 6: Schematic diagram of the collection process of the microlens array.

In the formula, ΔL_1 and ΔL_2, respectively, refer to the foreground depth and the back depth of field, F refers to the F number of the microunit lens, 8 is the allowable size of the diffuse spot, that is, the CCD/CMOS pixel size, and f is the focal length of the microunit lens. In general, since the focal length f of the microunit lens is very small, the depth of field of the optical elements used in the acquisition process in the integrated imaging system is very large. The use of the light field camera's acquisition method can make all the scenes fall within the depth of field. Since all objects in the scene can fall within the depth of field of the microlens without blurring due to defocusing, the microlens array can be equivalently regarded as a pinhole array during analysis.

The following will analyze the light field information parameters that can be obtained through the analysis of the collection process of the microlens array. The unit microlens is equivalently regarded as a small hole, as shown in Figure 6.

The number of macro pixels is equal to the number of microlenses, and the number of angular sampling points is the same as the number of pixels covered under each microlens. The spatial sampling range, that is, the range occupied by the microlens array, can be obtained by the following formula [19]:

$$L_x = N_{plx} \times D. \tag{6}$$

The angular sampling range is the angular range within which the pixels covered by each microunit lens can receive light, which can be obtained by the following formula [20]:

$$\Theta_{\text{angle}} = \arctan \frac{D}{2g}. \tag{7}$$

The application of the micro-unit lens solves the problem of simultaneous spatial sampling and angular sampling in the light field sampling process. However, when the micro-unit lens array is directly used for light field image collection, the range of light field collection is similar to the size of the micro-unit lens array. In a real shot scene, because the scene is usually much larger than the micro-unit lens array, the information collection in the scene is incomplete. In the process of collecting the real scene, it can be found that there is little difference in the angle sampling of the scene between two points very close in space. If the approximate continuity of the angle sampling of the micro-unit lens array is discarded, and the spacing between the micro-unit lenses is enlarged, the range of spatial sampling can be increased.

As shown in Figure 7, when using a parallel projection camera array to collect the light field, the main optical axis directions of all cameras are parallel, and the parameters (focal length, F number, etc.) are set to the same. At this time, it can be considered to collect the light field at the position where the camera's common focus plane is located. The spatial sampling range is the union of all the fields of view in the camera array, and the angular sampling range is the

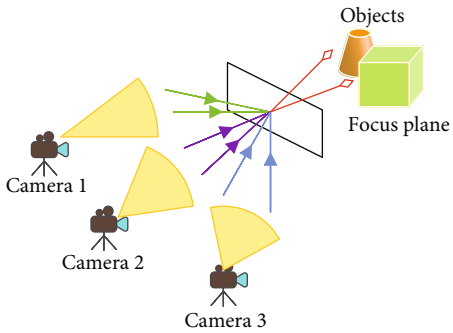

Figure 7: The acquisition process of the light field by the camera array.

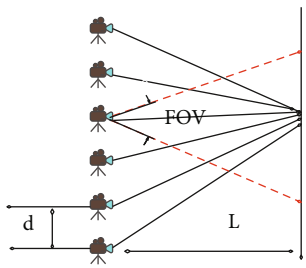

Figure 8: Schematic diagram of the parameters of the camera array collecting light field information.

same as the field of view of a single camera. In order to make the captured image clear, each camera in the camera array must have a sufficiently large depth of field.

As shown in Figure 8, the interval between the cameras in the camera array is d, the distance between the focus plane and the camera is l, and the field of view of a single camera is FOV. Then, in the process of sampling the light field, the angle sampling range is also FOV, and the number of angle sampling points is

$$N_{\text{angle}} = \frac{\text{FOV} \cdot l}{d}. \tag{8}$$

The number of spatial sampling points is approximately equal to the number of pixels of the camera's photosensitive element.

The application of the camera array can solve the problem that the sampling range of the microunit lens array is too small for the light field. However, the camera array device is huge, and the optical axis of each camera in the array needs to be aligned during use, and a complicated calibration process is required. On this basis, scholars proposed many improved light field cameras with similar structures and different parameters.

As shown in Figure 9, the light field camera transforms the scene into a reduced image through the transformation of the main mirror and then uses the microunit lens array to shoot the image formed by the main mirror to expand its collection range. At this time, the light field recorded by the microunit lens is no longer the original light field but the light field transformed by the main mirror. Therefore,

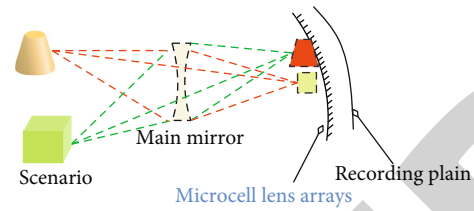

Figure 9: Schematic diagram of the structure of the light field camera.

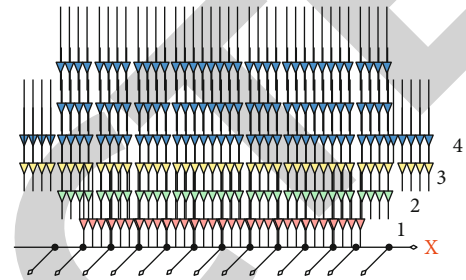

Figure 10: Schematic diagram of light field propagating in one direction.

the acquisition capability of the light field camera is closely related to the parameters of the main mirror, and its acquisition range can be characterized by the angle of view as follows:

$$FOV = 2 \arctan \frac{S}{2f}. \tag{9}$$

In the formula, S is the size of the recording panel, and f is the focal length of the main lens. The angle sampling range of the scene depends on the position of the point in the scene relative to the camera. The angle can be characterized by the angle formed by the camera lens to the object point as follows:

$$\theta \approx \frac{D}{L}. \tag{10}$$

In the formula, D refers to the diameter of the lens, and L refers to the distance between the object point and the camera.

The display modes of integrated imaging include real image mode, virtual image mode, and focus mode. When the display mode works in the focus mode, the microlens array can be approximately equivalent to a small hole model. The display process and the acquisition process are exactly the reverse process, and the parameter derivation is similar to the shooting process of the microlens array, and only the pixel parameters of the display panel need to be replaced with the pixel parameters of the acquisition panel.

Under the existing conditions, the pixels of the display panel cannot be small enough to meet the display requirements. Therefore, in the display of integrated imaging, in order to obtain a better viewing effect, it usually works in

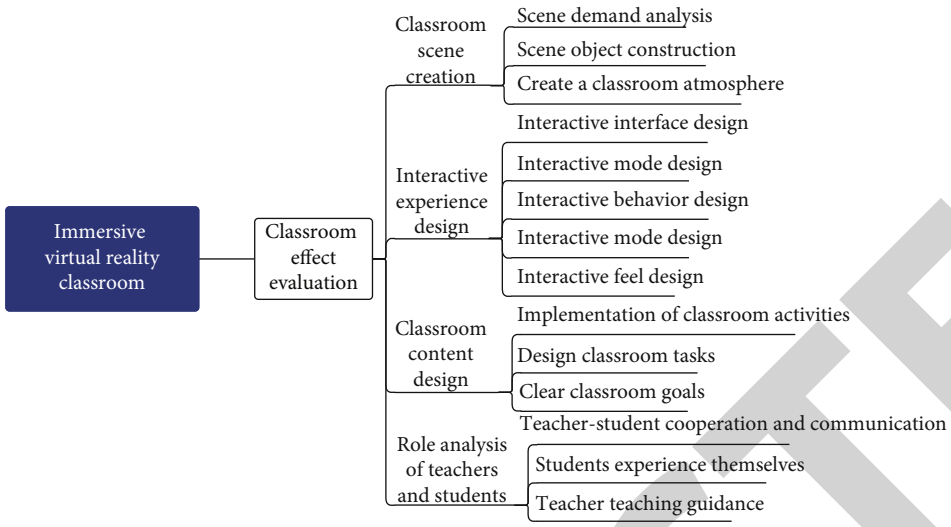

Figure 11: The overall structure of the immersive virtual reality classroom.

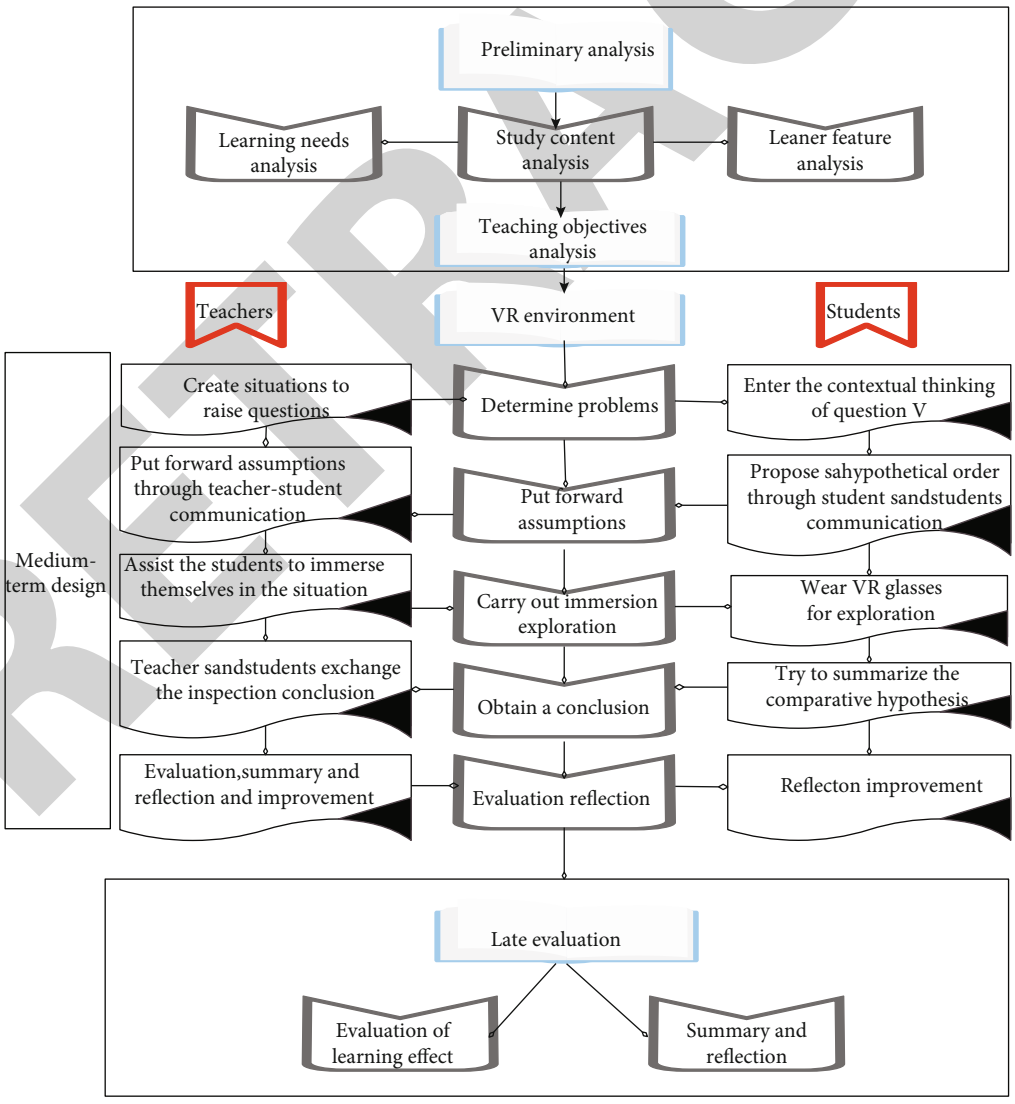

Figure 12: Immersive teaching mode based on VR.

Table 1: Verification of the effect of VR-based immersive teaching mode.

Number	Immersion	Teaching effect	Number	Immersion	Teaching effect
1	84.26	86.38	21	88.01	93.01
2	78.69	86.27	22	82.46	89.01
3	77.17	89.63	23	84.82	85.68
4	79.12	83.74	24	89.92	84.64
5	77.55	85.64	25	77.01	94.53
6	78.29	89.84	26	77.39	94.81
7	76.04	83.17	27	84.36	88.82
8	88.71	83.49	28	86.75	84.92
9	88.96	87.00	29	85.68	92.02
10	88.57	93.44	30	80.70	86.67
11	80.62	91.57	31	76.52	83.80
12	87.85	93.29	32	81.57	94.52
13	78.79	83.34	33	86.59	84.84
14	84.74	92.43	34	80.08	88.97
15	91.00	87.17	35	89.06	90.97
16	87.61	86.70	36	82.52	83.88
17	79.44	90.16	37	78.11	90.00
18	82.35	83.58	38	82.96	89.86
19	89.18	86.54	39	84.64	85.43
20	85.46	88.05	40	81.60	87.75

the real image mode and the virtual image mode. At this time, in each microunit lens in the lens array images, the corresponding microunit image on its common surface and the microunit lens can no longer be equivalent to a small hole model.

Through calculation, it can be known that the spatial sampling range becomes

$$L = L_{kns}\left(N_{kns} + \frac{l}{g}\right). \tag{11}$$

However, the spatial sampling range without angular sampling loss is reduced, which can be expressed as follows:

$$L = L_{kns}\left(N_{kns} - \frac{l}{g}\right). \tag{12}$$

In the formula, L_{kns} refers to the size of a single micro lens, and N_{kns} is the number of micro lenses.

The four-dimensional light field function is only a subset of the seven-dimensional plenoptic function, and the information loss is caused by the sampling during the acquisition of the four-dimensional light field. It, respectively, shows the distribution of light field sampling points on the sampling plane ($z = 0$) and several special interfaces (corresponding to the planes ① ~ ④ in Figure 10).

It can be seen from the figure that the spatial sampling rate on plane ① has reached a maximum. If the object (Lambertian) is just on plane ①, then the finest spatial sampling of the surface information of the object can be completed. However, the maximum spatial sampling rate sacrifices the angular sampling rate. The angular sampling rate on this plane is extremely small (no matter where, only one angle of light can be sampled at that point), and it no longer has viewing angle information.

In the method given in this paper, only two transmission processes are used: the propagation of optics in free space and the transformation of light by an ideal lens. The transmission matrix of light propagating in free space is

$$L_t = \begin{bmatrix} 1 & t \\ 0 & 1 \end{bmatrix}. \tag{13}$$

The transmission matrix of light passing through the lens is

$$L_f = \begin{bmatrix} 1 & t \\ -\frac{1}{f} & 1 \end{bmatrix}. \tag{14}$$

4. Immersive Classroom Teaching Model in Colleges and Universities Based on Virtual Reality

The overall structure of the immersive virtual reality classroom is shown in Figure 11.

The VR-based immersive teaching mode caters to the requirements of the new curriculum standards, and it is necessary to return the classroom to the students and pay

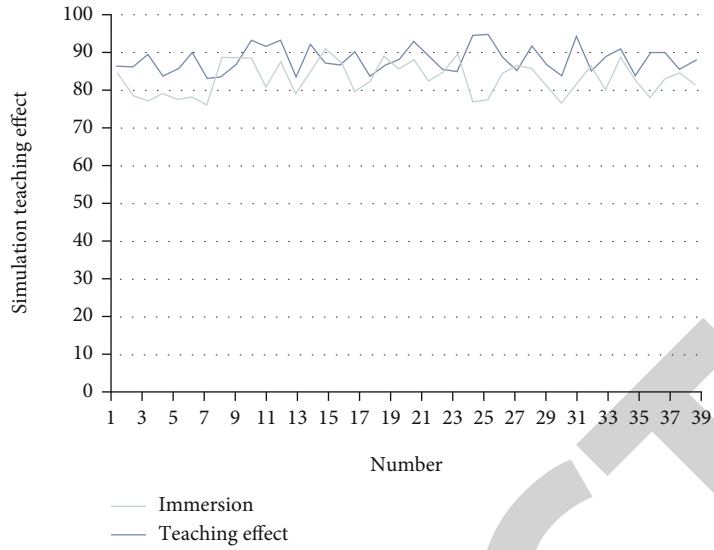

Figure 13: Statistical diagram of the simulation teaching effect.

attention to the student-oriented. Moreover, VR-based immersive teaching emphasizes that students are the mainstay and teachers are supplemented. The VR-based immersive teaching design model is shown in Figure 12.

On this basis, the simulation teaching effect of the model proposed in this paper is verified, and the results shown in Table 1 and Figure 13 are obtained.

From the above research, we can see that the VR-based immersive teaching model proposed in this paper can effectively change the shortcomings of the traditional teaching model and promote the improvement of teaching quality in universities.

5. Conclusion

Major breakthroughs in VR technology are accompanied by the emergence of 5G technology. The application of VR virtual reality in the field of education is becoming more and more extensive. In this context, it is also very important to study virtual reality immersive classrooms. The use of virtual reality technology can greatly improve the concentration of students. The concentration of students in the immersive virtual reality environment is 6 times that of the traditional environment. Moreover, students who study in an immersive virtual reality environment greatly improved in their ability to acquire and retain knowledge. This article combines virtual reality technology to reform the teaching mode of colleges and universities, constructs an immersive teaching classroom in colleges and universities, and adopts the immersive teaching model to improve the teaching quality of colleges and universities. Through the research of experimental results, it can be seen that the VR-based immersive teaching model proposed in this paper can effectively change the shortcomings of the traditional teaching model and has a certain role in improving the quality of teaching in colleges and universities.

Data Availability

The labeled dataset used to support the findings of this study is available from the corresponding author upon request.

Conflicts of Interest

The authors declare no competing interests.

Acknowledgments

This study is sponsored by 2020 Guangdong Province General Colleges and Universities Characteristic Innovation Project (Natural Science) "Research and Realization of Immersive Teaching System Based on VR/AR Technology" (No. 2020KTSCX172).

References

[1] M. S. Elbamby, C. Perfecto, M. Bennis, and K. Doppler, "Toward low-latency and ultra-reliable virtual reality," *IEEE Network*, vol. 32, no. 2, pp. 78–84, 2018.

[2] D. Shin, "Empathy and embodied experience in virtual environment: to what extent can virtual reality stimulate empathy and embodied experience?," *Computers in Human Behavior*, vol. 78, pp. 64–73, 2018.

[3] H. K. Kim, J. Park, Y. Choi, and M. Choe, "Virtual reality sickness questionnaire (VRSQ): motion sickness measurement index in a virtual reality environment [J]," *Applied Ergonomics*, vol. 69, pp. 66–73, 2018.

[4] R. Yung and C. Khoo-Lattimore, "New realities: a systematic literature review on virtual reality and augmented reality in tourism research," *Current Issues in Tourism*, vol. 22, no. 17, pp. 2056–2081, 2019.

[5] G. Makransky, T. S. Terkildsen, and R. E. Mayer, "Adding immersive virtual reality to a science lab simulation causes more presence but less learning," *Learning and Instruction*, vol. 60, pp. 225–236, 2019.

Hindawi
Journal of Sensors
Volume 2023, Article ID 9810962, 1 page
https://doi.org/10.1155/2023/9810962

Retraction

Retracted: Research on the Architecture of Digital Song and Dance Costume Design System Based on Intelligent Deep Learning Algorithm

Journal of Sensors

Received 19 December 2023; Accepted 19 December 2023; Published 20 December 2023

This article has been retracted by Hindawi following an investigation undertaken by the publisher [1]. This investigation has uncovered evidence of one or more of the following indicators of systematic manipulation of the publication process:

(1) Discrepancies in scope
(2) Discrepancies in the description of the research reported
(3) Discrepancies between the availability of data and the research described
(4) Inappropriate citations
(5) Incoherent, meaningless and/or irrelevant content included in the article
(6) Manipulated or compromised peer review

The presence of these indicators undermines our confidence in the integrity of the article's content and we cannot, therefore, vouch for its reliability. Please note that this notice is intended solely to alert readers that the content of this article is unreliable. We have not investigated whether authors were aware of or involved in the systematic manipulation of the publication process.

Wiley and Hindawi regrets that the usual quality checks did not identify these issues before publication and have since put additional measures in place to safeguard research integrity.

We wish to credit our own Research Integrity and Research Publishing teams and anonymous and named external researchers and research integrity experts for contributing to this investigation.

The corresponding author, as the representative of all authors, has been given the opportunity to register their agreement or disagreement to this retraction. We have kept a record of any response received.

References

[1] W. Wang, "Research on the Architecture of Digital Song and Dance Costume Design System Based on Intelligent Deep Learning Algorithm," *Journal of Sensors*, vol. 2022, Article ID 1545334, 10 pages, 2022.

Hindawi
Journal of Sensors
Volume 2022, Article ID 1545334, 10 pages
https://doi.org/10.1155/2022/1545334

Research Article

Research on the Architecture of Digital Song and Dance Costume Design System Based on Intelligent Deep Learning Algorithm

Wenli Wang

Apparel and Art Design College, Xi'an Polytechnic University, Xi'an 710048, China

Correspondence should be addressed to Wenli Wang; 20020722@xpu.edu.cn

Received 2 December 2021; Revised 4 January 2022; Accepted 15 January 2022; Published 7 February 2022

Academic Editor: Wei Zhang

In order to improve the intelligence and reliability of song and dance costume design, this article combines the intelligent deep learning algorithm to improve the digital costume design process. In order to solve the problem of minimizing the energy of image deformation, this paper proposes to transform it into a sparse matrix to solve the problem, which is solved by constructing a coefficient matrix and multiple iterations. After the algorithm is improved, this article combines the digital intelligence method to construct the digital song and dance costume design system structure based on the intelligent deep learning algorithm and analyzes its work flow. Finally, this paper verifies the method in this paper through feasibility analysis and system performance test. From the experimental results, it can be seen that the digital song and dance costume design system based on the intelligent deep learning algorithm proposed in this article has a good effect in the song and dance costume design.

1. Introduction

The three-dimensional clothing virtual deformation display system is to summarize the successful design historical materials and design experience accumulated by clothing designers and display personnel over the years and establish a digital clothing sampling system in the computer. The operator can perform a three-dimensional panoramic view of the selected clothing and adjust the deformation of its specific parts according to the needs. The computer simulates the dressing effect of the sample according to the selected size, thereby completing the generation process from style design to clothing design display adjustment. The ideal state of the intelligent clothing virtual deformation display system is "zero tool" and "dumb" operation. The former refers to the style design of clothing that does not use traditional paper and pen. It only needs software to model and adjust the clothing, and many related different styles can be derived. The latter is simple to operate and can be used by professionals and nonprofessionals. It is as convenient and quick to operate as point-and-shoot cameras on the market [1]. The intelligent clothing deformation system must be based on scientific and reasonable "design knowledge" as a platform to enable its intelligent design module to operate normally. To truly realize the intelligent display of three-dimensional clothing, there are still many problems that need to be solved. Ensuring the rationality of "design knowledge," how to transform "design knowledge" into computer-recognizable mathematical codes, how to use computer programming language to realize clothing deformation, etc., will all become high-end technologies for clothing three-dimensional virtual deformation display [2]. The digital realization and transformation of clothing models are the key to the development of its intelligent technology [3].

All human progress is a linear movement from shallow to deep, from simple to complex, from extensive to detailed, stone axes and choppers of the Paleolithic era, bone needles and spinning wheels of the Neolithic era, and today's CNC machine tools and electronic collider, the same helper who works for humans. Perhaps there are similar appearances and internal performances in similar times, while qualitative and conceptual drastic changes will occur in distant times. This is why today's design is different from the original design. The development of clothing design has generally

gone through this process, using primitive animal skins and leaves to simply drape. The emergence of cotton and linen fabrics in thousands of years of development and evolution gradually determined the garment shape of Chinese upper garments and lower garments. After thousands of years to the Ming and Qing dynasties, the princes and nobles' clothing embroidery overlaps, and they are extremely complicated and inexhaustible, which seems to indicate that feudal society is at its extreme. After the human history entered the modern society, clothing design has gone from simple tailoring and sewing, sheltering the body from the cold, through many revolutionary changes, and more and more infiltration of rational elements, from daily wear to fashion, from underwear to outerwear, classification strict, and the production process is more precise and perfect. Due to the intervention of high technology, clothing has undergone a qualitative leap from design to craftsmanship and fabrics. All this shows that the development of clothing also shows a linear movement. Due to this phenomenon of development, in musicals, according to the needs of the repertoire or the choreographer, the costume design will also be handled appropriately from the style and color, complicated or simple, until a satisfactory costume positioning is found.

This article combines the deep learning algorithm to improve the digital algorithm, builds a song and dance costume design system, improves the effect of song and dance costume design, and improves the intelligence of the song and dance costume design process.

2. Related Work

With the improvement of virtual technology, the development of virtual fitting technology abroad is very rapid. The Russian company AR Door has innovatively launched a "virtual fitting room" solution and conducted an application test in a Moscow store. This solution is in cooperation with Topshop, a British fashion brand company. It uses the Kinect, a somatosensory device launched by Microsoft, as the sensor. When using it, consumers do not have to actually try on clothes. They can try it virtually through simple gestures. Wear all the clothes built into the system [4]. NDP has customized a virtual fitting system for Japanese clothing company Uniqlo. This system consists of a peripheral camera, a large screen, and a tablet terminal. The system will recognize the type and color of the clothes selected by the user and can display the effect of the clothes on the user on the large screen through augmented reality technology [5]. The user can intuitively see the effect of the selected clothing on the model. The system proposed in [6] also has the function of helping users interact with their friends. Users can use the system to send virtual images of their clothes after trying on them to relatives and friends in the form of MMS or e-mail for them to comment. Virtual fitting has gradually developed in my country. In literature [7], the fitting software of the pot lift successfully realized the online virtual fitting of customers. Consumers can log on to their website and enter their height, weight, chest circumference, waist circumference, and other key body dimensions, and the system will soon be able to generate a three-dimensional virtual model with consumers' own body shape characteristics. The "online fitting room" proposed in literature [8] provides a variety of body models. Users can choose models that are similar to their own body types and wear their selected clothing, shoes, and hats on the model to roughly simulate these models and the effect of clothing on yourself. Literature [9] proposes "3D interactive virtual fitting room." In foreign countries, virtual reality technology has long been used in many areas of business activities, such as art, education, entertainment, medicine, and sales. Virtual reality technology is applied to the education industry. As a new teaching medium, its superiority is obvious. It can be a vivid and intuitive display of complex and boring theories to learners, and it also makes more theoretical knowledge available. The possibility of experimentation has greatly improved the learning efficiency [10].

At present, the basic research in this field in the United States mainly focuses on four aspects: perception, background software, user interface, and hardware. Japan is also one of the leading countries in the current research and development of virtual reality technology, and it is mainly dedicated to the research of establishing a large-scale knowledge base [11]. In addition, a lot of work has been done in the research of virtual reality games. However, most of Japan's virtual reality hardware is imported from the United States [12].

Literature [13] uses the repeated textile block (Lumislice) to realize the simulation and rendering of knitted fabrics at the same time and achieves a very fine effect. Literature [14] studies the internal structure of cloth to simulate gloss, but this method uses a highly simplified cloth model, and the result is also lack of verification. Literature [15] used ray tracing geometric models of small-scale cloth to calculate the BRDF of velvet and nylon fibers. Literature [16] used CT scan cloth surface structure to perform volume rendering. This method provides high-quality and close-range rendering, but this method requires the use of complex measuring equipment to measure samples; otherwise, it cannot be directly extended to other types of cloth. Literature [17] established a complete model that can regenerate the appearance of fabric cloth, using the bidirectional texture function (BTF) at short distances and the bilinear reflection distribution function (BRDF) at long distances. This is the most advanced method that can reproduce the appearance of various fabrics. It is an empirical model established by simulating the interaction of light on the fiber. Literature [18] established an anisotropic model based on the yarn's bidirectional scattering distribution function (BSDF) model and the yarn weaving method. This model mainly determines the optical properties of the cloth by the scattering properties of the yarn and the tangent direction of the yarn.

3. Digital Algorithm Based on Intelligent Deep Learning

The global optimization problem of image distortion in this paper is essentially a convex optimization problem. How to solve this convex optimization problem most efficiently is a problem that needs to be solved. First, we first abstract the

specific problem into a minimization problem of finding a generic function. For an unconstrained problem as described in [19]

$$\min f(x), \quad x \in R^n. \tag{1}$$

Among them, the function $f(x)$ has a first-order continuous partial derivative.

To solve such problems, we always hope to find the fastest path to the minimum.

The steepest descent method assumes that the rate of change of the function $f(x)$ along the direction d at the point x can be expressed by the directional derivative. For a differentiable function, the directional derivative is equal to the inner product of the gradient and the direction, that is,

$$Df(x;d) = \nabla f(x)^T d. \tag{2}$$

Therefore, finding the fastest declining direction of the function $f(x)$ at point x can be attributed to solving the following nonlinear programming [20]:

$$\begin{aligned} \min \quad & \nabla f(x)^T d \\ \text{s.t.} \quad & \|d\| \le 1. \end{aligned} \tag{3}$$

From the Cauchy-Schwarz inequality, we can get

$$\left|\nabla f(x)^T d\right| \le \left\|\nabla f(x)^T\right\| \|d\| \le \|\nabla f(x)\|. \tag{4}$$

By removing the absolute value sign, we can get

$$\nabla f(x)^T d \ge -\|\nabla f(x)\|. \tag{5}$$

Then, we know when

$$d = -\frac{\nabla f(x)}{\|\nabla f(x)\|}. \tag{6}$$

The equal sign holds, and the rate of change along the direction defined by the above formula is the smallest at point x, that is, the negative gradient direction. In this design, $f(x)$ corresponds to the image deformation energy, and x corresponds to the corresponding pixel coordinate value. The multidimensional convex optimization problem can be expressed as

$$\min \|E(x)\|_0. \tag{7}$$

Among them,

$$E(x) = \lambda_d E_d + \lambda_h E_h + \lambda_v E_v. \tag{8}$$

From the above derivation, it can be known that in order to minimize the objective function, it should be along the x negative gradient direction. This topic is aimed at the independent variables of 2D coordinate pixels, and the gradient direction is the xy direction differential.

After formula (8) is differentiated in xy direction and set to O, formula (9) can be obtained [21]:

$$\lambda_d \frac{\partial E_d}{\partial_{x,y}} + \lambda_d \frac{\partial E_v}{\partial_{x,y}} + \lambda_d \frac{\partial E_h}{\partial_{x,y}}, x, \mathrm{y} \in \{\text{All block nodes}\}. \tag{9}$$

In the formula, the items E_h and E_v are the f subitems of the above structural item E_s, which represent the energy subitems in the vertical and horizontal directions, respectively. The three component calculation formulas will be derived in detail below.

For the disparity term, each piece of energy is produced by a feature point (x, y):

$$E_d = \sum S(X_{\text{old}} - X_{\text{new}} - d)^2, \quad x \in \{\text{All matching feature points}\}. \tag{10}$$

Among them, the S term is the attention degree weight, X_{old} is the corresponding coordinate in the original image, and X_{new} is the corresponding coordinate in the virtual view point image.

For convenience, the abscissa of the vertices of each block is

$$\frac{\partial E_d}{\partial x_p} = \frac{\partial E_d}{\partial x_{\text{new}}} \frac{\partial x_{\text{new}}}{\partial x_p} = 2S(X_{\text{old}} - X_{\text{new}} - d) \frac{\partial x_{\text{new}}}{\partial x_v}, \tag{11}$$

$$\frac{\partial x_{\text{new}}}{\partial x_p} = \frac{\partial x_{\text{new}}}{\partial x_1} + \frac{\partial x_{\text{new}}}{\partial x_2} + \frac{\partial x_{\text{new}}}{\partial x_3} + \frac{\partial x_{\text{new}}}{\partial x_4}. \tag{12}$$

Based on the above formula, the following formula can be obtained:

$$\begin{aligned} \frac{\partial E_d}{\partial x_1} &= 2Sk_1(k_1x_1 + k_2x_2 + k_3x_3 + k_4x_4) - 2Sk_1(x_{\text{new}} + d), \\ \frac{\partial E_d}{\partial x_2} &= 2Sk_2(k_1x_1 + k_2x_2 + k_3x_3 + k_4x_4) - 2Sk_2(x_{\text{new}} + d), \\ \frac{\partial E_d}{\partial x_3} &= 2Sk_3(k_1x_1 + k_2x_2 + k_3x_3 + k_4x_4) - 2Sk_3(x_{\text{new}} + d), \\ \frac{\partial E_d}{\partial x_4} &= 2Sk_4(k_1x_1 + k_2x_2 + k_3x_3 + k_4x_4) - 2Sk_4(x_{\text{new}} + d). \end{aligned} \tag{13}$$

Among them, k_1, k_2, k_3, k_4 represents the current feature point and the ratio coefficient of the four vertices, respectively.

The energy constraint in the horizontal direction is generated by the horizontal edge of each block. Similarly, for convenience, t and j are used to indicate the position of the current block in the entire image. The specific expression is as follows:

$$E_h = \sum S_{i,j}\left(x_{i+1,j} - x_{i,j} - w\right)^2. \tag{14}$$

It takes the partial derivative of all the block vertices x_{ij}:

$$\begin{cases} \dfrac{\partial E_h}{\partial x_{ij}} = -2S_{i,j}\left(x_{i+1,j} - x_{i,j} - w\right), \\ \dfrac{\partial E_h}{\partial x_{i+1,\mathrm{j}}} = 2S_{i,j}\left(x_{i+1,j} - x_{i,j} - w\right). \end{cases} \tag{15}$$

It can be found from the formula that the periodicity of the horizontal energy item is mainly manifested between two adjacent blocks. In other words, for the horizontal item, only the horizontal adjacent block coefficient is not zero, and the rest are zero.

For the vertical term, each piece of energy is produced by a longitudinal edge of a block:

$$E_h = \sum S_{i,j}\left(x_{i,j+1} - x_{i,j}\right)^2. \tag{16}$$

It takes the partial derivative of all the block vertices $x_{i,j}$:

$$\begin{cases} \dfrac{\partial E_v}{\partial x_{ij}} = -2S_{i,j}\left(x_{i,j+1} - x_{i,j}\right), \\ \dfrac{\partial E_v}{\partial x_{i,j+1}} = 2S_{i,j}\left(x_{i,j+1} - x_{i,j}\right). \end{cases} \tag{17}$$

Similarly, the periodicity of the vertical term is mainly manifested between two adjacent blocks in the vertical direction, and its corresponding coefficient is nonzero.

By combining the above formulas into one, we can get the total $\partial E_v/\partial x_{ij}$. When we set it equal to 0, it can then be transformed into a multidimensional linear equation:

$$Ax = b. \tag{18}$$

This topic takes 640 ∗ 360 resolution as an example, the block size is 16 ∗ 16, and then A is a 861-order sparse square matrix with 7749 nonzero values. Through the analysis in this section, we have transformed a multidimensional convex optimization problem into a sparse matrix solution problem, thus bypassing the computationally intensive differential operation and QP solution algorithm implementation.

A convex optimization problem is transformed into a sparse matrix solution problem. Usually, the common method for solving linear matrix equations is to solve the linear equation coefficient matrix by matrix decomposition, mainly including triangular decomposition, singular value decomposition, and QR decomposition. The triangular decomposition method is also called LU decomposition, which is mainly solved directly after decomposing a matrix into an upper triangular matrix or a lower triangular matrix. QR decomposition is to decompose the matrix into a normal orthogonal matrix and upper triangular matrix. Singular value decomposition is an orthogonal matrix decomposition method, but it is an unavoidable problem that involves the amount of calculation after orthogonalization. Therefore, solving the energy equation by matrix decomposition is not a good choice. It is not only a matter of the amount of calculation but also some other reasons that the coefficient matrix in the energy equation is not suitable for matrix decomposition. The reason is that the dimension of the coefficient matrix is very large. Taking a 640 × 480 resolution image as an example, if the block size is 16 × 16, the number of unknowns is 640 + 1480 + 1 = 1271, that is, the A matrix is a large matrix of 1271 × 1271.

If the matrix decomposition method is used to solve the problem, it is necessary to store the coefficients of the relevant upper triangular or orthogonal matrix. For a 1271 ∗ 1271 matrix, it takes several millions to store the coefficients in 32 bits. This hardware resource consumption is obviously unacceptable. Since it is a specific engineering problem in this design, the solution can be analyzed in detail according to the specific situation.

Similarly, we take a 640 × 480 image as an example, the block size is 16 × 16, and the coefficient matrix is shown in Figure 1. Among them, (a) is a schematic diagram of the coefficient matrix, each pixel corresponds to a value in the coefficient matrix, the white dots are the nonzero points of the coefficient matrix, and the black dots are the zero-value points; (b) is an enlarged view of the red frame area in (a), and a small white block in (b) is a pixel, and the dashed line indicates periodicity.

It can be seen that the coefficient matrix is a matrix with block cyclicality, and there are also side-to-corner blocks of the same size on the top, bottom, left, and right sides of the main diagonal block. The size of the block is $(M + 1) \times (M + 1)$, which is partly different from the general strip diagonal matrix. Among them, although the main diagonal blocks are all a periodic three-diagonal matrix, the two adjacent main diagonal blocks are completely separated. The side-to-corner block is also a diagonal matrix, but there will be nonzero values on some diagonal neighboring pixels. These are generated by the disparity term, so the distribution is random. It can be observed from the figure that the coefficient matrix is a sparse band matrix. It can be seen from the formulae deduced above that the coefficient matrix has a certain periodicity. We can make full use of this periodicity to access data and use Gaussian iteration to solve approximate solutions.

Gaussian iterative solution is an improvement of Jacobian iterative solution. In each round of iterative process, a new solution is added to the iterative sequence in time, thereby accelerating the convergence speed of the iteration. During operation, it only needs to store one row of corresponding coefficients and solutions for vector multiplication. At the same time, there are many zero values in the matrix that do not need to be stored, and the magnitude of the required storage is on the order of 3 diagonals, which is reduced by more than 60% compared with the matrix decomposition, which greatly reduces the storage resources. The Gaussian iteration formula is as follows:

$$\begin{cases} x_i^{k+1} = \dfrac{\left(b_i - \sum_{j=1}^{i-1} a_{ij} x_j^{k+1} - \sum_{j=i=1}^{\mathrm{in}} a_{ij} x_j^k\right)}{a_{ii}}, \\ i = 1, 2, \cdots, n\,;\ k = 0, 1, 2, \cdots \end{cases} \tag{19}$$

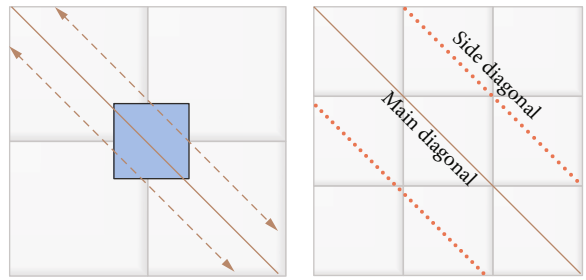

Figure 1: Coefficient matrix of the energy equation.

Among them, k is the number of iterations, and a_{ij} is the coefficient value. It can be seen from formulas (13), (15), and (17) that the coefficient matrix A satisfies

$$|a_{kk}| \geq \sum_{\substack{j=1 \\ j \neq k}}^{n} |a_{kj}|, \quad (k = 1, \cdots, n). \tag{20}$$

Obviously, the coefficient matrix A is a strictly diagonally dominant matrix, so the Gaussian iteration method is used to solve the convergence. As shown in Figure 2, the algorithm flow is described in detail below.

In the circle 2 flowchart, the system first reads in the data, that is, the input coefficient matrix A, constant vector b, initial value, stop condition, and the maximum number of cycles N. In the flowchart, k is the number of iterations and N is the maximum number of cycles. According to the input data, the system performs the first round of iteration according to formulas (4)–(18), judges whether the output data meets the termination condition, and outputs the result if it meets the termination condition; otherwise, it continues to iterate. If the iterative process has not met the termination condition, it is judged whether the number of iterations has exceeded the preset number of iterations, and a failure flag is output if it exceeds.

In the software implementation, the coefficient matrix generated by the horizontal term and the vertical term can be directly superimposed to form a part of the matrix coefficients, and the disparity term generated by the feature points is the equation coefficient matrix to be calculated. In the hardware implementation process, the stored data is only for nonzero coefficients, and there is no need to process a large amount of zero-valued data. It is necessary to use storage resources as much as possible to avoid processing a large amount of zero-valued data. We divide the coefficient matrix into two parts as shown in Figure 3: predictability data and randomness data. The predictability data is also the coefficient matrix generated by the previous structure item, and the randomness data comes from the disparity item of the feature point.

The predictability part can be divided into 5 categories according to the position of the unknown solution order in the grid: (1) four vertices of the grid, (2) vertical edges of the grid, (3) horizontal edges of the grid, (4) periodic edges of the grid, and (5) arbitrary edges of the grid. Module input

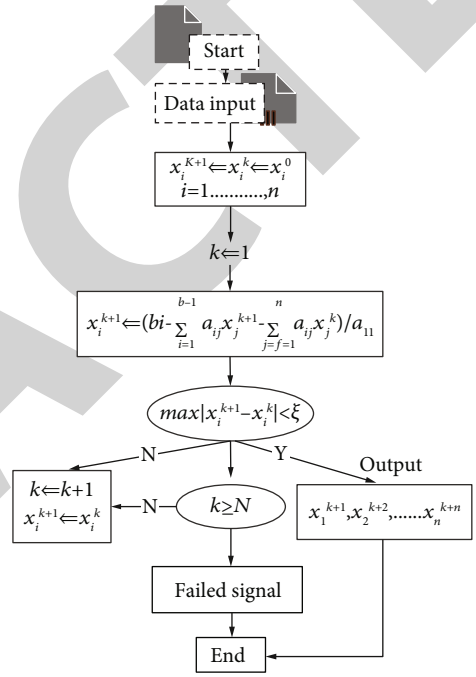

Figure 2: Iterative flowchart.

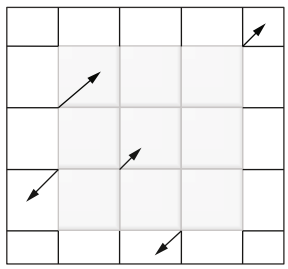

Figure 3: Schematic diagram of the predictable part of the coefficient matrix classification.

signals include system clock, enable signal, attention information, disparity information, and matching feature point coordinates, and output includes read and write address signals, predictable coefficients, and unpredictable coefficients.

In Figure 3, the upper left dashed box calculates the predictable part of the coefficient, and the lower left box calculates the unpredictable part of the coefficient. The STATE_

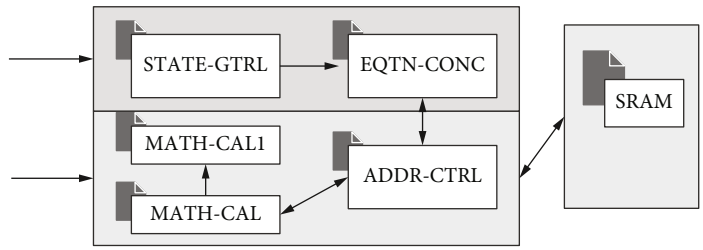

Figure 4: Block diagram of coefficient matrix equation.

CTRL module determines which category position the currently calculated coefficient is in, calculates the coefficient under the current category accordingly, and stores it in SRAM. The unpredictable part is responsible for processing the coefficients of the parallax part, and the input data has parallax, coordinates, and attention degree weights. There are two mathematical operation modules shown in Figure 4. Among them, MATH_CALl is responsible for calculating the precoefficient in the formula, and ADDR_CTRL reads the predictable part of the coefficient that has been stored before from SRAM. MATH_CAL is responsible for superimposing the disparity item on the data and then storing it back into SRAM through ADDR_CTRL.

It is worth noting that although the coefficient matrix has strong regularity and periodicity, it is also random due to the existence of characteristic points. This makes it more difficult for us to read and store correlation coefficient data. Usually, when we do a row of vector multiplication, we first take out the entire row of coefficients and then perform the multiplication in order. Once there are feature points in this row, the coefficient matrix will be very different. As shown in Figure 5, the green dots represent the impact of feature points, usually in 4 locations near them. Taking into account the convenience of storing data, we have adopted a certain margin for each row in the design process to ensure that there will be no overflow in the case of feature points. For the nonzero value of each row in the matrix, 12 storage units are opened up. If there is no coefficient storage at this position, the system skips directly, so as to ensure that the addressing is correct during the next iteration after one iteration.

The most important thing for the iterative method is the number of iterations, which is related to efficiency, resource consumption, and timing stability. Therefore, we need to set a good threshold and maximum number of iterations to ensure that we will not enter an endless loop. The measurement standard is that the accuracy is as close to the real solution as possible. However, considering that decimal points are not supported in FPGAs, we use fixed-point decimals instead of floating-point numbers.

Fixed-point decimal operations assume that x represents an actual number (floating-point number), and q represents its on-type fixed-point decimal number (an integer).

$$\begin{aligned} q &= (\text{int})(x * 2^n), \\ x &= (\text{float})\left(\frac{q}{2^n}\right). \end{aligned} \tag{21}$$

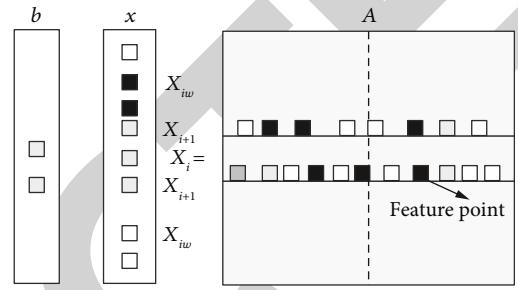

Figure 5: Schematic diagram of iterative solution operation.

From the above formula, we can get the "+," "-," and "∗" operations for fixed-point decimals.

If it is assumed that the values represented by q_1, q_2, and q_3 are x_1, x_2, x_3, respectively, we can define four arithmetic modes as follows:

$$\begin{cases} q_3 = q_1 \pm q_2 \Rightarrow x_3 = x_1 \pm x_2, \\ q_3 = q_1 \times \dfrac{q_2}{2^n} \Rightarrow x_3 = x_1 \times x_2, \\ q_3 = q_1 \times \dfrac{2^n}{q_2} \Rightarrow x_3 = \dfrac{x_1}{x_2}. \end{cases} \tag{22}$$

We can see that there is no difference between addition and subtraction operations and general addition and subtraction. For multiplication and division, a shift operation is used to keep the position of the decimal point unchanged, which involves rounding. For 32 digits with 10 fixed-point decimals, the accuracy can reach 0.000976. The method used in this paper is compared with the two sets of solutions of the matrix equation direct floating-point number solution. Because of the use of fixed-point decimals in this article, the iterative convergence judgment cannot achieve the same high-precision results as floating-point numbers. Therefore, the solution obtained by the method used in this article has a certain degree of deviation. The higher the fixed-point decimal places, the smaller the deviation. The average deviation for 8-digit fixed-point decimals is 0.89%, the deviation for 9-digit fixed-point decimals is 0.51%, and the deviation for 10-digit fixed-point decimals is 0.23%. For a virtual viewpoint image with a resolution of 640 ∗ 360, an error of 0.89% means that the overall horizontal offset has reached 5 pixels, a deviation of 0.51% has an offset of 3

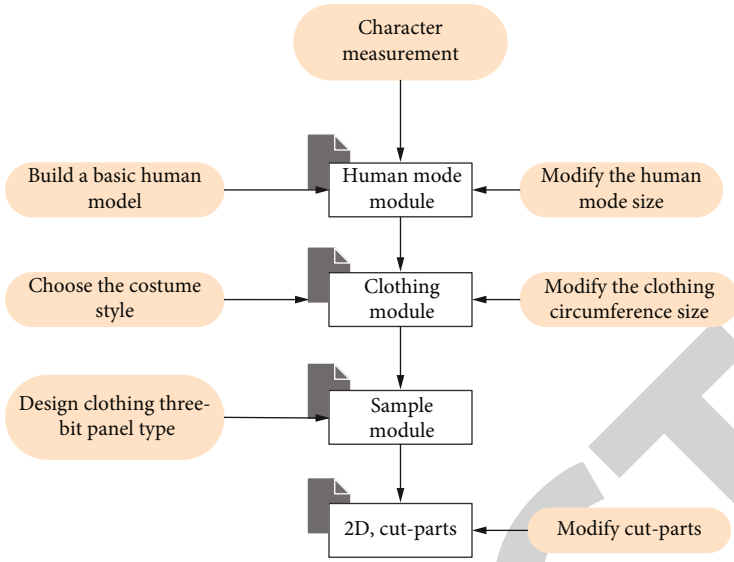

Figure 6: Operation flowchart of virtual design.

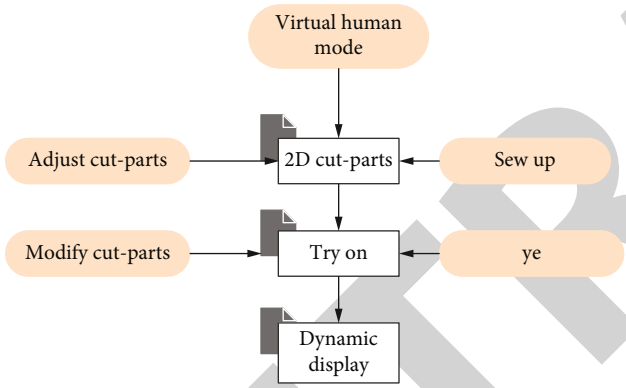

Figure 7: Operation flowchart of 3D virtual fitting software.

pixels, and an error of 0.23% as a pixel, the naked eye will not make a strong sensory distinction. When the number of digits is higher, the deviation will be smaller, and higher fixed-point decimals can be used when higher precision is required.

4. Digital Song and Dance Costume Design System Based on Intelligent Deep Learning Algorithm

Three-dimensional cutting software is a form of computer-aided virtual song and dance costume design system development. It integrates the advantages of three-dimensional cutting and plane plate making and adopts a more scientific and reasonable method in the conversion of 3D and 2D in song and dance costume design, which has set off a more time-saving and efficient era of machine electronics industry in the field of song and dance costumes. The operating steps of the three-dimensional virtual three-dimensional cutting software operating system are shown in Figure 6, and the operating flowchart of the three-dimensional virtual fitting software is shown in Figure 7.

Figure 8: A case of a mannequin in digital song and dance costume design.

Based on the support of the above models, the three-dimensional mannequin constructed in this article when designing digital song and dance costumes is shown in Figure 8.

Figure 9: Case of song and dance costume design.

Table 1: Feasibility evaluation of virtual design of song and dance costumes.

No.	Feasibility	No.	Feasibility
1	92.61	17	95.87
2	96.00	18	96.07
3	96.78	19	96.14
4	95.10	20	95.93
5	93.52	21	91.91
6	92.22	22	95.44
7	91.71	23	95.54
8	96.68	24	91.28
9	94.02	25	95.87
10	96.42	26	93.25
11	94.78	27	92.29
12	93.60	28	96.42
13	92.02	29	91.74
14	91.78	30	91.95
15	96.91	31	91.98
16	93.73	32	93.50

The costume design of song and dance is carried out in the system model invested and built in this article. Figure 9 shows a case of song and dance costume design.

After the song and dance costume simulation is completed, it needs to be subjectively evaluated to analyze the feasibility of the song and dance costume virtual design. First of all, the model establishes subjective evaluation items and evaluation scales for visual simulation effects based on the virtual evaluation of song and dance costumes, which is convenient for evaluators to evaluate the similarity between the

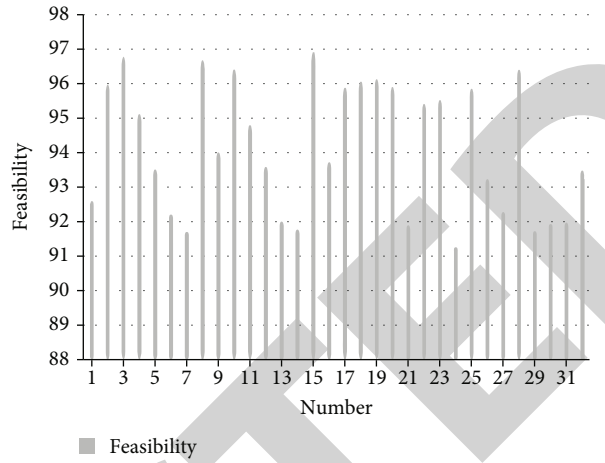

Figure 10: Statistical diagram of feasibility evaluation.

Table 2: Evaluation of the design effect of song and dance costumes.

No.	Design effect	No.	Design effect
1	87.20	16	87.76
2	83.17	17	88.50
3	89.23	18	89.92
4	88.69	19	90.03
5	82.94	20	87.71
6	83.26	21	87.53
7	82.99	22	88.54
8	88.86	23	84.27
9	84.16	24	88.07
10	86.68	25	90.35
11	90.18	26	81.84
12	90.72	27	91.02
13	86.96	28	83.31
14	88.25	29	90.77
15	88.95	30	86.41
16	87.76	31	88.98
17	88.50	32	91.00

simulation effects of song and dance costumes and the physical objects. Then, it analyzes the similarity between each song and dance costume simulation and the real object based on each evaluation item. Finally, it analyzes the grade evaluation scores of each evaluation item based on all simulated song and dance costumes and obtains conclusions related to the simulation effect. The feasibility of the system proposed in this paper for virtual design of song and dance costumes is evaluated, and the results are shown in Table 1 and Figure 10.

From the above research, we can see that the digital song and dance costume design system based on intelligent deep learning algorithm proposed in this paper has certain feasibility. Afterwards, the digital song and dance costume design system based on the intelligent deep learning algorithm is

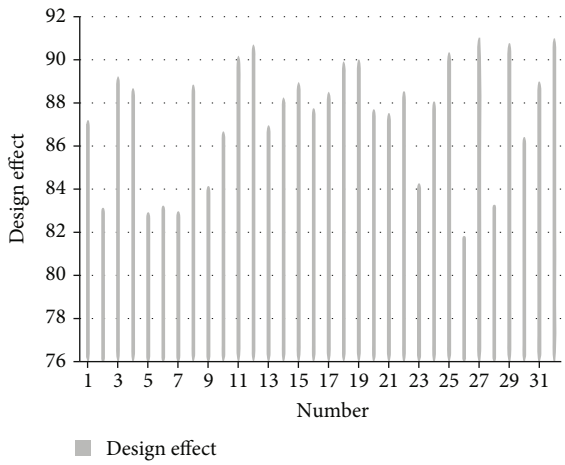

Figure 11: Statistical diagram of the evaluation of the design effect of song and dance costumes.

evaluated for the effect of the song and dance costume design, and the results shown in Table 2 and Figure 11 are obtained.

From the above research, it can be seen that the digital singing and dancing costume design system based on intelligent deep learning algorithm proposed in this article has good effects in the design of singing and dancing costumes.

5. Conclusion

On the stage, general costumes become special, which draw the audience's attention to the role around a certain event, script requirements, and drama creator's ideas. Characters are composed of body, movements, sounds, expressions, costumes, makeup, and other components, and costumes are part of the characters, which exist in the specific theater space and stage scenes. Moreover, it expresses certain drama content through intuitive image packaging. For musicals, it is established that people can look at their faces. Whether the costume is the "trademark" of the protagonist or the "trademark" of the supporting role, it can turn actors into kings or tramps, soldiers or servants, ladies or prostitutes. In musicals, costumes are the most external and common means of determining a character. Whether it is realism or symbolic suggestion, clothing can express gender, age, social class, occupation, nationality, ethnicity, religion, etc. Sometimes, it also reflects the spirit of a particular era. This article combines the deep learning algorithm to improve the digital algorithm, builds a song and dance costume design system to improve the effect of song and dance costume design, and improves the intelligence of the song and dance costume design process.

Data Availability

The labeled dataset used to support the findings of this study are available from the corresponding author upon request.

Conflicts of Interest

The author declares no competing interests.

Acknowledgments

This study is sponsored by Project of the Key Research Plan of the Education Department of Shaanxi Province in 2021 (Project of Key Philosophy and Social Science Research Base) "Cabaret clothing research in Shaanxi province" (21 JZ028) and the Key Philosophy and Social Science Project of Xi'an Polytechnic University "Clothing diversity research of ethnic song and dance along the silk road countries" (2019 ZSZD02).

References

[1] S. Cho, "Exploring theatrical costume design as a pedagogical tool for empathic design," *International Journal of Fashion Design, Technology and Education*, vol. 12, no. 1, pp. 12–22, 2019.

[2] T. Helve, "Political by design: costume design strategies within the Finnish contemporary dance productions AmazinGRace, noir? And the earth song," *Nordic Journal of Dance*, vol. 9, no. 1, pp. 14–31, 2018.

[3] P. Li, C. Yu, and C. Wu, "Customer-centered co-design modularization: the skirt design on mobile application," *The Journal of The Textile Institute*, vol. 110, no. 11, pp. 1538–1544, 2019.

[4] P. Wei, J. Jiang, and L. Li, "The application of image analysis technology in the extraction of human body feature parameters," *EURASIP Journal on Image and Video Processing*, vol. 2018, no. 1, 2018.

[5] E. Brayshaw, "Unraveling psychologically: knitting in performance costume and the themes of you got older (2015)," *TEXTILE*, vol. 18, no. 4, pp. 344–354, 2020.

[6] S. Churchill, "Revolutionary threads: the mediation of gender and political identity in the 'new Irish dance costume', 1917–37," *Gender & History*, vol. 31, no. 1, pp. 153–177, 2019.

[7] A. S. D. Fashion, "Dress, costume: a proposed terminological clarification in the historical research of women's clothing," *Anuarul Institutului de Cercetări Socio-Umane Gheorghe Șincai al Academiei Române*, vol. 24, pp. 194–212, 2021.

[8] K. H. Karamova, A. A. Mukhametshin, M. M. Makhmutova, and S. F. Usmanov, "Role of the "green" philosophy and bionics on the development of ecodesign clothing," *Helix*, vol. 9, no. 4, pp. 5204–5207, 2019.

[9] I. Sirotkina, "Costume as truth and as a new mythology: dressed performances of perestroika," *Fashion Theory*, vol. 22, no. 2, pp. 199–217, 2018.

[10] J. Olsson, "Shooting and shopping: suiting grant and dressing saint," *Film, Fashion & Consumption*, vol. 8, no. 1, pp. 49–69, 2019.

[11] A. Mochama, "Interpretations of television aesthetics: a mise-en-scene analysis in audio-visual Coca-Cola commercials," *International Journal of Research and Scholarly Communication*, vol. 3, no. 1, pp. 14–30, 2020.

[12] L. Colpaert, "Costume on film: how the femme fatale's wardrobe scripted the pictorial style of 1940s film noir," *Studies in Costume & Performance*, vol. 4, no. 1, pp. 65–84, 2019.

Hindawi
Journal of Sensors
Volume 2023, Article ID 9804026, 1 page
https://doi.org/10.1155/2023/9804026

Retraction

Retracted: Optimization of Agricultural Machinery Task Scheduling Algorithm Based on Multiobjective Optimization

Journal of Sensors

Received 19 December 2023; Accepted 19 December 2023; Published 20 December 2023

This article has been retracted by Hindawi following an investigation undertaken by the publisher [1]. This investigation has uncovered evidence of one or more of the following indicators of systematic manipulation of the publication process:

(1) Discrepancies in scope
(2) Discrepancies in the description of the research reported
(3) Discrepancies between the availability of data and the research described
(4) Inappropriate citations
(5) Incoherent, meaningless and/or irrelevant content included in the article
(6) Manipulated or compromised peer review

The presence of these indicators undermines our confidence in the integrity of the article's content and we cannot, therefore, vouch for its reliability. Please note that this notice is intended solely to alert readers that the content of this article is unreliable. We have not investigated whether authors were aware of or involved in the systematic manipulation of the publication process.

Wiley and Hindawi regrets that the usual quality checks did not identify these issues before publication and have since put additional measures in place to safeguard research integrity.

We wish to credit our own Research Integrity and Research Publishing teams and anonymous and named external researchers and research integrity experts for contributing to this investigation.

The corresponding author, as the representative of all authors, has been given the opportunity to register their agreement or disagreement to this retraction. We have kept a record of any response received.

References

[1] L. Zheng, "Optimization of Agricultural Machinery Task Scheduling Algorithm Based on Multiobjective Optimization," *Journal of Sensors*, vol. 2022, Article ID 5800332, 12 pages, 2022.

Hindawi
Journal of Sensors
Volume 2022, Article ID 5800332, 12 pages
https://doi.org/10.1155/2022/5800332

Research Article

Optimization of Agricultural Machinery Task Scheduling Algorithm Based on Multiobjective Optimization

Liang Zheng

School of Mechanical Engineering, Xihua University, Chengdu 610039, China

Correspondence should be addressed to Liang Zheng; zhengliang@mail.xhu.edu.cn

Received 2 December 2021; Revised 3 January 2022; Accepted 17 January 2022; Published 7 February 2022

Academic Editor: Wei Zhang

In order to improve the effect of agricultural machinery task scheduling, this paper starts from the perspective of multiobjective optimization to achieve task scheduling based on multiobjective particle swarm optimization algorithm. The position of each particle is a combination of resource options for each construction activity, and the displacement range and speed range of the particles are determined. Moreover, this paper uses the method of introducing an external storage library to store the current noninferior solutions and uses the adaptive grid method and the roulette selection method to select the global optimal solution of the particles. In addition, this paper proposes a task scheduling algorithm suitable for modern agricultural machinery based on the actual needs of current agricultural machinery task scheduling. The experimental results show that the agricultural machinery task scheduling algorithm based on multiobjective optimization proposed in this paper has a good agricultural machinery task scheduling effect and meets the basic purpose of optimizing the algorithm in this paper.

1. Introduction

With the development of the times, farmers' demand for agricultural machinery has become more and more urgent, and organizations such as agricultural cooperatives have gradually emerged. However, with the rapid development of agricultural mechanization, many problems have gradually emerged, which restrict the rapid development of agricultural mechanization. First, traditional agricultural production does not have a sound management system and lacks a reasonable number of management personnel, and agricultural production personnel are not strong in technical ability, have insufficient knowledge of agricultural machinery, and have weak maintenance capabilities. Second, due to the constraints of geographical location and economic level, some areas cannot increase investment in agricultural machinery, which largely restricts the development of regional agricultural mechanization. Third, with the development of agricultural mechanization, the increasing investment in agricultural machinery, and the expansion of management scale, the problems of lagging agricultural management informatization, poor timeliness, and low information utilization have emerged. Moreover, it is difficult for managers to obtain agricultural machinery operation information and operating conditions in a timely and accurate manner, and they cannot reasonably schedule and allocate agricultural machinery [1].

With the further development of science and technology, Geographic Information System (GIS), Communication Packet Radio Service (GPRS), and Global Positioning System (GPS) have made considerable progress. Remote monitoring and management systems using 3S (GIS, GPRS, and GPS) and other key technologies have been widely used in transportation, logistics, and other fields. The application of these technologies also provides effective means for agricultural machinery information supervision services. A complete agricultural supervision system is composed of computer hardware and software, and it has functions such as automatic data collection, automatic monitoring, and business processing and integrates 3S technology and network technology to realize the system of remote collection and real-time monitoring of agricultural resources [2]. With the rise of land transfer policies, farmers have formed large-scale management entities by transferring land contractual management rights.

Moreover, the vast majority of farmers continue to explore in actual production, which promotes the formation of agricultural machinery service organizations and the emergence of agricultural machinery social services [3].

Agricultural machinery socialization services connect limited agricultural machinery with scattered farmers. Farmers no longer face huge purchase pressure and do not need to bear the high cost of operation and maintenance of agricultural machinery. On the other hand, it also improves the utilization rate of agricultural machinery resources. The agricultural machinery service organization is the carrier of the socialized agricultural machinery service. It has gone through multiple stages of development: agricultural machinery giants, agricultural machinery associations, agricultural machinery joint-stock cooperative organizations, and intermediary service organizations. Over the years, the forms of socialized agricultural machinery services have also continued to innovate, from organic households' mutual assistance to farming, to joint household operations, to joint-stock cooperative operations and cross-regional operations, fundamentally solve the problems of large-scale operation of agricultural machinery and small-scale production of hundreds of millions of farmers. The socialization of agricultural machinery services includes agricultural machinery service providers and demanders. Agricultural machinery service providers include agricultural machinery cooperative organizations and agricultural production operation contracting companies. They purchase agricultural machinery of different types of operations on a large scale to provide agricultural machinery demanders. Agricultural machinery operation services, agricultural machinery service demanders, such as contracted land managers and individual farmers, buying agricultural machinery by themselves is neither realistic nor economical, but there is an urgent need for agricultural machinery operations. The agricultural machinery service demand side publishes its own operation requirements, including constraints on the operation site, operation type, and operation time. The agricultural machinery service provides a large number of operation requirements, combined with the existing agricultural machinery resources, and requires the allocation of each farmland operation appropriate agricultural machinery and planning an appropriate driving route for each agricultural machinery, so as to maximize the use of resources. This new agricultural machinery operation mode has derived a new research topic, that is, the agricultural machinery scheduling problem studied in this article.

Based on the above analysis, this paper applies the multiobjective optimization research algorithm to agricultural machinery task scheduling and proposes a task scheduling algorithm suitable for modern agricultural machinery to improve the efficiency of agricultural machinery task scheduling and improve agricultural machinery management efficiency and agricultural machinery production efficiency.

2. Related Work

Reasonably plan the time for a variety of agricultural production operations. In this process, the available time, labor, agricultural machinery resources, operation priority, and crop conditions are considered as important factors. Literature [4] proposes that there are two basic scheduling problems in the field of agricultural production: the first is a pure scheduling problem. For each job, the start time and end time of the job need to be determined in advance; the second is that the continuous scheduling problem requires that the resources shared by multiple jobs need to be organized in an orderly manner. He also first proposed a scientific method to solve scheduling problems in the agricultural field, which was mainly based on linear programming and simulation. Early methods could only solve pure scheduling problems. Literature [5] applies typical scheduling problems in the industrial field (such as job shop scheduling problems and flow shop scheduling problems) to continuous scheduling of agricultural field operations. Literature [6] proposes a special operation method for the VRP problem in the agricultural field to solve the planning and scheduling problems of field operations and has achieved good results in the scheduling of various types of agricultural operations. Literature [7] established a complete set of mathematical models for agricultural machinery continuous operation scheduling. The model includes input, data preprocessing, scheduling, and output. The output results include the agricultural machinery operation Gantt chart and the estimated cost of the scheduling plan. Solve the problem of continuous operation scheduling of agricultural machinery. Literature [8] combines neural network (NN) and genetic algorithm (GA) to optimize the path of agricultural robots. Through the high learning ability of NN, it can recognize the movement of the complex agricultural robot nonlinear system. The literature [9] improved the BRUSPLAN model based on the idea of integer planning for the planting of vegetable crops and established a two-stage stochastic linear programming (stochastic linear programming) model. Literature [10] established a linear programming model for rapeseed harvesting operations. The model considered resource constraints and operating time constraints and proposed two heuristic algorithms to solve the problem. The first method takes the operating rate as the primary optimization objective. The two methods meet the time window requirements as much as possible and optimize the starting time of each job. Literature [11] uses greedy algorithm and tabu search algorithm to optimize the scheduling path of agricultural machinery. The scheduling model takes into account the time lag caused by factors such as limited equipment and staff. The solution method of commercial integer programming software is adopted to solve a feasible scheduling plan within a reasonable calculation time. Literature [12] divides the agricultural machinery scheduling process into four independent steps: agricultural machinery allocation, farmland area coverage, agricultural machinery scheduling path generation, and secondary adjustment of the scheduling plan. Literature [13] studied the minimization of nonoperating mileage (that is, the transfer distance, excluding the mileage during internal operations of farmland) in the process of agricultural machinery scheduling. Regarding the problem as a binary integer programming problem, the path is optimized by calculating the traversal

sequence of parallel paths. Experiments show that the best traversal sequence is the optimal solution for minimizing nonoperating mileage.

Literature [14] proposed a two-stage metaheuristic algorithm combining simulated annealing algorithm and genetic algorithm and hybrid Petri network model to optimize the allocation and scheduling of agricultural machinery resources. In the first stage, the simulated annealing algorithm is used to optimize the resource allocation plan; in the second stage, the genetic algorithm is used to determine the priority of the job and generate the agricultural machinery scheduling plan according to the hybrid Petri network model. Literature [15] conducts detailed research and classification of agricultural machinery operation scheduling in order to abstract the common characteristics of different operation scenarios, establish a connection with traditional vehicle scheduling problems, and distinguish between agricultural machinery scheduling problems and vehicle scheduling problems with time windows. Literature [16] studied the dynamic agricultural machinery scheduling problem containing uncertain factors and proposed an abstract two-dimensional grid to create discrete transition nodes in the grid state space. Use the graph search algorithm to generate the optimal path. This algorithm improves the operation efficiency of agricultural machinery, and the calculation efficiency of the algorithm is high. It is suitable for multiple types of agricultural machinery to participate in the large-scale dynamic agricultural machinery scheduling problem at the same time.

3. Task Scheduling Algorithm Based on Multiobjective Optimization

The velocity update formula of the single-objective particle swarm optimization algorithm is shown in Equation (1), and the position update formula is shown in Equation (2). The optimal solution satisfying the termination condition is obtained through continuous iterations.

$$v_i(t+1) = w \cdot v_i(t) + c_1 \cdot r_1(p_i(t) - x_i(t)) + c_2 \cdot r_2\left(p_g(t) - x_i(t)\right), \tag{1}$$

$$x_i(t+1) = x_i(t) + v_i(t+1). \tag{2}$$

In the formula, $i = 1, 2, 3, \cdots, I$. I is the total number of particles in the particle population; $t = 1, 2, 3, \cdots, T$. T is the limit number of iterations; $v_i(t)$ is the velocity of the (i) particle at the (t)-th iteration; $x_i(t)$ is the position of the (i) particle at the (t)th iteration; $p_i(t)$ is the individual historical optimal solution of the pbest particle; p_g(t) is the global optimal solution of the gbest particle; w is the inertia weight, which is nonnegative and is used to control the effect of the previous velocity on the current velocity; r_1 and r_2 are two random numbers, taking values in the range $[0, 1]$; c_1 and c_2 are acceleration constants, that is, learning factors.

Since the optimization objective of this paper is to trade-off the duration of agricultural machinery operations, the cost of agricultural machinery operations, and the quality of agricultural machinery operations, achieving this optimization search process requires the use of a multiobjective particle swarm optimization algorithm (MOPSO). In the multiobjective particle swarm optimization algorithm, (t) and $Rh(t)$ in Equation (3) are used instead of $pi(t)$ and $pg(t)$, respectively. The velocity update equation of the particle is shown in [17]

$$v_i(t+1) = w \cdot v_i(t) + c_1 \cdot r_1(P_i(t) - x_i(t)) + c_2 \cdot r_2\left(R_g(t) - x_i(t)\right). \tag{3}$$

In the formula, $p_i(t)$ is the individual historical optimal solution of the particle selected by the dominating relationship; $p_g(t)$ is the global optimal solution of the particles selected from the external storage library in t iterations.

Particle position and velocity have a range of values. After the particle initialization and update, the particle position and velocity values that are out of the range should be adjusted. Values smaller than the lower limit are changed to the lower limit, and values larger than the upper limit are changed to the upper limit. The inertia weight ω is used to control the effect of the previous velocity on the current velocity. In this paper, a typical linear decreasing inertia weight is used, as shown in Equation (4). The inertia weight decreases linearly with the number of iterations, and the inertia weight is maximum at the beginning to explore larger regions and quickly locate the approximate location of the optimal solution; after which the inertia weight gradually decreases and fine local exploration begins. Two random numbers r_1 and $r_2$are randomly taken in the range of $[0, 1]$ to increase the randomness of the search. The learning factors c_1 and c_2 are used to regulate the maximum step size of learning, and both are taken as 2 in this paper.

$$w(t) = w_{\max} - \frac{w_{\max} - w_{\min}}{t_{\max}} \times t. \tag{4}$$

In the formula, $w(t)$ is the value of inertia weight in t iterations. $w_{\max}$ is the maximum value of inertia weight, which is set to 0.95 in this paper. $w_{\min}$ is the minimum value of inertia weight, which is set to 0.4 in this paper, and $t_{\max}$ is the maximum number of iterations [18].

To establish a multiobjective particle swarm optimization model, the following key issues need to be solved: one is how to choose the individual historical optimal solution of the particle; the other is how to choose the global optimal solution of the particle. Regarding the individual historical optimal solution of selecting particles and for multiobjective optimization problems, it is impossible to directly compare the pros and cons of the two solutions. We use the dominance relationship to select, that is, select the nondominated solution as the individual historical optimal solution based on the Pareto principle. If the dominance relationship between the two cannot be judged, it is selected at random. Regarding the selection of the global optimal solution of the particles, there are various solutions such as the elite set strategy, the niche mirror method, and the adaptive mesh density method. This paper adopts the method of

introducing an external storage library to determine the global optimal solution. The function of the external storage library is to store the current noninferior solutions and select the global optimal solution of the particles in it. The external repository consists of two parts: archive controller and grid. This method uses both the adaptive grid density method and the roulette method.

The role of the archive controller is to determine whether to add a solution to the grid of the external repository. After the particle swarm has selected the current new noninferior solution, the process of judging whether the solution NS (new solution) is stored in the external storage library is as follows. If the external repository is empty, the solution is stored. If solution $S1$ already exists in the external storage and $S1$ dominates NS, then solution $S1$ is still stored. If solution $S1$ already exists in the external storage and NS dominates $S1$, then solution NS is stored and solution $S1$ is removed. If solution $S1$ already exists in the external repository and NS and $S1$ have no dominance relationship, then the solutions NS and $S1$ are stored, that is, the dominated solution will not be stored in the external repository, as shown in Figure 1.

The role of the grid is to generate a Pareto solution set with uniform distribution. In this paper, the density of the particles in the noninferior solution set is determined according to the adaptive grid density, and the global optimal solution is selected according to the particle density information. The grid is actually an objective function space formed by multiple hypercubes (unit grids), and the dimension of the hypercube is consistent with the number of objective functions. Take the optimization problem in this paper as an example; the grid is a three-dimensional space, and the specific steps are as follows:

The first step is to determine the boundary of the grid. In the t-th iteration, the grid boundary is $(\min \mathrm{PT}^t, \max \mathrm{PT}^t)$, $(\min \mathrm{PC}^t, \max \mathrm{PC}^t)$, and $(\min \mathrm{PQ}^t, \max \mathrm{PQ}^t)$, and $\min \mathrm{PT}^t$ and $\max \mathrm{PT}^t$ are the smallest and largest calculated by the PT objective function of the particles that have been stored in the external storage library. The fitness value is the same for the rest.

The second step is to calculate the modulus length of each grid, as shown in Equation (5). The grid in this paper is the objective function space formed by $D \times D \times D$ hypercubes.

The third step is to calculate and determine the grid numbers of all particles stored in the external storage library, as shown in Equation (6) [19].

$$\begin{aligned} \triangle \mathrm{PT}^t &= \frac{\max \mathrm{PT}^t - \min \mathrm{PT}^t}{D} \triangle \mathrm{PC}^t = \frac{\max \mathrm{PC}^t - \min \mathrm{PC}^t}{D} \triangle \mathrm{PQ}^t \\ &= \frac{\max \mathrm{PQ}^t - \min \mathrm{PQ}^t}{D}. \end{aligned} \tag{5}$$

In the formula, $\Delta \mathrm{PT}^t$ is the modulus length of the grid in the direction of the objective function PT during t iterations. $\Delta \mathrm{PC}^t$ is the modulus length of the grid in the direction of the objective function PC during t iterations. $\Delta \mathrm{PQ}^t$ is the modulus length of the grid in the direction of the objective function PQ during t iterations. D is the divisor, which can determine the number of hypercubes (unit grids) in the grid, and the study by Coello and Lechuga suggests a value range of 30-50.

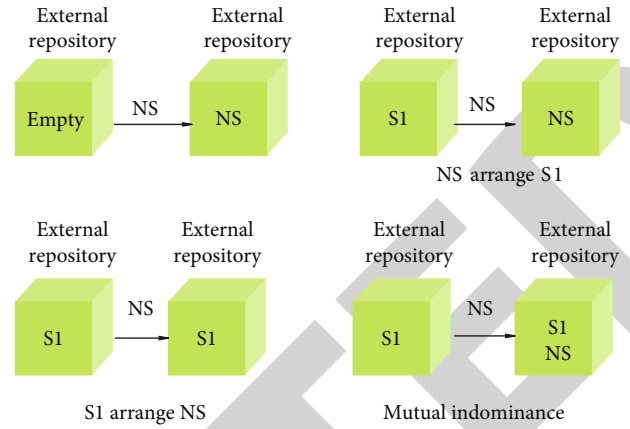

Figure 1: Schematic diagram of the role of the archive controller.

$$\mathrm{Int}\left(\frac{\mathrm{PT}_i^t - \min \mathrm{PT}^t}{\triangle \mathrm{PT}^t}\right) + 1\, \mathrm{Int}\left(\frac{\mathrm{PC}_i^t - \min \mathrm{PC}^t}{\triangle \mathrm{PC}^t}\right) + 1\, \mathrm{Int}\left(\frac{\mathrm{PQ}_i^t - \min \mathrm{PQ}^t}{\triangle \mathrm{PQ}^t}\right) + 1. \tag{6}$$

In the formula, PT_i^t is the fitness value calculated by the PT objective function of particle i in t iterations. Int is a function of rounding down.

The fourth step is to determine the number of particles in each grid, that is, the particle density. The fifth step uses the roulette selection method to select the global optimal solution.

In order to ensure the diversity of noninferior solution sets and explore more space, the lower the particle density in the grid, the greater the probability of being selected. Coello and Lechuga proposed to use 10 divided by the number of particles in the unit grid x_i as the fitness of the i-th unit grid $f(x_i)$ $(i = 1, 2, \cdots, N)$, and N is the number of unit grids that hold particles. The algorithm calculates the fitness ratio, that is, the ratio of the fitness of the i-th unit grid to the sum of all fitness, as shown in Equation (7). The algorithm calculates the cumulative probability q_i, that is, the sum of the fitness ratios from the first unit grid to the i-th unit grid, as shown in Equation (8). The algorithm randomly generates $r \in [0, 1]$. The algorithm starts from q_1. If $q_1 > r$, the unit grid 1 is selected. If $q_1 < r$, then $i + 1$, and then, the algorithm judges q_2 until $q_i > r$, the unit grid i is selected. Then, the algorithm randomly generates $r \in [0, 1]$ again to judge from q_1 and makes a total of N selections. The algorithm determines the unit grid that has been selected the most times (the number may be greater than 1) and randomly selects a particle in the determined grid as the global optimal solution.

$$p(x_i) = \frac{f(x_i)}{\sum_{j=1}^{N} f(x_j)}. \tag{7}$$

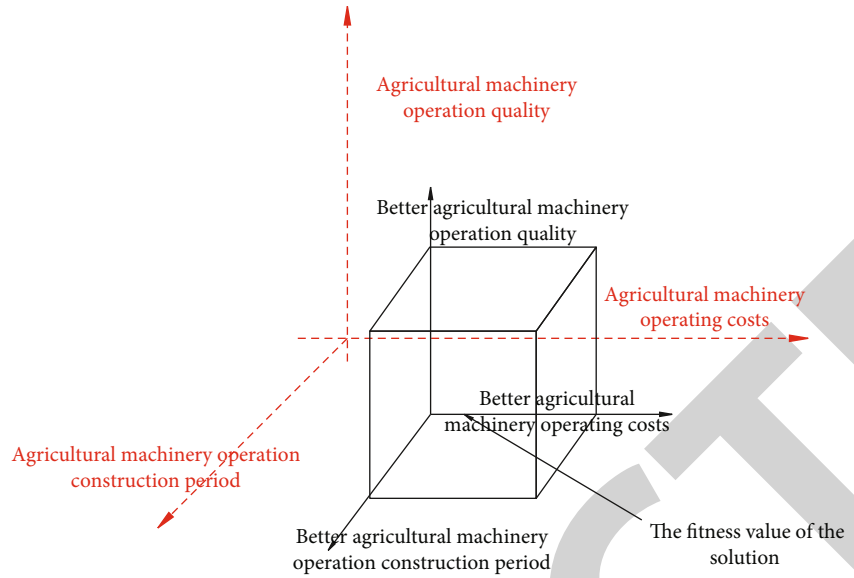

Figure 2: Schematic diagram of the optimization goal of agricultural machinery operation scheduling.

In the formula, $p(x_i)$ is the fitness ratio of the unit grid x_i and $f(x_i)$ is the fitness of the unit grid x_i.

$$q_i = \sum_{j=1}^{i} p(x_j). \tag{8}$$

In the formula, q_i is the cumulative probability of the unit grid x_i.

If the particles in the external storage library have reached the set maximum allowable capacity, it is necessary to remove the relatively low-quality solutions (particles). In order to ensure the uniformity and diversity of the noninferior solution set, the particles in the grid with higher density are removed. Particle removal only considers the unit grid with the number of particles greater than or equal to 2, which is expressed in the research of Yang Junjie and others, as shown in

$$\mathrm{CO}_k = \mathrm{Int}\left(\frac{|A_t| - L}{|A_t|} \times \mathrm{G}_{k,2}\right) + 0.5. \tag{9}$$

In the formula, CO_k is the number of particles that need to be removed in the unit grid k. L is the maximum allowable capacity of the number of particles stored in the external storage library, which is artificially specified. $|A_t|$ is the number of particles in the external storage library at t iterations. $G_{k,2}$ is the number of particles in the unit grid k where the number of particles is greater than or equal to 2.

The optimization objective of this paper is to minimize the duration and cost of agricultural machinery operations while maximizing the quality performance of agricultural machinery operations, that is, to obtain a Pareto optimal solution that weighs duration-cost-quality of agricultural machinery operations.

The optimization model of agricultural machinery operation scheduling in this paper takes the resource options of each agricultural machinery operation activity of the project as the decision variables, considers the priority constraints among agricultural machinery operation activities, and contains the following three objective functions, as shown in Equations (10), (11), and (12), to evaluate the duration of agricultural machinery operation, cost of agricultural machinery operation, and quality of agricultural machinery operation of the project, respectively. The objective functions are used to calculate the fitness values as a basis for meritocracy among particles, as shown in Figure 2.

The minimized agricultural machinery operation duration is

$$PT_{\min} = \sum_{i=1}^{I} T_{i,n}. \tag{10}$$

In the formula, i is the serial number of the agricultural machinery operation activity, $i = 1, 2, \cdots, I$. n is the serial number of the resource option, $n = 1, 2, \cdots, N$. $T_{i,n}$ is the agricultural machinery operation activity on the critical path (i) selection of resource options (n) continuous agricultural machinery operation duration.

Since the optimization model considers the priority constraints among agricultural machinery operation activities, the minimized agricultural machinery operation duration is the minimized critical path agricultural machinery operation duration, and the critical path is the route with the longest duration among agricultural machinery operation routes.

The minimized agricultural machinery operation cost is

$$PC_{\min} = \sum_{i=1}^{I} C_{i,n}. \tag{11}$$

In the formula, $C_{i,n}$ is the agricultural machinery

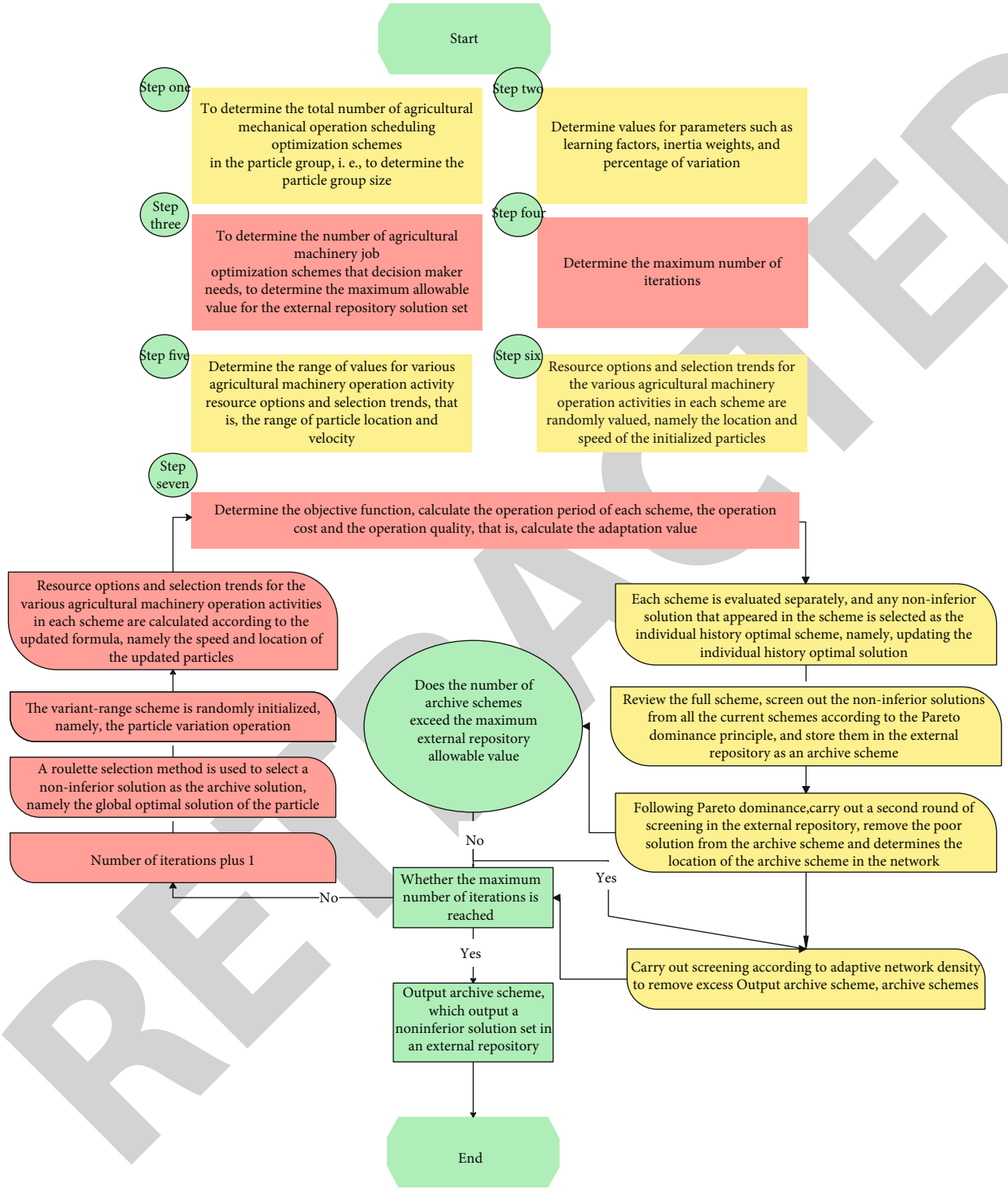

Figure 3: Flowchart of the MOPSO-CSO model.

operating cost consumed when the agricultural machinery operating activity (i) selects the resource option (n).

Due to the need to consider the individual costs of various agricultural machinery operations, the agricultural machinery operating costs in this paper are the direct construction costs of the project quota, that is, the sum of labor costs, material costs, and agricultural machinery operating equipment. The agricultural machinery operating cost of this optimization model does not include enterprise management fees, general risk fees, profits, measurement fees, supervision fees, safe and civilized agricultural machinery operating fees, and taxes. In the case of constant rates, these costs do not affect the comparison of optimization plans, and decision-makers can schedule the final agricultural

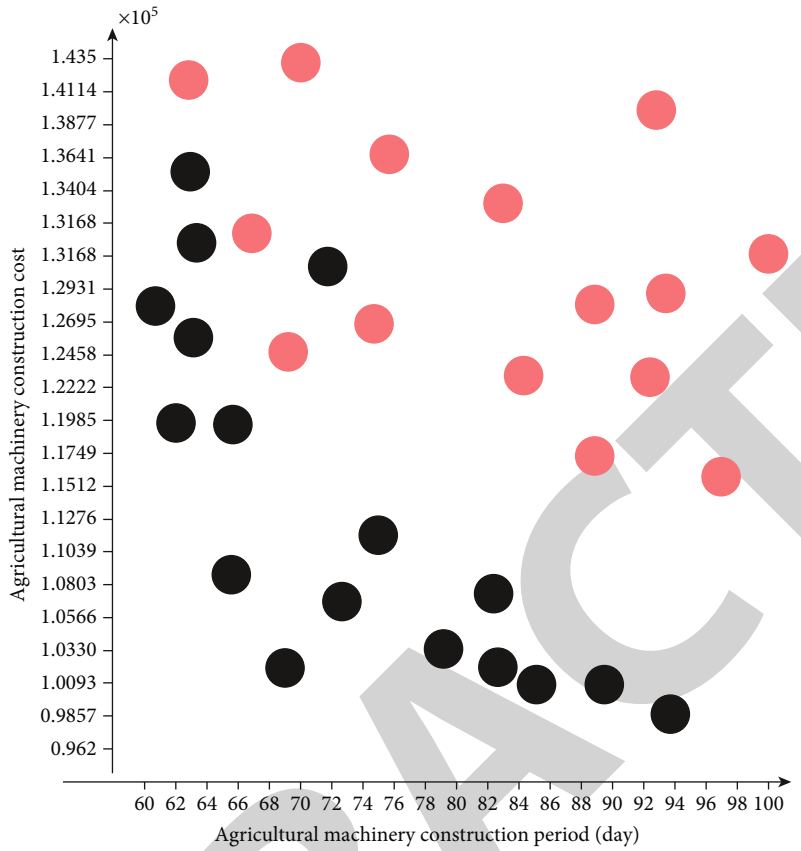

Figure 4: Optimization and iteration results of the MOPSO-CSO model.

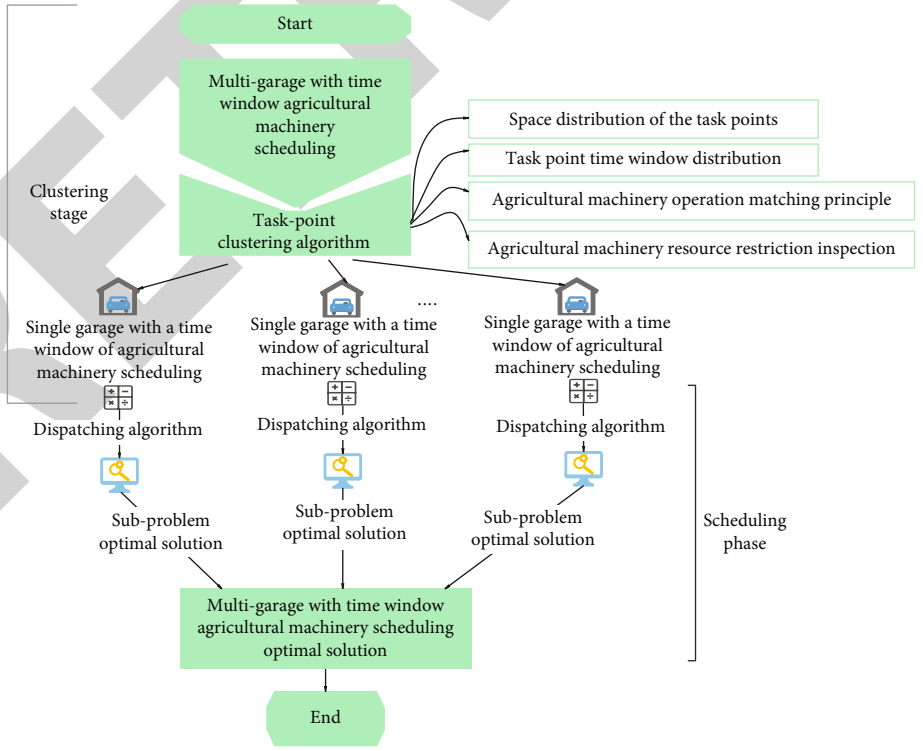

Figure 5: The basic framework of agricultural machinery task scheduling algorithm.

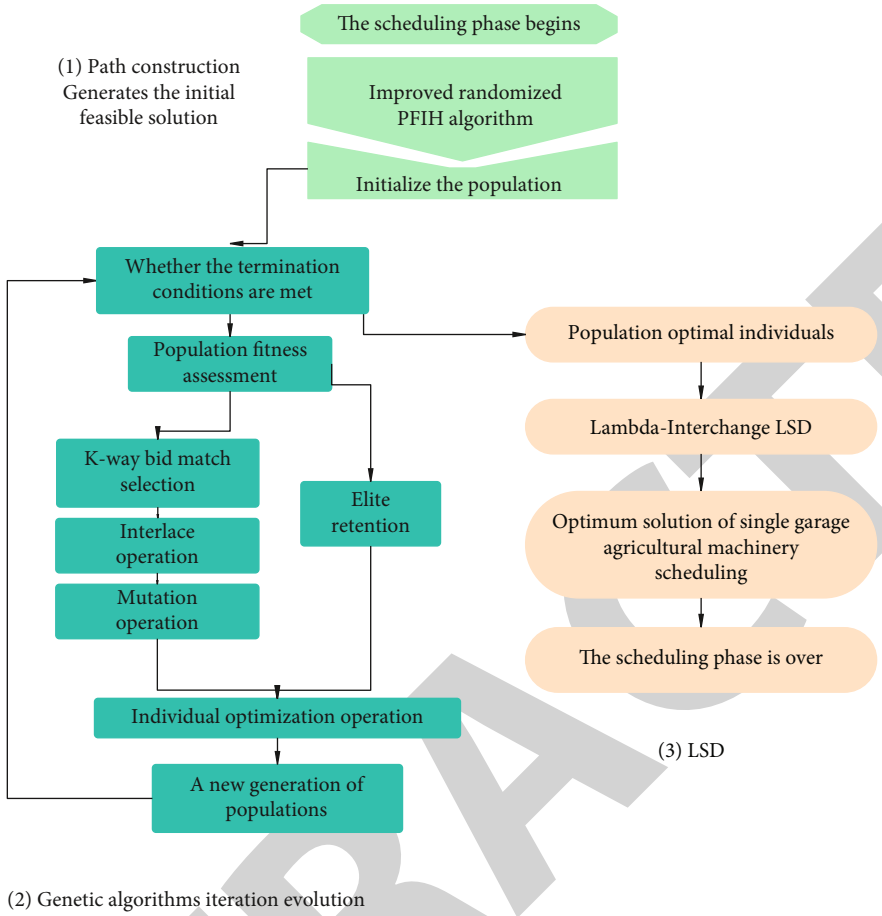

Figure 6: Algorithm flowchart of the scheduling stage.

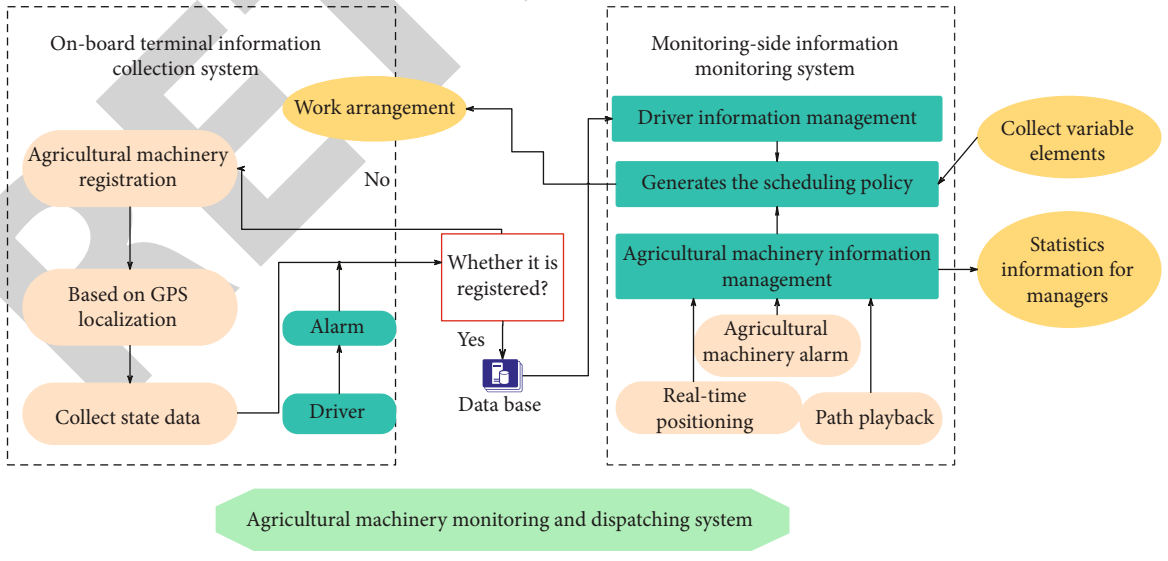

Figure 7: Agricultural machinery monitoring and dispatching system.

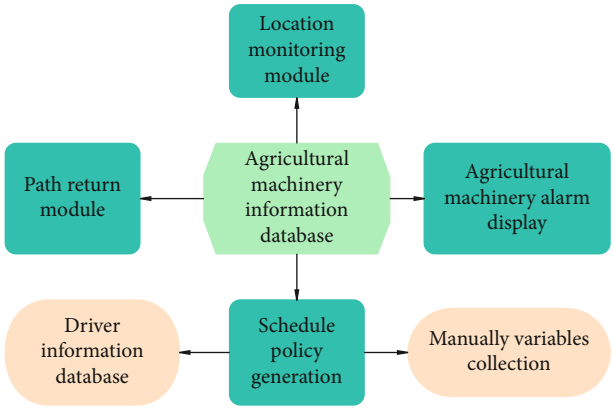

Figure 8: Data acquisition and display.

machinery operation plan. It calculates the standards of various companies in each region based on the resulting fixed direct project costs and different rates.

The maximized quality of agricultural machinery operations is

$$PQ_{\max} = \sum_{i=1}^{I} wi * Q_{i,n}. \tag{12}$$

In the formula, $w_{i,n}$ is the weight of the agricultural machinery operation activity (i) in the overall quality performance of the project, and $Q_{i,n}$ is the agricultural machinery operation quality performance when the resource option (n) is selected for the agricultural machinery operation activity (i).

This model of agricultural machinery operation scheduling optimization (MOPSO-CSO) is developed. The model is implemented in such a way that each particle represents an agricultural machinery operation scheduling scheme (referred to as a scheme in the pseudocode and flowchart). The combination of resource options for each agricultural machinery operation activity in the agricultural machinery operation scheduling scheme is used as each particle position with integer values ranging from 1 to M_i $(i = 1, \cdots, N)$; M_i is the total number of resource options to be considered for agricultural machinery operation activity i. Thus, the range of particle positions is limited to $[1, M_i]$. Its corresponding next selection trend, that is, the particle velocity range, is limited to $[1 - M_i, M_i - 1]$. Furthermore, the values of each dimension of the initial and updated positions of the particles should be rounded to integers in $[1, M_i]$. The implementation process of the MOPSO-CSO model, that is, the pseudocode, is summarized as follows.

(1) The algorithm determines the total number of agricultural machinery operation scheduling schemes in the particle swarm, that is, the algorithm determines the size of the particle swarm

(2) The algorithm determines the value of the learning factor, inertia weight, and mutation operator and other parameters

(3) The algorithm determines the upper limit of the number of agricultural machinery operation scheduling schemes that the decision-maker needs, that is, the algorithm determines the maximum allowable value of the solution set of the external storage library

(4) The algorithm determines the maximum number of iterations

(5) The algorithm determines the value range of the resource options and selection trends of various agricultural machinery operation activities, that is, the algorithm determines the value range of the particle position and velocity

(6) The algorithm randomly initializes the resource options and selection trend values of each agricultural machinery operation activity in each scheme, that is, the algorithm initializes the position and velocity of the particles

(7) The algorithm determines the objective function (Equations (10)–(12)). The algorithm calculates the agricultural machinery operation duration, agricultural machinery operating cost, and agricultural machinery operating quality of each scheme, that is, the algorithm calculates the fitness value

(8) The algorithm evaluates each plan individually. According to the principle of Pareto dominance, the algorithm selects the best

The combination of resource options for agricultural machinery operation activities is taken as the individual historical optimal solution, that is, the algorithm updates the individual historical optimal solution.

(9) Algorithmic evaluation of all schemes: according to the principle of Pareto dominance, the algorithm filters out the noninferior solutions in all current solutions and stores them in an external repository as archive solutions

(10) According to the principle of Pareto dominance, the algorithm performs a second round of screening in the external repository to remove the inferior solutions in the archive plan

(11) The algorithm judges whether the number of archive schemes exceeds the maximum allowable value of the external storage library. If it exceeds, the algorithm filters according to the adaptive grid density to remove redundant schemes. Otherwise, the algorithm proceeds to the next step

(12) The algorithm judges whether the maximum number of iterations is reached or the solution set converges. If it exceeds, the algorithm goes to Step 16

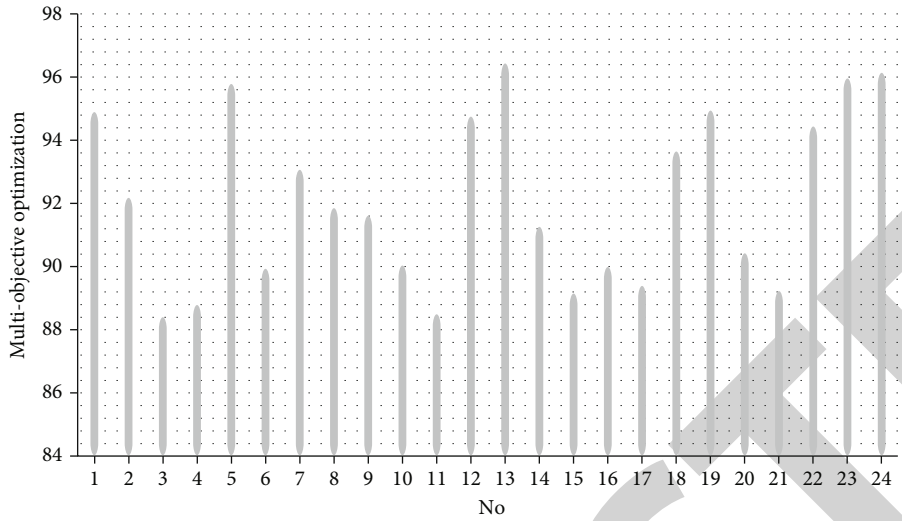

Figure 9: Multiobjective optimization effect.

to exit the loop; otherwise, the algorithm goes to the next step to loop

(13) According to the adaptive grid density, the algorithm uses the roulette selection method to select the optimal combination of agricultural machinery operation resource options in the archive plan as the global optimal plan, that is, the global optimal solution of the particles

(14) The algorithm initializes the schemes within the mutation range randomly, that is, the algorithm performs particle mutation operations

(15) The algorithm calculates the resource options and selection trends of each agricultural machinery operation activity in each scheme according to the update formula of the multiobjective particle swarm optimization algorithm (Equations (2) and (3)), that is, the algorithm updates the speed and position of the particles, and the algorithm goes to Step 7 to continue to loop

(16) The algorithm outputs archive scheme, that is, the algorithm outputs the noninferior solution set in the external storage library

Above, 1 to 6 are the initial stage, 7 to 15 are the cycle stage, and 16 is the end stage. The flowchart of the MOPSO-CSO model is shown in Figure 3.

The optimization iteration results of the MOPSO-CSO model in this paper are shown in Figure 4.

In Figure 4, the black particles represent the selected Pareto optimal solution, and the red particles represent the particles eliminated in the external storage during the iteration process. It can be seen that the particles gradually converge to the Pareto optimal solution. The position of the solution is evenly distributed, indicating that the model has a strong global search ability.

4. Agricultural Machinery Task Scheduling Algorithm Based on Multiobjective Optimization

The basic framework of agricultural machinery task scheduling algorithm is shown in Figure 5.

In the scheduling stage, a multiobjective algorithm is used to solve the agricultural machinery scheduling problem with time windows. The algorithm is divided into three steps. The first step uses an improved insertion path construction algorithm to generate an initial feasible solution to the problem. In the second step, multiple initial feasible solutions form the initial population. By designing suitable chromosome codes, fitness evaluation functions, genetic operators, etc., genetic algorithms are used to perform evolutionary operations such as selection, crossover, mutation, and individual optimization on the initial population. In the third step, after the evolution reaches the termination condition, the neighborhood search technology is used to further improve the optimal individual of the population and obtain a better solution. The algorithm flowchart of the scheduling phase is shown in Figure 6.

The location monitoring of agricultural machinery is conducive to the unified management of scattered agricultural machinery, coordinated deployment of agricultural machinery, and timely and accurate provision of the addresses of agricultural machinery that need to be repaired for maintenance personnel. Moreover, it provides idle agricultural machinery for the farmland that needs to be operated in time, prevents the resources of the agricultural machinery from being idle, saves time, and reduces costs. The system needs to facilitate the management of agricultural machinery information statistics and management, including agricultural machinery workload, working hours, repairs, location information, agricultural machinery model, license plate number, and fuel consumption. The operation status information of agricultural machinery is obtained in

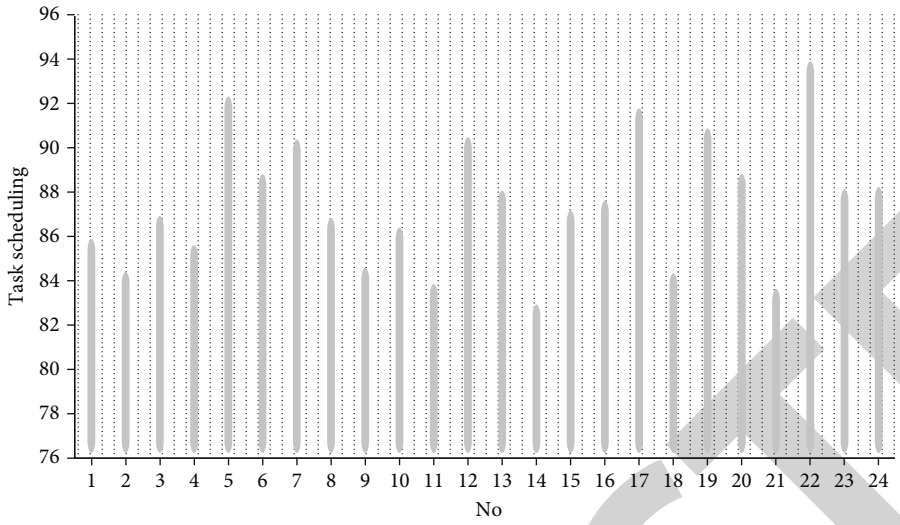

Figure 10: Task scheduling effect of agricultural machinery.

real time by the vehicle terminal and transmitted to the database of the monitoring system.

The monitoring terminal system automatically generates instructions for the optimal dispatch path or an emergency situation requires notification to the vehicle terminal. Moreover, it can interact (voice or text) with the in-vehicle App through text messages or directly through the communication network to inform the operator of the vehicle. The system uses MySQL database to store data. The system development idea is shown in Figure 7.

The relationship of the system data table is very simple. The agricultural machinery is successfully registered, and the agricultural machinery information database allows this agricultural machinery to upload data. The data in the agricultural machinery information database provides data support for agricultural machinery location monitoring, path playback and scheduling strategy generation, and alarm agricultural machinery display modules. The data relationship flowchart is shown in Figure 8.

In this paper, the performance verification of the multiobjective agricultural machinery task scheduling algorithm introduced in this paper is carried out. First, the multiobjective optimization effect of the algorithm in this paper is evaluated through simulation experiments, and the results shown in Figure 9 are obtained.

Through the above research, we can see that the algorithm proposed in this paper has certain advantages in multiobjective optimization. On this basis, this paper evaluates the effect of agricultural machinery task scheduling of agricultural machinery task scheduling algorithm based on the multiobjective optimization proposed in this paper and obtains the results shown in Figure 10.

From the above research, it can be seen that the agricultural machinery task scheduling algorithm based on multiobjective optimization proposed in this paper has a good agricultural machinery task scheduling effect and meets the basic purpose of optimizing the algorithm in this paper.

5. Conclusion

The research and development of a remote agricultural machinery monitoring service system integrating technology and management mode can realize remote monitoring, management, and mobilization of agricultural machinery and truly improve the efficiency of human and agricultural machinery and the level of agricultural information management. This paper designs an agricultural machinery operation and maintenance management system, which has the functions of agricultural machinery information management, agricultural machinery location monitoring, and communication scheduling. It is mainly aimed at agricultural machinery cooperatives and other agricultural machinery cooperative organizations and can conduct real-time and accurate monitoring and management of agricultural machinery at all levels across the country. At the same time, it also gives full play to the advantages of the development of mobile communication and the popularity of the development of mobile terminals, which effectively compensates for the disadvantages of poor flexibility and mobility of the traditional agricultural machinery monitoring and management end. In addition, it breaks through the constraints of agricultural machinery management in terms of time and space in the true sense and maximizes the efficiency of agricultural machinery production. This paper applies the multiobjective optimization research algorithm to agricultural machinery task scheduling and proposes an algorithm suitable for modern agricultural machinery task scheduling. The experimental results show that the multiobjective agricultural machinery task scheduling algorithm proposed in this paper has a good agricultural machinery task scheduling effect and meets the basic purpose of optimizing the algorithm in this paper.

Data Availability

The labeled dataset used to support the findings of this study are available from the corresponding author upon request.

Hindawi
Journal of Sensors
Volume 2023, Article ID 9813624, 1 page
https://doi.org/10.1155/2023/9813624

Retraction

Retracted: English Education Translation System Based on 5G Network Virtualization

Journal of Sensors

Received 19 December 2023; Accepted 19 December 2023; Published 20 December 2023

This article has been retracted by Hindawi following an investigation undertaken by the publisher [1]. This investigation has uncovered evidence of one or more of the following indicators of systematic manipulation of the publication process:

(1) Discrepancies in scope
(2) Discrepancies in the description of the research reported
(3) Discrepancies between the availability of data and the research described
(4) Inappropriate citations
(5) Incoherent, meaningless and/or irrelevant content included in the article
(6) Manipulated or compromised peer review

The presence of these indicators undermines our confidence in the integrity of the article's content and we cannot, therefore, vouch for its reliability. Please note that this notice is intended solely to alert readers that the content of this article is unreliable. We have not investigated whether authors were aware of or involved in the systematic manipulation of the publication process.

Wiley and Hindawi regrets that the usual quality checks did not identify these issues before publication and have since put additional measures in place to safeguard research integrity.

We wish to credit our own Research Integrity and Research Publishing teams and anonymous and named external researchers and research integrity experts for contributing to this investigation.

The corresponding author, as the representative of all authors, has been given the opportunity to register their agreement or disagreement to this retraction. We have kept a record of any response received.

References

[1] M. Hou, "English Education Translation System Based on 5G Network Virtualization," *Journal of Sensors*, vol. 2022, Article ID 8763849, 12 pages, 2022.

Hindawi
Journal of Sensors
Volume 2022, Article ID 8763849, 12 pages
https://doi.org/10.1155/2022/8763849

Research Article

English Education Translation System Based on 5G Network Virtualization

Manman Hou

Shaanxi Open University, Xi'an 710119, China

Correspondence should be addressed to Manman Hou; 1817300019@e.gzhu.edu.cn

Received 28 November 2021; Revised 24 December 2021; Accepted 29 December 2021; Published 27 January 2022

Academic Editor: Wei Zhang

In order to improve the effect of English education translation, this paper improves the 5G network virtualization algorithm and uses the typical correlation analysis method in data mining to extract the correlation relationship between the data content contained in the massive English translation user equipment. Furthermore, this paper adopts the similarity-based clustering method to realize the self-organization construction of English translation virtual community. On this basis, this paper proposes a spectrum allocation algorithm based on convex optimization, which effectively solves the problem of spectrum allocation in virtual cells. Finally, this paper constructs the functional architecture of the English education translation system based on 5G network virtualization and conducts experimental research. The experimental research results show that the English education translation system based on 5G virtualization constructed in this paper can play an important role in smart English teaching.

1. Introduction

With the introduction of the concept of "smart earth," under the research and development of artificial intelligence, cloud computing, and other technologies, the concept of "smart" has penetrated into all fields of society. In the field of education, researchers have conducted theoretical and practical discussions and research on smart classrooms, smart campuses, and smart education [1].

The emergence of smart teaching tools provides a full range of smart teaching environments for college teaching. Among them, the intelligent assistant Yu Class, developed by the Online Education Office of Tsinghua University, has powerful functions in the teaching process before, during, and after class. In particular, the application in classroom teaching is more obvious. Its "screen projection function" can not only project the content of learning to the student's mobile phone but also stimulate students' enthusiasm for learning through functions such as "barrage" [2].

In the context of smart education, the optimization of English translation classroom teaching ecology can analyze students, teachers, teaching organization, and teaching environment from the perspective of ecology and build an ecological teaching model for English translation classrooms in a smart education environment. According to ecological theory, English translation teaching can be regarded as an organic, complex, and unified system [3].

In traditional translation teaching, due to the influence of a fixed teaching environment (such as classrooms), the teaching content is generally based on theory and exercises, and students lack sufficient practice and knowledge input and application. In the process of teaching, students often lack interest due to the limitations of the language in the textbooks. However, the ecological translation teaching model in the context of smart education breaks through the limitations in this respect, and the forms of teaching organization present a trend of diversification. With the help of smart teaching tools, teachers can strengthen the learning content in three links before class, during class, and after class, so that the input of knowledge presents a natural ecological inheritance, and the degree of internalization of students' knowledge is more effective. In addition, it also balances the learning of basic English knowledge and professional knowledge. English translation teaching and learning

involve the basic knowledge of English as well as the professional knowledge. If you do not handle the relationship between each other, you may lose sight of one another. The three aspects of learning before class, during class, and after class effectively avoid this problem. Teachers can choose the way of teaching according to the difficulty of knowledge. For example, the basic knowledge of English such as vocabulary, grammar, and sentence patterns is relatively easy, but it is difficult to grasp quickly. Then, in the preclass session, teachers can set tasks for students through video commentary, audio commentary, or article reading. Students can have a deeper understanding of certain knowledge points by watching or reading repeatedly. As for the more difficult parts, you can analyze in depth through classroom discussion and solve such problems in the classroom. For the problem of insufficient translation practice, students can be organized to gradually improve through activities such as translation workshops and translation companies to observe knitting internships. Teaching and learning before class, during class, and after class is an organic whole, and the three are independent of and complementary to each other.

Based on the above analysis, this article studies an English education translation system based on 5G network virtualization, which provides a theoretical reference for improving the wisdom of subsequent English education.

2. Related Work

In the edge computing network system, the network architecture that combines network function virtualization and software-defined networking transforms traditional network functions from dedicated hardware devices to virtual network function software running on standardized commercial server virtual machines [4]. On the one hand, virtual machine-based software network functions use underlying virtualization technology to bring benefits that traditional networks do not have, such as accelerating time to market, reducing hardware and operating costs, and improving security and scalability [5]; on the other hand, the use of standardized programmable interfaces that separate the data plane and the logically centralized control plane can effectively simplify maintenance operations and reduce network management costs. It is an important means to provide network flexibility [6]. Sun and Li [7] put the network function of compressing the data stream at the front and the network function of augmenting the data stream at the back, thereby reducing the bandwidth overhead of the physical link between the front and rear network functions. However, they do not take into account the computational resource overhead required by the network functions that process the data flow. Literature [8] designed a corresponding buffer for the service chain. When the buffer data packet volume exceeds the threshold, the NFVnic will appropriately limit the data flow rate to avoid the downstream virtual network function from becoming the bottleneck of the entire service chain; when it is lower than the threshold, it will appropriately increase the data rate. Literature [9] proposes to place network functions with strong processing capabilities in front of the service chain and network functions with weak processing capabilities behind the service chain to avoid performance degradation of the service chain and to sacrifice resources in exchange for performance. How to find the proportional relationship between the data flow rate and the service chain deployment resources and directly determine the resource allocation based on the data flow rate is a very difficult problem [10]. In addition, the network architecture based on software-defined networking and network function virtualization is more flexible than traditional network architectures, but this flexibility also makes the state of edge computing networks constantly change and service chain updates occur frequently. Network operators must not only ensure that the update process of the service chain is correct and consistent but also avoid loopholes in the network update process, resulting in network performance degradation or even crash [11]; faster update speed means that the time occupied by resources at the same time will be reduced, and the use of network resources will be avoided. The rate is further reduced [12]. Literature [13] chooses to wait for the current data stream to be processed before routing the new data stream to process it, but this increases the time and cost of updating. Literature [14] replicates and transfers the state of network functions in a fine-grained manner to ensure consistent properties during the update process. At the same time, in order to avoid network performance degradation, they will cache data packets in the controller during the update process. Avoid packet loss or error handling. Literature [15] arranges the update sequence between service chains under the consideration of network resource constraints, so as to complete the update of the entire network state. Literature [16] uses an OpenNF or Split/Merge update mechanism to realize the update of a single service chain. Literature [17] is too coarse-grained to study the update sequence of the service chain, and it is difficult to minimize the update time of the network state. At the same time, because their update of a single service chain relies on the OpenNF or Split/Merge update mechanism, there is no further analysis of a single service chain. The update mechanism of the service chain is optimized.

3. 5G Network Virtualization Processing

Next, this article defines the relevant concepts and elements in the English education translation system network.

Definition 1. The base station set $S = \{s_m, m = 0, 1, 2, \cdots, N_s\}$ under the coverage area of the macro base station is composed of one macro base station and N_s small base stations, where s_0 is the macro base station and $s_1, \cdots, s_{N_s}$ represents the small base station [18].

Definition 2. A large number of user equipment are randomly distributed in the area, $U = \{s_m, m = 0, 1, 2, \cdots, N_U\}$ is the set of user equipment, and N_U is the number of users.

Definition 3. The user equipment is running various types of applications and needs to transmit various modal data, and the vector $X = \{x_1, x_2, \cdots, x_n\}$ representing the modal data is obtained through the data analysis method.

Definition 4. Similarity $\mathrm{sim}(u, v)$ refers to the similarity between user equipment u and v that needs to transmit data when communicating.

Definition 5. This article introduces a "user-centered" virtual cell, breaking the concept of traditional access network centered on base stations. The cell is no longer associated with the base station. However, it is associated with the user. At the same time, it realizes the decoupling of signal transmission and base station ID and further supports network virtualization management.

Definition 6. This article assumes that the defined macro base station area is allocated logically continuous spectrum resources; that is, the available spectrum resource is C. The spectrum allocation strategy among macro base stations is beyond the scope of this article, so this article will not discuss it.

There are a large number of user equipment in the network, and a large amount of data of various modalities needs to be transmitted in real time. As shown in Figure 1, each user equipment needs to transmit multiple modal data, and there is a certain correlation between modal data blocks describing the same or similar objects.

In this paper, two modal data blocks are represented as vectors $X = \{x_1, x_2, \cdots, x_n\}$ and $Y = \{y_1, y_2, \cdots, y_n\}$, respectively. The canonical correlation analysis extracts a linear combination of a set of variables from each vector representing the data to form two canonical vectors $w_X^T X$ and $w_Y^T Y$. Then, we use these two typical vectors to calculate the Pearson coefficient describing the correlation, as shown in the following formula [19]:

$$X\rho(X, Y) = \rho\left(w_X^T \mathrm{X}, w_Y^T Y\right) = \frac{\mathrm{cov}\left(w_X^T \mathrm{X}, w_Y^T Y\right)}{\sqrt{\mathrm{var}\left(w_X^T \mathrm{X}\right)\ \mathrm{var}\left(w_Y^T Y\right)}}. \quad (1)$$

In order to fully discover the correlation relationship between the data, the typical correlation analysis objective selects the optimal w_X and w_Y to maximize the value of formula (1), thus forming an optimization problem, as shown in the following formula:

$$\max \frac{\mathrm{cov}\left(w_X^T \mathrm{X}, w_Y^T Y\right)}{\sqrt{\mathrm{var}\left(w_X^T \mathrm{X}\right)\ \mathrm{var}\left(w_Y^T Y\right)}} \quad (2)$$
$$\mathrm{s.t.var}\left(w_X^T \mathrm{X}\right) = \mathrm{var}\left(w_Y^T Y\right) = 1.$$

The Lagrangian multiplier method is usually used to solve this problem, and the Lagrangian equation is constructed:

$$L = \mathrm{cov}\left(w_X^T \mathrm{X}, w_Y^T Y\right) - \frac{\lambda}{2}\left(\mathrm{var}\left(w_X^T \mathrm{X}\right) - 1\right) - \frac{\theta}{2}\left(\mathrm{var}\left(w_Y^T Y\right) - 1\right). \quad (3)$$

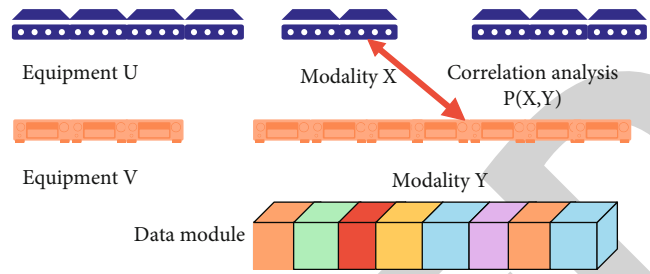

Figure 1: Modal data model.

By deriving and calculating the Lagrangian equation, we obtain [20]

$$w_Y = \frac{1}{\lambda}\sum_{yy}^{-1}\sum_{yx} w_x,$$
$$\sum_{xy}\sum_{yy}^{-1}\sum_{yx} w_x = \lambda^2 \sum_{xx} w_x. \quad (4)$$

Among them, $\sum_{xy}$ is the covariance matrix, $\sum_{xx}$ and $\sum_{yy}$ are the variance matrices, and the goal is to find the maximum λ, that is, the canonical correlation coefficient. When the maximum λ is obtained, it corresponds to w_X and w_Y is a typical vector.

We assume that two user equipment u and v and the data sets formed by transmitting data of multiple different modalities are $\Phi(u) = \{X_1^u, X_2^u, \cdots, X_{N_\Phi^u}^u\}$ and $\Phi(v) = \{X_1^v, X_2^v, \cdots, X_{N_\Phi^v}^v\}$, respectively. Using the data correlation discovery method introduced in the previous section, the correlation $\lambda(X_a^u, X_b^v)$ between any two pieces of different modal data X_a^u and X_b^v of two user equipment can be obtained. Thus, the similarity $R(u, v)$ between user equipment can be obtained, as shown in the following formula [21]:

$$R(u, v) = \sum_{a=1}^{N_\Phi^u}\sum_{b=1}^{N_\Phi^v} \lambda(X_a^u, X_b^v)\theta_{a,b}. \quad (5)$$

Among them, $\theta_{a,b}$ is determined according to the application type and the importance of the data in the user equipment, and the weight between these different associated data is obtained.

This research mainly focuses on the coverage area of the macro base station. Therefore, only the user equipment within the coverage of the same macro base station is clustered. And when two user devices are far apart, even if they have a strong similarity, it is difficult for the collaborative operation and data sharing between the devices to occur. In addition, it is not conducive to the optimization of virtualized spectrum resource allocation if devices that are far apart are divided into the same cluster. Therefore, the distance factor needs to be considered in the process of user equipment clustering and division, and the distance between the equipment is defined as

$$D(u, \mathrm{v}) = \sqrt{(x_u - x_v)^2 + (y_u - y_v)^2}. \quad (6)$$

Among them, (x_u, y_u) and (x_v, y_v) are the location information of user equipment u and v, respectively. In the process of clustering, this study defines the distance threshold $D_{\max}$. When the distance between two user equipment exceeds the threshold, that is, $D(u, v) > D_{\max}$, the similarity between the two user equipment is considered to be zero. The distance threshold $D_{\max}$ is dynamically adjusted according to the coverage area of the macro base station, the distribution of small base stations, and the supply and demand of spectrum resources.

To implement similarity-based clustering, firstly, it is necessary to define the similarity between user devices. This study uses data correlation and location information to define similarity as follows:

$$\mathrm{sim}(u, v) = \frac{\sigma R(u, v)}{D(u, v)}. \quad (7)$$

Among them, δ is the balance factor used to coordinate the relationship between the distance between the equipment and the degree of association. And $\mathrm{sim}(u, v) \in [0, 1]$. The greater the similarity, the greater the value of $\mathrm{sim}(u, v)$. When the data of two devices are not correlated, $\mathrm{sim}(u, v) = 0$. This article defaults that the similarity between the user equipment and itself is 1, that is, $\mathrm{sim}(u, u) = 1$. Then, the similarity matrix of user equipment in the network can be obtained, and it is shown in the following formula:

$$M_{N_U \times N_U} = \begin{bmatrix} sim(u_1, u_2) & \cdots & sim(u_1, u_{N_U}) \\ \vdots & \ddots & \vdots \\ sim(u_{N_U}, u_1) & \cdots & sim(u_{N_U}, u_{N_U}) \end{bmatrix}. \quad (8)$$

The elements on the main diagonal of the matrix are all 1, and $\mathrm{sim}(u, v) = \mathrm{sim}(v, u)$, so the similarity matrix is a symmetric matrix. In this case, we only need to store the upper triangular part of the matrix. This effectively reduces storage space and reduces computing costs. Then, an undirected graph $G = (U, E)$ is constructed according to the user equipment similarity matrix, where the node set $U = \{u_1, u_2, \cdots, u_{N_U}\}$ describes the user equipment in the network and the edge set $E = \{(u_i, u_j) \mid u_i, u_j \in U\}$ describes the similarity between the user equipment. The boundary value is defined as the similarity of two user devices. The larger the boundary value, the greater the similarity.

When the user equipment clusters are formed, it is necessary to judge the pros and cons of the cluster division. It mainly considers the similarity of user equipment in clusters and the similarity between user equipment in different clusters. The modularity is usually used to measure the quality of the clustering structure, that is, $Q = \sum(e_{ii} - a_i^2) = \mathrm{Tre} - \|e^2\|$, where $\mathrm{Tre} = \sum e_{ii}$. It describes the proportion of the number of connections between each user equipment in the cluster to the total number of connections, and $a_i = \sum e_{ii}$ represents the proportion of the number of connections between the user equipment in the cluster and the user equipment outside the cluster in the total number of connections. However, the measurement standard based on modularity has certain limitations, such as being not applicable to the situation where the cluster size difference is too large and the problem of inaccurate discovery of small-scale clustering. This paper studies the use of module density to measure the clustering structure, and as the exit condition of the clustering process, it is defined as follows:

$$\rho = \sum_{i=1}^{N_\Omega} \frac{L(V_i, V_i) - L(V_i, \bar{V}_i)}{|V_i|}. \quad (9)$$

Among them, $\bar{V} = V - V_i$ and N_Ω are the number of user equipment clusters, $L(V_i, V_i)$ is the number of internal connections in cluster i, $L(V_i, \bar{V}_i)$ is the number of connections to other clusters, Ω_k is the number of user equipment in cluster i, and N_Ω is the number of user equipment clusters formed.

In the research of this article, this article considers that each user equipment participates in the cluster division and is divided into only one cluster; then, the user equipment in the network will eventually form N, nonoverlapping user equipment clusters; that is, it will satisfy

$$\begin{aligned} U &= \bigcup_{k=1}^{N_\Omega} U(\Omega_k), \\ \Omega_k &\neq \varnothing, \quad k = 1, 2 \cdots, N_\Omega, \\ \Omega_i \cap \Omega_j &= \varnothing, \quad i, j = 1, 2, \cdots, N_\Omega, i \neq j. \end{aligned} \quad (10)$$

Among them, U is the user equipment set in the network and $U(\Omega_k)$ is divided into the user equipment set of cluster Ω_k.

Through the abstract management of user equipment information, the clustering method based on similarity is used to divide the user equipment in the coverage area of the macro base station online to form N user-centric virtual cells, forming a virtual cell set $G = \{g_1, g_2, \cdots, g_{N_g}\}$. As shown in Figure 2, each user equipment participates in the formation of a virtual cell. Through the construction of virtual cells, the data center conducts abstract management of user equipment distributed in various locations in the network. At the same time, in the process of constructing a virtual cell, by sensing the data content transmitted by the user equipment and then predicting the data flow information of each user equipment, the spectrum resource demand of the user equipment in the network is finally determined.

Within the coverage area of a certain macro base station, various types of user equipment form a user equipment set $U = \{u_n, n = 0, 1, 2, \cdots, \mathrm{N}_U\}$. Through the self-organizing construction of virtual cells, the user equipment forms multiple virtual cells to form a virtual cell set $G = \{g_1, g_2, \cdots, g_{N_g}\}$. At the same time, collect and analyze various valuable user information in the network. Furthermore, the abstract and unified global information in the data center is used to perform virtualized management of spectrum resources in units of virtual cells.

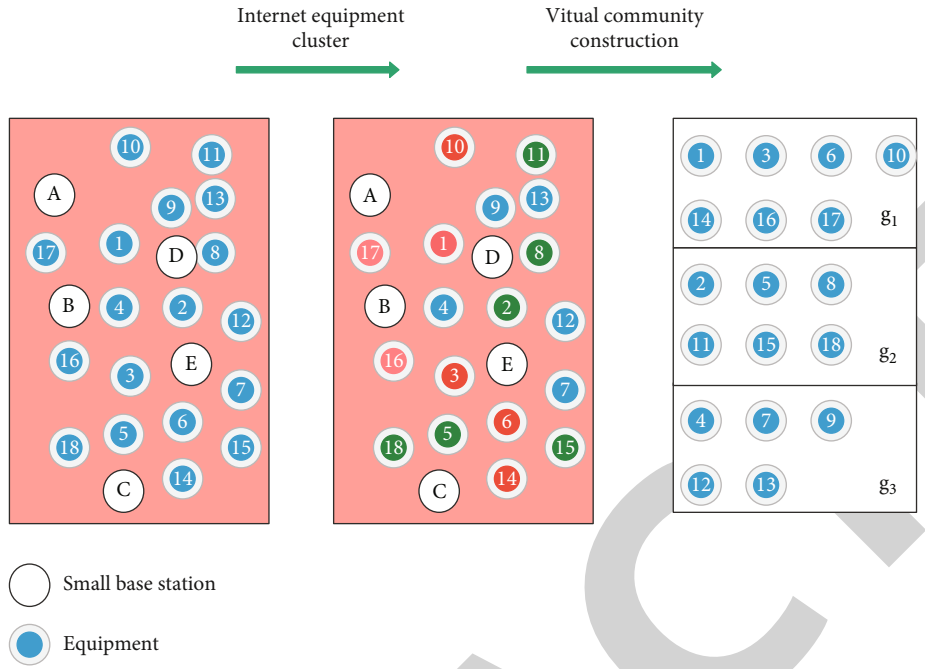

Figure 2: Virtual cell formation process.

It is assumed that the logically continuous spectrum resource obtained in the coverage area of the macro base station is C. In order to effectively reduce the interlayer interference, the spectrum resources are divided into two parts C_M and C_G orthogonally, and an appropriate spectrum guard band C is added between the two to reduce the adjacent channel interference between the macro base station and the small base station. Then, there are $C = C_M \cup C_G \cup C_p$ and $C_M \cap C_G \cap C_p = \varnothing$. Among them, the macro base station exclusively occupies the spectrum resource C_M, while the small base stations in the virtual cell use the spectrum resource C_G together. Furthermore, using the global user equipment distribution and resource demand information, the available spectrum resources are allocated to the virtual cell during the construction of the virtual cell. Using the data mining method, the data flow of each user equipment is obtained as $f(u)$. At the same time, the real-time demand $r(u)$ of user equipment communication is predicted. Furthermore, in the data center, the load information of the user equipment is obtained by calculation, and it is as follows:

$$D(u) = \psi(f(u), r(u)). \tag{11}$$

In order to determine the allocation ratio of C_M and C_G, it is necessary to calculate the load situation of the macro base station and the small base station in each virtual cell. First, this study uses global information to determine the base station selection situation of the user equipment, that is, which base station to choose to communicate with. Furthermore, the load generated by the user equipment on the base station is determined. This study defines $D(u, s_0)$ and $D(u, s)$ to describe the load situation of the user equipment on the macro base station and the small base station. Then, the load generated by the user equipment communicating with the macro base station in each virtual cell is calculated, and the total load of the macro base station is obtained as $D_M = \sum_{g\in G}\sum_{u\in U^g} D(u, s_0)$. At the same time, the load generated by the user equipment communicating with the small cell in the virtual cell is calculated, and the total load of the small cell in the network is calculated as $D_S = \sum_{g\in G}\sum_{s\in S^g} \sum_{u\in U^g} D(u, s)$, $s \neq s_0$, where U^g is the set of user equipment in the virtual cell and S^g represents a set of small base stations that provide communication services to the virtual cell g. Furthermore, this solution can dynamically adjust the size of C_M and C_G using the global load distribution, as shown below:

$$\frac{C_M}{C_G} = \sigma \frac{D_M}{D_S}. \tag{12}$$

Among them, σ is the distribution ratio factor to control the fairness of distribution. The spectrum resource $C_。$ obtained by all small base stations is allocated to each virtual cell as needed according to the load condition of the virtual cell in the network and when the spectrum resource is sufficient. At the same time, in order to reduce interference, C_G is orthogonally divided into $|G|$ parts; then, the small base stations in the virtual cell h obtain spectrum resources as

$$C_h = \frac{\sum_{g\in G}\sum_{u\in U^g} D(u, s)}{\sum_{g\in G}\sum_{s\in S^g}\sum_{u\in U^g} D(u, s)} \cdot C_G, \quad h \in G, s \neq s_0. \tag{13}$$

Therefore, this solution allocates corresponding spectrum resources to each virtual cell through the virtualized management of user equipment information and spectrum resources.

Specifically, spectrum resources need to be allocated to user equipment in the virtual cell. In the allocation process, the user's spectrum requirements and interference control

are mainly considered. First, communicating with the macro base station in the virtual cell g occupies the spectrum resource ;(eCx,). Whether the device g, communicating with the small cell in the virtual cell u, occupies the spectrum resource $r(\in \mathrm{Ca})$ is expressed as = 1or0 (g, eG, s, cS8, s, ≠ so u EU).

$$x_{i,0,k}^{r_1} = \begin{cases} 1, & \text{if UE } u_k \text{ in MBS is assigned resource } r_1, \\ 0, & \text{otherwise.} \end{cases} \tag{14}$$

In the same way, $x_{i,j,\mathrm{k}}^{r_2}$ has a similar definition. In this study, the macro base station equipment and the small base station equipment use orthogonal spectrum resources C_M and C_G, respectively. And by setting a spectrum guard band, the problem of adjacent channel interference between the macro base station and the small base station is overcome. Then, there is no interference between the macro base station equipment and the small base station equipment under the same macro base station coverage area. When the macro base station equipment and the small base station equipment use spectrum resources to communicate, the interferences they suffer are as follows:

$$\begin{cases} I_{i,0,k}^{r_1} = \sum_{\pi \in \mathrm{neigh}} P_{\pi,0}^{r_1} \varphi_{\pi,\mathrm{k}}^{r_1} + \sum_{\pi \in \mathrm{neigh}} \sum_{s_j \in S^{\pi}} P_{i,0}^{\xi} \varphi_{i.0,k}^{\xi}, \\ I_{i,j,k}^{r_2} = \sum_{\xi \in \psi_{r_2}} \sum_{g_i \in G} \sum_{s_j \in S^{g_i}} P_{i,j}^{\xi} \varphi_{i.j,k}^{\xi}. \end{cases} \tag{15}$$

When the macro base station equipment and the small base station equipment occupy resources, the SINR, respectively, meets

$$\begin{cases} \delta_{i,0,k}^{r_1} = \dfrac{P_{i,0}^{r_1} \varphi_{i,0,k}^{r_1}}{\sum_{\pi \in \mathrm{neigh}} P_{\pi,0}^{r_1} \varphi_{\pi,k}^{r_1} + \sum_{\pi \in \mathrm{neigh}} \sum_{s_j \in S^{\pi}} P_{\pi,j}^{r_1} \varphi_{\pi,j,k}^{r_1} + \sum_{\xi \in \psi_{r_1}} P_{i,0}^{\xi} \varphi_{i.0,k}^{\xi} + \sigma^2}, \\ \delta_{i,j,k}^{r_2} = \dfrac{P_{i,j}^{r_2} \varphi_{i,j,k}^{r_2}}{\sum_{\xi \in \psi_{r_2}} \sum_{g_i \in G} \sum_{s_j \in S^{g_i}} P_{\pi,j}^{\xi} \varphi_{\pi,j,k}^{\xi_1} + \sigma^2}. \end{cases} \tag{16}$$

Among them, δ^2 is the noise power. This study assumes that different channels have the same noise. neigh is the set of macro base stations that interfere with the macro base station. Therefore, in the virtual cell g_i, when the macro base station equipment and the small base station equipment occupy resources, the data transmission rates obtained are, respectively,

$$\begin{cases} R_{i,0,k}^{r_1} = W_{i,0,k}^{r_1} \log\left(1 + \delta_{i,0,k}^{r_1}\right), \\ R_{i,j,k}^{r_2} = W_{i,j,k}^{r_2} \log\left(1 + \delta_{i,j,k}^{r_2}\right). \end{cases} \tag{17}$$

Among them, according to the load information of the user equipment, $W_{i,0,k}^{r_1}$ and $W_{i,j,k}^{r_2}$ are the calculated resources, respectively. In addition, the data transmission rate needs to ensure that the user equipment successfully completes the communication. The transmission rate limitation of macro base station equipment and small base station equipment meets

$$\begin{cases} R_{i,0,k}^{r_1} \geq Y(D(u_k, s_0), t), \\ R_{i,j,k}^{r_2} \leq Y\left(D\left(u_k, s_j\right), t\right). \end{cases} \tag{18}$$

Among them, $Y(D(u_k, s_0), t)$ and $Y(D(u_k, s_0), t)$, respectively, represent the data transmission rate requirements of the macro base station equipment and the small base station equipment, that is, the transmission rate requirements for completing the data volume transmission within the effective time t. At the same time, considering the overall performance of the system, before spectrum allocation, by calculating the data transmission rate of each user equipment, the minimum data transmission rate limit $R_{\min}$ of the user equipment can be determined. According to the above description, this research builds a virtualized spectrum allocation model based on virtual cells. On the premise of effectively coordinating interference and maximizing system capacity, the virtualized spectrum allocation model can be expressed as

$$\begin{aligned} &\max \sum_{m=1}^{2} \sum_{i=1}^{N_G} \sum_{j=0}^{N_S} \sum_{k=1}^{N_U} x_{i,j,k}^{r_m} R_{i,j,k}^{r_m} \\ &\text{s.t. } C1: \sum_{i=1}^{N_G} \sum_{k=1}^{N_U} x_{i,0,k}^{r_1} W_{i,0,k}^{r_1} \leq C_M \\ &C2: \sum_{i=1}^{N_G} \sum_{j=0}^{N_S} \sum_{k=1}^{N_U} x_{i,j,k}^{r_2} W_{i,j,k}^{r_2} \leq C_G \\ &C3: \sum_{m=1}^{2} \sum_{i=1}^{N_G} \sum_{j=0}^{N_S} x_{i,j,k}^{r_m} R_{i,j,k}^{r_m} \geq R_{\min}, \quad \forall k = 1, 2, \cdots, N_U \\ &C4: W_{i,j,k}^{r_2} \geq 0, \quad \forall m = 1, 2, i = 1, 2, \cdots, N_G, \forall j = 1, 2, \cdots, N_S. \\ &\forall k = 1, 2, \cdots, N_U. \end{aligned} \tag{19}$$

In addition, while maximizing system capacity, focusing on user fairness, this article rewrites the optimization goal as $\max \sum_{m=1}^{2}\sum_{i=1}^{N_G}\sum_{j=0}^{N_S}\sum_{k=1}^{N_U} x_{i,j,k}^{r_m} \log\left(R_{i,j,k}^{r_m}\right)$ to achieve user fairness in virtualized spectrum allocation.

For the problem of virtualized spectrum allocation based on virtual cells, the data center obtains the load information of the user equipment in the network through perception and calculation. Therefore, for the spectrum allocation model based on virtual cells, this research introduces a convex optimization method to realize virtual spectrum allocation.

Theorem 7. *The virtualized spectrum allocation problem is a convex optimization problem; that is, there is an optimal spectrum allocation scheme to enable the system to obtain the maximum capacity.*

Proof. For the objective function $\max \sum_{m=1}^{2}\sum_{i=1}^{N_G}\sum_{j=0}^{N_S}\sum_{k=1}^{N_U} x_{i,j,k}^{r_m} \log\left(R_{i,j,k}^{r_m}\right)$, first of all, the method of slack variables is used to make $x_{i,j,k}^{r_m}$ become a continuous value in the range of 0 to 1. Then, after calculation, it is proven that $Sx_{i,j,k}^{r_m} \log\left(R_{i,j,k}^{r_m}\right)$ is a concave function. Therefore, the problem of virtualized spectrum allocation is equivalent to the following optimization problem:

$$\min\left(-\sum_{m=1}^{2}\sum_{i=1}^{N_G}\sum_{j=0}^{N_S}\sum_{k=1}^{N_U} x_{i,j,k}^{r_m} \log\left(R_{i,j,k}^{r_m}\right)\right). \tag{20}$$

At the same time, it is easy to determine that the constraints of formula (19) constitute a convex set. Furthermore, the virtualized spectrum allocation problem is proven to be a convex optimization problem with constraints on the variable $W_{i,j,k}^{r_m}$. Therefore, there is a globally optimal allocation scheme for the virtualized spectrum allocation problem, which can obtain the maximum system capacity. □

Next, this research transforms the optimization goal into $\min\left(-\sum_{m=1}^{2}\sum_{i=1}^{N_G}\sum_{j=0}^{N_S}\sum_{k=1}^{N_U} x_{i,j,k}^{r_m} \log\left(R_{i,j,k}^{r_m}\right)\right)$. Then, the Lagrangian duality method and KKT (Karush-Kuhn-Tucker) conditions are used to solve the virtualized spectrum allocation problem. First, construct the Lagrangian function of the virtualized spectrum allocation problem as follows:

$$\begin{aligned} L\left(W_{i,j,k}^{r_m}, \lambda^m.\lambda_k, v_{i,j,k}^{r_m}\right) &= -\sum_{m=1}^{2}\sum_{i=1}^{N_G}\sum_{j=0}^{N_S}\sum_{k=1}^{N_U} x_{i,j,k}^{r_m} \log\left(R_{i,j,k}^{r_m}\right) \\ &+ \sum_{m=1}^{} \lambda^m\left(\sum_{m=1}^{2}\sum_{i=1}^{N_G}\sum_{j=0}^{N_S}\sum_{k=1}^{N_U} x_{i,j,k}^{r_m} W_{i,j,k}^{r_m} - C_M\right) \\ &+ \sum_{m=2}^{} \lambda^m\left(\sum_{m=1}^{2}\sum_{i=1}^{N_G}\sum_{j=0}^{N_S}\sum_{k=1}^{N_U} x_{i,j,k}^{r_m} W_{i,j,k}^{r_m} - C_C\right) \\ &+ \sum_{k=1}^{} \lambda^m\left(R_{\min} - \sum_{i=1}^{N_G}\sum_{j=0}^{N_S}\sum_{k=1}^{N_U} x_{i,j,k}^{r_m} R_{i,j,k}^{r_m}\right) \\ &- \sum_{m=1}^{2}\sum_{i=1}^{N_G}\sum_{j=0}^{N_S}\sum_{k=1}^{N_U} v_{i,j,k}^{r_m} W_{i,j,k}^{r_m}. \end{aligned} \tag{21}$$

Among them, λ^m, λ_k, and $v_{i,j,k}^{r_m}$ are Lagrange multipliers. Then, the dual function of the virtualized spectrum allocation problem is

$$g\left(\lambda^m, \lambda_k, v_{i,j,k}^{r_m}\right) = \inf_{W_{i,j,k}^{r_m}} L\left(W_{i,j,k}^{r_m}, \lambda^m, \lambda_k, v_{i,j,k}^{r_m}\right). \tag{22}$$

Theorem 8. *The optimal solution $W_{i,j,k}^{r_m}$ of the virtualized spectrum allocation problem has a corresponding relationship with the optimal solution $(\lambda^m, \lambda_k, v_{i,j,k}^{r_m})$ of the dual problem.*

Proof. According to the literature, for any feasible Lagrangian multiplier $(\lambda^m, \lambda_k, v_{i,j,k}^{r_m})$, the dual function value is the lower limit of the spectrum allocation optimization function p, that is, $p \geq g(\lambda^m, \lambda_k, v_{i,j,k}^{r_m})$. In addition, the spectrum allocation problem is a convex optimization problem, which usually has a strong duality. Then, the optimal value p of the original problem is equal to the optimal value a of the dual problem, that is, $p' = d'$. Therefore, W has a corresponding relationship. □

Therefore, the optimal solution of the virtualized spectrum allocation problem can be obtained by solving the following dual problem:

$$\begin{aligned} &\max g\left(\lambda^m, \lambda_k, v_{i,j,k}^{r_m}\right) \\ &\text{s.t. } \lambda^m \geq 0, \lambda_k \geq 0, v_{i,j,k}^{r_m} \geq 0. \end{aligned} \tag{23}$$

Solving the above problems has greater complexity. This paper uses the interior point method to solve the problem and finally obtains the maximum value of $g(\lambda^m, \lambda_k, v_{i,j,k}^{r_m})$. At this time, the optimal Lagrangian multiplier value is λ^m, λ_k, $v_{i,j,k}^{r_m}$.

For convex optimization problems, the KKT condition is a sufficient and necessary condition for the optimal solution; that is, the specific value that meets the KKT condition is the optimal solution of the virtualized spectrum allocation problem and its dual problem. Next, this study combines the calculated best Lagrangian multiplier $(\lambda^m, \lambda_k, v_{i,j,k}^{r_m})$ and uses the KKT condition to calculate $W_{i,j,k}^{r_m}$. For KKT conditions, according to the virtualized spectrum allocation problem,

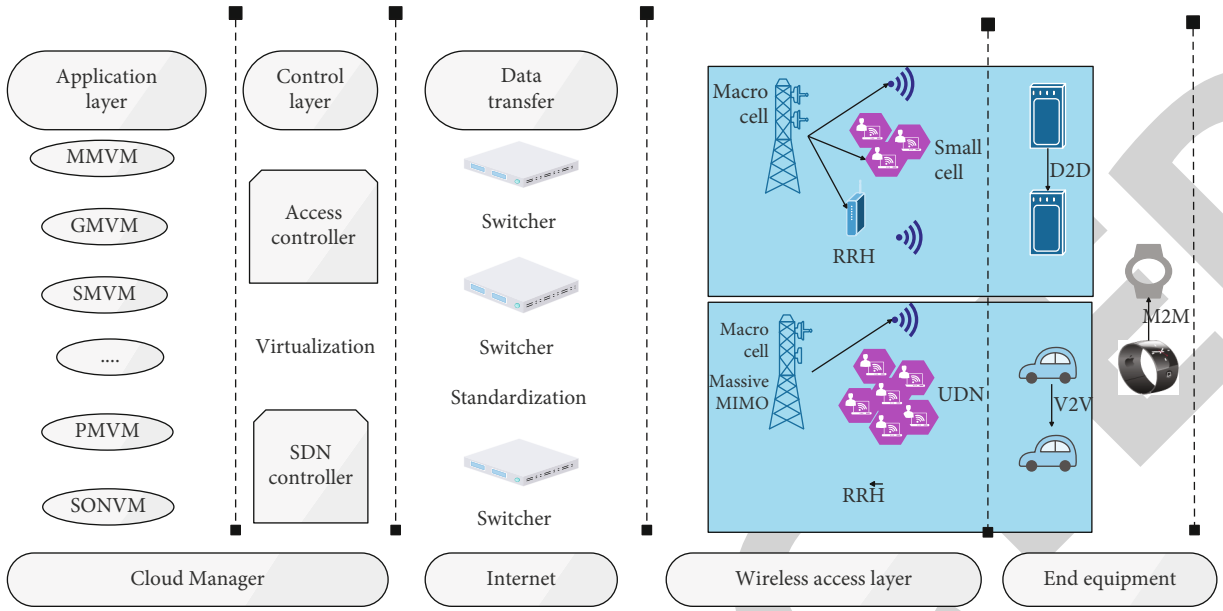

Figure 3: Schematic diagram of 5G network architecture of the English education translation system.

the feasibility conditions are determined as follows:

$$\sum_{i=1}^{N_G}\sum_{k=1}^{N_U} x_{i,0,k}^{r_1} W_{i,0,k}^{r_1} - C_M \le 0,$$

$$\sum_{i=1}^{N_G}\sum_{k=1}^{N_U}\sum_{k=1}^{N_U} x_{i,j,k}^{r_2} W_{i,j,k}^{r_2} - C_G \le 0,$$

$$R_{\min} - \sum_{i=1}^{N_G}\sum_{k=1}^{N_U}\sum_{k=1}^{N_U} x_{i,j,k}^{r_m} R_{i,j,k}^{r_m} \le 0, \quad \forall k = 1, 2, \cdots, N_U,$$

$$-W_{i,j,k}^{r_2} \le 0, \quad \forall m = 1, 2, i = 1, 2, \cdots, N_G, \forall j = 1, 2, \cdots, N_S,$$

$$\forall k = 1, 2, \cdots, N_U. \tag{24}$$

Then, it is ensured that the optimal solution $W_{i,j,k}^{r_m *}$ of the original problem is reachable. By analyzing the relationship between the virtualized spectrum allocation problem and the dual problem, the conditions for the complementary slack relationship are as follows:

$$\lambda^{m^*}\left(\sum_{i=1}^{N_G}\sum_{k=1}^{N_U} x_{i,0,k}^{r_m} W_{i,0,k}^{r_m} - C_M\right) = 0,$$

$$\lambda^{m^*}\left(\sum_{i=1}^{N_G}\sum_{k=1}^{N_U}\sum_{k=1}^{N_U} x_{i,j,k}^{r_m} W_{i,j,k}^{r_m} - C_C\right) = 0,$$

$$\lambda_k^*\left(R_{\min} - \sum_{m=1}^{2}\sum_{i=1}^{N_G}\sum_{j=0}^{N_S} x_{i,j,k}^{r_m} R_{i,j,k}^{r_m}\right) = 0, \tag{25}$$

$$v_{i,j,k}^{r_m *} W_{i,j,k}^{r_m *}.$$

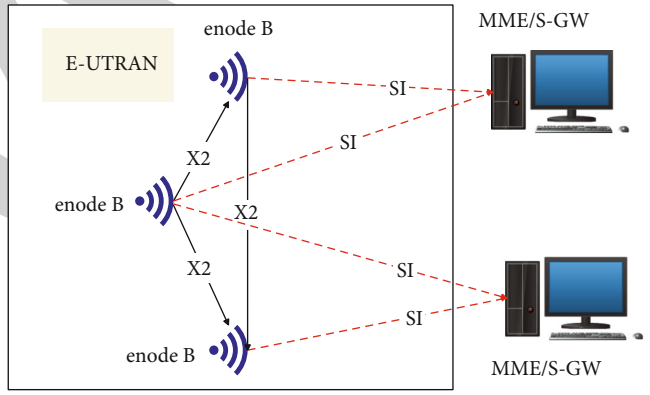

Figure 4: Schematic diagram of LTE architecture of the English education translation system.

The optimal value of $L(W_{i,j,k}^{r_m *}, \lambda^{m*}, \lambda_k^*, v_{i,j,k}^{m *})$ is obtained at $W_{i,j,k}^{r_m *}$; when the derivative is 0, the first-order constraint is satisfied:

$$\nabla\left(W_{i,j,k}^{r_m *}, \lambda^{m*}, \lambda_k^*, v_{i,j,k}^{m *}\right) = 0. \tag{26}$$

Among them, the feasible solution satisfies $W_{i,j,k}^{r_m *} \ge 0$, $\lambda^{m*} \ge 0, \lambda_k^* \ge 0, v_{i,j,k}^{m *} \ge 0$. The above formulas (24)–(26) are KKT conditions. Then, combine the obtained best Lagrangian multiplier $(\lambda^{m*}, \lambda_k^*, v_{i,j,k}^{m *})$ and KKT condition calculation:

$$\frac{\partial L\left(W_{i,j,k}^{r_m *}, \lambda^{m*}, \lambda_k^*, v_{i,j,k}^{m *}\right)}{\partial W_{i,j,k}^{r_m}} = 0. \tag{27}$$

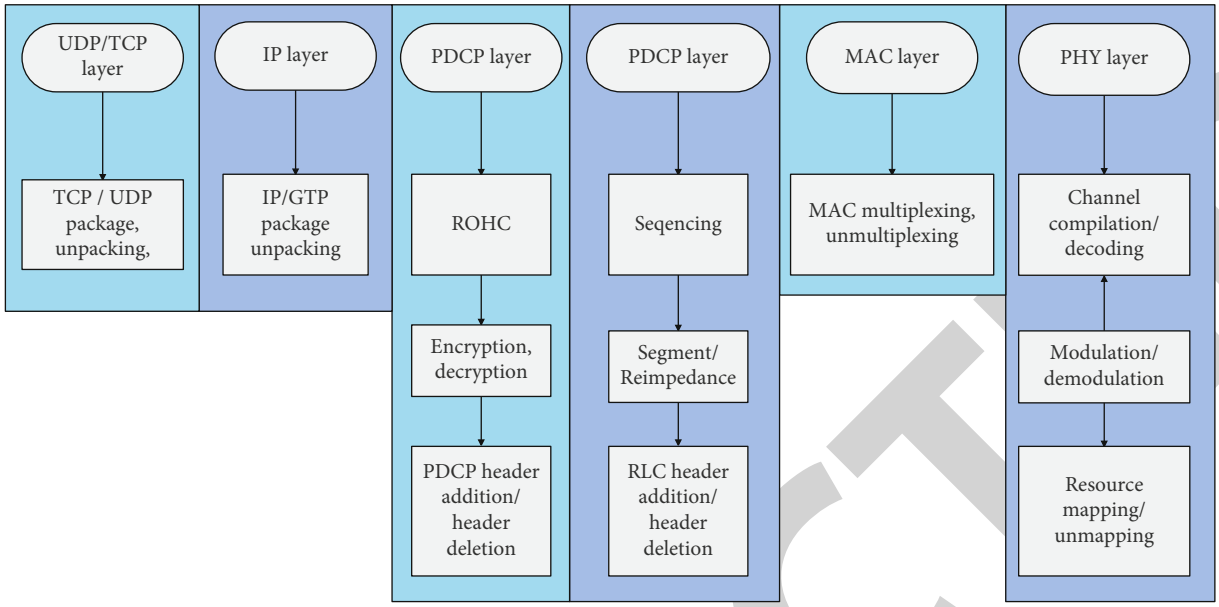

Figure 5: Schematic diagram of each functional module of the data plane.

Finally, the optimal solution to the virtualized spectrum allocation problem is

$$W_{i,j,k}^{r_m} = \frac{x_{i,j,k}^{r_m}}{\lambda^{m*}\left(x_{i,j,k}^{r_m} + x_{i,0,k}^{r_m}\right) - \lambda_k^{*} x_{i,j,k}^{r_m} \log\left(1 + \delta_{i,j,k}^{r_m}\right) - \nu_{i,j,k}^{r_m}}. \tag{28}$$

4. English Education Translation System Based on 5G Network Virtualization

The English education translation system network will introduce more communication modes, such as D2D (device-to-device), M2M (machine-to-machine), and V2V (vehicle-to-vehicle). To maintain an optimal user experience in such a complex network environment, RAT selection and management must be done on the network side and the device terminal side at the same time. Heterogeneous networks are still the development direction of future communication networks. Therefore, flexible deployment and cost have become important factors for 5G networks. This requires 5G systems to be based on software implementation and virtualization technology to enable them to build different virtual core networks to meet the needs of specific applications. As shown in Figure 3, it briefly describes the diversified services, application scenarios, different network integration modes, and cloud-based layered architecture ideas of the wireless network of the English education translation system.

The continuous evolution of the English education translation system has put forward stricter delay requirements for the LTE system, especially the delay requirements of the control plane and the user plane. Therefore, the LTE system not only optimizes the radio frame length and transmission time interval (TTI) but also adjusts the network architecture. The current LTE system architecture is mainly composed of two parts, namely, the evolved core network EPC and the evolved access network E-UTRAN, as shown in Figure 4.

Figure 5 shows the functional division of the data processing module in the English education translation system eNB-D. As shown in the figure, some sublayers have control logic tightly coupled with data, such as HARQ in the MAC layer and ARQ in the RLC layer. Here, these control functions are still attributed to the data plane.

The 5G network will not only adjust the access network architecture but also improve the forwarding plane. Moreover, it uses a distributed gateway with a sinking user plane to realize distributed deployment. Through the local cloud service system, the streaming media services originally obtained from the service center through the complicated Internet network can be cached to the local cloud server. Figure 6 shows the business flow network transmission model of the English education translation system.

As shown in Figure 7, a service chain flow needs to update its internal network functions VNF1, VNF4, and VNF5 from the old routing path to the new routing path based on performance optimization reasons. The update time required for each network function can be obtained according to the time prediction model in the previous section. If we use OpenNF's update mechanism to update the service chain in the figure, we first start from the data flow, and the data packets flow along the old deployment path of the service chain. It is found that the source network function "Old VNF1" needs to be updated, so it is updated.

Figure 8 is the hardware composition of this intelligent translation system, which is mainly composed of a database server, gateway server, client, and human-computer interaction terminal, including information processing module, AD module, and controller module. When translating English

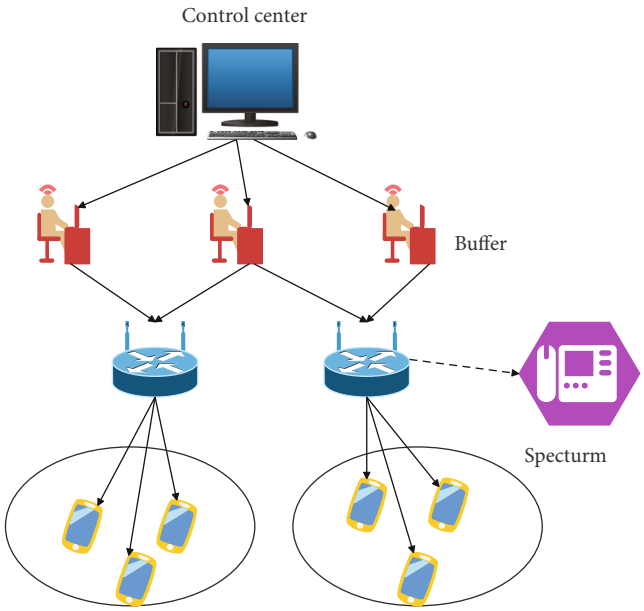

Figure 6: The new network service transmission model of the English education translation system.

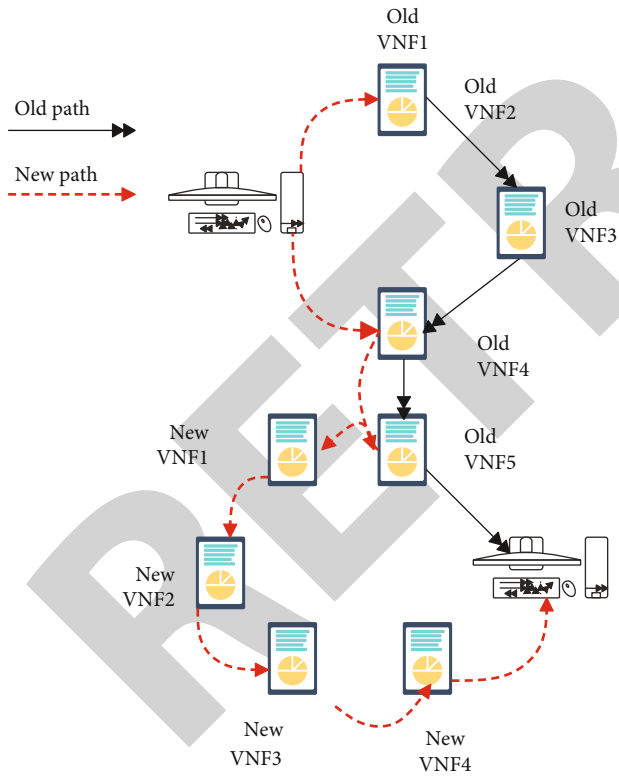

Figure 7: An example of updating the service chain of the English education translation system.

literary works, the user inputs the content to be translated from the client and uploads it to the database server through the gateway server for information processing. When encountering ambiguity judgments, the interpersonal interaction mode is turned on, and the human-computer interaction terminal is used for manual judgment, and the judgment results are fed back to the client and server at the same time.

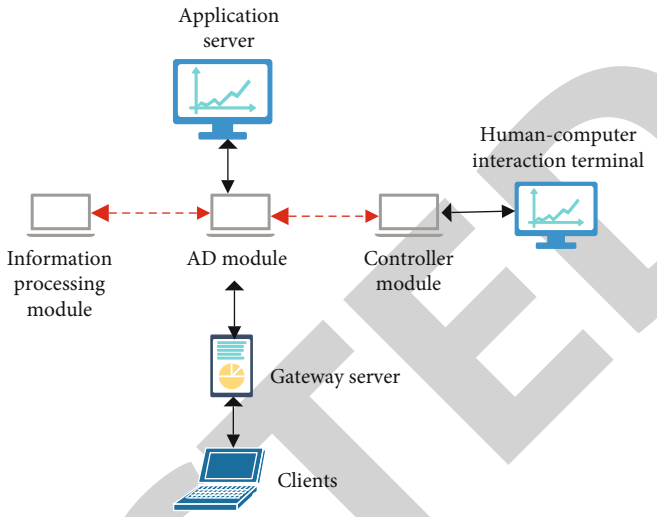

Figure 8: The hardware structure of the English education translation system.

Table 1: Data processing and transmission effect of the English education translation system based on 5G virtualization.

Number	5G data processing	Number	5G data processing	Number	5G data processing
1	89.09	17	89.92	33	90.06
2	89.91	18	88.65	34	93.82
3	86.08	19	92.38	35	85.87
4	85.88	20	91.46	36	86.60
5	90.67	21	89.74	37	86.76
6	85.86	22	92.39	38	87.28
7	85.78	23	86.59	39	88.43
8	87.34	24	85.87	40	88.68
9	92.17	25	91.89	41	89.94
10	92.01	26	88.91	42	93.01
11	93.30	27	86.70	43	89.39
12	90.24	28	85.32	44	87.12
13	89.91	29	91.14	45	90.43
14	85.27	30	88.43	46	92.14
15	93.01	31	89.08	47	88.79
16	85.60	32	89.94	48	86.09

On the basis of the above research, this article studies the English education translation system based on 5G virtualization built in this article. This paper conducts experimental research by inputting multiple sets of English data and counts the experimental data, evaluates the system's 5G data transmission and the translation effect of the English education translation system, and obtains the results shown in Tables 1 and 2.

From the above research, it can be seen that the English education translation system based on 5G virtualization constructed in this paper can play an important role in smart English teaching.

Table 2: Translation effects of the English education translation system based on 5G virtualization.

Number	Translation evaluation	Number	Translation evaluation	Number	Translation evaluation
1	83.92	17	82.05	33	84.74
2	85.12	18	89.50	34	78.86
3	88.96	19	82.28	35	82.54
4	78.98	20	88.93	36	86.54
5	91.89	21	79.08	37	84.60
6	89.10	22	79.95	38	86.06
7	82.10	23	80.33	39	86.34
8	83.66	24	88.90	40	90.51
9	89.40	25	86.03	41	87.49
10	87.79	26	87.05	42	79.52
11	85.83	27	83.05	43	82.47
12	83.33	28	86.89	44	78.72
13	86.33	29	79.34	45	84.56
14	79.25	30	91.98	46	82.30
15	82.01	31	83.60	47	89.96
16	82.52	32	80.33	48	87.69

5. Conclusion

With the advent of the 5G era and the continuous development of computer technology, many technologies are affecting and improving the quality of people's lives. At the same time, it also affects the teaching mode of college classrooms. In particular, the gradual popularization and improvement of virtual reality technology under 5G networks have enabled immersive classroom teaching to be realized. The traditional classroom teaching centered on the knowledge imparted by teachers will gradually be replaced by immersive classroom teaching based on virtual reality technology with the popularization of 5G networks. The application of virtual reality technology is very extensive. In the future, classroom teaching has a broader platform and a more open environment. How to combine the advantages of 5G in the construction of classroom teaching in colleges and universities to better serve education has become a very important and urgent research topic. Based on the above analysis, this article studies an English education translation system based on 5G network virtualization and provides theoretical references for improving the effect of smart teaching in subsequent English education. The experimental research results show that the English education translation system based on 5G virtualization constructed in this paper can play an important role in smart English teaching.

Data Availability

The labeled dataset used to support the findings of this study are available from the corresponding author upon request.

Conflicts of Interest

The author declares no competing interests.

Acknowledgments

This study is sponsored by Research on the Professional Development of English Teachers Based on the Status Quo of College English Teaching in Higher Vocational Colleges (No. 18JK0057).

References

[1] F. Chaume, "An overview of audiovisual translation: four methodological turns in a mature discipline," *Journal of Audiovisual Translation*, vol. 1, no. 1, pp. 40–63, 2018.

[2] E. Brynjolfsson, X. Hui, and M. Liu, "Does machine translation affect international trade? Evidence from a large digital platform," *Management Science*, vol. 65, no. 12, pp. 5449–5460, 2019.

[3] R. Schulte, "Expanding the horizon of translation studies," *Translation Review*, vol. 106, no. 1, pp. 1–3, 2020.

[4] K. Gurumurthy, D. Anand, and K. Karthik, "Democratizing translation using digital methods," *Language and Language Teaching*, vol. 10, no. 1, pp. 30–36, 2021.

[5] K. Karlgren, M. Lakkala, A. Toom, L. Ilomäki, P. Lahti-Nuuttila, and H. Muukkonen, "Assessing the learning of knowledge work competence in higher education–cross-cultural translation and adaptation of the Collaborative Knowledge Practices Questionnaire," *Research Papers in Education*, vol. 35, no. 1, pp. 8–22, 2020.

[6] C. Dinneen, "Students' use of digital translation and paraphrasing tools in written assignments on Direct Entry English Programs," *English Australia Journal*, vol. 37, no. 1, pp. 40–51, 2021.

[7] Y. Sun and D. Li, "Digital humanities approaches to literary translation," *Comparative Literature Studies*, vol. 57, no. 4, pp. 640–654, 2020.

[8] M. M. J. F. Farooque and B. Jadad, "A comparative analysis of translation software using data science approach to Arabic

Hindawi
Journal of Sensors
Volume 2022, Article ID 6477297, 11 pages
https://doi.org/10.1155/2022/6477297

Research Article

Research on Seismic Vulnerability of High-Pier and Long-Span Bridges Based on Improved IMK Resilience Model

Yifan Wang[1] **and Lihui Yin**[1,2]

[1]*School of Civil Engineering, Northeast Forestry University, Harbin 150040, China*
[2]*School of Civil Engineering, Heilongjiang University, Harbin 150080, China*

Correspondence should be addressed to Lihui Yin; yinlihui@nefu.edu.cn

Received 29 November 2021; Revised 24 December 2021; Accepted 5 January 2022; Published 27 January 2022

Academic Editor: Wei Zhang

After the fragility curve is established, the probability of structural damage reaching each level of damage under the action of the ground motion can be determined according to the ground motion parameters, so as to calculate the direct and indirect loss caused by the structural damage and complete the earthquake damage prediction. This paper combines the improved IMK resilience model to study the seismic vulnerability of high-pier and long-span bridges. Moreover, this paper obtains the parameter calculation model based on the regression analysis of PEER's 255 column specimen data. The improved IMK model needs to modify the elastic stiffness and strain hardening rate of the rotating spring to ensure the accuracy of the lateral stiffness of the component. The experimental research shows that the seismic vulnerability research model of high-pier and long-span bridges based on the improved IMK restoring force model has a certain analytical effect.

1. Introduction

The seismic design strength of existing ordinary small and medium-span bridges is generally based on the national unified seismic zoning. The seismic design parameters of the same structural type of bridges in the same zoning are the same, so the structural strength reserve when encountering an earthquake is the same [1]. However, during the actual earthquake, the seismic intensity of various places within the same seismic zone is not consistent or even significantly different, which leads to bridges with insufficient redundancy of individual structures that are prone to damage [2]. Therefore, it is necessary to use the probabilistic seismic hazard analysis method considering the temporal and spatial inhomogeneity of seismic activity to obtain the regional seismic hazard analysis results from the perspective of seismic subdivision. At the same time, it is necessary to combine dynamic time history analysis and structural vulnerability analysis to calculate the failure probability of the bridge under a given earthquake [3]. On this basis, the connectivity reliability of the traffic network after the earthquake is calculated, the vulnerability of the traffic network under the influence of the earthquake is studied, and a calculation model for solving the optimal path is proposed. In order to further improve the calculation efficiency and reduce the amount of calculation storage, the Target Order algorithm is proposed and the effectiveness of the algorithm is verified in the actual road network. The data obtained from the research can provide references for future engineering construction planning in the region. At the same time, predicting the connectivity reliability of the transportation network after the earthquake will help the government to be effective and timely in making daily maintenance decisions and postearthquake disaster relief decisions. As a result, the loss caused by the earthquake is reduced as much as possible, and the overall earthquake prevention and disaster reduction capabilities of the region are improved.

Over the past few decades, bridge engineering, which is an important foundation for national development, has developed significantly. With the gradual advancement of the national infrastructure construction process, the number and span of newly built bridges have been greatly improved.

At the same time, relevant seismic codes for bridge engineering are gradually improving. However, bridge damage caused by frequent earthquakes is becoming more and more common. Once the bridge is damaged, the transportation network may be paralyzed; in the earthquake rescue and relief, the bridge acts as a lifeline, and the consequences of its damage will be more serious. The reasonable implementation of bridge seismic fortification needs to be established on the basis of reasonable bridge seismic damage prediction model. On the one hand, a reasonable bridge earthquake damage prediction model can make a more accurate assessment of local earthquake losses from a macro perspective, including preearthquake assessment to control possible losses within an acceptable range, and establish a reasonable earthquake early warning and monitoring mechanism. It can quickly formulate rescue plans after an earthquake to provide support for government decision-making; on the other hand, the bridge earthquake damage prediction model can also provide a more accurate reference for the seismic design of specific bridges. Although my country has carried out a lot of research on earthquake damage prediction models of highway bridges, the researches are usually only for single bridges, there are few studies on the seismic damage assessment of bridge networks, and there is still a lack of relatively unified highway bridge earthquake damage prediction models. This restricts the development of earthquake damage prediction systems for highway bridges to a certain extent. In contrast, some developed countries in the world (such as the United States) have established standardized earthquake damage prediction methods. The most typical representative is HAZUS, which was jointly promoted by FEMA and NIBS in 1997. In HAZUS, it is believed that the key to earthquake damage prediction of highway bridges is to classify bridges based on their seismic performance and define five failure states of bridges, including no damage, slight damage, medium damage, severe damage, and complete damage, and then be able to determine the vulnerability curve of each type of bridge in each failure state. The seismic vulnerability curve is a function of ground motion parameters as an independent variable (defined as a cumulative distribution function that obeys a lognormal distribution in HAZUS).

This paper combines the improved IMK resilience model to study the seismic vulnerability of high-pier and long-span bridges and builds an intelligent model to provide a theoretical reference for the subsequent performance improvement of high-pier and long-span bridges.

2. Related Work

Literature [4] used expert investigation to analyze the seismic vulnerability of highway bridges and formed the seismic vulnerability curve of highway bridges. However, the limited number of samples limits the credibility of the research results. Literature [5] studied the contribution rate of various structural features to the seismic vulnerability of bridge structures and formed seismic vulnerability curves of railway bridges under the action of earthquakes of different intensities. The method proposed in [6] forms an earthquake vulnerability curve. It is assumed that each seismic vulnerability curve is a standard log-normal cumulative distribution function with unknown location parameters and known proportional parameters, so as to consider both capacity and demand. It is assume that each seismic vulnerability curve is a standard log-normal cumulative distribution function with unknown location parameters and known constant scale parameters, so as to integrate the random uncertainties of both capacity and demand. Literature [7] formed the seismic vulnerability curve of bridge piers by using the bridge damage data observed in the Kobe earthquake. In the research, the log-normal distribution function of two parameters is used to characterize the seismic vulnerability curve, and the relevant parameters are estimated by the maximum probability method. Literature [8] formed the seismic vulnerability curve of the bridge structure based on the bridge damage data obtained in the Northridge earthquake using logistic regression analysis. The seismic vulnerability curve formed by the empirical analysis method is usually based on the actual seismic damage data and the corresponding statistical results of ground motion parameters and has high reliability. The damage curve is only suitable for situations similar to the data source. Therefore, the empirical vulnerability curve is difficult to promote and use, and it is necessary to establish a reliable theoretical analysis method for the seismic vulnerability curve of bridge structures.

When analyzing the seismic vulnerability of bridge structures, different researchers have adopted different analysis methods. Reference [9] combines the characteristics of the bridge structure to systematically study the seismic vulnerability of the pier column at the most vulnerable part of the regular beam bridge and proposes an analysis based on the numerical simulation to form the seismic vulnerability curve of the pier column method. Literature [10] formed seismic vulnerability curves of reinforced concrete piers based on traditional reliability methods and numerical simulation methods and compared the seismic vulnerability curves obtained by the two methods. Literature [11] uses the Monte Carlo sampling simulation method to form the seismic vulnerability curve of the bridge structure. The response of the structure is calculated by two different methods, namely, the nonlinear dynamic time history analysis method and the capacity spectrum method. The comparison results of the seismic vulnerability curves formed by the two methods show that the consistency of the seismic vulnerability curves of the bridge in the two states of severe damage and complete failure is not as good as that of the slightly damaged state. Literature [12] proposed a method of forming seismic vulnerability curve through numerical simulation. The bridge pier is idealized as a single-degree-of-freedom vibration system, the seismic records of the Hanshin earthquake and the Northridge earthquake are used as input to calculate the Park-Ang damage index of the pier, and then the Park-Ang damage index and ground motion strength measurement parameters are used to form the reinforced concrete pier Earthquake vulnerability curve. Literature [13] analyzed the seismic vulnerability of a four-span simply supported girder bridge, obtained the seismic response data of the structure through nonlinear dynamic

time history analysis, and used a logical model to determine that the structure surpassed the specified ground motion intensity measurement parameters and used a logic model to determine the conditional probability that the structure exceeded the specified ground motion intensity measurement parameters. In this method, whether a certain vector in the Bernoulli random variable is 1 or 0 is determined according to whether the bridge maintains a certain damage state, and the parameters in the model are determined by regression analysis. Literature [14] formed the seismic vulnerability curves of four typical bridges through a comprehensive analysis of bridges in the central and southeastern regions of the United States. In the literature [15], the nonlinear analysis model and artificial seismic records were used to first form the seismic vulnerability curve of each bridge component (pier or support), and then the first order reliability principle was used to obtain the seismic vulnerability of the entire bridge system and then the seismic vulnerability damage curve of the bridge is obtained by using the first-order reliability principle. The research results show that among the four types of bridges, the most prone to damage are multispan simply supported beam bridges and multispan continuous steel beam bridges, and the least likely to be damaged are multispan continuous prestressed concrete beam bridges.

3. Improved Ibarra-Medina-Krawinkler Restoring Model

The hybrid simulation of seismic response of reinforced concrete frame structures and the analysis of their collapse resistance require a restoring force model that can effectively simulate the hysteresis characteristics of reinforced concrete members and accurate model parameters. The plastic dumpling model is a model often used in the nonlinear simulation of frame structures. It not only reflects the mechanical characteristics of the member but also is closely related to the material, restraint condition, and spatial layout of the member. Since decades, the plastic dumpling model has developed rapidly. The improved IMK model, as a plastic dumpling model with a trifold as the skeleton curve, introduces a degradation parameter β based on energy dissipation, which can consider a variety of degradation characteristics of the member under reciprocal loading. Compared with other plastic dumpling models, it can better simulate the hysteresis characteristics of reinforced concrete beams and columns effectively [16].

The main model skeleton parameters include elastic stiffness K_e, yield moment M_y, plastic corner $\theta_{cap,pl}$, post-yield hardening stiffness M_c/M_y, and postpeak corner θ_{pc}. An important feature of this model is the postpeak unloading section [17]. It can simulate the strain softening behavior associated with physical phenomena such as concrete crushing, steel buckling fracture, and bond damage. Figure 1 shows the skeleton curve of the modified IMK model.

The improved IMK model includes three types of models, that is, the bilinear model, the peak pointing model, and the pinched model.

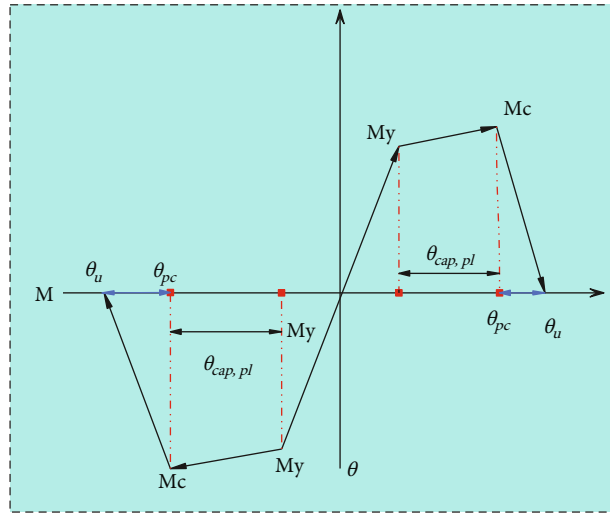

Figure 1: Improved IMK model skeleton curve.

The bilinear model is based on the bilinear hysteresis rule with strain hardening, which retains the main part of the bilinear hysteresis rule and introduces the degradation section after the peak and the residual strength section. The bilinear model is shown in Figure 2.

After unloading from point 3, the model sets the strength at point 3 as the strength limit in the positive direction. When the load is unloaded from point 5 in the negative direction, the maximum value of the restoring force is the previously set strength limit value, that is, the vertical coordinate of point 6. The load is then loaded from point 6 to point 3 with O stiffness and then continues with the degraded segment stiffness.

The peak pointing model retains the basic hysteresis rule and adds the degraded section and the residual strength section after the peak, and the model is shown in Figure 3 [18].

Compared with the bilinear model, the peak pointing model is unloaded at the positive 2 points and then loaded from the point on the horizontal axis to the previously unloaded 2 points after a hysteresis half-loop, that is, 8 points and 2 points are the same point, without considering the strength degradation. When unloading, the reloading stiffness changes after each arrival at the horizontal axis, and its value is determined by the intersection point with the horizontal axis and the peak displacement point in the previous cycle together.

The pinch model is similar to the peak pointing model; however, its reloading phase consists of two parts, as shown in Figure 4. In the reloading process, it is first loaded to the breakpoint 8 and then loaded to the previous unloading point 2. The breakpoint is determined by the maximum permanent deformation and the maximum force in the direction of loading. The parameter k_d is introduced in determining the transverse coordinate of the breakpoint, and the parameter k_f is introduced in determining the longitudinal coordinate of the breakpoint. If the deformation δ_{per} at the intersection of the reloading section with the transverse coordinate is greater than $(1 - k_d)/\delta_{per}$, and if strength

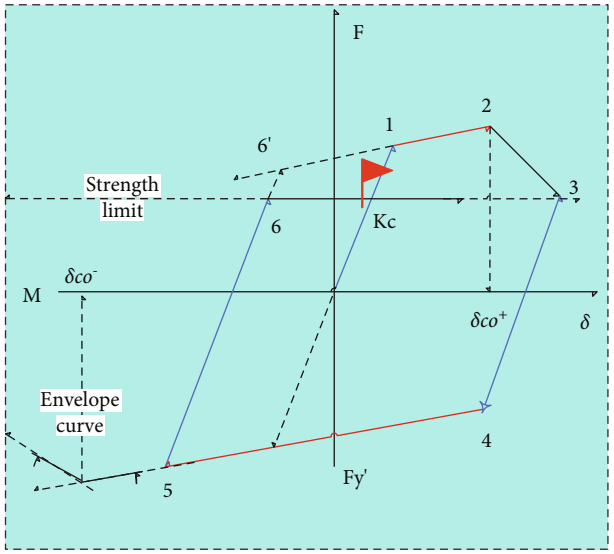

Figure 2: Bilinear model.

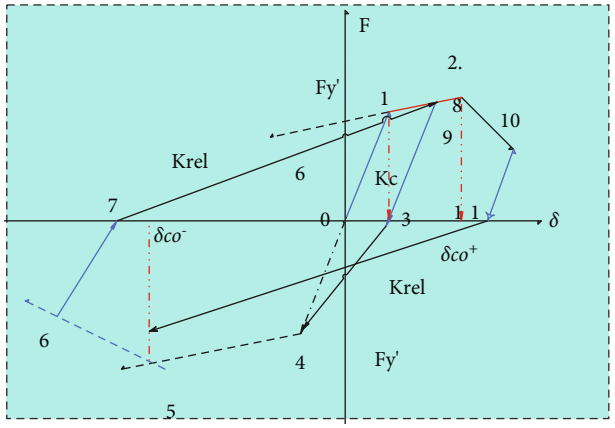

Figure 3: Peak pointing model.

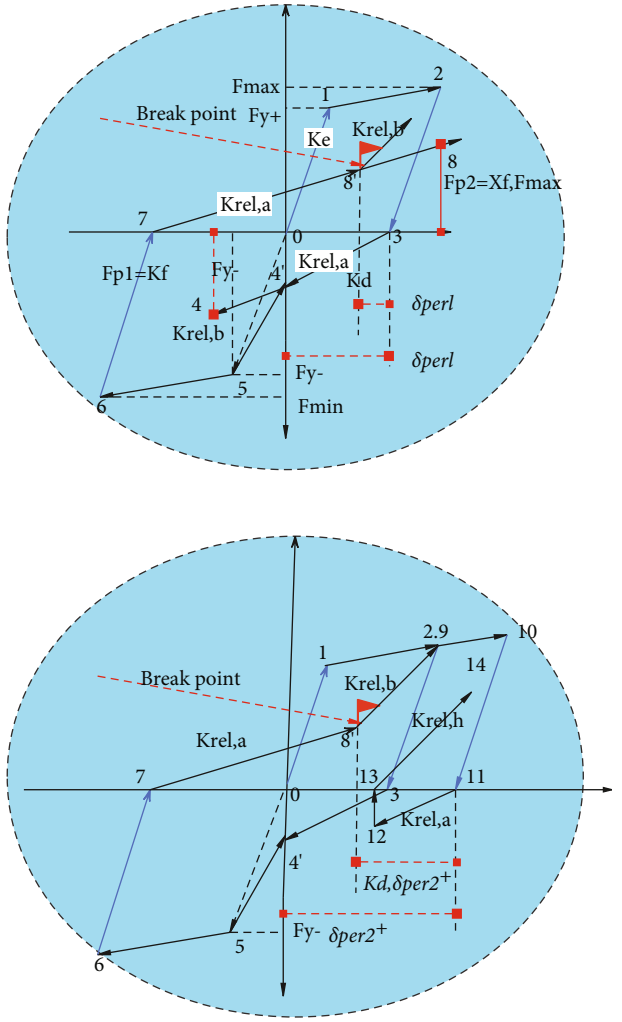

Figure 4: Pinch type model.

degradation is not considered, then the reloading path is loaded only for the straight line section from point 13 to the previous unloading point 10 [19].

The improved IMK model can depict four basic cyclic degradation modes of the member, that is, basic strength degradation, softening segment strength degradation, unloading stiffness degradation, and reloading stiffness degradation. The peak pointing model is used as an example to introduce the four degradation modes of the improved IMK model.

The cyclic degradation rate β is determined by the energy dissipation of the member under reciprocal loading. It assumes a reference value for the energy dissipation capacity of each member and does not consider the effect of the member loading history. The cyclic degradation rate β is calculated as follows [20]:

$$\beta_i = \left(\frac{E_i}{E_i - \sum_{j=1}^{i=1} E_j} \right). \quad (1)$$

Among them, β_i denotes the degradation coefficient calculated in the cycle numbered i, E_i denotes the reference value of the energy consumption of the component, $E_i = \gamma F_y \delta_y$, and γ is the coefficient calibrated from the experimental results. For each degradation mode is different, E_i refers to the energy consumption of the component in the cycle numbered i, the second bias E_i refers to the energy consumption of the component in the cycle numbered $i-1$, c denotes the exponential term coefficient of the degradation rate, and c is taken from 1.0 to 2.0. If the loading cycle consists of a sequence of cycles of constant amplitude, then $c = l$ indicates an almost constant degradation rate, while $c = 2$ indicates a slowing down of the degradation rate of the earlier cycles and an acceleration of the degradation rate of the later cycles [21].

Throughout the loading history, the value of β must be taken to satisfy $0 \le \beta_i \le 1$, that is

$$\gamma F_y \delta_y - \sum_{j=1}^{i} E_j \le E_i. \quad (2)$$

After each half turn of the cycle, the yield strength of the member will be degraded accordingly, and the degradation of the yield strength satisfies the expression as follows:

$$F_i^+ = \left(1 - \beta_{s,i}\right) F_{i=1}^+, \tag{3}$$

$$F_i^- = \left(1 - \beta_{s,i}\right) F_{i=1}^-. \tag{4}$$

Among them, $F_i^{+/-}$ denotes the yield strength value after the cycle numbered i in positive and negative directions, and $F_{i=1}^{+/-}$ denotes the yield strength value before the cycle numbered i.

For each degradation parameter $\beta_{s,i}$, which contains values in the positive direction and values in the negative direction, the basic intensity degradation rates in these two directions are calculated independently. That is, the value of F_i^- is updated after the end of each cycle in the positive direction, and the value of F_i^+ is updated after the end of each cycle in the negative direction.

The degradation mode of the basic strength also includes the degradation of the hardened stiffness, and the form of the hardened stiffness degradation is as follows:

$$K_{s,j}^+ = \left(1 - \beta_{s,i}\right) K_{s,j=1}^+, \tag{5}$$

$$K_{s,j}^- = \left(1 - \beta_{s,i}\right) K_{s,j=1}^-. \tag{6}$$

Similar to the yield strength, the hardening stiffness is calculated independently in both positive and negative directions.

Figure 5 illustrates the degradation pattern of the basic strength. After the loading path is loaded from 0 to 3, the degradation rate $\beta_{s,i}$ is calculated, at which time the negative yield strength of the member degrades from F_y^- to F_1^- and the negative stiffness of the member degrades from $K_{s,0}$ to $K_{s,1}{}^-$. After the loading path is loaded from 3 to 7, the value of the degradation rate $\beta_{s,i}$ is recalculated. At this time, the positive yield strength of the member is degraded from F_y^+ to F_1^+, and the positive stiffness of the member is degraded from $K_{s,0}$ to $K_{s,1}{}^+$.

Unlike the basic strength degradation, the softening segment strength degradation means that after the peak point, the slope of the softening segment remains constant. However, the intensity value of the intersection of the extension line and the vertical coordinate degrades with the number of cycles. The softening segment strength degradation equation is shown below:

$$F_{ref,1}^{+/-} = \left(1 - \beta_{e,i}\right) F_{ref,i-1}^{+/-}. \tag{7}$$

$F_{ref}^{+/-}$ is the intensity value at the intersection of the extension of the softened segment with the vertical coordinate after the peak, and similarly, the positive and negative degradation rates $\beta_{e,i}$ are calculated independently. The softening segment strength degradation rate is calculated each time it intersects the horizontal axis, which may not affect the loading path in the early stages of the nonlinearity. Figure 6

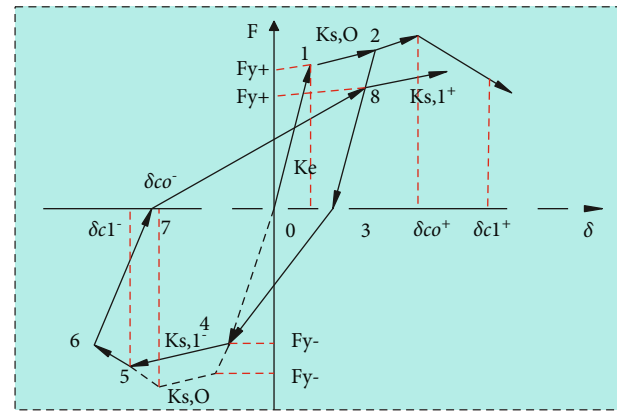

Figure 5: Basic strength degradation.

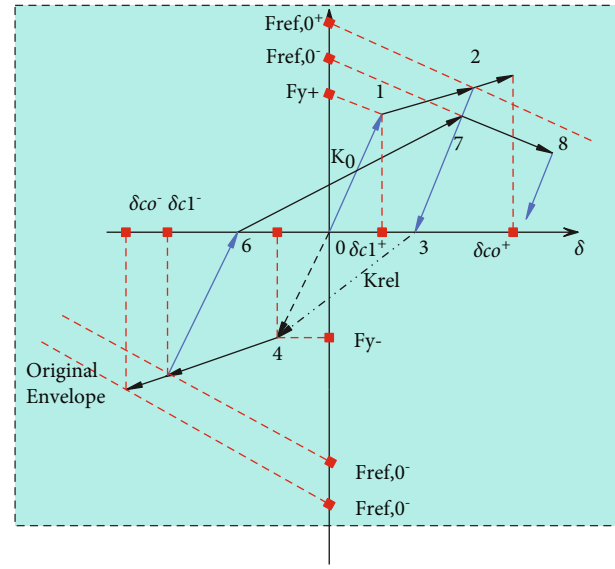

Figure 6: Strength degradation of softened section.

shows the softening section strength degradation. This shows that the softening segment strength degradation rate is first calculated when loading to point 3, where the intersection of the softening segment extension with the vertical coordinate in the negative direction degrades from $F_{ref,0}^-$ to $F_{ref,1}^-$. At loading up to 6, the softening segment strength degradation rate is recalculated, and the intersection of the positive softening segment extension with the longitudinal coordinate degrades from $F_{ref,0}^+$ to $F_{ref,1}^+$.

The unloading section contains negative unloading section and positive unloading section, the unloading stiffness degradation does not distinguish between positive and negative direction, and its stiffness degradation is calculated by the following formula:

$$K_{u,i} = \left(1 - \beta_{k,i}\right) K_{u,i-1}. \tag{8}$$

$K_{u,i}$ and $K_{u,i-1}$ denote the unloading stiffness before and after the half-turn of the cycle numbered i, respectively.

Among them, the zone is calculated by equation (1) and the appropriate cyclic degradation parameter γ_k. Unlike the degradation rates of the remaining three cases, the unloading stiffness degradation rate is the only one that is calculated when the load is reversed in the nonlinear phase. In addition, the unloaded stiffness is updated in both positive and negative directions. Therefore, the degradation of the unloaded stiffness is twice as high as that of the other degradation types.

Figure 7 illustrates the degradation of unloading stiffness. The unloading stiffness degrades from K_e to $K_{u,1}$ when loading to point 2 and then continues to degrade from $K_{u,1}$ to $K_{u,2}$ when loading to point 5.

The reloading stiffness degradation increases the magnitude of the target displacement. Depending on the direction of loading, the increased target displacement is defined by the maximum displacement of the last corresponding directional cycle. The reload stiffness degradation is only applicable to the peak pointing model and pinched model with the following expressions:

$$\delta_{i,j}^{+/-} = \left(1 + \beta_{a,i}\right)\delta_{i,j-1}^{+/-}. \tag{9}$$

Figure 8 shows an illustration of the reload stiffness degradation. The value of the reload stiffness degradation rate $\beta_{a,i}$ is updated each time it is unloaded to intersect with the horizontal axis. The cyclic half-turn target displacement $\delta_{i,j-1}^{+/-}$ with the corresponding direction number i is calculated from the cyclic half-turn target displacement $\delta_{i,j}^{+/-}$ with that direction number $i-1$.

The improved IMK model requires the determination of seven parameters, and the seven parameters are initial stiffness K_e, yield moment M_y, plastic turning angle $\theta_{cap,pl}$, post-yield hardening stiffness M_c/M_y, postpeak turning angle θ_{pc}, normalized hysteretic energy dissipation parameter λ, and exponential term degradation parameter c.

The empirical prediction equations for the above parameters were established based on 255 column specimens in the PEER structural performance database, and the empirical prediction equations for the seven parameters are shown below.

At present, there is no good definition for the initial stiffness of steel composite members. Two forms are used to quantify the effective stiffness, that is, the cut-line stiffness value EI_y past the yield point, and the cut-line stiffness EI_{suf_40} past the 40% yield value point, and the empirical prediction formulas for both forms are as follows:

(1) The cut line stiffness past the yield point is calculated as follows:

$$\frac{EI_y}{EI} = -0.07 + 0.59\left[\frac{P}{A_g f_c'}\right] + 0.07\left[\frac{L_s}{H}\right], 0.2 \le \frac{EI_y}{EI} \le 0.6. \tag{10}$$

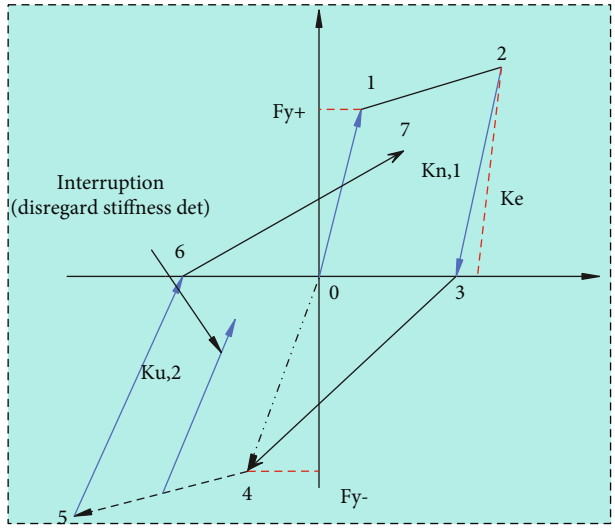

Figure 7: Unloading stiffness degradation.

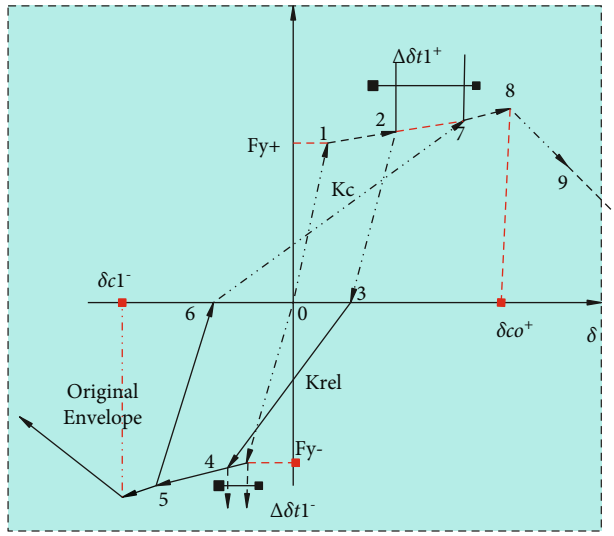

Figure 8: Reloading stiffness degradation.

(2) The simplified calculation formula for the secant stiffness past the yield point is as follows:

$$\frac{EI_y}{EI} = 0.065 + 1.05\left[\frac{P}{A_g f_c'}\right], 0.2 \le \frac{EI_y}{EI} \le 0.6. \tag{11}$$

(3) The formula for calculating the secant stiffness at the point of over 40% yield value is as follows:

$$\frac{EI_{suf\_40}}{EI} = -0.02 + 0.98\left[\frac{P}{A_g f_c'}\right] + 0.09\left[\frac{L_s}{H}\right], 0.35 \le \frac{EI_{suf}}{EI} \le 0.8. \tag{12}$$

(4) The simplified calculation formula for the secant stiffness at the point of over 40% yield value is as follows:

$$\frac{EI_{suf\_40}}{EI} = 0.17 + 1.61\left[\frac{P}{A_g f_c'}\right], 0.35 \le \frac{EI_{sf}}{EI} \le 0.8. \tag{13}$$

Among them, $P/A_g f_c'$ is the axial compression ratio of the column, and L_s/H is the aspect ratio of the column.

The empirical prediction formula of yield bending moment, the prediction formula of bending strength, and the formula are calculated as follows:

$$M_y = bd^3\phi_y\left\{E_c\frac{k_y^2}{2}\left(0.5\left(1+\delta'\right) - \frac{k_y}{3}\right) + \frac{E_s}{2}\left[\left(1-k_y\right)\rho + \left(k_y - \delta'\right)\rho' + \frac{\rho_v}{6}\left(1-\delta'\right)\right]\left(1-\delta'\right)\right\}. \tag{14}$$

Among them, the yield curvature is the smaller value in equations (15) and (16).

(1) If the yield of the section is determined by the yield of the tension steel bar, the calculation formula of the yield curvature is as follows:

$$\phi_y = \frac{f_y}{E_s\left(1-k_y\right)d}. \tag{15}$$

(2) If the yield of the section is due to the significant nonlinear phenomenon of the compressed part of the concrete, that is, the strain of the compressed part of the concrete exceeds its limit $\varepsilon_e \approx 1.8f_c'/E_c$, then, the calculation formula of the yield curvature is calculated as follows:

$$\phi_y = \frac{\varepsilon_e}{k_y d} \approx \frac{1.8f_c'}{E_e k_y d} \tag{16}$$

The depth k_y of the compressed part when the section yields (normalized by d) is

$$k_y = \left(n^2A^2 + 2nB\right)^{1/2} - nA. \tag{17}$$

Among them, $n = E_s/E_c$. If the reason for the section yielding is formula (1), then, the calculation formulas of A and B are formula (18) and (19). If the cause of section yielding is equation (2), then, the calculation formulas for A and B are equations (20) and (21).

$$A = \rho + \rho' + \rho_v + \frac{N}{bdf_y}, \tag{18}$$

$$B = \rho + \rho'\delta' + 0.5\rho_v\left(1+\delta'\right) + \frac{N}{bdf_y}, \tag{19}$$

$$A = \rho + \rho' + \rho_v - \frac{N}{\varepsilon_c E_c bd} \approx \rho + \rho' + \rho_v - \frac{N}{1.8nbdf_c'}, \tag{20}$$

$$B = \rho + \rho'\delta' + 0.5\rho_v\left(1+\delta'\right). \tag{21}$$

In the formula, ρ, ρ', and ρ_v, respectively, represent the reinforcement ratios of the longitudinal reinforcement of the compression part, the longitudinal reinforcement of the tension part, and the web reinforcement. $\delta' = d'/d$, d' refers to the distance from the center of the steel bar in the compression part to the outer edge of the concrete in the compression part. b and d are the width and height of the section, respectively, and N refers to the axial load (compression is positive).

Studies have shown that the axial compression ratio and concrete strength are the key factors that determine the hardening stiffness. The hardening stiffness M/M is expressed as follows:

$$\frac{M_c}{M_y} = (1.25)(0.89)^{\nu}(0.91)^{0.01c_{\text{units}}f_c'}. \tag{22}$$

The simplified constant equation for hardening stiffness after yielding is as follows:

$$\frac{M_c}{M_y} = 1.13. \tag{23}$$

Among them, ν is the axial compression ratio, f_c' is the concrete axial compressive strength, and c_{units} is the unit conversion variable. If the unit of f_c' is MPa, then c_{units} takes 1. If the unit of f_c' is ksi, then c_{units} takes 6.9.

The complete calculation formula of the plastic turning angle is as follows:

$$\theta_{cap,pl} = 0.12(1+0.55a_{sl})(0.16)^{\nu}(0.02+40\text{p}_{sh})^{0.43} \times (0.54)^{0.01c_{\text{units}}f_c'}(0.66)^{0.1s_n}(2.27)^{10.0\rho}. \tag{24}$$

The simplified calculation formula of the plastic turning angle is as follows:

$$\theta_{cap,pl} = 0.13(1+0.55a_{sl})(0.13)^{\nu}(0.02+40\text{p}_{sh})^{0.65}(0.57)^{0.01c_{\text{units}}f_c'}. \tag{25}$$

Among them, a_{sl} refers to the possibility of slippage of the longitudinal reinforcement at the end of the column (1 or 0), v represents the axial compression ratio of the member, s_n is the buckling coefficient of the reinforcement, $s_n = (s/d_b)(f_y/100)^{0.5}$, d_b is the diameter of the longitudinal reinforcement, f_y is the yield strength of longitudinal bars, ρ_{sh} is the area ratio of transverse steel bars in the column plastic dumpling zone, and ρ is the ratio of longitudinal bars.

Equations (24) and (25) are only applicable to the case where the cross-section is symmetrical. For the case of asymmetrical reinforcement, the analysis item of asymmetrical reinforcement is introduced into the formula, and the calculation formula of plastic rotation angle that can be used for asymmetrical reinforcement is obtained:

$$\theta_{cap,pl} = 0.12\left(\frac{\max\left(0.01, \left(\rho' f_y/f_c'\right)\right)}{\max\left(0.01, \left(\rho f_y/f_c'\right)\right)}\right)^{0.25} \cdot (1 + 0.55a_{sl})(0.16)^{v} \times (0.02 + 40\rho_{sh})^{0.43} \cdot (0.54)^{0.01c_{\text{units}}f_c'}(0.66)^{0.1s_n}(2.27)^{10.0\rho}, \tag{26}$$

$$\theta_{cap,pl} = 0.13\left(\frac{\max\left(0.01, \left(\rho' f_y/f_c'\right)\right)}{\max\left(0.01, \left(\rho f_y/f_c'\right)\right)}\right)^{0.225} \cdot (1 + 0.55a_{sl})(0.13)^{v} \times (0.02 + 40\rho_{sh})^{0.65} \cdot (0.54)^{0.01c_{\text{units}}f_c'}. \tag{27}$$

The calculation formula of the postpeak rotation angle is as follows:

$$\theta_{pc} = (0.76)(0.031)^{v}(0.02 + 40\rho_{sh})^{1.02} \le 0.10. \tag{28}$$

Among them, v is the axial compression ratio, and ρ_{sh} is the transverse steel area ratio.

The improved IMK model contains four degradation modes, namely, basic strength degradation, softening section strength degradation, unloading stiffness degradation, and reloading stiffness degradation. Each degradation mode is defined by two parameters: the normalized capacity dissipation capacity (λ) and the exponential term of the cyclic degradation speed (c). In order to reduce the complexity, assuming that the two parameters of the four cases are the same, the cycle degradation parameters are reduced from 8 to 2. The calculation formula 29 is a simplified calculation formula of a, and the corresponding c is taken as 1.0.

$$\lambda = (170.7)(0.27)^{v}(0.10)^{s/d}. \tag{29}$$

The cyclic energy dissipation capacity a is incorporated into OpenSees in the form of an input parameter, and the calculation formula of $\wedge$ is as follows:

$$E_t = \lambda \cdot \theta_{cap,p;} \bullet M_y = \wedge \bullet M_y, \tag{30}$$

$$\wedge = \lambda \bullet \theta_{cap,pl}. \tag{31}$$

a is the parameter of normalized energy dissipation capacity, which is defined by the total energy of the component:

$$E_i = \lambda \bullet \theta_y \bullet M_y. \tag{32}$$

In the above formula, when the model adopts the initial stiffness instead of EI_y/EI_g, the value of λ should be adjusted.

When the residual strength is 0, it sometimes causes errors in the OpenSees program. In order to avoid errors, the residual intensity can be taken as a nonzero positive number (0.01 is enough), so that errors in the program can be avoided in most cases.

For the flexural member that may deform to the inelastic range, a rotating spring of zero length is simulated at the end of the member, and the rotating spring at the end of the member (simulated by the zero-length unit) and the upper elastic unit are modeled in series. The overall stiffness of the member is a combination of the stiffness of the rotating spring and the stiffness of the elastic unit, and the expression is as follows:

$$K_{mem} = \frac{1}{(1/K_s) + (1/K_{bc})} = \frac{K_S K_{bc}}{K_s + K_{bc}}. \tag{33}$$

Among them, K_{mem} is the stiffness of the member, K_{bc} is the stiffness of the elastic unit, and K_s is the stiffness of the rotating spring. Analyzing the above equation, we can see that when the stiffness of the elastic unit is much larger than the stiffness of the rotating spring, the stiffness of the member is approximately the stiffness of the rotating spring. When the stiffness of the elastic beam-column unit is much smaller than the stiffness of the rotating spring, the member stiffness is approximately the stiffness of the elastic beam-column unit. In Ibarra's analysis, n times the stiffness of the elastic beam-column unit is used to represent the stiffness of the rotating spring, that is, $K_s = \text{nK}_{\text{bc}}$. Bringing $K_a = \text{nK}_{\text{bc}}$ into equations (33)–(35) are obtained. To make the stiffness of the member equal to the stiffness of the elastic unit, the cross-sectional moment of inertia of the elastic unit is the original cross-sectional moment of inertia of the elastic unit.

$$K_{bc} = \frac{n+1}{n} K_{mem}, \tag{34}$$

$$K_s = (n+1)K_{mem}. \tag{35}$$

After correcting the stiffness of the rotating spring, the strain hardening ratio, which is the ratio of the hardened stiffness to the elastic stiffness, needs to be corrected as well. The angle of rotation $\Delta\theta_{mem}$ of the member in the plastic phase consists of the angle of rotation of the rotating spring and the angle of rotation of the elastic unit, which is calculated as shown in equation (36). Equation (37) is obtained by taking $K_{s,s} = \alpha_{s,s}K_s$ and equations (34) and (35) into equation (36). Taking into account the angle of rotation $\Delta\theta_{mem} = \Delta M_{\text{in}}/$

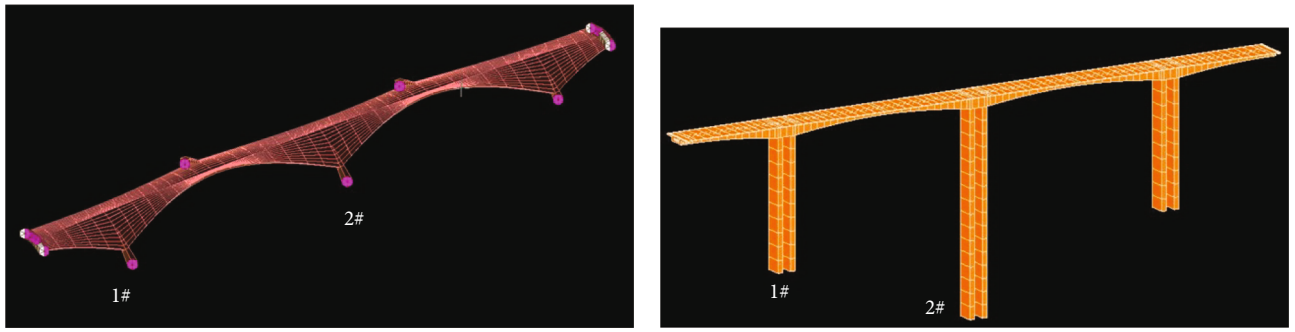

(a) Grid diagram of high pier and long-span bridge body (b) Overall structure drawing of high-pier and long-span bridge

Figure 9: Structure diagram of high pier and long-span bridge model.

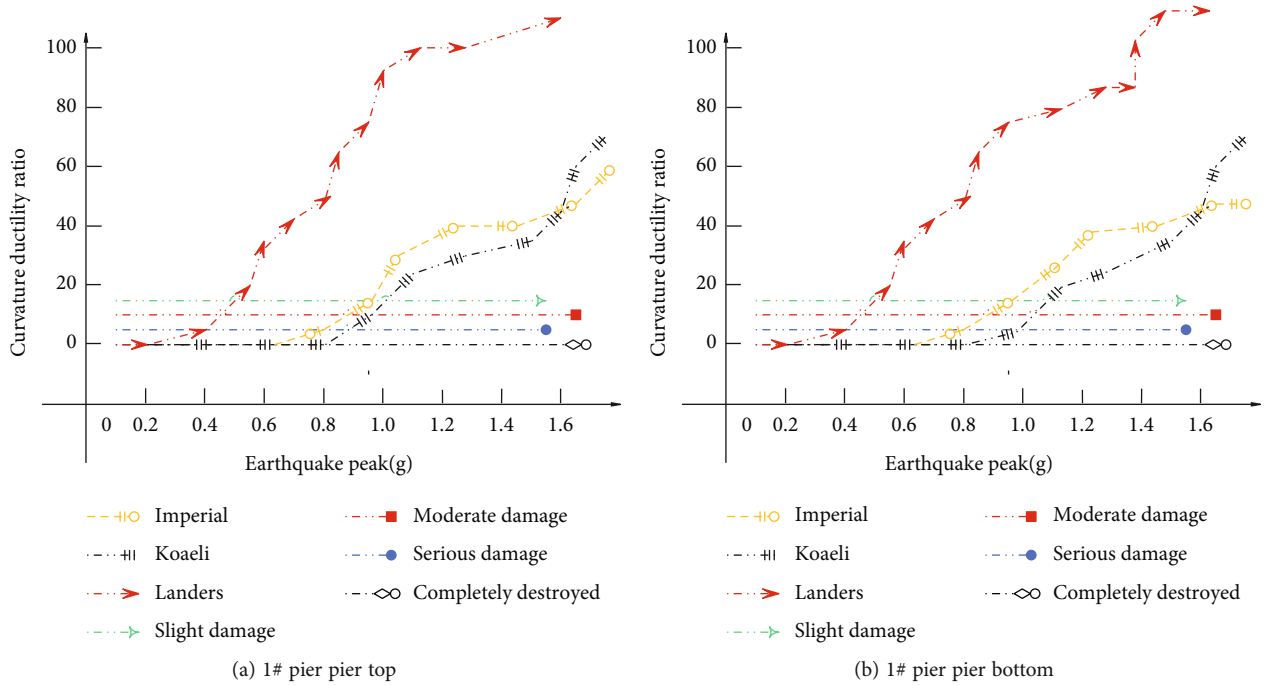

(a) 1# pier pier top (b) 1# pier pier bottom

Figure 10: IDA curve of 1# pier control section curvature ductility ratio.

$\alpha_{mem}K_{mem}$ of the member in the plastic phase, the expression (38) for the strain hardening coefficient of the rotating spring can be solved by combining it with equation (37).

$$\Delta\theta_{mem} = \Delta\theta_s + \Delta\theta_{bc} = \frac{\Delta M_{\text{in}}}{K_{s,s}} + \frac{\Delta M_{\text{in}}}{K_{bc}}, \tag{36}$$

$$\Delta\theta_{mem} = \Delta M_{\text{in}}\left(\frac{1 + n\alpha_{s,s}}{n\alpha_{s,s}K_{bc}}\right), \tag{37}$$

$$\Delta\theta_{mem} = \Delta\theta_s + \Delta\theta_{bc} = \frac{\Delta M_{\text{in}}}{K_{s,s}} + \frac{\Delta M_{\text{in}}}{K_{bc}}. \tag{38}$$

Among them, $\Delta\theta_s$ denotes the angle of rotation in the plastic phase of the rotating spring, $\Delta\theta_{bc}$ denotes the angle of rotation in the plastic phase of the elastic unit, ΔM_{in} is the increased bending moment in the plastic phase, $K_{s,s}$ and K_{bc} denote the stiffness of the rotating spring and the elastic unit in the plastic phase, respectively, $\alpha_{s,s}$ and $\alpha_{s,mem}$ denote the strain hardening rate of the rotating spring and the member, respectively, and n is the ratio of the rotating spring stiffness K_s to the elastic stiffness K_{bc} set in the elastic phase.

4. Research on Seismic Vulnerability of High-Pier and Long-Span Bridges Based on Improved IMK Resilience Model

Figure 9 shows a high-pier long-span bridge model. Three types of ground motions are applied longitudinally to obtain the bridge response, and the maximum curvature ductility ratio of the control section is obtained. In this paper, PGA is used as the independent variable, and the curvature ductility ratio is the dependent variable, and the IDA curve that controls the section curvature ductility ratio is drawn, as shown in Figures 10 and 11.

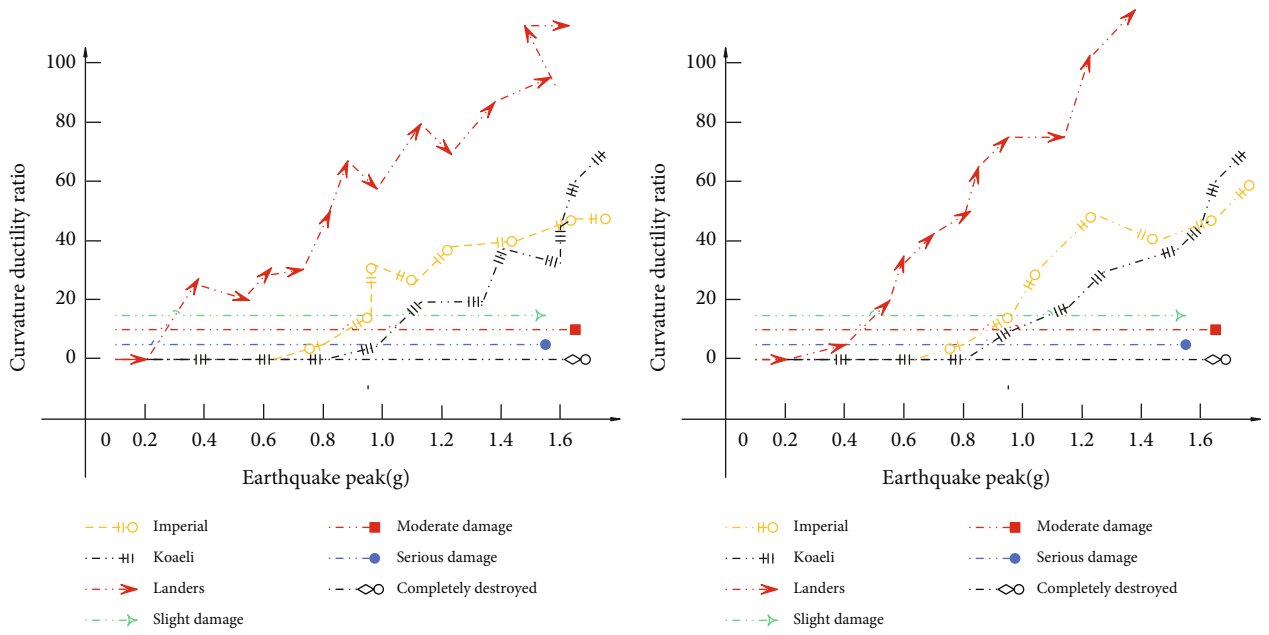

(a) 2# pier pier top

(b) 2# pier pier bottom

Figure 11: IDA curve of 2# pier control section curvature ductility ratio.

It can be clearly seen from Figures 10 and 11 that with the continuous increase of PGA, the maximum curvature ductility ratio of the critical section of the bridge is also increasing, which shows that it is appropriate to use PGA to represent the index of ground motion intensity. Due to the differences in the characteristics of the three types of ground motions, the damage caused is quite different. Compared with the other two ground motions, the Landers wave has a greater seismic response, while the other two ground motions have little difference in response, which is related to the original intensity of the ground motions. Under the action of a single ground motion, with the continuous increase of PGA, the specific damage state of the key section of the bridge can be seen more intuitively from the damage state histogram.

From the above research, it can be seen that the seismic vulnerability research model of high-pier and long-span bridges based on the improved IMK restoring force model has a certain analytical effect.

5. Conclusion

Through the analysis and research on the seismic damage evolution and vulnerability of the bridge structure, it is possible to evaluate the seismic performance of the bridge, provide a basis for the seismic design of the bridge, provide a theoretical basis for the assessment of bridge damage after the earthquake, and provide a certain theoretical basis for post-disaster decision-makers to formulate emergency plans for earthquake resistance and disaster reduction. However, high-pier long-span continuous rigid-frame bridges have more complex seismic performance and seismic response compared to low- and medium-span bridges, such as traveling wave effects, pile-soil interaction, and various complex nonlinear problems are more obvious. This paper combines the improved IMK resilience model to study the seismic vulnerability of high-piers and long-span bridges and builds an intelligent model. The test results show that the seismic vulnerability research model of high-pier and long-span bridges based on the improved IMK restoring force model has a certain analytical effect.

Data Availability

The labeled dataset used to support the findings of this study are available from the corresponding author upon request.

Conflicts of Interest

The authors declare no competing interests.

Acknowledgments

The research is supported by the 2nd Batch of Industry-University Cooperation Collaborative Education Project in 2021 by Department of Higher Education of Ministry of Education (Lihui Yin, School of Civil Engineering, Heilongjiang University) and the Natural Disaster Survey and Scientific Research Project of Heilongjiang Province in 2021 (Lihui Yin, School of Civil Engineering, Heilongjiang University).

References

[1] S. Deshan, Z. Erhua, D. Jun, and G. Shan, "Ground motion attenuation characteristics of Wenchuan earthquake and seismic response law of long-span continuous rigid frame bridge with high-rise pier," *China Civil Engineering Journal*, vol. 50, no. 4, pp. 107–115, 2017.

[2] L. Ren, G. Zhang, Y. Zhang, and S. He, "Seismic fragility analysis of V-shaped continuous girder bridges," *KSCE Journal of Civil Engineering*, vol. 24, no. 3, pp. 835–846, 2020.

[3] Z. Q. Chen, S. X. Zheng, Q. Zhou, Z. W. Chen, and X. Li, "Extreme value distribution and dynamic reliability estimation of high-pier bridges subjected to near-fault impulsive ground motions," *Advances in Structural Engineering*, vol. 23, no. 7, pp. 1367–1382, 2020.

[4] L. Tong, R. Wang, and D. Wang, "Seismic cracking mechanism and control for pre-stressed concrete box girders of continuous rigid-frame bridges: Miaoziping bridge in Wenchuan earthquake as an example," *Advances in Bridge Engineering*, vol. 2, no. 1, pp. 1–25, 2021.

[5] W. Q. Yue, H. Y. Jia, C. H. Zhao, X. L. Lan, and H. R. Liu, "Influence of actual site soil layers on pounding of a high-pier bridge occurred between deck and abutment," *Journal of Highway and Transportation Research and Development (English Edition)*, vol. 14, no. 1, pp. 55–64, 2020.

[6] R. Feng, X. Wang, W. Yuan, and J. Yu, "Impact of seismic excitation direction on the fragility analysis of horizontally curved concrete bridges," *Bulletin of Earthquake Engineering*, vol. 16, no. 10, pp. 4705–4733, 2018.

[7] F. Cui, H. Li, X. Dong et al., "Improved time-dependent seismic fragility estimates for deteriorating RC bridge substructures exposed to chloride attack," *Advances in Structural Engineering*, vol. 24, no. 3, pp. 437–452, 2021.

[8] G. Falsone, A. Recupero, and N. Spinella, "Effects of near-fault earthquakes on existing bridge performances," *Journal of Civil Structural Health Monitoring*, vol. 10, no. 1, pp. 165–176, 2020.

[9] M. Miari, K. K. Choong, and R. Jankowski, "Seismic pounding between bridge segments: a state-of-the-art review," *Archives of Computational Methods in Engineering*, vol. 28, no. 2, pp. 495–504, 2021.

[10] W. Guo, C. Zeng, H. Gou, Y. Hu, H. Xu, and L. Guo, "Rotational friction damper's performance for controlling seismic response of high speed railway bridge-track system," *Computer Modeling in Engineering & Sciences*, vol. 120, no. 3, pp. 491–515, 2019.

[11] R. Zhao, Y. Yuan, X. Wei et al., "Review of annual progress of bridge engineering in 2019," *Advances in Bridge Engineering*, vol. 1, no. 1, pp. 1–57, 2020.

[12] W. Zhai, Z. Han, Z. Chen, L. Ling, and S. Zhu, "Train–track–bridge dynamic interaction: a state-of-the-art review," *Vehicle System Dynamics*, vol. 57, no. 7, pp. 984–1027, 2019.

[13] S. Yang, D. Kwak, and T. Kishida, "Development of seismic fragility curves for high-speed railway system using earthquake case histories," *Geomechanics and Engineering*, vol. 21, no. 2, pp. 179–186, 2020.

[14] B. Shrestha, H. Hao, and K. Bi, "Devices for protecting bridge superstructure from pounding and unseating damages: an overview," *Structure and Infrastructure Engineering*, vol. 13, no. 3, pp. 313–330, 2017.

[15] K. Wei, C. Zhou, M. Zhang, Z. Ti, and S. Qin, "Review of the hydrodynamic challenges in the design of elevated pile cap foundations for sea-crossing bridges," *Advances in Bridge Engineering*, vol. 1, no. 1, pp. 1–30, 2020.

[16] X. Huang, C. Liu, Y. Tian, C. Chen, J. Xu, and J. Wu, "Analiza inovativnog projekta mosta Liyutuo Lounge u Dujiangyanu," *Građevinar*, vol. 72, no. 5, pp. 437–446, 2020.

[17] J. Neto, P. A. Montenegro, C. Vale, and R. Calçada, "Evaluation of the train running safety under crosswinds-a numerical study on the influence of the wind speed and orientation considering the normative Chinese hat model," *International Journal of Rail Transportation*, vol. 9, no. 3, pp. 204–231, 2021.

[18] H. Gou, X. Shi, W. Zhou, K. Cui, and Q. Pu, "Dynamic performance of continuous railway bridges: numerical analyses and field tests," *Proceedings of the Institution of Mechanical Engineers, Part F: Journal of Rail and Rapid Transit*, vol. 232, no. 3, pp. 936–955, 2018.

[19] L. L. Chen, J. F. Lu, and Q. S. Feng, "A coupled model for a moving mass and the periodic viaduct subjected to seismic waves," *Archive of Applied Mechanics*, vol. 91, no. 6, pp. 2761–2780, 2021.

[20] Y. Zhou, S. Di, C. Xiang, W. Li, and L. Wang, "Damage identification in simply supported bridge based on rotational-angle influence lines method," *Transactions of Tianjin University*, vol. 24, no. 6, pp. 587–601, 2018.

[21] X. Huang, C. Liu, Y. Tian, C. Chen, J. Xu, and J. Wu, "Analysis of innovative structural design of Liyutuo Lounge Bridge in Dujiangyan," *Građevinar*, vol. 72, no. 5, pp. 437–446, 2020.

Hindawi
Journal of Sensors
Volume 2023, Article ID 9812126, 1 page
https://doi.org/10.1155/2023/9812126

Retraction

Retracted: A Systematic Pipelaying Control Method Based on the Sliding Matrix for Dynamically Positioned Surface Vessels

Journal of Sensors

Received 19 December 2023; Accepted 19 December 2023; Published 20 December 2023

This article has been retracted by Hindawi following an investigation undertaken by the publisher [1]. This investigation has uncovered evidence of one or more of the following indicators of systematic manipulation of the publication process:

(1) Discrepancies in scope
(2) Discrepancies in the description of the research reported
(3) Discrepancies between the availability of data and the research described
(4) Inappropriate citations
(5) Incoherent, meaningless and/or irrelevant content included in the article
(6) Manipulated or compromised peer review

The presence of these indicators undermines our confidence in the integrity of the article's content and we cannot, therefore, vouch for its reliability. Please note that this notice is intended solely to alert readers that the content of this article is unreliable. We have not investigated whether authors were aware of or involved in the systematic manipulation of the publication process.

Wiley and Hindawi regrets that the usual quality checks did not identify these issues before publication and have since put additional measures in place to safeguard research integrity.

We wish to credit our own Research Integrity and Research Publishing teams and anonymous and named external researchers and research integrity experts for contributing to this investigation.

The corresponding author, as the representative of all authors, has been given the opportunity to register their agreement or disagreement to this retraction. We have kept a record of any response received.

References

[1] X. Li, Z. Jin, and L. Wang, "A Systematic Pipelaying Control Method Based on the Sliding Matrix for Dynamically Positioned Surface Vessels," *Journal of Sensors*, vol. 2022, Article ID 9702532, 16 pages, 2022.

Hindawi
Journal of Sensors
Volume 2022, Article ID 9702532, 16 pages
https://doi.org/10.1155/2022/9702532

Research Article

A Systematic Pipelaying Control Method Based on the Sliding Matrix for Dynamically Positioned Surface Vessels

Xinfei Li,[1] Zhongyu Jin,[1] and Lihui Wang[2]

[1]*College of Shipbuilding Engineering, Harbin Engineering University, Harbin, Heilongjiang 150001, China*
[2]*College of Intelligent Systems Science and Engineering, Harbin Engineering University, Harbin, Heilongjiang 150001, China*

Correspondence should be addressed to Lihui Wang; wanglihui406@hrbeu.edu.cn

Received 21 October 2021; Revised 8 November 2021; Accepted 20 November 2021; Published 25 January 2022

Academic Editor: Wei Zhang

A pipelaying control method is presented in this paper which includes path planning, path guidance, and path tracking controller for dynamically positioned (DP) surface vessels based on the characteristics of the predefined path in marine pipelaying operation. The pipelaying control method depends on path coding, path selection logic system, and a sliding matrix. The sliding matrix contains a vessel local path and its specified control requirements, which can be updated by sliding down the waypoint table line by line as the vessel is traveling from one path to the next. A line of sight (LOS) algorithm is developed to calculate the desired vessel position and heading on a circular arc path. The motion controller, which can simultaneously control the vessel speed at the directions of surge and sway, is designed by decomposing the desired inertial resulting velocity into the desired body velocity components. A DP simulator for pipelaying operation is developed, and in order to verify the proposed method, a pipelaying simulation is carried out. The simulation results show that the proposed method enables the vessel to move along the desired path while maintaining a set crab angle, a specified speed, and a turning radius. The pipeline can be laid onto the specified waypoints even when the vessel is subjected to drift forces caused by ocean currents, wind, and waves.

1. Introduction

Over the last two decades, deep-water pipelaying has gone through a spectacular development and the present methods and trends in deep-water pipelay systems are described in [1] by Fossen. Three basic pipelay methods are commonly in use: S-lay, J-lay, and reeling which are described in [2, 3] by Heerema and Ai et al., respectively. Xu et al. [4] proposed a simple and feasible VFIFE model for the static and dynamic analysis of deepwater S-lay and J-lay pipelines. In order to realize the design of continuous pipe laying method of rolling pipe laying method, it is necessary to take into account the characteristics of pipe laying operation and the research of ship path tracking control method and organically combine the two to realize this method. The predecessors have not discussed the specific methods to realize continuous pipe laying, which will be described in this paper.

The path planning, path guidance, and path tracking of pipelaying vessels have their own unique characteristics. Firstly, it is difficult to follow the desired pipeline path precisely by indirectly controlling vessel position and heading [5, 6]. Secondly, it is necessary to consider the vessel position, heading, speed, and turning radius simultaneously during pipelaying operation because of pipelaying requirements. Guidance algorithm is an important part of ship path tracking control. It can provide the desired position, heading angle, speed, and other information for ship control and guide the ship to complete the relevant tracking tasks [7, 8]. Therefore, dynamic positioning (DP) control and pipeline dynamics are the two main parts of the deepwater pipelaying simulation model [3].

The desired pipe paths consist of a few straight-line paths. In order to achieve a smooth transition between two straight-line paths, a circular arc path is inserted between the adjacent straight-line paths. The methods used to generate such circular arc path have been extensively studied in recent years, and the Dubins path is highly recognized in [9]. The curvature of the Dubins path is usually discontinuous at the intersection of a straight-line path and its adjacent

circular arc path. Accordingly, the Pythagorean hodographs [10] and the clothoid arcs [11] had been developed to obtain path with continuous curvature. Lekkas and Fossen [12] proposed the monotonic cubic Hermit spline interpolation (MCHSI) to realize the continuous change of path curvature with low computational cost in ship path planning. However, it is not easy to lay the pipe onto the desired pipeline path by indirectly controlling vessel path. Fu et al. [5, 13] developed a method of path analysis and mapping relation between the desired pipeline path and the desired vessel path and used sliding mode control to study the tracking control of pipe laying operation of pipelaying ship [14]. Rout et al. [15] presents a modified line-of-sight (LOS) guidance law and an adaptive neural network (NN) controller for underactuated marine vehicles in the presence of uncertainties and constraints. Lekkas and Fossen [16, 17] proposed a time-varying lookahead-distance LOS method. When the vessel moves close to the desired path, the heading is gradually adjusted to the desired direction, which is beneficial for reducing the overshoot and oscillation of the vessel position. Among all existing methods, the sideslip motion is easy to occur during path-following due to environmental interferences. Therefore, a nonlinear adaptive path-following controller is proposed by Fossen et al. [18] to compensate for vessel sideslip. For the plane path tracking problem of underactuated ships, Peymani and Fossen [19] designed a dynamic controller by using the idea of integral backstepping, explicitly considering the geometric error and ensuring the path convergence. In addition, aiming at the linear path tracking problem of fully driven ships, they derived the control law using the least square method and adjusted the ship speed according to the geometric distance and the convergence speed of the path [20]. Moe et al. [21] developed a guidance and control system for underactuated surface vessels to solve the control objective of making the vessel to follow a curved path in the presence of unknown ocean currents. Heshmati-Alamdari et al. [22] presented a robust nonlinear model predictive control (NMPC) scheme for the case of underactuated autonomous underwater vehicles (AUVs). Nie and Lin [23] proposed an adaptive fuzzy path following control law, which is based on the improved adaptive integrated line of sight (IAILOS) guidance law for the control of underactuated ship in the case of time-varying ocean current and sideslip. Abdurahman et al. [24] used path-following control and speed allocation to solve the three-dimensional path-following problem of underactuated underwater vehicles. Path-following control was achieved by defining a slip angle relative to the desired heading angle. Lamraoui and Zhu [25] presented an improved active disturbance rejecter control (ADRC) for path-following control of autonomous underwater vehicles under significant fast-varying disturbances caused by waves and sea currents. Du et al. [26] established a robust nonlinear control law by using disturbance observer, auxiliary power system, and dynamic surface control (DSC) technology to keep the ship's position and heading at the expected value. Yu et al. [27] presented an improved guidance law that transforms 3D path-following errors into controlled speed errors and designed a simplified nonlinear single-input fuzzy controller against unknown disturbances. Huang et al. [28] presented a 2D path-following control method for autonomous underwater vehicles (AUVs) based on dynamic circle heading modification (DCHM). Loginov et al. [29] proposed special control functionality for trailing suction dredgers in dynamic positioning (DP) systems that focused mainly on the dredging track controller, and the method was verified by the simulation and sea-trial results. Shi et al. [5, 30] presented a pipelaying control method for DP vessels, and it was tested in the pipelaying operation. Here, it refers to the control method. Healey and Lienard [31] designed the autopilot of the six degree of freedom underwater vehicle through sliding mode control, which has a good response to the speed, steering, and heave motion of the low-speed AUV. Mu et al. [32] investigated the path-following control problem for an underactuated unmanned surface vehicle (USV) in the presence of dynamical uncertainties and time-varying external disturbances. Rout and Subudhi [33] designed an explicit model predictive controller (Ex-MPC) for implementing a LOS guidance law.

The pipeline dynamic model is the other key and important problem in pipelaying operation. Ai et al. [3] proposed a pipelaying nonlinear dynamic model, which integrates the major aspects related to numerical simulation, including coupled pipeline motion and roller contact forces. Jensen [34, 35] proposed a nonlinear dynamic model which was capable of undergoing shearing, twist, and bending for the pipe string, and the model is suitable for pipelaying operations by a dynamically positioned surface vessel. Szczotka [36] studied a dynamic and quasi-static model that showed the high dynamic forces in the pipelaying equipment during pipelaying simulation operated in the sea for analysis of a pipelay spread. Different pipelaying models were studied in the above. However, applications of this method to pipelaying operation, especially for a series of waypoints, are not discussed in detail. In order to study a pipelaying system with DP vessels in time domain, it is necessary to simplify appropriately the pipeline dynamic model.

In this study, a systematic method, including path planning, guidance algorithm, and path tracking for pipelaying vessels, is presented from the prospect of the whole DP control system. One of the key steps to achieve path tracking finally is to combine the desired path information and the guidance algorithm with control strategy. The realization of the system depends on the coding method of the pipeline desired path. The method of sliding matrix is proposed to extract the required path information from the waypoint table for continuous pipelaying at specified speed, heading, and turning radius. The sliding matrix contains the vessel local desired path, the desired crab angle, and turning radius and the desired pipelaying speed. A simple and reliable guidance algorithm is also designed for circular arc paths of the pipelaying vessel, which is convenient for the guiding system to execute quickly. Then, the vessel speed and the yaw controllers are also designed. Finally, the effectiveness of the proposed control method of pipelaying control is verified using a DP simulator.

2. The Method of Pipelaying Path Based on a Sliding Matrix

2.1. Definition of Coordinates. Two coordinate systems adopted to define ship motions are presented in this section first. The North-East-Down (NED) coordinate system $\{n\} = (x_n, y_n, z_n)$ with origin o_n defined relative to the Earth's reference ellipsoid. It is usually defined as the tangent plane on the surface of the Earth moving with the marine craft. x_n axis points towards true north, y_n axis points towards east, and z_n axis points downwards from the Earth surface to its geocentric. This is usually referred to as flat Earth navigation, and it can be simply denoted by $\{n\}$, as shown in Figure 1.

The body-fixed reference frame $\{b\} = (x_b, y_b, z_b)$ with origin o_b is a moving coordinate frame that is fixed to the craft, and it can be simply denoted by $\{b\}$. The body axes are chosen to coincide with the principal axes of inertia, as shown in Figure 2. The x_b is the longitudinal axis pointing from aft to fore. The y_b is the transversal axis pointing to starboard. The z_b is the normal axis pointing from top to bottom.

2.2. Waypoints and Its Coding Method for Pipelaying Paths. The desired path of pipeline to be laid is expressed as a set of waypoints. The waypoint table for pipelaying contains the information of all waypoints, including north and east coordinates, crab angle, laying speed, and turning radius of pipeline, as shown in Table 1.

The waypoint table gives a detailed expression of the characteristics of each segment of pipelaying paths, and it also specifies the control requirements of the pipelaying vessel. The pipelaying paths are divided into several straight-line segments which are separated by different waypoints. As shown in Table 1, N_k and E_k are the north coordinate and east coordinate of the waypoint P_k, respectively. γ_k represents the crab angle which is a fixed angle between the desired vessel heading and the path tangential direction. V_k represents the desired pipelaying speed when the vessel is tracking the desired straight-line pipe path P_kP_{k+1} which is also represented by S_k. R_k represents the turning radius of the desired pipe circular arc path C_k, so as to obtain a smooth circular arc transition between a straight-line path to its adjacent next straight-line path, as shown in Figure 3.

In order to make the analysis of pipelaying path easier and achieve automatic identification in path tracking by programming, all the straight-line and circular arc paths in Figure 3 need to be coded.

As shown in Figure 3, P_k, $k = 1, \cdots, n$ denotes the waypoint k. A straight-line path is denoted as S_k, $k = 1, \cdots, n-1$, and S_1 represents the first straight-line path P_1P_2. A circular arc path is denoted as C_l, $l = 1, \cdots, n-2$, and C_1 represents the first circular arc path between S_1 and S_2. χ_1 is the path-tangential angle between the desired pipe straight-line path P_1P_2 (S_1) and x_n axis of $\{n\}$. γ_1 is the set crab angle, which is a specified angle between the desired vessel heading and the tangential direction of the straight-line path.

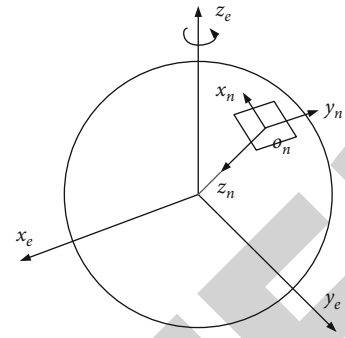

Figure 1: NED reference frame.

2.3. Pipelaying Path Planning Based on the Sliding Matrix. The desired paths of pipeline usually consist of straight-line paths and circular arc paths in sequence. For a straight-line path, it is only necessary to consider the start point and end point whereas for a circular arc path, the circular arc center also needs to be considered. A sliding matrix may be constructed using the information in the waypoint table.

As shown in Figure 3, the desired vessel heading ψ_k for straight-line path S_k is obtained by

$$\psi_k = \chi_k + \gamma_k, \tag{1}$$

where χ_k is the path-tangential angle of the desired pipe path S_k relative to χ_n axis of $\{n\}$. γ_k is the set crab angle when the vessel is tracking S_k.

As shown in Table 1, the control information of a sliding matrix is composed of a set of waypoints. The sliding matrix slides down the waypoint table and traverses all waypoints during pipelaying operation, as shown in Table 2.

The sliding matrix used to calculate the guidance law is proposed to resolve path-tracking problem in pipelaying operation. The sliding matrix, three rows and five columns, includes position coordinates of three waypoints, the desired heading angle, the desired speed of straight-line path, and the desired turning radius of circular arc path. From Table 2, the second column contains north coordinates of three waypoints, the third column contains east coordinates of three waypoints, the fourth column contains the desired heading, the fifth column contains the desired pipelaying speed of straight-line path, and the sixth column contains the desired turning radius.

The turning radius of pipelaying is related to characteristics of the pipeline, the gyration radius of the pipelaying vessel, and desired pipelaying speed on circular arc paths. The circular arc path represents the natural circular arc path when the vessel is traveling from one straight-line path to the next one at a specified turning radius and speed. The desired state of the start point of the circular arc path is $q_1 = (N_{q_1}, E_{q_1}, \psi_{q_1})$, and the desired state of the end point is $q_2 = (N_{q_2}, E_{q_2}, \psi_{q_2})$.

The steps for the analysis of the path based on sliding matrix are as follows:

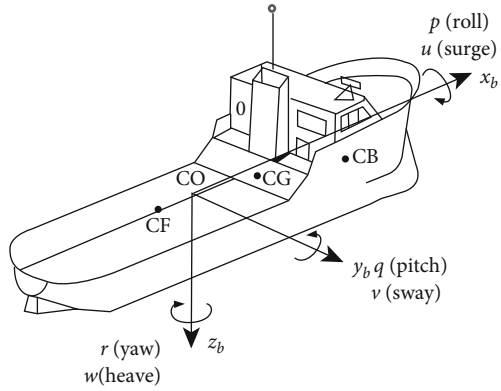

Figure 2: Body-fixed reference frame.

Table 1: The waypoint table for pipelaying operation.

No.	North	East	Crab angle	Speed	Turn radius
1	N_1	E_1	—	—	—
2	N_2	E_2	γ_1	V_1	—
3	N_3	E_3	γ_2	V_2	R_1
...	...	...	...	...	...
k	N_k	E_k	γ_{k-1}	V_{k-1}	R_{k-2}

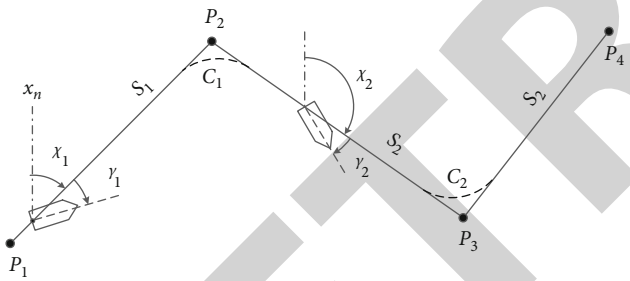

Figure 3: The coding method of the pipelaying path.

Table 2: The control information of a sliding matrix.

No.	North	East	Heading	Speed	Turn radius
k	N_k	E_k	—	—	—
$k+1$	N_{k+1}	E_{k+1}	ψ_k	V_k	—
$k+2$	N_{k+2}	E_{k+2}	ψ_{k+1}	V_{k+1}	R_k

Step 1. To calculate the angle between two adjacent straight-line paths.

The sketch of desired pipelaying paths is shown in Figure 4. Here, χ_2 is the path-tangential angle between P_2 P_3 (S_2) and the x_n axis of $\{n\}$. α_1 is the angle between the two straight-line paths S_1 and S_2.

The calculation method of α_1 is related to the rotation direction of circular arc path. When $0 \le \chi_1 < \pi$, the angle between P_1P_2 and P_2P_3 can be obtained using

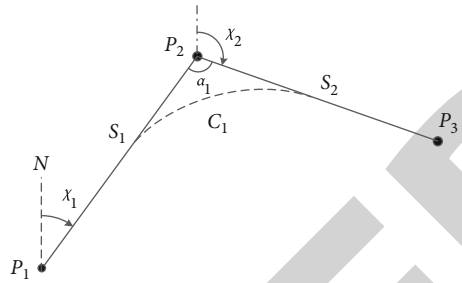

Figure 4: Sketch diagram of the angle between pipe paths.

$$\alpha_1 = \begin{cases} \pi - (\chi_1 - \chi_2)\mathrm{rg} = 0 & 0 \le \chi_2 < \chi_1, \\ \pi - (\chi_2 - \chi_1)\mathrm{rg} = 1 & \chi_1 \le \chi_2 < \chi_1 + \pi, \\ \chi_2 - (\chi_1 + \pi)\mathrm{rg} = 0 & \chi_1 + \pi \le \chi_2 < 2\pi, \end{cases} \tag{2}$$

where $\mathrm{rg} = 1$ implies that the rotation direction of a circular arc path is clockwise and $\mathrm{rg} = 0$ implies that the rotation direction is counterclockwise.

When $\pi \le \chi_1 < 2\pi$, the value of angle α_1 between the two straight-line paths can be obtained using

$$\alpha_1 = \begin{cases} (\chi_1 - \pi) - \chi_2\mathrm{rg} = 1 & 0 \le \chi_2 < \chi_1 - \pi, \\ \chi_1 - \chi_2\mathrm{rg} = 0 & \chi_1 - \pi < \chi_2 < \chi_1, \\ \pi - (\chi_2 - \chi_1)\mathrm{rg} = 1 & \chi_1 < \chi_2 \le 2\pi. \end{cases} \tag{3}$$

Step 2. To calculate the distance between a waypoint point and its tangent point.

To calculate the distance between a waypoint point and its adjacent tangent point, the sketch is shown in Figure 5. As shown in Figure 5, O_1 is the center of the circular arc path C_1, and R_1 is the turning radius. The points, q_1 and q_2, are the tangent points between the circular arc path and its two adjacent straight-line paths, respectively. θ_{Oq_1} is the angle between the vector O_1q_1 and x_n axis of $\{n\}$. θ_{Oq_2} is the angle between the vector O_1q_2 and x_n axis of $\{n\}$.

It is straightforward to calculate the distance between the waypoint P_2 and the tangent point q_1, which can be expressed as L_{2q_1}. Similarly, L_{1q_1} is the distance between the waypoint P_1 and q_1. Additionally, L_{2q_1} is equal to L_{2q_2}. It is assumed that R_1 and α_1 are known and consequently, L_{2q_1} can be expressed as

$$L_{2q_1} = L_{2q_2} = \frac{R_1}{\tan(\alpha_1/2)}. \tag{4}$$

Step 3. To calculate the coordinates of the tangent points.

Let L_{12} denote the distance between the waypoint P_1 and P_2. Hence, L_{1q_1} can be obtained from

$$L_{1q_1} = L_{12} - L_{2q_1}. \tag{5}$$

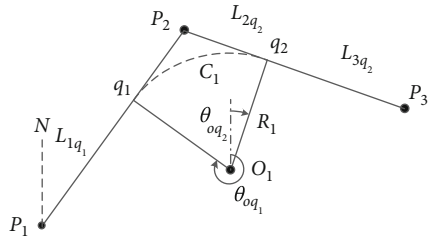

Figure 5: Sketch of the desired pipelaying path.

Here, it is necessary to make sure that $L_{12} > L_{2q_1}$ when the waypoints are specified.

Thereafter, the coordinates of the center of C_1, O_1 satisfy

$$\begin{bmatrix} N_{O_1} \\ E_{O_1} \end{bmatrix} = \begin{bmatrix} \cos\chi_{S_1} & -\sin\chi_{S_1} \\ \sin\chi_{S_1} & \cos\chi_{S_1} \end{bmatrix} \begin{bmatrix} L_{1q_1} \\ L_{Oq_1} \end{bmatrix} + \begin{bmatrix} N_1 \\ E_1 \end{bmatrix}. \quad (6)$$

Here, L_{Oq_1} is the vertical distance between the tangent point q_1 and the center O_1. For a clockwise circular arc path, L_{Oq_1} equals to R_1, and for a counterclockwise circular arc path, L_{Oq_1} equals to $-R_1$.

The coordinates of the tangent point q_1 satisfy

$$\begin{bmatrix} N_{q_1} \\ E_{q_1} \end{bmatrix} = \begin{bmatrix} \cos\chi_{S_1} & -\sin\chi_{S_1} \\ \sin\chi_{S_1} & \cos\chi_{S_1} \end{bmatrix} \begin{bmatrix} L_{1q_1} \\ 0 \end{bmatrix} + \begin{bmatrix} N_1 \\ E_1 \end{bmatrix}. \quad (7)$$

Consequently, the coordinates of the tangent point q_2 satisfy

$$\begin{bmatrix} N_{q_2} \\ E_{q_2} \end{bmatrix} = \begin{bmatrix} \cos\chi_{S_2} & -\sin\chi_{S_2} \\ \sin\chi_{S_2} & \cos\chi_{S_2} \end{bmatrix} \begin{bmatrix} L_{2q_2} \\ 0 \end{bmatrix} + \begin{bmatrix} N_2 \\ E_2 \end{bmatrix}. \quad (8)$$

Step 4. To calculate the angle between two straight lines.

The angle range is chosen to represent the part of a circular arc pipe path, as shown in Figure 5. Accordingly, it is necessary to calculate the angle between two straight lines connecting two tangent points to the center of the circular arc path. Moreover, it is also used to calculate the LOS point if it is required. In order to ensure angle continuity as a circular arc path passes across x_n axis of $\{n\}$, it is necessary to analyze the angle ranges of θ_{Oq_1} and θ_{Oq_2} further.

When $\theta_{oq_2} > \theta_{oq_1}$, it implies that the angle range of the circular arc path does not contain zero point, and the circular arc path does not pass across x_n axis of $\{n\}$. Whereas when $\theta_{oq_2} < \theta_{oq_1}$, it implies that the angle range of the circular arc path contains zero point, and the circular arc path passes across x_n axis of $\{n\}$.

Hence, the relationship mentioned above can be expressed as

$$\begin{cases} \theta'_{oq_1} = \theta_{oq_1} \\ \theta'_{oq_2} = \theta_{oq_2} \end{cases} \text{rg} = 1, \theta_{oq_2} > \theta_{oq_1} \text{ or } \text{rg} = 0, \theta_{oq_2} < \theta_{oq_1}. \quad (9)$$

Here, θ'_{oq_1} and θ'_{oq_2} are the updated values of θ_{oq_1} and θ_{oq_2}, respectively.

Consequently, Equations (10) and (11) are obtained:

$$\begin{cases} \theta'_{oq_1} = \theta_{oq_1} - 2\pi \\ \theta'_{oq_2} = \theta_{oq_2} \end{cases} \text{rg} = 1, \theta_{oq_2} < \theta_{oq_1}, \quad (10)$$

$$\begin{cases} \theta'_{oq_1} = \theta_{oq_1} \\ \theta'_{oq_2} = \theta_{oq_2} - 2\pi \end{cases} \text{rg} = 0, \theta_{oq_2} > \theta_{oq_1}. \quad (11)$$

2.4. Mapping from the Desired Pipelaying Path to the Desired Vessel Path. The horizontal projection distance between the pipe touchdown point at seabed and the vessel rotation center during pipelaying operation is defined as the touchdown distance. The desired vessel path needs to be calculated so that the pipe touchdown point can be placed on the desired path during turning in pipelaying operation. It is necessary to estimate the desired vessel path from the pipeline desired path and the touchdown distance. The touchdown distance can be modified anytime if it is necessary during pipelaying operation. The touchdown distance is mainly influenced by the method of pipelaying operation, sea depth, pipe mechanical properties, etc. The desired vessel path can be calculated based on the desired pipelaying path, and their geometric relationship is shown in Figure 6.

V_1 is the desired pipelaying speed when tracking S_1. ψ_{C_1}, V_{C_1}, and β_{C_1} are the desired heading angle, pipelaying speed, and sideslip angle when tracking the path C_1, respectively. R_V and R_1 are the radius of the desired circular path of the DP vessel and pipeline, respectively. L_{td} is the touchdown distance. P_{s_1} and P_{s_2} are the start point and end point of the path C_1, respectively. P_L is the LOS point on the path C_1. θ_{OL} is the azimuth angle of the straight-line O_1P_L.

The desired pipeline paths are composed of a few straight-line paths and circular arc paths in sequence. It is necessary to control precisely the ship heading angle to make smooth progress of pipelaying operation when the pipelaying vessel runs along the desired path. When the value of the crab angle is set to 0, the desired vessel heading angle is equal to the tangent direction of pipeline path; when the crab angle is a constant value, the desired vessel heading angle is obtained using Equation (1).

2.4.1. To Calculate the Desired Vessel Path from a Desired Straight-Line Pipe Path. Let $q_1(x_1, y_1)$ and $q_2(x_2, y_2)$ denote the start point and end point of the circular arc path of pipeline, respectively, χ_1 denotes the straight path angle, and L_{td} denotes the touchdown distance. Let $P_{s_1}(x_{s_1}, y_{s_1})$ and $P_{s_2}(x_{s_2}, y_{s_2})$ denote the start point and end point of the circular arc path of vessel, respectively. Accordingly, the coordinates of $P_{s_1}(x_{s_1}, y_{s_1})$ can be obtained using Equation (12), as shown

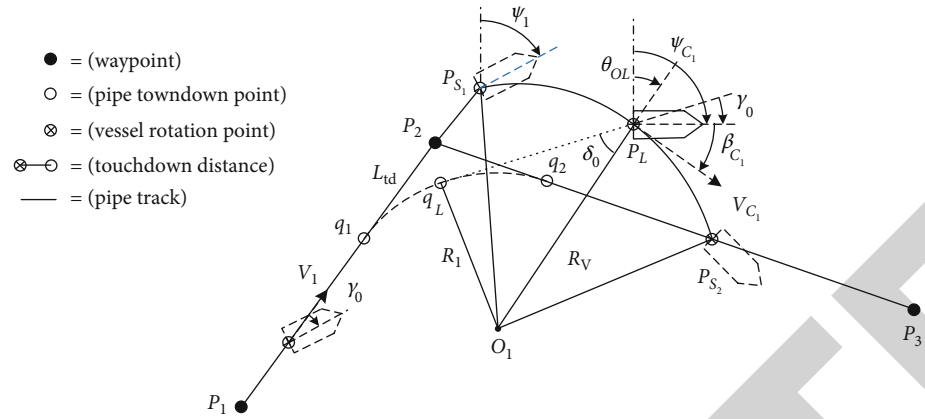

Figure 6: Mapping relationship between the desired vessel path and pipelaying path.

in Figure 6.

$$\begin{cases} x_{s_1} = x_1 + L_{\text{td}} \cos \chi_1, \\ y_{s_1} = y_1 + L_{\text{td}} \sin \chi_1. \end{cases} \tag{12}$$

Consequently, the coordinates of $P_{s_2}(x_{s_2}, y_{s_2})$ can be obtained using

$$\begin{cases} x_{s_2} = x_2 + L_{\text{td}} \cos \chi_2, \\ y_{s_2} = y_2 + L_{\text{td}} \sin \chi_2. \end{cases} \tag{13}$$

In this study, when the crab angle is set to 0, the desired vessel heading angle is equal to the tangent angle of desired pipeline paths.

2.4.2. To Calculate the Desired Vessel Path from a Desired Circular Arc Pipelaying Path. The desired circular arc path of pipe to be laid should be tangent to its adjacent straight-line path. This means that the desired vessel circular path is not tangent to its adjacent vessel straight-line path. Here, all crab angles for the desired straight-line and circular arc paths are set to γ_0. Accordingly, the desired heading angle for the first desired straight-line pipeline path is obtained using Equation (14), as shown in Figure 6.

$$\psi_1 = \chi_1 + \gamma_0, \tag{14}$$

where ψ_1 is the desired heading when tracking the straight-line path S_1 and γ_0 is the set crab angle.

When the vessel is tracking the circular arc path C_1, the desired heading angle ψ_{C_1} can be expressed as

$$\psi_{C_1} = \begin{cases} \theta_{OL} + \delta_0 + \gamma_0 & \text{Clockwise path}, \\ \theta_{OL} - \delta_0 + \gamma_0 & \text{Counterclockwise path}. \end{cases} \tag{15}$$

Here, the crab angle γ_0 is a constant during pipelaying operation.

The value of δ_0 can be obtained using

$$\delta_0 = \arcsin \frac{R_1}{R_{\text{V}}}. \tag{16}$$

Hence, the relationship between the desired turning radius of DP vessel and the desired turning radius of pipeline path can be expressed as

$$R_{\text{V}} = \sqrt{R_1^2 + L_{\text{td}}^2}. \tag{17}$$

Here, L_{td} is the touchdown distance.

2.5. A Guidance Law of Circular Arc Paths for DP Vessels. It is necessary to construct a guidance system that is suitable for DP vessels so that the vessel actual path can converge to the desired path smoothly. The common LOS guidance law is only suitable for path following of straight-line or circular arc path for underactuated water surface ships or underwater vehicles. Therefore, a new LOS guidance algorithm of circular arc paths for DP vessels is presented.

2.5.1. The Guidance Law for a Straight-Line Path. Let $P_{\text{L}}(N_{\text{LOS}}, E_{\text{LOS}})$ be the desired LOS point on a straight-line path. The points (N_k, E_k) and (N_{k+1}, E_{k+1}) are the start point and end point of the straight-line path, respectively. Let (N_t, E_t) be the real-time position of DP vessels. Thereafter, the following relationship can be obtained.

$$\begin{aligned} &(N_{\text{LOS}} - N_t)^2 + (E_{\text{LOS}} - E_t)^2 = R_{\text{LOS}}^2, \\ &\tan \alpha_k = \frac{\Delta E}{\Delta N} = \frac{E_{k+1} - E_k}{N_{k+1} - N_k} = \frac{E_{\text{LOS}} - E_k}{N_{\text{LOS}} - N_k}, \end{aligned} \tag{18}$$

where R_{LOS} is the radius of the LOS guidance law specified by the practice requirements.

2.5.2. A Guidance Algorithm for Circular Arc Paths. The guidance law of a curved path also takes the vessel position as the center and makes a circle with a radius value based on the principle of LOS guidance law of the straight-line path. One of the intersections of the circle and the circular

arc path is chosen as the LOS point. Meanwhile, the direction of the desired resultant speed of the vessel passes through the LOS point. The schematic diagram of the LOS guidance algorithm of the circular arc path is shown in Figure 7.

As shown in Figure 7, P_L denotes the LOS point on the desired vessel circular arc path. p_s denotes the real-time position of the vessel set rotation center. O_1 denotes the center of C_1. θ_{OL} denotes the azimuth angle of O_1P_L, and b denotes the angle between O_1P_C and x_n axis of $\{n\}$. σ_C is the angle between O_1P_C and O_1P_L.

It is necessary to know the angle of the straight-line segment connecting the LOS point and the circle center O_1P_L for calculating the coordinates of the LOS point on the circular arc path.

The following relationship between θ_{OL} and b can be obtained from Figure 7.

$$\theta_{OL} = \sigma_C - b. \tag{19}$$

The value of the angle σ_C is calculated using

$$\sigma_C = \frac{\pi}{2} - \delta_0. \tag{20}$$

The value of the angle b can be obtained using

$$b = \begin{cases} \theta_{OC} & 0 < \theta_{OC} < \dfrac{\pi}{2}, \\ \theta_{OC} - \dfrac{\pi}{2} & \dfrac{\pi}{2} < \theta_{OC} < \pi, \\ \theta_{OC} - \pi & \pi < \theta_{OC} < \dfrac{3\pi}{2}, \\ 2\pi - \theta_{OC} & \dfrac{3}{2}\pi < \theta_{OC} < 2\pi. \end{cases} \tag{21}$$

Thereafter, the coordinates of LOS point on a circular arc path can be obtained using

$$\begin{cases} N_{LOS} = N_{O_1} + R_L \cos(\theta_{OL}), \\ E_{LOS} = E_{O_1} + R_L \sin(\theta_{OL}). \end{cases} \tag{22}$$

The LOS point is the desired vessel position on a desired path. Hence, the desired heading angle during the circular path following can be obtained using Equation (15).

3. Control System Designing for Pipelaying Operation

As shown in Figure 8, the pipelaying simulation system of DP vessels is constructed, which includes the waypoint table, path planning module, path guidance module, thrust allocation module, propeller system module, vessel hydrodynamic module, environment force module, state observer module, and motion controller.

The data transmitted between the modules are represented by the numbers and ①—the coordinates, heading angle, laying speeds, turning radius; ②—the desired vessel path; ③—the desired LOS point, speed, heading; ④—the desired forces; ⑤—the desired thrusts; ⑥—the actual sum forces; ⑦—the estimated wind loads; ⑧—the LOS point.

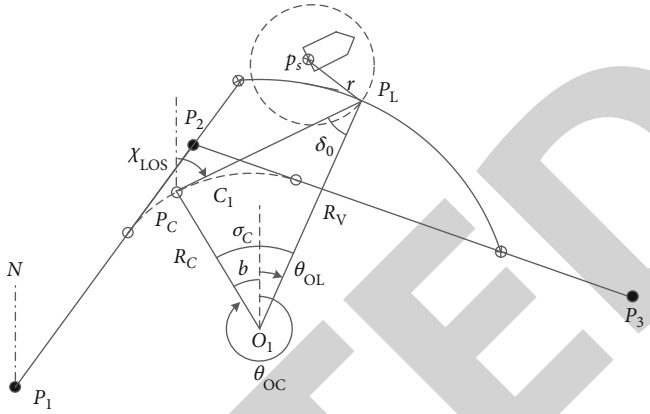

Figure 7: A LOS guidance algorithm for a circular arc path.

The principle of pipelaying operation of the DP simulation is presented as follows:

(1) The waypoint coordinates, crab angle, pipelaying speed, and turning radius of the pipe are input in the waypoint table according to the operational requirements of a pipelaying task

(2) The desired pipelaying path, the desired vessel path, and heading angle are generated by the path planning module from the waypoint table. Then, they are input into the path guidance module

(3) The vessel real-time position, speed, and heading angle are input into the module of state filter and observer, and the vessel drift (Low Frequency, LF) motion is estimated by filtering out the first-order wave-induced (Wave Frequency, WF) motion

(4) The LOS point is calculated using the path guidance module by inputting the vessel real-time position, heading angle and speed, the desired vessel path, and control requirements. Then, the LOS points are input into the motion controller module

(5) The desired forces in three degrees of freedom are estimated by the motion controller module through calculating the deviation between LOS point and estimated real-time motion. Then, they are input into the thrust allocation module

(6) The desired thrust and the azimuth angle of each thruster are calculated according to the configuration of the propulsion system and thrust allocation method chosen by the DP operator

(7) The actual thrust vector is generated by each thruster according to the desired thrust and azimuth angle

(8) The propeller system produces the sum forces in three degrees of freedom through the actual thrust vectors. Then, the sum forces will be applied to the DP vessel

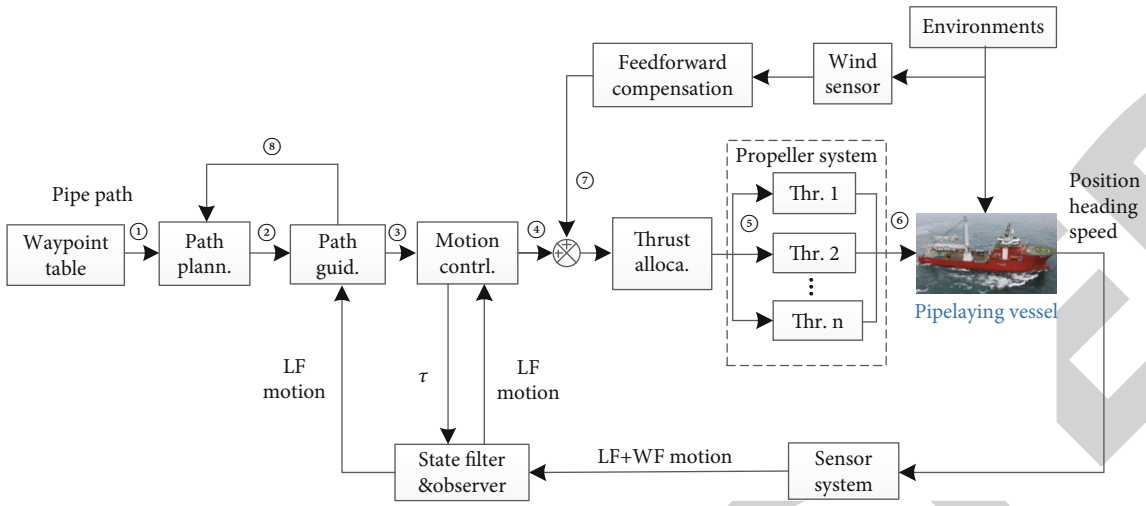

Figure 8: DP simulation system for a pipelaying vessel.

(9) The DP vessel is moved along the desired path at the given speed and heading angle by the pipelaying controller, even the vessel is exposed to the drift forces caused by ocean currents, wind, and waves

3.1. Path Selection Method in the Pipelaying Operation. The desired path of the pipelaying vessel can be obtained by making use of the waypoint table and mapping relationship between the pipelaying path and the vessel path. Hence, it is necessary to know the type of pipe path it is traveling along so the corresponding LOS point of the pipelaying vessel can be calculated. The flow chart of the path selection method is shown in Figure 9, and the details are explained in the following:

(1) Specify an index number for each straight-line path and each circular arc path of the pipelaying vessel, as well as the initial LOS point. And the first point in the waypoint table is usually set as the initial LOS point

(2) Let k and l be the indices for a straight-line path and a circular arc path, respectively. And the initial values are set as $k = 1$, $l = 0$

(3) The sliding matrix is generated according to the waypoint table and the initial value of k

(4) The desired pipelaying path expressed by the sliding matrix is analyzed to determine the end point of straight-line path and circular arc pipe path, the circle center, and rotation direction of the circular arc path of pipeline. The desired vessel path is calculated from the desired pipelaying path

(5) Determine which path type the vessel is going to track when the present path range is exceeded by the pipelaying vessel

(6) The condition $k > l$ implies that the vessel is going to travel along a straight-line path, and when $k = l$, it implies that the vessel is going to travel along a circular arc path

(7) When the vessel is traveling along a straight-line path and does not exceed its range, the start and the end points of the straight-line path are output to the LOS point calculating module. When the straight-line path range is exceeded, i.e., the vessel has just reached a circular arc path, then set $l = l + 1$. Consequently, now $k = l$, and the LOS point on the circular arc path is calculated

(8) When the vessel is traveling along a circular arc path and exceeds its range, it implies that the vessel has just reached the next straight-line path, then set $k = k + 1$. Consequently, now $k > l$, it is necessary to update the sliding matrix, and it will continue to run from the third step

It can be summarized as follows: when the value of k is increased by one, the sliding matrix is required to be updated and path analysis is also performed so that the related parameters of the next path are obtained. When the value of l is increased by one, the sliding matrix is not required to be updated. However, it is necessary to determine whether the vessel is sailing on a straight-line path or a circular arc path, and the related LOS point is required to be calculated.

3.2. Coordinate Calculation of LOS Point. The LOS point is defined as the desired vessel position on a specified path. It is a dynamically changing point that guides the vessel approach to the desired path along with a specified heading. The vessel path selection is based on the previous LOS point. The flow chart for calculation of LOS points is shown in Figure 10 and is explained in the following:

(1) The initializing parameters are input into LOS point calculating module

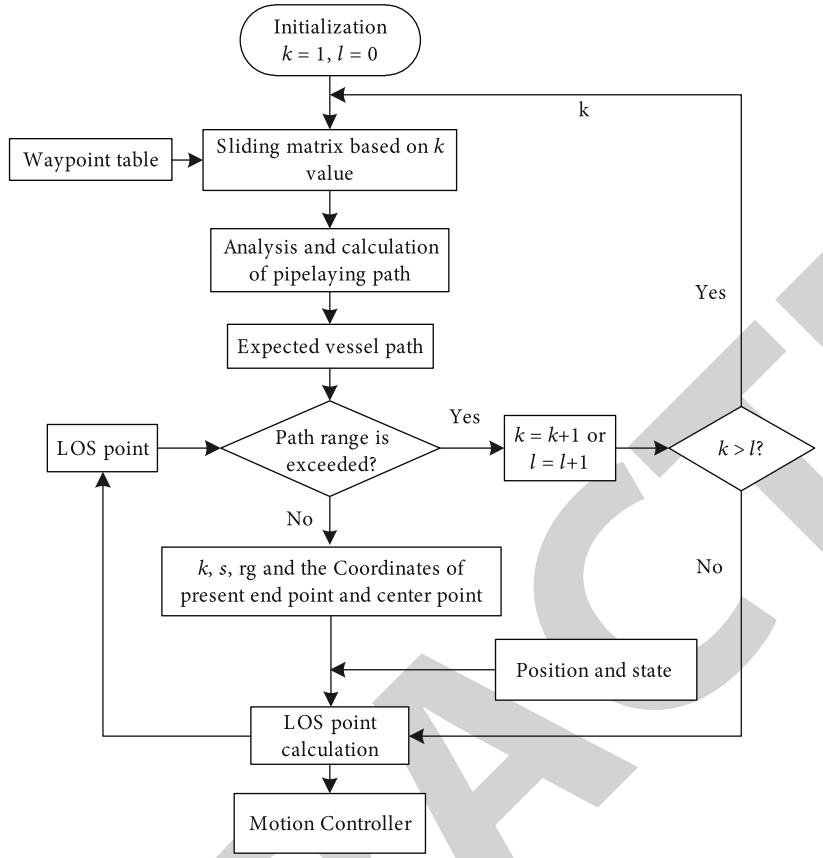

Figure 9: Execution process of the path selecting method.

(2) Check whether the path is required to be updated by comparing the value of k and k_{pre} in the process of calculating LOS point

(3) The condition $k = k_{pre}$ implies that the path does not need to be updated, where k is the index value of the present straight-line path and k_{pre} is the index value of the previous straight-line path

(4) When $k > k_{pre}$, it implies that the path is required to be updated, and the start and the end points of a straight-line path are also required to be recalculated and updated

(5) Determine the type of vessel path by comparing the values of k and l. If $k > l$, it implies that it is a straight-line path, and the method used to calculate LOS point of a straight-line path should be chosen. If $k = l$, it implies that it is a circular arc path, and the method used to calculate LOS point of a circular arc path should be selected

(6) The LOS point of the desired vessel path is obtained

3.3. Multiobjective Motion Controller of DP Vessels. The LOS point is the desired position of the ship moving on the desired path during path following, and its coordinates are changing dynamically when the vessel reaches a new position. The sliding matrix also contains such control requirement information which is obtained by the waypoint table. The diagram of the multiobjective controller of a DP vessel is shown in Figure 11.

When the vessel real-time position and the LOS point are known, the deviation of the vessel position in $\{n\}$ coordinate frame is converted into the deviation in $\{b\}$ coordinate frame. Then, the desired surge force, sway force, and yaw moment of the vessel can be calculated in combination with the deviations of the vessel speed and heading. The deviations of position and heading angle in $\{b\}$ can be obtained using

$$\begin{cases} \tilde{N} = N_{los} - N, \\ \tilde{E} = E_{los} - E, \\ \tilde{\psi} = \psi_d - \psi, \end{cases} \tag{23}$$

where $\tilde{N}$ and $\tilde{E}$ are the deviations of north and east positions, respectively. $\tilde{\psi}$ is the deviation of the heading angle. N and E are the real-time north and east positions, respectively; ψ is the real-time heading angle.

Hence, when the vessel is tracking the first desired circular arc path, the desired body velocity components decomposed from the pipelaying speed in the coordinate frame $\{n\}$ can be expressed as

$$\begin{cases} u_d = \cos\left(\beta_{C_1}\right) V_d, \\ v_d = \sin\left(\beta_{C_1}\right) V_d, \end{cases} \tag{24}$$

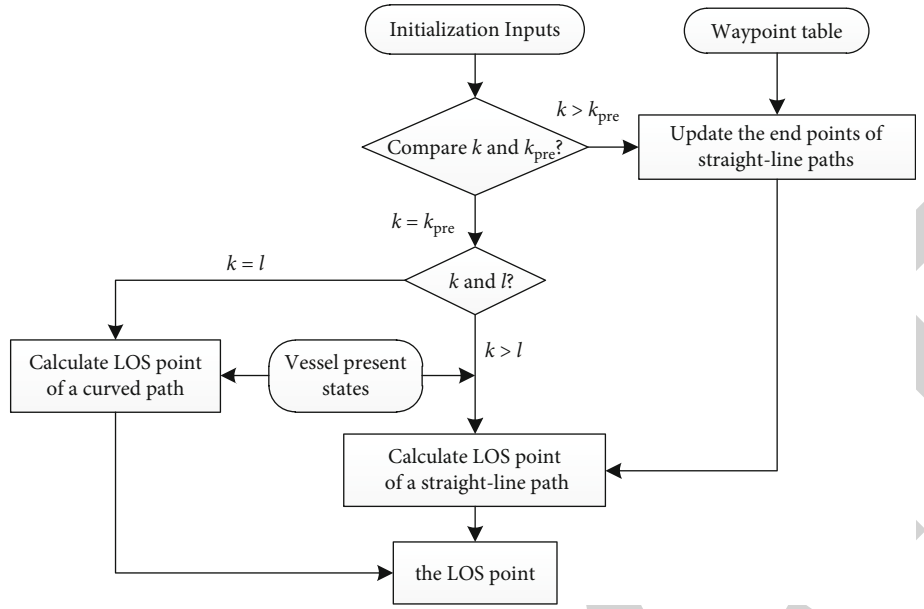

Figure 10: The calculation process of the LOS point.

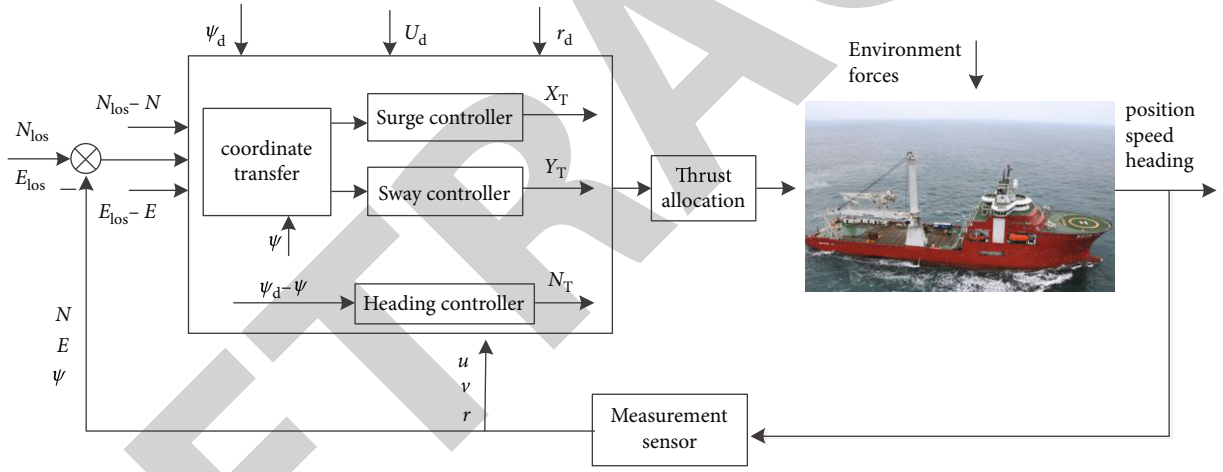

Figure 11: Multiobjective controller of DP vessel.

Table 3: The waypoint table of the pipelaying operation.

No.	N (m)	E (m)	Crab angle (degree)	Speed (m/s)	Turn radius (m)
1	0	0	0	2	0
2	1000	1000	0	2	300
3	1000	2000	0	2	300
4	200	2600	0	2	300
5	500	4000	0	2	300
6	1500	4100	0	2	0

where V_d is the desired speed in the coordinate frame $\{n\}$; β_{C_1} is the desired sideslip angle; u_d and v_d are the desired velocity components in the body coordinate frame, respectively.

When the vessel is tracking the desired circular arc path, the desired vessel speed is obtained using

$$V_d = V_{C_1}. \tag{25}$$

From Figure 6, when the rotational direction is clockwise and the circular arc path is clockwise, the value of β_{C_1} is obtained by

$$\beta_{C_1} = \frac{\pi}{2} - \delta_0 - \gamma_0. \tag{26}$$

The deviations of the vessel position in the coordinate frame $\{b\}$ can be expressed as

$$\begin{cases} \tilde{x} = \cos\left(\psi_{C_1}\right)\tilde{N} + \sin\left(\psi_{C_1}\right)\tilde{E}, \\ \tilde{y} = -\sin\left(\psi_{C_1}\right)\tilde{N} + \cos\left(\psi_{C_1}\right)\tilde{E}. \end{cases} \tag{27}$$

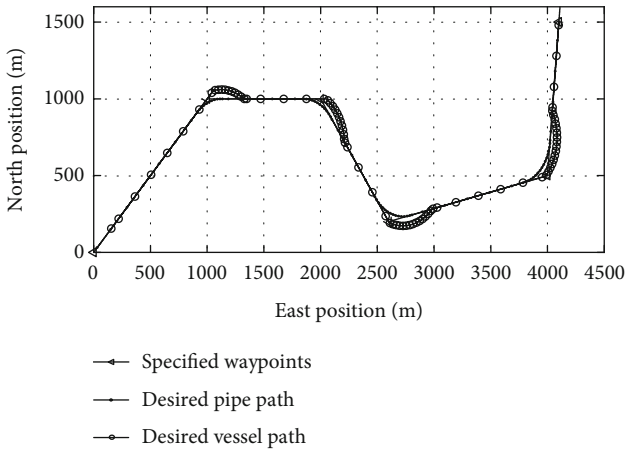

Figure 12: The specified waypoints, desired pipe path, and desired vessel path.

The deviations of the body velocity components by the vessel position deviation in the coordinate frame $\{b\}$ can be expressed as

$$\begin{cases} \tilde{u} = u_{\mathrm{d}} - u + k_{\mathrm{p}x}\tilde{x}, \\ \tilde{v} = v_{\mathrm{d}} - v + k_{\mathrm{p}y}\tilde{y}, \\ \tilde{r} = r_{\mathrm{d}} - r + k_{\mathrm{p}\psi}\tilde{\psi} + k_{\mathrm{d}\psi}\dot{\tilde{\psi}}, \end{cases} \tag{28}$$

where k_{px} is the control parameter used to convert the position deviation to the velocity deviation in surge direction. k_{py} is the control parameter used to convert the position deviation to the velocity deviation in sway direction. $k_{p\psi}$ and $k_{d\psi}$ are the control parameters used to convert the heading deviation to the rotational speed deviation.

Hence, the desired control forces generated by the propulsion system can be obtained using

$$\begin{cases} X_T = k_{\mathrm{p}u}\tilde{u} + k_{\mathrm{i}u}\int_0^t \tilde{u} + k_{\mathrm{d}u}\dot{\tilde{u}}, \\ Y_T = k_{\mathrm{p}v}\tilde{v} + k_{\mathrm{i}v}\int_0^t \tilde{v} + k_{\mathrm{d}v}\dot{\tilde{v}}, \\ N_T = k_{\mathrm{p}r}\tilde{r} + k_{\mathrm{i}r}\int_0^t \tilde{r} + k_{\mathrm{d}r}\dot{\tilde{r}}, \end{cases} \tag{29}$$

where k_{pu},k_{iu}, and k_{du} are the speed controller parameters of the dynamic positioning system in surge direction. k_{pv}, k_{iv}, and k_{dv} are the speed controller parameters of the dynamic positioning system in sway direction. k_{pr}, k_{ir}, and k_{dr} are the speed controller parameters of the dynamic positioning system in yaw direction.

4. Simulation Analysis of the Pipelaying Operation

The method presented in this study is a systematic control method, including pipeline path coding, pipeline path analysis based on the sliding matrix, mapping conversion between the desired pipeline path and the desired vessel path, the LOS guidance law of circular arc paths, and pipelaying controller design. To verify the effectiveness of the proposed method, a simulation is performed by setting a series of waypoints, pipelaying speed, crab angle, and turning radius.

A DP simulator for pipelaying operation is built using Qt software. As shown in Figure 8, the simulator consists of the waypoint table, path planning module, path guidance module, thrust allocation module, propeller system module, hydrodynamic module, environment force module, state observer module, and motion controller. It is assumed that the pipelaying water depth is a constant, and the tension of pipe tensioner is also a constant. For this simulation, the pipeline is assumed to be rigid without deformation in the pipelaying operation. Hence, the touchdown distance is also a constant.

The relevant parameters of the waypoint table need to be specified before starting pipelaying operation. All coordinates of six waypoints are set as shown in Table 3. All crab angles of the desired pipe path are set to 0 degree which means that the desired vessel heading angle is specified to be the same as the tangential angle of the desired pipeline path. The desired pipelaying speed on straight-line paths is set to 2 m/s, and the turning radius of the pipeline is set to 300 m. In addition, the touchdown distance is set to 200 m, and the desired speed on circular arc paths is set to 0.3 m/s.

Simulation environment parameters of the pipelaying operation are set as follows: the wind speed is 2 m/s, the current velocity is 1 m/s, and the wave height is 1.5 m. All environmental disturbances are assumed collinear with a direction of 40°.

4.1. Pipelaying Precision Analysis. The time step is set to 0.5 s. The results from the pipelaying simulation are shown in Figures 12–16.

For the results plotted in Figure 12, the desired pipelaying path is derived from the specified waypoints in Table 3 via the proposed method of path planning. Then, the desired vessel path is generated from the desired pipelaying path based on the parameters such as touchdown distance and turning radius in Table 3 using the presented method of pipeline path mapping. It can be seen that the vessel takes a turn at the outside of the pipeline circular arc path due to the touchdown distance and this is consistent with the theoretical results of the pipelaying path. From the simulation results shown in Figure 12, it is found that the pipelaying method of path analysis and path mapping works as expected.

The results of the vessel path obtained from the simulation and its cross-track error against the desired path are plotted in Figure 13.

As shown in Figure 13(a), the vessel path from the simulation matches well with the desired vessel path on the segments of straight-line paths and circular arc paths, even when the vessel is subjected to drift forces caused by ocean waves, wind, and currents. Therefore, these confirm that the vessel can track the desired path well through the application of the proposed method that combines path analysis, path selection, path guidance, and control technology.

As shown in Figure 13(b), the cross-track error of the vessel path is less than 0.1 m on straight-line paths. However,

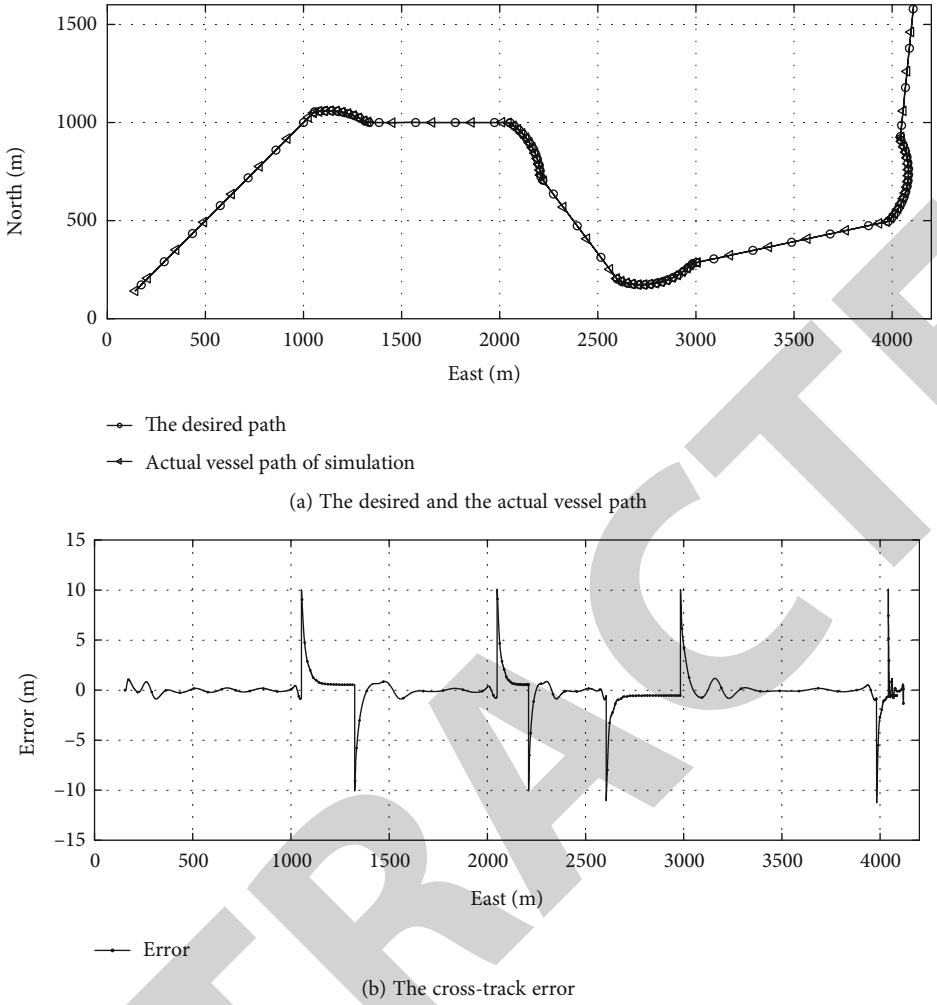

(a) The desired and the actual vessel path

(b) The cross-track error

Figure 13: Path following of the vessel.

the vessel cross-track error suddenly increases at the junction of a straight-line path and its adjacent circular arc path where the error reaches to 8.3 meters. This increased error may be the result of the continuous changing of the desired heading angle on circular arc paths, especially a sudden change of desired heading on the transition between a straight-line and its adjacent circular arc path. Then, the cross-track error gradually reduces, and finally, the path from simulation converges to the desired vessel path. Therefore, Figure 13(b) demonstrates that the proposed pipelaying controller method can make the vessel continuously track the desired vessel path.

The results of the pipe path from the simulation and its cross-track error against the desired pipe path are plotted in Figure 14.

As shown in Figure 14(a), the pipeline path from simulation matches well with the desired pipeline path during straight-line path following, and the simulated turning radius of the pipeline is the same as the specified turning radius. Therefore, it is reasonable to believe that the actual pipeline can be laid onto the desired pipelaying path by indirectly controlling the vessel motion. Additionally, Figure 14(a) also demonstrates that continuous pipelaying operation can be achieved via the proposed pipelaying control method. Consequently, the proposed method can be applied to various laying paths of pipelines and it is robust.

The cross-track error of the pipe path is shown in Figure 14(b). The cross-track error is less than 0.5 m on the segments of straight-line paths. However, the cross-track error suddenly increases at the junction of a straight-line path and its adjacent circular arc path. The maximum value of the cross-track error of the pipeline is approximately 9.5 m, which may be caused by a sudden change of the desired heading when the vessel is traveling between a straight-line path to its adjacent circular arc path. Besides, it may also be caused by the assumption that the pipe is rigid, and the cross-track error of the pipeline should be less than this value if the pipeline dynamic model [3, 6, 36] is considered. However, the cross-track error is gradually converged to zero when the vessel travels past the transition points.

4.2. Speed Analysis in Pipelaying Operation. The curves of speed performance during pipelaying operation are shown in Figure 15.

The pipelaying speed is 2 m/s on straight-line paths, and the speed is decreased to 0.3 m/s on the circular arc paths, which are consistent with the specified speed in the

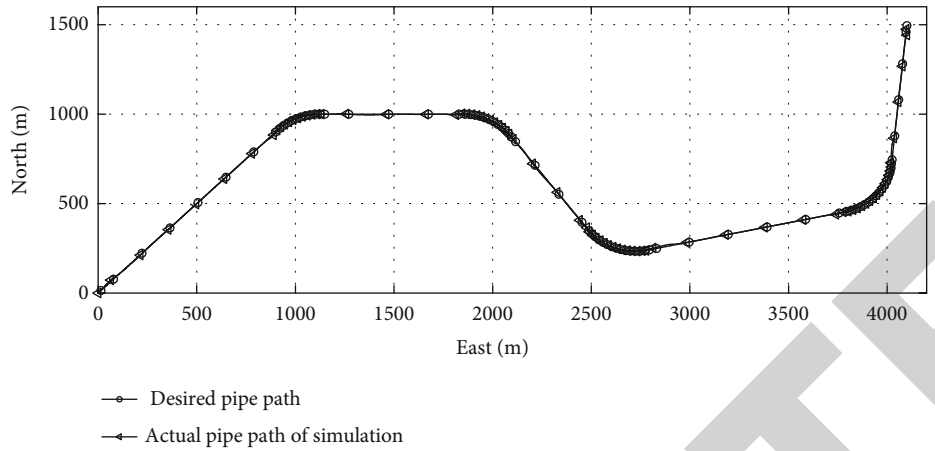

(a) The desired and the actual pipelaying path

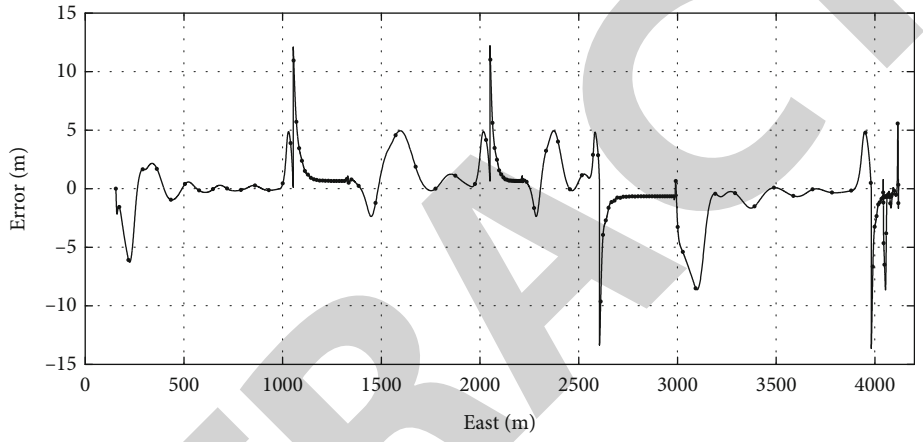

(b) The cross-track error

Figure 14: The pipelaying results of the pipeline.

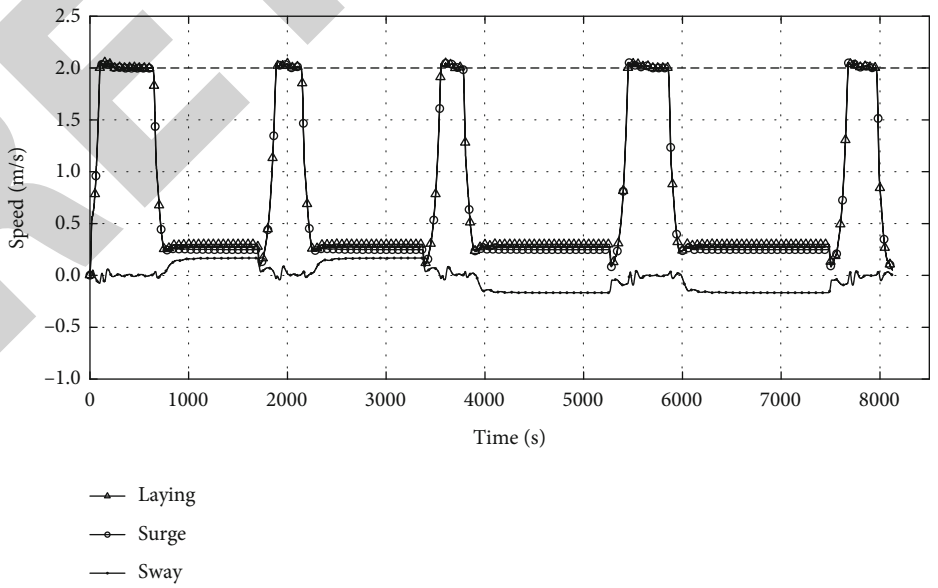

Figure 15: The vessel speed and pipelaying speed.

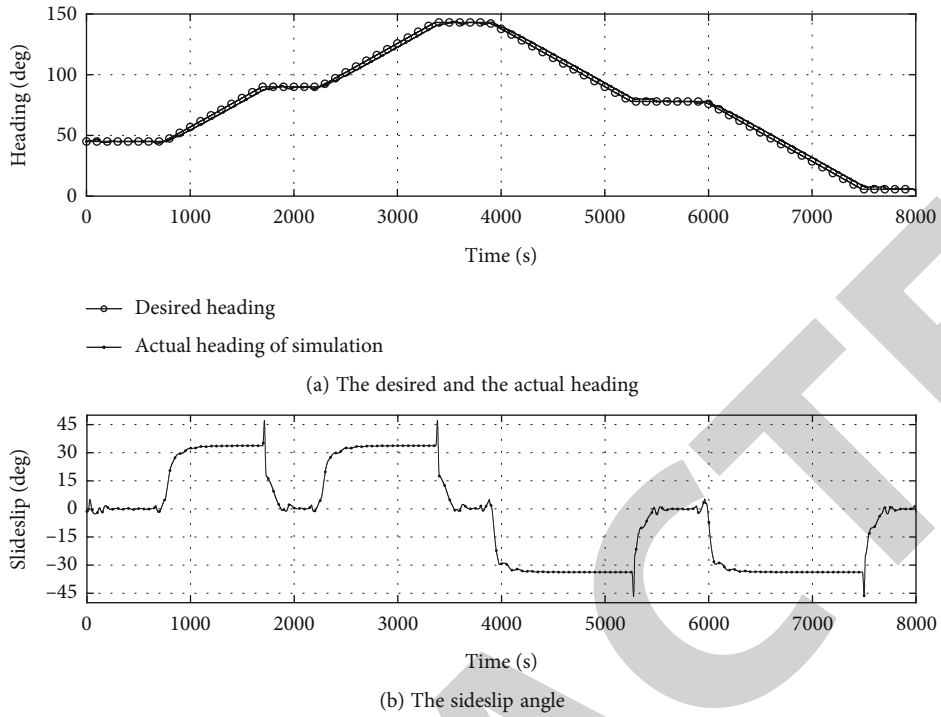

(a) The desired and the actual heading

(b) The sideslip angle

Figure 16: The vessel heading angle and sideslip angle.

waypoint table. As shown in Figure 15, the vessel speed along the surge direction is close to the pipelaying speed when the vessel is moving along a straight-line path. However, there is a relatively constant offset between the vessel speed along the surge direction and the pipelaying speed when the vessel is moving along a circular arc path, which is due to the vessel sway speed on the circular arc paths. Figure 15 also shows that the vessel speed along the sway direction is up to 0.18 m/s; this is the result of continuous changing of the desired heading angle which is consistent with the tangent of the desired pipe path despite that the predefined pipelaying speed on circular arc paths is reduced to 0.3 m/s. It is noticed that the vessel speed along the sway direction is decreased to zero on the straight-line paths. Hence, it is proved that the pipelaying controller designed in this study can control the vessel position and speed simultaneously during pipelaying operation.

4.3. Analysis of the Heading and Sideslip Angle. The vessel attitude performance in the pipelaying simulation, including the heading angle and sideslip angle, is shown in Figure 16.

As shown in Figure 16(a), the desired heading angle on the segments of the straight-line path is a constant, which is equal to the direction of the straight-line path. The desired heading angle on the segments of circular arc paths is a straight line with a constant slope, which is equal to the tangent direction of circular arc paths. Due to the limitation of the response speed of the vessel propulsion system, the propellers cannot immediately produce the desired thrusts, and there is always a time lag between the actual heading angle and the desired heading angle during path following on circular arc paths. However, the time lag is quite small. Therefore, it proves that the actual heading angle can track the desired value during operation using the designed pipelaying controller.

As shown in Figure 16(b), the sideslip angle fluctuates around zero on the segments of straight-line paths, which may be caused by the environmental forces from wind, wave, and currents. However, the vessel actual heading angle converges to the tangential direction of the desired circular arc paths and it is obtained by allowing a certain sideslip angle. The sideslip angle increases from 0° to 33° or decreases from 0 to -33°when the vessel is traveling along a circular arc path.

The proposed method, including path planning, path guidance, path tracking, and controlling, based on the sliding matrix for pipelaying operation in the study is effective. It is also proved by pipelaying simulation and analysis that the method is accurate in terms of the actual path, pipelaying speed, heading angle, and sideslip angle. The pipeline can be continuously laid onto the predefined path according to the specified pipe path, crab angle, pipelaying speed, and turning radius.

5. Conclusions

Through the operation simulation of pipelaying by DP ship and the analysis of the simulation results of pipeline trajectory, ship trajectory, pipelaying accuracy, pipelaying speed, and heading angle, the following conclusions can be obtained:

(1) A systematic method of pipelaying motion planning, guidance, and control of DP ship is proposed in this paper, which can control the pipelaying ship to switch smoothly between straight line and curve path, automatically update the path and relevant

control information along the waypoint table, and realize the continuous laying of offshore pipeline at a specified speed

(2) A pipeline path analysis and coding method based on a sliding matrix are proposed, which can realize automatic pipeline path analysis, automatic coding storage, and path mapping. With the progress of pipelaying, the relevant path and control information are automatically updated, which simplifies the preprocessing of the whole waypoint table and improves the automatic analysis ability of DP pipelaying path

(3) A circular path guidance method is proposed, and a multiobjective motion controller of DP ship is designed, which can effectively control the position, turning radius, speed, and attitude of DP pipelaying ship

Relevant simulation results show that the control method of pipelaying is effective and works reasonably well. This method is adopted in this paper to achieve the continuous pipelaying of the DP vessel, and it can also provide a valuable reference for path planning, guidance, and path tracking control of other surface vessels and underwater vehicles.

Data Availability

The raw data supporting the conclusions of this article will be made available by the authors, without undue reservation.

Conflicts of Interest

The authors declared that they have no conflicts of interest regarding this work.

Acknowledgments

This work was supported by the National Key Research and Development Program of China (2018YFC1406000).

References

[1] T. I. Fossen, *Handbook of Marine Craft Hydrodynamics and Motion Control*, Wiley, New York, USA, 2011.

[2] E. P. Heerema, "Recent achievements and present trends in deep-water pipe-lay systems," in *Proceedings of the 37th Offshore Technology Conference, OTC*, p. 17627, 2005.

[3] S. Ai, L. Sun, and L. Tao, "Modeling and simulation of deepwater pipeline S-lay with coupled dynamic positioning," *Journal of Offshore Mechanics and Arctic Engineering*, vol. 140, no. 5, pp. 1–10, 2018.

[4] P. Xu, Z. Du, F. Huang, and A. Javanmardi, "Numerical simulation of deepwater S-lay and J-lay pipeline using vector form intrinsic finite element method," *Ocean Engineering*, vol. 234, p. 09039, 2021.

[5] M. Panda, B. Das, B. Subudhi, and B. B. Pati, "A comprehensive review of path planning algorithms for autonomous underwater vehicles," *International Journal of Automation and Computing*, vol. 17, no. 3, pp. 321–352, 2020.

[6] Y. Ma, Y. Gong, C. Xiao, Y. Gao, and J. Zhang, "Path planning for autonomous underwater vehicles: an ant colony algorithm incorporating alarm pheromone," *IEEE Transactions on Vehicular Technology*, vol. 68, no. 1, pp. 141–154, 2019.

[7] N. A. Shneydor and D. Ingenieu, *Missile Guidance and Pursuit: Kinematics, Dynamics and Control*, Horwood Publishing Limited, Chichester, 1998.

[8] M. Breivik, "Topics in guided motion control of marine vehicles," in *Recent achievements and present trends in deepwater pipe-lay systems*, pp. 29–56, Doctor Dissertation of Norway University of Science and Technology, 2010.

[9] L. E. Dubin, "On curves of minimal length with a constraint on average curvature, and with prescribed initial and terminal positions and tangents," *Amer. J. Math.*, vol. 79, no. 3, pp. 497–516, 1957.

[10] R. T. Farouki and T. Sakkalis, "Pythagorean hodographs," *IBM Journal of Research and Development*, vol. 34, no. 5, pp. 736–752, 1990.

[11] H. Bruyninckx and D. Reynaerts, "Path planning for mobile and hyper-redundant robots using Pythagorean hodograph curves," in *1997 8th International Conference on Advanced Robotics. Proceedings. ICAR'97*, pp. 595–600, Monterey, CA, USA, 1997.

[12] A. M. Lekkas and T. I. Fossen, "Integral LOS path following for curved paths based on a monotone cubic Hermite spline parametrization," *IEEE Transactions on Control Systems Technology*, vol. 22, no. 6, pp. 2287–2301, 2014.

[13] M. Fu, A. Zhang, and J. Xu, "Adaptive dynamic surface tracking control for dynamic positioning cable laying vessel," in *2012 IEEE International Conference on Automation and Logistics*, pp. 266–271, Zhengzhou, China, 2012.

[14] M. Fu, B. Wu, and X. Zhang, "Modeling and analysis of trajectory tracking for DP vessel pipelaying based on back-stepping sliding mode method," *The Journal of New Industrialization*, vol. 4, no. 3, pp. 17–22, 2014.

[15] R. Rout, R. Cui, and Z. Han, "Modified line-of-sight guidance law with adaptive neural network control of underactuated marine vehicles with state and input constraints," *IEEE Transactions on Control Systems Technology*, vol. 28, no. 5, pp. 1902–1914, 2020.

[16] A. M. Lekkas and T. I. Fossen, *Line-of-sight guidance for path-following of marine vehicles*, Lamber Academic Publishing, 2013.

[17] A. M. Lekkas and T. I. Fossen, "A time-varying lookahead distance guidance law for path following," *IFAC Proceedings Volumes*, vol. 45, no. 27, pp. 398–403, 2012.

[18] T. I. Fossen, K. Y. Pettersen, and R. Galeazzi, "Line-of-sight path following for Dubins paths with adaptive sideslip compensation of drift forces," *IEEE Transactions on Control Systems Technology*, vol. 23, no. 2, pp. 820–827, 2015.

[19] E. Peymani and T. I. Fossen, "Direct inclusion of geometric errors for path maneuvering of marine craft," *IFAC Proceedings Volumes*, vol. 45, no. 27, pp. 293–298, 2012.

[20] E. Peymani and T. I. Fossen, "2D path following for marine craft: a least-square approach," *IFAC Proceedings Volumes*, vol. 46, no. 23, pp. 98–103, 2013.

[21] S. Moe, K. Y. Pettersen, T. I. Fossen, and J. T. Gravdahl, "Line-of-sight circular arc path following for underactuated USVs and AUVs in the horizontal plane under the influence of ocean

Hindawi
Journal of Sensors
Volume 2022, Article ID 6391238, 11 pages
https://doi.org/10.1155/2022/6391238

Research Article

BSIRNet: A Road Extraction Network with Bidirectional Spatial Information Reasoning

Hai Tan[1], **Hao Xu**[2,3] **and Jiguang Dai**[2,3]

[1]*Land Satellite Remote Sensing Application Center, Ministry of Natural Resources, Beijing 100048, China*
[2]*School of Geomatics, Liaoning Technical University, Fuxin 12300, China*
[3]*Institute of Spatiotemporal Transportation Data, Liaoning Technical University, Fuxin 12300, China*

Correspondence should be addressed to Hai Tan; tanh@lasac.cn

Received 22 September 2021; Accepted 17 December 2021; Published 12 January 2022

Academic Editor: Wei Zhang

Automatic extraction of road information from remote sensing images is widely used in many fields, such as urban planning and automatic navigation. However, due to interference from noise and occlusion, the existing road extraction methods can easily lead to road discontinuity. To solve this problem, a road extraction network with bidirectional spatial information reasoning (BSIRNet) is proposed, in which neighbourhood feature fusion is used to capture spatial context dependencies and expand the receptive field, and an information processing unit with a recurrent neural network structure is used to capture channel dependencies. BSIRNet enhances the connectivity of road information through spatial information reasoning. Using the public Massachusetts road dataset and Wuhan University road dataset, the superiority of the proposed method is verified by comparing its results with those of other models.

1. Introduction

Roads play an important role in urban planning, traffic navigation, map updating, and other fields [1]. With the rapid development of remote sensing satellites and sensors, it is becoming increasingly easy to collect very high-resolution (VHR) satellite imagery, which can provide sufficient data sources for road extraction. Therefore, extracting road information from VHR satellite imagery has become a popular topic of research. To date, researchers have developed many different road extraction methods [2], which can be generally divided into traditional methods and deep learning methods.

Traditional road extraction methods rely on road image features and the construction of a theoretical model [3]. For example, Song and Civco used a shape index and density features to extract road features [4], Valero et al. proposed the use of directional morphological operators that can flexibly fit straight and slightly curved structures for road extraction [5], and Dai et al. used a multiscale directional histogram and sector descriptor to extract road information through heuristic tracking [6]. However, the image features used to extract roads in these methods are manually designed and lack an automatic learning process. Consequently, traditional road extraction methods have the disadvantages of low automation, complex operation, and high time consumption.

Deep learning methods rely on a hierarchical feature expression framework to mathematically model specific problems in the real world and then use the resulting models to solve similar problems [7]. Different from traditional road extraction methods, deep learning methods have the characteristics of high automation and a strong learning ability [8], allowing them to better handle occlusion and shadows on roads. For example, a road structure refined convolutional neural network (CNN) was proposed by Wei et al. [9], which incorporates the geometric information of the road structure in the network learning process; Kestur et al. used a U-shaped fully convolutional network (U-FCN) that combines shallow fine-grained layers with a final-score layer to extract roads [10]; and Zhang et al. proposed a deep residual U-Net model [11], which combines the advantages of residual learning and U-Net [12, 13], for the road extraction task.

Although deep learning methods have achieved good results in automatic road extraction, these methods still often produce discontinuous road segments, which cause great difficulties in practical applications. There are two main reasons for this: (1) the occlusions and shadows caused by trees, buildings, etc., may cause a deep learning model to fail to correctly capture the information of occluded and shadowed roads. (2) The texture of a road may be very similar to that of the surrounding ground features, causing the model to be unable to extract clear road boundaries and locations. Both of these situations will lead to incomplete road extraction results, resulting in discontinuous roads.

At present, to address the discontinuity problem in road extraction, researchers have proposed various network models to directly improve the road extraction results. For example, He et al. proposed a road extraction network that relies on an encoder–decoder structure [14]. In the decoder component of this network, the spatial resolution of the feature maps is gradually restored by upsampling, but the details of the road edges are also lost. To prevent the loss of road edge details, Zhou et al. proposed a boundary and topologically-aware neural network (BT-RoadNet) [15]. This network extracts both rough features and fine features and then fuses them to improve the road extraction results. However, each channel contains a specific semantic feature, and BT-RoadNet ignores the relationships between the channels. Lu et al. proposed a globally aware road detection network with multiscale residual learning (GAMSNet) [16]. This network uses global average pooling to process channels and then uses a fully connected layer to establish the relationships between channels to improve the accuracy of road extraction. Although this network considers the relationships between channels, a large amount of road information will inevitably be lost when the channels are subjected to global average pooling. The above semantic segmentation network undeniably improves the accuracy of road extraction to a certain extent and improves the overall effectiveness on this task. However, the above network will still produce road discontinuities during the road extraction process.

To better solve the problem of road discontinuity, a road extraction network with bidirectional spatial information reasoning (BSIRNet) is proposed in this paper. In BSIRNet, a spatial reasoning perception module (SRPM) is established to capture spatial context dependence, a channel reasoning perception module (CRPM) is established to capture interchannel dependencies, and a multiscale skip connection structure is used to capture more semantic information.

The major contributions of this research are summarized as follows:

(1) A road extraction network with bidirectional spatial information reasoning (BSIRNet) is proposed. BSIRNet captures the dependencies of the road information in the spatial dimension and the channel dimension simultaneously. Moreover, BSIRNet extracts multiscale features of roads and integrates them to capture more road information. The BSIRNet method proposed in this research enhances the information reasoning ability applied in the road extraction process to solve the problem of discontinuous road extraction

(2) A spatial reasoning perception module (SRPM) and a channel reasoning perception module (CRPM) are proposed. The SRPM is aimed at capturing spatial context dependence such that at each location, the characteristics of the neighbourhood can be adaptively inferred to expand the receptive field. The CRPM is aimed at establishing the relationships between channels and capturing the dependencies between channels. Together, the SRPM and CRPM can solve the problem that road information cannot be captured due to occlusion and shadows

(3) A multiscale skip connection structure is used to extract multiscale semantic features and perform feature fusion processing. Feature maps of different scales contain different road information. A low-level feature map captures rich spatial information and can highlight the road boundaries, while a high-level semantic feature map reflects the road location information [17]. Our multiscale skip connection structure can solve the problem of unclear road boundaries caused by similar textures of roads and background features

The BSIRNet model proposed in this paper was verified on road datasets from Massachusetts and Wuhan University. The experimental results show that this method is superior to the existing deep-learning-based road extraction methods.

The rest of the paper is structured as follows. Section 2 introduces related network architectures. Section 3 describes the details of BSIRNet. Section 4 describes the datasets used in the experiments, the experimental setup, and the experimental results and presents a comprehensive analysis. Section 5 discusses the methods and advantages of BSIRNet. Finally, we summarize our conclusions in Section 6.

2. Related Architectures

As shown in Figure 1, the basic network used in BSIRNet is DeepLabV3+ [18], which, in turn, uses the improved Xception network as its backbone [19]. In the entry flow of the improved Xception network, all max pooling layers are changed to depthwise separable convolutions with stride = 2. In the middle flow, the residual blocks are repeated 16 times instead of 8 times. The atrous spatial pyramid pooling (ASPP) unit includes 5 different convolution operations, which extract different feature maps, and concatenation is then applied for multiscale feature fusion. DeepLabV3+ uses depthwise separable convolution to reduce the number of parameters to improve its computational efficiency.

A spatial information inference structure (SIIS) enables multidirectional message passing between pixels when it is integrated to a typical semantic segmentation framework [20]. Since the spatial information could be propagated

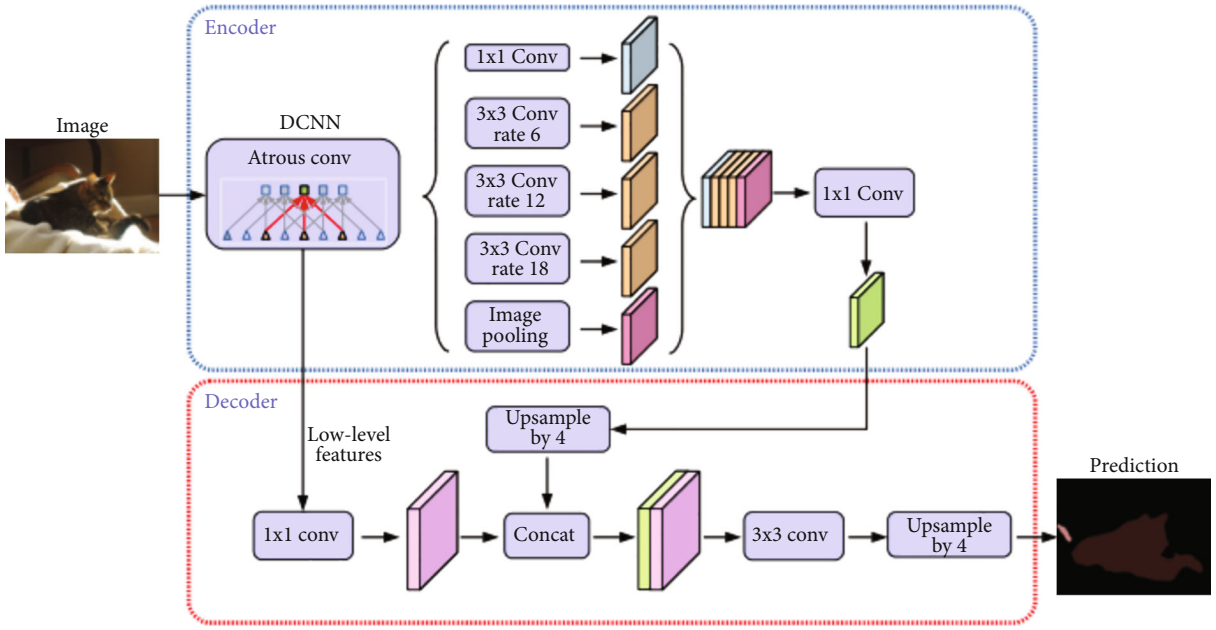

Figure 1: The architecture of DeepLabV3+.

and reinforced via interlayer propagation, SIIS can learn both the local visual characteristics of the road and the global spatial structure information. We also take inspiration from the advantages of SIIS. As shown in Figure 2, in SIIS, each feature map is divided into blocks by rows or columns, and information processing units with a recurrent neural network are sequentially applied to establish the semantic context [21].

Although DeepLabV3+ is an efficient semantic segmentation network, its convolutions can process only one local neighbourhood at a time, and it cannot effectively capture the long-range dependencies of the road information in the road extraction task. Similarly, although SIIS can establish contextual semantic relations, its convolutions can handle only one local neighbourhood at a time, and SIIS does not consider the relationships between channels.

Consequently, DeepLabV3+ and SIIS will both result in road discontinuities to varying degrees. To address the shortcomings of these existing architectures, we propose our road extraction network with bidirectional spatial information reasoning (BSIRNet).

3. Method

Figure 3 shows the overall flow chart of BSIRNet. BSIRNet is based on DeepLabV3+ and consists of Xception, ASPP, SIIS, SRPM, and CRPM components and a multiscale skip connection structure. The SRPM is used to capture the spatial context dependence, the CRPM is used to capture the dependence between channels, and the multiscale skip connection structure is used to capture more semantic information. The detailed architecture of BSIRNet is described in the following.

As shown in Figure 3, four outputs are generated from the input image after the deep convolutional neural network (DCNN): three low-level feature maps of different scales and one high-level semantic feature map. The three low-level feature maps of different scales correspond to the output_stride of the entry flow in Xception, which takes values of 4x, 8x, and 16x. These low-level feature maps represent the extracted spatial information, boundary information and location information of the roads in the input image.

The high-level semantic feature map is the output of the exit flow and serves as the input to the ASPP structure. The high-level semantic feature map undergoes five different convolution operations in the ASPP structure to yield outputs corresponding to five different scales. The five different convolution operations include a 1×1 convolution, three dilated convolutions with different dilation rates, and an image pooling operation. Among the three dilated convolutions with different dilation rates, the 3×3 dilated convolution with a dilation rate of 6 yield features with a smaller receptive field and clearer boundaries (fine features). In contrast, the 3×3 dilated convolution with a dilation rate of 18 yield features with a larger receptive field and blurred boundaries (rough features). The image pooling operation consists of global average pooling of the input features, followed by upsampling to the original size.

In summary, the road boundaries in the fine features are clear, but the receptive field is small. The road boundaries in the rough features are fuzzy, but the receptive field is large. If the fine feature pixels can be associated with the neighbourhood pixels corresponding to the rough features, not only can a reasoning relationship be established between each location and its neighbourhood but the receptive field in each region can also be expanded.

3.1. Spatial Reasoning Perception Module (SRPM). Since the convolution operations of DeepLabV3+ can process only one local neighbourhood at a time, the spatial context

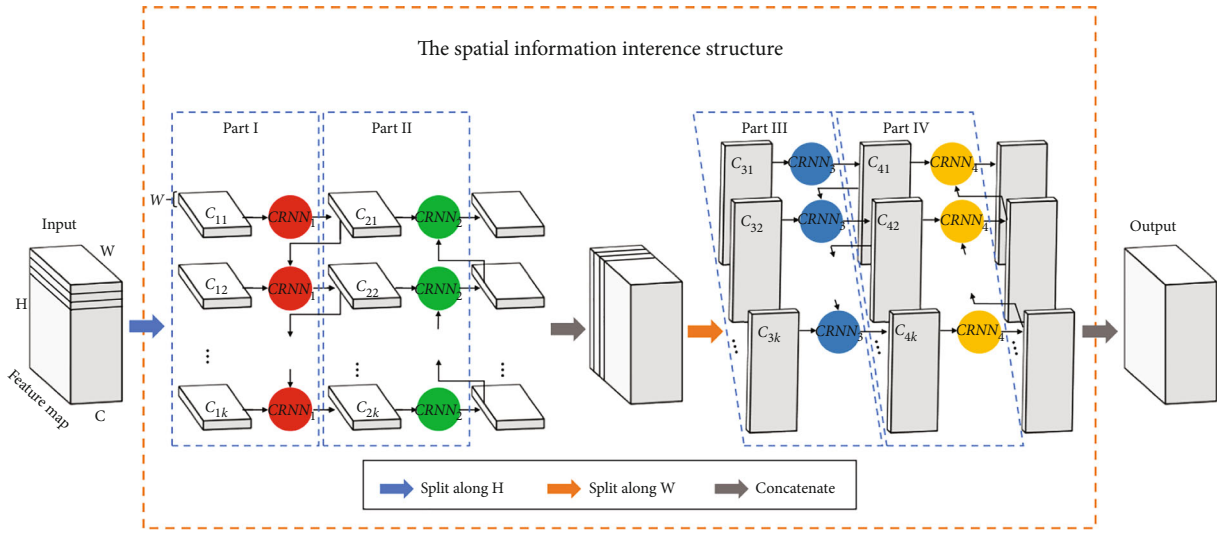

Figure 2: The architecture of the spatial information inference structure (SIIS).

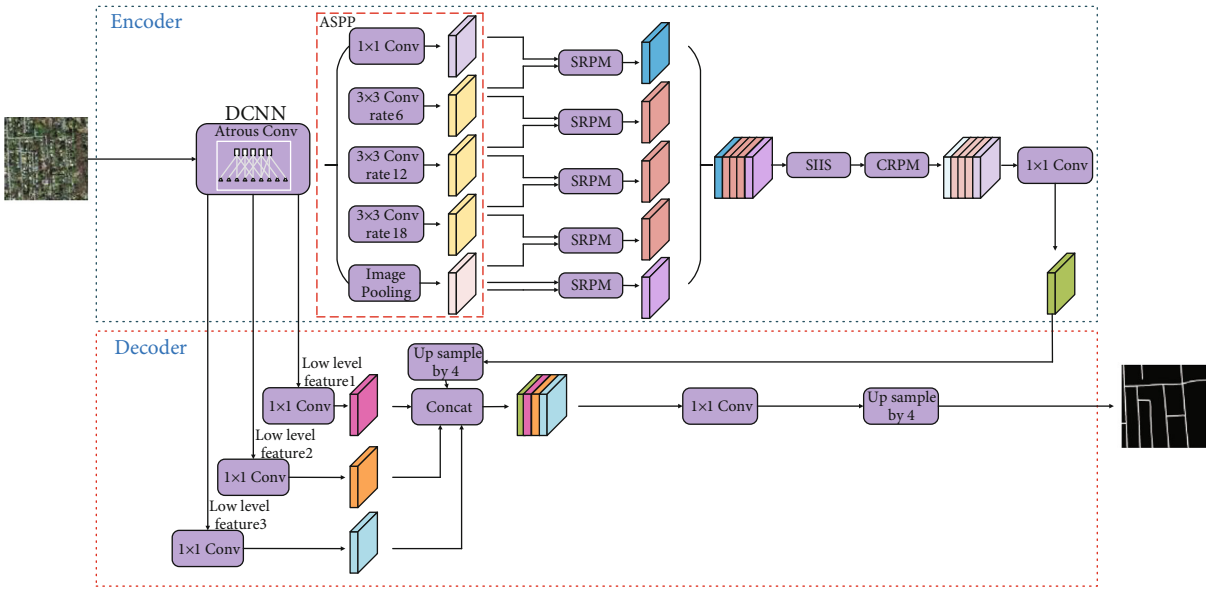

Figure 3: Overall flow chart of BSIRNet.

information obtained is limited, which prevents the network from capturing the long-range dependence of the road information. Therefore, we propose the SRPM to capture the spatial context dependence so that neighbourhood characteristics can be adaptively inferred for different locations, and the receptive field can be expanded.

In the SRPM, we use t different repeated paddings to expand the edge pixels of the feature map, such that each pixel of the feature map has a relative translation; thus, a set of feature map sequences $\{m_1, m_2, \cdots, m_t\}$ is obtained. We then apply concatenation to fuse the feature map sequence $\{m_1, m_2, \cdots, m_t\}$ to establish the inference relationship between each location and its corresponding neighbourhood and expand the receptive field of the feature map. The detailed structure of the SRPM is shown in Figure 4. The SRPM takes a rough feature map (pink) and a fine feature map (orange) as input. For the fine features, we use repeated padding (green) to fill in a layer of edge pixels in each of the four directions of the fine feature map to obtain f.

For the rough features, first use repeated padding to fill the rough feature map with one layer of edge pixels in the up and down directions and two layers of edge pixels on the right to obtain r_1. Second, we fill in two layers of edge pixels on the right and bottom sides of the rough feature map to obtain r_2. Then, we fill the rough feature map with one layer of edge pixels in the left and right directions and two layers of edge pixels on the bottom to obtain r_3. Analogously, we also fill in layers of edge pixels to obtain r_4, r_5, r_6, r_7, and r_8. Finally, concatenation is used to merge f, r_1, r_2, r_3

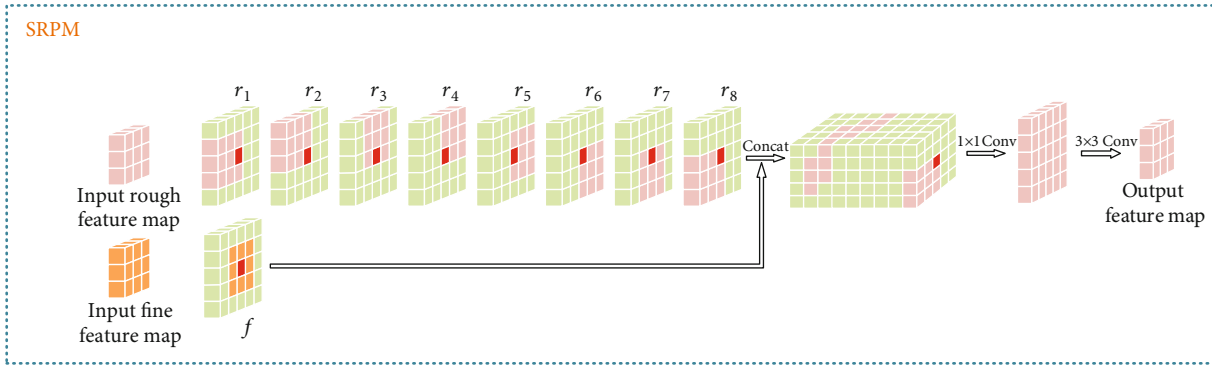

Figure 4: The architecture of the spatial reasoning perception module (SRPM).

, r_4, r_5, r_6, r_7 and r_8 obtained via the above operations. Let us consider the middle pixel of the fine feature map (red in f) as an example. When f is combined with r_1, a reasoning relationship is established between the middle pixel of the fine feature map and the pixel to the right in the corresponding rough feature map (red in r_1). Then, as the result continues to be merged with r_2, a reasoning relationship is established between the middle pixel of the fine feature map and the pixel to the lower right in the corresponding rough feature map (red in r_2). As the result continues to be merged with r_3, a reasoning relationship is established between the middle pixel of the fine feature and the pixel below in the corresponding rough feature map (red in r_3). Finally, r_4, r_5, r_6, r_7, and r_8 are sequentially merged to establish reasoning relationships between the middle pixel of the fine feature map and each pixel in its neighbourhood in the corresponding rough feature map. Because the receptive field of the rough feature map is larger, not only are reasoning relationships established between the fine feature map and the corresponding neighbours in the rough feature map but the receptive field of the fine features is also increased.

As shown in Figure 3, the SRPM is used to establish spatial reasoning perception relations for the five different scales of the ASPP output features. Since the output of the last image pooling operation does not have a corresponding rough feature map, the image pooling output can be used as both rough features and fine features to establish spatial reasoning perception relations.

3.2. Channel Reasoning Perception Module (CRPM). Each channel contains a specific semantic feature, but existing deep learning networks do not consider the relationships between channels when performing road extraction [16]. Therefore, we propose the CRPM to capture the interdependencies between channels to mitigate the discontinuity of roads. The proposal of the CRPM is also inspired by SIIS [20]. Although SIIS can efficiently establish semantic context relationships, it does not consider the transfer of information among recurrent neural network information processing units, easily leading to gradient disappearance or gradient explosion. Therefore, based on the above consideration, the number of skip connections in the CRPM is increased relative to SIIS to prevent gradient disappearance or gradient explosion.

The detailed structure of the CRPM is shown in Figure 5. As shown in part I of Figure 5, the input to the CRPM is a tensor with dimensions of $C \times H \times W$ consisting of SIIS output, where C, H, and W represent the numbers of channels, rows and columns, respectively. The tensor is first divided into k chunks along C, with the thickness of each chunk being $w = C/k$. Then, each chunk in the obtained sequence $S_1 = \{C_{11}, C_{12}, \cdots, C_{1k}\}$ is sent into CRNN_1 one by one. To prevent the gradient from disappearing or exploding, a skip connection is added after every four chunks. CRNN_1 is the first information processing unit of the CRPM. The main structure of a convolutional RNN (CRNN) unit is shown in Figure 6. This unit takes a three-dimensional tensor as input and produces an output in the same form to establish the reasoning relationships between channels. Specifically, the first chunk C_{11} is optimized by CRNN_1 to generate a new chunk C_{21} of equal size. When CRNN_1 optimizes the second chunk C_{12}, the most recent new chunk C_{21} will also be taken as input to provide the channel information. When the skip connection is optimized for the fifth chunk C_{15}, the generated chunks C_{21} and C_{24} are used as inputs to provide channel information. This process continues until the last chunk C_{k1} is updated, and during this process, the channel information is continuously transmitted downward.

In part II of Figure 5, the new chunks $C_{21}, C_{22}, \cdots, C_{2K}$ form a sequence $S_2 = \{C_{2K}, \cdots, C_{22}, C_{21}\}$ from bottom to top, which is then sent into CRNN_2 for optimization in the same way as in part I to produce k new chunks. These new chunks are then connected in the C dimension to form a complete tensor with dimensions of $C \times H \times W$, which is returned as the output tensor of the CRPM.

3.3. Multiscale Skip Connection Structure. Combining multiscale features is important for achieving accurate segmentation because feature maps of different scales contain different information. Low-level feature maps capture rich spatial information and can highlight the boundaries of roads, while high-level semantic feature maps reflect the location information of roads [17]. DeepLabV3+ operates at a single scale in the improved Xception. Therefore, in this work, multiscale features are extracted from Xception to extract more road information. Our multiscale skip connection structure fuses feature maps of different scales and then

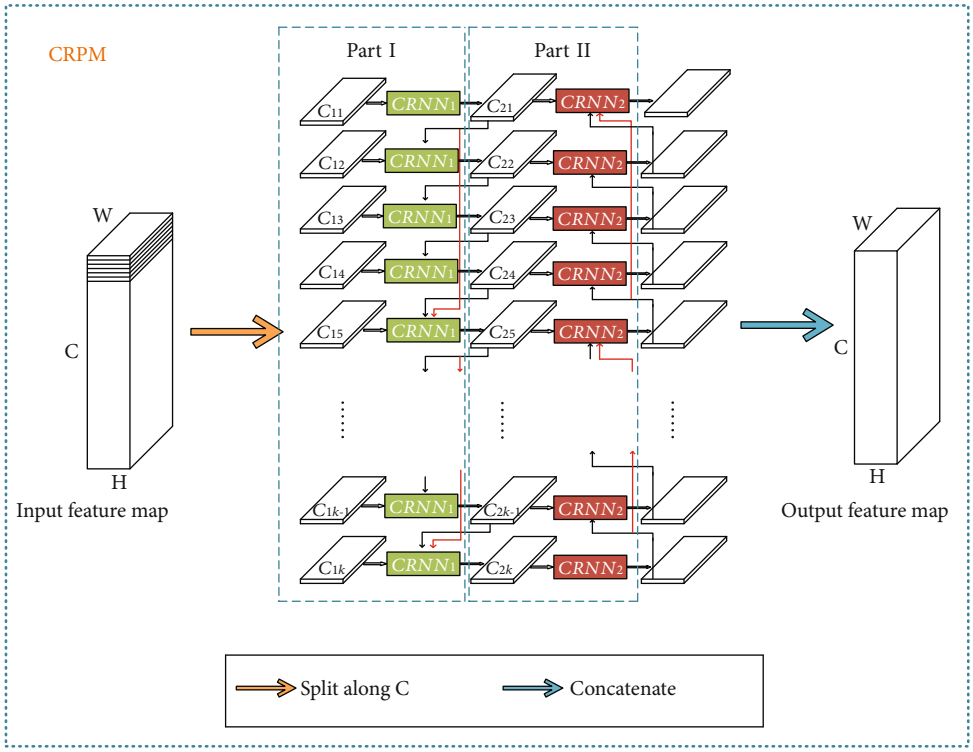

Figure 5: The architecture of the channel reasoning perception module (CRPM).

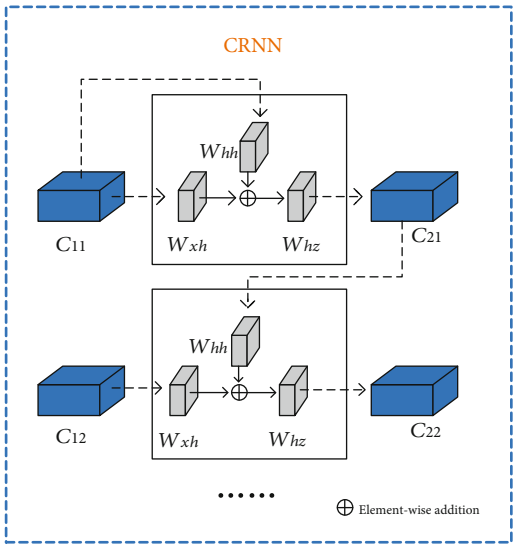

Figure 6: The architecture of a CRNN information processing unit.

learns a hierarchical representation of the aggregated multiscale feature maps.

In the multiscale skip connection structure, we use concatenation to fuse the three low-level feature maps of different scales with the processed high-level semantic feature map to capture more road information and improve the accuracy of road extraction. Then, 1×1 convolution and upsampling are used to process the fused multiscale features to obtain the final output.

4. Experiments and Analysis

4.1. General Details of the Experiments

4.1.1. Datasets. In our experiments, we use the Massachusetts road dataset and the Wuhan University road dataset. The Massachusetts road dataset consists of 1171 images, of which 1108 images are used for training, 14 images are used for validation, and 49 images are used for testing [22]. The size of each image is 1500×1500 pixels, and the resolution is 120 cm/pixel. The Wuhan University road dataset contains images from Boston and its surrounding cities in the United States, Birmingham in the United Kingdom, and Shanghai in China [16].

4.1.2. Data Preprocessing. For the Massachusetts road dataset and Wuhan University road dataset, since there are more background (nonroad) pixels in each image than road pixels, erroneously predicting road pixels to be background pixels is the main source of loss. Optimizing the semantic segmentation network can reduce the overall loss, but with the optimized semantic segmentation network, there is a high probability that uncertain pixels will be misidentified as background instead of as road pixels. To solve this problem, we adopt a simple and effective data preprocessing strategy known as the category ratio cropping (CRC) method [20].

As shown in Figure 7, we take an image I in the training set and its corresponding ground-truth label image L as an example. First, we use the same stride s and a $w \times w$

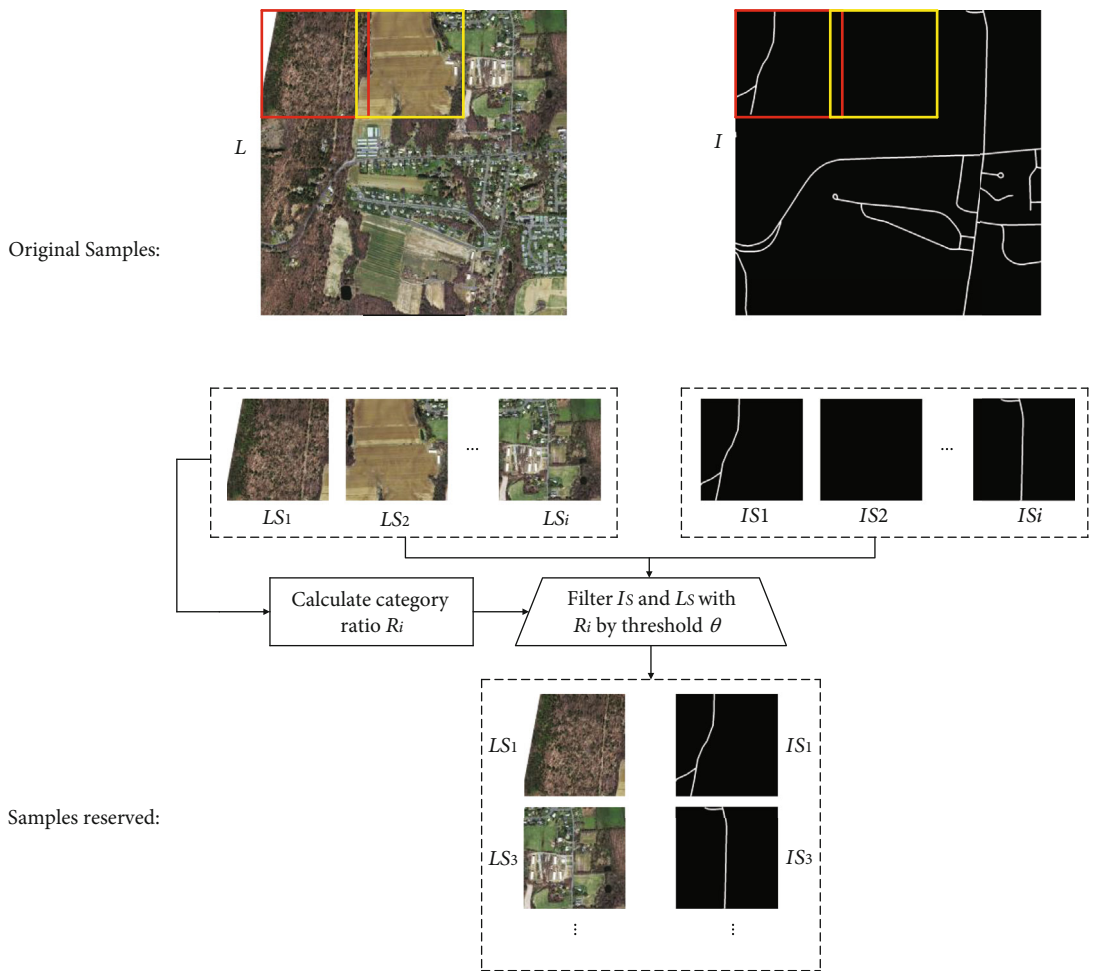

Figure 7: The process of applying the category ratio cropping (CRC) method to a typical sample from the Massachusetts road dataset.

cropping window to perform sliding cropping on $\{I, L\}$ to obtain a set of subimages and corresponding sublabels $\{I_{si}, L_{si}\}$, where $s = 494$ and $w = 512$. Second, L_{si} is used to calculate the ratio $R_i = [n1/ns, n2/ns, \cdots, nc/ns]$, where n_c denotes the number of pixels belonging to class C in L_{si} and n_s denotes the total number of pixels in L_{si}. Finally, the minimum value in R_i, min (R_i), is compared against a specified threshold θ. For pairs of I_{si} and L_{si}, only images with min (R_i) greater than the threshold θ are retained. We set the ratio threshold θ, which is a user-defined constant, to 0.01 [20].

After CRC data preprocessing, the imbalance in the numbers of road pixels and background pixels is effectively alleviated, thereby improving the efficiency of model training. In the end, we obtain 8988 images from the Massachusetts road dataset for training, 124 images for validation, and 386 images for testing. Similarly, we obtain 4568 images from the Wuhan University road dataset for training, 30 images for validation, and 127 images for testing.

4.1.3. Analysis of Experimental Parameters. To prevent excessively regular data from causing network overfitting or nonconvergence, we preprocess the training dataset using a data enhancement method that disrupts the order of the data. Second, considering that resizing will result in the loss of detailed image information, all images are used in their original size (512×512) to train the network. All models are trained with the same parameter settings and in the same environment. Specifically, we use the Adam optimizer for model training on a Windows 10 computer. The computer is equipped with an NVIDIA GeForce RTX 2080 Ti graphics card (with 11 GB of memory), allowing a batch size of 2 images. The learning rate for the Massachusetts road dataset is initially set to $1e-3$ and reduced by 0.85 every three epochs. The learning rate for the Wuhan University road dataset is initially set to $1e-4$ and reduced by 0.85 every three epochs. On these two datasets, the proposed network (BSIRNet) converges within only 50 epochs.

4.1.4. Evaluation Metrics. To evaluate the performance of a road extraction method, we adopt the following three evaluation metrics:

(1) The $F1$ score is an evaluation metric defined as the harmonic mean of the precision (P) and recall (R), and it is calculated as shown in

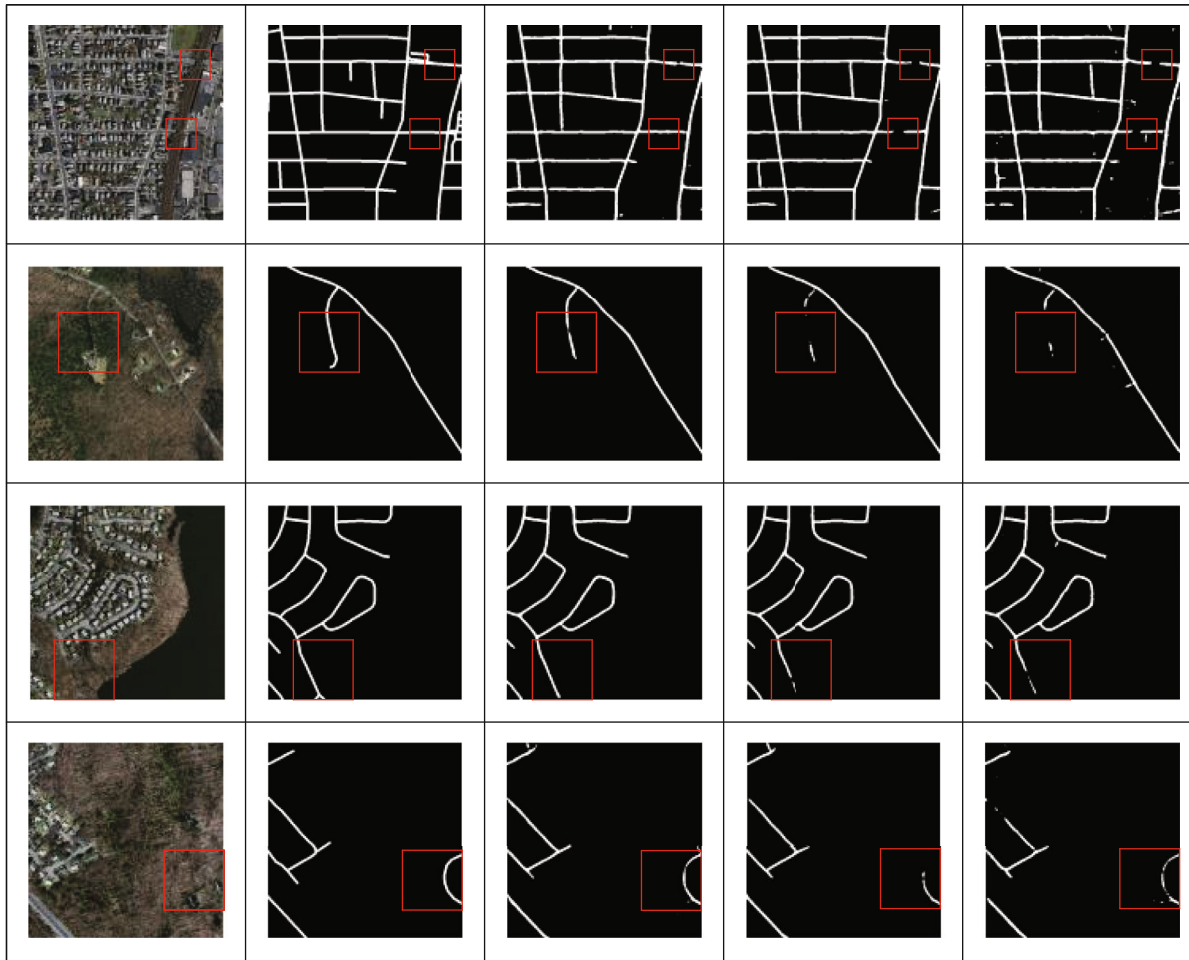

Figure 8: Road extraction results on the Massachusetts road dataset.

$$F1 = 2 \times \frac{p \times R}{P + R}. \tag{1}$$

(2) The intersection over union (IoU) is a comprehensive metric. It is defined as the ratio of the overlap area to the union area between the ground-truth map and the predicted map, and it is calculated as shown in

$$\text{IoU} = \frac{\text{TP}}{\text{FN} + \text{FP} + \text{TP}}, \tag{2}$$

where TP, FN, and FP denote the numbers of true positives, false negatives, and false positives, respectively. True positives are correctly identified road pixels; false negatives are road pixels incorrectly identified as nonroad pixels, and false positives are nonroad pixels incorrectly identified as road pixels

Table 1: Quantitative evaluation results on the Massachusetts road dataset.

Method	$F1$ score	Kappa	IoU
BSIRNet	0.7548	0.7392	0.6062
GAMSNet	0.7454	0.7311	0.5941
SII-Net	0.7199	0.7094	0.5623

(3) The kappa coefficient is an indicator for a consistency test and can also be used to measure the accuracy of semantic segmentation [23]. It may take values in the range of -1 to 1 but usually falls between 0 and 1. The greater the value of the kappa coefficient is, the higher the accuracy. The kappa coefficient is calculated as shown in

$$\text{kappa} = \frac{\text{Pa} - \text{Pe}}{1 - \text{Pe}}, \tag{3}$$

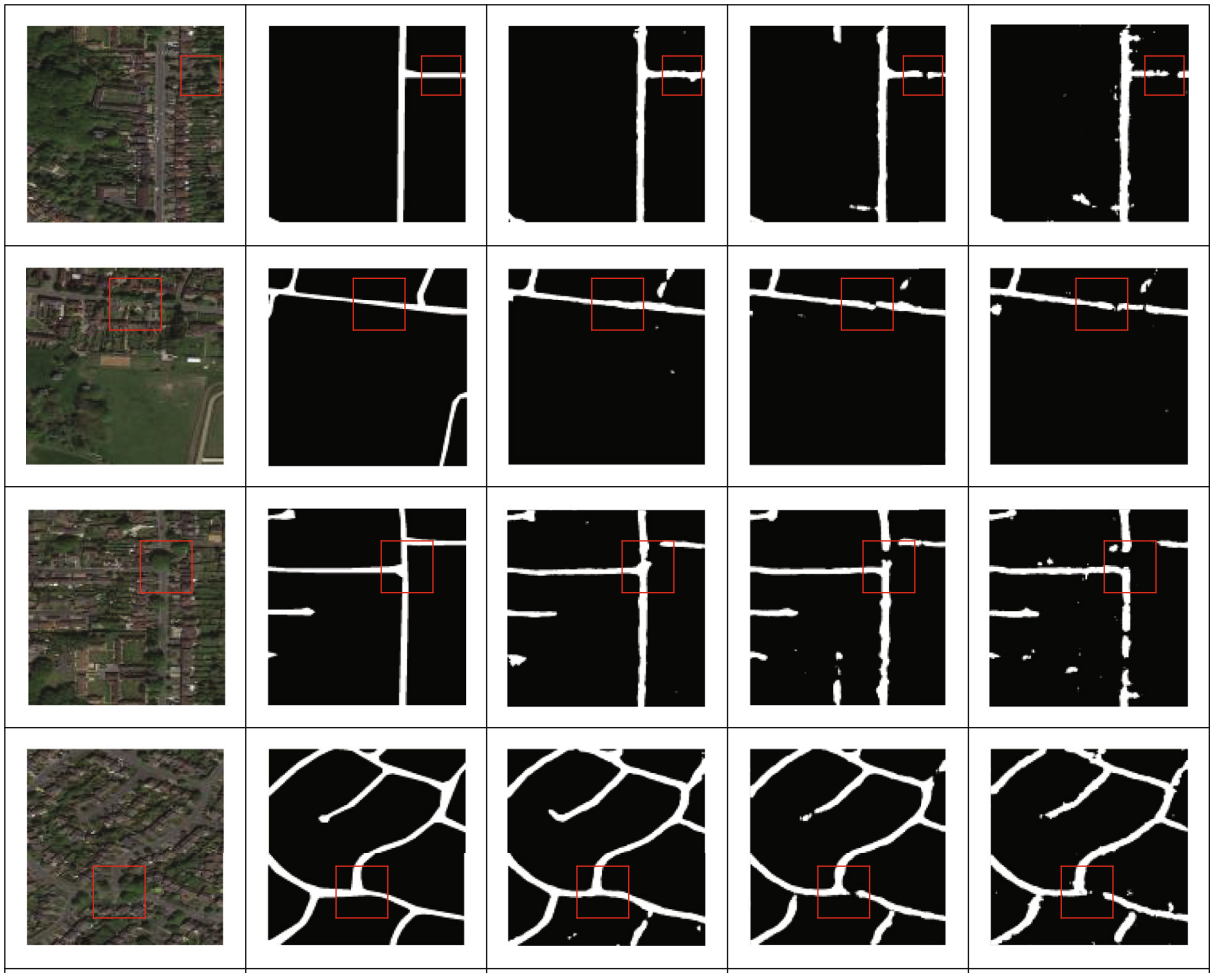

Figure 9: Road extraction results on the Wuhan University road dataset.

where Pa is the "actual agreement rate," and Pe is the "theoretical agreement rate."

4.2. Experiment Using the Massachusetts Road Dataset. In this experiment, road extraction is regarded as a semantic segmentation problem, focusing on the extraction of complete roads. We compare the proposed BSIRNet with two other road extraction methods based on semantic segmentation, namely, GAMSNet and the DeepLabV3+ network with SIIS (SII-Net). As shown in the first and second rows of Figure 8, our proposed BSIRNet completely extracts the occluded road, while the other two networks do not achieve complete extraction of this road. As shown in the third and fourth rows of Figure 8, for roads whose texture is similar to that of surrounding ground features, BSIRNet can also extract these roads completely. This shows that BSIRNet does not only solely depend on the visual characteristics of roads but also has some spatial information reasoning ability by virtue of modelling the specific context of roads. In particular, compared with GAMSNet and SII-Net, BSIRNet has a stronger spatial reasoning ability.

We also conduct a quantitative evaluation to compare the effectiveness of these methods. As shown in Table 1, the BSIRNet proposed in this study obtains an $F1$ score of 0.7548 and a kappa coefficient of 0.7392, greater than those of GAMSNet (with an F1 score of 0.7199 and a kappa coefficient of 0.7094). Compared with those of SII-Net, the F1 score and kappa coefficient of BSIRNet are increased by 3.49% and 2.98%, respectively. Because of the multiscale skip connection structure of BSIRNet, the extracted roads have clear boundaries. Compared with GAMSNet and SII-Net, BSIRNet also achieves a higher IoU. This shows that our spatial information reasoning perception network combined with a multiscale skip connection structure can effectively extract roads. The above experimental results verify the superiority of BSIRNet.

4.3. Experiment Using the Wuhan University Road Dataset. Using the Wuhan University road dataset, we further compare BSIRNet with the above two road extraction methods based on semantic segmentation. As shown in Figure 9, BSIRNet is able to completely extract roads occluded by

Table 2: Quantitative evaluation results on the Wuhan University road dataset.

Method	$F1$ score	Kappa	IoU
BSIRNet	0.7684	0.7392	0.6238
GAMSNet	0.7556	0.7261	0.6072
SII-Net	0.7343	0.7015	0.5801

trees, unlike GAMSNet and SII-Net. Moreover, as shown in the third row of Figure 9, in complex situations, the BSIRNet extraction results have stronger continuity than the results of the other two networks.

Similarly, we conduct a quantitative evaluation of the road extraction results on the Wuhan University road dataset. In Table 2, it can be clearly seen that BSIRNet outperforms the other two networks on the Wuhan University road dataset. Compared with those of GAMSNet, the $F1$ score and kappa coefficient of BSIRNet are increased by 1.28% and 1.31%, respectively. Compared with those of SII-Net, the $F1$ score and kappa coefficient of BSIRNet are increased by 3.41% and 3.77%, respectively. In addition, the extraction results of BSIRNet have stronger continuity, and the IoU value is also significantly higher than those of the other two networks. These experimental results show that our method results in fewer false extractions and missing extractions, thus further verifying that our method can alleviate the problem of discontinuity in road extraction results based on deep learning in the presence of occlusion and texture similarity.

5. Discussion

In the BSIRNet model proposed in this paper, the SRPM is established to capture spatial context dependence, the CRPM is established to capture interchannel dependencies, and the multiscale skip connection structure is used to capture more semantic information. The SRPM and CRPM together solve the problem that road information sometimes cannot be effectively captured due to occlusion and shadows. The multiscale skip connection structure solves the problem of unclear road boundaries caused by road textures similar to those of surrounding ground features. BSIRNet does not solely depend on the visual characteristics of roads but instead achieves some spatial information reasoning ability by modelling the specific context of roads, thereby solving the problem of road discontinuity caused by noise and occlusion.

In the above experiments, we use the Massachusetts road dataset and the Wuhan University road dataset to compare the BSIRNet model proposed in this paper with GAMSNet and SII-Net. The experimental results prove the effectiveness and superiority of BSIRNet, especially in overcoming the influence of occlusion to maintain the continuity of the extracted roads. The experimental results on the Massachusetts road dataset show that BSIRNet can completely extract roads affected by occlusion. Furthermore, when the road texture is very similar to the texture of surrounding ground object, BSIRNet can also extract roads with clear boundaries. As shown in Table 1, compared with those of SII-Net, the $F1$ score, kappa coefficient, and IoU of BSIRNet on the Massachusetts road dataset are increased by 3.49%, 2.98%, and 4.39%, respectively. The road extraction results of BSIRNet are also significantly better than those of GAMSNet on this dataset. Moreover, as shown in Table 2, the experimental results on the Wuhan University road dataset further prove the effectiveness and superiority of BSIRNet. Additionally, the method proposed in this paper has certain reference significance for the discontinuous extraction of other linear ground objects such as railways, power lines, pipelines, and rivers.

6. Conclusions

This paper proposes a road extraction network with bidirectional spatial information reasoning (BSIRNet), which can effectively improve the accuracy of road extraction. Roads possess natural connectivity; however, when an existing method extracts a road, discontinuity problems can easily arise due to interference from noise and occlusion. To solve this problem, we establish a spatial reasoning perception module (SRPM) to capture spatial context dependence and a channel reasoning perception module (CRPM) to capture interchannel dependence in BSIRNet. At the same time, we use a multiscale skip connection structure to capture more semantic information. Using the public Massachusetts road dataset and the Wuhan University road dataset, the superiority of the proposed method is verified by comparing its results with those of other models. When a road is occluded or shadowed by trees, buildings, etc., or the texture of the road is very similar to that of surrounding objects, BSIRNet can effectively improve the accuracy of road extraction. The quantitative results of our experimental evaluation also confirm the superiority of the proposed method. However, using very high-resolution (VHR) satellite imagery to classify road materials still presents great challenges. Therefore, in future work, we will conduct related research and propose a model for classifying road materials.

Data Availability

The data used to support the findings of this study are included within the article.

Conflicts of Interest

The authors declare that there is no conflict of interest regarding the publication of this paper.

Acknowledgments

This research was funded by the Natural Resources Satellite Remote Sensing Technology System Construction Sub-Project: Satellite Data Product Quality Inspection System (AA2111-9) and the National Natural Science Foundation of China (42071428).

References

[1] Q. Zhu, Y. Zhang, L. Wang et al., "A global context-aware and batch-independent network for road extraction from VHR satellite imagery," *ISPRS Journal of Photogrammetry and Remote Sensing*, vol. 175, pp. 353–365, 2021.

[2] J. Dai, Y. Wang, Y. Du et al., "Development and prospect of road extraction method for optical remote sensing image," *Journal of Remote Sensing (Chinese)*, vol. 24, no. 7, pp. 804–823, 2020.

[3] J. Dai, T. Zhu, Y. Zhang, Y. Wang, and X. Fang, "Line segment fusion method for high-resolution optical satellite image," *Acta Geodaetica et Cartographica Sinica*, vol. 49, no. 4, pp. 489–498, 2020.

[4] M. Song and D. Civco, "Road extraction using SVM and image segmentation," *Photogrammetric Engineering & Remote Sensing*, vol. 70, no. 12, pp. 1365–1371, 2004.

[5] S. Valero, J. Chanussot, J. A. Benediktsson, H. Talbot, and B. Waske, "Advanced directional mathematical morphology for the detection of the road network in very high resolution remote sensing images," *Pattern Recognition Letters*, vol. 31, no. 10, pp. 1120–1127, 2010.

[6] J. Dai, T. Zhu, Y. Wang, R. Ma, and X. Fang, "Road extraction from high-resolution satellite images based on multiple descriptors," *IEEE Journal of Selected Topics in Applied Earth Observations and Remote Sensing*, vol. 13, pp. 227–240, 2020.

[7] L. Ma, Y. Liu, X. Zhang, Y. Ye, G. Yin, and B. A. Johnson, "Deep learning in remote sensing applications: a meta-analysis and review," *ISPRS Journal of Photogrammetry and Remote Sensing*, vol. 152, pp. 166–177, 2019.

[8] X. Lu, Y. Zhong, Z. Zheng, J. Zhao, and L. Zhang, "Edge-reinforced convolutional neural network for road detection in very-high-resolution remote sensing imagery," *Photogrammetric Engineering & Remote Sensing*, vol. 86, no. 3, pp. 153–160, 2020.

[9] Y. Wei, Z. Wang, and M. Xu, "Road structure refined CNN for road extraction in aerial image," *IEEE Geoscience and Remote Sensing Letters*, vol. 14, no. 5, pp. 709–713, 2017.

[10] R. Kestur, S. Farooq, R. Abdal, E. Mehraj, O. S. Narasipura, and M. Mudigere, "UFCN: a fully convolutional neural network for road extraction in RGB imagery acquired by remote sensing from an unmanned aerial vehicle," *Journal of Applied Remote Sensing*, vol. 12, no. 1, article 016020, 2018.

[11] Z. Zhang, Q. Liu, and Y. Wang, "Road extraction by deep residual U-net," *IEEE Geoscience and Remote Sensing Letters*, vol. 15, no. 5, pp. 749–753, 2018.

[12] K. He, X. Zhang, S. Ren, and J. Sun, "Deep residual learning for image recognition," in *Proceedings of the IEEE conference on computer vision and pattern recognition*, pp. 770–778, Las Vegas, NV, USA, 2016.

[13] O. Ronneberger, P. Fischer, and T. Brox, "U-net: convolutional networks for biomedical image segmentation," in *International Conference on Medical image computing and computer-assisted intervention*, vol. 2, pp. 234–241, Munich, Germany, 2015.

[14] H. He, S. Wang, D. Yang, S. Wang, and X. Liu, "An road extraction method for remote sensing image based on encoder-decoder network," *Acta Geodaetica et Cartographica Sinica*, vol. 48, no. 3, pp. 330–338, 2019.

[15] M. Zhou, H. Sui, S. Chen, J. Wang, and X. Chen, "BT-RoadNet: a boundary and topologically-aware neural network for road extraction from high-resolution remote sensing imagery," *ISPRS Journal of Photogrammetry and Remote Sensing*, vol. 168, pp. 288–306, 2020.

[16] X. Lu, Y. Zhong, Z. Zheng, and L. Zhang, "GAMSNet: globally aware road detection network with multi-scale residual learning," *ISPRS Journal of Photogrammetry and Remote Sensing*, vol. 175, pp. 340–352, 2021.

[17] H. Huang, L. Lin, R. Tong et al., "UNet 3+: a full-scale connected UNet for medical image segmentation," in *ICASSP 2020-2020 IEEE International Conference on Acoustics, Speech and Signal Processing (ICASSP)*, Barcelona International Convention Centre, Spain, 2020.

[18] L. Chen, Y. Zhu, G. Papandreou, F. Schroff, and H. Adam, "Encoder-decoder with atrous separable convolution for semantic image segmentation," in *Computer Vision–ECCV 2018*, pp. 833–851, Munich, Germany, 2018.

[19] F. Chollet, "Xception: deep learning with depthwise separable convolutions," in *2017 IEEE Conference on Computer Vision and Pattern Recognition (CVPR)*, vol. 1, pp. 1800–1807, Hawaii, America, 2017.

[20] C. Tao, J. Qi, Y. Li, H. Wang, and H. Li, "Spatial information inference net: road extraction using road-specific contextual information," *ISPRS Journal of Photogrammetry and Remote Sensing*, vol. 158, pp. 155–166, 2019.

[21] W. Zaremba, I. Sutskever, and O. Vinyals, "Recurrent neural network regularization," 2014, https://arxiv.org/abs/1409.2329.

[22] V. Mnih and G. E. Hinton, "Learning to detect roads in high-resolution aerial images," in *Proceedings of the European Conference on Computer Vision (ECCV)*, pp. 210–223, Heraklion, Crete, Greece, 2010.

[23] R. Fan, Y. Chen, Q. Xu, and J. Wang, "A high-resolution remote sensing image building extraction method based on deep learning," *Acta Geodaetica et Cartographica Sinica*, vol. 48, no. 1, pp. 34–41, 2019.

Hindawi
Journal of Sensors
Volume 2023, Article ID 9765036, 1 page
https://doi.org/10.1155/2023/9765036

Retraction

Retracted: Application of Multiobjective Particle Swarm Optimization in Rural Credit System

Journal of Sensors

Received 19 December 2023; Accepted 19 December 2023; Published 20 December 2023

This article has been retracted by Hindawi following an investigation undertaken by the publisher [1]. This investigation has uncovered evidence of one or more of the following indicators of systematic manipulation of the publication process:

(1) Discrepancies in scope
(2) Discrepancies in the description of the research reported
(3) Discrepancies between the availability of data and the research described
(4) Inappropriate citations
(5) Incoherent, meaningless and/or irrelevant content included in the article
(6) Manipulated or compromised peer review

The presence of these indicators undermines our confidence in the integrity of the article's content and we cannot, therefore, vouch for its reliability. Please note that this notice is intended solely to alert readers that the content of this article is unreliable. We have not investigated whether authors were aware of or involved in the systematic manipulation of the publication process.

Wiley and Hindawi regrets that the usual quality checks did not identify these issues before publication and have since put additional measures in place to safeguard research integrity.

We wish to credit our own Research Integrity and Research Publishing teams and anonymous and named external researchers and research integrity experts for contributing to this investigation.

The corresponding author, as the representative of all authors, has been given the opportunity to register their agreement or disagreement to this retraction. We have kept a record of any response received.

References

[1] W. Xue, "Application of Multiobjective Particle Swarm Optimization in Rural Credit System," *Journal of Sensors*, vol. 2021, Article ID 3468479, 9 pages, 2021.

Hindawi
Journal of Sensors
Volume 2021, Article ID 3468479, 9 pages
https://doi.org/10.1155/2021/3468479

Research Article

Application of Multiobjective Particle Swarm Optimization in Rural Credit System

Wuxia Xue

Department of Economics, Wenzhou Vocational College of Science and Technology, Zhejiang 325006, China

Correspondence should be addressed to Wuxia Xue; xuewuxia@wzvcst.edu.cn

Received 29 October 2021; Revised 17 November 2021; Accepted 24 November 2021; Published 23 December 2021

Academic Editor: Wei Zhang

In China's rural credit system, the problem of credit constraints is prominent. Due to the imperfect credit market, a large number of rural residents have credit constraints. Rural credit constraint is a serious problem restricting China's rural economic development. Aimed at solving the rural credit constraints, this paper makes an optimization analysis on the rural credit system and loan decision-making. To more reasonably evaluate customers' borrowing ability, the credit risk based on farmers' data on the big data platform is evaluated in this paper. The stacked denoising autoencoder network is improved by adopting the deep learning framework to improve the accuracy of credit evaluation. For improving the loan decision-making ability of rural credit system, a loan optimization strategy based on multiobjective particle swarm optimization algorithm is proposed. The simulation results show that the optimization ability, speed, and stability of the proposed algorithm have achieved good results in dealing with the loan portfolio decision-making problem.

1. Introduction

In the period of market economy, farmers' consumption has been monetized and socialized to a great extent. On the one hand, the products and services needed by farmers are no longer self-sufficient. Like urban residents, it uses money as the medium to exchange needed products. On the other hand, the income level of farmers is low, and the income and expenditure are highly inaccurate. There is often an imbalance between farmers' income and consumption expenditure, so the need of the forming productive and consumer financing is exiting. A serious problem facing China's rural economic development is rural credit constraints [1]. Due to the imperfect credit market, a large number of rural residents have credit constraints. The probability of farmers getting loans is very low, which has also become one of the important reasons to curb farmers' consumption [2].

China's rural residents have strong credit constraints [3]. In 2007, the People's Bank of China and the National Bureau of statistics conducted a special survey on 20000 farmers in 10 provinces. The results show that 46 percent of farmers have loan needs, but only about 26 percent of farmers with loan needs can obtain loans through formal financial institutions. According to the survey, the network coverage of financial service institutions in rural areas is insufficient. By the end of June 2009, there were 2945 townships in China without any financial institutions. There are more than 8000 townships and towns with only one bank network. Among all townships and towns in China, the serious shortage of financial service accounts for 1/3.

The rural credit constraints are caused with four reasons as follows: (1) There are defects in the rural financial system. The Agricultural Development Bank has a single business, which is limited to the issuance of grain and cotton loans. At the same time, the business scope of most banks has not yet involved rural areas. (2) The construction of rural social credit system lags behind, and there is information asymmetry. The reasons why formal financial institutions are unwilling to lend to farmers also include that financial institutions are unable to understand the accurate information of rural borrowers. For example, farmers' credit level and repayment ability, what is the actual purpose of their loans, what risks will there be, and so on. This makes financial institutions reluctant to extend loans to rural residents.

(3) Rural financial institutions generally require mortgage guarantee. However, the main properties owned by rural residents are land with only use right and real estate without mobility. These properties can not be used as collateral for bank loans in the existing financial regulations. Other properties owned by farmers are mainly livestock and means of production. These can not be used as collateral for loans. (4) The credit products issued by financial institutions are not suitable for the consumption needs of rural residents. The important characteristics of Chinese rural residents' loan behavior are the huge number of farmers, high dispersion, and small loan amount. These require financial institutions to have very high operation efficiency in order to meet the needs of rural loan business [4]. The analysis of this paper focuses on the second and fourth points here, which study to improve the accuracy of credit assessment and optimize the loan program.

The business purpose of the bank is to maximize profits and minimize risks. It follows the principle of efficiency, safety, and liquidity. Risk loan portfolio rationing decision-making is a process of selecting combining appropriate loan objects from many loan objects on the premise of comprehensively considering loan income and risk. Literature [5] established a loan portfolio optimization decision-making model based on the principle of maximum unit risk return. The above combinatorial optimization problem belongs to NP (nondeterministic polynomial) hard problem [6]. The solving process of the problem is simple and easy when the scale is small, but with the increase of the scale of the problem, the amount of calculation increases exponentially. Therefore, it is necessary to design a better algorithm that takes into account the quality of solution and running time.

Particle swarm optimization (PSO) is inspired by the research results of bird swarm foraging behavior [7, 8]. The particle swarm optimization algorithm has the advantages of fast convergence, simple operation, and easy implementation. The algorithm has attracted extensive attention of scholars in the fields of evolutionary computing [9], computer science [10], and management science [11] and has achieved a lot of research results [12]. Most of these research results are obtained from the research of various multidimensional continuous space optimization problems, but there are few application research results in discrete optimization problems [13].

The innovations and contributions of this paper are listed below:

(1) In order to evaluate farmers' borrowing ability more reasonably, the deep learning framework is used to evaluate farmers' personal credit. Due to the existence of high-dimensional data in the bank's big data platform, the stacked denoising autoencoder network is firstly used for feature compression and extraction

(2) Different from the previous bank credit evaluation, this paper takes bank big data as the data source of risk evaluation. It enriches the characteristics of credit evaluation and improves the accuracy of evaluation

(3) In order to improve the loan decision-making ability of rural credit system, an adaptive decomposition multiobjective particle swarm optimization algorithm is designed in this paper. Then, by calculating the optimal solution and the membership information of the subspace, the appropriate solution in the external file is selected, and an external file update strategy based on decomposition method is designed. Finally, the convergence of the algorithm is improved by balancing the exploration and development ability of the algorithm

The structure of this paper is as follows. The related theories are described in Section 2. Section 3 focuses on the proposed algorithm model in this paper. Section 4 is experiment and analysis. Section 5 is the conclusion.

2. Related Theories

2.1. Selection of Risk Assessment Features. The data used by banks to assess personal credit risk mainly comes from the collection of customer data, such as the central bank's credit investigation data, basic personal information, financial status, credit records, and debts [14]. With the expansion of various businesses of the bank, especially the cross-marketing of internal customers, customer information is constantly enriched. Bank customers no longer belong to a single business category, and the footprints left by customers in multiple business areas of the bank will become the data source of personal credit risk assessment. These data have also become a necessary supplement to personal credit portrait.

Based on the traditional evaluation features, namely, credit card lending and loan repayment data, this paper relies on the big data platform of a commercial bank. Customer cross-business information is added to the evaluation system to integrate the two parts of data, so as to build a complete bank personal credit portrait. Figure 1 shows the logical representation of data splicing and integration.

2.2. Multiobjective Optimization Problem. For a multiobjective optimization problem (MOP) [15], its objective function can be described as

$$\text{Min } (H(i)) = [h_1(i), h_2(i), \cdots, h_W(i)], \tag{1}$$

where i is an n-dimensional decision variable. $h_W(i)$ is the wth objective function. W is the number of objective functions.

For a set of decision variables i and j, it is assumed that the problem to be optimized is the minimization target value. If $h(i)$ is less than or equal to $h(j)$ for any target value, and at least one target of $h(i)$ is less than $h(j)$, then i dominates j.

$$\begin{aligned} &\forall x : h_x(i) \le h_x(j), \\ &\exists y : h_y(i) < h_y(j), \end{aligned} \tag{2}$$

where $x = 1, 2, \cdots, W, y = 1, 2, \cdots, W$. If i and j are dominant, then i and j can be compared. Otherwise, i

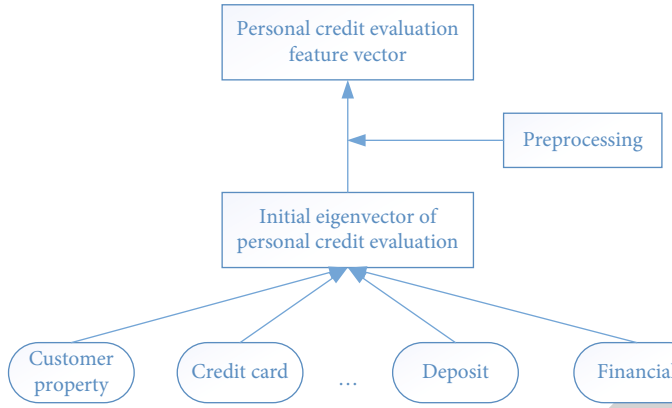

Figure 1: Construction of personal credit evaluation characteristics.

and j cannot be compared. When a solution is not dominated by any solution, it is called a nondominated solution. All the nondominated solutions finally obtained by the algorithm are the optimal solution set obtained by the algorithm.

Multiobjective particle swarm optimization algorithm uses a group of randomly distributed populations to guide the population to search the optimization space by selecting the appropriate solution. A multiobjective optimization algorithm is used to obtain the optimal solution set of MOP. In each iteration, the update formulas of particle velocity and position are

$$i_x(n+1) = i_x(n) + q_x(n+1), \tag{3}$$

$$q_x(n+1) = \omega_x q_x(n) + e_{x,1}R_{x,1}(u_x(n) - i_x(n)) + e_{x,2}R_{x,2}(a(n) - i_x(n)), \tag{4}$$

where ω_x is the inertia weight. $e_{x,1}$ and $e_{x,2}$ are learning factors. $R_{x,1}$ and $R_{x,2}$ are random values. $u_x(n)$ is the individual optimal position of the particle in the nth iteration. $a(n)$ is the global optimal position of the tth iteration. $i_x(n)$ is the position of the ith particle in iteration n. $q_x(n+1)$ is the velocity of the ith particle at iteration n.

3. Application of Multiobjective Particle Swarm Optimization Algorithm

3.1. Credit Evaluation Based on Deep Learning. The stacked autoencoder network applied in this paper is a special structure of deep learning. It is mainly applied to dimensionality reduction of high-dimensional data, namely, feature compression [16]. Firstly, a shallow neural network is constructed for the input item, hidden layer, and output item, and the hidden layer is solved when the output item is closest to the input item. Then, the hidden layer is used as the input of the next shallow network. Repeat the above process to solve the new hidden layer. Finally, the hidden layers are stacked layer by layer in the form of stack to form a deep neural network.

Big data samples have noise caused by data deviation, error, and missing. In order to enhance the antinoise ability of the autoencoder, the denoising autoencoder (DAE) adds noise to the original data to generate a shallow neural network structure and then compresses and extracts its features [17]. The algorithm has good performance in multidimensional and high noise data scenarios. Firstly, the training sample $i(i \in R^t)$ is subjected to a series of random transformations $v_f(i' \mid i)$, and the variable i' is obtained after corrosion. Then, the reconstructed input i'' is obtained by learning and training the autoencoder of i'.

In the neural network, the gradient descent method is used for iterative solution, so that i'' is closest to the original data i. At this time, the corresponding hidden layer j (or compressed feature layer) is

$$j = \operatorname{argmin}\left[\sum_{x=1}^{t} \frac{1}{t} L\left(i_x, i_x'\right) + Y_m\right], \tag{5}$$

where $i_x \in i, i_x' \in i''(x = 1, 2, \cdots, t)$ are the corresponding elements belonging to the original feature and reconstruction feature, respectively. L is the loss function of mean square error or cross entropy. Y_m is a norm constraint added to prevent overfitting in the process of model learning.

The random transformation generated by the original denoising autoencoder network only adds a small change to the characteristics of the original data. It does not take into account the noise correlation between input features, which is obviously insufficient to improve the robustness of the model. On the premise of considering the correlation of sample noise, in order to improve the quality of noise generation, its truncation form is used to improve the computational efficiency.

Firstly, by analyzing the correlation between input features, the positive definite correlation matrix is determined Σ_{II}. For any $t \times 1$ vector g_z and diagonal matrix $\Lambda = \operatorname{diag}[\lambda_1, \lambda_2, \cdots, \lambda_t]$, equation (6) can be established.

$$\Sigma_{II} g_z = \Lambda g_z, \tag{6}$$

where λ_x is a nonzero characteristic term of the correlation matrix Σ_{II}. Expansion can be defined as the decomposition of correlation matrix.

$$\Sigma_{II} = \sum_{x=1}^{t} \sqrt{\lambda_x} q_x q_x^N, \tag{7}$$

where q_x is the normalized eigenvalue of λ_x. Therefore, the random variable can be expressed as

$$I = \mu_I + \sum_{x=1}^{t} \sqrt{\lambda_x} q_x I_x, \tag{8}$$

where μ_I represents the mean of the random variable I. Since normalization will be carried out first in the calculation process, it can be assumed that $\mu_I = 0$. I is a random number. It follows the standard normal distribution, $I \sim T(0, 1)$. In practice, in order to reduce the amount of calculation, the truncated approximation can be obtained only by obtaining the W term $(w < t)$.

$$\hat{I} = \sum_{x=1}^{W} \sqrt{\lambda_x} q_x I_x. \tag{9}$$

The item W needs to ensure that the truncation error is less than 0.05. The truncation error is defined as

$$\mathrm{err}_{r-\mathrm{Var}} = \frac{\mathrm{Var}\left[I - \hat{I}\right]}{\mathrm{Var}[I]} = \frac{\sum_{x=W+1}^{t} \lambda_x q_x^2}{\sum_{x=1}^{t} \lambda_x q_x^2}. \tag{10}$$

The stacked denoising autoencoder (SDAE) network is formed by cascading a single autoencoder layer by layer. Specifically, the middle hidden layer obtained from the training of the previous autoencoder participates in the training as the input of the next autoencoder. This stack in turn form a deep neural network structure, as shown in Figure 2.

The big data platform of commercial banks takes personal credit card data as the main data to construct the personal credit portrait. And the personal credit portrait will also concatenate personal business attributes and transaction data. Because personal information is scattered in various data sources, it needs to be integrated and spliced in order to facilitate the use and unified management of upper business logic. With individual customers as the granularity and credit dimension as the starting point, splice and integrate other business data of individual customers in the big data platform. Finally, it can form a complete view of personal credit based on bank big data. The following is a formal expression of the overall algorithm of personal credit risk assessment.

(1) Data preprocessing: first, extraction, integration, cleaning, and conversion of the original data are preprocessed. The feature vector $[i_1, i_2, \cdots, i_z]$ is formed from the traditional credit evaluation features. The intrabank business data of individual customers are preprocessed to form feature vectors $[i_{z+1}, i_{z+2}, \cdots, i_t]$. Two parts of features are fused to form the input features of the model; that is, $I = [i_1, i_2, \cdots, i_t]$ is used as the input data for model training

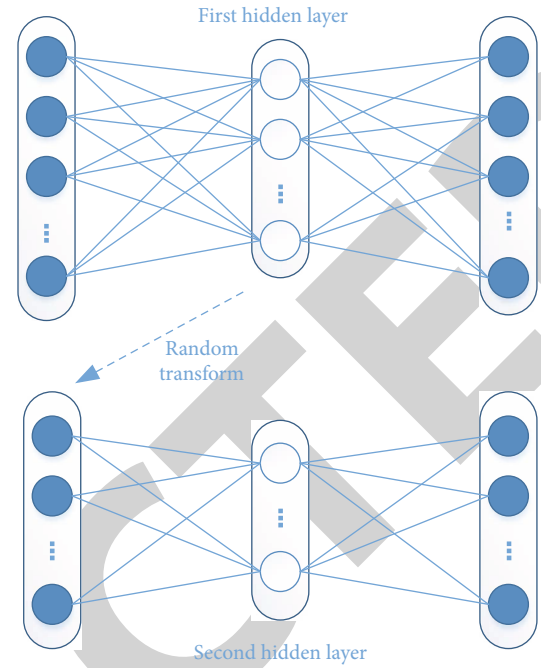

Figure 2: Stacked denoising autoencoder network.

(2) Model training: the input feature set is constructed based on big data, and an improved SDAE network is constructed

(i) Construct layer 1 network

We obtain the correlation matrix between features Σ_{II}.

The random disturbance transformation $v_f(i' \mid i)$ is carried out through decomposition to obtain the input term i' after corrosion. According to the denoising autoencoder calculation flow, the first hidden layer h_1 is obtained and changed into the first input layer.

(ii) Construct layer 2 to layer N networks

Obtain the correlation matrix between implicit features Σ_{hh}.

The hidden layer of the previous neural network is used as the input of the next neural network.

All hidden layers $h_i(i = 1, 2, \cdots, N)$ after the second layer are retained and constructed as a deep neural network structure.

(iii) Reverse tuning

SVM is used for final recognition and classification. BP is used to inversely optimize the network parameter weight w_i and bias b_i; that is, the gradient descent method is used to adjust $[w_i, b_i](1 \le i \le N)$.

3.2. Credit Decision Based on Multiobjective Particle Swarm Optimization. Text multiobjective particle swarm optimization algorithm is mainly improved around the external file update strategy and speed parameter update strategy. The external file update strategy improves the spatial search ability of the algorithm by optimizing the spatial distribution

information of the solution. The speed parameter updating strategy mainly uses the evolution direction information of particles to realize the adaptive adjustment of parameters and balance the global exploration ability and local development ability of the algorithm.

3.2.1. Spatial Distribution Information of Optimization Solution. Given a set of uniformly distributed direction vectors, $Q = \{q_1, q_2, \cdots, q_z\}$. The target domain O is uniformly decomposed into z subspaces $(\Omega_1, \Omega_2, \cdots, \Omega_z)$. The spatial distribution information of the optimal solution $s_x(n)$ is determined by the angle between its position vector and direction vector$<\boldsymbol{\lambda}(s_x(n)), q>$ decision, where $\boldsymbol{\lambda}(s_x(n)) = [\lambda_1(s_x(n)), \lambda_2(s_x(n)), \cdots, \lambda_W(s_x(n))]$ is the position vector of the optimal solution $s_x(n)$.

$$\lambda_w(s_x(n)) = \arccos\left(\frac{|h_w(s_x(n)) - r_w(n)|}{\sqrt{\sum_{y=1}^{W}\left(h_y(s_x(n) - r_y(n)\right)^2}}\right), \quad (11)$$

where $w = 1, 2, \cdots, W$. W is the number of objective functions. $R = [r_1, r_2, \cdots, r_w]$ is the reference point on the target space, $r_w(n) = \min(h_w(S(n)))$. The position vector satisfies the following conditions.

$$\sum_{w=1}^{W} \cos^2(\lambda_w(s_x(n))) = 1. \quad (12)$$

If the direction vector q_y satisfied $<\lambda(s_x(n)), q_z> \leqslant <\lambda(s_x(n)), q_y>$, then the xth optimization solution $s_x(n)$ belongs to the subspace Ω_Z determined by the direction vector q_z in the target space.

3.2.2. External File Update Strategy. In order to ensure the search ability of the algorithm in the optimization space, an external file update strategy based on the optimal solution spatial distribution information in the external file is designed. The update strategy includes two parts: subspace solution set allocation process and subspace solution set selection process.

The angle between the newly generated optimization solution $s_x(n)$ and all given direction vectors is calculated. The subspace of the direction vector with the smallest included angle is selected as the attribution space. The home space of all optimal solutions is allocated. For any subspace α, the optimal solution set $e_\alpha(n)$ is as follows:

$$\begin{aligned} e_\alpha(n) = \{s_x(n) \mid \langle \lambda(s_x(n)), q_\alpha \rangle \\ \leq \left\langle \lambda(s_x(n)), q_y \right\rangle, s_x(n) \in S(n), x = 1, 2, \cdots, |S(n)|\}, \end{aligned} \quad (13)$$

where q_y is any other direction vector, and $y = 1, 2, \cdots, Z$. In order to avoid the problem of poor search ability in algorithm space, this algorithm filters the optimal solution set in subspace. The upper limit of the number of optimization solutions for each subspace is $\eta(n)$, where $\eta(n)$ is defined as below:

$$\eta(n) = \left\lfloor \frac{R}{B(n)} \right\rfloor, \quad (14)$$

where R is the default value of the given external file. $B(n)$ is the number of subspaces with optimal solutions in the current iterative process. When the algorithm does not fully explore the target space, $B(n)$ is small. At this time, more optimization solutions need to be reserved in the subspace to ensure that the algorithm can be fully explored in the target space. With the optimization process, $B(n)$ gradually increases. At this time, the subspace needs to retain the optimal solution with good convergence to ensure the convergence of the algorithm.

3.2.3. Adaptive Flight Parameter Adjustment Mechanism. To enhance particle exploration, if particle $i_x(n)$ is dominated by $u_x(n)$, the value of $e_{x,1}$ needs to be lowered. At the same time, the values of ω_i and $e_{x,2}$ need to be increased. In order to enhance particle development capability, if particle $i_x(n)$ dominates $u_x(n)$, the value of $e_{x,1}$ needs to be increased. At the same time, lower the values of ω_i and $e_{x,2}$. Therefore, in order to adapt to the characteristics of particle search, a flight parameter adjustment mechanism based on the information of particle evolution direction is designed in this paper. The adaptive flight parameter $\delta_x = [\omega_x, e_{x,1}, e_{x,2}]$ adjustment mechanism of particle $i_x(n)$ is as follows:

$$\delta_x(n+1) = \begin{Bmatrix} \delta_x(n)\lambda_{x,1}(n), & u_x(n) > i_x(n) \\ \delta_x(n)\lambda_{x,2}(n), & u_x(n) < i_x(n) \\ \delta_x(n), & \text{otherwise} \end{Bmatrix}, \quad (15)$$

where $\lambda_{x,1}(n)$ and $\lambda_{x,2}(n)$ is the exploration parameter matrix and development parameter matrix of particle $i_x(n)$, respectively.

$$\lambda_{x,1}(n) = \begin{bmatrix} U_x(n)+1 & 0 & 0 \\ 0 & U_x(n) & 0 \\ 0 & 0 & U_x(n)+1 \end{bmatrix}, \quad (16)$$

$$\lambda_{x,2}(n) = \begin{bmatrix} U_x(n) & 0 & 0 \\ 0 & U_x(n)+1 & 0 \\ 0 & 0 & U_x(n) \end{bmatrix}, \quad (17)$$

where $U_x(n)$ is the fine tuning parameter.

$$U_x(n) = \left(1 + g^{\left(\bar{F}(n) - F_x(n)\right)}\right)^{-1}, \quad (18)$$

where $F_x(n)$ is the Euclidean distance between particle $i_x(n)$ and global guidance point $a_x(n)$. $\bar{F}(n)$ is the average value of the distance between all particles and the guide point $a_x(n)$. When the particle $i_x(n)$ is close to $a_x(n)$, the

$U_x(n)$ value is low. At this time, the particles can be deeply developed in the $a_x(n)$ neighborhood. When the particle $i_x(n)$ is far away from $a_x(n)$, the $U_x(n)$ value is higher. At this time, particles can fully explore the optimization space of $a_x(n)$ neighborhood. The exploration parameter matrix and development parameter matrix will be updated with the change of particle harmonic parameters. The particle velocity is effectively adjusted according to the flight characteristics of particles.

3.2.4. Algorithm Steps. The calculation flow of adaptive decomposition multiobjective particle swarm optimization algorithm is as follows.

Step1. Randomly initialize the velocity $q_x(0)$, position $i_x(0)$, and inertia weight of each particle in the particle swarm $\omega_x(0)$ and learning factors $e_{x,1}(0)$ and $e_{x,2}(0)$. Set the initial position of each particle as the current historical optimal position $U_x(n)$.

Step2. Calculate the fitness value of each particle. The direction vector of the optimization solution is calculated from equation (11). The angle value between the optimization solution and the given direction vector is calculated from equation (13), and the attribution region of the optimization solution is determined.

Step3. Update the policy according to the external file. Select the appropriate optimization solution for the subspace solution set to update the external file.

Step4. Arbitrarily select the optimization solution from the external file as the gbest of the population, and update the pbest point of each particle.

Step5. Influences the evolution direction of each particle guidance point. The evolutionary harmonic coefficients are calculated from equations (16)–(18). The flight parameters of particles are adaptively adjusted by equation (15).

Step6. Update the position and velocity of particles according to equations (3) and (4).

Step7. Determines whether the algorithm meets the termination conditions. If so, it exits the loop and outputs the final optimization solution set. Otherwise, return to step 2.

In the implementation process, the external file update strategy based on the spatial distribution information of the optimized solution is used to ensure the distribution of the solution set of the algorithm. At the same time, combined with the evolution direction information of particles to adaptively update the flight parameters, the algorithm can obtain the optimal solution set with good distribution and convergence.

4. Experiment and Analysis

4.1. Credit Risk Assessment. The data of this paper comes from the big data platform of a commercial bank in China. In order to get a more comprehensive user portrait, the data required for modeling is centered on personal credit card data. Then, splice the customer's business data in the bank, including deposit, loan, financial management, guarantee, tripartite deposit, fund, debit card, and e-banking transaction. A total of 540000 customers were collected as modeling data, including 521361 nondefaulting customers.

Table 1: Effectiveness verification of DAE layers.

Model	Recall (%)	Precision (%)	MCC
SDAE3	83.5	83.9	0.736
SDAE4	84.3	85.7	0.759
SDAE5	84.8	86.4	0.773
SDAE6	84.4	85.3	0.766
SDAE7	83	83.8	0.745

The evaluation indexes commonly used in machine learning classification tasks are used to measure and evaluate the methods in this paper, such as recall, precision, accuracy, Matthews correlation coefficient (MCC) [18], F-score, and AUC-ROC [19]. Since the number of DAE layers of stacked denoising autoencoder network has an impact on the learning results of the model, this paper evaluates and verifies the models with different DAE layers, and the results are shown in Table 1.

Table 1 lists the different comparative experimental results when the number of DAE layers increases from 3 to 7. It can be seen from Table 1 that with the increase of DAE layers, the recall rate, the precision, and the MCC gradually increase. When the number of DAE layers increases to 5, the index values have reached the highest. This shows that the deep neural network is not the deeper the better but needs to be dynamically adjusted and selected according to the application scenarios and data of specific business. Therefore, in the subsequent experiments, the model with 5 DAE layers is used for related experiments.

In order to illustrate the advantages of the improved algorithm in this case study, the comparison results between the improved algorithm and other common algorithms in personal credit risk assessment are described in detail below. This algorithm is compared with traditional feature selection algorithm and advanced deep learning algorithm, where the traditional feature selection algorithms include paper [20] and paper [21]. Advanced deep learning algorithms include paper [16] and paper [17]. The experimental results of comparison are shown in Figure 3.

It can be seen from the results in Figure 3 that the results of the credit evaluation algorithm proposed in this paper are better than other traditional methods. At the same time, it is better than the original stacked denoising autoencoder network, and the accuracy is improved by about 3%. In particular, compared with the original feature set (Raw Feat without any feature selection), AUC-ROC, ACC, and F-score increased by 15%, 18%, and 21%, respectively. The above results illustrate this. In the big data scenario, this algorithm based on the deep learning framework can fully extract the potential essential characteristics of personal credit risk. It effectively compresses and embeds high-dimensional sparse features, so that the relationship between credit features can be expressed in low-dimensional space, so as to improve the final credit evaluation ability. The autoencoder network based on denoising stack improves the antinoise ability of the model when the data quality in big data environment is not high, so as to obtain better credit evaluation results.

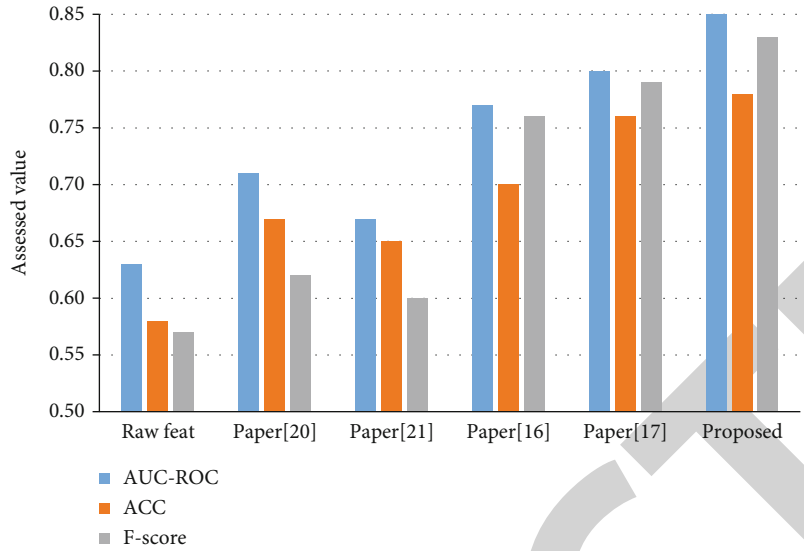

Figure 3: Comparison of evaluation results of different feature selection methods.

Table 2: Basic information table of loan portfolio options.

Project	Applied loan limit	NPV (good credit)	NPV (medium credit)	NPV (bad credit)	Average NPV
1	17.5	38.59	23.59	8.59	23.59
2	14	32.61	22.61	12.61	22.61
3	19.95	47.7	2.7	-12.3	12.7
4	15.75	48.095	38.095	23.095	36.43
5	28	51.225	6.225	-23.775	11.225
6	13.125	38.385	3.385	-10.615	10.385
7	31.5	73.38	63.38	8.38	48.38
8	10.5	39.835	19.835	4.835	21.505
9	12.25	41.045	15.045	9.045	21.71
10	5.6	19.88	13.88	-0.12	11.21

4.2. Loan Portfolio Decision. In order to better illustrate the operation effect of this algorithm in loan portfolio decision-making, the following two simulation examples are tested.

4.2.1. Simulation Example 1. The total loan amount of a bank's rural project is 1.5 million yuan. The minimum loan task required by the superior bank is 1.35 million yuan. At present, 10 farmer enterprises apply for loans, and the net present value (NPV) of the enterprises applying for loans under good, medium, and bad credit is shown in Table 2.

The multiobjective particle swarm optimization algorithm proposed in this paper is used to solve the simulation example 1. The population size of the algorithm and the maximum capacity of external files are set to 100. The initial inertia weight is 0.5, and the learning factor is set to 1. The maximum number of iterations for all test functions is set to 200. The algorithm runs independently for 30 times, and the results are taken as the average value. The operation result of one time and the convergence curve of objective function are shown in Figure 4. The results of 30 runs have reached the optimal value, and the average time is less than 1 s.

4.2.2. Simulation Example 2. In order to better illustrate that the algorithm proposed in this paper can be used to solve the optimization decision-making problem of large-scale loan portfolio, a simulation example 2 is designed in this paper. Simulation example 2 repeats the data of simulation example 1 10 times, so as to construct an example in which 100 farmer enterprises apply for loans. This not only does not affect the test of the algorithm in this paper but is more conducive to the test of the algorithm. Because the solution of the above problem requires exponential order time of the problem scale, for the simulation example 2 constructed according to this method, this can really test the effect of this algorithm in large-scale loan portfolio optimization decision-making problem. To sum up, this paper uses the above method to construct simulation example 2, and the specific data are as follows.

The total loan amount of a bank's rural project is 15 million yuan. The minimum loan task required by the superior bank is 13.5 million yuan. At present, 100 farmer enterprises apply for loans, and the net present value of the enterprises applying for loans under good, medium and poor operation

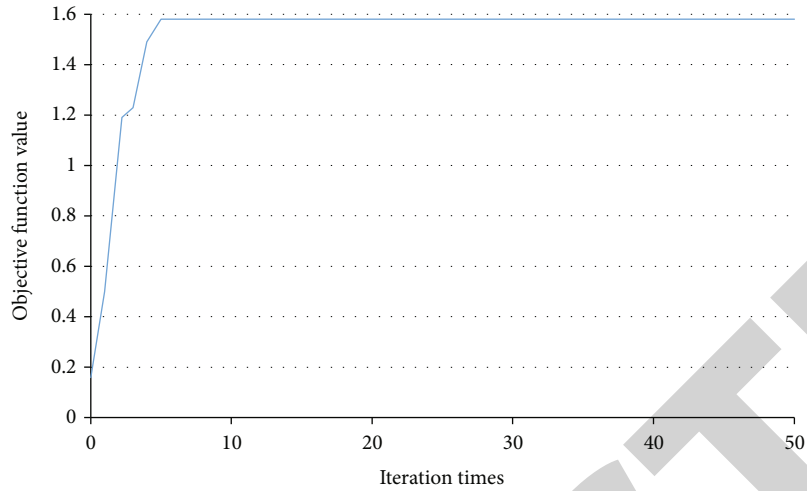

Figure 4: Convergence curve of simulation example 1.

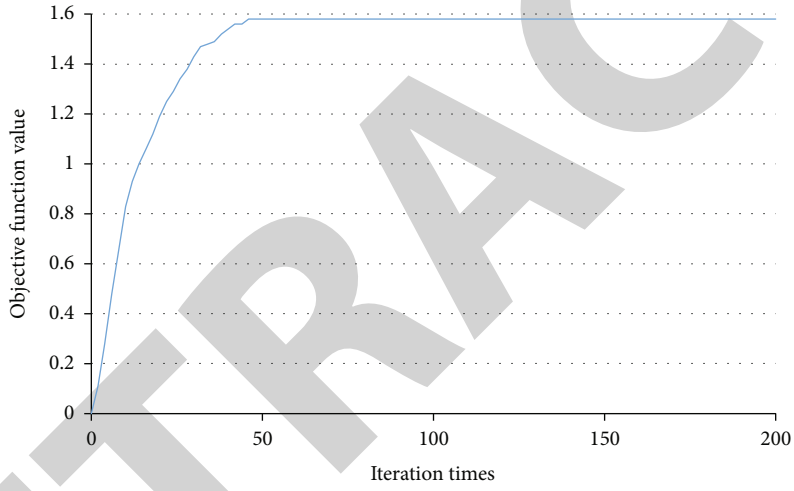

Figure 5: Convergence curve of simulation example 2.

is known. Here, the net present value, that is, repeat the data in Table 1 10 times. The population size of the algorithm and the maximum capacity of external files are set to 1000. The initial inertia weight is 0.5 and the learning factor is set to 1. The maximum number of iterations for all test functions is set to 200. The algorithm runs independently for 30 times, and the results are taken as the average value. The operation result of one time and the convergence curve of objective function are shown in Figure 5. The results of 30 runs have reached the optimal value, and the average time is less than 10 s. This algorithm finds the optimal solution in an average time of less than 10 s, which shows that this algorithm has achieved good results in solving speed and optimization ability. In 30 independent random experiments, the proposed algorithm has reached the optimal solution, which shows that the proposed algorithm has strong stability.

To sum up, the multiobjective particle swarm optimization algorithm proposed in this paper has achieved good results in optimization ability, solution speed, and stability in solving large-scale loan portfolio optimization decision-making problems.

5. Conclusion

Rural credit constraint is a serious problem facing China's rural economic development. China's rural credit market is imperfect, and the probability of a large number of farmers getting loans is very low. For solving these problems, this paper optimizes the rural credit system and loan decision-making. To solve the problem of data quality in big data applications, this paper improves the stacked denoising autoencoder depth network and improves the accuracy of credit evaluation. In order to improve the loan portfolio strategy, an adaptive decomposition multiobjective particle swarm optimization algorithm is proposed. Its main advantages include the following two aspects. (1) The external file update strategy based on spatial optimization can effectively balance the convergence and diversity of external files, so as to improve the spatial search ability of the algorithm. (2) The adaptive flight parameter adjustment mechanism can balance the exploration and development ability of the algorithm, so as to improve the convergence of the algorithm. Experimental results show that the proposed algorithm is

Hindawi
Journal of Sensors
Volume 2023, Article ID 9820609, 1 page
https://doi.org/10.1155/2023/9820609

Retraction

Retracted: Mining and Evaluation of Teaching Civics Courses Based on Apriori-TIDS Algorithm

Journal of Sensors

Received 19 September 2023; Accepted 19 September 2023; Published 20 September 2023

This article has been retracted by Hindawi following an investigation undertaken by the publisher [1]. This investigation has uncovered evidence of one or more of the following indicators of systematic manipulation of the publication process:

(1) Discrepancies in scope
(2) Discrepancies in the description of the research reported
(3) Discrepancies between the availability of data and the research described
(4) Inappropriate citations
(5) Incoherent, meaningless and/or irrelevant content included in the article
(6) Peer-review manipulation

The presence of these indicators undermines our confidence in the integrity of the article's content and we cannot, therefore, vouch for its reliability. Please note that this notice is intended solely to alert readers that the content of this article is unreliable. We have not investigated whether authors were aware of or involved in the systematic manipulation of the publication process.

Wiley and Hindawi regrets that the usual quality checks did not identify these issues before publication and have since put additional measures in place to safeguard research integrity.

We wish to credit our own Research Integrity and Research Publishing teams and anonymous and named external researchers and research integrity experts for contributing to this investigation.

The corresponding author, as the representative of all authors, has been given the opportunity to register their agreement or disagreement to this retraction. We have kept a record of any response received.

References

[1] H. Yang, "Mining and Evaluation of Teaching Civics Courses Based on Apriori-TIDS Algorithm," *Journal of Sensors*, vol. 2021, Article ID 5956429, 10 pages, 2021.

Hindawi
Journal of Sensors
Volume 2021, Article ID 5956429, 10 pages
https://doi.org/10.1155/2021/5956429

Research Article

Mining and Evaluation of Teaching Civics Courses Based on Apriori-TIDS Algorithm

Haiying Yang

Anyang Normal University, Anyang, 455000 Henan, China

Correspondence should be addressed to Haiying Yang; yanghy@aynu.edu.cn

Received 21 October 2021; Revised 9 November 2021; Accepted 20 November 2021; Published 16 December 2021

Academic Editor: Wei Zhang

The thinking course is an innovative move to implement the fundamental task of moral education and realize the whole process of education and all-round education in universities. The Apriori-TIDS algorithm proposed in this paper adopts the TID list of transaction identifiers to calculate the support count and generate the frequent item set of the Hou option set, and the whole frequency set generation process only needs to scan the transaction database once, which greatly improves the operation efficiency of the mining algorithm. The course is based on the three focus points of ideological and political education, such as "matters, times, and situations", to explore the elements of ideological and political education hidden in the course, and to give the principles and criteria for evaluating the effectiveness of ideological and political teaching in the course, in order to make the professional degree course become the main channel to lead the ideological and political education of postgraduate courses and improve the effectiveness of the course in educating people.

1. Introduction

In July 2020, the first conference on postgraduate education in China was held, which made important arrangements for the reform and innovation of postgraduate education in our country in the new era [1]. In September 2020, proposing to further improve the ideological and political education system, Xi Jinping's socialism with Chinese characteristics in the new era thought into the teaching materials was promoted, into the classroom and into the mind, and to comprehensively improve the level of ideological and political education of postgraduates [2].

At present, degree course of information master students includes public degree courses and professional degree courses, and the credits of professional degree course are generally about 2/3 of the total credits of degree course, which has a large proportion [3]. Moreover, professional degree courses are the core and basic contents of the professional work that graduate students can engage in after graduation. Therefore, professional degree courses are a very important part of the curriculum of master's degree students, and only by integrating as many elements of political education as possible in professional degree course can we realize the situation of comprehensive political education for people [4]. In addition, professional degree course of information graduate students contains rich elements and resources for thinking and political education, which has high feasibility in the actual education and teaching process. In this paper, based on the characteristics of the professional degree courses of information master students, we will focus on the three points of "events, times, and situations" [5], dig deeper into the elements of Civics Education hidden in them, make the professional degree courses become the main channel to lead the Civics Education of graduate students, and gradually cultivate the patriotism and social responsibility of graduate students.

The focus of teaching civics course is to explore the explicit and implicit civics education elements embedded in the course content and to combine them with subject knowledge. It should be said that any course contains rich elements of thinking and political education, and how to reasonably and effectively explore these elements is an important issue in the implementation of thinking and political teaching [6]. This requires the teachers of professional

degree courses to be good at discovering and identifying the resources of the political thinking hidden in them on the basis of fully mastering the content and system of subject knowledge and integrating and linking them with classroom teaching, experimental practice, and other teaching links, so as to realize the effective unification of knowledge transfer and all-round education goals. Information graduate degree course has their own characteristics, and the characteristics of the time are more prominent, so they can focus on the three points of "events, time, and situations" when the elements of the course's political thinking education [7].

The so-called "things" mainly emphasize the objective existence of things, that is, the objective existence of Civics Education elements in the postgraduate professional degree courses, and the postgraduate professional Civics Education courses must explore the philosophical ideas and Civics Education elements embedded in the course contents [8]. For example, the philosophical relationship between the most basic binary in digital communication and the ancient Chinese Yin-Yang Bagua and I Ching, the moving stories of Academician Deng Zhong-Han, the chief director of the "Starlight China Core Project", and Academician Wu De-Xin, an expert in integrated circuits [9], one of the greatest scientists in the 20th century, Shannon, who "one man built the world," Shannon's story of "a man who built a discipline." The "transformation" of the teaching of the civics course is to implant the philosophical ideas and civics elements implied in the stories into the minds of students in a silent way, and to infect and shape them through objective and concrete examples [10]. The points of "things" should carry the facets of teaching purpose and should be interlinked with the contents and knowledge points of professional course, so as to achieve the watery blend between reasoning and statement.

The so-called "time" refers to the advancement of time and the development of the era. The postgraduate professional degree course of Civics Science focuses on the changes of the era, so it must follow the development of social progress and grasp the reality of life, summarize the frontier and hot issues in the curriculum that students are most interested in, and talk through the progress of information technology and the development of disciplines and specialties for the country and society [11, 12]. The history of the development of communication technology, for example, is a history of the development of the country and society. For example, the history of the development of communication technology is a history of the development and progress of China's information industry, highlighting the great achievements made by China since the founding of New China, especially since the reform and opening up. By telling the story of the development of the information industry of the motherland to the postgraduates with the content of the course, they can experience the historical achievements of reform and opening up, strengthen the four self-confidence, and enhance the national pride of young students, so as to further stimulate the patriotism enthusiasm and enterprising spirit of study of the postgraduates [13, 14].

In the past decades, the rapid development of computer hardware has led to the upgrading of powerful computer mainframes, data collection devices, and storage media, while greatly promoting the development of databases and the information industry, making a large amount of data and information stored in the transaction management, information retrieval, and data analysis. However, most database systems are still limited to transactional database operations, i.e., simple entry, query, modification, and statistics [15]. The amount of information people obtains through these operations is only a part of the information contained in the whole database, but more importantly, the potential information hidden behind the data, which has important reference value in the decision-making process, cannot be discovered. Decision makers make decisions not on the basis of information-rich data in databases, but often on the basis of decision makers' intuition, because decision makers lack the tools to extract valuable knowledge from massive data. Therefore, there is an urgent need for effective information analysis tools to help mine the "mineral deposits" contained in the "data mountain" and refine them into useful knowledge [16].

2. Improvement of Apriori Algorithm

2.1. Introduction of Apriori-TIDS Algorithm. In this paper, we propose a new algorithm—Apriori-TIDs (transaction identifier set) algorithm—to improve the Apriori algorithm [17], which requires repeated scanning of the original database. First, the transaction database is scanned, and the transaction identifier TID containing each item set is recorded at the same time to generate a marquis set C_1. C_1 is structured as (Item_set, Support_count Support, Transaction_Identifier_list Tid_silt). Then, the set of items whose support count is lower than the minimum support appendix is removed from C. Then, the set of item sets in C_1 is the frequent 1 item set L_1.

L_{k-1} is concatenated with L_{k-1} to generate C_k. The transaction identifier list of C_k is equal to the intersection of two L_{k-1} transaction identifier lists that generated it. Counting the number of TIDs in the list of transaction identifiers corresponding to the set of items in C_k gives the count of each set of items in C_k.

2.2. Example of Apriori-Tlns Algorithm. Let a transaction database be as shown in Table 1. Let the minimum support count be 2, i.e., min_sup = 29/ = 22%.

(1) Scan the database to generate, as shown in Table 2

(2) According to C_1 determining L_1, as shown in Table 3

(3) Concatenate L_1 to generate C_2. After each new item set is generated, the Tid _list of the set is generated and counted. If the count is less than min_ sup, the set is removed from C_2; otherwise, the set is kept

Generate C_2, as shown in Table 4.

Table 1: Transaction Database.

TID	List of IDS
T100	I1, I5
T200	I4
T30	I2, I3
T400	I1, I2, I4
T500	I1, I3
T60	I2
T700	I1, I3
800	I1, I2, I3
T900	I1, I2, I3

Table 2: Marquee l a set collection C_1.

Item set	Support count	Transaction list
I1	6	T100, T400, T500
I2	7	T100, T200, T300, T800, T900
I3	5	T300, T500, T600, T700, T800, T900
I4	3	T20
I5	2	T100, T800

Table 3: Frequent 1 item set L_1.

Item set	Support count
I1	6
I2	7
I3	6
I4	2
I5	2

Table 4: Margin 2 a collection C_2.

Item set	Support count	Transaction list
I1, I2	4	T100, T0, T900
I1, I3	3	T500, T700, T800, T900
I1, I5	2	T100
I2, I3	3	T300, T600, T900
I2, I4	2	T2400
I2, I5	1	T100800

(4) Generated L_2, as shown in Table 5

(5) Generate C_3

According to the Apriori property, {I,J3,15},{I2,I3,I4}, {12,3,J5}, and {12,4,5} are pruned.

The generated C_3, as shown in Table 6.

(6) Generate L_3, as shown in Table 7

Table 5: Frequent 2 item set L_2.

Item set	Support count
I1, I2	4
I1, I3	4
I1, I5	2
II, I5	4
I2, I3	4
I2, I4	2
I2, I5	2

Table 6: Margin 3 a collection C_3.

Item set	Support count	Transaction list
I1, I2, I3	2	T800, T900
I1, I2, I5	2	T100, T800

Table 7: Frequent 3 item set L_3.

Item set	Support count
I1, I2, I3	2
I1, I2, I5	2

(7) Generate C_4

$$\{112.\text{I3, S}\}\ \text{Tid\_list} = \{\text{T800}\}, \text{Delete} L_4 = \phi. \quad (1)$$

The algorithm terminates, and all frequent item sets are found.

3. Algorithm Performance Comparison Analysis

The advantage of the Apriori-TIDS algorithm over the Apriori algorithm is that the original database only needs to be scanned once. In other words, only in the first step of generating the Hounset 1-item set C_1, it is necessary to scan through the database to obtain the TID list of each item set, while in calculating the count of any other Hounset C_K, it is only necessary to count the number of TIDs in the corresponding transaction identifier list in C_K [18, 19]. Let the number of item sets C_1 in Apriori set be $|C_I|$, the number of records in the database be n, and the average capacity of each record be p. The time required to compute apriori set C_1 is $O(|C_1|np)$, and the total time required is $O(|C_1|np)$ since the database is scanned only once (the time required to run in memory is negligible compared to the time required to access external memory). Compared to the total time overhead of $O(\sum_{k\}} C_k|np)$for the Apriori algorithm, the Apriori I TIDS algorithm saves a significant amount of time overhead.

Table 8: Experimental data records.

Min – sup = 0.03	Algorithm	Test time sampling (unit: ms)	Average value (unit: ms)
	Apriori	51328, 50703, 50203, 51422, 51812, 50765, 51532, 51125, 50859, 51297	51105
	Apriori–TIDS	1563, 1984, 1812, 1766, 1766, 1844, 1797, 1781, 1625, 1938	1788

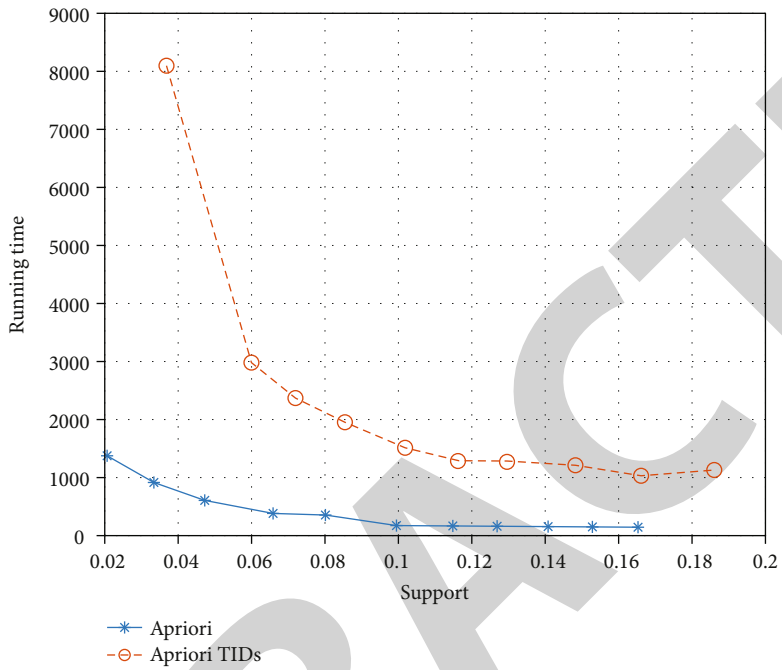

Figure 1: Comparison of the time overhead of the two algorithms.

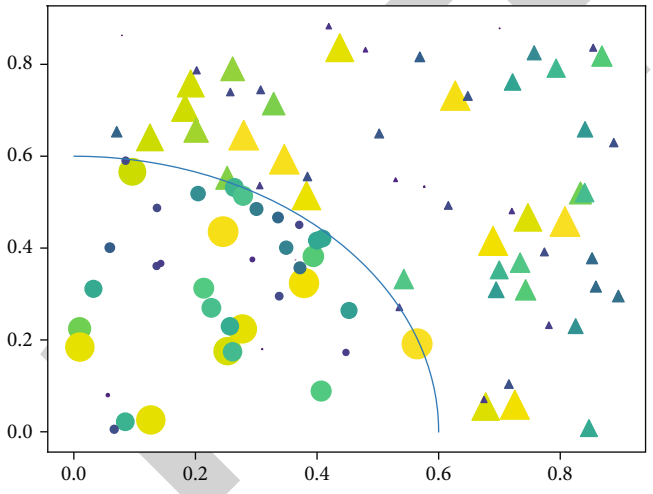

Figure 2: Classification of different mining information.

For comparison, we wrote a program to run the Apriori algorithm on the same ORAcLE database with the same table structure and the same data to test its running time. If we set "SETTIMNIGON" in SQL/pLUs of ORAcLE [20], the running time is automatically displayed after the algorithm finishes running, and the time is simply the algorithm running time, excluding the network communication overhead. We use "Course Related Topics" as the experimental data, and there are 102 records in Table 8. Each record has 36 fields. We set different support Min values, and the results are shown in Table 8:

The time pairs of the two algorithms at each support degree are shown in Figure 1.

From Figure 1, it can be seen that the improved algorithm runs significantly more efficiently than the original Apriori algorithm, especially when the support elucidation value is low.

4. Analysis and Evaluation of the Results of the Civics Excavation

4.1. Factors Affecting Mining Results. There are three main factors that affect the mining results:

(1) Classification of achievement bands: different criteria for the classification of achievement intervals will result in a different distribution of student achievement levels, which will affect the results of mining all topics related to achievement [21, 22]

(2) The choice of the gap value: the settings of support and credibility are directly related to the number of rules mined and the degree of interest of users in the rules. If the Min value is set lower, the number of rules mined is higher, and vice versa is lower

(3) Selection of data source: this system selects the data of students in the Department of Computer Science of Grade 01, and all the theme mining is based on the data of this one department. If you select data from more than one department or grade, the result will be changed to some extent. For example, there is a reserved function in this system to select data from multiple departments for mining. If more than one department is selected, the topic "Student Basic Information Linkage" will be mined based on the data of all the departments selected, and the results will be more generalized [23, 24]

4.2. Classification of Mining Results. In addition, to explore the elements of Civics Education in the three aspects of "events, times, and situations" in the information graduate degree course, it is necessary to adhere to the student-centered approach, combine the elements of Civics Education course with the vivid cases around them, ground them, keep them close to the social reality, so that students like to listen, are willing to do and actively do, and then guide them in a subtle way. Graduate students should be guided to think and discern in a subtle way [25]. At the same time, the civics science course cannot be separated from the professional content, but must be combined with the actual, scientific, and reasonable, objective civics science elements. One is to borrow the thinking political elements from different course, enhance the connection and integration between courses, and strengthen the diversity and richness of thinking political education elements. Secondly, combining with the characteristics of colleges and universities and regional features, we integrate university history, school training, regional culture, and red gene into the civics science course, so as to enhance the infectious and attractive power of teaching contents.

The application of ARMEMD system has mined a large number of rules, which can be classified into different categories according to different methods [26]. For the characteristics of this system, we can classify the mined rules according to three different criteria:

(1) According to the relationship between rules and common sense, the rules of mining can be divided into three categories: rules that are consistent with common sense, rules that are consistent with the phenomena that people take "for granted" [27, 28]. We believe that these rules are not necessarily redundant but provide a factual basis for these "taken-for-granted" common knowledge from a data mining perspective

(i) Rules that contradict common sense

This part of the rule is the opposite of what people take for granted and is therefore often of great interest to users.

(ii) Rules that cannot be explained based on existing common sense

This part of the rule cannot be adequately explained according to common sense, possibly because of the low confidence of support, or because the amount of data is relatively small and there is a certain degree of chance.

(2) According to the degree of interest, they can be divided into two categories:

(i) Interesting rules

Such rules reflect facts or laws that are unique, universal, and previously undiscovered, and therefore of high interest.

(ii) Uninteresting rules

These rules reflect the facts that are consistent with common sense, are universal, and have been known for a long time, so they are not of interest to users。

(3) According to the guiding role of rules on reality, they can be divided into three categories, as shown in Figure 2, among which the triangle reflects the rules of negative problems in teaching management, such rules reflect some problems in teaching management, and can reflect the causes of the problems to a certain extent, which can assist the decision-making level to take corresponding measures to solve such problems. The circle reflects the rules of some positive phenomena, and such rules reflect some experience in teaching management that is worth promoting [29, 30]. The size of the graph is a rule that has no guiding value, which only confirms known common knowledge or has low support and credibility, and is not representative and not much guidance for teaching management decisions

4.3. Rule Interpretation and Evaluation. In order not to miss the valuable rules, we set the elucidation value low, and thus, the number of association rules mined is large. Here, only a few representative rules are extracted for explanation and analysis [31].

Rule group a:

$$\begin{aligned}&\text{Professional foundation course grade} = \text{A} = > \text{Professional course grade IIA}(0.083, 0.727).\cdots\cdots\cdots(\text{al}),\\ &\text{Professional Course Grade} = \text{A} = > \text{Professional Foundation Course Grade} = \text{A}(0.083, 0.889)\cdots\cdots\cdots(2\text{a}),\\ &\text{Professional Course Grade II C} = > \text{Professional Foundation Course Grade II C}(0.146, 0.737)..\cdots(3\text{a}).\end{aligned} \quad (2)$$

The meaning of this set of rules is 72.7% of students with good grades in major foundation courses also have good grades in major courses (rule al), 73.7% of students with poor grades in major courses have bad grades in major foundation courses (rule 3a), and 88.9% of students with good grades in major courses also have good grades in major foundation courses (rule 2a).

This set of rules shows that there is a strong relationship between professional foundation courses and professional courses, which are consistent with known common knowledge and confirms this objective law from the fact. Therefore, we should pay attention to the teaching quality of professional foundation courses.

Rule group b:

$$\begin{aligned}
&\text{Public course grade IIA into professional foundation course grade IIA} = > \text{professional course grade recognition}(0.073, 0.875) \cdots (3b),\\
&\text{Public course grade recognized eight professional course grades} = A > \text{professional basic course grade} = A(0.073,)bl, \cdots \cdots (4b),\\
&\text{Professional course grades} = A = > \text{public course grades II } A(0.073, 0.778) .. \cdots \cdots \cdots \cdots \cdots \cdots \cdots \cdots \cdots (bl),\\
&\text{Professional Foundation} = AA \text{ Professional} = A = > \text{Public} = A(0.073, 0.875) \cdots (bz). \qquad (3)
\end{aligned}$$

The meaning of this set of rules is 87.5% of students with good grades in public courses and professional foundation courses also have good grades in professional courses (rule bl), 100% of students with good grades in public courses and professional courses also have good grades in professional foundation courses (rule bZ), 77.8% of students with good grades in professional courses also have good grades in public courses (rule b3), sand tudents with good grades in professional courses and professional foundation courses 87.5% of students with good grades in major and basic courses also had good grades in public courses (rule b4).

This set of rules suggests that public course has a strong influence on the basic and specialized courses, which are consistent with new common knowledge. For science and technology students [32], public courses such as advanced mathematics and linear algebra can cultivate students' ability to reason logically, and public courses such as English and listening are basic language tools, which are necessary for learning professional course well.

Rule group c:

$$\begin{aligned}
&\text{Mao Zedong Thought II } A = > \text{English } (I) = A(0.11, 5.0647) .. \cdots \cdots \cdots \cdots \cdots \cdots \cdots \cdots \cdots \cdots (d),\\
&\text{Mao Zedong Thought IIA} = > \text{Probability Theory} = A(0.125, 0, 706) . \cdots \cdots \cdots \cdots \cdots \cdots \cdots (2c),\\
&\text{Mao Zedong Thought} = A = > \text{Discrete Mathematics} = A(0.1 \text{ coincidence}, 0.647) . \cdots \cdots \cdots \cdots \cdots \cdots \cdots \cdots \cdots (3c),\\
&\text{Advanced Mathematics } A(I) = CA \text{ Introduction to Computers II } C = > \text{Mao Zedong Thought II } C(.0o73, 1) .. \cdots (4c),\\
&\text{University Physics } (I =) AA \text{ Probability Theory} = AA \text{ Advanced Mathematics } A(II)\\
&\quad = A \text{ II} > \text{Mao Zedong Thought} = A(.073, 1) ., \cdots \cdots \cdots \cdots \cdots \cdots \cdots \cdots \cdots \cdots \cdots \cdots \cdots \cdots \cdots (5c),\\
&\text{Advanced Mathematics } A(II) = C \text{Advanced Language Programming} = C\\
&\quad = > \text{Mao Zedong Thought} = C.(073, .778) . \cdots \cdots \cdots \cdots \cdots \cdots \cdots \cdots \cdots , .. \cdots \cdots \cdots \cdots (6c),\\
&\text{Advanced Mathematics } A(II) = AA \text{ Physics Experiment} = A = > \text{Mao Zedong Thought } C.(.063, .857) . \cdots \cdots (7c). \qquad (4)
\end{aligned}$$

This set of rules reflects a high degree of correlation between Mao Zedong thought and various other public, professional basis, and specialized courses. Considering this set of rules by itself, it seems to be unexplainable by common sense. However, we observed a large number of such similar rules and found that all the rules mined were of this form:

$$\text{Course X} = A \text{ II} > \text{Course Y IIA, Course X II } C = > \text{Course Y} = C. \qquad (5)$$

That is, a course grade is excellent, then another course grade is excellent; a course grade is poor, then another

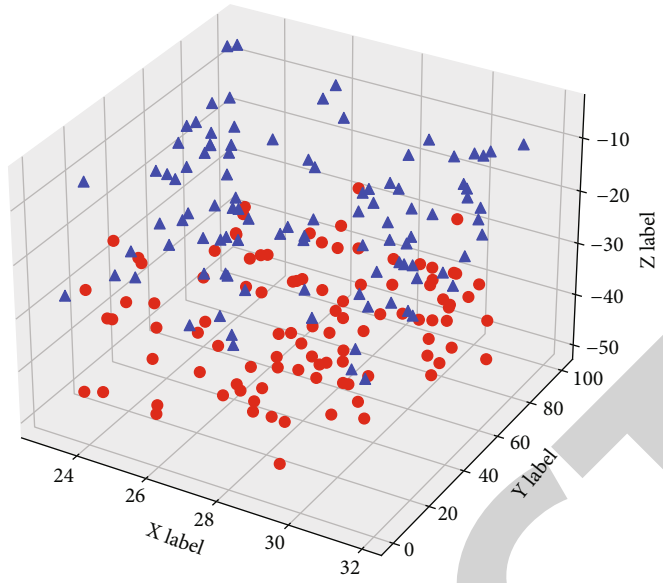

Figure 3: Visualization of rule interpretation and evaluation in different dimensions.

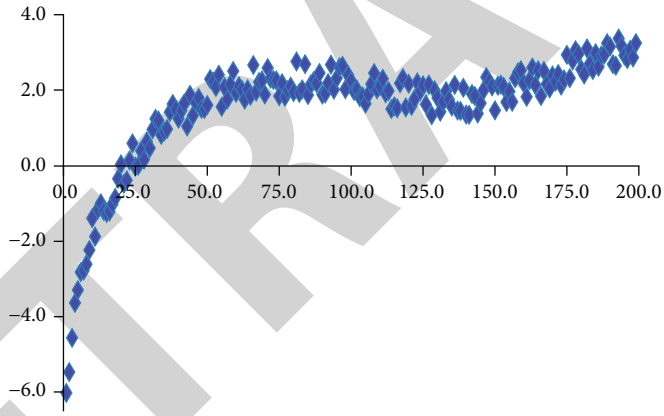

Figure 4: Students' evaluation of the Civics course by different study hours.

course grade is poor, and there is not found a type such as "course X = A two > course Y two C" or "course X two C => course Y = A". The rule of "Course X = A II > Course Y II C" or "Course X II C = > Course Y = A" was not found. This indicates that students with good academic performance tend to have better grades in all subjects, and even if there are cases of bias, the number is very small, so no such rule is found. In this way, it is easy to understand the phenomenon reflected in the rules of rule group 3.

Rule group d:

$$\begin{aligned}&\text{Level 6 = failed II > gender = male}(0.604, 0.866)\cdots\cdots\cdots\cdots\cdots\cdots\cdots\cdots\cdots\cdots(\text{dl}),\\&\text{Gender II Male = >Grade VI II Failed}(0.604, 0.784)\cdots\cdots\cdots\cdots\cdots\cdots\cdots\cdots(\text{d2}).\end{aligned}\tag{6}$$

That is, 86.6% of the students who did not pass English 6 were male, and 78.4% of all male students did not pass 6. This is in line with the commonly held view that boys are slightly less gifted than girls in learning languages. It is recommended that emphasis be placed on strengthening the tutoring of male students when teaching English.

Rule group e:

$$\begin{aligned}
&\text{Gender} = \text{Female ii} > \text{Health status} = \text{A}(0.208, .0909).\cdots\cdots\cdots\cdots\cdots\cdots\cdots\cdots\cdots\cdots\cdots(\text{el}),\\
&\text{Interests II Sports} = >\text{Gender} = \text{Male}(0.729, 1)\cdots, \cdots\cdots\cdots\cdots\cdots\cdots\cdots\cdots\cdots\cdots(\text{e2}),\\
&\text{Gender} = \text{Male II} > \text{Interests} = \text{Sports}\,(0.729, 946).\cdots\cdots\cdots\cdots\cdots\cdots\cdots\cdots\cdots(\text{e3}).
\end{aligned} \tag{7}$$

Rule el means 90.9% of female students are in good health. Health status here is mainly calculated based on the students' physical education results in four semesters, and this rule indicates that the overall level of physical fitness of female students in the computer science department is relatively good. There is no corresponding rule found for male students, which indicate that the level of physical fitness of male students in this department is slightly lower compared to female students. Interestingly, rules ez and e3 indicate that male students are basically into sport but do not perform well in physical education classes.

Rule group f:

$$\begin{aligned}
&\text{Mean score II A} = >\text{teaching mode} = \text{teacher lecture}\,(0.188, 1)..\cdots\cdots\cdots\cdots(\text{n}),\\
&\text{Mean score} = \text{C} = >\text{Instructional mode} = \text{Teacher lecture}(0.167, 1)\cdots\cdots\cdots\cdots(2\text{f}),\\
&\text{Mean score II A} = >\text{Education} = \text{Master}'\text{s degree}\,(0.125, .0667)\cdots\cdots\cdots\cdots\cdots\cdots\cdots\cdots\cdots(\text{ez})\\
&\text{Mean score II C} = >\text{Education} = \text{Master}'\text{s}(0.125, .075)\cdots\cdots,.\cdots\cdots\cdots\cdots\cdots\cdots\cdots\cdots(4\text{f}),
\end{aligned} \tag{8}$$

Grade point average II C II > assessment method = closed book exam (0.146, .0875).⋯ ⋯ ⋯ ⋯ ⋯ ⋯ ⋯ (5f), Grade point average II C II > Practice hours = less than 5% (.146, .0875).⋯ ⋯ ⋯ ⋯ ⋯ ⋯ ⋯ (6f).

The visualization of rule interpretation and evaluation in different dimensions is shown in Figure 3, where rule n means that 100% of classes with good average performance are taught by teachers, while rule several means that 100% of classes with poor average performance are also taught by teachers, and these two rules indicate that there is no necessary connection between the use of teacher teaching and teaching performance. Similarly, rules 4 and 4f show that there is no necessary relationship between teachers' education and teaching performance.

Rule 5f means that 87.5% of the classes with a poor grade point average used a closed-book test. No corresponding rule was found for classes with good average score. This indicates that the results of using closed book exams tend to be less desirable than those of open-book exams. It indicates that the department's closed book exams are more difficult than open-book exams, or that the evaluation criteria for closed book exam papers are less rigorous than those for open-book exams.

Rule 6f means that 87.5% of the classes with a bad grade average had a very low percentage of practical hours (less than 5%). No corresponding rule was found for classes with good grade point averages. This indicates that the percentage of practical class time is too low for students' knowledge acquisition. It is recommended to increase the percentage of practical lessons in the teaching arrangement as much as possible.

In addition, no correlation was found between "gender" and "academic performance," indicating that the academic performance of computer science majors is not significantly related to gender. We did not find any connection between humanities and other course. It is suggested that the humanities course in our school has no significant influence on the overall quality of students, and it is suggested that the current humanities course in our school should be adjusted.

4.4. Civics Teaching Evaluation. The final teaching effect is often not determined by a single party but may depend on the cooperation and synergy of teachers, counselors, and postgraduate supervisors, and it is difficult to judge the root cause of the changes produced by postgraduates. Moreover, there is no more systematic and unified index on how to reasonably and effectively evaluate the effectiveness of the civics course. Professional Civics course is generally considered to be the most critical and difficult part of the Civics course, and the reasonable and effective evaluation of professional Civics course is one of its most core problems.

As shown in Figure 4, the evaluation of students' Civics courses with different learning duration, x-axis is time (minutes), and the axis is an evaluation score, we can know the evaluation principle, standard, and application of teaching effect of Civics courses for research information graduate degree, which can positively stimulate the enthusiasm of teaching reform of Civics courses for teachers in charge, help teachers reflect on the teaching effect of Civics, further optimize the teaching content and way of Civics courses, and effectively promote the sustainable development of the teaching of Civics and Political Science.

5. Conclusions

The professional degree courses are an important part of the master's degree course, and only by incorporating as many elements of education in the professional degree course as possible can we realize the situation of educating people in a more comprehensive way. Taking the professional degree courses of information master students as an example, this paper discusses the ways to explore the educational elements of the Civics and Political Science courses based on the three factors of "matter, time, and situation" and gives the corresponding teaching evaluation principles and standards considering the characteristics of Civics and Political Science courses.

Data Availability

The datasets used in this paper are available from the corresponding author upon request.

Conflicts of Interest

The author declared that he/she has no conflicts of interest regarding this work.

References

[1] T. Zhang, X. Chen, and K. Cai, "Evaluation of teaching quality in colleges and universities based on association rule algorithm," *Agro Food Industry Hi Tech*, vol. 28, no. 1, pp. 2611–2614, 2017.

[2] C. L. Mao, S. L. Zou, and J. H. Yin, "Educational evaluation based on Apriori-Gen algorithm," *Eurasia Journal of Mathematics Science and Technology Education*, vol. 13, no. 10, pp. 6555–6564, 2017.

[3] Yangzhao, "Research on the application of university teaching management evaluation system based on Apriori algorithm," *Journal of Physics: Conference Series*, vol. 1883, no. 1, p. 012033, 2021.

[4] R. Jin, Q. Lin, B. Zhang et al., "A study of association rules in three-dimensional property-taste-effect data of Chinese herbal medicines based on Apriori algorithm," *Zhong Xi Yi Jie He Xue Bao*, vol. 9, no. 7, pp. 794–803, 2011.

[5] H. Yu, "Online teaching quality evaluation based on emotion recognition and improved Apriori Tid algorithm," *Journal of Intelligent and Fuzzy Systems*, vol. 40, no. 5, pp. 1–11, 2020.

[6] C. Wang and X. Zheng, "Application of improved time series Apriori algorithm by frequent itemsets in association rule data mining based on temporal constraint," *Evolutionary Intelligence*, vol. 13, no. 1, pp. 39–49, 2020.

[7] Y. Y. Ye, "Research and application of Apriori algorithm for mining association rules," *Advanced Materials Research*, vol. 1079-1080, pp. 737–742, 2014.

[8] C. Blackmore, "How to queer the past without sex: queer theory, feminisms and the archaeology of identity," *Archaeologies*, vol. 7, no. 1, pp. 75–96, 2011.

[9] C. Ozan, "Authentic assessment increased academic achievement and attitude towards the educational measurement of prospective teachers," *International Journal of Evaluation and Research in Education*, vol. 8, no. 2, pp. 299–312, 2019.

[10] W. J. Zhang, M. A. Dong-Lai, and W. Yao, "Mining decision rules based on the improved Apriori algorithm," *Journal of Agricultural University of Hebei*, vol. 36, no. 2, pp. 122–124, 2013.

[11] G. Zhu, G. Zhu, and J. Zhang, "Computer simulation of ideological and political teaching under big data of complexity," *Complexity*, vol. 2021, no. 10, 13 pages, 2021.

[12] T. Xie, C. Zhang, Z. Zhang, and K. Yang, "Utilizing active sensor nodes in smart environments for optimal communication coverage," *IEEE Access*, vol. 7, pp. 11338–11348, 2018.

[13] Z. Zhang, C. Zhang, M. Li, and T. Xie, "Target positioning based on particle centroid drift in large-scale WSNs," *IEEE Access*, vol. 8, pp. 127709–127719, 2020.

[14] J. Pohjankukka, T. Pahikkala, P. Nevalainen, and J. Heikkonen, "Estimating the prediction performance of spatial models via spatial k-fold cross validation," *International Journal of Geographical Information Science*, vol. 31, no. 10, pp. 2001–2019, 2017.

[15] S. Zhong, Z. Yan, Y. Li, J. Luo, and H. Zhang, "Numerical study on plane and radial wall jets to validate the 2D assumption for an idealized downburst outflow," *Advances in Civil Engineering*, vol. 2021, Article ID 9993981, 17 pages, 2021.

[16] W. Jiang, "Problems and countermeasures of ideological and political management of college students based on network information," *Journal of Physics Conference Series*, vol. 1744, no. 4, article 042005, 2021.

[17] J. X. Chen, "Application of data mining technology based on Apriori algorithm," *Applied Mechanics and Materials*, vol. 543-547, pp. 2036–2039, 2014.

[18] S. Z. Sousa, "Avaliação da Educação Infantil: questões controversas e suas implicações educacionais e sociais/Evaluation of early childhood education: Controversial issues and their educational and social implications," *Revista de Educação PUC-Campinas*, vol. 23, no. 1, pp. 65–78, 2018.

[19] P. J. Wang and Y. L. Zhao, "Research on data mining based on Apriori algorithm," *Advanced Materials Research*, vol. 532-533, pp. 1675–1679, 2012.

[20] Q. Li, Y. Zhang, H. Kang, Y. Xin, and C. Shi, "Mining association rules between stroke risk factors based on the Apriori algorithm," *Technology and health care : official journal of the European Society for Engineering and Medicine.*, vol. 25, Supplement 1, pp. 197–205, 2017.

[21] C. Zhang, T. Xie, K. Yang et al., "Positioning optimisation based on particle quality prediction in wireless sensor networks," *IET Networks*, vol. 8, no. 2, pp. 107–113, 2019.

[22] J. Giersch and C. Dong, "Required civics courses, civics exams, and voter turnout," *The Social Science Journal*, vol. 55, no. 2, pp. 160–170, 2018.

[23] A. Cohen, "Teaching to discuss controversial public issues in fragile times: approaches of Israeli civics teacher educators," *Teaching and Teacher Education*, vol. 89, article 103013, 2020.

[24] C. H. Cao, Y. N. Tang, D. Y. Huang, W. M. Gan, and C. Zhang, "IIBE: an improved identity-based encryption algorithm for WSN security," *Networks*, vol. 2021, article 8527068, 8 pages, 2021.

[25] A. Cohen, "Teaching to teach civics in fragile times: a conceptual framework," *European Journal of Teacher Education*, vol. 44, no. 2, pp. 249–270, 2021.

[26] B. Graham and R. Weingarten, "The power of active citizenship: a renewed focus on teaching civics education," *American Educator*, vol. 42, no. 2, p. 4, 2018.